SMSI 2025

Proceedings

Proof reading version

Authors can report corrections to
contact@smsi-conference.com

A1: Atmospheric Measurement

Chair: Andreas Fischer, Universität Bremen, Bremen (Germany)

A1.1 **Development of an Optical Real-Time Measurement System for Air Change Rates in Indoor Environments** **24**
R. Grüttner, C. Friebe, Institut für Luft- und Kältetechnik gemeinnützige Gesellschaft mbH, Dresden (Germany)

A1.2 **Wireless Network Architecture for Comprehensive Indoor Environmental Quality Monitoring in Public Schools** **26**
F. Sievers, N. Langer, S. Palzer, TU Dortmund University, Dortmund (Germany)

A1.3 **Validation of a Sensor Node Prototype for Multimodal Climate Measurement Network** **28**
M. Bankwitz, S. Hirsch, Brandenburg University of Applied Sciences, Brandenburg/Havel (Germany), C. Engel, TEPROSA GmbH, Magdeburg (Germany)

A1.4 **Optimizing OF-CEAS for the Detection of stable methane isotopes in the atmosphere** **31**
C. Dinc, P. Nitzsche, J. Goldschmidt, University of Freiburg, Freiburg (Germany), K. Schmitt, J. Wöllenstein, Fraunhofer IPM, Freiburg (Germany)

A2: Magnetic and inductive Measurement

Chair: Michael Heizmann, Karlsruher Institut für Technologie KIT, Karlsruhe (Germany)

A2.1 **Digital Signal Processing for Eddy Current Parameter Identification in Measurement Applications** **33**

A2.2 **Wireless Eddy Current Telemetry System for Measuring Axial Piston Ring Movement in a Combustion Engine** **35**
A. Higgs, B. Rossegger, M. Engelmayer, LEC GmbH, Graz (Austria), N. Wermuth, Graz University of Technology, Graz (Austria)

A2.3 **Three-axis Joystick as Stray Field Robust Magnetic Position System** **38**
M. Ortner, P. Malagò, F. Slanovc, Silicon Austria Labs, Villach (Austria), S. Leisenheimer, Infineon Technologies AG, Neubiberg (Germany)

A2.4 **Airgap-Dependent “Pole Eating” Effect in Magnetic Scales** **40**
F. Slanovc, D. Markó, M. Ortner, Silicon Austria Labs, Villach (Austria)

A3: Bio Medical Aplications

Chair: Dinko Oletic, University of Zagreb, Zagreb (Croatia)

A3.1 **Development of a Biosensor Platform Measuring the Electrical Resistance in a Tailor-Made System for Biological Barriers to Assess the Barrier Integrity** **42**
V. Vogel, D. Brück, R.-K. Zäh, B. Faupel, University of Applied Sciences, Saarbrücken (Germany), S. Schnur, S.-M. Klär, M. Schneider, M. Hittinger, Saarland University, Saarbrücken (Germany)

A3.2 **Application of NeRF and RGB-D Camera for the Generation of Digital Twins of Biological Soft Tissues** **44**
M. C. Mezei, F. Auletta, C. M. Oddo, Sant’Anna School of Advanced Studies, Pisa (Italy), A. Gavazza, G. Rossi, University of Camerino, Matelica (Italy)

A3.3 **Towards Smart Face Masks by a Reusable,Wireless Sensor Patch and Tailored Data Analysis** **46**
S. Schäfer, S. Schmitt, J. Magomajew, Fraunhofer IMM, Mainz (Germany), M. Tagliani, H. Theuer, E. Dahrmann, IMSTec GmbH, Klein-Winternheim (Germany)

A3.4 **Platform for the Development of Robust Magnetomotive Ultrasound Imaging Algorithms** **48**
C. Heim, S. J. Rupitsch, Albert Ludwig University of Freiburg, Freiburg (Germany), C. Huber, H. Ermert, S. Lyer, Universitätsklinikum Erlangen, Erlangen (Germany), I. Ullmann, Friedrich-Alexander-Universität Erlangen-Nürnberg, Erlangen (Germany)

A4: Revised SI

Chair: Joao Alves Sousa, Instituto Portugues da Qualidade, Caparica (Portugal)

A4.1 **New opportunities in Revised SI: Traceable measurement quantities and improved uncertainties in small mass/force metrology** **50**
S. Vasilyan,V. Shmagun,N. Rogge,T. Kissinger,T. Fröhlich,Technische Universität Ilmenau,Ilmenau (Germany)

A4.2 **Novel Sensor Principle for High-Precision SI-Traceable Force Measurements** **51**
M. Wittke, M. A. Torres Melgarejo, M. Wolf,R. Theska, T. Fröhlich, Technische Universität Ilmenau, Ilmenau (Germany)

A4.3 **Effect of Helium Contamination on Rubidium Clocks - A Possible Error Source for Absolute Gravimeters and Kibble Balances** **53**
C. Rothleitner, J. Konrad, Physikalisch-Technische Bundesanstalt, Braunschweig (Germany)

A5: Acoustic Sensing

Chair: Eric Starke, SICK Engineering GmbH, Ottendorf-Okrilla (Germany)

A5.1 **Low-Cost Acoustic Measurments by Calibration of Consumer Grade Hardware** **55**
F. Huber, F. Toth, TU Wien, Vienna (Austria)

A5.2 **Electro-acoustic Properties of Li(Nb,Ta)O3 Solid Solutions in Harsh Environments** **57**
H. Fritze, F. El Azzouzi, U. Yakhnevych, Y. Suhak, Technische Universität Clausthal - IEPT, Goslar (Germany), H. Schmidt,Technische Universität Clausthal - IMET, Clausthal-Zellerfeld (Germany), S. Ganschow, Leibniz-Institut für Kristallzüchtung, Berlin (G

A5.3 **A Compact, Cost Efficient, Modular, Intelligent Ultrasound Sensor Platform** **59**
W. Bost, C. Grandinetti, H. Hewener, S. Tretbar, Fraunhofer IBMT, Sulzbach (Germany)

A5.4 **Ultrasonic phased array interface using programmable I/O and microprocessor clock synchronisation** **61**
T. Nellius, K. Henne, M. Hartinger, L. Meihost, T. Hetkämper, H. Zeipert, L. Claes, B. Henning, Measurement Engineering Group, Paderborn University, Paderborn (Germany)

A6: Flexible Sensors

Chair: Veda Sandeep Nagaraja, Tyndall National Institute, Cork, T12R5CP (Ireland)

A6.1 **Sustainable sensors research on food, environment; Research on healthcare and wearables by Tyndall National Institute: Offerings on INFRACHIP** **63**
A. O'Riordan, B. O'Flynn, D. Iacopino, S. Konigulu, V. S. Nagaraja, Tyndall National Institute, Cork (Ireland)

A6.2 **Flexible, Printed Sensors research in Joanneum Reasearch and access through INFRACHIP** **65**
O. Werzer, G. Scheipl, B. Stadlober, Joanneum Research Forschungsgesellschaft mbH, Weiz (Austria)

A6.3 **AMO research in graphene and 2D material devices for sensing applications and their access through INFRACHIP** **67**
G. Rinke, S. Suckow, H. Kleinjans, Z. Wang, M. C. Lemme, AMO GmbH, Aachen (Germany)

A6.4 **Flexible Magnetoresistive Sensors for Novel Applications** **69**
A. Nicolicea, M. Pelkner, M. Melzer, Bundesanstalt für Materialforschung und -prüfung, Berlin (Germany), E. S. Oliveros-Mata, Y. Zabila, D. Makarov, Helmholtz-Zentrum Dresden-Rossendorf e.V., Dresden (Germany)

A7: Metrology in the digital age

Chair: Joao Alves Sousa, Instituto Portugues da Qualidade, Caparica (Portugal)

A7.2 **Determining Data Centre PUE with a Digital Twin** **71**
A. Kammeyer, F. Burger, D. Lubbert, Physikalisch-Technische Bundesanstalt, Berlin (Germany), K. Wolter, Freie Universität Berlin, Berlin (Germany)

B1: Multimodal IoT Devices

Chair: Andreas Schütze, Universität des Saarlandes, Saarbrücken (Germany)

B1.1 **Overview: Multimodal Smart Sensor Networks for Plant Monitoring and Improved Energy Efficiency** **73**
D. Arendes, C. Fuchs, C. Bur, A. Schütze, Saarland University, Saarbrücken (Germany), J. Kelleter, GTE Industrieelektronik GmbH, Viersen (Germany), T. Baur, 3S Technologies GmbH, Saarbrücken (Germany), W. Simmendinger, Sciosense Germany GmbH, Reutlingen (Germany)

B1.2 **Gas Source State Estimation with Reynolds-Averaged Dispersion Model and Time-Averaged Measurements** **75**
A. Raffeiner, R. Pohle, Siemens AG, Munich (Germany), J. Chen, A. J. Lilienthal, Technical University of Munich (Germany)

B1.3 **Performance Assessment of Methane and Carbon Dioxide Sensors for Drone-Based Environmental Gas Monitoring** **77**
M. Stanisavljevic, J. Zirzow, P. P. Neumann, Bundesanstalt für Materialforschung und -prüfung, Berlin (Germany), S. Essel, Infraserv GmbH & Co. Höchst KG, Frankfurt am Main (Germany), N. Karbach, T. Hoffmann, Johannes Gutenberg University Mainz, Mainz (Germany)

B1.4 **Mobile Test Bed for Development and Validation of Networked Multimodal Gas Leakage Detection** **79**
C. Fuchs, A. Almohemied, D. Arendes, A.Schütze, Saarland University, Saarbrücken (Germany)

B2: MEMS Resonators

Chair: Stefan J. Rupitsch, Albert-Ludwigs-Universität Freiburg, Freiburg (Germany)

B2.1 **Structural Investigations of Pore Nucleation after Electrochemical Porosification of 4H-SiC for MEMS** **81**
G. Pfusterschmied, C. Zellner, D. Schock, U. Schmid, TU Wien, Vienna (Austria)

B2.2 **Avoided mode-crossing in MEMS resonators under different dissipation mechanisms** **83**
A. Loch Gesing, E. Gietl, M. Stixenberger, D. Platz, U. Schmid, TU Wien, Vienna (Austria)

B2.3 **Simultaneous Analysis of Local Device Layer Thickness and Film Stress on Cantilevered MEMS Structures** **85**
D. Huber, C. Schallert, G. Pfusterschmied, U. Schmid, TU Wien, Vienna (Austria)

B2.4 **Nanoelectromechanical System Fourier Transform Infrared Spectroscopy (NEMS-FTIR) for Nanoplastic Analysis** **87**
J. Timarac-Popovic, A. Giesriegl, H. Besic, S. Schmid, TU Wien, Vienna (Austria), J. Hiesberger, N. Luhmann,J. P. Lafleur, Invisible-Light Labs GmbH, Vienna (Austria)

B3: Pressure Sensors and their Applications

Chair: Marc Christopher Wurz, Leibniz Universität Hannover, Garbsen (Germany)

B3.1 **High-Sensitive Chromium Strain Gauges on Steel Surfaces** **89**
R. Ottermann, T. Steppeler, M. C. Wurz, Leibniz University Hannover, Garbsen (Germany)

B3.2 **Analysis of positioning parameters at glazing of pressure measurement cells** **91**
I. Jenei, R. Wagner, M. Nikolic, ETO SENSORIC GmbH, Nürnberg (Germany), A. Grün, CiS Forschungsinstitut für Mikrosensorik GmbH, Erfurt (Germany)

B3.3 **Advanced Glass Packaging with Integrated Stress Relief Structures for MEMS Pressure Sensors** **93**
M. Bertke, S. Schudak, LPKF Laser & Electronics SE, Garbsen (Germany)

B3.4 **Sensors on PEEK - Advantages of Plastic Substrates in Microsystem and MEMS Technology** **95**
S. Bengsch,E. Fischer,S. Bur,Ensinger GmbH,Nufringen (Germany)

B4: Optical Sensor Systems

Chair: Petr Klapetek, Czech Metrology Institute (CMI), Brno (Czech Republic)

B4.1 **Small Optical Measurement System for Stable Detection of Mold Growth** **97**
V. Rathnayake, T. Schweizer, S. van den Driesche, M. J. Vellekoop, University of Bremen (Germany)

B4.2 **Low-Noise Silicon APD with Enhanced Blue-Violet Sensitivity** **99**
L. Long, X. Xu, M. Schaedel, G. Brokmann, T. Ortlepp, CiS Forschungsinstitut für Mikrosensorik GmbH, Erfurt (Germany)

B4.3 **Fiber Optic Current Sensor System for Long-Term Monitoring of Geomagnetically Induced Currents in the Power Grid** **101**
J. Mandl, P. Trampitsch, A. Fröhlich, R. Klambauer, A. Bergmann, University of Technology, Graz (Austria)

B5: Modeling

Chair: Eric Benoit, Université Savoie Mont Blanc, Chambéry (France)

B5.1 **Model-based Reconstruction of Freeform Surfaces with Radial Basis Functions** **103**
F. Fleischmann, D. Hilbig, Hochschule Bremen, Bremen (Germany), T. Binkele, OPTIMARE Systems GmbH, Bremerhaven (Germany), N. Müller, ATLAS ELEKTRONIK GmbH, Bremen (Germany)

B5.2 **OPC UA for IO-Link Wireless in a Cyber Physical Finite Element Sensor Network for Shape Measurement** **105**
H. Beuster, L.-M. Bretthauer, G. Scholl, Helmut Schmidt University, Hamburg (Germany)

B5.3 **OEFPIL: An Alternative Method for Curve Fitting** **107**
A. C. Campbell, R. Slesinger, M. Sira, Czech Metrology Institute, Okruzni (Czech Republic), V. Witkovsky, G. Wimmer, Slovak Academy of Sciences, Bratislava (Slovakia)

B5.4 **Methods of uncertainty evaluation using virtual experiments with the example of the tilted-wave interferometer** **109**
M. Stavridis, M. Marschall, F. Hughes, I. Fortmeier, C. Elster, Physikalisch-Technische Bundesanstalt Braunschweig and Berlin (Germany)

B6: Event Based Vision

Chair: Daniel Platz, Technische Universität Wien, Wien (Austria)

B6.1 **Fast Tracking using Event-based Vision Sensors and Binary Frames** **111**
J. Baßler, M. Heizmann, Karlsruhe Institute of Technology, Karlsruhe (Germany)

B6.2 **Performance Comparison of Area-scan and Event-based Image Sensors** **113**
A. Manakov, B. Jähne, Heidelberg University, Heidelberg (Germany)

B6.3 **Motion Compensation of Event-Streams for Multitarget Tracking in Sensor-Based Sorting** **115**
P. Bäcker, G. Maier, Fraunhofer IOSB, Karlsruhe (Germany)

B6.4 **Ev2Gray: Generating Intensity Images from Event Streams** **117**
J. Basler, M. Heizmann, Karlsruhe Institute of Technology, Karlsruhe (Germany)

B7: Bio Sensing

Chair: Georg Pfusterschmied, Technische Universität Wien, Wien (Austria)

B7.1 **Enhanced Signal Detection for Chlorophyll a Fluorescence Signal** **119**
S. Baghbani, A. Sarlak, S. J. Rupitsch, Albert Ludwig University of Freiburg, Freiburg(Germany)

B7.2 **A second generation dispatchable fibre-optic biosensor reader for monitoring sediment toxicity (Sundanse)** **121**
R. S. Marks, A. A. Paul, G. Carmeli, Ben Gurion University of the Negev, Be'er-Sheva (Israel)

B7.3 **Field Enabled Bioluminescent Fiber-Optic Whole-Cell Bioreporter Biosensors for Toxicity Monitoring of Water and Sediments (Sundanse) 123**
R. S. Marks,vA. A. Paul, G. Carmeli, Ben Gurion University of the Negev, Be'er-Sheva (Israel), O. Menashe, Kinneret College on the Sea of Galilee, D.N. Emek Ha'Yarden (Israel)

C1: Flow Sensing

Chair: Jens Zosel, Kurt-Schwabe-Institut für Mess- und, Waldheim (Germany)

C1.1 **Comparison of Polyimide to Silicon Nitride Membranes for Robust Thermal Flow Sensors 125**
T. Trautmann, A. Schander, M. Vellekoop, University of Bremen, Bremen (Germany)

C1.2 **Multichannel electrical conductivity sensor for gas-liquid flow imaging 127**
M. Bliem, S. Puttinger, M. Da Silva, Johannes Kepler University Linz, Linz (Austria)

C1.3 **Measurability of changes of the laminar-turbulent transition on wind turbines by means of thermographic flow visualization and a co-rotating measurement platform 129**
J. Dieckmann, A. von Freyberg, A. Fischer, University of Bremen, Bremen (Germany), N. Balaresque, Deutsche WindGuard Engineering GmbH, Bremerhaven (Germany)

C1.4 **Advances in Magnetic Flow Metering: A Clamp-on Device 131**
L. Schmieder, P. Koss, Fraunhofer IPM, Freiburg im Breisgau (Germany)

C2: Sensor-Intelligence - Devices and Applications

Chair: Thomas Velten, Fraunhofer-Institut - IBMT -, Sulzbach (Germany)

C2.1 **Sensor-Intelligence Devices for optimized condition and process monitoring 134**
K. Becker, D. Koster, H.-G. Herrmann, Fraunhofer IZFP, Saarbrücken (Germany)

C2.2 **Bioreactor Intelligence for Real-Time Monitoring and Automation of Stem Cell Cultivation 137**
D. Amelin, T. Knoll, M. Jochem, S. Altmaier, F. Musiol, F. R. Ihmig, M. M. Gepp, R. Ruff, Fraunhofer IBMT Sulzbach (Germany)

C2.3 **Real-time, Parallelized and Non-contact Read-Out of 3D Cardiac Tissue Models 139**
R. Le Harzic, F. Stracke, D. Amelin, R. Ruff, F. Musiol, H. Zimmermann, Fraunhofer IBMT Sulzbach (Germany), R. Kettenhofen, D. Bauer, S. Herrmann, J. Neubauer, Fraunhofer Project Center for Stem Cell Process Engineering, Würzburg (Germany)

C2.4 **Implementation of Sensor-Intelligence Devices (SIDs) for Condition Monitoring Applications in the Sense of Smart Predictive Maintenance 141**
S. Klein, P. Stopp, D. Koster, Fraunhofer IZFP, Saarbrücken (Germany)

C3: Gas Sensing I

Chair: Stefan Zimmermann, Leibniz Universität Hannover, Hannover (Germany)

C3.1 **3D Density Field Reconstruction of Vehicles Exhaust Plumes using Background Oriented Schlieren Tomography based on Windowed Fourier Transform and Graphical Phase Analysis 143**
H. H. Imtiaz, P. Schaffer, T. Forstinger, M. Kupper, A. Bergmann, Graz University of Technology, Graz (Austria)

C3.2 **Fast Gas Chromatography Setup for Online Contaminant Monitoring in Plastics Recycling 145**
W. Reimringer, O. Brieger, T. Sauerwald, Saarland University, Saarbrücken (Germany)

C3.3 **Chromatographic VOC Sensing using Molecularly Cross-Linked Metal Nanoparticle Networks 147**
L. Mielke, H. Schlicke, Leibniz Institute of Polymer Research Dresden, Dresden (Germany), S. C. Bittinger, J. N. Beyer, T. Vossmeyer, University of Hamburg, Hamburg (Germany)

C3.4 **Towards Low-Cost Portable GC Systems for VOC Analysis 148**
O. T. Penagos Carrascal, G. Zeh, T. Sauerwald, Fraunhofer IVV, Freising (Germany)

C4: Robotics

Chair: André Schäfer, Hottinger Brüel & Kjaer GmbH, Darmstadt (Germany)

C4.1 **Additive Manufactured Capacitive Sensor for Slip Detection with Seamless Integration of Object Recognition and Differentiation in Robot Grippers** **151**
N. Hangst, S. Schröder, T. M. Wendt, Offenburg Universtiy of Applied Sciences, Offenburg (Germany), S. J. Rupitsch, University of Freiburg, Freiburg (Germany)

C4.2 **Novel Characterisation and Modeling of the Thermal Behavior of Multi-Wire SMA Actuators for Robot Grippers** **153**
A. Dierle, T. M. Wendt, T. Seifert, A. Schnebel, Offenburg University of Applied Sciences, Offenburg (Germany)

C4.3 **Optimized Grasp Planning for Bin-Picking Robots with 2D and 3D Sensor Data** **155**
R. Haas, N. Hangst, T. M. Wendt, Offenburg University of Applied Sciences, Offenburg (Germany)

C5: Gas Sensing II

Chair: Jens Zosel, Kurt-Schwabe-Institut für Mess- und, Waldheim (Germany)

C5.1 **Programable Printing Technology Based on Spark Ablation for the Develoment of Gas Sensors** **157**
L. N. Sacco, Nigel Rising, N. Schouten, VSParticle, Delft (The Netherlands), L. Egger, M. Popov, A. Köck, Materials Center Leoben Forschung GmbH, Leoben (Austria), C. Dösinger, L. Romaner, Montanuniversität Leoben, Leoben (Austria)

C5.2 **Continuous Estimation of Particle Emissions in Flue Gas of Wood Combustion using Gas Sensor Measurements** **159**
G. Hagen, R. Moos, University of Bayreuth, Bayreuth (Germany)

C5.3 **Optomechanical Gas Pressure Sensing over Broad Pressure and Temperature Ranges** **161**
C. Reinhardt, S. Croatto, L. Stankewitz, M. Kunze, J. Schaffran, A. Lindner, Deutsches Elektronen-Synchrotron DESY, Hamburg (Germany), H. Masalehdan, A. Franke, N. Sültmann, R. Schnabel, University of Hamburg, Hamburg (Germany)

C5.4 **A Calibration-free Mid-Infrared TDLAS Sensor for Stand-Off Detection of Carbon Dioxide operating at 2004 nm** **163**
P. Schaffer, H. H. Imtiaz, B. Lang, M. Kupper, A. Bergmann, University of Technology, Graz (Austria)

C6: Hydrogen Sensor Technology

Chair: Matthias Bartholmai, BAM Bundesanstalt für Materialforschung, Berlin (Germany)

C6.1 **Toward a Digital Twin of Hydrogen Pressure Vessels Enabled by Distributed Fiber Optic Sensors** **165**
C. Karapanagiotis, M. Schukar, M. Breithaupt, K. Hicke, Bundesanstalt für Materialforschung und-prüfung, Berlin (Germany)

C6.2 **Hydrogen Safety - Dealing with Closed Spaces** **167**
K. Nattuveettil, C. Liebner, C. Tiebe, Bundesanstalt für Materialforschung und -prüfung, Berlin (Germany)

C6.3 **Analysis of Methods for Predicting H2 Sensor Responses** **169**
R. Sarif, C. Tiebe, Bundesanstalt für Materialforschung und-prüfung, Berlin (Germany), C. Herglotz, Brandenburgische Technische Universität Cottbus-Senftenberg, Cottbus (Germany)

C6.4 **Digital Certificates: Enabling Automation in Quality Assurance and Metrological Traceability** **171**
M. Melzer, N. Brunner, Bundesanstalt für Materialforschung und -prüfung (BAM), Berlin (Germany)

C7: Gas Sensing III

Chair: Ulrich Kaiser, DHBW Lörrach, Lörrach (Germany)

C7.1 **Simulation and determination of the coupling efficiency to photoacoustic resonators** **173**
D. Sieg, V. Kuczius, G. Rodriguez Gutierrez, J. Gaworski, S. Palzer, TU Dortmund University, Dortmund (Germany)

C7.2 **Design of a Refrigerant Leak Sensor based on the Photoacoustic Dual Chamber Detection Method** **175**
H. Yassine, C. Weber, N. Brugger, K. Schmitt, J. Wöllenstein, University of Freiburg, Freiburg (Germany), M. El-Safoury, Fraunhofer IPM,Freiburg (Germany)

C7.3 **Optimizing Analog Front End Architectures for Enhanced SNR in Photoacoustic Imaging** **177**
S. Kindorf, C. Weber, B. Bierer, J. Wöllenstein, Fraunhofer IPM, Freiburg (Germany)

D1: IR Sensing

Chair: Ulrich Schmid, Technische Universität Wien, Wien (Austria)

D1.1 **eNDIRi² evaluation kit – evaluation system for IR components** **179**
J. Knossalla, A. Isserstedt-Trinke, A. Sachse, S. Biermann, Micro-Hybrid Electronics GmbH, Hermsdorf (Germany)

D1.2 **Investigation of the suitability of MEMS-FPI-based NIR spectral detectors for the analysis of cooling lubricants** **181**
J. Otto, K. L. Krieger, University of Bremen, Bremen (Germany)

D1.3 **A gonioreflectometer for the measurement of bidirectional reflectance distribution functions in the thermal infrared** **183**
H. Noori, K. Ma, R. Schmoll, A. Kroll, University of Kassel, Kassel (Germany)

D1.4 **Development of a Computationally Efficient Person Detection Procedure for Low-Resolution Infrared Sensor Arrays** **185**
A. Rehmer, Heimann Sensor GmbH, Dresden (Germany)

D2: Sensors for Agrifood Quality

Chair: Camilla Baratto, National Research Council (CNR-INO), Brescia (Italy)

D2.1 **Innovative Sensor Technologies for Agrifood Quality Assessment** **188**
F. Venturini, ZHAW Zurich University of Applied Sciences, Winterthur (Switzerland)

D2.2 **Quality assessment of raw fresh milk from several sources by no-destructive Raman sensor** **190**
I. Petrignani, S. Almaviva, A. Lai, ENEA, Italian National Agency for New Technologies, Energy and Sustainable Economic Development, Frascati (Italy)

D2.3 **Investigating biotic and abiotic stresses on green-leaf plants by means of hand-held Raman spectroscopy** **192**
L. Pandolfi, G. Faglia, C. Baratto, CNR-INO,University of Brescia,Brescia (Italy), N. Miotti, M. Turina, M. Ciuffo, E. Gobbi, CNR-IPSP,Turin (Italy), T. Tonto, V. Locato, L. de Gara, Università Campus Bio-Medico di Roma, Rome (Italy)

D2.4 **Portable Raman Spectroscopy Based Prototype for the Clostridia Detection in Milk** **194**
D. Barbiero, F. Melison, L. Cocola, M. Fedel, L. Poletto, National Research Council, Padua (Italy), C. Andrighetto, P. De Dea, Veneto Agricoltura, Thiene (Italy)

D3: IR and Temperature Measurement

Chair: Bernd Henning, Universität Paderborn, Paderborn (Germany)

D3.1 **Rapid measurement of the Size-of-Source Effect by using an Iris aperture** **196**
M. Mendez, R. Schmoll, A. Kroll, University of Kassel, Kassel (Germany)

D3.2 **Fast MEMS-IR-Emitters for NDIR Sensors** **198**
T. Schildhauer, A. T. Winzer, J. Baldauf, T. Ortlepp, CiS Forschungsinstitut für Mikrosensorik GmbH, Erfurt (Germany)

D3.3 **Accelerated Life Tests for Determining the Expected Lifetime – Test Strategy for IR-MEMS-Emitter** **200**
L. Bindel, F. Huwald, L. S. Oechler, A. Isserstedt-Trinke, S. Biermann, Micro Hybrid Electronic GmbH, Hermsdorf (Germany)

D3.4 **Power control and app connection via Bluetooth for NDIR-Sensor-applications** **202**
M. Ueberschär, M. Jung, F. Liebold, Cooperative University Gera-Eisenach, Gera (Germany)

D4: Temperature Sensing

Chair: Michael Schneider, Technische Universität Wien, Wien (Austria)

D4.1 **Thin-film sensors on thrust bearing washers for temperature measurement directly in the mechanical rolling contact** **205**
T. Steppeler, R. Ottermann, F. Dencker, M. C. Wurz, D. Konopka, F. Pape, G. Poll, M. Marian, Leibniz University Hannover, Garbsen (Germany)

D4.2 **Characterization of the Thermal Conductivity of Silica Aerogels** **207**
T. M. de Rijk, T. Wendland, M. J. Vellekoop, University of Bremen, Bremen (Germany)

D4.3 **Enhancing Dynamic Measurement Methods: From Concepts to Calibration Standards** **209**
B. Tallawi, J. O. Favreau, K. Romieu, LNE-CETIAT, Villeurbanne (France)

D5: Piezoelectric MEMS I

Chair: Michael Schneider, Technische Universität Wien, Wien (Austria)

D5.1 **Noncontacting Determination of the Piezoelectric Coefficient d33 of Lithium Tantalate up to 400 °C** **212**
H. Wulfmeier, N. Warnecke, D. Kohlmann, H. Fritze, Clausthal University of Technology, Goslar (Germany)

D5.2 **Evaluation of piezoelectric micromachined ultrasonic transducers (PMUT) for the broadband detection of ultrasonic elastic waves** **214**
H. Zeipert, L. Claes, B. Henning, Paderborn University, Paderborn (Germany), C. Stoeckel, S. Mulay, Fraunhofer ENAS, Chemnitz (Germany)

D5.3 **Experimental comparison of receive sensitivity of circular and ring piezo-electrodes geometries for PMUT resonator membranes designed in PiezoMUMPS process** **216**
N. Plantak, M. Katalenic, D. Oletic, University of Zagreb, Zagreb (Croatia)

D5.4 **Impact of Damping Effects on Piezoelectric Actuation Used in Acoustofluidic Cell Trapping** **218**
B. Leikam, S. Pandey, O. Hayden, G. Schrag, Technical University of Munich, Munich (Germany)

D6: Piezoelectric MEMS II

Chair: Stefan J. Rupitsch, Albert-Ludwigs-Universität Freiburg, Freiburg (Germany)

D6.1 **High Throughput Magnetron Sputtering of Tilted c-Axis AlN Films for Biosensing Applications** **220**
P. Bergmann, E. Loos, M. Nestler, scia Systems GmbH, Chemnitz (Germany)

D6.2 **Noise in Piezoelectric MEMS: Modeling and Experimental Characterization** **222**
S. Zarepakzad, P. Egger, N. R. Haghighi, S. Muringakodan, M. Mortada, P. T. Das, U. Schmid, M. Schneider, TU Wien, Vienna (Austria), K. C. Schwab, Kavli Nanoscience Institute and Thomas J. Watson, Sr., Laboratory of Applied Physics, California (USA)

D6.3 **DC Voltage Induced Parametric Potential Energy Modulation in Bistable Piezoelectric MEMS Membranes** **224**
S. Muringakodan, U. Schmid M. Schneider, TU Wien, Vienna (Austria)

D6.4 **Characterization of AlN-Based MEMS Kineto-Electric Transducer for Cultural Heritage Conservation** **226**
C. Trigona, S. Ahmed, A. M. Gueli, S. Baglio, University of Catania, Catania (Italy), M. Liuzzo, F. L. Iacono, G. Navarra, University of Enna “Kore”, Enna (Italy)

D7: Radar Sensors

Chair: Michael Heizmann, Karlsruher Institut für Technologie KIT, Karlsruhe (Germany)

D7.1 **Recognising Wild Animals on Roads: Radar-based Sensor Systems for Accident Avoidance** **228**
M. Schneider, H. Mantz, T. Walter, Ulm University of Applied Sciences, Ulm (Germany), M. Montoya-Capote, J. Berger, A. Reichel, N. Hollmach, tecVenture, Leipzig (Germany)

D7.2 **Portable Radar-Based Measurement System for Vibration Analysis of Large Infrastructures** **230**
V. C. Ramankutty, R. Martin, C. Sohrmann, Fraunhofer IIS, Dresden (Germany)

D7.3 **Millimeter-Wave Spectroscopy for Evaluating Blood Coagulation and Clotting** **231**
T. Liebchen, G. Ulisse, V. Krozer, Goethe Universität Frankfurt am Main, Frankfurt am Main (Germany)

P01 **Identification of Foraging Bumblebees by Pulse Compression of their Unique Doppler Radar Signature** **233**
H. Aumann, M. Aumann, Maine Biosensors LLC, Dover-Foxcroft, Maine (USA), F. Drummond, University of Maine, Orono,Maine (USA)

P02 **APPLICATION OF ENVIRONMENTAL MEASUREMENT IN PORTS USING CLEVER SENSE** **235**
J. Garcia Fernández, Geomodel LDA / University of Lisbon, Lisbon (Portugal)

P03 **NFC Based Current Sensor for Medium-Voltage Lines** **237**
M. Lenzhofer, D. Holzmann, Silicon Austria Labs GmbH, Villach (Austria), D. Sturm, KNG-Kärnten Netz GmbH, Klagenfurt (Austria)

P04 **UHF RFID Based Strain Sensor for Hydropower Generators** **239**
M. Lenzhofer, A. Horn, Silicon Austria Labs GmbH, Villach (Austria), S. Culetto, KELAG-Kärntner Elektrizitäts-Aktiengesellschaft, Flattach (Austria)

P05 **Self-built low-cost pyrolyzer using Curie-Point temperature coupled to a gas chromatograph-ion mobility spectrometer** **241**
D. Röckrath, M. Hitzemann, M. Lippmann, C. Thoben, A. Eckhardt, S. Zimmermann, Leibniz University Hannover, Hannover (Germany)

P06 **Comparison of Point-to-Point LPWA Smart Sensors with Low-Power Local Mesh Networking Solutions for Industrial Refrigeration and Operational Parameter Detection** **243**
Z. Kiss, Endrich Bauelemente Vertriebs GmbH, Nagold (Germany)

P07 **A Concept for Form-Adaptive and Force-Controlled Gripping with Magnetorheological Material** **245**
J. J. Blöchle, T. M. Wendt, T. Seifert, Hochschule Offenburg, Offenburg (Germany)

P08 **The SI 2019 approach to redefine units does not apply to the mole** **247**
R. Kacker, K. Irikura, National Institute of Standards and Technology, Gaithersburg (USA)

P09 **Piezoelectric pressure mapping sensors using the poling effect induced by surface chemical modification** **249**
D. Tadaki, S. Matsumoto, S. Yamamiya, A. Hirano-Iwata, M. Niwano, Tohoku University, Sendai (Japan), T. Ma,Beijing Institute of Technology, Beijing (China), Y. Imai, National Institute of Technology, Sendai College, Sendai (Japan)

P10 **Morphology Evolution of Snow-flakes Pattern and its Effect on Nano-/Micro-particles Embedded PbSe Photoconduc-tive Thin Film Characteristics** **251**
R. S. Kim, S. Guduru, Y. Zhang, Laser Components Detector Group, Chandler (USA), K. H. Lee, J. H. Park, USMX Technologies LLC, Las Vegas (USA), S. J. Kim, University of Louisville, Louisville (USA)

P11 **Split-Ring Resonator as Transducer for Metal-Organic Framework Based Sensors** **253**
C. Thoben, M. Hitzemann, L. A. Ruff, C. Reinbacher, S. Zimmermann, T. Hennig, E. Rohloff, A. M. Schneider, A. Schaate, Leibniz University Hannover,Hannover (Germany)

P12 **Multi-sensor pothole detection and monitoring system** **255**
I. Romero, H. Mantz, T. Walter, M. Schneider, Ulm University of Applied Sciences, Ulm (Germany)

P13 **Why a DCC Makes Life Easier with Multi-Component Sensors for Forces and Moments** **257**
D. Schwind, GTM Testing and Metrology GmbH, Bickenbach (Germany)

P14 **Automatic Multisensory Measurement of the Borehole Length during Drilling of Inhomogeneous Materials** **259**
A. Boaron, D. Stöbener, A. Fischer, University of Bremen, Bremen (Germany)

P15 **Shape Measurement of Large Scale Components Employing Wireless Sensor Networks** **261**
L.-M. Bretthauer, G. Scholl, R. Heynicke, Helmut Schmidt University,Hamburg (Germany)

P16 **Optical signal transmission solutions for electromobility and renewable energies in favor of a low carbon future** **263**
A. Schäfer, Hottinger Brüel and Kjaer GmbH (HBK), Darmstadt (Germany)

P17 **Influence of Length on the Electromigration of Aluminum through Molybdenum disilicide Thin films** **265**
J. Baldauf, A. T. Winzer, T. Ortlepp, CiS Forschungsinstitut für Mikrosensorik GmbH, Erfurt (Germany)

P18 **Changes in Amorphous Molybdenum Disilicide Thin Films Caused by Electrical Current Stressing** **267**
J. Baldauf, S. Reiß, A. T. Winzer, T. Ortlepp, CiS Forschungsinstitut für Mikrosensorik GmbH, Erfurt (Germany)

P19 **Benchmarking Robot and Cobot Performance for an Assembly Application** **269**
M. Gapp, A. Fischer-Janzen, D. Pfister, T. M. Wendt, University Offenburg, Offenburg (Germany), S. J. Rupitsch, University Freiburg, Institut für Mikrosystemtechnik – IMTEK, Freiburg (Germany)

P20 **Practical Realization of Johnson's Noise Thermometer** **271**
J. Martinek, V. Hortvík, P. Klapetek, Czech Metrology Institute, Brno (Czech Republic)

P21 **Elastically stable tensile force sensors for belt tension monitoring** **273**
T. Frank, A. Cyriax, S. Hermann, A. Grün, CiS Forschungsinstitut für Mikrosensorik, Erfurt (Germany)

P22 **Optimized hardness testing: Precise force application and measurement at low forces** **275**
T. Frank, S. Hermann, A. Grün, H. Wünscher, CiS Forschungsinstitut für Mikrosensorik GmbH, Erfurt (Germany), P. Beisel, KB Prüftechnik GmbH, Hochdorf-Assenheim (Germany)

P23 **Signal evaluation of force sensors based on silicon strain gauges using artificial neural networks** **277**
T. Frank, S. Hermann, CiS Forschungsinstitut für Mikrosensorik GmbH, Erfurt (Germany)

P24 **Add-on kit for non-invasive pressure measurement on process pipes** **279**
T. Frank, A. Cyriax, A. Grün, S. Hermann, M. Kermann, S. Jagomast, A. Grün, CiS Forschungsinstitut für Mikrosensorik GmbH, Erfurt (Germany)

P25 **Membrane Characterization of Transparent Photodiodes** **280**
C. Möller, D. Mitrenga, T. Klein, A. T. Winzer, T. Ortlepp, CiS Forschungsinstitut für Mikrosensorik GmbH, Erfurt (Germany)

P26 **Combined Stationary Fluorescence and Nanosecond Time Resolved Laser Flash Photolysis Setup** **282**
N. Lange, M. Regehly, University of Applied Sciences Wildau, Wildau (Germany)

P27 **Improved Inductive Measurement System for Monitoring Electromagnetic Properties of Steel Sheets During Production** **284**
M. Simoneit, T. Thuilot, A. Hennig, University of Applied Sciences Ruhr West, Mülheim an der Ruhr (Germany), O. Kanoun, Technical University Chemnitz, Chemnitz (Germany)

P28 **Enhancing Predictive Maintenance with Temporal Convolutional Networks** **286**
F. Rieger, R. Schilling, F. Heinrich, F. Wenninger, Fraunhofer EMFT, Munich (Germany)

P29 **Non-radioactive Electron Capture Detection for Process and Quality Control in Brewery Production** **288**
M. Lippmann, M. J. Kueddelsmann, D. Claassen, M. Kaschytza, S. Deicke, E. Bunert, S. Zimmermann, Leibniz University Hannover, Hannover (Germany), M. Wigger, S. Sielemann, Hamm-Lippstadt University of Applied Sciences, Hamm (Germany)

P30 **Identification of plastics in foodstuff using Rapid-FLIM and neural networks** **290**
S. Heitzmann, A. S. Rajan, M. Versen, N. Leiter, University of Applied Sciences Rosenheim, Rosenheim (Germany)

P31 **In-Situ and Operando Measurements for the Characterization of Next-Generation Sensor Materials** **292**
R. Tschammer, C. Morales, K. Henkel, J. I. Flege, BTU Cottbus-Senftenberg, Cottbus (Germany), C. Tiebe, Bundesanstalt für Materialforschung und -prüfung, Berlin (Germany)

P32 **Measurement Systems for In-Situ Monitoring of Fuel Cell Systems Using Fiber Optical Sensors and Colorimetric Fluorescence Technology** **294**
M. Reiter, A. Klug, AVL List GmbH, Graz (Austria), G. Auböck, Silicon Austria Labs GmbH, Graz (Austria), A. Bergmann, C. Sommitsch, M. Bodner, Graz University of Technology, Graz (Austria)

P33 **A MEMS-SPM for dynamic nanomechanical measurements of soft materials** **296**
U. Brand, Z. Li, Physikalisch-Technische Bundesanstalt, Braunschweig (Germany)

P34 **Point Cloud Data Processing in Scanning Probe Microscopy** **298**
P. Klapetek, M. Valtr, Czech Metrology Institute, Brno (Czech Republic), D. Necas, CEITEC Brno University of Technology, Brno (Czech Republic), E. Heaps, A. Yacoot, National Physical Laboratory, Teddington (United Kingdom)

P35 **Calibration of Temperature Probes on Heat Pipes** **300**
J. O. Favreau, E. Georgin, CETIAT, Villeurbanne (France)

P36 **Mass value correction method for weighing cell based on digital plD state-locking control Presentation preference: 303**
P. Sun, J. Wang, C. Peng, National Institute of Metrology, Beijing (China)

P37 **Improved impulse magnetization of magnetic measurement scales 305**
R. Slatter, B. Böhle, U. Rother, ELSOMA GmbH, Schwerte (Germany)

P38 **Fabrication and Characterization of CO2 Sensor Using ZnO<In> Nanograins 307**
M. Aleksanyan, G. Shahkhatuni, Z. Simonyan, G. Shahnazaryan, R. Papovyan, D. Kananov, A. Grigoryan, G. Gevorgyan, G. Stepanyan, A. Sayunts, Yerevan State University, Yerevan (Armenia)

P39 **Development of a universal instrument system for locking intramedullary nails....309**
T. Reuter, A. Grundmann, S. Walther, Institut Chemnitzer Maschinen und Anlagenbau e.V., Chemnitz (Germany)

P40 **Branching Wall-less Vessel System in Tissue-Mimicking Materials for Magnetomotive Ultrasound Imaging 311**
C. Heim, S. J. Rupitsch, University of Freiburg, Freiburg (Germany), C. Huber, H. Ermert, S. Lyer, Universitätsklinikum Erlangen, Erlangen (Germany), I. Ullmann, Friedrich-Alexander-Universität Erlangen-Nürnberg, Erlangen (Germany)

P41 **Innovating THz Detectors: Unmatched Sensitivity at Room Temperature,Infinite Possibilities....313**
A. Rämer, E. Nöske, E. Dischke, V. Krozer, W. Heinrich, Ferdinand-Braun-Institut, Berlin (Germany)

P42 **Neuromorphic Spiking Sensory Conversion System Based on the STDP Learning Rule of Biological Synapses....315**
H. Abd, A. Joshy, A. König, RPTU University Kaiserslautern Landau, Kaiserslautern (Germany)

P43 **Viscosity Analysis of Liquid Food Using Hyperspectral Imaging....317**
A. Ghezal, A. König, RPTU University Kaiserslautern Landau, Kaiserslautern (Germany)

P44 **Supervised Self-Calibration for Fault-Tolerant xMR-Based Angular Decoders under Dynamic Perturbations 319**
E. Gerken, A. König, RPTU University Kaiserslautern Landau, Kaiserslautern (Germany)

P45 **Determination of the phase proportions of austenitic steels using artificial intelligence....321**
T. Schroeter, J. Wichmann, ifw Günter Köhler Institut für Fügetechnik und Werkstoffprüfung GmbH, Jena (Germany), G. Polte, Technische Universität Ilmenau, Ilmenau (Germany), L. Kaufhold, Ernst Abbe-Hochschule Jena, Jena (Germany)

P46 **Soft Sensor Approach to Detect Failures in Circuit Breaker Components....323**
M. Fuhrländer, J. Gebhardt, H. Rahmeh, A. Boyaci, ABB AG, Mannheim (Germany)

P47 **Stop ignoring units outside the SI....325**
J. Valdés, Universidad Nacional de San Martín, San Martín, Buenos Aires (Argentina)

P48 **Application-Oriented In-Situ Testing Methods for Permanent Magnet Characterization 327**
M. Lanz, G. Martinek, T. Kresse, G. Schneider, D. Goll, Aalen University, Aalen (Germany), A. Georgiadis, Leuphana University, Lüneburg (Germany)

P49 **Modeling of High-Sensitivity SAW Magnetic Field Sensors with Au-SiO2 Phononic Crystals....329**
M. Samadi, M. Gerken, Kiel University, Kiel (Germany), J. M. Meyer, F. Lofink, Fraunhofer ISIT, Itzehoe (Germany)

P50 **Effect of Matrix Gas Variations on NO2 Measurements by a PEMS Device for Real Driving Emissions Tests 332**
M. E. Kim, H. Bohlius, V. Ebert, J. Nwaboh Physikalisch-Technische Bundesanstalt, Braunschweig (Germany)

P51 **ThinKIsense – Thin Edge Artificial Intelligence for Process Automation 334**
G. Erdler, S. Klehr,S. von Dosky, M. Mussler, Siemens AG, Karlsruhe (Germany)

P52 **Modelling Membrane-Based Compact Fiber-Interferometric Gas Pressure Sensors in Cryogenic Environments 336**
D. Hartwig,C. Reinhardt,L. Stankewitz,S. Croatto,S. Karstensen,J. Schaffran,A. Lindner,Deutsches Elektronen-Synchrotron DESY,Hamburg (Germany),H. Masalehdan, N. Sültmann,R. Schnabel,Universität Hamburg,Hamburg (Germany)

P53 **Simultaneous DTGS and DTS Measurements for Temperature Estimation in a Bubble Column Reactor 338**
D. F. Gomes,G. Heim Weber,C. Martelli,Federal University of Technology - Paraná UTFPR,Curitiba (Brazil), M. W. Hlawitschka,Y. Schick,M. J. da Silva,Johannes Kepler Universität,Linz (Austria)

DOI 10.5162/SMSI2025/C1.1

Development of an Optical Real-Time Measurement System for Air Change Rates in Indoor Environments

Rebekka Grüttner[1], Christian Friebe[1]
[1] Institut für Luft- und Kältetechnik gemeinnützige Gesellschaft mbH, 01309 Dresden, Germany
rebekka.gruettner@ilkdresden.de

Summary:
This article presents a novel measurement system and method for determining air change rates in real-time using an optical principle. It measures the attenuation of light intensity through fog aerosols in an indoor volume, employing a light source (laser) and a detector to capture transmitted intensity, allowing measurements across distances of 1 to 50 m. Results were validated against conventional methods, such as the SF_6 tracer gas decay method and volumetric air change measurement. Disturbances like temperature variations and external light were successfully mitigated.

Keywords: real-time air change measurement, optical measurement, local air change rate, indoor air quality, energy efficiency

Background

Nowadays, people spend most of their time indoors, making healthy air quality essential for their well-being and performance. The air change rate (ACR), measured in h^{-1}, is a key parameter for assessing air quality, indicating how often indoor air is replaced. By measuring the ACR, the effectiveness of ventilation systems can be evaluated and improved as necessary. However, measured ACR values may, for practical reasons, deviate from the intended design values [1]. ACR measurement is typically performed by analyzing tracer gas concentrations at defined points within a room [2-5]. The commonly used tracer gas, SF_6, has the highest global warming potential. Real-time measurements require relatively high tracer gas concentrations, while lower concentrations require sampling in containers and time-consuming laboratory analysis, leading to delays and potential uncertainties in measurement quality. Various methods are used for ACR measurement, with the constant decay method using SF_6 considered especially accurate according to Weis et al., and thus widely applied [2-6]. Nevertheless, uncertainties for this method range from 10 % to 80 %, depending on the distribution of concentration and the measurement location, while device uncertainty itself ranges from only 1.5 % to 5 %.

A new optical measurement system for measuring ACR has been developed, tested, and validated. It provides real-time air change rates, is climate-friendly, and is significantly more cost-effective, achieving accuracy levels comparable to those of traditional measurement methods.

Measuring Method and Basics

The measuring system is based on the attenuation of light as the beam passes through an aerosol-air mixture. Depending on the aerosol particle concentration (aerosol used DEHS), the continuous-wave laser beam (laser class 2M) is attenuated as it traverses the measuring area, with only a portion of the light directed to the detector (CMOS sensor), see Figure 1.

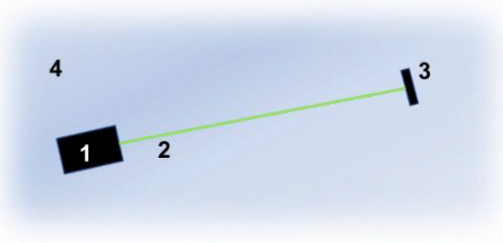

Fig. 1. Function principle: 1 laser, 2 Laser beam through measuring area, 3 Detector, 4 air-aerosol mixture

The measurement is conducted optically by analyzing the recorded brightness curve. The measurement process is shown in Figure 2 and is divided into four distinct phases. Initially, the baseline brightness without aerosol is measured, followed by the introduction and uniform distribution of the aerosol. After a brief settling period, the recording of the decay curve begins. Based on the formula principles for the ACR from concentrations according to the tracer gas decay

method and the Beer-Lambert law, the ACR can be calculated according to eq. (1) using two defined points in time t_1 and t_2 and the corresponding brightness values. The brightness I_1 is lower than I_2 due to the higher aerosol concentration.

I_0 represents the initial brightness, measured without the introduction of aerosol particles. Additionally, the natural decay rate (NDR), which accounts for processes such as particle adhesion and evaporation, must be subtracted. This value is either known or measured in advance under the given ambient conditions. The result represents an average ACR between two timesteps.

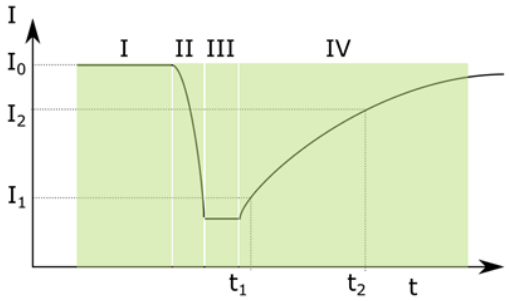

Fig. 2. Measurement phases' light intensity: I: baseline without aerosol concentration; II: aerosol introduction; III: uniform aerosol distribution; IV: aerosol dilution by ventilation

$$ACR = \frac{1}{t_2 - t_1} ln\left(\frac{ln\frac{I_0}{I_1}}{ln\frac{I_0}{I_2}}\right) - NDR \quad (1)$$

The ACR is also obtained from the exponent of the exponential regression fit according to eq. (2) and (3), which takes into account the entire curve.

$$\log\left(\frac{I_0}{I(t)}\right) = I_0 \cdot e^{-N\,t} \quad (2)$$

$$ACR = N - NDR \quad (3)$$

Description and Results

The measurement requires a constant laser intensity. Temperature-related fluctuations are compensated by using a reference beam measurement, while the influence of ambient light is minimized with the help of a bandpass filter and a stray light trap (baffle). Since the sensor records brightness values between 0 and 255, the radiation intensity is adjusted before measurement using a polarisation filter. CFD simulations of room airflow showed that local ACR measurements at a single point can deviate by up to 20% from the room's average ACR. The new measurement system is suitable for areas between 1 and 50 metres, allowing determination of both local ACR for specific areas and average ACR for the entire room. The brightness curve is analysed in real time using software. Validation measurements showed a maximum deviation of

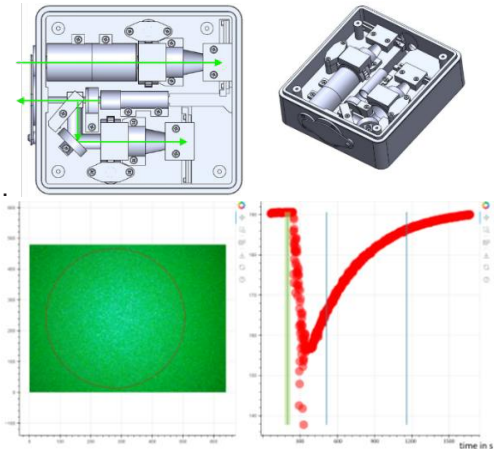

Fig. 3. Set-up of the measuring device (top); measuring software with signal and its progression (bottom)

ACR of 6 % compared to volumetric ACR measurements and a maximum deviation of 6 % compared to SF_6 tracer gas decay measurements. For the first time, the new measurement system enables precise ACR determination in real time without climate-damaging tracer gases. By using comparatively simple and harmless components, a time- and cost-efficient measurement system was developed that, in addition to determining average and local air change rates, can also measure the cleaning efficiency of filter-based devices in relation to aerosols.

This work was granted and supported by the German Federal Ministry for Economic Affairs and Climate Action.

References

[1] K. Noh, M.-D Oh, Variation of clean air delivery rate and effective air cleaning ratio of room air cleaning devices. *Build. Environ.* 84 (2014)

[2] ISO 12569, Thermal performance of buildings and materials - Determination of specific airflow rate in buildings (2017)

[3] ASTM E741-23, Standard Test Method for Determining Air Change in a Single Zone by Means of a Tracer Gas Dilution (2023)

[4] VDI 4300-7, Indoor-air pollution measurement - Measurement of indoor air change rate (2001)

[5] ASHRAE Handbook - Fundamentals, Chapter 4: Ventilation Requirements and Infiltration (2017)

[6] ISO 16000-8: Indoor air - Part 8: Determination of local mean ages of air in buildings for characterizing ventilation conditions (2007)

[7] N. Weis, C.V. Hutter-Sumowski, A. Meyer, B. Neuweger, Qualitätssicherung d. Bestimmung d. Luftwechselrate in Innenräumen [*Quality assurance of determining air change rates in indoor environments – comparison of methods*]. Bremer Umweltinstitut GmbH im Auftrag des Umweltbundesamtes (2019)

DOI 10.5162/SMSI2025/C1.2

Wireless Network Architecture for Comprehensive Indoor Environmental Quality Monitoring in Public Schools

Fabian Sievers[1], Nils Langer[1], Stefan Palzer[1]
[1] TU Dortmund, Professorship for Sensors, Friedrich-Wöhler Weg 4, 44227 Dortmund, Germany
stefan.palzer@tu-dortmund.de

Summary:
School buildings require a high level of thermal comfort and good indoor air quality to provide a healthy environment. At the same time, automated heating, ventilation, and air conditioning systems are too costly, thus public school buildings typically feature a low level of automatization. Retrofitting by means of low-cost components has the potential to improve overall building performance until they can be reformed. Here a scalable wireless sensor and actor system architecture that is suitable for large scale monitoring and control of thermal comfort in entire buildings with single room resolution is presented.

Keywords: Indoor environmental quality, Wireless Sensor and actuators network, thermal control systems, air quality, thermal comfort

Introduction

Many public-school buildings in Germany lack investments in thermal insulation and digitization of building operation [1]. This leads to increased operating costs with schools having a particularly high energy consumption. For example, public buildings in Germany feature an energy consumption of 211,4 kWh/m^2 [2]. At the same time, large scale, complex retrofitting is not feasible on a short timescale thus highlighting the need for cost-effective, scalable solutions to reduce energy consumption in buildings that may be quickly implemented.

To optimize energy consumption of complete buildings, continuously monitoring the environmental quality in all rooms is a prerequisite. The collected data can then be used to characterize the thermal behaviour and point towards weaknesses that may be addressed using small-scale, cost-effective energetic renovations. Furthermore, adding wireless thermostats, the room temperature can be controlled based on environmental data to reduce energy consumption while maintaining high thermal comfort. Controlling individual rooms is knows to increase environmental air quality [3] and a reduction in energy consumption [4] of 21,81 – 44,36 % can be achieved while improving the average comfort.

Network architecture

To monitor the environmental quality at an individual room level, a sensor node for monitoring humidity and temperature featuring a Sensirion SHT31 and a carbon dioxide (CO_2) sensor by SenseAir (K30) has been developed in three schools in the town of Holzwickede. In total 155 sensor nodes and 328 thermostats were installed in 149 rooms. The data from each sensor node is collected in a time-series database on a central server and transmitted via the respective WLAN networks. The hand adjusted thermostats at the school have been replaced with custom-designed, wireless battery-powered thermostats, which are remotely controllable from the central server.

The system is implemented as a mesh network between sensor nodes, thus increases flexibility for node placement, lowering the dependence on WLAN range, and alleviating congestion on the WLAN and stress on WLAN access points, because less network participants need to be managed.

Crucially, the connection of radiator thermostats has to be low power consuming in order to ensure a sufficiently long battery lifetime. To this end, the ESP-NOW wireless protocol by Espressif Systems has been established since it provides a suitable connectionless communication protocol for IEEE802.11-enabled IoT allowing for power consumption reduction of more than 30% as compared to WiFi [5].

For the low power communication, the sensor nodes are configured to answer to specific thermostats only, based on their mac address. All communication is initialized by the thermostat with a broadcast message. The configured sensor node answers with a unicast message. After the thermostats have received the message successfully it responds with sensor data. This

communication sequence ensures that the thermostat's microcontroller (MCU) does not have to listen for wireless messages continuously and therefore can sleep most of the time saving energy.

Fig. 1 shows an exemplary network topology made up of sensor nodes, thermostats and a router. It marks the connections and their type between all network participants.

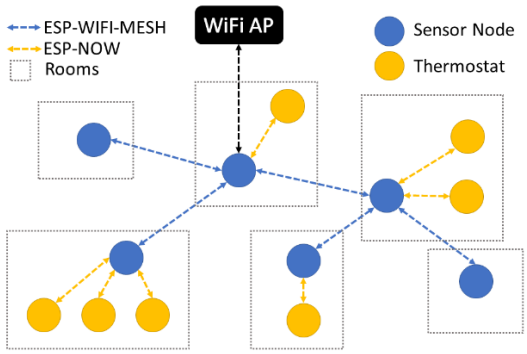

Fig. 1. Exemplary network topology made up of sensor nodes, radiator thermostats and a WLAN access point. The access point provides internet connectivity for the sensor node mesh. The thermostats connect through ESP-NOW for low power communication.

To minimize active time of the thermostat's MCU the communication window is optimized to be as short as possible

Results

The current consumption for data transfers between sensor node and a thermostat have been optimized and determined. The thermostat uses two AA alkaline batteries in series resulting in a supply voltage of 3 V. In Fig. 2 two different scenarios are shown. Initially the thermostat searches for the sensor node, which takes approximately 1493 ms. The usual data exchange is shorter with a total current consumption of 3,8 µAh per exchange.

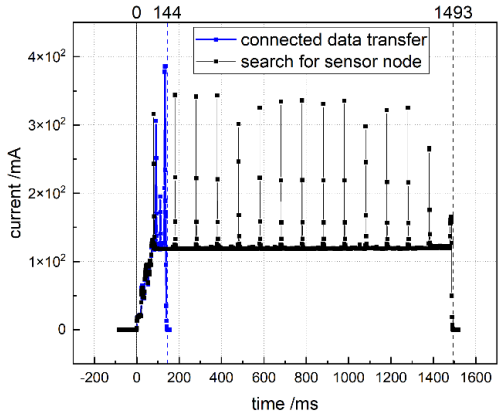

Fig. 2. Current consumption over time of a thermostat (a) while searching for a sensor node without success, (b) during successful data exchange between connected sensor node and thermostat

Data is exchanged in an interval of 4 minutes leading to a total current consumption of 1,37 mAh per day for communication. This leads to an expected lifetime of approximately 1459 days assuming 2000 mAh battery capacity.

Fig. 3 shows data collected with the novel installation for one room during the 27.11.2024. Collected is high resolution data for CO_2, relative humidity and temperature.

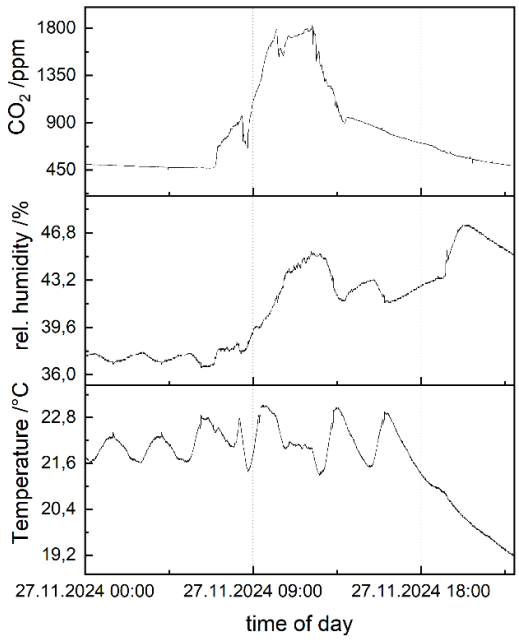

Fig. 3. Collected data for one room during 27.11.2024. Captured temperature, humidity and CO2 concentration data.

References

[1] S. Brand, J. Salzgeber: „Kosten steigen schneller als die Investitionen: Bedarfe für Schulen weiter hoch", *KfW Research*, Nr. 401, KfW

[2] Kluttig, H.; Dirscherl, A.; Erhorn, H.: Energieverbräuche von Bildungsgebäuden in Deutschland. *gi-Gesundheits-Ingenieur* 122, Heft 5, Seite 221-233

[3] A. Ortiz Perez et al., "A Wireless Gas Sensor Network to Monitor Indoor Environmental Quality in Schools," *Sensors*, vol. 18, no. 12. MDPI AG, p. 4345, Dec. 09, 2018. doi: 10.3390/s18124345.

[4] G. Halhoul Merabet et al., "Intelligent building control systems for thermal comfort and energy-efficiency: A systematic review of artificial intelligence-assisted techniques," *Renewable and Sustainable Energy Reviews*, vol. 144. Elsevier BV, p. 110969, Jul. 2021. doi: 10.1016/j.rser.2021.110969.

[5] [1] D. Urazayev, A. Eduard, M. Ahsan, and D. Zorbas, "Indoor Performance Evaluation of ESP-NOW," *2023 IEEE International Conference on Smart Information Systems and Technologies (SIST)*. IEEE, pp. 1–6, May 04, 2023. doi: 10.1109/sist58284.2023.10223585.

DOI 10.5162/SMSI2025/C1.3

Validation of a Sensor Node Prototype for Multimodal Climate Measurement Network

Madeleine Bankwitz[1], Christian Engel[2], Sören Hirsch[1]
[1] Brandenburg University of Applied Sciences, Magdeburger Str. 50, 14770 Brandenburg/Havel, Germany,
[2] TEPROSA GmbH, Paul-Ecke-Str. 6, 39114 Magdeburg, Germany
madeleine.bankwitz@th-brandenburg.de

Summary:

This work introduces a multimodal microsensor system for intelligent building analysis. The sensor captures temperature, humidity, brightness, and acceleration on a building facade. Analog measurements are processed as a data matrix and analyzed using correlation coefficients against commercially available weather data. The results demonstrate reliable performance, supporting its potential in smart building applications.

Keywords: multimodal sensor system, sensor network, climate monitoring, building, digitilization

Background

There are a number of areas in which the use of digital analysis is essential. It is of the most crucial importance to ensure efficiency and predictive planning, particularly in regard to the objective of achieving sustainability. To facilitate mathematical and trend analyses, access to digital data is important [1]. It is therefore necessary to develop measuring systems that can be installed in a variety of environments, are compact in size and measure a range of parameters. Due to the major influence of the building sector on the greenhouse gas effect, we are concentrating on measuring systems for climate monitoring [2,3].

Arnesano et al. conducted a literature review identifying horizontal air temperature distribution as a critical aspect of climate characterization. The review emphasizes the importance of accounting for external influences—such as solar radiation, shadowing elements, and seasonal variations—in comprehensive indoor climate assessment and monitoring strategies [4]. Coulby et al. (2021) presented an indoor environmental quality (IEQ) sensor system that measures CO2 concentration, temperature, humidity, atmospheric pressure, and light intensity. While the system successfully indicates and adapts to changes in environmental quality, potential biases in accuracy limit its applicability in more rigorous contexts, such as occupational health assessments and compliance with industry standards [5]. Chen et al. (2024) introduced an innovative multimodal intelligent flooring system capable of detecting position, pressure, material type, user identity, and activity. The system demonstrated strong signal robustness and achieved high sensitivity and linearity, underscoring its potential for responsive environments and intelligent building applications [6]. Yun et al. developed a wireless sensor network for indoor climate monitoring, which collects diverse environmental parameters, including temperature, humidity, CO2 levels, light, and occupancy. This system provides insights into building climate dynamics, supporting informed adjustments for indoor comfort and energy efficiency [7].

Method

A preliminary prototype has been developed for the current stage of the project. It is based on an ultra-low energy and miniaturized but nevertheless modular multi-channel data-capture platform with an advanced microcontroller platform at its core (Fig. 1). It is intended to measure crucial environmental parameters like temperature, humidity, brightness as well as mechanical loads. The integration of this system into various components and spaces requires a novel approach, combining advanced circuit design and packaging technologies to create a super compact but robust design. For this purpose, a sensor system was designed, combining six channels of analog-to-digital conversion, complemented by a high bandwidth preprocessing stage used for filtering and signal con-

ditioning. Following data processing, analysis and compression performed by the microcontroller, data is sent via standard UART interface to the communications module which allows wired as well as wireless communication. By using multilayer circuit design together with minimum copper structure width of 50 µm together with innovative stacked micro-via technology and state-of-the-art sub-miniature XQFN and BGA packages, we were able to integrate all mentioned components of the sensor system within dimensions of only 10 mm x 50 mm.

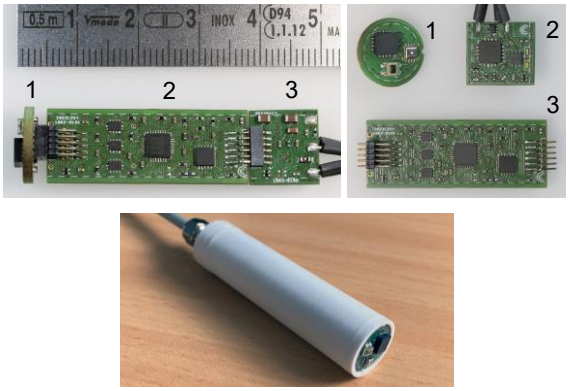

Fig. 1. Sensor Node Prototype

A single-digit mA average power consumption was achieved with standby currents in the lower µA range. This allows the use of energy harvesting as power source together with next generation solid-state batteries.

The sensor was installed on the outside of a building on a window sill. In order to validate the sensor system, commercially available weather data from the nearest weather station was also obtained via the weather application programming interface (API), which is provided via the Visual Crossing website. The Pearson correlation coefficient of the sensor and weather data is calculated for the statistical validation and allows a statement to be made about the linear correlation of the metric variables.

Experimental Results

Meteorological data were obtained from Visual Crossing Weather's online platform, which offers an accessible, cost-effective API that sources data from proximate weather stations. This weather dataset provides hourly readings and is likewise saved in a .csv file format for consistency with the sensor data.

Figure 2 shows a comparison of the measured parameters over 10 hours. A similar trend can be seen between the measured data from the sensor (solid line) and the meteorological data (dashed line). It is particularly noticeable that the temperature and humidity data from the sensor show an indirectly proportional behavior. This is confirmed by the negative correlation coefficient in Table 1.

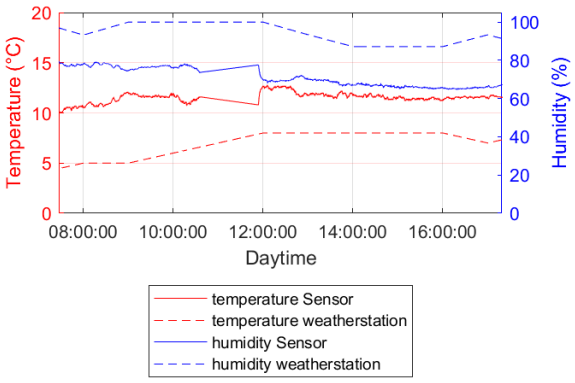

Fig. 2. Multiple Parameters in- and outdoor over time

To calculate the correlation index, the weather data was adjusted to the sample size of the sensor's measuring points. For temperature, there is a weak positive correlation between the data from the weather station and the sensor with a coefficient of 0.41. For humidity, on the other hand, a medium-strong positive correlation between the measured data can be recognised.

Tab. 1: Pearson's Correlation Coefficient r

	r
Temperature weather x sensor	0.41
Humidity weather x sensor	0.67
Sensor temperature x humidity	-0.43

Conclusion

A multimodal sensor node prototype was developed and its measurements were compared with data from commercially available weather monitoring systems. The results show that the measurement system exhibits comparable behavior to its meteorological counterparts, indicating its potential suitability for environmental monitoring applications. In the next step, the accuracy of the sensor will be investigated by controlling the environmental variables, for example using a climate chamber. In this way, precise error tolerances for the system can be determined.

The next phase of hardware development involves integrating a CO_2 sensor to enhance atmospheric monitoring capabilities. By adopting wireless communication, the new prototype aims to address the limitations by dependence on wiring, reducing infrastructural demands while enabling a more extensive deployment of sensors across different locations [8].

References

[1] Arabshahi, M., Wang, D., Sun, J., Rahnamayiezekavat, P., Tang, W., Wang, Y. & Wang, X. (2021). Review on Sensing Technology Adoption in the Construction Industry. *Sensors, 21*(24), 8307. https://doi.org/10.3390/s21248307

[2] Li, Y., Han, M., Liu, S. & Chen, G. (2019). Energy consumption and greenhouse gas emissions by buildings: A multi-scale perspective. *Building And Environment*, 151, 240–250. https://doi.org/10.1016/j.buildenv.2018.11.003

[3] Lamb, W. F., Grubb, M., Diluiso, F. & Minx, J. C. (2021). Countries with sustained greenhouse gas emissions reductions: an analysis of trends and progress by sector. *Climate Policy, 22*(1), 1–17. https://doi.org/10.1080/14693062.2021.1990831

[4] Arnesano, M., Revel, G. & Seri, F. (2016). A tool for the optimal sensor placement to optimize temperature monitoring in large sports spaces. *Automation in Construction,* 68, 223–234. https://doi.org/10.1016/j.autcon.2016.05.012

[5] Coulby, G., Clear, A. K., Jones, O. & Godfrey, A. (2021). Low-cost, multimodal environmental monitoring based on the Internet of Things. *Building And Environment*, 203, 108014. https://doi.org/10.1016/j.buildenv.2021.108014

[6] Chen, Y., Hong, J., Xiao, Y., Zhang, H., Wu, J. & Shi, Q. (2024). Multimodal Intelligent Flooring System for Advanced Smart-Building Monitoring and Interactions. *Advanced Science.* https://doi.org/10.1002/advs.202406190

[7] Yun, J. & Kim, J. (2013). Deployment Support for Sensor Networks in Indoor Climate Monitoring. *International Journal Of Distributed Sensor Networks*, 9(9), 875802. https://doi.org/10.1155/2013/875802

[8] Yang, Y., Xu, W., Gao, Z., Yu, Z. & Zhang, Y. (2023). Research Progress of SHM System for Super High-Rise Buildings Based on Wireless Sensor Network and Cloud Platform. *Remote Sensing*, 15(6), 1473. https://doi.org/10.3390/rs15061473

DOI 10.5162/SMSI2025/A1.4

Optimizing OF-CEAS for the Detection of stable methane isotopes in the atmosphere

Cem Dinc[1], Ponkanok Nitzsche[1], Jens Goldschmidt[1], Katrin Schmitt[1,2], Jürgen Wöllenstein[1,2]
[1] Laboratory for Gassensors, Department of Microsystems Engineering - IMTEK, University of Freiburg, Georges-Köhler-Allee 102, 79110 Freiburg, Germany
[2] Fraunhofer Institute for Physical Measurement Techniques IPM, Georges-Köhler-Allee 301, 79110 Freiburg, Germany
cem.dinc@imtek.uni-freiburg.de

Summary:
This work presents an approach to detect and measure the specific isotopic ratio of the stable methane isotopes $^{12}CH_4$ and $^{13}CH_4$ using a high-finesse cavity within an Optical Feedback CEAS system. The development of this approach is ongoing with the aim of precisely measuring the isotopic ratio under atmospheric conditions in the mid-infrared (MIR) spectral region around 3001.2 cm^{-1}, where the absorption lines of the two stable isotopologues are located and well separated under a pressure of 40 mbar enabling the simultaneous measurement of both within a spectral range of 1 cm^{-1}.

Keywords: Optical Feedback CEAS, Methane Isotopic Ratio, Absorption Spectroscopy, MIR Environmental Sensor, Greenhouse Gas

Motivation

To understand the impact of climate change, it is important to investigate greenhouse gases such as methane (CH_4) and carbon dioxide (CO_2). The current CH_4 concentration in the atmosphere is 1.9 ppm, which is still rising and has doubled over the last 200 years. In addition, it has a global warming potential that is almost 30 times higher than that of CO_2, it is for this reason that CH_4 is the second most important greenhouse gas after CO_2 [1]. This is why it is of great importance to identify and monitor CH_4 sources and sinks and thus to study the CH_4 cycle and its influence on global warming. The identification is based on the isotopic ratio ($\delta^{13}C$) of the two stable isotopes $^{12}CH_4$ and $^{13}CH_4$ referenced to the Vienna Pee Dee Belemnite (VPDB) standard, which is a specific value for each source and every sink. For instance, one of the largest anthropogenic sources of CH_4 is natural gas, which has an isotopic ratio of $\delta^{13}C$ = -43‰. A natural source of CH_4 is that of wetlands, which has a value of $\delta^{13}C$ = -60‰ [2]. Precise measurement of the isotopic ratio can be achieved through established methods like isotope ratio mass spectrometry (IRMS) with the necessary sample preparation and cavity ring down spectroscopy (CRDS) [2]. We present an alternative to CRDS with a higher sensitivity: optical feedback cavity enhanced absorption spectroscopy (OF-CEAS). Based on the feedback of the resonant light into the laser that is transmitting from the cavity (OF), the laser is self-locked to the resonance of the cavity. The effect of this process is the reduction of the laser line width, the improvement of the frequency stability and thus a higher signal-to-noise ratio (SNR) as well as a higher coupling efficiency [3].

The strongest absorption lines of CH_4 are in the MIR spectral region and to be able to determine the isotopic ratio of CH_4 within a single scan, a suitable region around 3001.2 cm^{-1} was selected. Both stable isotopologues are located here and well separated from each other under low pressure.

Experimental Setup

The cavity design allows to adjust crucial parameters, such as the effective absorption path length (L_{abs}) and the free spectral range (FSR).

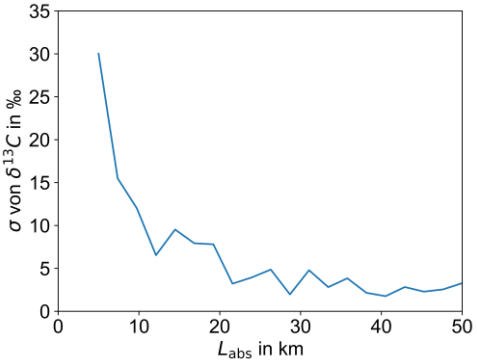

Fig. 1: Monte Carlo simulation to assess the uncertainty of the $\delta^{13}C$ value for different L_{abs}.

These parameters significantly influence the investigation of the spectral range and consequently the determination of the isotope ratio. Hence, a range of investigations and simulations were conducted utilizing the HITRAN database, comprising a Monte Carlo simulation to determine the L_{abs} necessary to optimize the precision of the $\delta^{13}C$ value [4]. The simulation parameters were a concentration of 1.9 ppm at a temperature of 298.15 K and a pressure of 40 mbar, with a noise level determined through measurements being introduced into the simulated spectrum. Using a fit of a Voigt profile-based physical model to the simulated signal including spectroscopic parameters from the HITRAN database, the isotope ratio could be determined for different L_{abs}. Ten simulations were run per L_{abs} to assess the uncertainty, which is shown in Figure 1. It is observable that the uncertainty reduces and stabilizes starting at a L_{abs} of 20 km. Therefore, the cavity was built in a V-shape with a planar mirror and two curved mirrors with a radius of curvature of 1000 mm. The reflectivity of the mirrors is 99.989 % and the arm lengths 905 mm. This results in a FSR of 82.8 MHz and a L_{abs} of 22.6 km. The advantage of the V-cavity is that it ensures that only the resonant light transmitted from the cavity is fed back to the laser and not the direct reflection. An interband cascade laser (ICL) with a central wavenumber of 2998.5 cm^{-1} was selected for operation within the specified spectral range. The beam is propagated through the cavity by passing a mirror, which is mounted on a piezo transmitter (PZT), enabling active control over the laser-cavity-distance to maintain the phase condition for the optical feedback [3]. To verify the ability of the system to detect atmospheric CH_4 the laser was tuned over a spectral range of approximately 1 cm^{-1} by applying a 1 Hz-sawtooth signal. The cavity which was housed with gas connections, pressure and temperature sensors, was flooded with ambient air under atmospheric condition. A measurement with a duration of 300 s was carried out for system characterization.

Results

As demonstrated in Figure 2, the system characterization results indicate a relatively stable methane concentration of 1 ppm in the ambient air over the measurement period. A deviation from the expected value of 1.9 ppm is clearly visible. The reason of this deviation includes cross-sensitivity to H_2O in this spectral range, which complicates baseline correction, and a deviation of the effective absorption path from the expected 22.6 km. The Allan deviation indicated an increasing precision with the integration time, which is not yet sufficient to precisely determine the stable isotopic ratio of CH_4.

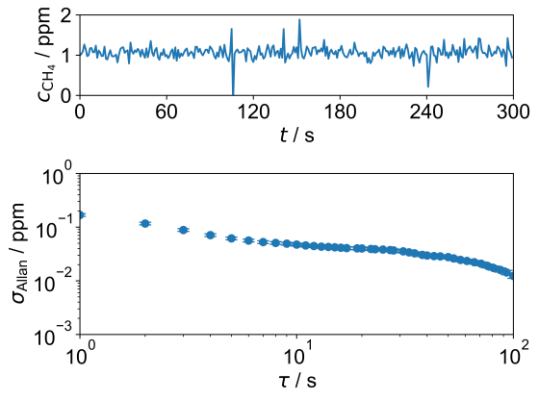

Fig. 2: Measured CH_4 concentration in ambient air under atmospheric conditions for 300 s and the corresponding Allan Deviation.

Conclusion

Here we have presented an OF-CEAS system capable of detecting CH_4 at atmospheric conditions in the selected spectral region, although still with a strong cross-sensitivity to H_2O. The system must be further optimized to be able to determine the isotopic ratio of CH_4 precisely. To enhance the accuracy of the baseline correction by reducing the cross-sensitivity, future measurements will be performed with dried air and low pressure. The application of a pressure of approximately 40 mbar permits the clear separation of the absorption lines of the stable isotopologues. Additional optimizations include the installation of the V-cavity within a custom-built Invar cell with active temperature control, which should enhance the stability of the cavity.

References

[1] Masson-Delmotte, V., et al. IPCC, 2021: Climate Change 2021: The Physical Science Basis. Contribution of Working Group I to the Sixth Assessment Report of the Intergovernmental Panel on Climate Change, Cambridge University Press, Cambridge, United Kingdom and New York, NY, USA, 2391 pp.; doi:10.1017/9781009157896

[2] Zhang, Z., et al. Novel Coalbed Methane (CBM) Origin Analysis and Source Apportionment Method Based on Carbon Isotope Ratio Using Infrared Dual-Wavelength Laser Absorption Spectroscopy, *Earth and Space Science*, 5.11, 721-735 (2018); doi: 10.1029/2018EA000437

[3] Morville, J., et al. Fast, low-noise, mode-by-mode, cavity-enhanced absorption spectroscopy by diode-laser self-locking, *Applied Physics B* 80, 1027-1038 (2005); doi: 10.1007/s00340-005-1828-z

[4] Gordon, Iouli E., et al. The HITRAN2020 molecular spectroscopic database, *Journal of quantitative spectroscopy and radiative transfer* 277, 107949 (2022); doi: 10.1016/j.jqsrt.2021.107949

DOI 10.5162/SMSI2025/A2.1

Digital Signal Processing for Eddy Current Parameter Identification in Measurement Applications

Sebastian Hütter[1], Gerhard Mook[1], Thorsten Halle[1]
[1] Institute of Materials, Technologies and Mechanics (IWTM), Otto-von-Guericke Universität, Universitätsplatz 2, 39106 Magdeburg, Germany
sebastian.huetter@ovgu.de

Summary:
This paper presents a simplified eddy-current testing system design that minimizes hardware complexity by leveraging digital signal processing (DSP). An architecture for the digital-to-analog and analog-to-digital converters is shown that ensures precise temporal correlation between transmitted and received signals. By converting these signals to in-phase and quadrature (IQ) format, additional filtering, spectral analysis and parameter tuning is possible. This design has been applied in both educational and spectroscopic measurement contexts, demonstrating the efficiency of its implementation.

Keywords: eddy current, digital signal processing, soft sensors, system modeling, material characterization

Introduction

When eddy-current methods are used in non-destructive testing (NDT) or evaluation (NDE), there are fundamentally two different kinds of measurements commonly carried out. Probably the more common one in NDE is the measurement of the impedance of the sensor system followed by some modeling of the obtained response. One of the first descriptions is that of Dodd and Deeds [1], resulting in analytical solutions for plates. An early lumped element model was developed by Libby [2] by treating the measurement chain as a transmission line, for which the total impedance can be calculated. The element parameters can be used to obtain the inductance of the coil, which allows inferring the properties of the material under investigation [3]. If the transmission line model is segmented, defects in the material or layered properties of a composite can be included explicitly [4]. The preceding models are preferred for a single-coil measurement setup. For sensors with separate transmission and receiver coils, the natural model is that of a transformer with losses [5].

Alternatively, the voltage transfer function can be used to achieve similar results, but with considerable simpler measurement devices. For transformer-style eddy current sensors, a model for a lossy transformer including different material elements has previously been described by the authors [6,7]. Besides the much simpler hardware requirements, voltage transfer based measurements lend themselves especially well to implementation in software defined logic. In this article, the system architecture underlying the previous work is described and its applicability to both non-destructive testing and evaluation are shown.

System Design

The fundamental principle underlying the present design is keeping the physical hardware as simple as possible and carrying out most of the data processing in digital signal processing (DSP). The eddy current sensor itself is a transformer-type, consisting of a transmitter and receiver coil on a common cylindrical core.

The only system components realized as electronic devices are the excitation coil driver which is a digital analog converter and an analog digital converter on the receiver coil. Both operate on time-domain low frequency signals using commercial-grade chip sets. To achieve accurate temporal correlation between the transmitted and received signal that is required for later processing of the material response, the transmitted analog signal is also fed into a secondary channel of the analog digital converter. This way, any time delay between generation of the digital transmitted signal and acquisition of the digital received signal can be neglected. This layout is illustrated in Fig. 1.

Once the digital signal has been acquired, both loop-back and received signal can be converted to in-phase and quadrature (IQ) format by applying a two all-pass filters designed to have a relative difference in phase response of 90° over a large frequency range [8]. In this form, further

processing such as filtering or spectral analysis is straightforward.

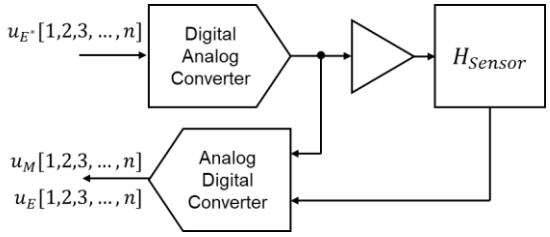

Fig. 1. Architecture of the digital-analog interface. u_E and u_M refer to the excitation and measured signal used in processing, u_{E^*} is the original generated signal.

One significant advantage of this design is that it does not require impedance measurement while still obtaining the full response characteristic. The digital nature of further processing also enables rapid development cycles for new analytic methods not easily possible in conventional circuits.

Application

This design has been applied first to eddy-current testing application in the form of an application for educational use. Here, the low hardware requirements are used to enable many students to participate in exercises while having the capability of modifying many parameters of test equipment [9]. The DSP here consists of a sinusoidal signal generator on the sending side and complex division of the measured and transmitted signal, offset/zero correction O, phase correction φ and amplification A which result in a value in the complex plane V that can be directly displayed, as shown in eq. (1):

$$V = \left(\frac{u_M}{u_E} - O\right) \cdot exp(-i\varphi) \cdot A \qquad (1)$$

A more complex application is found in the spectroscopic application previously mentioned. In this case, the excitation is a broadband noise signal. The response is therefore also an uncorrelated noise-like signal which is affected by the material under test. Since only the sensor itself is in the analog loop, its transfer function can be found by Fourier transform of the time domain signal and complex division. As the only system part interacting with the material, this transfer function must include all effects of the material's electromagnetic properties (as well as those of the coils). The details have been described in [7], but most importantly this transfer function can be modeled as that of a lossy transformer with two major contributions: the direct transfer of energy between the sender and receiver coil with a phase delay depending on the material as well as a part relating to the eddy currents themselves which involves the induced currents and the leakage coefficient. In this case, the main advantage of the digital system is in its ability to identify the model parameters using the entirety of the available information.

Summary

Using DSP techniques, rapid development of new analysis techniques for the application of eddy currents in the field of non-destructive evaluation and material characterization is possible. This advantage has been used to develop a new modeling approach for the voltage transfer function of eddy current sensors in transformatoric circuit.

Acknowledgements

The authors thank the German Research Foundation DFG for the support of the depicted research within the priority program SPP2183 through project grant no. HA 5209/11-3.

References

[1] C.V. Dodd, W.E. Deeds, Analytical Solutions to Eddy-Current Probe-Coil Problems, Journal of Applied Physics 39, 2829–2838 (1968); doi:10.1063/1.1656680

[2] H.L. Libby, Introduction to electromagnetic nondestructive test methods, Wiley-Interscience, New York [u.a.], 1971

[3] F. Wendler, R. Laue, S. Härtel, B. Awiszus, O. Kanoun, Design of a multi-modal sensor for the in-process measurement of material properties based on inductive spectroscopy, Measurement 227, 114187 (2024); doi:10.1016/j.measurement.2024.114187

[4] H.A. Sabbagh, R.K. Murphy, E.H. Sabbagh, L. Zhou, R. Wincheski, Advanced Electromagnetic Models for Materials Characterization and Nondestructive Evaluation, Springer International Publishing, 2021; doi:10.1007/978-3-030-67956-9

[5] Y.L. Bihan, Study on the transformer equivalent circuit of eddy current nondestructive evaluation, NDT&E International 36, 297–302 (2003); doi:10.1016/s0963-8695(03)00003-3

[6] S. Hütter, J. Simonin, G. Mook, T. Halle, Equivalent network modeling of eddy-current transfer functions, Measurement 235, 114943 (2024); doi:10.1016/j.measurement.2024.114943

[7] S. Hütter, Y. Simonin, G. Mook, T. Halle, Soft sensor system for in-process eddy current microstructure characterization, Journal of Sensors and Sensor Systems 13, 237–244 (2024); doi:10.5194/jsss-13-237-2024

[8] K. Vetter, Complexify a Real Signal, https://www.katjaas.nl/hilbert/hilbert.html (accessed 2024-04-09)

[9] G. Mook, J. Simonin, EddyCation - the All-Digital Eddy Current Tool for Education and Innovation, in: G. Busse, D. Van Hemelrijck, I. Solodov, A. Anastasopoulos (Eds.), Emerging Technologies in Non-Destructive Testing, Taylor & Francis, London, Leiden, New York, Philadelphia, Singapore, 2008: pp. 289–293

DOI 10.5162/SMSI2025/A2.2

Wireless Eddy Current Telemetry System for Measuring Axial Piston Ring Movement in a Combustion Engine

Ansel Higgs[1], Bernhard Rossegger[1], Michael Engelmayer[1], Nicole Wermuth[2]
[1] LEC GmbH, Inffeldgasse 19, 8010 Graz, Austria
[2] Institute of Thermodynamics and Sustainable Propulsion Systems, Graz University of Technology
Ansel.higgs@lec.tugraz.at

Summary:
This paper presents an approach to measuring axial piston ring movement in a running combustion engine using a wireless telemetry system. The electrical design of the telemetry is discussed as well as steps taken to enable operation under the extreme conditions inside an engine. Emphasis is placed on the embedded system, power supply, signal acquisition, and data post-processing techniques. The paper concludes with an outlook for future applications and measurements with eddy current sensors.

Keywords: wireless telemetry, inductive position measurement, piston ring movement, embedded systems, harsh environment

Background

Ongoing development of sensor technology and electronics is making it possible to solve more and more measurement tasks that were not possible in the past. Modern sensor systems are becoming increasingly popular in the field of combustion engines, the further development of which is essential in the fight against climate change with regard to the use of alternative fuels [1]. Conventional sensor systems are typically not suited for application inside the engine or on the piston, due to the high temperatures, vibration, and size constraints. While measurements of piston temperature and pressure are possible with both wired [2] and wireless [3] methods, until now, the piston ring kinetics could only be calculated with the help of simulation models [3],[4].

In piston engines, the combustion of fuel initiates an oscillating movement of a piston, which is then converted into a rotational movement at the crankshaft. The combustion chamber, between the moving piston and the cylinder in which it moves, is sealed with the aid of piston rings. The kinetics of the ring are crucial regarding the efficiency and reliability of the engine, as this system causes up to 50 percent of internal friction losses [5] and 20 percent of the total mechanical losses of the engine [6].

Methodology

Piston ring movement in the axial direction is measured with a wireless telemetry system developed for application in the crankcase of a combustion engine. The embedded measurement system is based on an ARM cortex-M33 microcontroller with extended operating temperature range to 125 °C. Measurement data is transmitted to a receiver on the testbench via a Bluetooth radio integrated in the microcontroller. Due to the low number and compact size of the auxiliary components and microchips required for the telemetry, the entire signal acquisition system, measuring 3 x 6 cm, can be mounted on the piston.

Power is supplied to the system via inductive coupling. A receiver coil, buffer, and voltage regulator are mounted on the side of the piston. When the piston reaches the bottom of the cylinder, the receiver coil becomes aligned with a transmitter coil mounted inside the engine. A changing magnetic field produced by the transmitter coil charges the receiver during their alignment. The stored energy allows for the telemetry to measure continuously over the complete engine rotation.

The axial ring movement is measured by eddy current sensors installed in the piston ring grooves. A cross-section of the sensor installation is shown in Fig. 1. The top ring position is measured with a sensor installed in the bottom flank of the groove, while the second and third rings are measured with sensors installed in the top flanks of the respective grooves. The sensors feature a sub 5 mm diameter and 2 mm height, allowing them to be installed in a piston with 19 cm bore without modifying the piston and potentially influencing its performance. Signal acquisition of the eddy current sensors is performed with Texas Instruments LDC1101 inductance to digital converter integrated circuits.

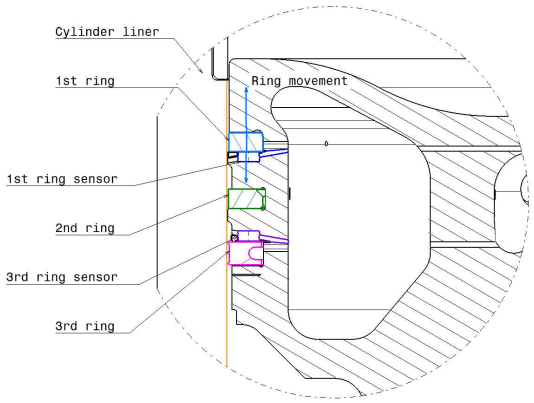

Fig. 1: Cross section of eddy current sensors in piston ring groove flanks

The LDC feature an internal sensor driver which brings inductive sensors into oscillation. Each sensor is paired with a parallel capacitor to set the resonant frequency around 2.5 MHz. Capacitors with C0G dielectric are used due to their low temperature coefficient of capacitance, as temperature on the telemetry PCB readily exceeds 100 °C during full engine load.

In most applications, the distance of a conductive target to an eddy current sensor is measured by the change in power input to the sensing coil as it induces eddy currents and dissipative power in the target. Due to the low Q factor of the small eddy current sensors required for installation in the piston ring, this parameter is out of the measurable range for the LDC1101. Instead, the position of the ring is acquired by measuring the change in inductance of the eddy current sensor. As the ring approaches the sensor, the sensor's inductance decreases and resonation frequency increases. This frequency is digitized by the LDC with an internal register and reference clock generated by the telemetry microcontroller.

The digitized frequency is polled at a sample rate of 10 kHz. For an engine operating at 1500 rpm, this corresponds to approximately 400 samples per revolution which is sufficient to capture transient motion during combustion. While the M33 microcontroller features a core clock speed of 38.4 MHz, there is insufficient time to simultaneously sample and transmit data from all sensors in real time at this rate. Therefore, a buffer solution using magneto-resistive random-access memory is employed to store data over an 8 second sample period. The high storage density, extended temperature range, and lack of write delays are essential for successful implementation of the telemetry. Time synchronization with other sensors on the testbench is achieved with a reference signal transmitted once per revolution via an infrared diode to a photodiode receptor on the telemetry. When a sampling period is complete, measurements are wirelessly transferred to the testbench.

Results

An example of the eddy current sensor output of the 2nd piston ring's axial movement is plotted in Fig. 2. As the measurements were performed on a 4-stroke engine, the x-axis covers 720 degrees of revolution, starting at 90 degrees before combustion and continuing to the compression stroke of the next cycle at 630 degrees. The measurement consists of 150 combustion cycles overlaid on the same plot in gray. For each crank angle, the most common result is displayed in navy and the average result in orange. This post processing strategy is required as the incremental resolution of the sensor is low, with approximately 10 increments of 12 µm corresponding to a maximal ring movement of 120 µm.

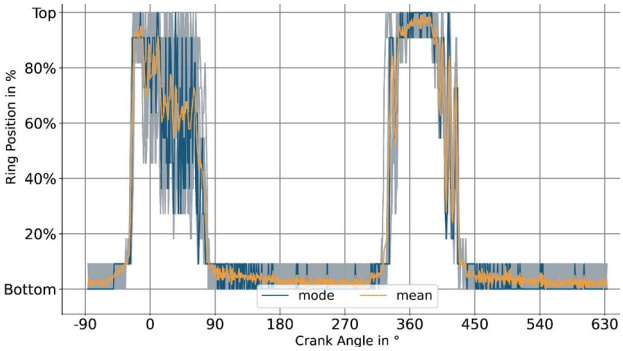

Fig. 2: Eddy current sensor measurement results

It can be seen that for some portions of the cycle, 45° before combustion for example, the mode and mean values agree with each other, indicating minimal variation between cycles. However, during combustion, from 0° to 80°, the mode and mean diverge, indicating larger variations between cycles due to irregularities in the combustion process.

Conclusion

The development and successful testing of the measurement system confirms that this technique is suitable for applications in combustion engines. The sensors and signal acquisition circuitry proved to hold up to the extreme conditions in the engine, although improvements are required to robustness of the first ring's sensor, as it failed during the first combustion cycles.

Future research will focus on broadening the application of wireless eddy current sensor telemetry systems. Current topics include measurement of cylinder liner distortion and oil film thickness, as well as improvements to sensor robustness and measurement quality in the second generation of the telemetry.

References

[1] C. Kendlbacher, K. Schrattbauer und R. Schimon, Alternative fuels and their applications on large engines,*18th Symposium "Sustainable Mobility, Transport and Power Generation", Graz, Austria* (2021)

[2] D. E. Richardson, Comparison of Measured and Theoretical Inter-Ring Gas Pressure on a Diesel Engine, *SAE Transactions,* Vol. 105, 1910-1923 (1996); doi: 10.4271/961909

[3] A. Higgs, B. Rossegger, A. Tilz, M. Vareka, M. Engelmayer, & A. Wimmer, The Development and Application of Advanced Sensor Solutions for Gaining New Insights Into Large Engines, *ASME 2023 ICE Forward Conference, (2023); doi:* 10.1115/ICEF2023-110623

[4] D. Weiß, S. Posch, M. Engelmayer und A. Wimmer, Development, Calibration and Validation of a Tribological Simulation Model for the Piston Ring Pack of a Large Gas Engine, *SAE International Journal of Advances and Current Practices in Mobility*, Vol 5, 642-651 (2022); doi: 10.4271/2022-01-0323

[5] A. Götze und D. Jaitner, Combined experimental and simulative approach for friction loss optimization of DLC coated piston rings, *Automotive and Engine Technology*, Vol 7-3, 283-293 (2022); doi: 10.1007/s41104-022-00115-7

[6] K. G. Mahmoud, O. Knaus, T. Parikyan, G. Offner und S. Sklepic, An integrated model for the performance of piston ring pack in internal combustion engines, *Proceedings of the Institution of Mechanical Engineers*, *Part K: Journal of Multi-body Dynamics*, Vol. 232-3, 371-384 (2018); doi: 10.1177/1464419317736676

DOI 10.5162/SMSI2025/A2.3

Three-axis Joystick as Stray Field Robust Magnetic Position System

Michael Ortner [1], *Perla Malagò*[1], *Florian Slanovc*[1], *and Stephan Leisenheimer*[2]
[1] Silicon Austria Labs (SAL), Europastraße 12, 9524 Villach, Austria
[2] Infineon Technologies AG, Am Campeon 1-15, 85579 Neubiberg, Germany
michael.ortner@silicon-austria.com

Summary: It was demonstrated that a specific arrangement of magnet and single 3D magnetic field sensor can effectively resolve the motion of a three-axis joystick. However, the proposed configuration lacks robustness against stray magnetic fields. Building on the original concept, this work explores the feasibility of achieving stray field immunity through differential measurement techniques. Our findings show that while a stray field robust design is attainable, it imposes stringent requirements on system design and sensor arrangement to ensure reliable operation under varying magnetic conditions.

Keywords: Magnetic position systems, Magnetic sensors, Magnetic field simulation, Magnetic system design,

Background, Motivation, and Objective

Magnetic position systems leverage magnetic fields from permanent magnets to translate relative physical position into electrical signals using magnetic field sensors [1]. Unlike mechanical or optical alternatives, magnetic systems operate contact-free and resist environmental factors like dirt and temperature variations, which enhances their reliability in industrial applications. [2]. Recent advancements include multi-dimensional sensing like three-axis joysticks [3] or six degrees of freedom systems [4].

In [3] Malagó et al. propose a design method for magnetic position systems based on geometric optimization, utilizing a differential evolution algorithm that relies on fast analytical solutions for magnetic field simulation. This method is applied to tracking three-axis joystick motion using only a single 3D magnetic field sensor. This solution provides a cost-effective, high-resolution option for three-axis joysticks and ball-joint motion tracking for applications that include gaming controls in simulators, steering in nautical and aerospace fields, robotic joint motion tracking, as well as mechanical systems like steering knuckles and multimedia control elements like the BMW iDrive.

However, the system proposed by Malagó et al. lacks stray field stability, meaning that small variations from external magnetic fields can lead to inaccurate position measurements. Robust designs, such as those in [5], ensure consistent performance, which is essential for safety and precision in industrial applications. The authors argue that a well-designed system can achieve a state separation of more than 1 mT per degree, offering significant robustness. However, industry standards like ISO 26262 [6] account for stray fields as high as 5 mT, posing a considerable challenge for maintaining measurement accuracy in compliant systems.

In this work, we build upon the system and simulation methods developed in [2] to design a stray-field-stable three-axis joystick by applying a differential measurement principle.

Methodology

Stray field robustness through differential measurement uses pairs of strategically positioned sensors to cancel a homogeneous external magnetic field by measuring the difference in their readings. This approach isolates the target magnetic signal, focusing on variations caused by the magnet rather than environmental interference, thus enhancing accuracy without complex shielding.

Analytical solutions are crucial to the magnetic system design approach proposed in [3], as they provide extremely fast computations of magnetic fields of permanent magnets. This allows the application of genetic algorithms in design spaces with dozens of variables, facilitating the discovery of novel solutions and optimal layouts. This design approach is implemented using the Magpylib Python package [7], which provides vectorized analytical solutions for rapid and efficient magnetic field computations.

The chosen system design parameters include the position and orientation of the magnet mounted on the joystick axis, as well as the position and orientation of the sensor with an airgap of 2 mm. Off-the shelf magnet sizes and cubical geometries with sides between 2 mm and 5 mm are chosen, with typical rare earth material with a polarization of 1 T. The sensor itself contains two 3D sensing elements (pixels) spaced realistically between 1 mm and 3 mm apart to allow integration of the differential sensing principle within a single sensor unit. For practical reasons related to PCB fabrication, two layout types are selected:

DOI 10.5162/SMSI2025/A2.3

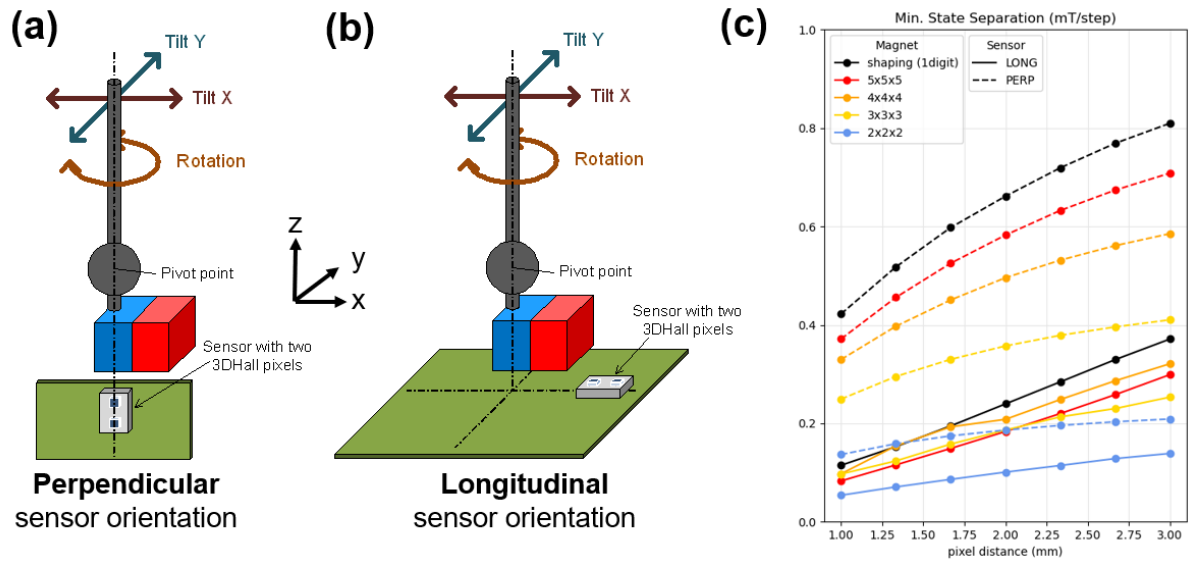

Fig. 1: Design layouts satisfying the design constraints (a) and (b). Simulation results (c).

the perpendicular layout, where the sensor pixels are aligned along the z-axis (Fig. 1a), and the longitudinal layout, where the two sensor pixels lie in the same x-y plane (Fig. 1b).

Results

Simulations confirm that a differential setup is possible for the three-axis joystick. As with the original single-pixel design, strict design constraints apply: the magnet must be mounted on the axis with an offset from the center, and its magnetization must be oriented perpendicular to both the displacement and the axis.

The perpendicular configuration is most effective when the sensor is positioned directly on the z-axis. Here, the second pixel is placed at a larger air gap, receiving significantly less magnetic field from the magnet and thus primarily serving to ”measure the stray field”. The longitudinal setup, however, is more challenging to implement. This setup requires the sensor to be laterally displaced beyond the magnet itself, with the pixels aligned radially. The two schemes are sketched in Fig. 1 (a) and (b).

Simulation results for optimal designs are presented in Fig. 1 (c), showing the minimum state separation in millitesla per degree of joystick tilt/rotation (step) for various magnet sizes and tilt angles up to 20°. As anticipated, state separation improves with greater inter-pixel distance. Perpendicular setups demonstrate significantly larger state separation, suggesting they are better suited for sensing applications.

Conclusion and Outlook

We have demonstrated that stray-field-stable magnetic detection of three-axis joystick motion is feasible using magnetic field sensors with dual 3D sensing elements. Simulations reveal that achieving a one-to-one correspondence between magnetic field states and joystick degrees of freedom imposes strict requirements on magnet and sensor arrangement, with perpendicular alignment generally yielding better results. The sensor-magnet configurations developed in this work are patented by Infineon Technologies AG.

References

[1] S. Lumetti, “Amr sensor array design for the realization of a 3d magnetic tactile sensor,” in *Proceedings*, vol. 97, p. 198, MDPI, 2024.

[2] C. Treutler, “Magnetic sensors for automotive applications,” *Sensors and Actuators A: Physical*, vol. 91, no. 1-2, pp. 2–6, 2001.

[3] P. Malagò, “Magnetic position system design method applied to three-axis joystick motion tracking,” *Sensors*, vol. 20, no. 23, p. 6873, 2020.

[4] D. Cichon, “A hall-sensor-based localization method with six degrees of freedom using unscented kalman filter,” *IEEE Sensors Journal*, vol. 19, no. 7, pp. 2509–2516, 2019.

[5] N. Dupre, “A stray-field-immune magnetic displacement sensor with 1% accuracy,” *IEEE Sensors Journal*, vol. 20, no. 19, pp. 11405–11411, 2020.

[6] W. Granig, “Calculation of failure detection probability on safety mechanisms of correlated sensor signals according to iso 26262,” *SAE International Journal of Passenger Cars-Electronic and Electrical Systems*, vol. 10, no. 2017-01-0015, pp. 144–155, 2017.

[7] M. Ortner, “Magpylib: A free python package for magnetic field computation,” *SoftwareX*, vol. 11, p. 100466, 2020.

DOI 10.5162/SMSI2025/A2.4

Airgap-Dependent “Pole Eating” Effect in Magnetic Scales

Florian Slanovc[1], *Daniel Markó*[1] *and Michael Ortner*[1]
[1]Silicon Austria Labs (SAL), Europastraße 12, 9524 Villach, Austria
florian.slanovc@silicon-austria.com

Summary: Magnetic scales and encoders are essential tools for precise measurement of linear displacement and angular rotation, especially in applications requiring long stroke lengths. However, material imperfections and errors in the magnetization process can result in inaccuracies within the magnetic zone patterns. This paper investigates the phenomenon of “pole eating”, where magnetic poles are partially diminished by neighboring poles at larger air gaps. A quantitative analysis of the impact of airgap variations on pole read-out accuracy is presented, focusing on three key error parameters: zone length variations, zone depth inconsistencies, and zone polarization irregularities. The findings provide insights into the tolerances necessary for reliable magnetic scale performance under varying air gap conditions, contributing to improved design and operational guidelines for magnetic measurement systems.

Keywords: magnetic encoder, scales, linear, rotary, pole errors

Background

Magnetic scales and encoders, linear and rotary, are vital for precise position and velocity measurements in industrial and scientific applications. Using Hall-effect or magnetoresistive sensors, they detect incremental or absolute magnetic patterns encoded on a scale [1].

Magnetic encoders outperform optical counterparts in robustness, tolerating dust, oil, and vibration, making them ideal for demanding environments like robotics, CNC machinery, and medical equipment.

Following [2], this study defines “zones” as magnetized material patterns and “poles” as the corresponding sensor signal patterns, with poles being the regions between consecutive zero crossings of the relevant field component.

Investigation of pole errors

Magnetic encoders are subject to various inaccuracies that can compromise their performance in precision applications [3]. Variations in the magnetic zones—specifically in their length, depth, and polarization (illustrated in Fig. 1)—often arise from material inhomogeneities, run-out errors, or imperfections during the magnetization process [4]. These variations manifest as distortions in the pole pattern of the measured signal, directly affecting both absolute and incremental position measurements.

This study demonstrates that these zone pattern variations influence the pole pattern in an airgap-dependent manner. This observation suggests that the exact configuration of the magnetic zones on the encoder scale is less critical than the resulting magnetic field measured above them. Notably, the magnetic field’s characteristics change with airgap distance, a phenomenon exemplified by the “pole eating” effect shown in Fig. 2. This insight provides a basis for reevaluating design and error mitigation strategies in magnetic encoder systems.

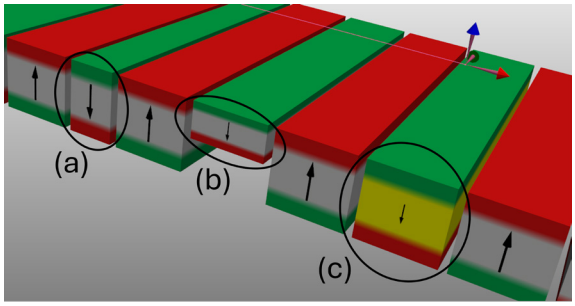

Fig. 1: Defects in zone patterns studied: (a) zone length variation, (b) zone depth variation, (c) zone polarization variation. A sensor above the scale detects the resulting field at a given airgap.

Results

To investigate the effects of pole length variation, we utilized Magpylib, an open-source library for analytical magnetic field calculations of permanent magnets [5]. Magnetic zones were modeled as idealized cuboid magnets, facilitating systematic parameter manipulation. The simulation parameters, representative of realistic linear and rotary encoder systems, are detailed in Tab. 1. The results are expressed as relative deviations, ensuring scaling invariance and minimizing dependence on the absolute parameter values of the system.

Starting from an ideal magnetic zone pattern, we introduced a single faulty zone and system-

DOI 10.5162/SMSI2025/A2.4

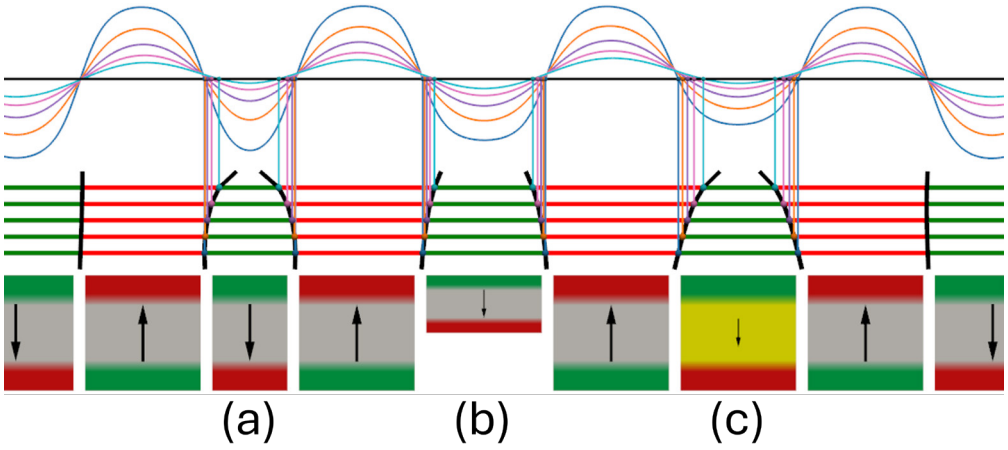

Fig. 2: Pole lengths measured above zone defects (Fig. 1a–c) at varying airgaps. Larger airgaps cause defect poles to be increasingly "eaten" by neighboring poles due to signal zero-crossing shifts (vertical field component).

Tab. 1: Input parameters for analytical simulations. Scaling invariance ensures results apply to systems of varying sizes.

zone length	$1\,\mathrm{mm}$
zone width	$5\,\mathrm{mm}$
zone depth	$0.5\,\mathrm{mm}$
magnetic polarization	$100\,\mathrm{mT}$ out-of-plane
read-out airgap	$\frac{1}{2}$ zone length = $0.5\,\mathrm{mm}$

atically varied three error types—zone length, zone depth, and zone polarization—by up to 10% of their original values. The deviations in pole length, expressed as percentages relative to the original pole lengths, were analyzed as a function of air gap variations. The results, summarized in Fig. 3, reveal how specific error types influence pole read-out under different air gap conditions.

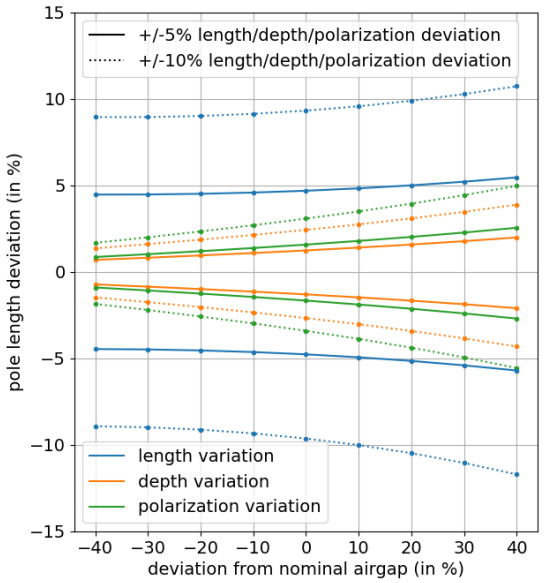

Fig. 3: Pole length deviations vs. airgap variations for different zone errors: length, depth, and polarization.

Outlook

Our presented simulations provide initial insights into the sensitivity of pole length deviations to zone pattern imperfections. Current efforts are focused on experimental validation of these findings to establish a comprehensive understanding of error sources and their impact on signal quality in practical encoder systems.

References

[1] A. Ellin and G. Dolsak, "The design and application of rotary encoders," *Sensor Review*, vol. 28, no. 2, pp. 150–158, 2008.

[2] DIN SPEC 91411:2021-09, *"Requirements for the technical representation of magnetic dimensional standards in construction drawings"*. Beuth Verlag, Berlin, 2021.

[3] T. Becker, T. Materne, and S. Cardoso de Freitas, "A1.2 - Surprising advances in magnetic encoder performance - Do not expect only better accuracy," in *Proceedings Sensor 2017*, pp. 32–35, AMA Service GmbH, Von-Münchhausen-Str. 49, 31515 Wunstorf, Germany, 2017.

[4] P. Campbell, "Magnetoresistive sensors for high resolution position encoding," in *SAE Technical Paper Series*, ANNUAL, SAE International, 1993.

[5] M. Ortner and L. G. C. Bandeira, "Magpylib: A free python package for magnetic field computation," *SoftwareX*, vol. 11, p. 100466, 2020.

DOI 10.5162/SMSI2025/A3.1

Development of a Biosensor Platform Measuring the Electrical Resistance in a Tailor-Made System for Biological Barriers to Assess the Barrier Integrity

Verena Vogel[1,2], Sabrina Schnur[2], Sophie-Marie Klär[2], Dietmar Brück[1], Marc Schneider[2], Marius Hittinger[2,3,4], Ralf-Kilian Zäh[1], Benedikt Faupel[1]
[1]University of Applied Sciences, School of Engineering, Saarbrücken, Germany;
[2]Department of Pharmacy, Biopharmaceutics and Pharmaceutical Technology, Saarland University, Saarbrücken, Germany; [3]Department of Drug Delivery, PharmBioTec Research and Development gGmbH, Schiffweiler, Germany; [4]MucosaTec GmbH, Schiffweiler, Germany
Verena.Vogel@htwsaar.de

Summary:
Monitoring the electrical resistance across biological barriers can serve as an indicator of barrier integrity. Our biosensor system offers an alternative for electrical resistance measurements in a tailor-made system for biological barriers. Measurements of agarose gels at different concentrations (0.5%, 2% w/v) and volumes (150, 300 µl) should demonstrate the ability to distinguish between different conductive barriers. Resistance differences of intact and perforated barriers should highlight the sensor´s potential to assess the barrier integrity and its application in pharmaceutical research.

Keywords: biosensor, electrical resistance, biological barrier, pharmaceutical research, transepithelial electrical resistance

Introduction

Biological barriers, such as the intestinal epithelium, play a crucial role in pharmaceutical research. Studying these barriers often involves monitoring their integrity using the transepithelial electrical resistance (TEER), an accepted technique that quantifies electrical resistance across the cellular layer [1,2]. A high electrical resistance indicates an intact barrier, while weakened cell junctions display a reduced resistance value. Commercially available devices have the drawback of limited flexibility concerning electrode placement [1,3]. Common "chopstick" electrodes, with fixed design and spacing, restrict customization options.
Our work presents a biosensor platform integrated in a 3D printed made tailor-made system for biological barriers, designed to measure electrical resistance. The continuous monitoring of the electrical resistance is essential to ensure a stable and intact barrier and prevent disturbances of the barrier during experiments. The sensor system offers an adaptable alternative for electrical resistance measurements across barriers, with flexibility in electrode positioning, electrode geometry, and the applied potential, current, and frequency. This adaptability makes it suitable for assessing barrier integrity in dynamic environments, such as during transport studies.

Methods

The 3D printed polylactic acid (PLA) based module, consisting of a cover component and a base component, is linked to a peristaltic pump (BMT Fluid Control Solutions GmbH, Germany). The cell culture insert (Corning, USA) includes a porous polyethylene terephthalate (PET) membrane with a pore size of 0.4 µm. Before starting the measurements, the modules are filled with Hanks' balanced salt solution (HBSS buffer, gibco, Thermo Fisher Scientific, USA). The sensor set-up features two stainless steel wires as electrodes, one in the upper compartment and one in the lower compartment (Fig. 1) The circuit consists of a voltage divider circuit linked to an Arduino microcontroller (Fig. 2). The space between the electrodes contains the buffer and the barrier, which includes the PET membrane and the barrier model. Agarose gel is prepared at varying concentrations (0.5%, 2% w/v) in HBSS buffer, boiled at 200 °C, and pipetted onto the membrane in volumes of 150 µl or 300 µl, to simulate a barrier model. To assess the sensor’s ability to distinguish between intact and disrupted barriers, the respec-

tive gel is perforated with a 1000 µl pipette tip and remeasured.

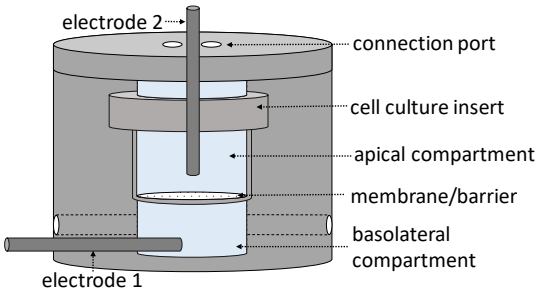

Fig. 1 Customized electrode set-up integrated into a specially designed module that can accommodate a cell culture insert with a barrier

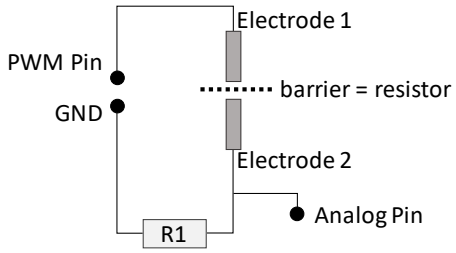

Fig. 2 The measurement principle involves a voltage divider with R1 as a resistor, two electrodes and a barrier that acts as a resistor.

Results

Initial data indicate the sensor´s potential to distinguish between an insert containing only buffer (without membrane), an insert with a PET membrane, and inserts filled with 150 µl 2% w/v or a 300 µl 2% w/v agarose gel. A 150 Ω resistor was chosen as R1.

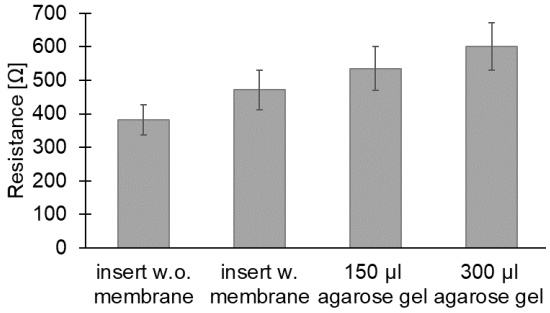

Fig. 3 Comparison of measured resistance across different barriers (n=5), including inserts without a membrane (w.o.), with a membrane (w.), and with 150 µl or 300 µl of 2% w/v agarose gel.

Preliminary resistance measurements (2000 Ω resistor chosen as R1) of the perforated gel resulted in a decrease in resistance for the disrupted agarose barriers of 105 Ω for the 150 µl 0.5% w/v gel and 131 Ω for the 150 µl 2% w/v gel (Fig. 4), showing the potential to differentiate between the intact barrier and a perforated gel barrier.

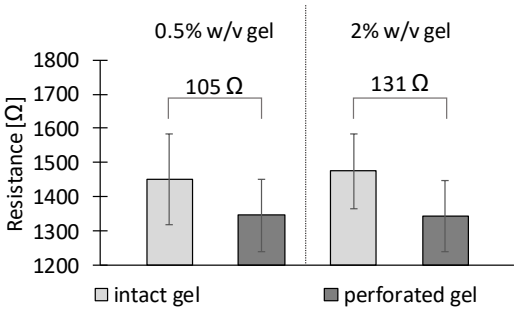

Fig. 4 Resistance measurements of agarose gels with 150 µl 0.5% w/v and 150 µl 2% w/v , comparing intact versus perforated gels (n=5).

Conclusion

In conclusion, a sensor platform was developed to perform electrical resistance measurements of biological samples. Measurements using different conductive substrates, such as varying concentrations and volumes of agarose gel, indicate the platform's potential to distinguish between substrates with different electrical conductivity properties and between intact and perforated gel barriers. This advantage shows great potential for pharmaceutical research, as monitoring the barrier integrity is crucial for assessing the impact of environmental factors on the cell or tissue models during experiments. This is especially important in *in-vitro* models designed to simulate physiologically relevant environments, intending to reduce the need for animal studies. Future steps will focus on integrating cell monolayers to further validate the sensor's functionality in a biologically relevant model. Additionally, the platform could offer the potential to assess pharmaceutical-induced toxicity, as reduced electrical resistance indicates cell barrier disruption, which might correlate to cytotoxicity.

References

[1] B. Srinivasan, A. R. Kolli, M. B. Esch, H. Abaci, M.L Shuler, J. J. Hickman, TEER measurement techniques for in vitro barrier model systems, *Journal of laboratory automation*, 20(2), 107-126 (2015); DOI: 10.1177/2211068214561025

[2] K. Benson, S. Cramer, H. J. Galla, Impedance-based cell monitoring: barrier properties and beyond, *Fluids and Barriers of the CNS*, 10, 1-11. (2013); DOI: 10.1186/2045-8118-10-5

[3] C. G. Jones, C. Chen, An arduino-based sensor to measure transendothelial electrical resistance, *Sensors and Actuators A: Physical*, 314, 112216 (2020); DOI: 10.1016/j.sna.2020.112216

Acknowledgment

The presented work was financially supported by the EFRE-project “LADME on Desk”.

DOI 10.5162/SMSI2025/A3.2

Application of NeRF and RGB-D Camera for the Generation of Digital Twins of Biological Soft Tissues

Marton C. Mezei[1], *Fabrizia Auletta*[1], *Alessandra Gavazza*[2], *Giacomo Rossi*[2] *and Calogero M. Oddo*[1]
[1] BioRobotics Institute, Sant'Anna School of Advanced Studies, Pisa, Italy
[2] School of Biosciences and Veterinary Medicine, University of Camerino, Matelica, Italy
Calogero.Oddo@santannapisa.it, Fabrizia.Auletta@santannapisa.it

Summary: We present an integrated scanning system designed for data collection and 3D reconstruction of macroscopic ex-vivo soft tissues. It combines a commercial RGB-D camera, a rotary stage, and a lighting system to capture high-resolution images with known and repeatable camera poses. The captured data enable the training of Neural Radiance Field (NeRF) models. The technical validation assesses the precision of the camera system and the accuracy of the NeRF-based 3D reconstruction. The demonstration of the system in clinical settings is illustrated on ex-vivo tissue scans, proving the system's potential for real-world deployment in medical environments.

Keywords: Medical Sensors, Digital Twin, Image-Based 3D Reconstruction, AI-Driven 3D Reconstruction, Data Fusion in Sensor Systems, AI in Measurement Systems, Ex-vivo Tissue Scanning.

Background, Motivation and Objective

The creation of high-fidelity digital twins and 3D virtual reconstructions of physical samples, especially in the medical field, is a rapidly advancing field. However, generating these detailed digital twins presents challenges, particularly for surfaces that are reflective, homogeneous or nearly symmetrical, such as soft tissues. Advancements in 3D reconstruction, notably through NeRF, have demonstrated great potential in solving these challenges. NeRF generates high-quality virtual representations of complex structures by training a neural network to describe the density and color information for each point of the scene in a continuous manner, even in challenging conditions [1, 2, 3]. For the clinical setting, a specialized scanning system is required to capture the precise datasets needed for NeRF-based and other RGB/RGB-D reconstruction methods. To meet this need, we present a novel surgical scanning system that reliably acquires NeRF-compatible data, enabling the rapid, high-quality digital twins of resected soft tissues for real-time surgical planning and post-operative analysis [4, 5].

Description of the New Method or System

We present a semi-automatic scanner platform designed for the rapid acquisition of RGB images, depth images, and point clouds, all with precisely known camera positions. The platform is further enhanced with NeRF-based algorithms to enable high-precision 3D reconstruction of soft tissues. The system integrates an RGB-D camera (Intel RealSense D405), a rotary stage (Standa 8MR190-2-28, 0.01° resolution), an LED lighting system, and a 3D-printed camera arm (Figure 1). The polylactic acid (PLA) camera arm allows the positioning of the pitch angle of the camera between 0° and 90° (5° resolution) and the positioning of the camera distance from the object between 60mm and 130mm (10mm resolution). The rotary stage automatically sets the yaw angle, whereas the pitch angle of the camera axis is adjusted manually on the camera arm. The soft tissues selected for macroscopic description vary in size and shape, ranging from 15mm to 65mm, and the adjustable camera distance ensures the preservation of their key features. The reconstruction process consists of (i) calibration phase with a ChArUco[1] marker-based camera pose detection, (ii) acquisition of RGB-D and point clouds phase, (iii) post-processing phase and (iv) training phase. The neural network was trained to create an implicit representation of the scene using Nerfstudio [4]. Nerfstudio also includes a tool for converting implicit representations to explicit formats, allowing for the export of point clouds. The training was performed on an NVIDIA T4 GPU within a Google Colab environment. The

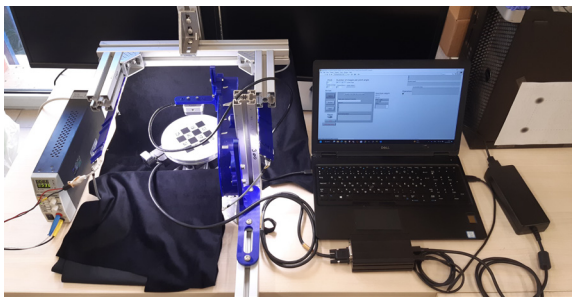

Fig. 1: Semi-Automatic RGB-D Scanning System.

[1] https://docs.opencv.org/4.x/d0/d3c/classcv_1_1aruco_1_1CharucoBoard.html

use of the Nerfacto method for the training of a single scene, comprising 200 images, typically required approximately 20 minutes, with a maximum of 10,000 iterations.

Results

To evaluate the effectiveness of both the scanning system and the algorithm, their outputs were benchmarked against a reference standard through two separate validation methods. The depth accuracy of the Intel RealSense camera was assessed at six sample pitch angles on the camera arm (25°, 35°, 45°, 60°, 75° and 90°), at multiple yaw angles for each pitch angle. This was repeated for three sample camera elevations (70mm, 90mm and 130mm). During these acquisitions, the ChArUco board was placed on the rotary stage with its width and height dimensions serving as the control parameter of the depth accuracy. The pattern real dimensions were measured with a caliper and compared with the same measurements carried out with CloudCompare[2] on the raw acquired point clouds. The average absolute distance error and the average standard deviation across all camera distances were 0.24mm and 0.354mm, respectively, which align with the manufacturer's submillimeter accuracy claim. The accuracy of the NeRF-based reconstruction method was assessed through the acquisition of 200 images, each at distinct yaw and pitch angles and camera elevation. The dataset comprised two objects with known geometries, specifically 30x30x30mm cubes made of aluminum and delrin. The NeRF reconstruction of each reference object was then compared to its original CAD model. As before, the mean distance error of each point in the point cloud was compared to the ground truth geometry of the CAD models with the CloudCompare software (see Figure 2). After a thorough tuning phase to optimize the scanning and reconstruction pipeline, the average mean distance error was 0.19 mm, and the standard deviation was 1.094 mm. The reconstruction pipeline proposed

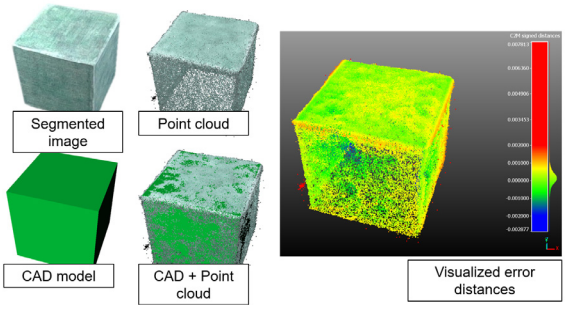

Fig. 2: Aluminum reference cube with mean error distances of the individual points.

[2]CloudCompare (version 2.13) [GPL software]. (2024). Retrieved from `http://www.cloudcompare.org/`

above was evaluated with resected animal soft tissues. An example is presented in Figure 3 to the reconstruction of an ex-vivo animal specimen. During the acquisition, the petri dish containing the specimen was placed on the rotary stage. Although no ground truth geometry was available for the soft tissue for thorough comparison, it is apparent that the reconstruction preserved the main geometric features while providing an accurate representation of the surface texture. Such tests revealed that the collected data can be effectively used for RGB and RGB-D based NeRF reconstruction methods and state-of-the-art 3D reconstruction methods. Therefore, the scanning system can be effectively utilized to collect data sets for the macroscopic description of ex-vivo soft tissues, with dimensions ranging between 15mm and 65mm [6]. Future work will focus on fine-tuning the presented algorithms to improve their performance and efficiency. This will include conducting comprehensive testing and parameter adjustments. Additionally, there will be an emphasis on gathering extensive and diverse datasets to enhance the accuracy, reliability, and generalizability of the system across various real-world scenarios.

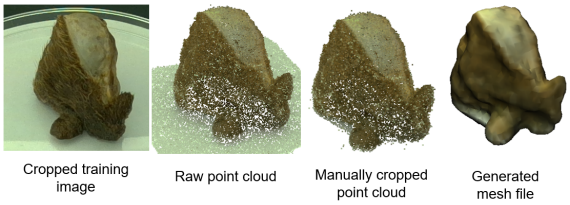

Fig. 3: Example of a 46x24x31mm canine mammary neoplasm, its reconstructed point clouds and generated mesh file.

References

[1] B. Mildenhall, P.P. Srinivasan, et al., Nerf: Representing scenes as neural radiance fields for view synthesis, *Commun. ACM*, 65, 99–106, 2021; doi: 10.1145/3503250

[2] A. Tewari, J. Thies, et al., Advances in neural rendering, *Comput. Graph. Forum*, 41, 703–735, 2022; doi: 10.1111/cgf.14507

[3] A. Yu, V. Ye, et al., pixelnerf: Neural radiance fields from one or few images, *CVPR*, 4578–4587, 2021; doi: 10.1109/CVPR46437.2021.00455

[4] M. Tancik, E. Weber, et al., Nerfstudio: A modular framework for neural radiance field development, *SIGGRAPH*, 1–12, 2023; doi: 10.1145/3588432.3591516

[5] A. Suvarna, R. Vempati, et al., DeltaAI: Semi-Autonomous Tissue Grossing Measurements and Recommendations using Neural Radiance Fields for Rapid, Complete Intraoperative Histological Assessment of Tumor Margins, *bioRxiv*; doi: 10.1101/2023.08.07.552349

[6] F. Auletta, M.C. Mezei, I. Benedetti, G. Rossi, A. Gavazza, C.M. Oddo, Digital Dataset of Formalin-Fixed Animal Tissues for Macroscopic Pathology: Image and Ultrasound Data, *in preparation*

DOI 10.5162/SMSI2025/A3.3

Towards Smart Face Masks by a Reusable, Wireless Sensor Patch and Tailored Data Analysis

Sören Schäfer[1], Stefan Schmitt[1], Juri Magomajew[1], Maximiliano Tagliani[2], Heiko Theuer[2], Erik Dahrmann[2]
[1] Fraunhofer Institute for Microengineering and Microsystems (IMM), Carl-Zeiss-Str. 18-20, 55129 Mainz, Germany,
[2] IMSTec GmbH | Auf dem Langloos 10, 55270 Klein-Winternheim, Germany
Soeren.schaefer@imm.fraunhofer.de

Summary:
The efficacy of FFP2 masks heavily depends on its fit and whether it is worn correctly. We present a reusable smart face mask sensor patch that detects mask fit by pressure modulation and alerts the user if it undershoots a certain threshold. The patch gets fixed on the outside of the mask fleece non-destructively, which opens the opportunity of adding other sensors, e.g. for hazardous gases. We test the patch with different subjects and discuss its sensitivity with respect to different external factors.

Keywords: wearable, smart face mask, health monitoring, data science

Background

Face masks have become ubiquitous during COVID-19 pandemic, underlining the importance of high-quality personal protective equipment. However, the efficacy of a face mask to protect the user against airborne viruses decreases if the mask is not worn correctly and/or does not match the user's physiognomy (mask fit or fit factor) or becomes too damp over time. Long-term users, e.g. healthworkers, are also advised to take breaks in wearing the mask to prevent fatigue.

Smart face masks can meet these challenges if they fulfill three tasks: i) monitoring environmental parameters that change within a respiratory cycle and are sensitive to mask fit, ii) processing this data on-board, and iii) alert the user in case of detected anomalies. An external device, e.g. a smartphone, may also carry out steps ii) and iii), in which case the mask should have a communication interface.

Description of the New Method or System

We design and construct a wireless sensor patch as shown in Fig. 1 that comes with a commercial sensor for pressure *p*, relative humidity *rH* and temperature *T* (BME280), a battery plug for power supply, a sound transducer and LEDs for alerting the user and a system-on-chip (SoC) that supports bluetooth low energy protocol (BLE). The patch is placed in a 3D-printed protective case with an opening at the position of the sensor. The diameter and height of the final case is 2,8 cm and 0,8 cm, respectively. We fix the patch on a FFP2 mask with a pair of magnetic rings, one within the case and the other on the far side of the mask fleece. Figure 1d) illustrates the case with the sensor patch being placed within the mask. We demonstrate, however, that the patch is also sensitive when placed at the outer layer of the mask, with the sensor facing the mask fleece.

In contrast to other approaches with reusable hardware components, the sensor patch can be used with commercially available masks [1-3] and is by design more robust and hygienic compared to devices placed within the mask [4-6]. The fixation on the outside of the filtering layers also opens the route for further hypothetical add-ons, e.g. sensors for CO_2 or other hazardous gases, to warn the user in an event of external threat.

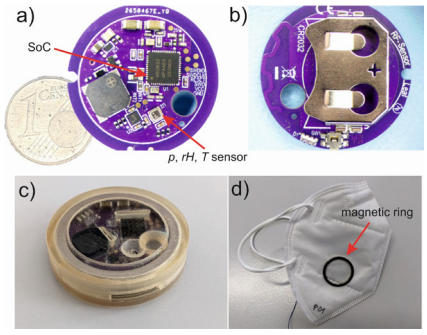

Fig. 1. Photograph of the a) top view and b) bottom view of the sensor patch. Red arrows mark the actual sensor and SoC, respectively. c) sensor patch in 3D-printed case with opening at sensor position. d) FFP2 mask with magnetic ring that fixates the patch from the outside. (Image Copyright: Fraunhofer IMM)

We test the device with respect to its capability to track the wear time and the fit quality of the mask for different users and under different conditions, like physical exercise, speech, etc.. We set up a suited algorithm that modifies and analyses the raw data under the constraints of being as time and power efficient as possible without losing sensitivity and selectivity.

Results and Discussion

While tracking mask wear time by signal modulation is straightforward, detecting the mask fit is rather challenging, as a defined leakage of about 2-3 mm reduces the efficacy of the mask significantly and must be detected by the sensors. User specific factors (tidal volume, physiognomy, physical activity, respiratory rate etc.) add further constraints. We test the sensitivity of the sensor patch when fixed on the outer layer of an FFP2 mask with different artificial leakages. We therefore punch holes of different diameter into the fleece and compare it to the best achievable fit with no intended leakage, i.e. zero leakage area. Figure 2 illustrates the effective pressure modulation Δp, where the ambient pressure, taken as a mean of intervals with a duration of Δt = 15 seconds, has been subtracted, for three leakage diameters, 0, 1 and 4 mm, respectively. The sampling rate is 20 Hz. In the example, the amplitude of the modulation decreases from about 50 Pa for the reference to about 30 and 25 Pa with increasing leakage area. Furthermore, the noise level of the measurement is between 5 and 10 Pa. A reliable statement on the fit quality therefore requires further data processing such as smoothing methods, treatment of outliers etc., as well as a (potentially) user-specific threshold value. We focus on the pressure signal since *rH* and *T* modulate less significantly once they reach equilibrium after a few minutes of wear time.

We record data sets from test subjects as they run through a predetermined performance profile on an ergometer. The acquisition time is 30 minutes. We split the datasets into intervals of 15 seconds, perform a smoothing and afterwards extract the signal stroke as well as the respiratory rate. Figure 3 shows the resulting correlation between both for a good (green circles) and bad (red diamonds) mask fit. Both datasets can be distinguished well by a threshold line (black dashed) that also accounts for the dependency of the signal stroke on the respiratory rate.

The proof of concept will be further discussed and tested with more and different subjects under different environmental conditions.

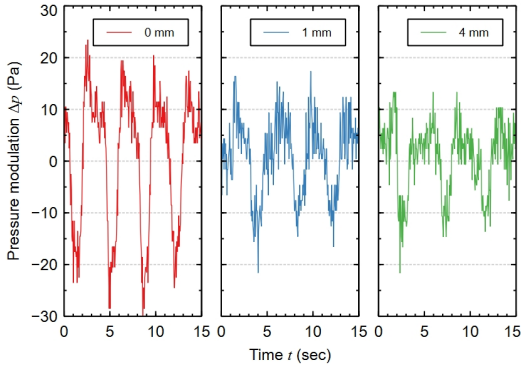

Fig. 2. Pressure signal minus the average (ambient) pressure for best achievable mask fit (0 mm) and two different artificial leakages (1 and 4mm) over a period of 15 seconds.

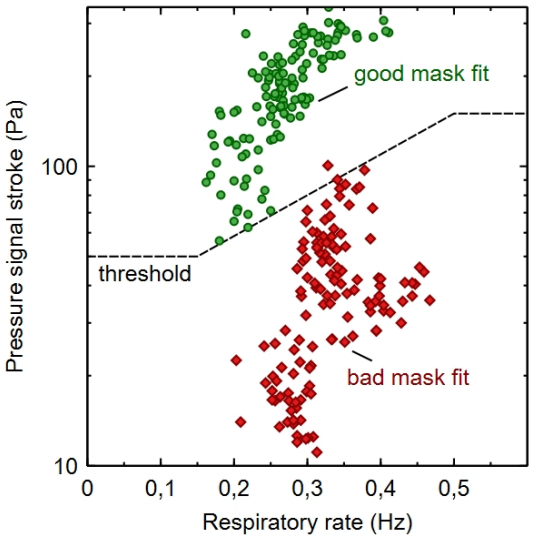

Fig. 3. Pressure signal stroke versus breathing frequency for a test subject having a good (green circles) and bad (red diamonds) mask fit. Each data point refers to a 15sec time interval of an overall acquisition time of 30 min. The dashed line marks a potential decision threshold.

References

[1] A. Fois, et al. , “Innovative Smart Face Mask to Protect Workers from COVID-19 Infection,” in 2021 IEEE MeMeA Symposium; doi: 10.1109/MeMeA52024.2021.9478739

[2] H. F. Fischer, et al., “Masquare: A Functional Smart Mask Design for Health Monitoring,” in 2021 Int. Symp. on Wearable Computers; doi: 10.1145/3460421.3478831

[3] J. Hyysalo, et al., *Internet of things* 18, 100511 (2022); doi: 10.1016/j.iot.2022.100511.

[4] Z. Ye, et. al., ACS nano 16, 5874 (2022); doi: 10.1021/acsnano.1c11041

[5] P. R. Priya, et al., IEEE Sensors J. 23, 13621 (2023); doi: 10.1109/JSEN.2023.3269388

[6] A. Curtiss, et al., Proc. ACM Interact. Mob. Wearable Ubiquitous Technol. 5, 1 (2021); doi: 10.1145/3494991

DOI 10.5162/SMSI2025/A3.4

Platform for the Development of Robust Magnetomotive Ultrasound Imaging Algorithms

Christian Heim[1], Christian Huber[2,3], Ingrid Ullmann[3], Helmut Ermert[2], Stefan Lyer[2], and Stefan J. Rupitsch[1]
[1] Department of Microsystems Engineering (IMTEK), Laboratory for Electrical Instrumentation and Embedded Systems, University of Freiburg, Georges-Köhler-Allee 106, Germany
[2] Department of Otorhinolaryngology, Head and Neck Surgery, Section of Experimental Oncology and Nanomedicine (SEON), Professorship for AI-Controlled Nanomaterials (KINAM), Universitätsklinikum Erlangen, Glücksstraße 10a, Germany
[3] Institute of Microwaves and Photonics (LHFT), Friedrich-Alexander-Universität Erlangen-Nürnberg, Cauerstraße 9, Germany
Christian.Heim@imtek.uni-freiburg.de

Summary:
In this contribution, we present a platform for the development and evaluation of Magnetomotive Ultrasound (MMUS) imaging algorithms for tissue mimicking materials. The presence of biological disturbances such as respiration or mechanical vibrations in in-vivo experiments interferes with MMUS imaging, which has to be considered for robust algorithm development. An electrodynamic shaker-based approach can be used instead of electromagnets to mimic magnetically induced displacements and biological disturbances to provide enhanced data for MMUS algorithm development and evaluation.

Keywords: Magnetic Drug Targeting (MDT), superparamagnetic nanoparticles (SPIONs), Magnetomotive Ultrasound (MMUS), local cancer treatment, ultrasound imaging.

Motivation

Magnetic Drug Targeting (MDT) with superparamagnetic nanoparticles (SPIONs) is an emerging cancer treatment method for a new local chemotherapy. A promising real-time imaging modality for monitoring the spatial distribution of SPIONs within tumorous tissue during the enrichment is Magnetomotive Ultrasound (MMUS) imaging [1]. A recent review of MMUS can be found in [2]. The basic idea behind MMUS is to induce mechanical displacements in the µm range within the SPION-laden tumorous tissue by using a time-varying magnetic excitation field. Over the past two decades, various magnetic excitation fields have been studied in tissue mimicking phantoms or in-vivo, including harmonic, pulsed, linear up-chirp, and frequency-shift keying [3]. An overview of phantom manufacturing can be found in [4]. However, the presence of biological disturbances such as respiration or mechanical vibrations in in-vivo experiments interferes with MMUS imaging. In order to include these additional disturbances in the development and evaluation of MMUS algorithms, we have realized an electrodynamic shaker-based platform, which allows the separate mechanical generation of magnetic excitation fields and different biological disturbances within a tissue mimicking phantom.

Experimental Setup

Common MMUS experimental setups require a very strong electromagnet to magnetically induce mechanical displacements in the µm range within a phantom. Without biological disturbances, only the internal SPION-laden tissue together with the surrounding tissue will move. Biological disturbances can instead be considered as global movement across both the SPION-laden and SPION-free tissue. Fig. 1 shows a schematic overview of the new MMUS platform. Internal movement can be generated using a shaker and a U-shaped element around the phantom and attached to the surfaces of the phantom parallel to the *xy*-image plane. Global movement can be mimicked by using another shaker to move an ultrasonic transducer. To reduce the complexity of in-vivo experiments to one-dimensional biological movements, the ultrasonic transducer can individually move either in *x*, *y* or *z* direction. Displacements are generated using two Tira TV 51110 vibration systems in combination with a Tektronix AFG3102 arbitrary function generator and are recorded using a Micro-Epsilon optoNCDT 1420 triangulation sensor. Ultrasound data is collected by means of an Ultrasonix SonixTouch ultrasound scanner in combination with a L9-4/38 ultrasonic transducer.

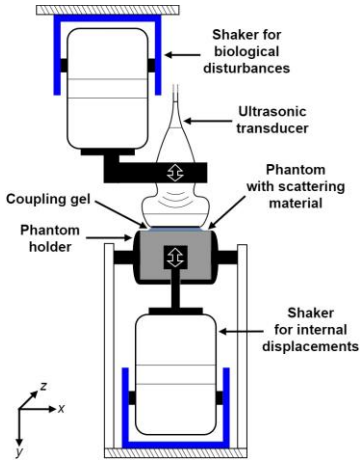

Fig. 1. Schematic overview of the platform for mimicking magnetically induced displacements and biological disturbances for MMUS experiments.

Experiment and Results

To demonstrate the working principle of the new development platform, we performed an experiment using a disturbed linear up-chirp and a MMUS algorithm explained in [5]. This MMUS algorithm uses a phased-based displacement estimator and cross-correlation filtering for each pixel. The excitation and disturbance generated by the shakers are shown in Fig. 2.

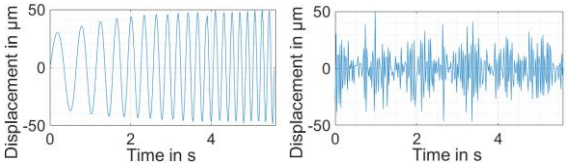

Fig. 2. Linear up-chirp excitation from 1 Hz to 6 Hz (left) and Gaussian noise disturbance (right).

The ultrasound imaging method selected was a clinically scanned B-mode with a center frequency of 6.6 MHz, 58 frames per second, mechanical index of 0.53, and thermal index of 0.37. Fig. 4 shows a B-mode image of the utilized phantom with scattering material. For comparison, a phase-based displacement estimation of a selected pixel with and without disturbance is depicted in Fig. 3.

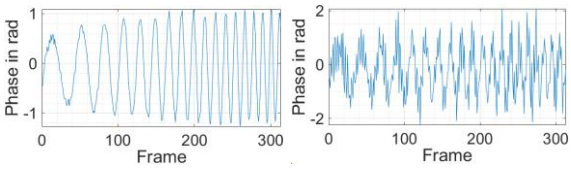

Fig. 3. Phase-based displacement estimation without disturbance (left) and with Gaussian noise disturbance (right).

The final MMUS image after evaluating each pixel for maximum displacement is illustrated in Fig. 4. It shows decreasing movement from the excitation through the surrounding area to the surface. The movement on the surface could be confirmed using the triangulation sensor.

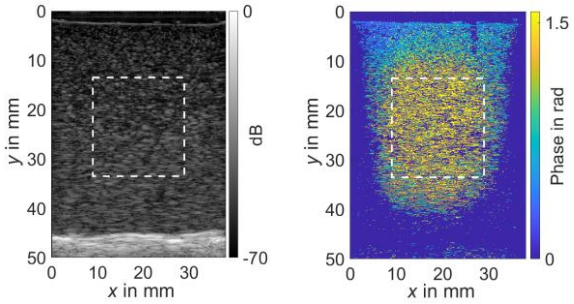

Fig. 4. B-mode image of utilized phantom (left) and MMUS image (right). The dotted box indicates the location of the attached U-shaped element.

Conclusion and Outlook

This contribution demonstrates a new shaker-based platform for MMUS algorithm development. It could be shown that one shaker allows mimicking very low internal displacements in the µm range, and that an additional shaker can be used to add disturbance on top. Finally, it was possible to mimic common MMUS setups and to perform MMUS imaging of disturbed internal displacement. This platform enables to study and develop new MMUS algorithms under new conditions. Future research will focus on different excitations and disturbances. In addition, an ultrasound-based method to determine the contours will be investigated to better differentiate between tumorous and healthy tissue.

References

[1] M. Fink, S. Rupitsch, S. Lyer, H. Ermert, In Vivo Study on Magnetomotive Ultrasound Imaging in the Framework of Nanoparticle based Magnetic Drug Targeting, *Current Directions in Biomedical Engineering* 6(3), 543–546 (2020); doi: 10.1515/cdbme-2020-3139

[2] K. Kubelick, M. Mehrmohammadi, Magnetic particles in motion: magneto-motive imaging and sensing, *Theranostics* 12(4), 1783–1799 (2022); doi: 10.7150/thno.54056

[3] M. Fink, S. Rupitsch, S. Lyer, H. Ermert, Quantitative Determination of Local Density of Iron Oxide Nanoparticles Used for Drug Targeting Employing Inverse Magnetomotive Ultrasound, *IEEE Transactions on Ultrasonics, Ferroelectrics, and Frequency Control* 68(7), 2482–2495 (2021); doi: 10.1109/TUFFC.2021.3068791

[4] C. Heim, C. Huber, H. Ermert, I. Ullmann, T. Saleem, S. Lyer, S. Rupitsch, Modelling and Construction of Complex Shaped Polyvinyl Alcohol based Ultrasound Phantoms for Inverse Magnetomotive Ultrasound Imaging, *Proceedings 22. GMA/ITG-Fachtagung Sensoren und Messsysteme 2024*, 313–318 (2024); doi: 10.5162/sensoren2024/D1.4

[5] M.Fink, H. Ermert, C. Alexiou, S. Lyer, Detection of Iron Oxide Nanoparticles for Local Chemotherapeutic Treatment Employing Coded Magnetomotive Ultrasound, *Proceedings Sensor 2017*, 323–328 (2017); doi: 10.5162/sensor2017/C2.2

DOI 10.5162/SMSI2025/A4.1

New opportunities in Revised SI: Traceable measurement quantities and improved uncertainties in small mass/force metrology

Suren Vasilyan[1], Vitalii Shmagun[1], Norbert Rogge[1], Thomas Kissinger[1], Thomas Fröhlich[1],
[1] Institute for Process Measurement and Sensor Technology, Technische Universität Ilmenau
Ehrenbergstraße 29, 98693 Ilmenau, Germany,
suren.vasilyan@tu-ilmenau.de

Summary:
The contribution discusses the new opportunities made possible by revised SI. On particular example of small force measurement (below 10 µN) the new traceability routes for the measurement quantities will be described. Additionally, the improvements deriving from the adopted new methodology will be shown. As a new concept adapted in small mass/force metrology the Photon Momentum method is employed. Thus, the traceability of the force measurements can be obtained in two complementary means. One, that is traceable via optical power detectors to quantum electrical standards, and the second one similarly, is traceable via Kibble balance principle using mass realization methodology to the quantum electrical standards. The Photon momentum method is especially advantageous to use for the small force calibrations below µN range where the dead weight force calibration method has already several limitations. E.g. during the calibration of small mass standards (to be used further for Force calibration) using conventional subdivision method the uncertainty of these masses grows, reaching a couple of percent level for masses below 0.1 mg.

Keywords: Photon momentum, small forces, small mass standards, optical power, traceability, quantum electrical standards, kibble balance,

DOI 10.5162/SMSI2025/A4.2

Novel Sensor Principle for High-Precision SI-Traceable Force Measurements

Martin Wittke[1], Mario André Torres Melgarejo[1], Matthias Wolf[1], Thomas Fröhlich[2], René Theska[1]
Technische Universität Ilmenau, Department of Mechanical Engineering, Ilmenau, Germany
[1]Institute for Design and Precision Engineering, Precision Engineering Group
[2]Institute of Process Measurement and Sensor Technology, Process Metrology Group
martin.wittke@tu-ilmenau.de

Summary:
Prior to 2019, force and mass measurements had to be traced back to the International Prototype Kilogram, which realized the SI unit kilogram. This definition required a long calibration chain with a series of relative mass comparisons. By setting Planck's constant to a fixed numerical value of $h = 6.626\,070\,15 \cdot 10^{-34}$ J s in the redefinition process, each instance of the calibration chain can now traceably measure absolute forces or masses. However, systems that provide a direct correlation between electrical and mechanical quantities are required. This work presents a novel sensor principle for high-precision SI-traceable force measurements. The sensor is based on the Planck Balance principle. Sub-mechanisms for compensating the stiffness of the compliant kinematic structure are integrated to maximize the resolution and minimize the uncertainty. The compensation mechanisms are based on preloaded springs to guarantee functionality in any orientation. The stiffness can be reduced to at least 0.04 % of the initial value. A force resolution below 40 pN is therefore achieved.

Keywords: force sensor, load cell, force measurement, electromagnetic force compensation, stiffness compensation, Planck Balance, SI, traceability

Introduction

Prior to 2019, the traceability of the SI unit kilogram had to be ensured via a long calibration chain back to the International Prototype Kilogram. By setting Planck's constant to $h = 6.626\,070\,15 \cdot 10^{-34}$ J s as a new SI reference, traceable measurements are open to all institutions independently. The sensor principle presented in this work offers a solution for force measurements in a wide field of precision engineering applications. It is based on the principle of a Planck balance and includes spring-based stiffness compensation mechanisms. Thus, the force resolution is increased and the measurement uncertainty is decreased independently of the orientation.

Methods

Planck Balance
The Planck Balance uses the compensation principle to determine the force F_M in Measurement Mode. The force is initiated translationally via a parallel spring guide, which is connected to a measurement lever by a coupling element. Once the force is applied, a position sensor measures the deflection of the lever. A controller processes the signal and energizes the electromagnetic actuator with the current i_{Ky} to keep the measurement lever in balance. To calculate the force F_M using equation (1), the actuator constant $B_{VC} \cdot L_{VC}$ needs to be determined.

$$F_M = i_{ky} \cdot B_{VC} \cdot L_{VC} \qquad (1)$$

The Velocity Mode is used for an in-situ calibration of the voice coil. A second actuator generates specific oscillations. The induced voltage $u_{ind}(t)$ in the voice coil is measured and synchronized with the velocity $v_{BC}(t)$ of the load carrier, which is determined using an interferometer. Therefore, equation (2) can be applied to calculate the actuator constant traceable to Planck's constant and the speed of light.

$$u_{ind}(t) = v_{BC}(t) \cdot B_{VC} \cdot L_{VC} \qquad (2)$$

Stiffness compensation
Due to the high motion reproducibility and negligible material friction, kinematic structures in precision applications are frequently designed as compliant mechanisms with concentrated compliances. However, even minimal hinge thicknesses of approx. 50 µm are still considerably limiting resolution and measurement uncertainty. Therefore, the residual stiffness needs to be compensated. Existing solutions use masses, magnets, or springs. Springs are advantageous since they work independently of their orientation and do not generate magnetic interference fields.

Sensor Principle

The novel force sensor principle (Figure 1) features the fundamental structure of the Planck balance. However, there is only one voice coil actuator. Investigations showed that a single actuator can be used to generate the oscillation for the Velocity Mode and to measure the induced voltage [1]. Spring-based stiffness compensation mechanisms [2] are integrated to compensate for the residual stiffness of the thin revolute joints. To eliminate static imbalances due to manufacturing-related position deviations of the joints and to prevent further function limitation [3], a double configuration of the mechanism is used. The Joints P_1 and

P_2 are purposefully displaced by the distance $\Delta_y P_n N_n$. The two compensation mechanisms thus generate two counter-directed moments about the lever joint H, which cancel each other out. The spring preload distances d_{Qx} can therefore be used to adjust the position d_{Ky} of the static equilibrium and simultaneously to reduce the stiffness to the target value.

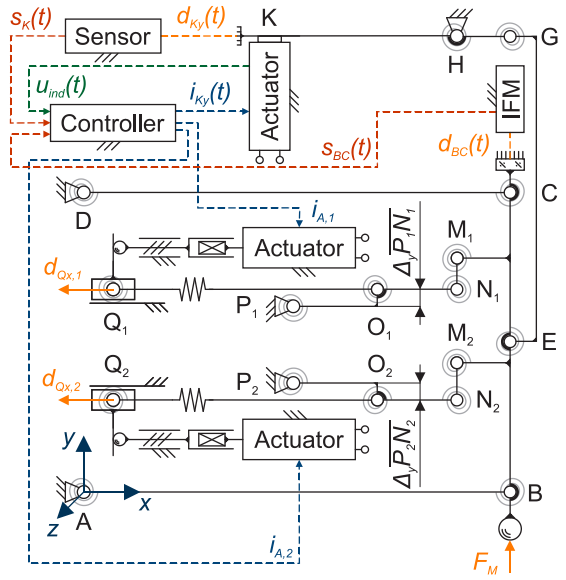

Fig. 1: Principle of the novel force sensor.

Simulation results

The kinematic structure was investigated using the rigid body model. The force-displacement diagrams are shown across the entire compensation range (Fig. 2) and around zero stiffness (Fig. 3).

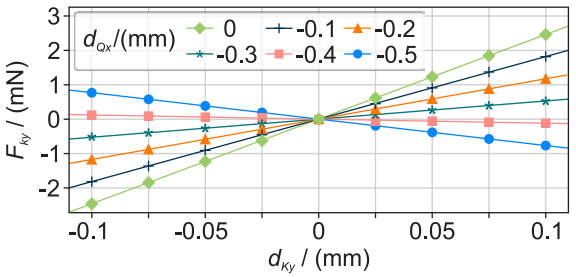

Fig. 2: Force-displacement diagram of the kinematic structure for a range from 0 mm to -0.5 mm for d_{Qx}.

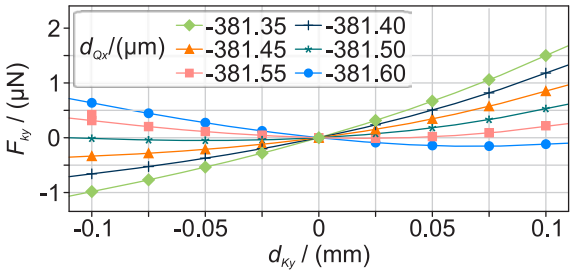

Fig. 3: Force-displacement diagram of the kinematic structure around zero stiffness for preload resolution steps of 50 nm for d_{Qx}.

Discussion

The results of the rigid body simulation confirm the feasibility of the principle. A reduction in stiffness is achieved by preloading the spring elements. There are linear correlations between the stiffness of the mechanism and the preload distance of the springs, as well as force and deflection. In the working range around zero stiffness, the force-displacement curve shows a slightly nonlinear behavior. For the considered configuration, the highest positive residual stiffness is achieved at d_{Qx} = -381.55 µm, if a preload adjustment resolution of 100 nm is assumed. The initial stiffness can thus be reduced from 24.61 N/m to $9.86 \cdot 10^{-3}$ N/m. With a position detection sensitivity of 1 nm at the operation point K and transmission ratio 4, forces F_M of 39.44 pN can be resolved.

Summary and Outlook

The redefinition of the SI unit kilogram allows every institution to perform directly traceable force and mass measurements. This paper presented a novel force sensor principle intended for precision engineering applications. It is based on the Planck balance using two spring-based mechanisms to compensate for the residual stiffness of the compliant kinematic structure. The principle theoretically allows a perfect stiffness reduction, practically down to at least 0.04 % of the initial value. The influences of critical manufacturing deviations are also eliminated by adjustment. The achievable force resolution is below 40 pN.
In future work, the complete kinematic structure will be designed as a compliant mechanism. All actuators and sensors will be specified and integrated into the system. The manufactured sensor will be put into operation and investigated experimentally.

Acknowledgment

The authors gratefully acknowledge the support of the Deutsche Forschungsgemeinschaft (DFG) within the framework of the Research Training Group “Tip- and laser-based 3D-Nanofabrication in extended macroscopic working areas” (GRK 2182) at the Technische Universiät Ilmenau, Germany.

References

[1] F. Hilbrunner, I. Rahneberg, T. Fröhlich, Wattwaage mit Hebelübersetzung auf Basis eines kommerziellen EMK-Wägesystems. *tm - Technisches Messen*, *85* (11), 658-679 (2018); doi: 10.1515/teme-2017-0065

[2] M.A. Torres Melgarejo, M. Wittke, R. Theska, Adjustable stiffness compensation for monolithic high-precision mechanisms, *Proceedings of the 22nd International Conference of the European Society for Precision Engineering and Nanotechnology*, 67-68 (2022)

[3] M. Wittke, M. A. Torres Melgarejo, M. Darnieder, R. Theska, Investigation of a novel monolithic stiffness-compensated mechanism for high-precision load cells, *Engineering for a changing world: Proceedings: 60th ISC, Ilmenau Scientific Colloquium, Technische Universität Ilmenau, September 04-08, 2023* (1.3.017). Ilmenau Scientific Colloquium. Technische Universität Ilmenau; 60 (Ilmenau): 2023.09.04-08. Ilmedia; doi: 10.22032/dbt.58735

DOI 10.5162/SMSI2025/A4.3

Effect of Helium Contamination on Rubidium Clocks – A Possible Error Source for Absolute Gravimeters and Kibble Balances

Christian Rothleitner, Johannes Konrad
Physikalisch-Technische Bundesanstalt (PTB), Bundesallee 100, 38116 Braunschweig, Germany
christian.rothleitner@ptb.de

Summary: When a Kibble balance is operated at highest accuracy level, often a Programmable Josephson Voltage Standard (PJVS) and a Free-Fall Absolute Gravimeter are located in the same room. The helium used in PJVS systems can evaporate into the laboratory air, potentially contaminating the rubidium clock used by the gravimeter. This contamination affects the absolute frequency of the clock and can lead to wrong measurements of the free-fall acceleration, and, as a consequence, wrong determination of the mass.

Keywords: Kibble balance, rubidium clock, frequency shift, mass determination, free-fall acceleration

Introduction

Since the re-definition of the SI unit kilogram in 2019, the Kibble balance [1] is one possible experiment to realize the unit at highest accuracy level. Because the Kibble balance compares the weight of a mass piece to an electro-magnetic force, the knowledge of the local acceleration due to free-fall (gravity) must be known to high accuracy. The accuracy of the most precise Kibble balances is at a relative level of 1×10^{-8}. For the force comparison a Kibble balance needs accurate timing, be it for velocity measurements or synchronization of data acquisition systems. Also, the absolute gravimeter requires accurate timing, as it measures the free-fall acceleration via laser interferometric length measurements, combined with accurate time stamps for all the measured positions along the free-fall trajectory. On the other hand, for measurements of voltage at the relative 1×10^{-9} level and better, a Programmable Josephson Voltage Standard (PJVS) is usually used in Kibble balance experiments. Those PJVS require liquid helium for cooling. An evaporation of some helium during operation or preparation of the measurement is unavoidable. The helium content in the laboratory room will thus increase, which can have significant negative effects on the frequency accuracy of a rubidium clock, as reported in the literature (see, e.g. [2]). Such clocks are usually used in free-fall absolute gravimeters, especially of kind FG5/X, from the company Microg-LaCoste, CO, USA. A helium-induced frequency shift has been observed and reported, e.g. in [3] or [4]. However, also for other components in the Kibble balance experiments, rubidium clocks can be used, e.g. for data acquisition systems or for the PJVS itself.
The Physikalisch-Technische Bundesanstalt (PTB), the German national metrology institute, is developing a compact Kibble balance, called *Planck-Balance* [5], for industrial applications. To this end, a PJVS is run in the laboratory of the Planck-Balance. At the same time, an FG5X gravimeter is located in the same lab room. Recently, we noticed a rapid increase in the absolute frequency of the rubidium clock, which is integrated in the FG5X, while a PJVS was in operation. In this short article, we report on the observed details.

Effect of Helium Contamination on Rubidium Clocks

The impact of helium on rubidium clocks is known among specialists. For example, in [3] or [4] this issue was reported for gravimeters. In [2] the authors investigated this effect systematically for different kinds of noble gases. Therein, it is stated that the effect is a result of the collisions of the Rb atoms with the noble gas atoms. In the case of He (as well as for Ne) atoms this shift is always positive, while for other noble gases (Ar, Kr, Xe) it is negative. Measured cross sections agree very well with a pseudo-potential model, as the authors reported. Thus, the effect can be theoretically predicted and quantified.

Observations in the Laboratory

In the Planck-Balance laboratory at the PTB we regularly perform measurements of the local free-fall acceleration with our free-fall absolute gravimeter FG5X-263, or we make investigations of it. For those measurements we usually either use PTB's $10\,\mathrm{MHz}$ signal that is provided via an optical fiber to our lab room, or we lock the gravimeter's rubidium clock to a GPS. For our Planck-Balance we also have a PJVS in the same lab, but during the last few months, the PJVS was not in operation, so that no helium dewar was in the lab.
End of October this year, for reasons of high-accuracy voltage measurements of the Planck-

Balance, the PJVS was prepared with a dewar of liquid helium. During this time the gravimeter was running as well, however, with the rubidium clock still locked to a GPS. After the gravimeter measurements were finished, the GPS was disconnected from the gravimeter, and in the following an increase of the absolute frequency was observed (see fig. 1). In the beginning, we assumed that the clock was broken, as the relative drift was on the order of $5 \times 10^{-10}\,\mathrm{d}^{-1}$, a rate that is very high, when compared to the clock specifications. Note that a positive relative bias of 5×10^{-10} in the clock frequency results in an error of $-1\,\mu\mathrm{Gal}$ (or 1×10^{-9} relative) in the measured gravity.

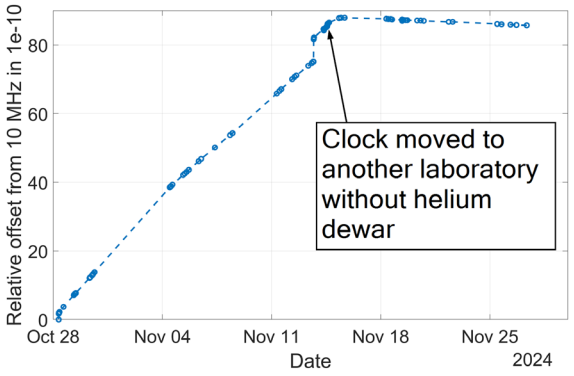

Fig. 1: The clock shows a rapid increase of its absolute frequency. The drift amounts to about $4 \times 10^{-10}\,\mathrm{d}^{-1}$. After the clock was moved to another room (see insert), the positive drift ceased, and a negative drift started, with an approximate rate of $-0.2 \times 10^{-10}\,\mathrm{d}^{-1}$.

Helium contamination was initially ruled out, as the dewar was connected to a silicone hose discharging the evaporated helium outside. It was assumed that this setup would prevent any significant helium concentration from accumulating in the room. But since the drift was positive, as the theory predicts, we decided to move the clock to another room to see if the effect diminishes or even reverses. In the following, first a further increase of the clock frequency was observed for one day, reaching a maximum of 87.9×10^{-10} of relative frequency offset (which is equivalent to a gravity error of about $-17.6\,\mu\mathrm{Gal}$– resulting in a relative error of 17.6×10^{-9} in a mass determination with a Kibble balance). After that a constant, but very slow decrease by about $2 \times 10^{-11}\,\mathrm{d}^{-1}$ set in, which is lasting since then. This fact suggests that the rubidium clock was not contaminated by a sudden surge, but that the helium diffused into the glass cell at a steady rate. Assuming a linear drop in frequency, it will probably take over a year for the frequency to return to exactly $10\,\mathrm{MHz}$. This rate, however, agrees quite well with a time constant of 90 to 100 days, as reported by [4]. For these reasons, we assume that the observed frequency deviation actually comes from the helium.

Conclusion

Although helium contamination-induced frequency shifts of rubidium clocks is known in clock community, and partly also in gravity community, it might not be well known to groups working on Kibble balances. In such experiments, the effect is of great importance, as usually in the same laboratory, where the mass is determined, a PJVS is operated with liquid helium. This cannot only introduce a bias in the gravity determination with the gravimeter, but also to the velocity determination of the Kibble experiment, when in this case also a rubidium clock is used. In our case, a two-week contamination of the rubidium clock by helium, with normal operation of a PJVS and a room size of approx. $90\,\mathrm{m}^3$, led to a relative frequency error of 87.9×10^{-10}. If this error were to be disregarded in a mass determination with the Kibble balance, the relative error in the mass determination would be around 17.6×10^{-9}, i.e. more than the combined measurement uncertainties of the best Kibble balances worldwide. Moreover, the real amount of evaporated helium can easily be underestimated, as some tests with a helium leak detector at our PJVS showed us. Taking into account that $1\,\mathrm{L}$ of liquid helium converts into $750\,\mathrm{L}$ of gaseous helium, a daily rate of realistic $3\,\mathrm{L}$ of liquid helium can occupy a non-negligible part of the lab room. Therefore, it is recommended to use clocks that are not prone to helium contamination, or at least discipline the rubidium clock by a GPS signal.

References

[1] I. A. Robinson and S. Schlamminger, “The watt or Kibble balance: a technique for implementing the new si definition of the unit of mass,” *Metrologia*, vol. 53, no. 5, p. A46, 2016.

[2] N. D. Zameroski, G. D. Hager, C. J. Erickson, and J. H. Burke, “Pressure broadening and frequency shift of the 5S1/2→ 5D5/2 and 5S1/2→ 7S1/2 two photon transitions in 85Rb by the noble gases and N2,” *Journal of Physics B: Atomic, Molecular and Optical Physics*, vol. 47, no. 22, p. 225205, 2014.

[3] J. Mäkinen, H. Virtanen, M. Bilker-Koivula, H. Ruotsalainen, J. Näränen, and A. Raja-Halli, “The effect of helium emissions by a superconducting gravimeter on the rubidium clocks of absolute gravimeters,” in *Third International Gravity Field Service (IGFS) General Assembly (IGFS 2014)*, (Shanghai, China), June 2014.

[4] D. Van Westrum, T. Bianchi, R. Bilson, B. Ellis, T. Niebauer, and H. Rohner, “The effect of helium conatamination on rubidium clock references in absolute gravity meters,” in *IAG Symposium on Terrestrial Gravimetry: Static and Mobile Measurements*, pp. 125–130, 2014.

[5] C. Rothleitner, J. Schleichert, N. Rogge, L. Günther, S. Vasilyan, F. Hilbrunner, D. Knopf, T. Fröhlich, and F. Härtig, “The Planck-Balance—using a fixed value of the Planck constant to calibrate E1/E2-weights,” *Measurement Science and Technology*, vol. 29, no. 7, p. 074003, 2018.

DOI 10.5162/SMSI2025/A5.1

Low-Cost Acoustic Measurments by Calibration of Consumer Grade Hardware

Felix Huber, Florian Toth
Institute of Mechanics and Mechatronics, TU Wien, Getreidemarkt 9, 1060 Vienna, Austria
felix.huber@tuwien.ac.at

Summary: Multiple sensors with excellent linearity and high precision are often necessary to investigate acoustic problems (e.g., beamforming, impedance tube, spacial decomposition). This paper explores a flexible acoustic measurement system consisting of low-cost consumer-grade hardware. A MEMS capsule is paired to a P48-compatible pre-amplifier to form the microphone, which can then be used with off-the-shelf microphone amplifiers and converters available from the consumer or pro audio industry. Because the converters use widely available protocols like ASIO, CoreAudio, and others, an open-source Python module can be used to conduct the measurements. The acoustic measurement system is first calibrated and then evaluated at each stage to examine its performance and find its weaknesses to be explored by future research.

Keywords: Acoustics, Microphone, Low-Cost, Calibration, Measurement

Motivation

Acoustic measurements demand a precise and frequency-independent measurement chain, starting from the electro-acoustic transducer over several signal conditioning and amplification stages, to finally reach AD conversion. Due to the trend towards integration, the MEMS microphone was established as a low-cost and better performance alternative to the standard integrated FET capsules [1]. There were previous attempts to use MEMS capsules in high-precision measurement [2]. They still lag behind in frequency response and noise, but the gap is narrowing [3]. The steady consumerization trend has made high-quality converters and amplifiers widely available and affordable, especially in the consumer and pro audio industry. Of course, the low price has disadvantages like missing specifications, no user support for measurement purposes, and no specialized software.

The low-cost alternative

With the motivation of a decentralized hardware and software approach and the inclination toward open-source projects, this paper assesses a complete audio measurement chain using only cheap and widely available resources. The proposed framework consists of a MEMS microphone capsule, the Infineon IM73A135. The centerpiece of the proposed measurement chain is an in-house developed pre-amplifier, signal- and power-conditioner circuit [4], enabling the connection between the capsule output and the interface input with P48 power supply [5]. The RME Fireface UFX+ is used as a microphone amplifier, power supply, and converter, offering up to 24bit depth and 192kHz sample rate. Due to the use of widely available audio protocols like ASIO on Windows or CoreAudio on MacOS, the list of compatible software is extensive and includes many open-source options. The measurement software used in this paper is the ASMU Python package [6]. It is an audio framework for sound measurement and manipulation purely written in Python and offers great flexibility for simple measurement tasks. Due to the pure Python implementation, integration in post-processing code is nearly effortless. All measurements for this paper are conducted with the described setup.

Measurement and Results

Before the measurements, the audio interface inputs are calibrated. We use a sine generator ($1\,\mathrm{kHz}$, $1\,\mathrm{Vp}$) and connect it to the audio interface input. A high-precision multimeter (Keithley 2000) is used to measure the input voltage, and due to the grounding of the generator, a $50\,\Omega$ resistor provides pseudo balancing (Fig. 1a). This calibrated input is now used to calibrate the outputs of the interface (Fig. 1b) by again using a $1\,\mathrm{kHz}$ sinusoidal signal. A microphone calibrator (B&K Type 4231) is used to calibrate the acoustics by prescribing a known sound pressure to the capsule for the microphone connected, as shown in Fig. 1f. This is done for the low-cost microphone and a reference microphone (B&K Type 4190).

We first evaluate the linearity of the interface's outputs and inputs. Therefore, we create a loopback connection (Fig. 1c) called LOOP. The interface is used to excite a pink noise signal while simultaneously recording it. Fig. 2 shows the latency-adjusted voltage transfer function of the

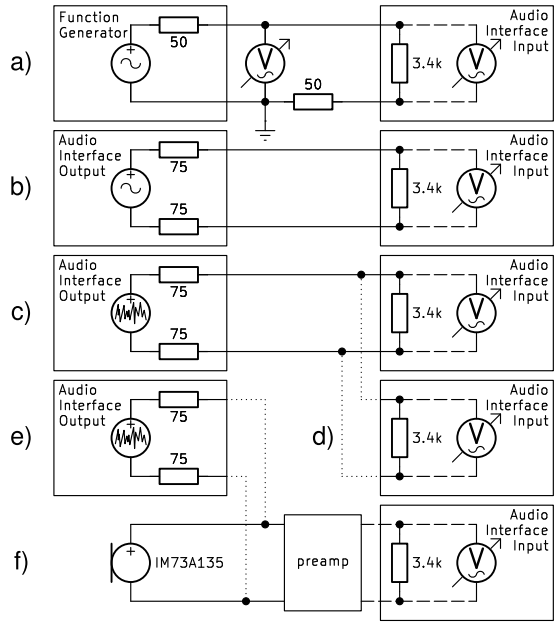

Fig. 1: Connection for input (a) and output (b) calibration. Measurement setups for loopback (c), channel mismatch (d), pre-amplifier (e), and acoustic measurements (f).

ideal and recorded signal. Additionally, we compute the input mismatch by comparing two inputs connected in parallel (Fig 1d). The $0.6\,\mathrm{dB}$ offset is explained by the active balancing circuit inside the interface, which exhibits different gains for balanced and unbalanced connections and by the changed generator impedance. Besides that the results show a frequency response from $6.3\,\mathrm{Hz}$ to $63\,\mathrm{kHz}$ within $0.5\,\mathrm{dB}$ deviation.

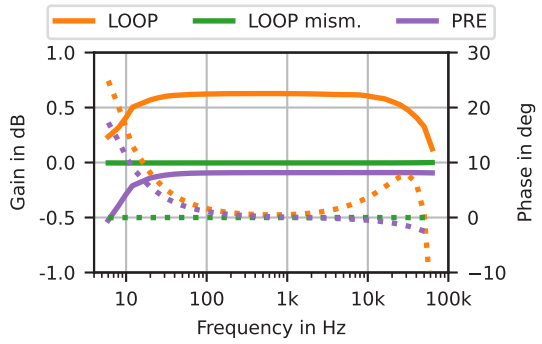

Fig. 2: Voltage frequency responses for the loopback (LOOP), channel mismatch (LOOP mism.), and pre-amplifier (PRE) measurements.

The pre-amplifier (PRE) is tested by inserting it into the discussed loopback connection (Fig. 1e) and again computing the voltage transfer function. The results in Fig. 2 show excellent linearity over the entire frequency range, with an expected highpass behavior due to internal coupling capacitors. The two microphones (low-cost and reference B&K) are placed membrane to membrane in an anechoic chamber, with a broadband speaker at $1\,\mathrm{m}$ distance. The speaker is calibrated (through the reference microphone) to excite a pink noise signal at $94\,\mathrm{dB}$. We finally compute the pressure transfer function between the two microphones and plot them over the frequency in Fig. 3. The results are characterized by a low-frequency drop and a significant rise in gain above $10\,\mathrm{kHz}$. The MEMS capsule frequency characteristics cause this behavior, which closely corresponds with the datasheet.

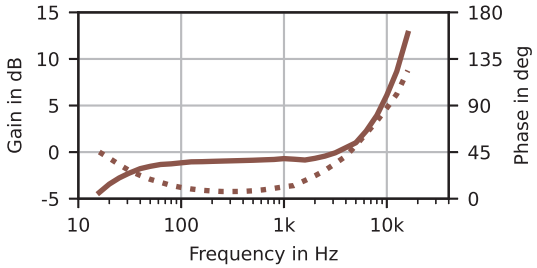

Fig. 3: Acoustic pressure frequency response between the low-cost MEMS microphone and the reference B&K Type 4190 microphone.

Summary and Outlook

The tested system shows outstanding electrical performance over a wide frequency range. Deploying the developed microphone for measurements below $10\,\mathrm{kHz}$ seems feasible. To overcome this limitation, the setup can be readily modified to accommodate newer, more linear MEMS capsules.

References

[1] P.R. Scheeper, A.G.H. Van der Donk, W. Olthuis, P. Bergveld, A review of silicon microphones, *Sensors and Actuators A: Physical* 44(1), 1-11 (1994); doi: 10.1016/0924-4247(94)00790-X

[2] A. Prato, N. Montali, C. Guglielmone, A. Schiavi, Pressure calibration of a digital microelectromechanical system microphone by comparison, *The Journal of the Acoustical Society of America* 144(4), EL297–EL303 (2018); doi: 10.1121/1.5059333

[3] S.A. Zawawi, A.A. Hamzah, B.Y. Majlis, F. Mohd-Yasin, A Review of MEMS Capacitive Microphones, *Micromachines* 11(5), 484 (2020); doi: 10.3390/mi11050484

[4] F. Huber, F. Toth, MEMS measurement microphone compatible to P48 amplifiers, *OSF* (2024); doi: 10.17605/osf.io/p5vjt

[5] Multimedia systems - Guide to the recommended characteristics of analogue interfaces to achieve interoperability, 61938, *IEC*, (2018)

[6] felhub, Acoustic Signal Measurement Utilities, *PyPI*, Accessed: Nov. 27, 2024.

DOI 10.5162/SMSI2025/A5.2

Electro-acoustic Properties of Li(Nb,Ta)O_3 Solid Solutions in Harsh Environments

F. El Azzouzi[1], U. Yakhnevych[1], Y. Suhak[1], H. Schmidt[2], S. Ganschow[3], S. Sanna[4], H. Fritze[1]
[1]

[1] Technische Universität Clausthal, IEPT, Am Stollen 19 B, D-38640 Goslar, Germany
[2] Technische Universität Clausthal, IMET, Robert-Koch-Str. 42, D-38678 Clausthal-Zellerfeld
[3] Leibniz-Institut für Kristallzüchtung, Max-Born-Straße 2, 12489 Berlin, Germany
[4] Justus-Liebig-Universität Gießen, Heinrich-Buff-Ring 16, 35392 Gießen, Germany

Summary:
The prospects of lithium-niobate-tantalate solid solutions ($LiNb_{1-x}Ta_xO_3$, LNT) for high-temperature sensors and actuators are presented from a physical and materials science perspective. The focus lies on defect mechanisms that are relevant for the acoustic losses that determine potential applications of such crystals at high temperatures. Further, tailoring of the materials properties by variation of the niobium-tantalum ratio is demonstrated.

Keywords: Lithium-niobate-tantalate solid solutions, ionic and electronic conductivity, high-temperature, oxygen partial pressure, defect models

Introduction and Motivation

Resonant sensors offer advantages for multiparameter in-situ monitoring and control of industrial processes. In particular, there is an increasing need in sensitive, robust and cost-effective sensors for gas composition, temperature and pressure for the application in harsh environments. Thereby, piezoelectric crystals offer the advantage that they can be directly excited to oscillate by applying a voltage of appropriate frequency. Changes in environmental conditions are directly transferred to frequency changes, which is feasible at very high temperatures with materials such as lithium niobate-lithium tantalate (LNT).

Moreover, LNT represents a piezoelectric material which combines high piezoelectric coefficients, low acoustic loss, and thermal stability which are crucial for the development of high-temperature sensors and actuators.

Objectives

LNT solid solutions are used as model system with the aim of exploring the correlation of defect structure, electronic and ionic transport, and electromechanical properties in polar oxides.

The specific aim of this presentation is to present and interpret the high-temperature electromechanical properties and, in particular, the acoustic losses in bulk LNT at high temperatures. Further, materials data required for modelling such as the temperature dependent piezoelectric coefficient should be determined.

Piezoelectric Resonators

LNT crystals grown by the Czochralski technique [1] are cut into circular disks, polished and, if required, coated with Pt-based electrodes. Such a device and a schematic profile of resonant mechanical displacement is shown in Fig. 1.

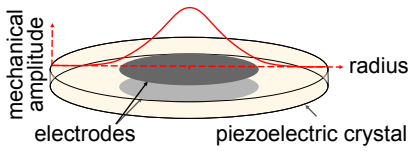

Fig. 1: Piezoelectric resonator with metal electrodes and displacement profile.

Results and Discussion

Crucial high-temperature properties of LNT solid solutions such as bulk conductivity as well as acoustic losses were determined as a function of temperature and oxygen partial pressure (p_{O2}) and correlated with the atomistic transport processes.

Above 400°C, the acoustic losses are governed by the relaxation of piezoelectrically excited charge carriers and thus the electrical conductivity [2]. Fig. 2 shows the related loss peak at about 850 °C.

Below this temperature, the losses decrease and reach values that correspond to that of phonon scattering. The electronic conductivity tends to be suppressed by high Ta contents, which becomes apparent above 600°C and allows a

reduction in losses. High mechanical resonance frequencies also lead to a reduction in losses, so that small structures or even thin films are desirable.

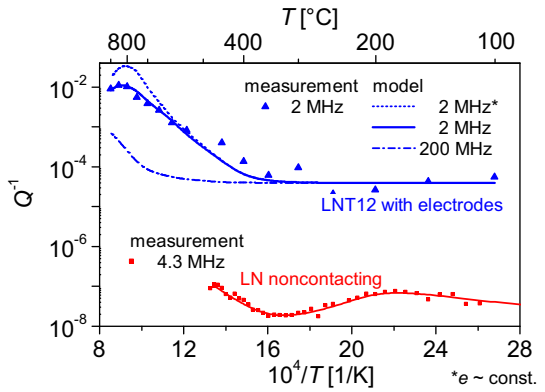

Fig. 2: Total losses of LN and $LiNb_{88}Ta_{12}O_3$ (LNT12) resonators with different composition determined with and without contacting metal electrodes (points) and modelling including variation of the operating frequency (lines).

To enable modeling of the losses, for example, the temperature dependent piezoelectric coefficient has been determined, see Fig. 3.

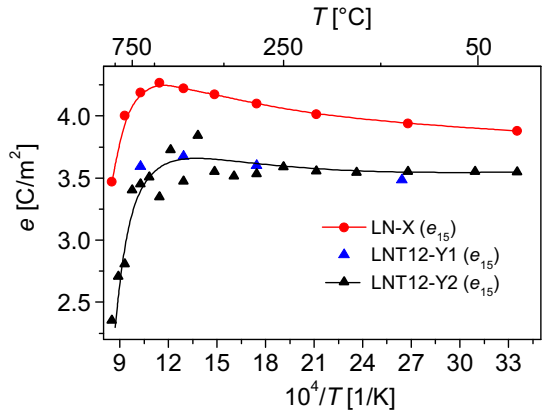

Fig. 3: Piezoelectric coefficient e_{15} for LN and $LiNb_{88}Ta_{12}O_3$ (LNT12) as a function of temperature [3].

Further, the p_{O2} dependence of the conductivity has been measured. It can be explained by a defect mechanism that is not linked to the unwanted evaporation of Li_2O. Fundamental findings, such as the unexpectedly strong change in the activation energy of the electrical conductivity at the transition between the ferroelectric and paraelectric phase, are now also discussed [4,5].

Conclusions

Extraction of materials data using a one-dimensional physical model for piezoelectric resonators together with atomistic models enables to identify the piezoelectric/carrier relaxation as the dominating loss mechanism at high temperatures.

Based on the results, the LNT system is seen as a platform for the development of novel high-tech components for resonant sensors, micro-actuators, integrated acoustics and photonics as well as quantum technologies even at high temperatures. The results can be transferred to other material systems such as multiferroics and perovskite-related materials.

Acknowledgements

The Deutsche Forschungsgemeinschaft (DFG, German Research Foundation) is gratefully acknowledged for financial support within the research unit FOR5044 *Periodic low-dimensional defect structures in polar oxides*.

References

[1] U. Bashir, K. Böttcher, D. Klimm, S. Ganschow, F. Bernhardt, S. Sanna, M. Rüsing, L. M. Eng, M. Bickermann, Ferroelectrics 613 (2023) 250.

[2] U. Yakhnevych, V. Sargsyan, F. El Azzouzi, A. Kapp, F. Bernhardt, Y. Suhak, S. Ganschow, H. Schmidt, S. Sanna, H. Fritze, Phys. Status Solidi A (2024) 2400106.

[3] F. El Azzouzi, D. Klimm, A. Kapp, L. M. Verhoff, N. A. Schäfer, S. Ganschow, K.-D. Becker, S. Sanna, H. Fritze, Phys. Status Solidi A (2024) 2300966.

[4] C. Kofahl, L. Dörrer, B. Muscutt, S. Sanna, S. Hurskyy, U. Yakhnevych, Y. Suhak, H. Fritze, S. Ganschow, H. Schmidt, Phys. Rev. Mat. 7 (2023) 033403.

[5] U. Yakhnevych, F. E. Azzouzi, F. Bernhardt, C. Kofahl, Y. Suhak, S. Sanna, K. D. Becker, H. Schmidt, S. Ganschow, H. Fritze, Solid State Ionics 407 (2024) 116487.

DOI 10.5162/SMSI2025/A5.3

A Compact, Cost Efficient, Modular, Intelligent Ultrasound Sensor Platform

Wolfgang Bost[1], Christian Grandinetti[1], Holger Hewener[1], Steffen Tretbar[1]
[1] Fraunhofer Institute for Biomedical Engineering IBMT, 66280 Sulzbach, Germany
wolfgang.bost@ibmt.fraunhofer.de

Summary:
We developed and evaluated a new modular concept for a modern compact ultrasound sensor platform. The hardware is designed as an inexpensive, matchbox-sized set of components that can be easily combined and configured for a wide range of applications including mobile and distributed technical or wearable biomedical ultrasound. The modular concept and flexible software architecture allows the adaptation to new applications with a short time to market and will be applied in distributed sensor networks including edge-AI based processing in the future.

Keywords: modular ultrasound device, artificial intelligence, networked system, flexible handheld device, cost efficient

Background, Motivation an Objective

Ultrasound (US) measurement technology is comparatively inexpensive, real-time capable, non-invasive and a flexible method used commercially in the medical and industrial applications. In both fields there is still great potential for application specific and dedicated ultrasound sensor systems including an automated signal analysis and classification using artificial intelligence. Using ultrasound measurements, material properties can be examined non-destructively as well as flow speeds, distances or fill levels of solids or liquids. Based on the objects being examined, application-specific solutions with adapted ultrasound transducers, transmit/receive electronics and signal analysis must be developed to match the individual requirements. Therefore, ultrasound systems with different levels of integration and complexity are available often realized as a dedicated solution tailored to a single or only a few applications. This circumstance makes these systems inflexible to match new requirements for slightly adapted use-cases or new product variations, results in high development costs and a relatively long time-to-market when transferring ultrasound technology to new fields of application. We developed a flexible ultrasound system and software architecture based with a modular design to realize innovative solutions and products in a wide range of applications with a low time-to-market.

Materials and Method

Our single channel system “SonoOne” is designed to be cost-efficient and modular. Based on a set of many different modules, a sensor system can be set up and configured depending on the application and requirements. A basic system configuration consists of 4 modules (see figure1):

1. A basic ultrasound electronics module for generation of US-transmission signals and digitization
2. A Communication interface module including wired (USB, Serial, …) and wireless data transfer via WiFi to mobile devices or a central server infrastructure.
3. Power supply module for the common supply low voltages.
4. A High voltage power supply module for the generation transmission signals (bipolar excitation of the transducer using a tri-state transmit pulser that can be arbitrary programmed allowing coded excitation).

The size of each PCB module is 50mm x 30mm. The modules can be flexibly configured via standardized hardware and software interfaces. In addition to those standard modules, the modular stacked design allows the usage of application specific extensions. An OLED display stack has been developed to be used on top of the stack to show important status information or measurement results. Another extension module allows a battery-powered and mobile usage by integrating a Li-Ion battery module and a charging circuit. Future modules can extend the SonoOne module stack by data storage modules integrating flash memory or storage cards to record data during long-term

measurements or hybrid sensor modules integrating other measurement modalities.

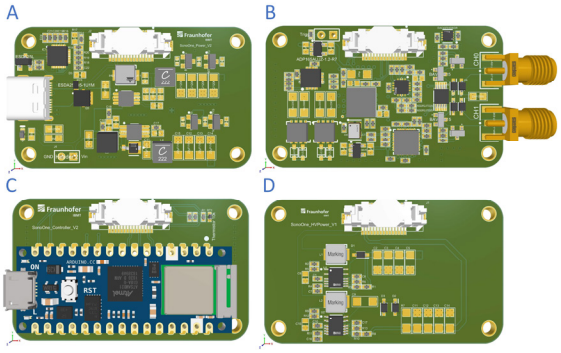

Fig. 1. 3D PCB Layout of the 4 basic modules (low voltage supply (A), US-module (B), control unit (C), high voltage supply (D))

Multiple of those ultrasound system stacks will be combined to form an intelligent sensor network via a wireless interface and data will be shared between the sensor systems. Currently, the communication module implements a standardized communication protocol for data transfer to a mobile device (i.e. a laptop) and the SonoOne hardware to connecting to a local WiFi infrastructure. This way, SonoOne is prepared to realize a distributed sensor network for larger scale measurement tasks in industrial setups.
The specification of the basic system configuration is listed below.

Tab. 1: System specification

power supply	5 VDC		Rx gain	0-50 dB
Tx voltage	up to 200 Vpp		Rx sampling rate	40 MHz / 80 MHz
Tx clock	80 MHz		ADC resolution	12 bit
Tx frequency	20 kHz - 10 MHz		samples per measurement	6600

Evaluation of the System

For evaluation of the System, several integration concepts including custom housing and mounting options for various applications (object detection in water, air or liquid flow measurements) have been realized. The basic configuration achieves an interactive wireless communication with repetition rate of approx. 25 Hz (using 2048 samples per measurement) transferring the digitized ultrasound raw data via WiFi to the connected PC/backend where storage and analysis with additional processing of the data can been performed. In combination with custom in-house developed wedge transducers, the flow of water in a pipe could be measured with high accuracy. Compared to a commercially available system, a flow of 500 l/min could be detected with an accuracy matching the commercial magnetic-inductive flow meter system (KROHNE Altometer SC 100 AS). Another demonstrator integrated a mobile air-coupled ultrasound measurement system using commercial 40 kHz ultrasound transducer capsules that provides not only distance information but radio-frequent raw ultrasound wave data for further analysis in new applications.

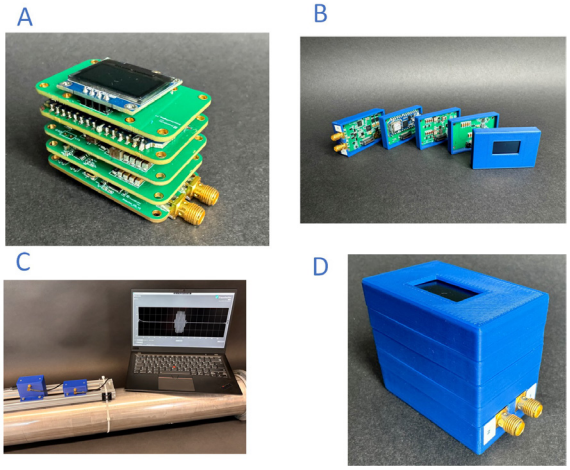

Fig. 2. Assembly of different prototypes (stack of all 5 developed modules (A), integrated in a 3D printed housing (B), integrated together with a Li-Ion battery (D), combined with in house developed transducers for clamp on flow measurements (C)

Results

The implementation of a modular circuit board concept into an application specific measuring system for gaseous, liquid and solid media was successfully realized and evaluated. A new technology platform for industrial applications has been implemented and can be adapted / extended easily. The developed modules are a basis for new product development in the context of cost-effective, intelligent and networked medical and industrial products.

Outlook

A main advantage of the modularity is that future technological leaps in individual components (efficient energy storage, new radio standards, new materials for ultrasonic sensors, improved manufacturing technologies in electronics and enhanced analysis algorithms) can be directly exploited by replacing the corresponding module without having to redesign the entire electronic unit, thus forming the basis for completely new applications, especially in the area of industry, medicine or sports. Automated intelligent evaluation processes can be carried out both in a cloud network or as Edge AI with integrated data processing capacity.

DOI 10.5162/SMSI2025/A5.4

Ultrasonic phased array interface using programmable I/O and microprocessor clock synchronisation

Tom Nellius[1], Kevin Henne[1], Maximilian Hartinger[1], Lars Meihost[1], Tim Hetkämper[1], Henning Zeipert[1], Leander Claes[1], and Bernd Henning[1]
[1]Measurement Engineering Group, Paderborn University, Paderborn, Germany
meihost@emt.uni-paderborn.de

Summary: This contribution constitutes an approach to ultrasonic phased array excitation using programmable input/output banks for fast, digital signal generation, a method to synchronise a number of microprocessors and a minimalistic analogue frontend. Exploiting the low-pass characteristic of the array's transducers, it is assumed sufficient to apply a binary signal to each element. These signals are generated synchronously by state machines implemented in hardware, a feature present on some microcontrollers designated as programmable input/output. To increase the number of channels, the clock of a number of microcontrollers is synchronised using a phase detection circuit. A digital-input MOSFET low-side driver circuit is used for each channel to amplify the digital signals. Synchronous signal generation for a 64-element array is demonstrated using schlieren imaging.

Keywords: Clock synchronisation, Interface, Programmable I/O, Signal generator, Ultrasonic phased array

Motivation

Controlling ultrasonic phased array systems commonly requires complex, specialised, multichannel hardware. Especially when many elements are to be excited simultaneously, an equal number of amplifiers and signal generators is required, increasing hardware size and costs. For an efficient, robust implementation, it is thus advantageous to minimise the hardware required for each channel. To facilitate this, it is assumed sufficient to drive the elements of the array with binary signals, taking advantage of their low-pass characteristics. If the binary signal can be modulated with sufficient frequency, coded signals can be used to generate arbitrary signals after the low-pass filtering. This circumvents the necessity of a large number of digital-to-analogue converters. Binary signals can further be generated using general-purpose outputs of microcontrollers, which are available on nearly every pin of a microcontroller, compared to digital-to-analogue converters.

The aim is to drive a 64-element array with up to 5 MHz. Nevertheless, the critical parameter is not the signal frequency itself, but the time delay possible between the different transducer signals. This delay is needed to perform beam steering and/or focussing [1]. Thus, to have fine-grained control, it is desirable to have an output switching frequency as high as possible, ideally the system's clock. This does not apply to most microcontrollers. However, some microcontrollers (e.g. RP2040, *Raspberry Pi Foundation*, [2]) are equipped with hardware state machines, which can be connected to the output pins. This feature is called programmable input/output and enables independently switching a number of outputs with up to the system's clock frequency. Currently, available microcontrollers with programmable input/output do not provide a sufficient number of outputs to provide signals for 64 elements. It is thus necessary to realise an external clock synchronisation of a number of microcontrollers. Further, the output current of the microcontrollers is insufficient to drive the elements of the array. The behaviour of each element can be approximated by a capacitance, requiring a fast driver circuit for capacitive loads.

Implementation

The RP2040 microcontroller used to implement the phased array interface includes programmable input/output with eight parallel hardware state machines. Each state machine is fed by two first-in-first-out (FIFO) registers and can be run with frequencies up to the system clock (133 MHz) [2]. To output binary signals to the phased array, the desired binary sequences are generated by a personal computer, transferred to the microcontroller, and stored in the controllers RAM to be transferred into a FIFO-register on data request. A specialised instruction set is used to program these state machines, with each instruction requiring a single cycle to execute. The instruction set includes an instruction to pull values from the FIFO-registers and write them to the output pins:

```
.program fifo_to_out_pin

loop:
    pull
    out pins, 16
    jmp loop
```

The `pull` instruction transfers a 32 bit word from the FIFO-register to an intermediate register called output shift register (OSR). The `out` instruction writes the first 16 bit of the word in the OSR to 16 pins determined by the controller's configuration and the `jmp` instruction resets the program counter to the beginning of the `loop` block. The programmable input/output functionality can also be configured to perform this operation in a single instruction using a feature called *autopull* and by configuring the state machine to handle the loop automatically, rendering the *pull* and *jmp* instructions obsolete. Programmable input/output is also used to trigger the state machines to start

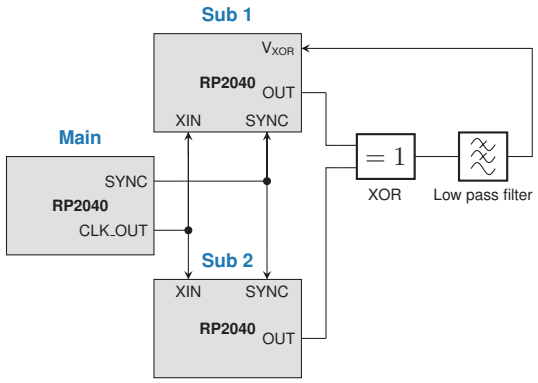

Fig. 1: Synchronisation setup with XOR phase detection between two microcontrollers.

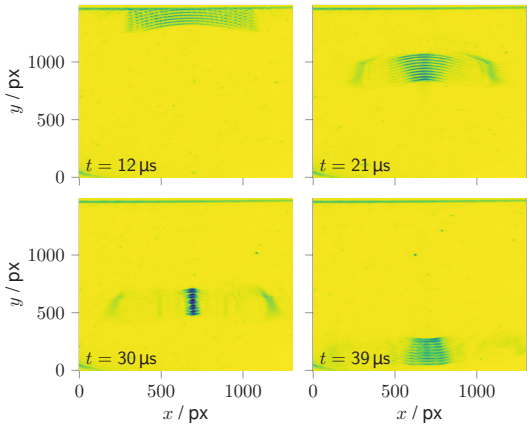

Fig. 2: Schlieren images showing the emission of the array focussing acoustic waves to a given point.

outputting the signals. On the RP2040, 30 pins are available. With one pin used as a trigger input, 29 pins are available to output signals. For the presented application, the signals for 16 channels of the array are generated by a single controller.

To implement the required number of channels four microcontrollers are used, which need to operate synchronously. The microcontroller at hand provides a pin designated XIN, which is directly linked to the system's internal phase-locked loop (PLL). To validate the synchronicity of two XIN-synced controllers, a periodic signal (SYNC) is applied to all controllers and replicated using programmable input/output at the OUT pins, see Figure 1. If the two controllers are synchronised their generated output would be identical, but a comparison shows a phase-shift (up to $\pm 1/2$ clock period) between the generated signals. This phase-shift, possibly caused by the post-dividers of the PLL, is generated at random during the initialisation process. For the quantification of the phase-shift an XOR-gate with analogue low-pass filter at the output is utilised. The output of this circuit is at high-level if both input signals are complementary and low-level if they are identical. Hence, while observing this output of the phase-detection circuit with an analogue-to-digital converter at V_{XOR}, one controller's PLL is reset until the phase-shift is (close to) zero. On average, this synchronisation process is completed under 1 s. As this clock synchronisation only needs to be carried out when powering up the array interface, it is considered sufficiently fast.

The current at the output of the microcontrollers is insufficient to drive the elements of the array. A minimalistic driver circuit is developed based on a low-side gate driver integrated circuit (UCC27517A-Q1, *Texas Instruments*). These integrated circuits (IC) are designed to drive the gates of large MOS transistors with high frequency signals and are thus particularly suited to drive other capacitive loads, such as piezoelectric elements of a phased array. The specific IC used here also provides a digital input u_{in} that can be directly connected to the output pin of a microcontroller. A supply voltage U_0 of 18 V is used, which defines the high level output voltage and thus the voltage at the elements of the array Z_{load}. No further active or passive components are required, however it is advisable to buffer the supply voltage U_0 with sufficiently large capacitances (220 nF) for each channel. The only circuit components that are required for each channel of the interface are thus the low-side gate driver and a single capacitor, leading to a minimalistic realisation of the array driver circuitry.

Evaluation

To evaluate the performance of the array interface, a 64-element phased array by *Imasonic* is used to excite acoustic waves in water. The resulting acoustic emission is visualised using schlieren imaging [3]. As an example application, a binary burst signal (10 Periods) with a frequency of 1 MHz is applied to the array. The delay times between the elements are chosen to focus the waves to a point with a distance of 30 mm in front of the array's surface. Figure 2 shows that the developed interface is able to generate the signals according to the specification and realise a successful focussing. Other beam-forming methods, such as a directed emission of planar waves with a given angle, are also evaluated successfully.

Conclusions

An interface to generate arbitrary, binary signals for a 64-element phased ultrasonic array is realised using four clock-synchronised microcontrollers and programmable input/output logic. No specialised analogue components or reconfigurable logic devices (FPGAs) are required. The presented approach can be extended to arrays with a higher number of elements by increasing the number of controllers or using an updated version (RP2350B, *Raspberry Pi Foundation*), which provides 48 programmable outputs. Future work will include an extension for simultaneous signal acquisition to realise full ultrasonic imaging capabilities.

References

[1] S. J. Rupitsch, *Piezoelectric sensors and actuators: fundamentals and applications*. Berlin: Springer, 2019, ISBN: 9783662586013.

[2] *RP2040 datasheet*, Raspberry Pi Ltd, 2021.

[3] T. Hetkämper, K. Koch, *et al.*, "Phase-preserving methods to visualise ultrasonic fields with schlieren imaging," *tm - Technisches Messen*, vol. 90, no. 2, pp. 103–112, 2023.

DOI 10.5162/SMSI2025/A6.1

Sustainable sensors research on food, environment; Research on healthcare and wearables by Tyndall National Institute: Offerings on INFRACHIP

Alan O'Riordan[1], Brendan O'Flynn[1], Daniela Iacopino[1], Sanatana Konigulu[1] Veda Sandeep Nagaraja[2]
[1] Tyndall National Institute, Cork, Ireland,
[2] Tyndall National Institute, Cork, Ireland
Corresponding Author veda.sandeep@tyndall.ie

Summary:
Tyndall National Institute is a research institute affiliated to University College Cork. Tyndall is the Coordinator of the free technology and infrastructure access programme INFRACHIP. Amongst the various technology pillars under which the offerings are available, sensors and sustainable sensors along with system development through packaging are most sought. At Tyndall National Institute we have given access to external users on sensors technology on biophotonics for healthcare, wearable sensors, sensors for food and environmental monitoring. This paper gives a brief overview of sensors research in Tyndall and what we have on offer through INFRACHIP to external users

Keywords: Biophotonics, sustainable sensors, wearables, free access

Title

Sensors technology is rapidly growing and advancing. A lot of emphasis is also being laid out to have sustainable sensors developed. The key roadblock one faces in research is access to state of the art infrastructure. At Tyndall National Institute we have infrastructure to carry out research in biophotonics sensors, sustainable food, agriculture and environment, flexible sensors and wearables. We also have a research platform for system development. All of these are made accessible for free to external users through the INFRACHIP platform.

Sustainable sensors on Food, Agriculture and environment

Miniaturization of working electrodes as electrochemical sensors has been found to offer many advantages such as a lower detection limits, lower solution resistance and a reduction in the use of expensive materials [1]. The electrochemical sensors, developed by Tyndall, as seen in figure 1 typically contain multiple interdigitated ultra-microelectrode arrays with critical dimension of 1 µm width and 45 µm length. The other electrode comb in the interdigitated setup can be used as an in-situ pH probe by monitoring the potential at which the gold oxide reduction peak occurs when undergoing cyclic voltammetry. This ability for pH tailoring on chip can allow for an enhanced sensitivity for detecting the analyte of interest.[2]

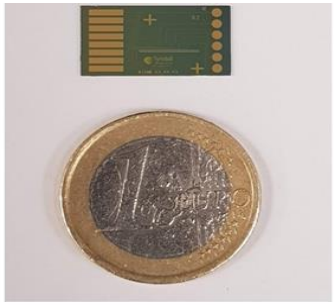

Figure 1:Fully fabricated Electrochemical chip containing 6 working IDT sensor, counter and reference electrode.

Robotics and wearable sensors

Tyndall's Collaborative Robotics Lab is equipped with cutting-edge technology, including the UR16e robot and Quantum Mocap Metagloves, for advanced robotics and VR research. Its comprehensive capabilities make it a leader in practical and innovative robotics and VR/AR applications. Human Biomechanics is an intriguing discipline that bridges biology and physics, examining human body movement and function through mechanical physics principles. This approach helps researchers unravel the complexity of human motion and understand the roles of force, torque, and equilibrium in controlling daily activities. It is a vital area of study in sports science, medicine, ergonomics, and engineering, providing critical insights that can improve performance, prevent injuries, and enhance overall well-being. Figure 2 gives an

overview of the AR VR applications of sensors research at Tyndall.

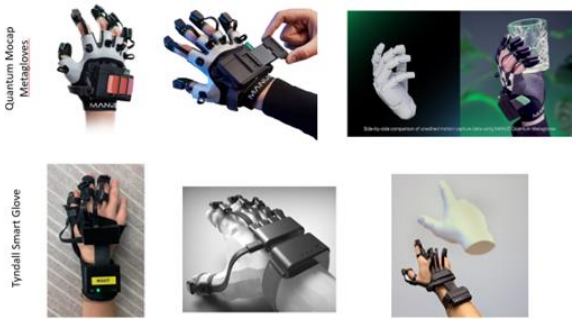

Figure 2: AR VR sensor development at Tyndall

Biophotonics Probe and sensors integration (BioProbe)

Advancements in biophotonics have opened new frontiers in medical diagnostics, environmental monitoring, and other critical fields. At the forefront of this innovation is the BioProbe initiative, a initiative focuses on the meticulous design and integration of miniature probes and sensors for prototyping, addressing the unique demands of biophotonics applications. Tyndall has experience in the design and development of miniature probes for wide range biophotonics technologies including time domain diffuse reflectance spectroscopy, fluorescence lifetime imaging, fluorescence and Raman probes. By leveraging their expertise, the team at Tyndall has developed number of demonstrators showcasing our highly specialized probes technology, that enhance performance at reduced probe footprint, driving forward the capabilities of biophotonic technology [3]. Figure 3 is an image of a Bioprobe developed at Tyndall.

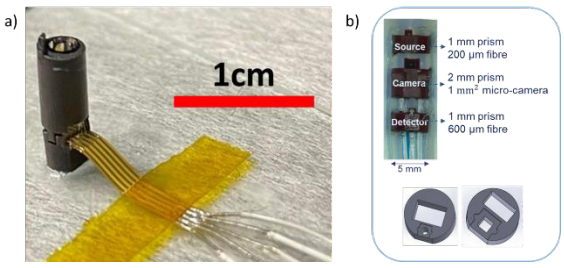

Figure 3: Bioprobe developed at Tyndall

Sensor development on flexible substrate

Tyndall has developed a research platform to develop and integrate sensors using the Direct laser writing facilities. Direct Laser Writing (DLW) is a fabrication technique that uses a focused laser beam to create precise three-dimensional graphitic micro- and nanostructures on various substrates from synthetic polymers and natural bioplastics. Engraving machines with different wavelengths, ranging from 405 nm to 450 nm and infrared (IR), are used for this process. Usinf this facility it is possible to fabricate the transducing components of wearable biosensing devices on flexible polymeric or bioplastic substrates. Figure 4 gives the DLW set up

Fig. 4. Direct Laser Writing set up at Tyndall

Conclusion

INFRACHIP is a free technology and infrastructure access programme open to researchers across all domains. It is open to industries, SMEs, research organisations and academic institutions. It helps a researcher or industry personnel to overcome the hurdle to access infrastructure which does not exist within their own organization. Tyndall has a large infrastructure available on sensor development in many areas and we welcome external users to make best use of INFRACHIP platform. For more queries, one can contact the corresponding author of this paper,

References

List and number all bibliographical references at the end of the paper. When referenced within the text, enclose the citation number in square brackets, i.e. [1]

[1] Forster, R. J.; Keyes, T. E. 6 - Ultramicroelectrodes; Zoski, C. G. B. T.-H. of E., Ed.; Elsevier: Amsterdam, 2007; pp 155–171.

https://doi.org/https://doi.org/10.1016/B978-044451958-0.50007-0

[2] O'sullivan, B.; Patella, B.; Daly, R.; Seymour, I.; Lovera, P.; Rohan, J. F.; Inguanta, R.; O'riordan, A. A Theoretical and Experimental Study of Electrochemical PH Control at Gold Interdigitated Microband Arrays

[3] Dario Angelone, Sanathana Konugolu Venkata Sekar, Walter Messina, Andrew Matheson, Ahmet T. Erdogan, Robert K Henderson, Ray Burke, Stefan Andersson-Engels, "Time resolved SPAD micro-camera probe for wide-field FLIm in microendoscopy," Proc. SPIE 12368, Advanced Biomedical and Clinical Diagnostic and Surgical Guidance Systems XXI, 1236807 (6 March 2023); https://doi.org/10.1117/12.2648340

DOI 10.5162/SMSI2025/A6.2

Flexible , Printed Sensors research in Joanneum Reasearch and access through INFRACHIP

Oliver Werzer[1], Gregor Scheipl[1], Barbara Stadlober[1]
[1]Joanneum Research Forschungsgesellschaft mbH/Department Materials, Franz-Pichler-Str. Nr. 30, 8160 Weiz, Austria
Mail: oliver.werzer@joanneum.at

Summary:
Realizing ideas is challenging especially if dedicated experimental stations or machinery are missing. INFRACHIP provides free access to state-of-the-art technologies in many fields so that fundamental research, feasibility or even prototypes can be achieved. As JOANNEUM RSEARCH (JOR) we are a partner in the project consortium. In this context, we present some of the technological focal points that we contribute to this project to give the reader an impression of how their own research/development ideas might benefit from collaborating with JOR via INFRACHIP.

Keywords: Infrastructure, functional printing, flexible electronics, sensors, R2R, high resolution structures & patterns, lab-on-chip, piezoelectric, PVDF-TrFE

Introduction

Technology is advancing rapidly, yet innovative ideas often face roadblocks due to limited access to state-of-the-art technologies or delays in securing funding - if funding is granted at all. EU-sponsored infrastructure projects are crucial for maintaining Europe's competitive edge in science and research. The INFRACHIP project addresses these challenges by offering a streamlined proposal process and rapid access to cutting-edge technologies. This initiative is funded by the European Union's Horizon Europe research and innovation program under Grant Agreement No. 101131822.

Joanneum Research (JOR), a non-profit RTO based in Austria, is a proud partner in this project. The department Materials holds extensive expertise in a wide range of advanced technologies. Highlights of our offerings are detailed in the following chapters, with additional resources available online [1].

Printed Sensor Fab (PrintSENS)

In recent decades, sensors have become indispensable in our everyday lives, with an ever-expanding array of innovative variants. At JOR, we host a comprehensive development chain for flexible, printed sensors, placing a strong emphasis on those based on the ferroelectric polymer P(VDF-TrFE) (poly(vinylidene fluoride trifluoroethylene). P(VDF-TrFE) has become very attractive as functional material for high-tech applications due to inherent physical properties like high piezo- and pyroelectric coefficients (up to 40 µC/K*m2) [2]. This material forms the core of a printed sensor technology (PyzoFlex®) which are able to measure slightest pressure changes (piezoelectric sensing) in a wide frequency range. At low frequencies, the sensor does force sensing, pressure distribution measurement or impact monitoring; at higher frequencies it can detect structure born sound, and vibration patterns. The sensor reacts to changes in temperature as by pyroelectric sensing and usable as touchless interaction or proximity sensing, among others.

PyzoFlex® technology enables the utilization of screen- or inkjet printing techniques and can be used to add new sensory functions to almost any surface. By leveraging CAD tools and finite element modelling, we achieve optimized sensor design to realize customized solutions for each given application. Tailored material selection ensures peak performance during printing, while post-processing techniques, such as high-voltage electrical poling, align the polymer's dipoles to enhance application-specific performance.

The development process is comprehensive, encompassing morphological and electrical characterization, followed by the assembly of complete sensor systems. This includes the integration of off-the-shelf components, electronic readouts, and custom software development, completing the value chain for printed sensor solutions (Fig.1).

Recent breakthroughs highlight the technology's versatility: measuring large-area pressure distributions in smart surfaces [3], realizing fully

organic pyroelectric sensor arrays by integrating P(VDF-TrFE) with organic thin-film transistors [4], monitoring the bending of alpine skis during downhill performance [5], and creating ultra-flexible organic active-matrix sensor sheets for biosignal monitoring [6].

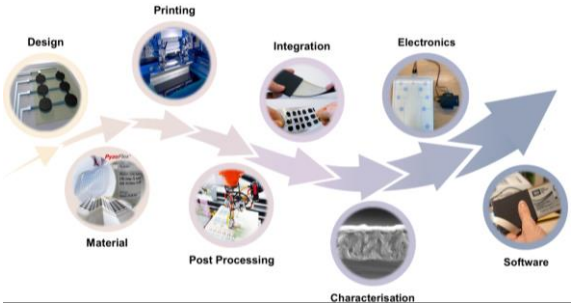

Fig. 1. Development path of PyzoFlex® sensor solutions covering the value chain up to prototype level.

Beyond sensing, this technology also unlocks opportunities for energy harvesting. Examples include ultra-thin, 1 mm floor tiles with bendable cantilevers [7], vibrating structures [8], and deformable elements within bicycle tubes or on wind turbine blated [9]—all capable of generating energy through mechanical deformation.

Roll-to-roll imprinting

Mass production of advanced tools and devices requires scalable manufacturing solutions. Roll-to-Roll (R2R) technology, long utilized in paper printing, offers fast, continuous production capabilities. In recent years, R2R technology has been adapted for the large-scale production of functional devices, including organic electronics, flexible micro-optics, and microfluidic systems. While some R2R developments facilitate just printing, additional capabilities arise from mechanically imprinting structures onto flexible substrates.

Using precision-engineered stamps, high-resolution structures can be transferred directly onto flexible foils, which are coated, for example with high-viscosity liquid resins in which the structure is embossed. These resins harden under UV exposure, capturing the desired features and enable the fabrication of high-resolution textures with a very high throughput (several m/minute). Key challenges in this process include designing and originating the stamp via maskless lithography, optimizing the stamp's surface chemistry, and tailoring the imprint resin. At JOR, proprietary technologies like NIL® and bioNIL® enable advanced customization of these resins, meeting diverse application requirements.

Flexible Microfluidics Fab (FLEXµFLU)

R2R imprinting enables the fabrication of sophisticated devices which enable applications like point-of-care diagnostics, organ-on-chip, mixing, crystallization amongst many more. For their realization many aspects need consideration starting from simulation of fluidics or reaction chemistry, over imprinting, lamination and more (see Fig. 2). At the FLEXµFLU all steps can be taken care of for achieving best functional devices.

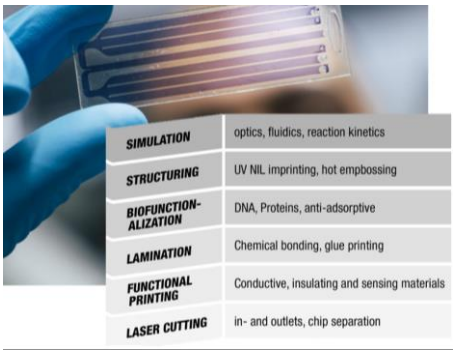

Fig. 2. Example of a Lab-on-chip produced in a R2R process at Joanneum Research and an explanation of the entire development and production chain offered.

Flexible Microoptics Fab (FLEXµOPT)

Microoptical elements are integral to various applications, including lighting, optical communications, camera lenses, and even decorative designs. While injection molding is commonly used for large-scale production, R2R processing offers a faster, more cost-effective, and adaptable alternative.

At JOR, the FLEXµOPT facility supports the entire development chain for 2D and 2.5D freeform microoptical elements. This includes raytracing, lithography up to small-scale production using step-and-repeat imprinting technology and high-throughput manufacturing explained above.

References

[1] https://infrachip.eu/showroom/access_provider_facility-joanneum/

[2] N. Neumann, et. Al. Ferroelectrics 1991, 118(319- 324)

[3] Asier Alvarez Rueda, et. al. *Sensors* **2023**, *23*(2)

[4] Marco Fattori, et. al. Nature Electronics 2022, 5(289–299)

[5] Christoph Thorwartl, et. al. *Sensors* **2022**, *22*(15), 5768

[6] Esther Karner-Petritz, et. al. Adv. Electron. Mater. 2023, 9, 2201333

[7] Asier Alvarez Rueda, et. al. Nano Energy 121 (2024) 109248

[8] Asier Alvarez Rueda, et. al. Adv. Eng. Mater. 2024, 26, 2302140

[9] https://www.symphony-energy.eu/applications/

DOI 10.5162/SMSI2025/A6.3

AMO research in graphene and 2D material devices for sensing applications and their access through INFRACHIP

Gordon Rinke[1], Stephan Suckow[1], Herbert Kleinjans[1], Zhenxing Wang[1], Max C. Lemme[1,2]
[1] AMO GmbH, Otto-Blumenthal-Str. 25, 52074 Aachen, Germany
[2] RWTH Aachen University, Chair of Electronic Devices, Otto-Blumenthal-Str. 2, 52074 Aachen, Germany
Mail: rinke@amo.de

Summary:
The EU-funded INFRACHIP project gives access to advanced technologies and addresses innovation and funding challenges. As an access provider, AMO GmbH offers infrastructure for deposition, etching, lithography and advanced characterization, as well as expertise in the fabrication of graphene and other 2D material-based devices. By integrating 2D materials into electronic and photonic devices with scalable fabrication processes and versatile photonic platforms, AMO supports cutting-edge R&D and delivers tailored solutions for next-generation sensing and electronic applications.

Keywords: Infrastructure, 2D Materials, Sensors, Photonics, Electronics

Introduction

Technology is advancing rapidly, yet ideas often face hurdles due to limited access to state-of-the-art or cutting-edge technologies. Securing funding can also be a lengthy process, if successful at all. EU-sponsored infrastructure projects play a crucial role in maintaining high standards of science and research within Europe. The INFRACHIP project addresses these challenges by offering a streamlined proposal process and quick access to relevant technologies. This initiative is supported by funding from the European Union's Horizon Europe research and innovation program under Grant Agreement No. 101131822.

AMO GmbH is a non-profit SME specializing in R&D for micro- and optoelectronic applications and one of the 11 service providers involved in the INFRACHIP initiative. The technology portfolio offered by AMO includes not only different deposition, etching, and lithography tools but also advanced characterization techniques and the fabrication of graphene and other 2D Materials devices for sensor applications. [1] What characterizes AMO as a service provider is flexibility, a short feedback loop with customers, and a broad range of solutions based on the know-how and technologies developed in our research projects.

Sensors and Detectors based on 2D Materials

Graphene and other two-dimensional materials appeared on the stage first in 2004, raising great expectations that they could revolutionize microelectronics. These expectations were largely driven by the excellent intrinsic properties of graphene: high carrier mobility, broadband optical absorption, ultimate thinness, and high mechanical strength.

At AMO, research on graphene and other 2D materials has been ongoing since 2006, with a particular focus on their potential applications in microelectronics and optoelectronics. Of particular interest is the integration of 2D materials with conventional silicon technology to develop new applications in electronics, sensing and photonics.

Graphene-based field-effect transistors for sensing application

Several advanced devices based on 2D materials have been demonstrated in various publications, including Hall sensors [2], pressure sensors [3], photodetectors [4], and diodes [5]. An example of graphene-based Hall sensors fabricated on a flexible substrate is shown in Fig. 1. These Hall sensors are created on a 50 µm thick flexible Kapton foil using large-scale graphene grown via the chemical vapor deposition technique on copper foil. The devices exhibit voltage and current normalized sensitivities of up to 0.096 V VT^{-1} and 79 V AT^{-1}, respectively—values comparable to those of rigid silicon-based Hall sensors. Notably, the sensors maintain their sensitivity even after being bent to a minimum radius of 4 mm, corresponding to a tensile strain of 0.6%, and after enduring 1000 bending cycles to a radius of 5 mm.

Our capabilities span both chip-scale fabrication and wafer-scale production, highlighting our commitment to bridging the gap between

innovative research and scalable manufacturing. As part of the 2D-EPL and 2D-PL projects [6], we have developed a reliable baseline process for fabricating graphene-based field-effect transistors (GFETs) on 6” silicon wafers. These GFETs are offered through multi-project wafer (MPW) runs [7], making 2D material-based devices accessible to a broader research and development community. As part of INFRACHIP, AMO offers this expertise to provide users with comprehensive support to drive their R&D initiatives forward.

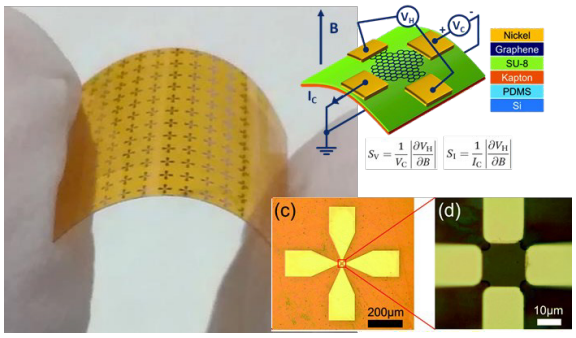

Fig. 1. Flexible Graphene Hall Sensor [2] fabricated at AMO.

Photonic Sensing

AMO's photonic platforms are built on advanced Silicon-On-Insulator (SOI) technology, available in 220 nm and 400 nm thicknesses, as well as Silicon Nitride (Si_3N_4) layers up to 450 nm thick. This versatile platform enables the fabrication of both passive and active photonic devices, with the added capability of integrating 2D materials for enhanced functionality like photodetectors. Our offerings are summarized in [8].

For sensing applications, the integration of 2D materials into photonic devices unlocks exciting possibilities beyond photodetection on any dielectric waveguide [9, 10], like using the 2D material as mid-infrared light emitter [11], as transparent microheater [12] or to build optical modulators for data communication [13]. By combining established photonic technologies with the unique properties of 2D materials, AMO supports the development of next-generation photonic sensing solutions.

We are also establishing aluminum nitride (AlN) as new dielectric waveguide platform with enhanced transparency in the blue/UV spectrum compared to Si_3N_4 and have recently published the lowest AlN waveguide loss in the data communication spectrum [14]. Finally, we are combining waveguides with plasmonics to create very sensitive biosensors with minimal footprint [15].

Summary

Through INFRACHIP, AMO leverages its expertise to provide comprehensive support for users, enabling them to advance their R&D initiatives. Whether researchers require guidance in prototyping, scaling up to wafer-level manufacturing, or integrating 2D materials into standard semiconductor processes, AMO offers tailored solutions and services to meet their needs. By combining cutting-edge technology, established manufacturing workflows, and customer-centric collaboration, we empower users to unlock the full potential of 2D materials in next-generation electronic and sensing devices.

Acknowledgments

This project received funding from the European Union’s Horizon Europe Research and Innovation Program under the Graphene Flagship 2D Experimental Pilot Line (2D-EPL, 952792), Graphene Flagship Core 3 (881603), INFRACHIP (101131822), AEOLUS (101017186), GRACED (101007448) and funding from BMBF under grant agreement No. 13N16116 (ATIQ).

References

[1] https://infrachip.eu/showroom/access_provider__facility-amo-gmbh/

[2] Wang, Z., Shaygan, M., Otto, M., Schall, D. & Neumaier, D. *Nanoscale* **8**, 7683–7687 (2016).

[3] Lukas, S. *et al. ACS Nano* **18**, 25614–25624 (2024).

[4] De Fazio, D. *et al. ACS Nano* **14**, 11897–11905 (2020).

[5] Wang, Z. *et al.*. *Advanced Electronic Materials* **7**, 2001210 (2021).

[6] https://graphene-flagship.eu/industrialisation/pilot-line/

[7] Canto, B. *et al.* Preprint at https://doi.org/10.21203/rs.3.rs-5032996/v1 (2024).

[8] A. Rahim *et al.*, *IEEE Journal of Selected Topics in Quantum Electronics*, **25**(5), pp. 1-18 (2019).

[9] D. Schall et al., ACS Photonics 1(9) 781–784 (2014).

[10] S. Parhizkar et al., ACS Photonics **9**(3), 859–867 (2022).

[11] N. Negm et al., *ACS Photonics* **11**(8), 2961–2969 (2024).

[12] D. Schall et al., Opt. Express **24**, 7871-7878 (2016).

[13] M. Mohsin et al., Sci Rep 5, 10967 (2015).

[14] R. Singh et al., Opt. Express **32**(25) (2024).

K. Fotiadis et al., ACS Photonics **10**(8), 2580–2588 (2023).

DOI 10.5162/SMSI2025/A6.4

Flexible Magnetoresistive Sensors for Novel Applications

Alberto Nicolicea[1], *Eduardo Sergio Oliveros-Mata*[2], *Yevhen Zabila*[2], *Denys Makarov*[2], *Matthias Pelkner*[1], *Michael Melzer*[1]
[1] Bundesanstalt für Materialforschung und -prüfung, Division 8.4 Acoustic and Electromagnetic Methods, Unter den Eichen 87, 12205 Berlin, Germany
[2] Helmholtz-Zentrum Dresden-Rossendorf e.V., Institute of Ion Beam Physics and Materials Research, Bautzner Landstraße 400, 01328 Dresden, Germany
Alberto.Nicolicea@bam.de

Summary: Recent developments in flexible electronics have lead to the appearance of flexible magnetic field sensors produced by thin-film deposition on flexible substrates which show promising capabilities for applications such spatial navigation, micro-fluidic particle detection, biomedical applications, intelligent textiles and non-destructive testing. In this work flexible anisotropic magnetoresistive sensors were used to scan curved and flat ferromagnetic samples with reference defects. Defects with depths down to 110 µm were detected with an signal-to-noise ratio of 2.7. A 2D magnetometer mapping of the surface of the samples was also obtained.

Keywords: Flexible magnetic field sensors, Flexible Electronics, Non-Destructive Testing, Thin Film Sensor Fabrication, Defect Detection

Introduction

Flexible electronics is an emerging field that has been gaining a lot of attention in recent years, with the appearance of flexible solar panels, screens and other such novel devices. Recent developments in this area have lead to the appearance of flexible magnetic field sensors which are produced by thin-film deposition on flexible substrates. These devices show promising capabilities for several applications such spatial navigation, micro-fluidic particle detection, biomedical applications and intelligent textiles [1]. One possible field of interest is the application of these devices for electromagnetic (EM) non-destructive testing (NDT), since it would enable in-contact scanning of surfaces with arbitrary shapes.

The novelty of this work consists of employing flexible anisotropic magnetoresistive (AMR) sensors mounted on a rotative mechanical holder to scan a semi-circular ferromagnetic sample with 3 reference defects via magnetic flux leakage (MFL) testing, thus demonstrating the applicability of this new method for the scanning of curved surfaces [2]. A flat ferromagnetic sample with 10 reference defects of different depths was also scanned employing flexible AMR field sensors. Defects with depths ranging from 110 µm up to 2240 µm were detected with an signal-to-noise ratio (SNR) of 2.7 up to 27.9. A 2D magnetometer mapping of the sample with a spatial scanning step of 10×50 µm^2 was also obtained using the flexible AMR sensors. This approach can be further extended to Eddy current testing, and structural health monitoring. In addition, sensor arrays and matrices can be fabricated to improve the scanning applicability.

Methodology and Results - NDT Scanning

In our study we employed flexible linear AMR sensors for MFL testing, fabricated with standard thin-film fabrication processes (photo-lithography and magnetron sputtering deposition) (Fig. 1a-b) and encapsulated with a layer of plastic lacquer which protects from corrosion. These sensors have an in-plane sensitive direction perpendicular to the magnetic bars (Fig. 1c) and their signal response is linearized by the barber-poles present in the gold layer (Fig. 1d).

To display the capability that these flexible sensors have for curved surface scanning, a semi-cylindrical ferromagnetic steel component with 3 reference defects along its surface was used (inset of Fig. 1e). Magnetization of the sample was performed diametrically. To scan this sample, the sensor is mounted on a rotative holder that also has the ability to move vertically along the *z*-axis. These two free axes of movement of the holder combined with the gravitational weight maintain the sensor conformal in contact with the curved sample surface during the motorized line-scans along the *x*-axis. Repeated scans for different positions along the *y*-axis produce an automated 2D magnetic mapping (Fig. 1f), with a scanning resolution of $(\Delta x \times \Delta y) = (5 \times 50$ µm$^2)$. The sensor-to-surface distance corresponds to the thickness (20 µm) of the flexible substrate (Kapton). A geometrical transition between the linear coordinates of the mechanical scanner and the cylindrical coordinates of the sensor was performed for the display of the signal.

A flat steel sample with several reference defects of decreasing depth was also scanned using a flexible AMR sensor, with the objective of studying the relation between defect depth the signal amplitude detected by the sensor. Once again, the steel plate was magnetized

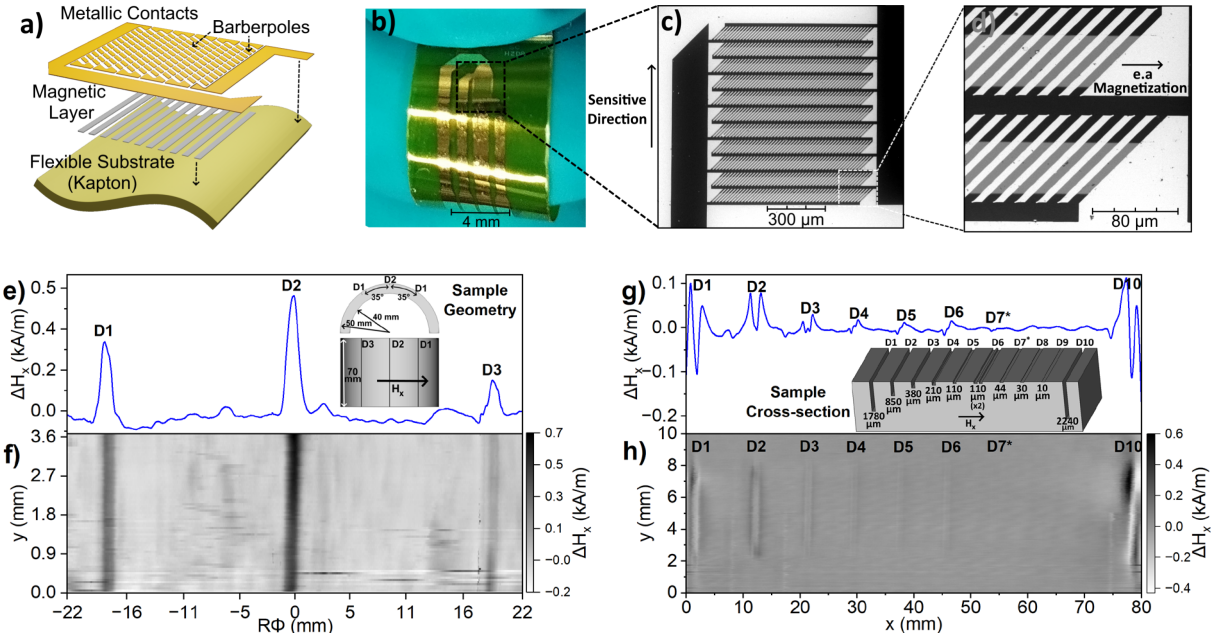

Fig. 1: Flexible AMR sensor: a) The magnetic layer of the sensor is deposited on a flexible substrate (Kapton), followed by the deposition of a gold layer forming the barber-pole structures and the electrical contacts. b) Photography displaying the flexibility of the sensor. c) Scanning electron microscopy (SEM) of the sensitive region (1 mm^2). d) SEM image focusing on the magnetic bars and the metallic barber-poles deposited on top. Scanning of a curved sample with reference defects: e) Average of 70 measurements, showing the signal amplitude of each defect. Inset shows the geometry of the sample scanned. f) 2D magnetometer scanning (cylindrical coordinates). Scanning of a flat sample: g) Levelled plot of the average centre-line signal (100 measurements). Inset showing the depth of defects (cross section view). h) 2D magnetometer mapping of the tangential magnetic field (ΔH_x). (at the limit of detection). Source: [2]*

close to saturation with a DC magnetic field directed along its length (perpendicular to the linear reference defects), before scanning. Fig. 1g) shows the average of the center-line signal of 100 scanned lines. The full-area 2D magnetometer mapping of the sample surface with an area of 10 $\times$ 80 mm^2 and a spatial scanning step of ($\Delta x \times \Delta y$) = (10 $\times$ 50 µm^2) was also obtained - Fig. 1h).

It is observed that deeper defects produce a stronger signal response when compared to more shallow ones. Defects down to 44 µm were detected, with defects D8 (30 µm) and D9 (10 µm) not detectable. Unfortunately, the AMR sensors used could not separate the signals from the double notch defect D6, since their separation distance was small compared to the sensor area. This can be fixed by further miniaturizing the sensors so as to increase the spatial resolution and capability of detecting more localized magnetic fields, since larger sensors average the signal beneath their area. However, this process might also affect the performance and characteristic parameters of the sensors. This is a future study to be performed.

Acknowledgements

This research work was funded in the framework of the BAM-internal funding instrument ”Menschen – Ideen; Ideen: Entwickeln” (”People - Ideas; Ideas: Develop”). This work is also financially supported via the European Union’s Horizon Europe Research and Innovation Programme, Grant Agreement # 101070066 (project REGO) and ERC grant 3DmultiFerro (Project number: 101141331).

References

[1] Makarov, Denys & Melzer, Michael & Karnaushenko, Daniil & Schmidt, Oliver. (2016). Shapeable magnetoelectronics. Applied Physics Reviews. 3. 011101. 10.1063/1.4938497.

[2] A. Nicolicea, E. S. Oliveros-Mata, Y. Zabila, D. Makarov, M. Melzer, M. Pelkner, Flexible anisotropic magnetoresistive sensors for novel magnetic flux leakage testing capabilities, NDT & E International 2024, 103160, https://doi.org/10.1016/j.ndteint.2024.103160.

DOI 10.5162/SMSI2025/A7.1

Determining Data Centre PUE with a Digital Twin

Alexander Kammeyer[1,2], *Florian Burger*[1], *Daniel Lübbert*[1] *and Katinka Wolter*[2]
[1] Physikalisch-Technische Bundesanstalt, Abbestraße 2-12, 10587 Berlin, Germany
[2] Freie Universität Berlin, Takustraße 9, 14195 Berlin, Germany
alexander.kammeyer@ptb.de

Summary: The Power Usage Effectiveness is an important metric in assessing data centre energy efficiency. Regulations require constant monitoring of data centre energy consumption. This paper presents a method to calculate the (Interim) Power Usage Effectiveness of an HPC data centre using a Digital Twin in a robust and flexible way by identifying all necessary meters, providing a robust, continuous data collection mechanism and arbitrary time ranges.

Keywords: HPC, digital twin, data centre, energy efficiency, metrics

Introduction

Data centres have become an integral part of modern, digital societies. They provide services for every day life, emerging trends such as AI, for research and the digital quality infrastructure. The growth of data centres has lead to an increase in energy consumption. Ireland forecasts that by 2027 the energy demand of data centres in the country will make up up 31 percent of the total energy consumption [1]. To ensure efficient energy usage, standards and efficiency requirements for data centres have been introduced. One such standard is the Blue Angel certificate for data centres [2]. It is mandated for new data centres of the federal government in Germany by the climate protection programme 2023 [3]. The Blue Angel defines the Power Usage Effectiveness (PUE) as the central metric to quantify efficient energy usage.

Measuring the PUE as required by the Blue Angel is challenging in a legacy setup. Several steps are necessary: the proper electric and heat meters must be identified; data needs to be acquired continuously; finally, the data must be converted into matching units for the eventual PUE calculation. This paper presents a method to perform these steps using an HPC data centre Digital Twin [4].

Measurement data acquisition for PUE

The Blue Angel uses the PUE definition of the ISO 30134 standard [5]:

$$\mathrm{PUE} = \frac{E_{\mathrm{DC}}}{E_{\mathrm{IT}}} \tag{1}$$

where E_{DC} is the total data centre energy consumption and E_{IT} is the IT equipment energy consumption. Both are annual values in $\mathrm{kW\,h}$. Building annual sums will cancel seasonal effects and one-off events. If the PUE is calculated for a shorter period, it becomes the Interim Power Usage Effectiveness (iPUE).

The Digital Twin needs to collect data from electricity meters. The data needs to be split between IT equipment, e.g. servers, network components, storage and backup, and other energy consumers in the data centre, such as cooling, lighting, lifts, fire alarm system and office spaces.

A standard electricity meter might be reset, e.g. due to maintenance or replacement. This will result in incorrect PUE calculation, if only the annual accumulated power consumption is read at the beginning and end of a year. To make the computation robust against such faults, the Digital Twin continuously collects the power consumption in 15 minute intervals from the electricity meters, stores these values and integrates over them to obtain the annual power consumption.

The electric energy used for cooling should be measured, but this is not feasible for all setups. The data centre at hand shares a central cooling infrastructure with the entire campus, making direct measurement impractical. Instead, heat meters in the cooling water supply line measure the power, with data collected by the Digital Twin. As per Annex B, a conversion factor of 0.4 is applied to convert chilled water power to electric energy, and all heat meter readings are multiplied by this factor.

Calculating PUE

Table 1 lists all relevant meters of the PTB data centre. The Sub-Distribution (SD) meters 1 – 4 measure the IT equipment energy usage in the data centre. Cooling is measured on the two supply lines via the so-called KMZ 12/17 and 6/12 heat meters. Since the PTB data centre is located in a mixed-use building, using the entire building energy consumption over-estimates the PUE. It was decided to only include energy con-

Table 1: Meters in the data centre

Meter	Unit	Factor
Sub-Distribution 1	kW	1.0
Sub-Distribution 2 (UPS)	kW	1.0
Sub-Distribution 3	kW	1.0
Sub-Distribution 4	kW	1.0
KMZ 12/17	kW	0.4
KMZ 6/12	kW	0.4

sumption directly associated with the data centre and exclude all office and shared spaces. With the selected meters, the PUE can be computed as:

$$\mathrm{E_{IT}} = \mathrm{SD\ 1} + \mathrm{SD\ 2} + \mathrm{SD\ 3} + \mathrm{SD\ 4} \tag{2}$$

$$\mathrm{E_{Cooling}} = 0.4 * (\mathrm{KMZ\ 12/17} + \mathrm{KMZ\ 6/12}) \tag{3}$$

$$\mathrm{E_{DC}} = \mathrm{E_{IT}} + \mathrm{E_{Cooling}} \tag{4}$$

$$\mathrm{PUE} = \frac{\mathrm{SD\ 1} + \mathrm{SD\ 2} + \mathrm{SD\ 3} + \mathrm{SD\ 4} + \mathrm{E_{Cooling}}}{\mathrm{SD\ 1} + \mathrm{SD\ 2} + \mathrm{SD\ 3} + \mathrm{SD\ 4}} \tag{5}$$

The Digital Twin calculates the PUE as follows: all metering results are put into mean windows. The heat power values are multiplied by the scalar conversion factor of 0.4. Three sums are calculated, the IT equipment work (2), the cooling work (3) and the overall data centre work (4). It is possible to use work and not power for the ratio. Figure 1 shows the iPUE development for September 2024 in the HPC data centre. Variations can be observed due to different use of the system, as well as ambient temperature. Figure 2 shows the correlation between the per day average outside temperature and the PUE. A linear fit describes the data well:

$$\mathrm{iPUE}(T) = 1.453 + 0.00285(T - 10) \tag{6}$$

The model is centred around 10 °C which corresponds to the approximate mean annual temperature for Germany.

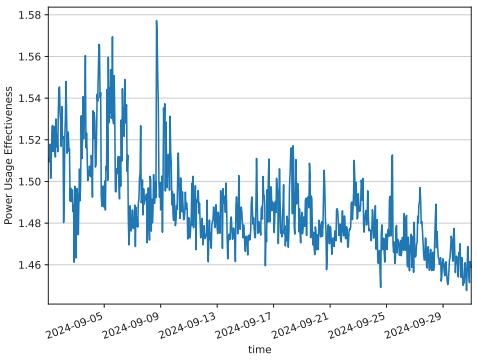

Figure 1: iPUE visualisation using 1h average window

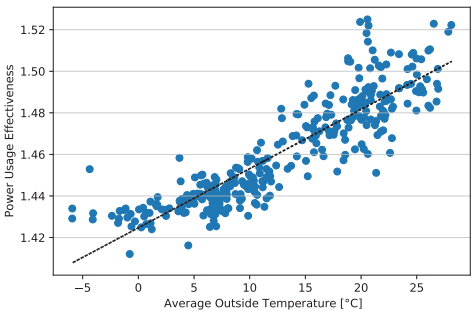

Figure 2: Correlation between outside temperature and iPUE calculated using a 24h average window with a linear model

Conclusion

This paper presented a way to compute the PUE of an HPC data centre with a Digital Twin. Two advantages of the Digital Twin have been shown: the possibility to correct data in case of meter faults and the ability to compute the iPUE through high data resolution.

The automatic PUE calculation can be used to generate automatic reporting on Green IT goals and the required yearly report for the Blue Angel certificate. Furthermore, it allows data centre operators to quantify events in terms of iPUE that are otherwise lost in the yearly average. A similar approach can be used for other data centre metrics. The PUE model can be included into the system simulation that is included with the Digital Twin.

References

[1] Department of the Environment, Climate & Communications, “Ireland’s integrated National Energy and Climate Plan 2021-2030,” July 2024.

[2] RAL UMWELT, *Energieeffizienter Rechenzentrumsbetrieb DE-UZ 161*. Bonn, D, 2 ed., Feb. 2015.

[3] Bundesministerium für Umwelt, Naturschutz und nukleare Sicherheit, “Klimaschutzprogramm 2030 der Bundesregierung zur Umsetzung des Klimaschutzplans 2050,” Oct. 2019.

[4] A. Kammeyer, F. Burger, D. Lübbert, and K. Wolter, “Developing a digital twin to measure and optimise hpc efficiency,” IMEKO World Congress 2024, in press, 2024.

[5] ISO/IEC JTC 1/SC 39, “Information technology – Data centres – Key performance indicators Part 2: Power usage effectiveness (PUE),” standard, International Organization for Standardization, Geneva, CH, Apr. 2016.

DOI 10.5162/SMSI2025/B1.1

Overview: Multimodal Smart Sensor Networks for Plant Monitoring and Improved Energy Efficiency

Dennis Arendes[1], Jörg Kelleter[2], Tobias Baur[3], Wolfram Simmendinger[4], Christian Fuchs[1], Christian Bur[1], Andreas Schütze[1]
[1]Saarland University, Lab for Measurement Technology, Saarbrücken, Germany
[2]GTE Industrieelektronik GmbH, Viersen, Germany
[1]3S Technologies GmbH, Saarbrücken, Germany
[1]Sciosense Germany GmbH, Reutlingen, Germany
d.arendes@LMT.uni-saarland.de

Summary:
The project MIMOSE-A is a combined work of industry and academia to improve the monitoring of chemical industry parks. The monitoring should detect and locate leakages, especially of energy sources incl. hydrogen, and anomalies (e.g. fire) to save energy and therefore money for the operator of the industry park. Mimose-A tries to realise this surveillance with small sensor nodes, equipped with a variety of sensors like microphones and metal oxide gas sensors. Together with advanced data evaluation and machine learning algorithms the sensor system is tested to detect anomalies.

Keywords: Multimodal IoT Sensors, Industrial Facility Monitoring, Leakage Detection, MOS Gas Sensors, Machine Learning

Motivation

Humans are able to recognize the state of their environment very quickly by taking in information via various sensory channels and processing it with each other **Fehler! Verweisquelle konnte nicht gefunden werden.**. Today, a large number of inexpensive sensors are available for technical systems, some of which are far more powerful than the human sensory **Fehler! Verweisquelle konnte nicht gefunden werden.**. Nevertheless, a similarly comprehensive assessment of the environment is not yet possible because the individual sensor data is not sufficiently fused and interpreted [1].

In plant monitoring, not only in the chemical industry, dedicated sensor systems, i.e. systems designed for precisely one specific application, are common today, usually associated with high costs, partly due to the low quantities, which do not allow an economy of scale. These limited technical systems are supplemented by humans, who can only selectively detect unusual conditions and potentially hazardous situations with their ‘sensors’.

The availability of sufficient computing power to interpret the resulting flood of data enables a paradigm shift in the sensory monitoring of systems, which is to be addressed for the first time in this project. The aim is to record multimodal plant data over a large area and thus significantly improve the assessment options, e.g. for the early detection of leaks in energy sources (compressed air, water vapour, gas and, increasingly in future, hydrogen). Suitable visualisation of spatially and temporally high-resolution measurement data allows the current situation to be recorded quickly and accurately, even if the data quality of individual measurement points is poor. The stationary sensor nodes are supplemented by mobile, autonomous sensor systems that can react to unknown situations in particular in order to offer significant added value with a lower use of resources. Wireless networking of the nodes and higher-level evaluation based on extracted features using distributed AI methods in the sense of edge or fog computing can further increase the sensitivity, selectivity and robustness of system monitoring thanks to the redundancy this provides.

Approach

The sensor nodes are designed and integrated by the two project partners GTE Industrieelektronik, Viersen, and 3S Technologies, Saarbrücken. They combine metal oxide semiconductor (MOS) gas sensors, operated in temperature cycled operation (TCO) with microphones and other miniaturized sensors in order to have transducers for all kind of possible signals. As MOS sensor the ENS170 sensor (ScioSense Germany GmbH, Germany) is

used. The ENS170 is a multipixel sensor, using different sensitive materials in four layers in order to boost the sensitivity and selectivity. One possible sensor node is depicted in Fig. 1. Communication between all sensor nodes is a challenge, which can be addressed by low-

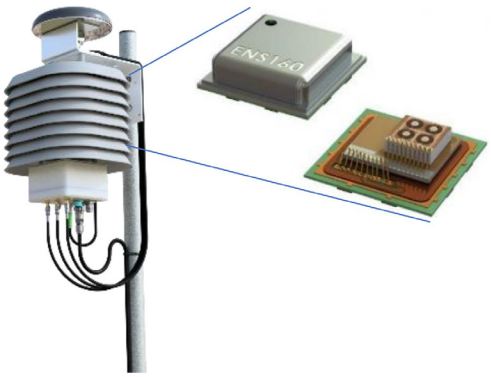

Fig. 1 Multimodal sensor node (3S GmbH, Germany) with the digital MOS-multisensor ENS160 (Sciosense Germany GmbH).

power communication protocols like LPWAN and is part of one work package.

Evaluation is done by multiple project partners, which try to use a various amount of Machine Learning Algorithms in order to detect the previously described anomalies. Especially Transfer Learning can be useful in order to solve inherent problems like sensor drift or domain shifts. The complete timeline of the project, structured in the designated work-packages, is displayed in Fig. 2.

Supplementary to the sensor nodes, mobile drones are deployed in case an anomaly is detected by the stationary nodes. These drones try to verify or falsify anomalies to allow for human actions only in real alarm cases. Otherwise, people's alarm tolerance is reduced.

Summary

Mimose-A is a project aiming to detect energy source leakages with a fine-meshed grid of sensor nodes in order to increase energy efficiency while also monitoring other anomalies. The overall goal is to save energy and thus money.

Acknowledgements

The project "Mimose-A" is funded by the German Federal Ministry for Economic Affairs and Climate Action (BMWK) under the grant number 03EN4057A-G. We acknowledge support by the Project Management Jülich (PTJ). Furthermore, the authors want to thank all project partners for the good, ongoing cooperation.

References

[1] Y. Cao, C. Summerfield, H. Park, B.L. Giordano, C. Kayser, Causal Inference in the Multisensory Brain, Neuron 102, 1076-1087 (2019); doi: 10.1016/j.neuron.2019.03.043

[2] G.F. Fine, L.M. Cavanagh, A. Afonja, R. Binions, Metal Oxide Semi-Conductor Gas Sensors in Environmental Monitoring, MDPI Sensors 10, 5469-5502 (2010); doi: 10.3390/s100605469

[3] M.A. Bakr, S. Lee, Distributed Multisensor Data Fusion under Unknown Correlation and Data Inconsistency, MDPI Sensors 17, 2472 (2017); doi: 10.3390/s17112472

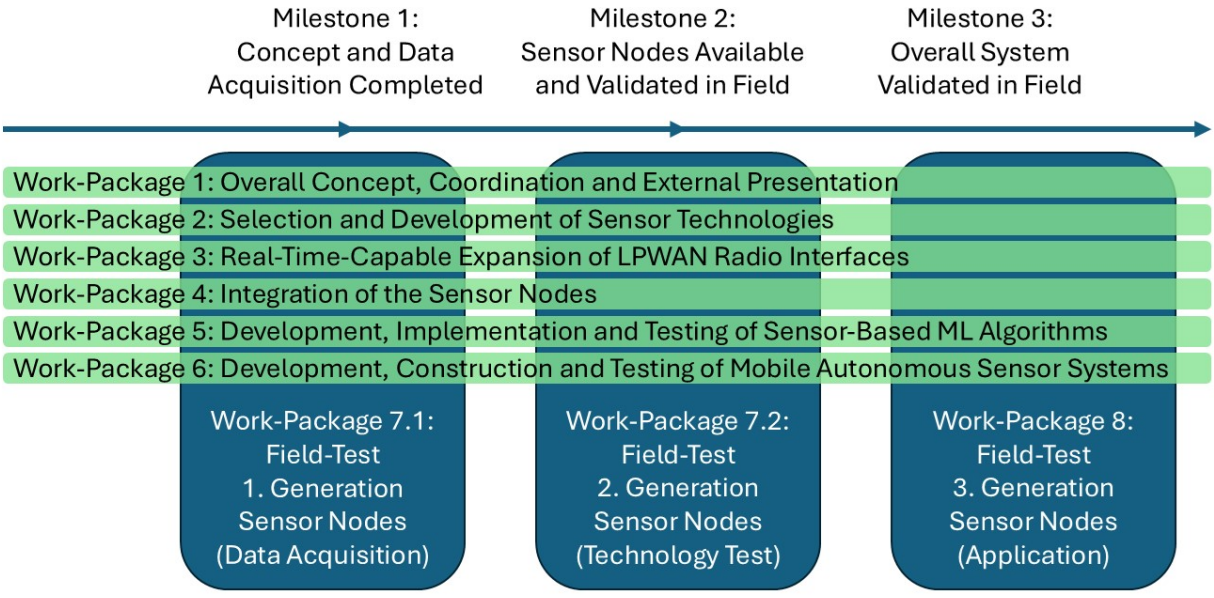

Fig. 2 Suggested solution with all scheduled work packages in the MIMOSE-A project.

DOI 10.5162/SMSI2025/B1.2

Gas Source State Estimation with Reynolds-Averaged Dispersion Model and Time-Averaged Measurements

Aaron Raffeiner[1,2], *Roland Pohle*[1], *Jia Chen*[2] *and Achim J. Lilienthal*[2]
[1]Siemens AG, Munich, Germany
[2]Technical University of Munich (TUM), Germany
aaron.raffeiner@siemens.com

Summary: In this work, the Gas Source State Estimation (GSSE) problem in non-trivial geometries is approached by combining a non-stationary gas dispersion Partial Differential Equation (PDE) with in-situ gas measurements under the assumption of known flow. The GSSE problem is formulated as an optimization problem with PDE constraints and solved efficiently using the adjoint method. The approach is simulatively validated on a 2D problem with laminar flow around a circular obstacle and data from gas dispersion simulations. Thereby, a single Gaussian gas source could be localized accurately for most trials with randomly placed sensor.

Keywords: gas source state estimation, sensor network, PDE-constraint optimization, Reynolds averaging

Background and Motivation

The early detection, localization and quantification of unwanted gas sources in industrial plants helps to increase their resource efficiency and at the same time reduces their environmental impact. However, estimating the state, i.e., the spatial distribution, of a gas source poses significant challenges due to the complex processes that govern atmospheric gas dispersion. For in-situ measurements, further difficulties arise since they can only be made at sparse locations. To address these challenges, this work uses a model-based GSSE approach that combines measurements with a dispersion model. Similarly, Wiedemann et al. modeled dispersion in a 2D domain with the non-stationary Advection-Diffusion (AD) PDE [1]. The required flow field was estimated from anemometer measurements. Though, an open domain without obstacles was assumed which is rarely the case in industrial plants. Khodayi-mehr et al. studied GSSE in geometrically more complex domains with stationary gas transport and fully known flow [2]. The problem was formulated as an optimization problem with PDE constraints. However, the stationary assumption is often violated in outdoor environments. This motivates to investigate GSSE in non-trivial geometries with non-stationary models and fully known flow.

Gas Dispersion Model

The proposed GSSE approach is studied on an exemplary 2D problem "flow around a cylinder". The modeling domain $\mathbf{\Omega}$ is a rectangular channel of and height H and length $L \gg H$ with a circular obstacle of radius r at position $\mathbf{x}_c$, see Fig. 1. In an industrial plant, the obstacle may correspond to a gas tank. The flow $\mathbf{v}(\mathbf{x}, t)$ and pressure $p(\mathbf{x}, t)$ at location $\mathbf{x} \in \mathbf{\Omega}$ and time t is modeled by the incompressible Navier-Stokes PDE

$$\rho \left(\frac{\partial \mathbf{v}}{\partial t} + (\mathbf{v} \cdot \nabla)\mathbf{v} \right) = \mu \nabla^2 \mathbf{v} - \nabla p \,, \tag{1a}$$

$$\nabla \cdot \mathbf{v} = 0 \,. \tag{1b}$$

A parabolic inflow velocity (left wall), no-slip conditions at the top/bottom wall and obstacle and a zero initial condition are assumed [3]. The gas concentration $c(\mathbf{x}, t)$ is described by the AD PDE

$$\frac{\partial c}{\partial t} = D \nabla^2 c - \mathbf{v} \cdot \nabla c + S \,, \tag{2}$$

with the positive source term $S(\mathbf{x}) \geq 0$. A zero initial condition and no-flux boundary conditions are assumed. For realistic gas dispersion with Reynolds Re and Péclet Pe numbers $> 10^5$, problem-specific Finite-Element (FE) solvers with small time/space discretization are required for numerical stability [3]. To avoid these difficulties, GSSE is studied in the laminar flow regime with $Re = 100$ and advection-dominated transport with $Pe = 10$. In this case, a triangular mesh with $n_e = 1038$ elements and a time step $\Delta t_s = 0.01\,\mathrm{s}$ can be used.

Gas Source State Estimation Method

GSSE aims to estimate the field $S(\mathbf{x})$ in eq. (2) from n_s gas measurements $y(\mathbf{x}_m^j)$ at locations $\mathbf{x}_m^j$ given the flow $\mathbf{v}$. The required data is artificially generated from simulations of eq. (1) and eq. (2). To cope with turbulence, only time-averaged flow $\bar{\mathbf{v}}$, concentration $\bar{c}$ and measurements $\bar{y}$ are used. The averaged quantities in the period $\Delta \bar{t}$ are computed using each $\Delta t_m \gg \Delta t_s$ time step to emulate sensors with sampling times Δt_m larger than turbulent effects. Time-averaging of eq. (2), using the Reynolds decomposition, leads to the Reynolds-averaged (RA) AD PDE [4]

$$\frac{\partial \bar{c}}{\partial \bar{t}} = \bar{D} \nabla^2 \bar{c} - \bar{\mathbf{v}} \cdot \nabla \bar{c} + \bar{S} \,, \tag{3}$$

where $\bar{D} = D + K$ is the sum of molecular D and turbulent $K \gg D$ diffusivity. Thus, turbulent mixing is modeled as diffusion. The GSSE problem is formulated as an optimization problem

$$\bar{S}^* = \arg\min_{\bar{S}} \sum_{i=1}^{n_T} \sum_{j=1}^{n_s} \left(\bar{c}_i^j - \bar{y}_i^j \right)^2 , \tag{4a}$$

$$\text{s. t.} \quad \text{eq. (3)} \quad \text{and} \quad \bar{S}(\mathbf{x}) \geq 0 , \tag{4b}$$

with the RA AD PDE as constraint. Here, the Crank-Nicolson scheme with time step $\Delta\bar{t}$ is used for temporal discretization [3]. The objective is to minimize the error between the average concentration measurements $\bar{y}_i^j = \bar{y}(\mathbf{x}_m^j, i\Delta\bar{t})$ of sensor j and the corresponding concentrations $\bar{c}_i^j = \bar{c}(\mathbf{x}_m^j, i\Delta\bar{t})$ at time step i. Note that Reynolds-averaging reduces the computational cost of solving eq. (4) since a larger time step $\Delta\bar{t} \gg \Delta t_m$ and thus less steps $n_T = T/\Delta\bar{t}$, can be used. The problem is minimized iteratively with the Conjugate-Gradient Method [3]. The required gradient w.r.t. $\bar{S}$ is computed with the adjoint method using the Firedrake package [5].

Results

The GSSE approach was tested with $n_s = 20$ spatially fixed gas sensors, fully known flow field $\bar{\mathbf{v}}$ and a single 2D Gaussian-shaped source

$$S(\mathbf{x}) = \frac{q}{2\pi\sigma^2} \exp\left(\frac{-1}{2\sigma^2} \left\| \mathbf{x} - \mathbf{x_s} \right\|_2^2 \right) , \tag{5}$$

at location $\mathbf{x_s}$, width σ and constant emission rate density q. The total emission rate Q is obtained by integrating $S(\mathbf{x})$ over the domain $\mathbf{\Omega}$. The center $\mathbf{x_s}$ and area A_σ, containing $\approx 0.68Q$ of the total emission rate is depicted in Fig. 1. From FE simulations for $T = 10\,\mathrm{s}$, the average fields and measurements are generated by averaging simulation data with a sampling time $\Delta t_m = 50\Delta t_s$. In eq. (4), time averaging over period $\Delta\bar{t} = T$ is performed and a diffusivity $\bar{D} = 0.8$ is used. The estimated source location $\mathbf{x}_s^*$ is obtained by searching for the midpoint of a circular area that includes the most emissions. The performance of the GSSE approach is statistically evaluated with histograms obtained from 80 trials of random sensor locations. The sensor locations $\mathbf{x}_m^j$ are sampled from a Sobol sequence to avoid sensor-clustering. The estimated field $\bar{S}^*(\mathbf{x})$ for a specific sample is shown in Fig. 1. The source was localized with a median error of $0.061L$ of the channel length L. In $71\,\%$ of the trials, the location error was below $0.1L$. The emission rate was overestimated in median to $1.842Q$, with $80\,\%$ of the trials in the range $[1.11Q, 2.54Q]$.

Conclusion

The proposed GSSE approach allows to estimate the spatial distribution of a gas source from in-situ gas measurements in geometrically non-trivial domains under the assumption of known flow. Thereby, measurements are combined with a non-stationary dispersion model with known initial and boundary conditions. Time-averaging of the model and measurements is performed to reduce the computational cost of the GSSE problem. From the estimated source field, the source-location could be determined accurately for most trials with different sensor placements. However, the emission rate was overestimated in all trials. It was observed that the source estimate improves when sensors are near the source. This indicates the importance of proper sensor placement for reliable GSSE. From an optimization perspective, it may also be beneficial to reduce the dimension of the problem by using a mesh-size-independent parametrization of the source field, e.g., a Neural Network with fewer parameters than the number of elements n_e [5]. Moreover, an approach to estimate the flow field from measurements is required to relax the restrictive assumption of known flow.

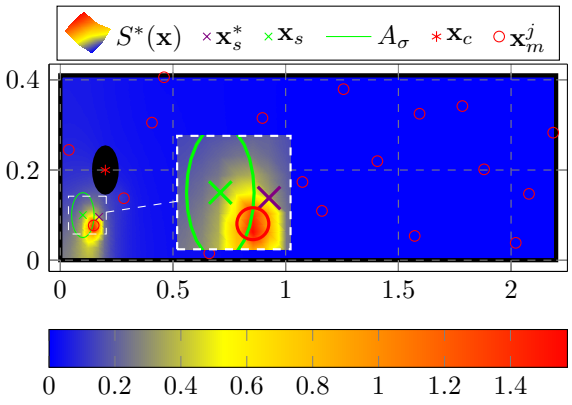

Fig. 1: Estimated source field $\bar{S}^*(\mathbf{x})$ from eq. (4) and location $\mathbf{x}_s^*$ for one trial. Ground truth $S(\mathbf{x})$ from eq. (5) indicated in green. Obstacle and channel boundaries shown in black. Sensor locations $\mathbf{x}_m^j$ shown as red circles.

References

[1] T. Wiedemann et al., "Gas Source Localization Based on Binary Sensing with a UAV," in *IEEE International Symposium on Olfaction and Electronic Nose (ISOEN)*, 2022. DOI: 10.1109/ISOEN54820.2022.9789553.

[2] R. Khodayi-mehr et al., "Model-Based Active Source Identification in Complex Environments," *IEEE Transactions on Robotics*, 2019. DOI: 10.1109/TRO.2019.2894039.

[3] H. Elman et al., *Finite Elements and Fast Iterative Solvers*. Oxford University Press, 2014. DOI: 10.1093/acprof:oso/9780199678792.001.0001.

[4] P. Zannetti, *Air Pollution Modeling*. Springer New York, 1990. DOI: 10.1007/978-1-4757-4465-1.

[5] N. Bouziani and D. A. Ham, "Physics-driven machine learning models coupling PyTorch and Firedrake," *ICLR 2023 Workshop on Physics for Machine Learning*, 2023. DOI: 10.48550/arXiv.2303.06871.

DOI 10.5162/SMSI2025/B1.3

Performance Assessment of Methane and Carbon Dioxide Sensors for Drone-Based Environmental Gas Monitoring

Mila Stanisavljevic[1], Sven Essel[2], Niklas Karbach[3], Johannes Zirzow[1], Thorsten Hoffmann[3], and Patrick P. Neumann[1]
[1]Bundesanstalt für Materialforschung und -prüfung, Unter den Eichen 87, 12205 Berlin, Germany
[2] Infraserv GmbH & Co. Höchst KG, Industriepark Höchst 65926, Frankfurt am Main
[3] Johannes Gutenberg University Mainz, 55128 Mainz, Germany
mila.stanisavljevic@bam.de

Summary:

This study evaluates the performance of methane (CH_4) and carbon dioxide (CO_2) sensors mounted on an unmanned aerial vehicle (UAV) for gas detection in open-field environments. Sensors were tested simultaneously during UAV flights over artificial gas sources, with wind data collected from two anemometers to understand plume dynamics. Field-deployed CH_4 sensors provided validation for the UAV-based measurements. The results demonstrate the sensors' effectiveness in gas detection.

Keywords: UAV-based gas sensing; Sensor comparison; Methane and carbon dioxide detection

1. Introduction

Detecting and monitoring methane (CH_4) and carbon dioxide (CO_2) is a key task that can be effectively accomplished using remotely operated platforms equipped with specialized sensors. Various sensor systems are currently available for deployment in mobile platforms such as unmanned aerial vehicles (UAVs) [1,2]. These payload systems typically are in conjunction with environmental sensors, enabling more accurate detection of CH_4 and/or CO_2 leaks and enhancing the monitoring of industrial gas sources [3]. To facilitate a transition from using individual sensors to an integrated network of mobile and stationary sensors, we initiated an experiment aimed at improving monitoring capabilities. This approach explores sensor limitations and enhances the understanding of their comparability across diverse deployment scenarios, including UAV-based applications.

2. Materials and Methods

2.1 UAV Platform

The DJI M300 RTK (Da-Jiang Innovations Science and Technology Co., Ltd, Hangzhou, China)(Fig1) is a commercially available quadcopter suitable for operating in harsh weather conditions. It offers a maximum flight time of 55 min and can carry up to 27 kg. In our case, the UAV was equipped with two different gas sensor setups:
1)Sniffer4D sensor (with a measurements range of 300-50, 000 ppm) mounted on the top of the platform: a Cubic SJH-5 (with a measurement range of 0–5000ppm CH_4) and SCD30 (with a measurement range of 400–10,000 ppm CO_2).
2)Cubic SJH-5 and SCD30 for CH_4 and CO_2 and MH-Z19B sensors for CO_2 mounted on the lower part of UVA.
The MH-219B sensor was operated on passive diffusion, while the Sniffer4D utilized its own integrated active gas inlet. In contrast, the SJH-5 and SCD30 sensors were connected to 2 m sampling tube for active sampling.

2.2. Experimental Setup

The experiments were conducted outdoors at BAM TTS (Technical Safety Test Site, Horstwalde Brandenburg, Germany). The experimental setup used 100% CH_4 and CO_2 gas cylinders as artificial sources connected to a tube and a fan to disperse the gas plume in the experimental area (Fig. 2).

Figure 1. DJI Matrice M300 RTK with i) Sniffer4D ii) SJH-5 and SCD30 sensors.

The fan's position was adjusted vertically between 0° and 80° to create different plumes. Two ultrasonic anemometers (uSonic-3, Metek GmbH) were placed approx. 5 m apart and mounted at a height of 3 m to monitor wind conditions. A network of 10 stationary CH_4 sensors (Dräger PIR 7000) was mounted on stands at 1 and 2 m height, respectively, providing high-resolution CH_4 data. In total, three experimental trials were conducted to survey the area near the fan and stationary sensor network. Two flights used sensor setup #1, while the other used sensor setup #2 for evaluating the aerial gas detection performance, see Sec. 2.1.

3. Results

3.1 Data Postprocessing

The first step in evaluating the results involved synchronizing the sensor data with geocoordinates, excluding takeoff and landing periods, and subtracting background CH_4 and CO_2. A time-lag detection algorithm was then applied, utilizing detrending, normalization, and cross-correlation to account for potential sensor delays [4]. The performance of the post-processed sensor data is presented in Tab 1.

Table 1. Summary of CH_4/CO_2 concentrations

Flight	*#1*		*#2*		*#3*	
(ppm)	*min*	*max*	*min*	*max*	*min*	*max*
Snifer4D	600	700	-		600	1500
SJH-5	1.98	3700	-		1.98	3300
SCD30	484	697	430	6228	480	857
MHZ19B	-		430	7322	-	
Dräger PIR 7000	-		-		2	2000

Flight #1: Sniffer4D detected concentrations between 600 and 700 ppm, while SJH-5 ranged up to 3700 ppm, showing its higher sensitivity.
Flight #2: Only CO_2 measurements were taken, with the SCD30 recording a maximum of 6,228 ppm and the MH-Z19B reaching 7,322 ppm.
Flight #3: After adjusting the fan position from 0° to 80°, the Sniffer4D sensor reached 1,500 ppm, still significantly lower than the SJH-5's 3,300 ppm. The stationary CH_4 sensors, which initially detected no signal with the fan at 0°, registered up to 2,000 ppm when the fan's position was changed, but only the three closest sensors were affected.
To confirm the Sniffer4D's limitations, laboratory tests were conducted with the Sniffer4D in ambient air and a 2.5% CH_4 cylinder, which confirmed similar results: the sensor could not detect ambient air and reported lower than expected values for the 2.5% cylinder, aligning with the field data.

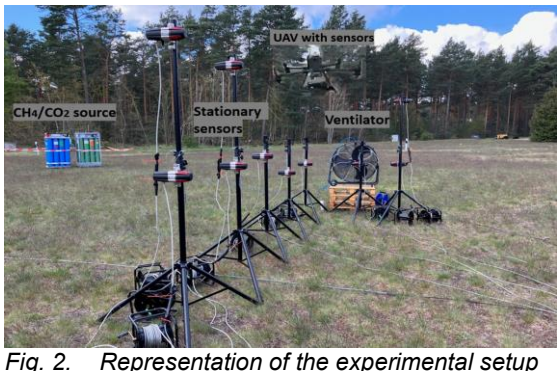

Fig. 2. Representation of the experimental setup

This comparison suggests that although we detected increased CH_4 and CO_2 concentrations, we were most likely not able to capture the whole extent of the plume during flights, especially with respect to its vertical extent. Moreover, we were unable to capture the entire plume with all sensors, highlighting potential limitations in the sensor placement, measurement limitations, and UAV's flight pattern. Factors such as UAV rotor downwash, fan position, sampling tube length, inlet type, and sensor position can all influence the results [3]. Additionally, Sniffer4D's factory calibration appears to be faulty and may have drifted over time, but this issue could be addressed with an external calibration, which is beyond the scope of this study.

Conclusions

This study demonstrated the feasibility of using UAV-mounted sensors for CH_4 and CO_2 plume detection in open-field conditions. Findings highlighted how sensor placement, fan angle adjustments, and sensor drift effects contribute to measurement variability, particularly for mobile setups. Future work should focus on refining sensor configurations and addressing environmental influences to enhance UAV-based gas detection systems' reliability.

References

[1] DJI, Matrice 300, Drone Safety (2024); accessed 28.10.2024. Available at: https://drone-safety.de/produkt/dji-matrice-300/

[2] D. Fosco, M. De Molfetta, P. Renzulli, B. Notarnicola, Progress in monitoring methane emissions from landfills using drones: An overview of the last ten years, *Science of The Total Environment*945,173981(2024);doi:10.1016/j.scitotenv.2024.173981

[3] P. P. Neumann, P. Hirschberger, M. Bartholmai, Influence of rotor downwash on vertically displaced nanobots in flight, Materials Today: Proceedings 2020; doi: 10.1016/j.matpr.2020.03.047

[4] P. Coïsson, K. Telali, B. Heumez, V. Lesur, X. Lalanne, C. J. Xin, Time-stamp correction of magnetic observatory data acquired during unavailability of time-synchronization services, Geosci. Instrum. Method. Data Syst. 6 (2017), 311–317 (2017); doi: 10.5194/gi-6-311-2017.

DOI 10.5162/SMSI2025/B1.4

Mobile Test Bed for Development and Validation of Networked Multimodal Gas Leakage Detection

Christian Fuchs, Ahmad Almohemied, Dennis Arendes, Andreas Schütze
Saarland University, Lab for Measurement Technology, Campus A5.1, 66123 Saarbrücken
c.fuchs@lmt.uni-saarland.de

Summary:
This work presents a mobile leakage test bed for gases (indoor and outdoor). This consists of a compressed gas cylinder on a cart that uses a mass flow controller to generate controllable leakage rates measured by multiple sensors. Bidirectional MEMS Microphones and MOS gas sensors are used for this purpose. Target is the development of multimodal sensor nodes combining different sensor signals with effective machine learning methods implemented on the sensor nodes for robust leak detection.

Keywords: Test Beds, Multimodal Measurements, Leakage Detection, MOS Gas Sensors, Directional MEMS Microphones.

Introduction

Leakages can occur in many places in an industrial context. Examples are gas containers and lines, compressed air, or rather pneumatics. The occurrence of leakages significantly reduces energy efficiency through loss of energy sources and can also result in safety risks. If these leakages can be detected and quantified, problem areas can be identified and fixed. Saving resources like compressed air or hydrogen is a significant benefit of leakage detection methods.

Various options are available to detect leakages. In previous publications, acoustic leakage detection was simulated [1] and performed with different sensor types [2-5]. Those sensor types used are vibration sensors [2], acoustic cameras [3], acoustic emission sensors [4,5], or a single microphone [6]. A different approach is the use of gas sensors [7]. To assess the combination of different sensor modalities for networked sensor nodes, a test bed was developed to simulate gas leakages. A compressed gas cylinder is installed on an aluminum cart and various leakages can be created, with the leak rate set by a mass flow controller. A pressure sensor is implemented to additionally monitor leakages with different sizes. Leakages can be simulated for any gas available in gas bottles.

Concept

The test bed is designed horizontally so that the gas cylinder is stored stably. The cylinder can be loaded from the back or front and is attached to the support surfaces with tension straps. Both 10 l and 50 l gas bottles are compatible, as the CAD model in Fig. 1 shows. Fig. 1 also shows

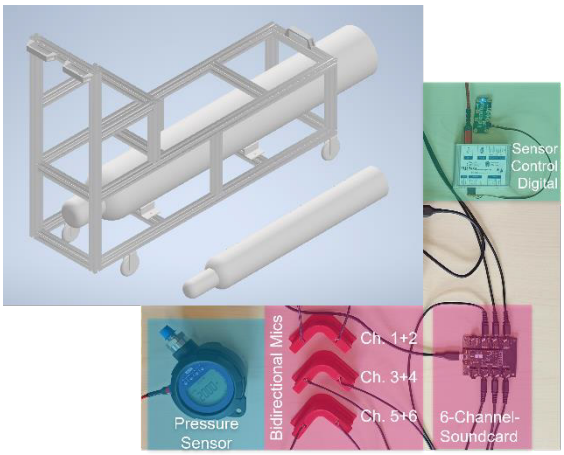

Fig. 1. CAD model of the test bed with gas cylinder and peripherals for flow control and data acquisition from microphones, gas sensors, and pressure sensor.

sensors and their data acquisition electronics implemented in the first iteration of the test bed.

To generate the targeted leak rates, a pressure reducer is attached to the gas bottle in front of a mass flow controller (MFC, MKS 1179A) allowing to set flow rates between 200 ml/min and 2000 ml/min (24 to 240 l/h). An outlet (in the first version a ¼ inch Swagelok pipe) is then used to allow the gas to flow into the environment. The pressure sensor is installed directly at the outlet in order to measure the relative pressure right in front of the restriction, which is shown in an example setup (Fig. 2).

The dynamic pressure depends on the outlet size and the flow rate. It is expected that the sound radiation increases significantly as the flow rate increases, but also depends on the outlet size and pressure. The sound characteristics

will also depend on the outlet shape (initially round) and gas type. From an acoustic point of view, the goal is to determine the flow rate for different outlet sizes and shapes based on sound radiation in characteristic frequency ranges (cf. experiments on pneumatic cylinders, [8]).

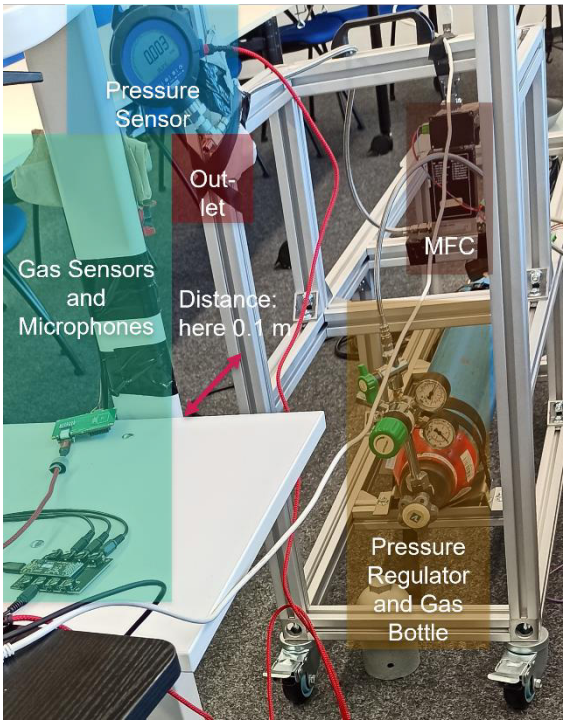

Fig. 2. Test bed setup for indoor experiments at different distances with four microphones (with/without housing, directed at the source/perpendicular to the source) and six gas sensors.

Regarding gas sensors, it is expected that complementary information can be gathered when gas is released due to the sensitivity of MOS sensors to a wide range of gases, e.g. hydrogen, methane, and VOC [9, 10] allowing more robust leak detection in industrial environments. Increased selectivity, i.e. based on multisensor arrays or dynamic operation, will provide further information on leak type and allow separation of various sources.

Design of Experiment

Experimental data, which will be presented in an upcoming journal, will include tests in indoor scenarios, i.e. with limited ambient influence, with sensors installed at different distances from the source. This experiment is intended to show how sensor signals change with distance. Further experiments will be conducted outdoors with different environmental conditions. This will allow optimization of the sensor set-up, i.e. directional information of microphones vs. undirected, optimal selection and operating mode of gas sensors for different sources as well as determination of the detection limit by combining microphones and gas sensors in different environments and at different distances. Further experiments will include acoustic and gas interferences as well as more complex sensor nodes, i.e. by implementing an anemometer for measuring wind speed and direction. This will also be tested under controlled conditions in indoor environments with fans to set defined wind directions and speeds.

The expected outcome are design recommendations for multimodal sensor nodes including the required signal processing for robust leak detection for various leak sources.

Acknowledgements

The project “Mimose-A” is funded by the German Federal Ministry for Economic Affairs and Climate Action (BMWK) under the grant number 03EN4057A-G. We acknowledge support by the Project Management Jülich (PTJ).

References

[1] K. Pugalenthi et al.: Leak detection in gas distribution pipelines using acoustic impact monitoring, *IECON* (2016). doi: 10.1109/IECON.2016.7793352

[2] S. Lee, B. Kim, Machine Learning Model for Leak Detection Using Water Pipeline Vibration Sensor, *Sensors*, *23*(21), 8935 (2023). doi: 10.3390/s23218935

[3] S. Ahmad et al.: A Method for Pipeline Leak Detection Based on Acoustic Imaging and Deep Learning, *Sensors 22*(4), 1562 (2022). doi: 10.3390/s22041562

[4] N. Ullah, Z. Ahmed, J.-M. Kim, Pipeline Leakage Detection Using Acoustic Emission and Machine Learning Algorithms, *Sensors 23*(6), 3226 (2023). doi: 10.3390/s23063226

[5] V.V. Shanbhag et al.: Condition monitoring of hydraulic cylinder seals using acoustic emissions, *Int J Adv Manuf Technol 109* (2020). doi: 10.1007/s00170-020-05738-4

[6] D. Diaz Ocampo et al.: Merkmalsbasierte luftakustische Diagnose von Druckluftleckage mithilfe maschineller Lernverfahren, *22. GMA/ITG-Fachtagung Sensoren und Messsysteme* (2024). doi: 10.5162/sensoren2024/A1.1

[7] A. Shrivastava et al.: GSM Based Gas Leakage Detection System, *Int. Journal of Technical Research and Applications* 1(2), 42-45 (2013).

[8] C. Fuchs et al.: Entwicklung akustischer Messungen für industrielles maschinelles Lernen. *DAGA Conference*, Stuttgart (2022).

[9] C. Schultealbert et al.: Measuring Hydrogen in Indoor Air with a Selective Metal Oxide Semiconductor Sensor. *Atmosphere*, *12*(3), 366 (2021). doi: 10.3390/atmos12030366

[10] A. Schütze et al.: Highly Sensitive and Selective VOC Sensor Systems Based on Semiconductor Gas Sensors: How to?, Environments 4, 20 (2017). doi: 10.3390/environments4010020

DOI 10.5162/SMSI2025/B2.1

Structural Investigations of Pore Nucleation after Electrochemical Porosification of 4H-SiC for MEMS

Georg Pfusterschmied[1,2], Christopher Zellner[1,2], Dominik Schock[1], Ulrich Schmid[1]
[1] TU Wien, Institute of Sensor and Actuator Systems, Gußhausstraße 27-29, 1040, Vienna, Austria
[2] Christian Doppler Laboratory for Sustainable Silicon Carbide Technology, Institute of Sensor and Actuator Systems, TU Wien, Gusshausstrasse 27-29, 1040 Vienna, Austria
Georg.Pfusterschmied@tuwien.ac.at

Summary:

The study emphasises the advantages of using electrochemical porosification to fabricate SiC-based MEMS devices, specifically focusing on improving pore nucleation control while preserving surface integrity. The results indicate that surface roughness plays a crucial role in pore nucleation, demonstrating the potential for improved MEMS device performance through carefully controlled substrate and etching conditions.

Keywords: SiC, electrochemical etching, nucleation layer, MEMS, resonator

Background, Motivation and Objective

Micro-electro-mechanical systems (MEMS) based resonators are pivotal in advancing technologies across various applications, such as precision timing devices, filters in communication systems, and sensors for automotive and aerospace industries [1, 2]. Silicon carbide (SiC), renowned for its exceptional material properties, including high thermal conductivity, mechanical robustness, and chemical stability, stands out as an ideal candidate for fabricating resonating MEMS devices, mainly when high quality factors are critical [3]. Despite the advantages of SiC, significant challenges remain in the cost-effective production of high-quality MEMS devices using this material. The integration of the cubic polytype 3C-SiC on silicon substrates has been vastly investigated. Still, SiC technology faces challenges such as significant differences in the coefficient of thermal expansion (CTE) of 8 % at room temperature and a lattice mismatch of about 20 %, leading to inherent stress and defects in the devices. These limitations hinder exploiting SiC's beneficial properties in MEMS applications [4]. As the cost of 4H-SiC wafers is anticipated to decrease in the foreseeable future, there is a growing interest in shifting focus towards manufacturing techniques that capitalise on 4H-SiC bulk wafers for MEMS device fabrication. One promising technology is photoelectrochemical etching [5], which facilitates the fast formation of porous 4H-SiC with tailored degrees of porosity. This technique enables the subsequent growth of a polycrystalline or even epitaxial 4H-SiC layer, potentially overcoming previous material integration challenges and paving the way for more cost-effective and high-performance SiC-based MEMS devices. With this technique, in combination with a thermal annealing step, mechanical structures such as membranes have already been reported [6]. During PEC etching of SiC and other semiconductors like silicon, a so-called cap layer is commonly observed in the initial few tens of nanometers of etching. This cap layer contributes to an irregular and difficult-to-control pore formation front, which has historically led researchers to develop nucleation layers to facilitate more controlled porosification. However, forming a nucleation layer with specific surface roughness can impede the deposition of subsequent epitaxial layers. The compromised surface quality induces certain defects during the growth of the epitaxial layer, negatively impacting both the layer quality and, hence, the quality factor of MEMS devices constructed from it [7].

Description of the New Method or System

The focus of this study is to provide deeper insights into the pore nucleation during the electrochemical etching of SiC to enable better control over porosification while maintaining a high degree of surface integrity for later epitaxial growth. This understanding is crucial to enhance the fabrication quality of MEMS devices, ensuring high performance and reliability.

4-inch wafers of n-type 4H-SiC with a 4 ° off-axis and a bulk resistivity of 0.02 Ω·cm were cut in 2.5 × 2.5 cm^2. The surface roughness of the C-face and the Si-face before EC etching is < 2 nm and < 0.1 nm, respectively. Electrochemical etching was performed in a tabletop etching cell from AMMT, shown in Fig. 1 a). The samples are placed between two etching cell compartments, acting as a separation wall between the two electrodes. When a bias is applied, SiC is oxidised at the cell's anode and dissolved by hydrofluoric acid (HF), etching pores on the face

adjacent to the electrode with the negative potential. A solution consisting of 5.52 mol/L HF and 1.7 mol/L ethanol was used. The corresponding etching profile is shown in Fig 1 b). Due to the relatively high conductivity of the used sample, no additional UV light illumination was required. Plasma etching from 10 s up to 30 s was conducted on porosified samples stepwise to expose the pore formation during the first 150 nm using 25 sccm O_2, 5 sccm SF_6 and a plasma power of 300 W in a parallel plate plasma etcher from STS.

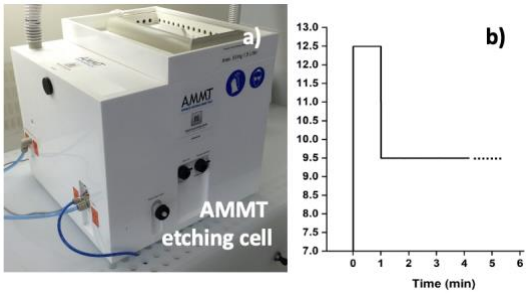

Fig. 1 a) Picture of the tabletop etching cell from AMMT, and b) Illustration of the applied voltage profile during electrochemical etching.

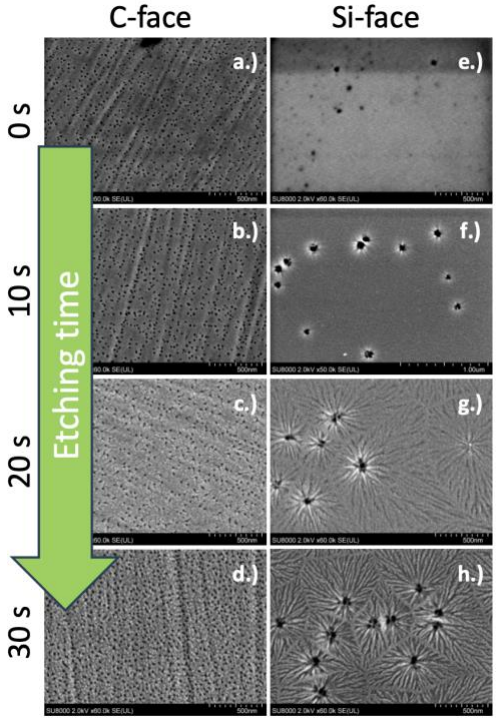

Fig 2 Results from plasma etching of a.-d.). the C-face etched sample and e.-h.) the Si-face etched sample. Etching rates of 300 nm/min and 225 nm/min were observed for the C- and the Si-face, respectively.

Results

Fig 2 shows the top-view SEM images for the C-face (a-d) and the Si-face (e-h). On the C-face etched samples, as shown in a.), extensive pore nucleation occurred, which can be explained by the minimal but sufficient surface roughness of < 2 nm. It can be seen that pore nucleation predominantly takes place along the nanometer-deep polishing scratches. No significant change in the porous structure was observed when the top surface was etched for 10-30s, as seen in Fig 2 (b-d). It is worth noticing that side branching was observed after 20 s of plasma etching. Furthermore, a significant increase in pore density from 250 pores/µm^2 (0 s) to 400 pores/µm^2 (30 s) took place. However, only scattered but larger pores were observed on the atomically flat Si-face with surface roughness values below 0.1 nm (Fig 2 e). After plasma etching of 20 s, a significant change in pore propagation was observed. Lichtenberg figures could be observed (see Fig 2 g and h).

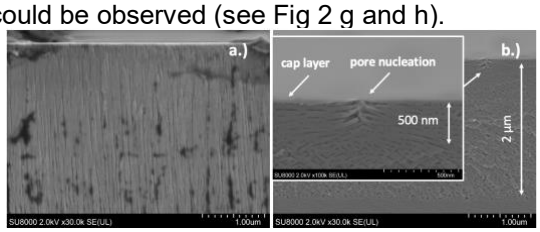

Fig 3 Cross-sectional SEM images of the samples etched from a.) the C-face and b.) the Si-face.

In Fig 3 cross-section SEM images of porosified samples for a) the C-face and b) the Si-face are shown. Continuous and cylindrical pores could be observed for the C-face, which are typical of C-faced etched samples. For the Si-face etched sample shown in b.), the impact of pore nucleation and the corresponding Lichtenberg figure are visible and cause a chaotic porosification profile. These findings indicate that even low energetic plasma surface treatment can facilitate pore nucleation on SiC.

References

[1] C. T. Nguyen, "MEMS technology for timing and frequency control," *IEEE Trans Ultrason Ferroelectr Freq Control,* vol. 54, no. 2, pp. 251-270, 2007, doi: 10.1109/TUFFC.2007.240.

[2] D. S. Eddy and D. R. Sparks, "Application of MEMS technology in automotive sensors and actuators," *Proceedings of the IEEE,* vol. 86, no. 8, pp. 1747-1755, 1998.

[3] Z. Liu, Y. Long, C. Wehner, H. Wen, and F. Ayazi, "4H silicon carbide bulk acoustic wave gyroscope with ultra-high Q-factor for on-chip inertial navigation," *Communications Engineering,* vol. 3, no. 1, p. 87, 2024.

[4] M. Albani *et al.*, "Solving the critical thermal bowing in 3C-SiC/Si(111) by a tilting Si pillar architecture," *Journal of Applied Physics,* vol. 123, no. 18, p. 185703, 2018, doi: 10.1063/1.5019325.

[5] J.-N. Chazalviel, R. Wehrspohn, and F. Ozanam, "Electrochemical preparation of porous semiconductors: from phenomenology to understanding," *Materials Science and Engineering: B,* vol. 69, pp. 1-10, 2000.

[6] M. Leitgeb, C. Zellner, G. Pfusterschmied, M. Schneider, and U. Schmid, "Porous Silicon Carbide for MEMS," in *EUROSENSORS 2017* vol. 1, ed. Paris, France, 2017, p. 297.

[7] S. E. Saddow *et al.*, "Structural Characterization Of Sic Epitaxial Layers Grown On Porous Sic Substrates," *MRS Proceedings,* vol. 640, p. H2.7, 2000, Art no. H2.7, doi: 10.1557/PROC-640-H2.7.

DOI 10.5162/SMSI2025/B2.2

Avoided mode-crossing in MEMS resonators under different dissipation mechanisms

Andre Gesing[1], *Erwien Gietl*[1], *Marco Stixenberger*[1], *Daniel Platz*[1], *and Ulrich Schmid*[1]
[1] TU Wien, Institute of Sensor and Actuator Systems, Gußhausstraße 27-29, 1040, Vienna, Austria
andre.gesing@tuwien.ac.at

Summary: This study investigates the phenomenon of avoided-crossing in MEMS resonators and its impact on the quality factor (Q-factor) under two key dissipation mechanisms: anchor losses and fluid-structure interaction. Numerical and experimental results reveal significant reductions in Q-factors during mode crossings and avoided-crossings, particularly in scenarios involving width variations and fluid density changes. These findings highlight the need to consider avoided mode-crossing in MEMS resonators for obtaining high Q-factors and hence, high device sensitivity as well as predictable bandwidth.

Keywords: MEMS, Avoided-crossing, Anchor losses, Fluid-structure interaction

Background, Motivation and Objective

MEMS are ubiquitous components in modern technology, integral to applications in sensing, communication, and energy harvesting [1]. MEMS resonators are characterized by the resonance frequency and quality factor (Q-factor) of their vibrational modes. When a parameter of the resonator or its surrounding environment changes, the resonance frequencies and corresponding vibrational modes also shift. A particularly intriguing phenomenon occurs when two resonance frequencies converge closely: vibrational modes often degenerate, and resonance frequencies "veer" apart in a phenomenon known as avoided-crossing or mode-veering [2, 3].

Understanding multimode effects, such as avoided-crossing and mode localization [4], is critical for optimizing MEMS resonators. Research has predominantly focused on changes in resonance frequencies and vibrational modes, leaving its impact on the Q-factor underexplored. This study addresses this gap by presenting a theoretical framework as well as experimental results to investigate the influence of avoided-crossing on the Q-factor in two distinct scenarios: anchor losses and fluid-structure interaction.

Description of the New Method or System

The Q-factor Q is defined as the ratio of stored energy in a structure to dissipated energy over an oscillation period. As different damping mechanisms contribute to the dissipated energy, we focus on anchor losses and fluidic losses. Anchor losses in MEMS resonators arise from the energy radiating into the substrate through the mechanical supports, leading to energy dissipation and a reduction in the Q-factor. To model and quantify these losses, we employ the Finite Element Method (FEM) with the governing equation as the linear elasticity in the absence of external forces

$$\nabla \cdot \sigma + \rho\omega^2 \mathbf{u} = \mathbf{0}, \tag{1}$$

where σ represents the Cauchy stress tensor, ρ is the density, ω is the angular frequency and $\mathbf{u}$ is the displacement tensor. The system is solved incorporating a Perfectly Matched Layer (PML) to simulate the energy absorption in the substrate effectively, yielding a complex eigenvalue $\tilde{\omega}$ problem from which the Q-factor is determined as

$$Q_{\mathrm{anchor}} = \frac{\mathrm{Re}(\tilde{\omega})}{2\mathrm{Im}(\tilde{\omega})}. \tag{2}$$

For the fluidic Q-factor, we adopt a semi-numerical approach based on the Kirchhoff plate equation coupled with the Stokes flow for fluid dynamics as

$$\frac{h^3}{12} C_{\alpha\beta\gamma\delta}\phi_{,\alpha\beta\gamma\delta} - \omega^2 \rho h \phi = P_{\mathrm{ext}} + P_z, \tag{3}$$

where $C_{\alpha\beta\gamma\delta}$ are the components of the fourth-order elasticity tensor. P_{ext} is a driving force and P_{hydro} is the hydrodynamic point force [5]. This equation is solved with Galerkin mode decomposition (GMD), which efficiently determines the spectral displacement ϕ of wide resonators in viscous fluids, from which Q and the resonance frequencies are obtained.

Results

We investigate avoided mode-crossing by considering a cantilevered silicon microplate with length equals 200 μm, thickness equals 15 μm and width varying from 250 μm to 500 μm. Selected resonance frequencies and Q-factors are shown in Fig. 1. Those are for the out-of-plane modes 1:3 and 2:1, as well as the lateral mode. At a width of 355.5 μm, the modes

2:1 and 1:3 are subject to an avoided-crossing phenomenon, where the resonance frequencies veer apart instead of simply crossing over each other. Crucially, note that avoided-crossing is accompanied by a significant decrease in the Q-factor of the 1:3 mode, as seen on Fig 1b. A different mode crossing occurs between the lateral and 1:3 modes at a width of 316.5 μm where no veering of the resonance frequencies is observed. Neverthelles, the mode crossing results in a pronounced reduction in the Q-factor for the 1:3 mode from $Q \approx 10^6$ to $Q \approx 10^3$. To confirm these observations, experiments were performed, whose results for the 1:3 mode are shown in Fig. 1c, where similar drops in Q are seen in $w \approx 365$ μm and $w \approx 320$ μm due to the crossing of the resonance frequencies of the 1:3 mode with other modes.

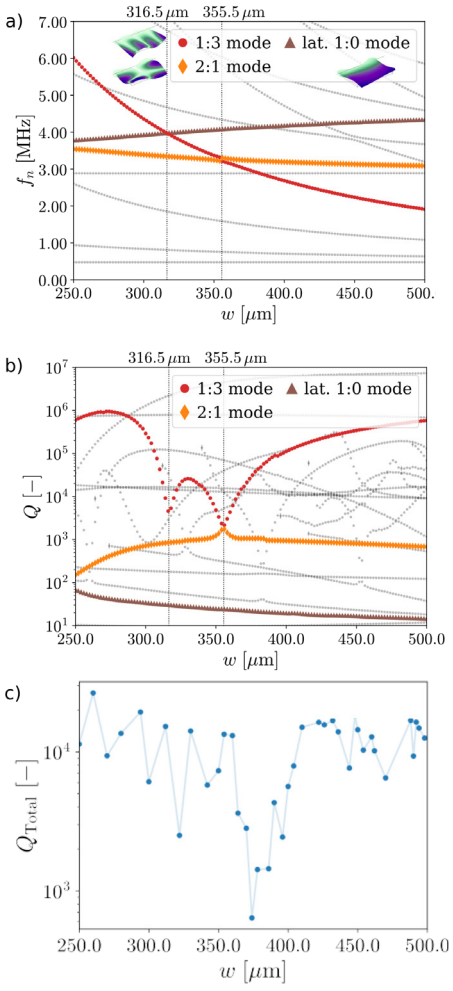

Fig. 1: a) Resonance frequencies and b) Q-factors (right) of MEMS resonator modes as a function of resonator width, varying from 250 μm to 500 μm. c) Experimentally measured Q-factor of the 1:3 mode showing similar drops at $w \approx 365$ μm and $w \approx 320$ μm.

In addition to the anchor losses analysis, we also consider fluidic damping. The resonance frequencies and Q-factors of the 5:0 and 3:2 modes were analyzed for a silicon microplate as a function of fluid density ranging from 1 kg/m^3 to 1000 kg/m^3. Note that a notable increase in the Q-factor in the 3:2 mode occurs at a fluid density of approximately 10 kg/m^3 as shown in Fig. 2. This sudden change indicates an interaction with another mode, where the energy dissipation mechanism of mode 3:2 is altered through the fluid-structure coupling.

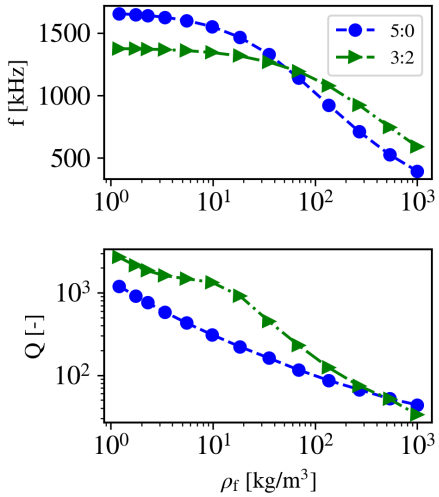

Fig. 2: Resonance frequencies (top) and Q-factors (bottom) of the 5:0 mode (blue circles) and 3:2 mode (green triangles) as a function of fluid density.

These findings demonstrate the sensitivity of MEMS resonator's Q-factors to avoided-crossing.

References

[1] L. Wei et al. The recent progress of MEMS/NEMS resonators, *Micromachines* 12, 724 (2021); doi: 10.3390/mi12060724

[2] H. Ouakad, S. Ilyas, M. Younis, Investigating Mode Localization at Lower- and Higher-Order Modes in Mechanically Coupled MEMS Resonators, *Journal of Computational and Nonlinear Dynamics* 15, 031001 (2020); doi: 10.1115/1.4045634

[3] N. alcheikh, H. Ouakad, S. Mbarek, and M. Younis, Crossover/veering in V-shaped MEMS resonators, *Journal of Microelectromechanical Systems* 15, 74-86 (2021); doi: 10.1109/JMEMS.2021.3126551

[4] Y. Wang et al. A mass sensor based on 3-DOF mode localized coupled resonator under atmospheric pressure, *Sensors and Actuators A: Physical* 279, 254-262 (2018); doi: 10.1016/j.sna.2018.06.028

[5] A. Gesing, T. Tran, D. Huber, D. teinmüller-Nethl, G. Pfusterschmied, D. Platz, M. Schneider and U. Schmid. The gas-liquid-Q-factor-inversion in MEMS plate resonators, *Journal of Sound and Vibration* 559, 117777 (2023); doi: 10.1016/j.jsv.2023.117777

DOI 10.5162/SMSI2025/B2.3

Simultaneous Analysis of Local Device Layer Thickness and Film Stress on Cantilevered MEMS Structures

Dominik Huber[1], Christoph Schallert[1], Georg Pfusterschmied[1], Ulrich Schmid[1]
[1] TU Wien, Institute of Sensor and Actuator Systems, Gußhausstraße 27-29, 1040, Vienna, Austria
Dominik.Huber@tuwien.ac.at

Summary:

This paper reports on a passive MEMS structure facilitating the local measurement of both, the device layer thickness and residual film stress with white light interferometry (WLI). The structure consists of a released single-side clamped plate (SSCP) and a step-profile etched through the device layer down to a silicon dioxide layer. In doing so, both the static deflection and the thickness are determined, independent of material parameters, such as the index of refraction or surface roughness. Both key properties can be efficiently measured with the same tailored WLI set-up.

Keywords: device layer thickness, film stress, WLI, SiC, automation

Background, Motivation, and Objective

Tolerances of the device layer properties, such as thickness or residual stress are common for standard SOI wafers in the MEMS industry as well as for any thin films deposited during device fabrication[1, 2]. Ellipsometry is a well-established technique for the analysis of the thickness of thin films [3]. It is a fast and non-destructive technique to measure the impact of the thin film on polarized light. To calculate the thickness of a thin film from that measurement, precise knowledge about material parameters, e.g., index of refraction, is necessary, and a smooth surface is highly recommended. On wafer-level the curvature measurement is widely applied to calculate the residual stress from Stoney's formula [4]. This technique has the disadvantage, that it is developed for uniform thin film thickness, which led to extensive progress on passive test structures for optical measurements of the static deflection[5, 6]. However, there is still the need to determine both parameters, static deflection, and thickness, with the same WLI set-up on-chip with a fully automated approach.

Description of the New Method or System

In this study, we present the simultaneous measurement of the static deflection of released SSCP structures and the device layer thickness with the same WLI set-up. This combination allows for the development of a high-precision residual stress map across a wafer with minimal time consumption. Test structures consisting of an SSCP and a step-profile close to the anchor region are presented in *Figure 1*. The step-profile consists of 50 µm wide trenches etched through the device layer. Utilizing deep reactive ion etching (DRIE), the plates are released from the substrate, whereas the stress in the device layer leads to a static deflection. Plates with a constant length of 500 µm and different widths ranging from 50 µm to 1000 µm were fabricated, enabling the characterization of local stress profiles. In general, a straightforward integration of such test structures is possible for MEMS devices, achieving local information, such as thin film thickness and in further consequence, the intrinsic film stress.

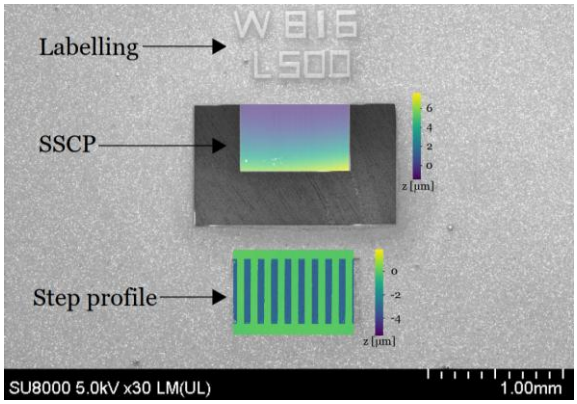

Figure 1: SEM image of the MEMS structure consisting of an 816 µm wide and 500 µm long SSCP released from the back, and a step-profile with 10 trenches etched only from the front side. A width of 50 µm per trench is realized by standard DRIE technique.

Results

In *Figure 1*, the SEM image of the MEMS structure indicates the extracted WLI measurement data. Automated WLI scans of MEMS structures spread across a 4" SOI-wafer are shown in *Figure 2*. Especially the data on the thin film thickness of the single crystalline silicon device layer displays the stated thickness variation of the wafer manufacturer of ±0.5 µm and gives a strong argument for the local knowledge of the device layer thickness for MEMS devices. Even more, a polycrystalline SiC thin film is analyzed with the same technique, and the thin film thickness, as well as the static deflection for two rows of devices, are shown in *Figure 3*. Following the considerations of Bao [7] on a beam under a bending moment, the residual stress values for the devices are calculated and shown in *Figure 4* as

a function of the device position on the wafer, thus proving the high potential of this approach.

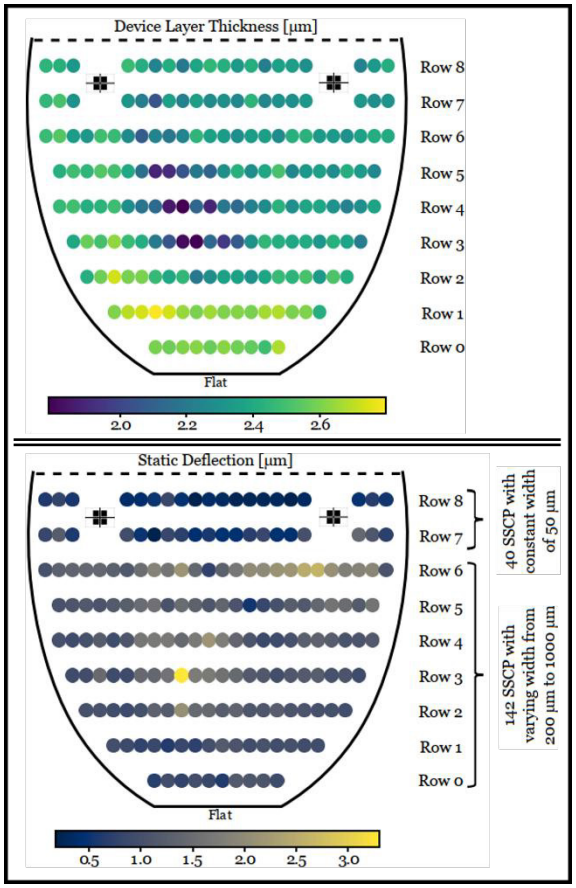

Figure 2: Scans of thin film thickness (top) and static deflection (bottom) on 182 MEMS structures positioned across half of the surface of a 4" wafer. The device layer material is single crystalline silicon from an SOI wafer with a stated thickness from the manufacturer of 2±0.5 µm. We find a rather large deviation in thin film thickness of 35 % but very low static deflection of the plates, resulting in low residual stress values below 10 MPa. The upper part of the wafer was used for investigations not relevant to this study.

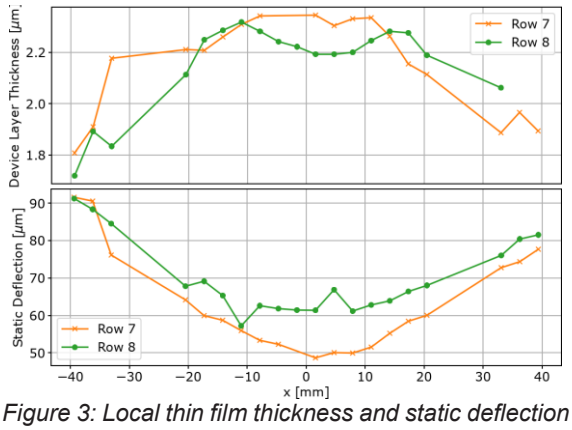

Figure 3: Local thin film thickness and static deflection of rows 7 and 8 across the center of a 4" wafer coated with polycrystalline SiC in an LPCVD process [8]. The wide spread of thin film thickness from 1.7 µm at the wafer edge to 2.3 µm in the center is expected due to the horizontal positioning of the wafer substrate in the quartz tube of the CVD furnace parallel to the gas flow. The static deflection at the tip of the SSCP ranges from 50 µm in the center to 90 µm at the edge.

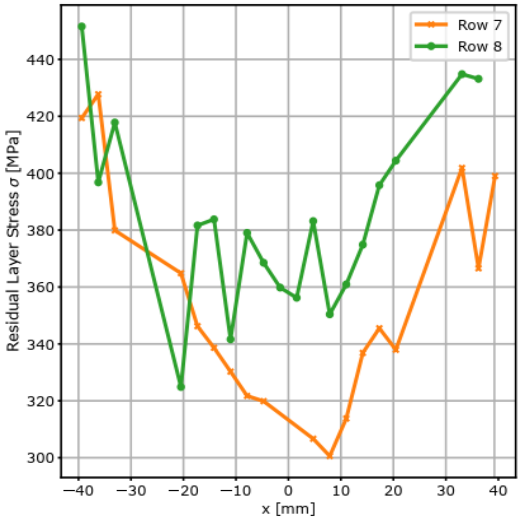

Figure 4: An experimentally determined Young's modulus of 217 GPa is used for the calculation of the residual stress for the measured SiC data in Figure 3, leading to a compressive stress in a range from 300 MPa to 450 MPa. Despite a reduction of the film thickness towards the edges of the wafer, there is an increase of the residual stress reflecting the increase of the static deflection of the SSCPs.

References

1. Brouzet, V., et al. *Full Wafer Stress Metrology for Dielectric Film Characterization: Use Case*. in *2019 30th Annual SEMI Advanced Semiconductor Manufacturing Conference (ASMC)*. 2019.
2. Moriceau, H., F. Fournel, and F. Rieutord, *1 - Materials and manufacturing techniques for silicon-on-insulator (SOI) wafer technology*, in *Silicon-On-Insulator (SOI) Technology*, O. Kononchuk and B.-Y. Nguyen, Editors. 2014, Woodhead Publishing. p. 3-51.
3. Tompkins, H.G., *A User's Guide to Ellipsometry*. 2006: Dover Publications.
4. Chen, K.-S. and K.-S. Ou, *Chapter 17 - MEMS Residual Stress Characterization: Methodology and Perspective*, in *Handbook of Silicon Based MEMS Materials and Technologies (Second Edition)*, M. Tilli, et al., Editors. 2015, William Andrew Publishing: Boston. p. 398-412.
5. Masters, N., et al., *Side-by-Side Comparison of Passive MEMS Strain Test Structures under Residual Compression*, in *Mechanical Properties of Structural Films*. 2001, ASTM International. p. 0.
6. Guckel, H., et al., *Diagnostic microstructures for the measurement of intrinsic strain in thin films.* Journal of Micromechanics and Microengineering, 1992. **2**(2): p. 86.
7. Bao, M., *Analysis and design principles of MEMS devices*. 2005: Elsevier.
8. Moll, P., et al., *Impact of alternating precursor supply and gas flow on the LPCVD growth behavior of polycrystalline 3C-SiC thin films on Si.* Sensors and Actuators A: Physical, 2024. **372**: p. 115376.

DOI 10.5162/SMSI2025/B2.4

Nanoelectromechanical System Fourier Transform Infrared Spectroscopy (NEMS-FTIR) for Nanoplastic Analysis

Jelena Timarac-Popović[1, 2], Johannes Hiesberger[2], Niklas Luhmann[2], Ariane Giesriegl[1], Hajrudin Bešić[1], Josiane P. Lafleur[2], and Silvan Schmid[1]

[1] TU Wien, Institute of Sensor and Actuator Systems, Gusshausstrasse 27-29, 1040 Vienna, Austria
[2] Invisible-Light Labs GmbH, Taubstummengasse 11, 1040 Vienna, Austria
jelena.popovic@tuwien.ac.at

Summary: We introduce a novel application of photothermal infrared spectroscopy based on nanoelectromechanical systems (NEMS), integrated with a commercially available FTIR spectrometer (NEMS-FTIR). We successfully detected 1 ng of polystyrene (PS) and 1 ng of polypropylene (PP) nanoplastic particles with diameters of 100 nm and 54 nm, respectively. As a case study, we detected small amounts of degradation products originating from plastic tubing. The technique enabled high-resolution spectral identification of samples from microliter to nanoliter volumes on NEMS chips.

Keywords: nanoplastics, trace substances, photothermal sensing, Fourier transform infrared spectroscopy, NEMS-FTIR, degradation

Introduction

The degradation and fragmentation of plastics, driven by various physical and chemical factors, results in the formation of microplastics (MPs) and nanoplastics (NPs), alongside the release of harmful substances and additives into the environment [1]. The growing prevalence of NPs in both the environment and the tissues and cells of living organisms has raised significant concerns regarding their potential biological effects [2].

Analytical techniques such as mass spectrometry-based techniques, surface-enhanced Raman spectroscopy (SERS), and atomic force microscopy-infrared spectroscopy (AFM-IR) offer good sensitivity with detection limits typically in the nanogram to picogram range, depending on the specific method [3]. However, their widespread application for routine environmental monitoring is hindered by factors such as expensive equipment, time-intensive procedures and sample preparation, which limit their practicality in large-scale studies [3].

Nanoelectromechanical infrared (NEMS-IR) spectroscopy, a new analytical approach based on NEMS chips comprising a resonator, has shown very good sensitivity down to the picogram level for the detection of various substances, including polymeric nanoparticles [4], and pharmaceutical compounds [5]. However, the reliance of NEMS-IR on expensive quantum cascade lasers (QCLs), which have a narrow spectral range, limits its applicability for routine nanoparticle monitoring.

In this study, we present NEMS-Fourier transform infrared spectroscopy (NEMS-FTIR) as a novel solution for the chemical analysis of NPs and other trace substances that exhibit IR absorption profiles. Here, in contrast to NEMS-IR, widely available FTIR spectrometers are used as light sources, providing a method with a wide spectral range for IR analysis.

Materials

Polystyrene-based nanoparticles (PS, ⌀100 nm) were purchased from Sigma Aldrich (USA) as a 10%w/v aqueous suspension and polypropylene particles (PP, ⌀54 nm) were obtained from Lab261 (USA) as a 1%w/v suspension. For 50 µg/mL suspensions, UHPLC-MS grade water (Thermo Fisher Scientific, USA) was used for dilution.

Tygon tubing (LMT-55) was used for the plastic degradation experiment. Tubing segments (8 mm long, 3 mm OD, 1 mm ID) were first washed with DI water (18 MΩ·cm; Millipore, USA) to remove potential surface contaminants and then soaked in ethanol (HPLC grade, Sigma Aldrich, USA), with exposure times ranging from 0.5 to 4 minutes. Segments were handled with clean metal tweezers to avoid contamination.

Methods

NEMS chips were fabricated using standard cleanroom lithography. At their center is a 1x1 mm^2 silicon nitride (SiN) membrane whose tensile stress is approximately 50 MPa. Electrical transduction is enabled by two gold electrodes extending along the membrane, each 10 µm wide, allowing the conversion of mechanical vibrations into electrical signals [6, 7].

Due to its robustness, the samples can be applied to the membranes using different sampling techniques [8]. A nanoliter dispenser (BioFluidix-Hamilton, Germany) was used to deposit 20 nL PS and PP suspensions, depositing 1 ng of particles on the membranes. Micropipettes were used to deposit 2 µL of ethanol in which parts of the plastic tubing were soaked.

During the measurement, NEMS chips were positioned at ~10^{-5} mbar inside the nanoelectromechanical IR analyzer (EMILIE™, Invisible-Light Labs GmbH, Austria). When exposed to IR light, the sample absorbs the radiation and heats up, causing thermal expansion and reduced tensile stress in the membrane. The change in oscillation frequency, monitored via a self-sustaining oscillator and a frequency counter [7], correlates with absorbed power. The IR spectrum was generated in the range of 4000 to 400 cm^{-1}, with FTIR settings for resolution, delay, co-additions, and aperture at 4 cm^{-1}, 30 ms, 200 and 6 mm, respectively.

Results

The NEMS-FTIR spectra of 1 ng of PS and PP NPs are shown in Fig. 1, where characteristic IR peaks of these materials are observed [9] and presented as vertical dashed lines.

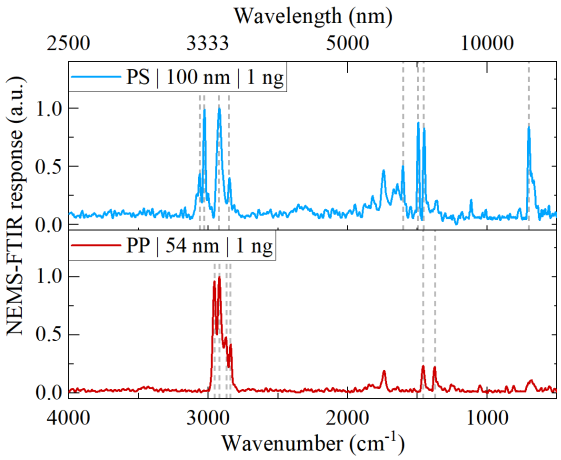

Fig. 1: NEMS-FTIR spectra of 1 ng of PS NPs (top) and PP NPs (bottom). Vertical lines mark the characteristic peaks of each polymer.

Fig. 2 presents NEMS-FTIR spectra of ethanol samples after plastic tubing immersion, showing increasing peak intensity with time, indicating progressive dissolution of the tubing due to its lack of ethanol resistance. IR database analysis identified alkyd varnish and polyurethane, which may originate from tubing additives or coatings dissolving in ethanol.

Summary and outlook

NEMS-FTIR presents as potential tool for detecting nanoplastic particles and degradation products of plastics, even from short exposure times, providing a sensitive alternative to more complex methods. The ability to use online available databases further enhances its practicality. While the technique can detect substances down to the low nanogram range, with the potential for detection in the picogram range, extraction from complex environmental matrices may be necessary.

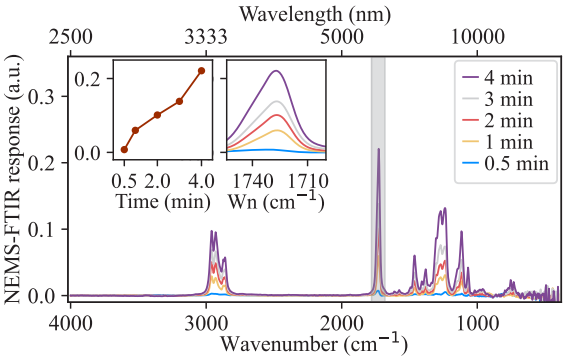

Fig. 2: NEMS-FTIR spectra of degradation products from plastic tubing in ethanol after immersion for different durations. The right inset shows an enlarged view of the 1727 cm^{-1} peak, while the left inset illustrates the change in intensity of this peak over time.

References

[1] A. A. Koelmans, E. Besseling, E. M. Foekema, Leaching of plastic additives to marine organisms, *Environmental Pollution* 187, 49-54 (2014); doi: 10.1016/j.envpol.2013.12.013

[2] N. Ali, J. Katsouli, E. L. Marczylo, T. W. Gant, S. Wright, J. B. de la Serna, The potential impacts of micro- and nanoplastics on various organ systems in humans, *eBioMedicine* 99, 104901 (2024); doi: 10.1016/j.ebiom.2023.104901

[3] J. Caldwell, P. Taladriz-Blanco, R. Lehner, A. Lubskyy, R. D. Ortuso, B. Rothen-Rutishauser, A. Petri-Fink, The micro-, submicron-, and nanoplastic hunt: A review of detection methods for plastic particles, *Chemosphere* 293, 133514 (2022); doi: 10.1016/j.chemosphere.2022.133514

[4] S. Yamada, S. Schmid, T. Larsen, O. Hansen, A. Boisen, Photothermal infrared spectroscopy of airborne samples with mechanical string resonators, *Anal. Chem.* 85(21), 10531–10535 (2013); doi: 10.1021/ac402585e

[5] M. Kurek, M. Carnoy, P. E. Larsen, L. H. Nielsen, O. Hansen, T. Rades, S. Schmid, A. Boisen, Nanomechanical infrared spectroscopy with vibrating filters for pharmaceutical analysis, *Angew. Chem.* 129(14), 3959–3963 (2017); doi: 10.1002/ange.201700052

[6] N. Luhmann, R. G. West, J. P. Lafleur, S. Schmid, Nanoelectromechanical Infrared Spectroscopy with In Situ Separation by Thermal Desorption: NEMS-IR-TD, *ACS Sensors* 8(4), 1462–1470 (2023); doi: 10.1021/acssensors.2c02435

[7] H. Bešić, A. Demir, V. Vukićević, J. Steurer, S. Schmid, Adaptable Frequency Counter with Phase Filtering for Resonance Frequency Monitoring in Nanomechanical Sensing, IEEE Sensors Journal (2024); doi: 10.1109/JSEN.2024.3355026

[8] R.G. West, K. Kanellopulos, S. Schmid, Photothermal microscopy and spectroscopy with nanomechanical resonators, *The Journal of Physical Chemistry C* 127, 21915–21929 (2023); doi: 10.1021/acs.jpcc.3c04361

[9] B. Smith, The infrared spectra of polymers III: Hydrocarbon polymers, *Spectroscopy* 36(11), 22-25 (2021); doi: 10.56530/spectroscopy.mh7872q7

DOI 10.5162/SMSI2025/B3.1

High-Sensitive Chromium Strain Gauges on Steel Surfaces

Rico Ottermann, Tobias Steppeler, Marc Christopher Wurz
Institute of Micro Production Technology, Leibniz University Hannover,
An der Universitaet 2, 30823 Garbsen, Germany
ottermann@impt.uni-hannover.de

Summary:
This article presents the photolithographic manufacturing and characterization of high-sensitive chromium-based strain gauges. They are produced polymer-free on stainless-steel tensile specimens and show high k-factors (strain sensitivity) of 11.0 ± 0.1. Their temperature coefficient (temperature sensitivity) of 591 ± 23 ppm/°C is comparably high which is why a full-bridge arrangement in cooperation with a temperature sensor next to it is used. This leads to a sensor system that can be used for harsh environment pressure measurements with a sensitivity of 1.71 µV/V/µm/m.

Keywords: Strain gauges, Chromium, Sputtering, Strain measurement, Polymer-free

Introduction

Strain sensors are crucial components in various industrial and research applications where precise measurement of deformation is essential. In industries such as aerospace and civil engineering, strain sensors provide real-time data on structural integrity, allowing for predictive maintenance, structural health monitoring and improved safety. Commercial strain gauges are polymer-foil based and attached with an adhesive to the measurement object [1]. Here, errors can occur due to different attachment conditions. Additionally, they have limitations when it comes to harsh environments like elevated temperature or chemical resistance [1],[2]. For this purpose, polymer-free thin-film sensors are used, for example for harsh environment pressure sensors [2]. Since mainly metallic components are of interest, the thin-film layers are deposited directly onto the surface based on the sputtering technology [3]. Because this technique allows not only the free choice of the sensor layer design but also its material, research is conducted concerning high-sensitivity materials. In comparison to standard materials like constantan or NiCr (k ≈ 2 [1]), extremely high k-factors of 174 can be reached with doped silicon but only in MEMS technology [4]. Sputtered materials such as Ni-DLC (Diamond-like-Carbon) show k-factors up to 15 with low temperature coefficient of resistance (TCR) [2]. CrN shows a strain sensitivity of 5-11 with TCR values of -5,500 ppm/°C to -186 ppm/°C [5],[6]. This article investigates sputtered chromium strain gauges on stainless-steel tensile specimens concerning their resistivity, k-factor, TCR as wells as full-bridge strain and temperature behavior.

Sensor Manufacturing

The strain gauges are produced on stainless-steel wafers (diameter: 100 mm, thickness: 0.8 mm). They are mirror polished with mean roughness values R_a = 20 ± 10 nm and R_z = 150 ± 80 nm. After a chemical cleaning step with acetone and isopropanol, sputter etching removes impurities and activates the surface for higher adhesion. First, a reactively RF sputtered Al_2O_3 insulation layer ensures electrical insulation of the following layer system.

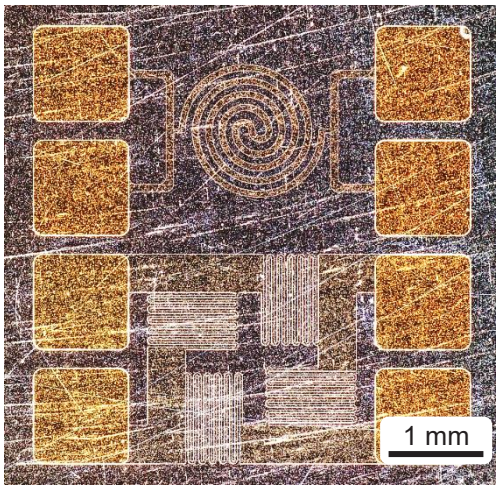

Fig. 1. Manufactured thin-film sensor system.

The total thickness of 2 µm is reached with two single steps of 1 µm with a chemical cleaning step in-between to enhance its functionality. Now, the photolithographic structuring takes place with the AZ5214E positive resist. The chromium sensor layer is sputtered with a power of 500 W (sputtering rate: 88 nm/min, sputtering

pressure $3.8 \cdot 10^{-3}$ mbar). A final liftoff process results in meander-shaped single strain gauges and Wheatstone full-bridge circuits with a sensor layer thickness of 500 nm. A Pt temperature sensor (500 nm) with a Ti adhesion promoter (10 nm) and Au contact pads (500 nm) are fabricated with two further liftoff processes (Fig. 1). In the end, the wafer is cut into a simplified tensile specimen with a width of 40 mm. Solder contacting completes the sensor manufacturing.

Characterization

The insulation layer properties show a resistance of $9.7 \cdot 10^{9} \pm 0.2 \cdot 10^{8}$ Ω that leads to a resistivity of $3 \cdot 10^{12} \pm 8 \cdot 10^{10}$ Ωcm. The breakdown field strength is 153 ± 25 kV/mm. The resistivity of Cr is $54.6 \cdot 10^{-6} \pm 1.5 \cdot 10^{-6}$ Ωcm that is approximately factor 4 of the bulk value which is in agreement with literature values [7]. The k-factor of four single strain gauges is characterized in a tensile test stand with forces between 400 and 2,400 N leading to a strain difference Δε of 312 µm/m. Based on the normalized resistance change $\Delta R/R_0$, eq. (1) is used.

$$k = (\Delta R/R_0)/\Delta\varepsilon \qquad (1)$$

High k-factor values of 11.0 ± 0.1 were achieved. Fig. 2 shows the linear curve of several test cycles for Cr in comparison to NiCr with a k-factor of 2. An explanation of the increased Cr k-factor is assumed in partly semiconductor behavior through doping with oxygen or nitrogen which cannot be clarified in detail. The k-factor of Pt was reduced to 0.8 as a result of the symmetrical spiral sensor design.

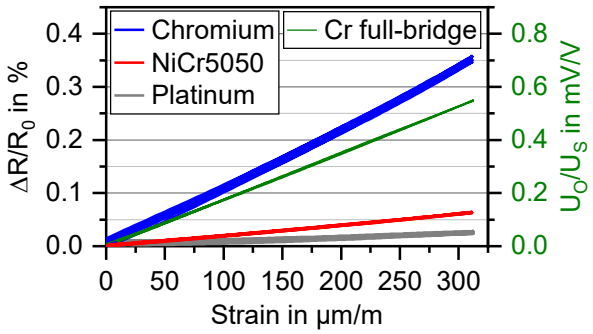

Fig. 2. Sensor signals for three different sensor materials and a Cr full-bridge.

Temperature investigations between 20 and 100 °C (ΔT = 80 °C) on a heating plate revealed TCR values of 591 ± 23 ppm/°C calculated with eq. (2). NiCr showed a value of 12 ± 5 ppm/°C.

$$TCR = (\Delta R/R_0)/\Delta T \qquad (2)$$

Now, Cr strain gauge full-bridges were tested concerning their strain sensitivity, temperature behavior and drift behavior. Initially, the bridge offset is 6.9 ± 2.7 mV/V. The sensitivity is calculated to 1.71 ± 0.03 µV/V/µm/m based on eq. (3) [1], see Fig. 2. Here, the strain ε is given by the k-factor k, the poisson's ratio v, the bridge output voltage U_O and supply voltage U_S.

$$\varepsilon = 4/k \cdot 1/2 \cdot 1/(1+v) \cdot U_O/U_S \qquad (3)$$

The temperature dependency leads to a high apparent strain of 4.4 µm/m/°C that can be reduced to a noise of only 11.7 µm/m in the temperature range from 20 °C up to 100 °C using the Pt thin-film temperature sensor. The drift at 20 °C is 0.36 µV/V/h that can be reduced with annealing.

Conclusion

This article presents sputtered chromium strain gauges on steel samples. With a k-factor of 11.0, the strain sensitivity is increased by a factor of 5 compared to conventional materials like NiCr. Due to the comparably high temperature coefficient of resistance of 591 ppm/°C (NiCr: 12 ppm/°C), Wheatstone full-bridge configurations were used leading to a strain sensitivity of 1.7 µV/V/µm/m. With an additional thin-film Pt temperature sensor, the remaining temperature induced apparent strain is 12 µm/m (20 °C up to 100 °C). These highly sensitive strain gauges can be used in harsh environments due to their polymer-free structure, and will be used for metal-based pressure sensors in the future.

References

[1] S. Keil, Dehnungsmessstreifen, *Springer Vieweg Wiesbaden*, Ed. 2, 1-485 (2017), doi: doi.org/10.1007/978-3-658-13612-3.

[2] M. Petersen, et al., Me-DLC films as material for highly sensitive temperature compensated strain gauges, *Diamond and Related Materials* 20, 814-818 (2011); doi: 10.1016/j.diamond.2011.03.036.

[3] R. Ottermann, M.C. Wurz, et al., Directly Deposited Thin-Film Strain Gauges for Force Measurement at Guide Carriages, *IEEE Sensors Journal* 24, 40471-40484 (2024); doi: 10.1109/JSEN.2024.3478821.

[4] S. Ling, et al., Novel Semiconductor Piezoresistive Thin-Film Strain Gauge With High Sensitivity, *IEEE Sensors Journal* 24, 13914-13924 (2024); doi: 10.1109/JSEN.2024.3373635.

[5] H.A. Mol, et al., Process for low temperature deposition of strain gauge materials based on Chromium nitride thin films, *IEEE Sensors*, 226-229 (2011); doi: 10.1109/ICSENS.2011.6127044.

[6] G.S. Chung, W.J. Lee, J.S. Song, Characteristics of Chromium Nitride Thin-Film Strain Gauges, *Sensors and Materials* 13, 13-23 (2001); sensors.myu-group.co.jp/article.php?ss=10426.

[7] P.A. Gould, The resistivity and structure of chromium thin films, *British Journal of Applied Physics* 16, 1481-1491 (1965); doi: 10.1088/0508-3443/16/10/309.

DOI 10.5162/SMSI2025/B3.2

Analysis of positioning parameters at glazing of pressure measurement cells

I. Jenei[1], R. Wagner[1], M. Nikolic[1], A. Grün[2]
[1] ETO SENSORIC GmbH, Löffelholzstraße 20, 90441 Nürnberg, Germany
[2] CiS Forschungsinstitut für Mikrosensorik GmbH, Konrad-Zuse-Straße 14, 99099 Erfurt, Germany
I.Jenei@etogruppe.com

Summary:
Glazing is increasingly used to join the silicon measuring cell to the steel diaphragm in pressure sensor production. This study examines the glazing process at ETO SENSORIC (Germany) using statistical analysis. The objective was to identify key positioning parameters that optimize signal yield. High sensor sensitivity and low deviation of the characteristic curve are maintained. A multivariable regression was performed with the measuring cell signal as the response. The analysis was extended with a µCT study of parts with unexplained signal deviations.

Keywords: pressure sensor, glazing, piezo resistive cell, steel membrane, statistic

Introduction

Glazing is a particularly sensitive process that directly affects the signal quality. During glazing, several objectives must be optimized, including the positioning of the measurement cell (strain gauge), thermal parameters, material selection, and process cost. This study aimed to determine the relationship between positioning parameters and both the signal level (sensitivity) and the piecewise variation of the characteristic lines [1]. These features, which characterize glazing quality, can easily be quantified using the measurement cell's signal. The cell contains four resistors forming a Wheatstone bridge, measured in the laboratory with a pressure-controlled measurement system.
Additionally, samples that deviated from the regression model were analysed using µCT to reveal the effect of bubble distribution in the glazing.

Samples

For the investigation, CiS set up steel measuring cells with differently positioned silicon strain gauges – 200 bar relative pressure sensor. Complete assemblies of pressure sensors with a steel diaphragm and a piezo resistive measuring cell joined by a glazing were produced in 46 functional parts, 28 of which were OK-calibrated (OK parts).
In the following section, only the OK parts were included in the analysis, but in the last sections. The variants (Tab.1) include test specimens with glass layer thicknesses of 50 µm and 150 µm and standard positioning (1.5 mm from the centre of the steel membrane at 0° rotation). The final three variants were produced with a 50 µm glass layer and an initial 45° rotation, followed by centre distances of 1 mm and 2 mm. The positioning parameter is set to the default value at the theoretical limits of the technology, showing no indication of a design of experiments (DoE).

Tab. 1 Variants of samples

	Thick. glass [µm]	Disp. centre/ mm	Angle / °	Functional parts	Calibration Ok
Thick. glass 50 µm	50	1,5	0	17	13
Thick. glass 150 µm	150	1,5	0	10	5
Angle 45°	50	1,5	45	7	0
Displacement 1 mm	50	1	0	5	4
Displacement 2 mm	50	2	0	7	6

Basic statistic of the signal

The raw values were extracted from the complete measurement protocol at specific temperatures (-25 °C, 20 °C, and 120 °C) and pressures (0 bar, 100 bar, and 200 bar) for further analysis. The standard deviation of these values for a given positioning parameter indicates the coherence of the derived characteristic curves. Fig. 1 and 2 display three pressure cycles for each temperature - cycle 1 at -25 °C, cycle 2 at 20 °C, and cycle 3 at 120 °C - with each cycle rising to 200 bar and falling back to 0 bar.
In Fig. 1, parts with a 150 µm thickness show very low deviation and raw values in contrast to those pieces with a 50 µm layer, indicating that a stable, functional sensor can be produced with a 150 µm layer. Additionally, Fig. 1 shows that the "50 µm" configuration with a 2 mm displacement exhibits the same deviation as the basic "50 µm" displacement (1.5 mm), while the "Angle 45°" configuration displays extremely large deviation throughout. The median value indicates sensor sensitivity; according to Fig. 2, all settings except "Angle 45°" are suitable for measurement, as a 45° rotation causes the resistors to cancel out the signal, and both scatter and median decrease with increasing temperature.

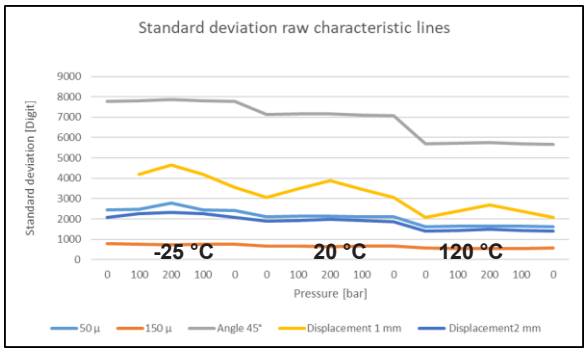

Fig. 1. Standard deviation of raw characteristic line vs. pressure

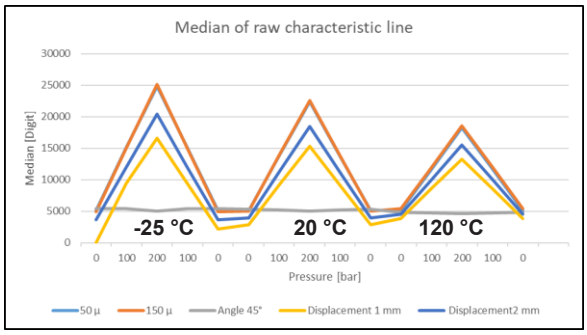

Fig. 2. Median of raw characteristic line vs. pressure

Variables of measuring cell positioning

To determine the parameters, several planes were first defined. The surface of the steel membrane was chosen as the reference plane (plane 0). The four bond pads on the strain gauge were designated as planes 1, 2, 3, and 4, while the surface of the strain gauge was assigned as plane 5 and the glazing surface as plane 6. Based on these planes, 11 geometric and positioning parameters were developed, covering features from the cross-section of the glass pad to the heights of the strain gauge cell elements. These variables were measured using a Keyence 4th Generation measuring microscope.

Analysis of measuring cell positioning

The following section analyses the influence of the glazing's geometric parameters on the raw values of the characteristic lines. A multivariable regression analysis was performed using MiniTab. Parts with a 50 µm layer thickness yielded significantly worse EMC results compared to those with a 150 µm layer; therefore, we focused on the 150 µm test specimens. Regression analyses were conducted over all temperature ranges (-25 °C, 20 °C, 120 °C) and pressure ranges (0 bar, 100 bar, 200 bar). For the 150 µm layer, the coefficients of determination were consistently high (>80%), though the significant variables varied. The influence of different parameters on the sensor signal was sometimes contradictory, suggesting other factors may also be at play.

A µCT analysis was then carried out to investigate whether bubbles or cracks in the glass solder could affect the results [2].

Deviation in trend

The NOK parts generally exhibit lower raw values than the OK parts, except for NOK part No. 29, whose raw value falls within the expected range for OK parts. The analysis of geometric parameters revealed no abnormalities, suggesting that other factors may be influencing the results. Four samples were therefore sent for µCT analysis. The selected samples included the conspicuous test piece No. 29, an OK part with a 50 µm layer (No. 16), a NOK part with a 150 µm layer (No. 25), and an OK part with a 150 µm layer (No. 38). Test piece 16 shows almost no bubbles in the glass pad (Fig. 3) and has an acceptable signal. In contrast, test piece 25 exhibits many large bubbles in the glass solder, especially beneath the strain gauge, resulting in significantly lower raw values. Test sample 29 has a large bubble beneath the strain gauge - though smaller than in test piece 25 - which places it just outside the acceptable range. Test sample 38, like test sample 16, displays only a small bubble beneath the strain gauge and shows no abnormalities in its characteristic curve.

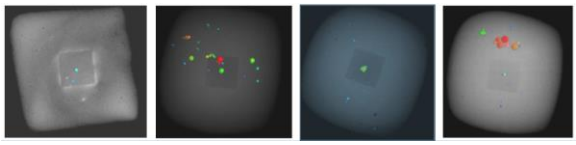

Fig. 3, µCT image of No. 16 IO/50µm; No. 25 NIO/150µm; No. 29 NIO/150µm; No. 38 IO/150µm;

Result and discussion

- A significant deviation from the ideal strain gauge positioning substantially affects the raw values and the consistency of the signal lines.
- Using a 150 µm layer thickness, sensitive sensors can be produced with a lower standard deviation than those with a 50 µm layer.
- The regression analysis of production parameters versus raw values yielded contradictory results, indicating that some factors were overlooked; hence, a µCT scan was performed.
- Bubbles in the glass beneath the strain gauge directly influence its raw signal values.
- A design of experiments (DoE) is currently underway to investigate the factors influencing bubble formation in glazing.

References

[1] Montgomery, D. (2013). Design and Analysis of Experiments. Eight Edition, John Wiley & Sons, Inc.

[2] H. Shao u.a. „Microstructure and Wettability of Glass Solder on Al2O3 Ceramic and Its Joints Properties" pp. 145-155. Feb. 2023

DOI 10.5162/SMSI2025/B3.3

Advanced Glass Packaging with Integrated Stress Relief Structures for MEMS Pressure Sensors

Maik Bertke, Svenja Schudak
LPKF Laser & Electronics SE, Osteriede 7, 30827 Garbsen, Germany
maik.bertke@lpkf.com

Summary:
Advanced glass packaging with integrated stress relief structures for MEMS pressure sensors, enabled by Laser Induced Deep Etching (LIDE) technology, effectively isolates sensing elements from package-induced stresses. Our simulations demonstrate that hermetically sealed corrugated membrane structures reduce thermal induced stress by up to 99,4 % when subjected to CTE mismatch between glass and FR4 substrates. The integrity and mechanical stability of the glass is maintained, as processing with the LIDE technology does not create any imperfections such as microcracks or internal stresses.

Keywords: MEMS sensors, glass packaging, stress relief structures, Laser Induced Deep Etching, glass micro features

Introduction

MEMS pressure sensors are critical components in numerous industrial, automotive, medical, and consumer applications, providing precise pressure measurements in increasingly demanding environments [1, 2, 3]. However, one of the most significant challenges remains the effective isolation of the sensing element from external mechanical and thermal influences [4]. The coupling between the silicon chip and its package, as well as between the package and substrate or circuit board, introduces substantial performance limitations due to thermal mismatch between different materials, creating stresses that directly transfer to the sensor membrane and result in measurement errors [4, 5]. Conventional approaches involve complex and costly stress relief structures that increase production costs and limit miniaturization or the use of soft adhesives that can degrade over time are limited in temperature and pressure stability [4, 6, 7]. This paper explores how Laser Induced Deep Etching (LIDE) technology can be leveraged to create integrated stress relief structures directly within glass packaging for MEMS pressure sensors, potentially enabling higher accuracy, improved reliability, and expanded operating temperature ranges while reducing manufacturing complexity and cost [8, 9].

Glass integrated stress relief structures

This study employed LIDE technology to fabricate integrated stress relief structures in glass packages for MEMS pressure sensors. LIDE is a two-step process: first, a specialized laser process that precisely modifies the glass; second, a selective wet etching process that etches modified regions much faster than unmodified glass. This approach allows for minimum feature sizes down to 5 µm with positional accuracy of ±1 µm with very low surface roughness [9]. We designed and fabricated hermetically sealed glass carrier substrates with corrugated membranes (10 - 30 µm thickness, 400 µm depth, 50 µm channel width) for stress relief as shown in Figure 1. In a previous publication we have demonstrated fracture strength of ~1 GPa of LIDE processed glass springs with cross-sections of 30 µm × 260 µm in mechanical testing confirming the absence of strength-limiting defects [10].

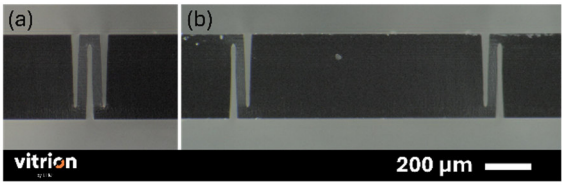

Figure 1: Cross section of double membrane structure and (b) platform with single membrane structures.

The test samples (2.5 × 2.5 mm²) were made of 500 µm thick Borosilicate glass (Schott BF33) that has a very similar coefficient of thermal expansion (CTE) to Si. We have carried out Finite Element Modeling simulations using Ansys Mechanical to optimize designs and predict performance, comparing the substrates with and without stress relief structures. The simulations analyze a thermal induced tensile stress of a Si pressure sensor membrane (20°C to 85°C) caused by the CTE mismatch between borosilicate glass (3.3 ppm/K) and FR4 (16 ppm/K). The Si die (1 × 1 mm²) was placed on the glass sample.

Simulation Results

FEM simulations of the stack of FR4, BF33 and Si show a significant reduction of the mean Von-Mises stress on the sensor membrane from 15.9 MPa to 0.277 MPa (98.26 % reduction) using a single corrugated membrane (30 µm thickness) for stress relief when subjected to thermal loading representing a 65°C temperature change with a CTE mismatch of 12.7 µm/m/K between borosilicate glass and FR4 substrate. A dual-membrane configuration reduces the induced stress to 0.104 MPa (99.35 % reduction).

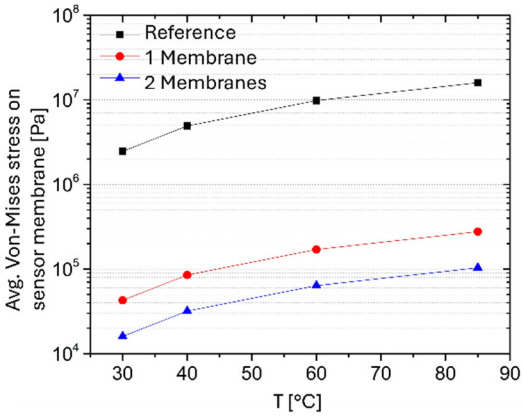

Figure 2: Simulation results of the average Van-Mises stress on the membrane of a 1 × 1 mm² silicon die placed in the middle of the glass substrate without microstructures (Reference), with one membrane and with two membranes (30 µm thickness).

Stress distribution analysis revealed that the microstructures created mechanical "breaks" in stress propagation paths, absorbing and redistributing induced stress while maintaining integrity and out-of-plane stability.

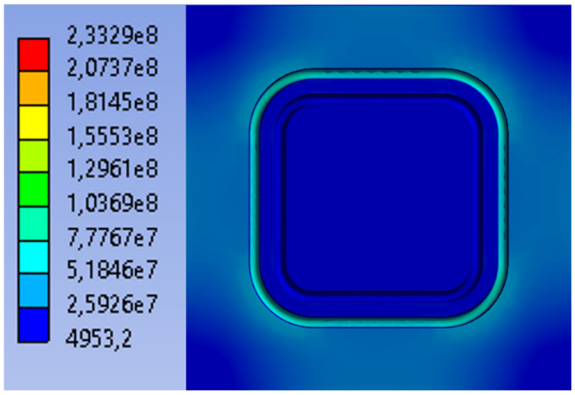

Figure 3: Stress distribution on the glass substrate with two corrugated membranes.

Conclusion

This study demonstrates that micro structured glass has enormous potential for improvements in thermal stability, mechanical stress isolation, and high-temperature operation of MEMS devices facing thermal and mechanical stress challenges. These advancements address critical limitations in current MEMS pressure sensor technology and open new possibilities for applications across automotive, industrial, medical, and aerospace sectors where accurate pressure measurement under varying environmental conditions is essential. Future work will be focused on process integration and optimizing design configuration.

References

[1] L. Jin, Applications and Prospectes of Mems Sensors in Automotive, *Journal of Physics: Conference Series* 1884, 012010 (2021); doi: 10.1088/1742-6596/1884/1/012010

[2] V. S. Balderrama, J. A. Leon-Gil, D. A. Fernández-Benavides, J. Ponce-Hernández and M. Bandala-Sánchez, MEMS Piezoresistive Pressure Sensor Based on Flexible PET Thin-Film for Applications in Gaseous-Environments, *IEEE Sensors Journal* 22 (3), 1939-1947 (2022), doi: 10.1109/JSEN.2021.3135543

[3] L. Gupta, G. Singh, V. Pandey, A study of piezoresistive pressure sensor technology, *AIP Conf. Proc.* 2327, 020008 (2021); doi: 10.1063/5.0039425

[4] Y. Zhang, B. Li, H. Li, S. Shen, F. Li, W. Ni, W. Cao, Investigation of Potting-Adhesive-Induced Thermal Stress in MEMS Pressure Sensor, *Sensors* 21, 2011 (2021); doi: 10.3390/s21062011

[5] X. Bie, X. Xiong, Z. Wang, W. Yang, Z. Li, X. Zou, Analysis of the Thermally Induced Packaging Effects on the Frequency Drift of Micro-Electromechanical System Resonant Accelerometer, *Micromachines* 14, 1556 (2023); doi: 10.3390/mi14081556

[6] M. Ghanam, P. Woias, F. Goldschmidtböing, MEMS Pressure Sensors with Novel TSV Design for Extreme Temperature Environments, *Sensors* 25, 636 (2025); doi: 10.3390/s25030636

[7] C. Cheng, Y. Lu, J. Yao, J. Chen, D. Chen, J. Wang, Development of a new MEMS resonant differential pressure sensor with high accuracy and high stability, *Measurement* 226, 114080 (2024); doi: 10.1016/j.measurement.2023.114080

[8] A. B. Shorey, Y. J. Lu, G. A. Smith, Leveraging Glass Properties for Advanced Packaging, *48th Annual Internationl Symposium on Microelectronics – IMAPS 2015,* Orlando, 000370-74 (2015)

[9] R. Santos, N. Anspach, N. Ambrosius, S. Schmidt, R. Ostholt, Fabrication of Panel-Level Glass Substrates with Complete Design Freedom Using LIDE, *IMAPS Symposium 2022*, Boston, 000371-77 (2023), doi: 10.4071/001c.74577

[10] M. Bertke, S. Schudak and R. Ostholt, Glass as A Functional Material for Micro Electromechanical Systems, IEEE 37th International Conference on Micro Electro Mechanical Systems (MEMS), Austin 2024, 646-649 (2024), doi: 10.1109/MEMS58180.2024.10439553

DOI 10.5162/SMSI2025/B3.4

Sensors on PEEK - Advantages of Plastic Substrates in Microsystem and MEMS Technology

Dr. Sebastian Bengsch[1], *Dr. Eike Fischer*[1], *Stefan Bur*[1]
[1] *Ensinger GmbH, Rudolf-Diesel-Str. 8, 71154 Nufringen, Germany,*

sebastian.bengsch@ensingerplastics.com

Summary:
Silicon, glass and ceramic substrates are generally used in the field of microsystems technology and MEMS. Thermoplastics play a subordinate role at most in the area of flexible substrates. However, substrates made of polyether ether ketone (PEEK) offer previously unimagined advantages for new sensor application scenarios where conventional substrates reach their limits. Especially the Ensinger Microsystems Technology (EMST) shows the various benefits using PEEK as a substrate material.

Keywords: Sensors, PEEK, Plastic, Substrates, EMST, MEMS

Introduction

Silicon and ceramic substrates are generally used in the field of microsystems technology and MEMS. Thermoplastics play a subordinate role at most in the area of flexible substrates. However, substrates made of polyether ether ketone (PEEK) offer previously unimagined advantages for new sensor application scenarios where conventional substrates reach their limits.

Polyether Ether Ketone

PEEK is a thermoplastic material with high chemical resistance and excellent temperature behavior. The material withstands 250 °C permanently and for bonding processes even 300 °C for short times. The material is also available as a compound material for Laser Direct Structuring and is adapted to metallization processes. The dielectric strength of 17.5 kV/mm shows ideal electrical resistivity for e.g. electronic or sensor applications.

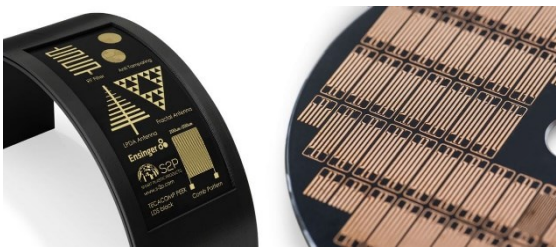

Fig. 1: PEEK based Substrates

Advantages of PEEK Substrates

Fig. 2 shows the properties of PEEK in comparison to the established substrates. Generally, no substrate is superior in every field of interest and the web diagram illustrates that the PEEK based TECAWAFER PEEK LDS substrate is beneficial in terms of electrical and chemical properties. It also has a lower environmental impact and allows for multiple packaging options.

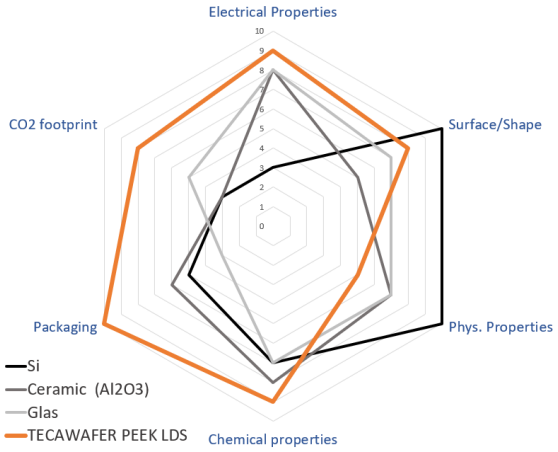

Fig. 2: TECAWAFER PEEK LDS in comparison

Ensinger Microsystems Technology

The Ensinger Microsystems Technology (EMST) consists of three basic process steps.

1. Injection molding
2. PVD coating
3. Chemical Mechanical Polishing (CMP)

Using highly precise molding inlays, microstructures are imprinted by the injection compression molding process into the PEEK material. This way a structural resolution in the single digit micrometer range is achied. Subsequent PVD processes include sputtering, evaporation and for insulation purposes PECVD. The following polishing step removes the applied layer apart from the metallization inside the structured cavities.

Advantages of the EMST Process Chain

The EMST process chain shows advantages not only regarding the number of process steps. It also allows the neglection of the clean room environment and robust choice of substrate material. The high reproducibility and excellent values of standard deviation of this process chain regarding mechanical an electrical values have to be emphasized. The references [1] – [5] show the use cases for the Ensinger Microsystems Technology.

Sensor Examples

Using the Ensinger Microsystems Technology, various thin film based sensors have already been manufactured. The first sensors evaluated on PEEK were temperature sensor elements, which are applicable between -70 and 250 °C [1]. Another major focus of sensor application lays in the field of magnetic field sensors. AMR and GMR Sensors were built using EMST and showed state of the art sensor signal and behavior on PEEK substrates [3]. Also strain gauge based sensor systems like torsion, strain and pressure sensors were evaluated in will be published shortly. A combination of heater and sensor elements can be manufactured in the case of calorimetric flow sensors, which are also available on PEEK substrates [5]. Fig. 4 shows various thin film based sensor samples based on the EMST process chain.

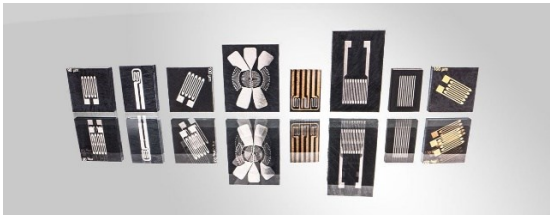

Fig. 4: Various Sensor Examples Based on PEEK and EMST Process Chain

Benefits of PEEK in Sensor Technologies

PEEK as substrate material and especially the used TECACOMP PEEK LDS as substrate for sensor manufacturing - also in the case of the EMST technology - shows various benefits for different sensor applications. Regarding temperature sensors the fast response behavior using PEEK as substrate has to be emphasized. Similar behavior on silicon substrates can only be realized using expensive backside thinning processes using dry etching. In case of calorimetric flow sensors, the same effect can be very beneficial. Flow sensors also need chemical and physical resistance for different media and therefore alternatives are looked for especially where silicon or ceramic show limitations (e.g. acids and alkaline). Looking at the manufacturing of pressure sensors on the basis of strain gauges , usually expensive thinning and mounting of the membranes to the body/housing is challenging and expensive. Using PEEK as a substrate increases the signal and manufacturing can be simplified by mechanical thinning of the membrane or direct production of membrane and housing in one process step.

Conclusion

PEEK as a substrate material opens up new possibilities in terms of manufacturing technologies. Physical and chemical limitations of existing substrate technologies are overcome with PEEK and in particular with TECAWAFER PEEK LDS, creating new possibilities for sensor applications and designs.

References

[1] Sebastian Bengsch; Marc Christopher Wurz; Maximilian Aue; Sascha de Wall; "Structuring Methods of Polymers for low Cost Sensor Manufacturing", 2018 IEEE 68th Electronic Components and Technology Conference (ECTC).

[2] Sebastian Bengsch; Eike Fischer; Sascha de Wall; Timo Schelm; Matthias Arndt; Marc Christopher Wurz, "Optical Platform for Highly Precise Optical Components", 2020 IEEE 70th Electronic Components and Technology Conference (ECTC).

[3] Eike Christian Fischer, Sebastian Bengsch, Sascha de Wall, Marc Christopher Wurz, "Giant Magneto-Resistive Effect based Sensor on Laser Direct Structured MID Substrates", 2020 IEEE 70th Electronic Components and Technology Conference (ECTC), pp.439-444, 2020.

[4] Sascha de Wall, Sebastian Bengsch, Eike Fischer, Folke Dencker, Marc Christopher Wurz, "Anisotropic Magneto-Resistive Sensor Effect based Sensor using Daisy Chain on Polyether Ether Ketone Substrate", 2021 IEEE Sensors, pp.1-4, 2021.

[5] Sebastian Bengsch; André Buelau; Andrea Knoeller; Volker Kible; Daniela Walter; David Helm, "Development of a Thermal Flow Sensor Based on the Ensinger Microsystems Technology", MikroSystemTechnik Kongress 2023.

DOI 10.5162/SMSI2025/B4.1

Small Optical Measurement System for Stable Detection of Mold Growth

Varuni Rathnayake [1,2], Thomas Schweizer[1,2], Sander van den Driesche [1,2,3], and Michael J. Vellekoop[1,2,3]
[1] Institute for Microsensors, -actuators and -systems, University of Bremen, Germany
[2]Microsystems Center Bremen (MCB), Germany
[3]MAPEX Center for Materials and Processes, University of Bremen, Germany
vrathnayake@imsas.uni-bremen.de

Summary: A small, stable sensor system is proposed to detect mold growth. The system measures the pH change in culture medium using the corresponding colour shift of pH indicator dyes in response to mold metabolism. The system employs a spectral sensor and a LED that measures the transmittance across 150 μl of culture media. The configuration of the optical system assures the accuracy of the measurements with a fixed optical path with no mold colony hindrance. A calibration method was introduced to calibrate small volumes of dyed culture medium.The system allows the detection of mold growth and identification of growth phases of mold measuring the pH value of the culture medium.

Keywords: mold, Bromocresol purple(BCP), agar, pH value, colour sensor

Background, Motivation and Objective

Mold contamination is a significant issue in agriculture, biogas facilities, industrial plants, and indoor environments. It can break down organic matter, can lead to structural damage in buildings and can result in crop losses. Additionally, mold spores have been shown to impair air quality, causing respiratory diseases such as asthma and allergies in both humans and animals. Conventional methods for detecting mold involve using Andersen impactors with agar-filled petri dishes and counting colony-forming units (CFUs). This is laborious process that requires several steps. Other methods, such as PCR, qPCR, and microscopic analysis, require experienced professionals. Colourimetric measurement methods have been previously investigated and shown to be effective for mold detection [1]. However, mold growth on the surface of agar plates disturb the optical pathway which leads to inaccurate measurement results.

Mold Detection System and Characterization

In this work a stable optical measurement setup was realized to detect the growth of mold. An optical path was chosen such that it does not cross the surface of agar where mold colonies are growing, which would otherwise affect the transmittance measurements [1]. Mold spores start germinating in environments, which are humid and have sufficient organic matter. Agar mixed with pH indicator dye is used as growth medium in the micro reactors to determine mold growth. When spores are in contact with Agar, they start germinating and feed on the organic matter. As a function of metabolism, when mold grows, they release acidic and basic waste [2]. These waste products changes the ionic composition of the culture medium and thus changing the pH of agar, which can be detected by pH indicator dyes. Spores can be introduced into the system by air or liquid samples. To prevent the agar from drying out caps are fitted onto the microreactors.

The system consists of a cylindrical microreactor that has a volume of 400 μl (diameter: 8mm, height: 8mm). It is filled with agar mixed with Bromocresol purple(BCP) dye with a concentration of 0.025% w/v. The measured dye colours for different pH values are shown in Fig. 1.

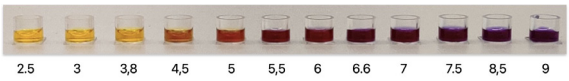

Fig. 1: Colour in BCP dyed Agar for different pH values

The optical setup to measure the colour intensity through a small optical path of 8 mm consist of a 3000K LED and a spectral colour sensor (AS7341) that were configured in such a way that light passes through the microreactor filled with agar. The LED was powered with 20 mA current to illuminate the microreactor. The colour sensor has 8 channels sensitive to different wavelengths in visible range and provides intensity data for each wavelength.

To measure the pH of the agar medium accurately, a calibration curve for BCP dyed agar is necessary. One significant challenge when measuring the pH of (semisolid) textured agar with a standard pH probe is that the sensitive membrane gets obstructed by agar particles resulting in inaccurate readings. Also, changing pH and measuring pH of small volumes of Agar is not straight forward. To address the above challenges, a liquid fraction with BCP dye is used. As the first step, a calibration curve of BCP dyed

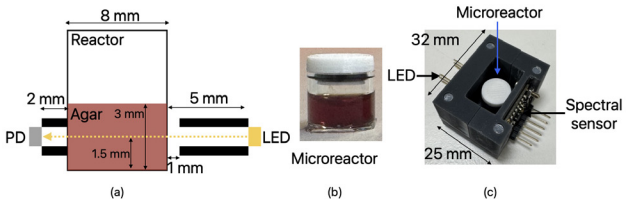

Fig. 2: (a) Optical setup (b) Microreactor (c) Resin printed holder for LED and color sensor

water for a pH range 2.5-9 was established as the first reference. By adding a liquid fraction with multiple samples covering a pH range of 0-14 on top of agar gel, the pH value of the liquid and the agar fractions reach equilibrium. Then by comparing the colour of the liquid fraction on top of the agar, the pH value of the two fractions can be read out using the first reference curve. A second reference curve can then be created for the agar fraction itself. This will be used further as the calibration curve to measure the pH of the medium when mold is growing. To minimize the possible drifts due to temperature fluctuations and varying LED properties, each wavelength was normalized using 680nm wavelength because it is not affected by the change in colour of the dye.

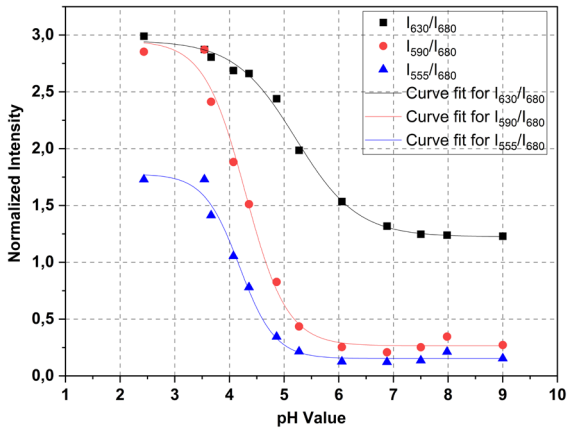

Fig. 3: Calibration curve for 0.025% w/v BCP dyed Agar, including sigmoidal Boltzmann curvefit

Fig. 3 outlines the correlation between pH values and the intensity ratios at three distinct wavelengths: 555 nm, 590 nm, and 630 nm, all normalized to the intensities at 680 nm. The I_{630}/I_{680} (black curve) is suitable for pH values ranging from 4 to 7. In contrast, the I_{590}/I_{680} (red curve) is effective for detecting pH values between 3 and 5.5. The normalized intensity at 555 nm (blue curve) does not offer any additional information compared to the other wavelengths. Therefore, the system can effectively operate along a pH range of 3 to 7 using only 3 wavelengths: 590 nm, 630 nm and 680 nm(reference).

Results

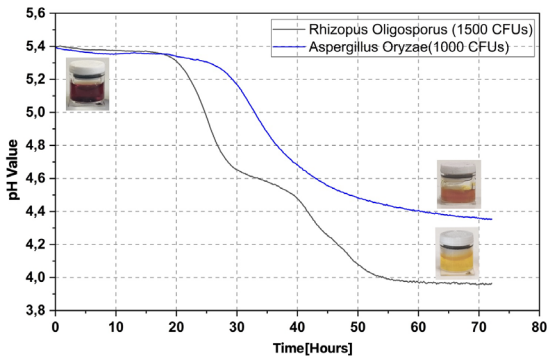

Fig. 4: pH change in the culture medium for 2 different species of mold

Fig. 4 shows the change in pH of the culture medium for two types of mold: *Rhizopus Oligosporus* and *Aspergillus Oryzae*. For the measurements, liquid samples with different spore concentrations were used for each species. The intensity measurements were recorded with a 10 minute sampling time. Initial pH of agar was determined as 5.4±0.2. During the lag phase, the pH value of the medium remains unchanged as the spores adjust to the moist medium. Following this phase, mold spores start growing and release waste into the agar, altering its pH. A pH change of -0.5 is shown within 25 hours for *R. Oligosporus*. For *A. Oryzae* spores, it takes a bit longer and is observed after 35 hours. Both species demonstrate a gradual decrease in pH over time, indicating that the medium becomes more acidic.

Conclusion

The growth of two mold species has been successfully detected using stable optical readings with 150 μl volume of culture medium. Intensity ratio measurements from 2 wavelengths and a reference wavelength enable the system to detect pH values in the range of 3 to 7. The results are very promising for the realization of a mold spore quantification platform.

Acknowledgement

We thank our partners STÖRK Umwelttechnik GmbH and MESA Electronic GmbH for fruitful discussions. This work is a part of the research project “MoldDetection, project number: KK5039203KS1, which is supported by the Federal Ministry for Economic Affairs and Energy (BMWi) under the framework of the Central Innovation Programme for SMEs (ZIM).

References

[1] Papireddy Vinayaka, et al., On-Chip monitoring of pH change in agar-gels during fungi growth by integrating impedance and colorimetric principles, *Procedia Eng.*, 2014: pp. 373–376. doi:10.1016/j.proeng.2014.11.739.

[2] H.G. Schlegel, General Microbiology, Seventh Edition, 2003.

DOI 10.5162/SMSI2025/B4.2

Low-Noise Silicon APD with Enhanced Blue-Violet Sensitivity

L. Long, X. Xu, M. Schaedel, G. Brokmann and Th. Ortlepp
CiS Forschungsinstitut für Mikrosensorik GmbH, Konrad-Zuse-Str. 14, D-99099 Erfurt, Germany.
llong@cismst.de

Summary: A theoretical two-carrier formalism for the calculation of the optoelectrical properties of APDs is established based on the independent Bernouilli trial and generating function method. The gain and excess noise factor can be calculated for any doping profile under any bias and illumination wavelength. This is applied to the design of a CMOS compatible low-noise silicon avalanche photodiode. The doping profile and antireflection layer are optimized to achieve enhanced blue-violet sensitivity and low-noise, while keeping the operating bias at a moderate level. The properties of the fabricated APDs are in good agreement with the theoretical analysis.

Keywords: Silicon, APD, gain, excess noise factor, blue-violet enhanced

Introduction

For PET and high-energy physics applications, gamma rays are converted to blue or violet photons with scintillators and detected by an APD or photomultiplier [1]. Therefore, it would be advantageous if the APD used has low noise and enhanced blue-violet sensitivity [2]. Since sensitivity and noise are strongly dependent on the device doping profile, the operating bias, and the wavelength of the incident photons, design and optimization using conventional TCAD simulation would be very time-consuming. To this end, we have derived a formalism to calculate the gain and excess noise factor from a given doping profile at any bias and for any wavelength of incident photons. This formalism is based on the independent Bernouilli trial and generating function method, which applies the impact ionization rate for electrons and holes. It is shown that the theoretical results are in good agreement with the TCAD simulation. Therefore, for the design of an APD, it is only necessary to perform a process simulation to realize the obtained doping profile and design an appropriate layout edge structure. Using this procedure, we developed a low-noise silicon APD with enhanced blue-violet sensitivity.

The opto electrical properties of APD

The impact ionization of accelerated charge carriers in an electric field generates a further generation of charge carriers for any given input charge carrier according to the ionization rate of electrons and holes. The initial carriers can be the light-generated carriers or thermally excited electron-hole pairs. The one dimensional multiplication zone is divided into N sections, where section i has a length of $l_i = \frac{e_a}{q|E(x_i)|}$. Here $E(x_i)$ is the electric field strength at x_i, e_a is the ionization energy of charge carriers. Therefore, in section i, the electron has an impact ionization probability of $\alpha_n(x_i)l_i$, the hole has an impact ionization probability of $\alpha_p(x_i)l_i$, where the α_n and α_p are the impact ionization rates of electrons and holes, respectively. For photon of wavelength λ, the light generation probability in section i is $\gamma(\lambda)l_i \exp(-\gamma(\lambda)x_i)$, where γ is the absorption coefficient of photon. This random process can be well described by the N independent Bernoulli trial [3]. If we take the generating function as $\phi_i(t)$ for section i, we get the gain as

$$G_i = \phi_i'(1) \tag{1}$$

and its variance as

$$Var(G_i) = \phi_i''(1) - \phi_i'^2(1) + \phi_i'(1) \tag{2}$$

The excess noise factor is

$$F_i = 1 + \frac{Var(G_i)}{G_i^2} \tag{3}$$

For a pn junction formed in n-type silicon doped with $1.3\times10^{15}cm^{-3}$ under a bias voltage of 202V, the calculated spectral gain and excess noise factor are shown in Fig. 1 and Fig. 2, respectively. It is shown that shorter wavelengths have higher gain and lower noise.

Low noise APD design and manufacture

To reduce the noise of the APD, it is important to achieve a lower ratio of hole to electron ionization rate, which means a lower electric field strength for silicon. Combined with the requirement of low leakage current and high blue-violet sensitivity, an n-type 3ohmcm (100) silicon wafer is used. A shallow trench is introduced to reduce possible edge breakdown and to achieve better surface isolation. Furthermore, the top layers are designed to realize antireflection and passivation at the same time. The active area of the APD is $4.5mm \times 4.5mm$. Shallow pn junction is formed by ion implantation.

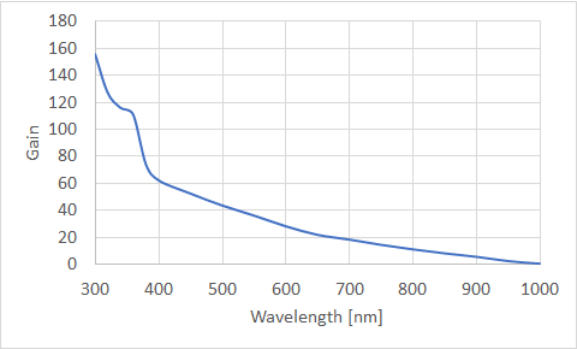

Fig. 1: The spectral gain characteristics of APD for a bias voltage of 202V.

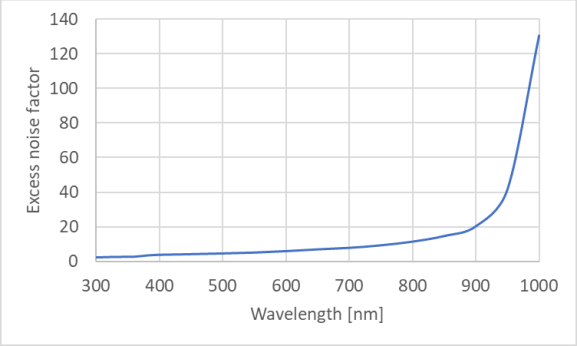

Fig. 2: The spectral excess noise factor characteristics of APD for a bias voltage of 202V.

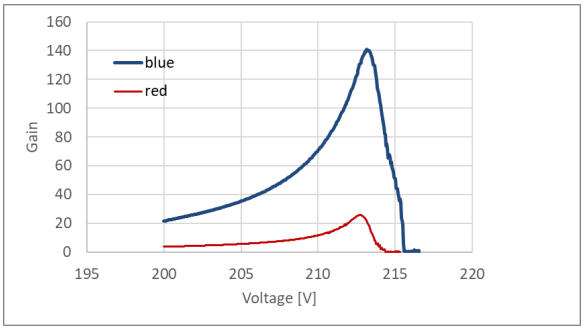

Fig. 3: The gain voltage characteristics of APD for two different LEDs with center wavelength 405nm and 850nm.

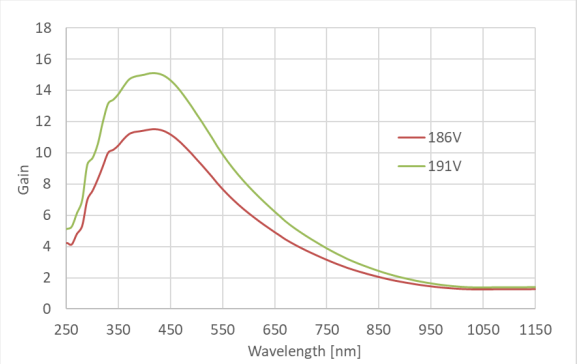

Fig. 4: The gain spectral response characteristics of APD for two bias voltages 186V and 191V.

Characterisation

After prototyping, the devices are systematically characterized. At low bias (20V), the dark current is 0.3 to 0.5nA at room temperature. The gain voltage relation for red and blue LEDs is shown in Fig. 3. The spectral response measured at bias voltage of 186V and 191V is shown in Fig. 4. Characterization results showed that the sensitivity in the blue-violet region is increased with the peak sensitivity is at 400nm wavelength, where the gain is 42 for a bias voltage of 210V. The noise spectrum under red and blue LED illumination is measured at a bias of 202V. The gain and excess noise factor are shown in Tab.1. The excess noise factor for blue light is 7.9. Compared with Fig. 1 and Fig. 2, the agreement is good. Small deviations may be due to the doping concentration used and the spectral profile of the LEDs.

Tab. 1: The gain and excess noise factor measured at 202V

LED	Gain	Excess noise factor
red	4.4	31.5
blue	26.2	7.9

Summary

A theoretical formalism for the optoelectrical properties of APDs is developed, which can effectively support the design and optimization of customer-specific APDs. A prototype of low-noise APD with enhanced blue-violet sensitivity is developed. The APDs have potential use in the PET of nuclear medicine and electromagnetic calorimeter of high-energy physics experiment.

References

[1] M. J. Paulus, J. M. Rochelle, and D. M. Binkley, Comparison of the Beveled-Edge and Reach-Through APD Structures for PET Applications, *Proceedings of 1994 IEEE Nuclear Science Symposium*, 1864-1868 (1994).

[2] C. H. Tan, A. Velichko, L. W. Lim, and J. O. S. Ng, Few-photon detection using InAs avalanche photodiodes, *Optics Express* 27, 5835-5842 (2019.

[3] K. M. van Vliet and L.M. Rucker, Theory of Carrier Multiplication and Noise in Avalanche Devices, *IEEE TRANSACTIONS ON ELECTRON DEVICES* ED-26, 746-751 (1979).

DOI 10.5162/SMSI2025/B4.3

Fiber Optic Current Sensor System for Long-Term Monitoring of Geomagnetically Induced Currents in the Power Grid

Johannes Mandl [1], *Philipp Trampitsch*[1], *Alexander Fröhlich* [2], *Reinhard Klambauer*[1] *and Alexander Bergmann*[1]
[1] EMS, Graz University of Technology, Inffeldgasse 33/I, 8010 Graz, Austria
[2] IEAN, Graz University of Technology, Inffeldgasse 18/I, 8010 Graz, Austria
johannes.mandl@tugraz.at

Summary: Within this work, we describe an interferometric fiber optic current sensor for the monitoring of geomagnetically induced currents in power grids. For the first time, the developed system is able to provide information about the distribution of these currents on individual phases and lines on high-voltage potential. During preliminary testing, a current sensitivity in the mA range was achieved. For in-field operation, the system was equipped with a custom electronics unit to enable on-board data processing, data storage as well as remote data access.

Keywords: fiber optic current sensor, geomagnetically induced current, Faraday effect, Field Programmabable Gate Array, power grid monitoring

Introduction

Monitoring the components of our electric power system is of great significance in order to ensure proper functionality and network stability. In particular, power transformers in the electric grid are affected by low frequency, (quasi-)direct currents (LFCs), disturbing the operating point of the device and causing half-cycle saturation as well as increased heating and reactive power demand. One well-known origin of LFCs is space weather, where the interaction of charged solar particles with the Earth's magnetosphere leads to so-called geomagnetically induced currents (GICs) on ground level.
At the moment, GICs are only monitored in transformer neutral points [1] and there is no information about their distribution on the grid's three phases and on individual lines, which would facilitate the choice of appropriate mitigation measures. While conventional current transformers suffer from several shortcomings, fiber optic current sensors (FOCS) based on the Faraday effect offer a practical solution for this task, given their ability to simultaneously measure alternating (ac) and direct (dc) currents with high bandwidth as well as being galvanically separated from the circuit, allowing their installation on high-voltage potential [2]. A current-related magnetic field in parallel to the propagation direction of light in a dielectric medium will lead to a rotation of the light's plane of polarization. For a closed fiber loop around a conductor, the resulting phase shift can be described by

$$\phi = VNI \tag{1}$$

where the Faraday phase shift ϕ is directly proportional to the current I through the Verdet constant V of the material and N, the number of fiber windings around the conductor.

Sensor setup

The used sensor setup (Fig. 1) is based on the polarization-rotated reflection interferometer [3] and exploits the non-reciprocity of the Faraday effect. The relative phase shift ϕ_r between two orthogonal light waves completing a forward and backward travel in the system will then be four times higher than described with (1).

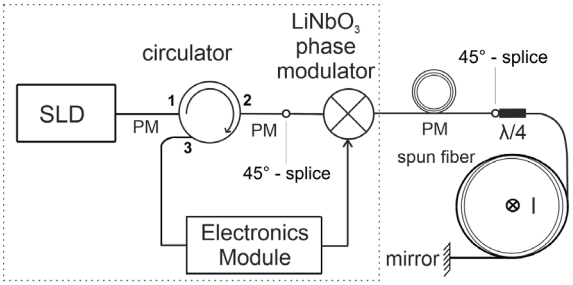

Fig. 1: Optical sensor setup of FOCS:
SLD - superluminescent diode,
PM - polarization-maintaining fiber leads, λ/4 - fiber quarter wave retarder, I - current-carrying conductor

Linear-polarized light from a superluminescent diode (SLD) at 1550 nm with a bandwidth of 60 nm is used to equally excite both slow and fast axis modes of a polarization-maintaining (PM) fiber at a 45° splice point. A birefringent $LiNbO_3$ phase modulator introduces a non-reciprocal phase shift between the two axes. The following PM fiber lead separates the two modes beyond their coherence length to minimize cross-coupling. A fiber $\lambda/4$ retarder transforms the two orthogonal linear polarization modes into left- and right hand circular polarizations, which then acquire a non-reciprocal phase shift twice caused by current's magnetic field on their round trip. Due to the interchange of polarization axes at the mirror, the optical setup is reciprocal and immune to perturbations experienced by both modes. An ideal modulation is achieved, when one full period of the sinusoidal modulation signal is equivalent to the time of flight for the light in the interferometer. The Faraday phase shift can then be inferred from the detected harmonics of the modulation frequency [3]. On their return trip, the two polarization modes are again mixed at the first 45° splice, one axis is blocked by going through Port 3 of the PM circulator and the optical signal is sent to the electronics module for signal processing.

The developed electronics module takes over the entire data processing from initial detection,

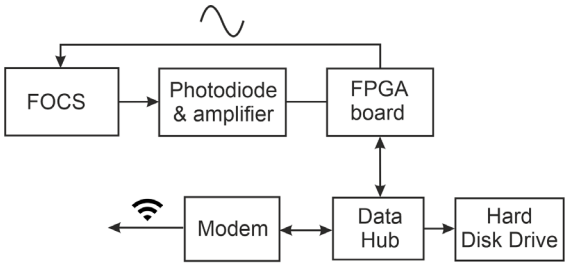

Fig. 2: Block diagram of electronic signal processing and data storage for the installed FOCS system.

calculation as well as data storage. In a first stage, the optical signal is converted into an electrical signal by a photo diode and then amplified. The FPGA (Field Programmable Gate Array) board contains an analog-to-digital converter and calculates the Faraday phase shift ϕ_r. Using a digital-to-analog converter, the $LiNbO_3$ phase modulator is controlled. The FPGA chip communicates via Ethernet with a commercial data hub (Artemes GmbH, Austria), allowing storage of data on a local hard disk drive and remote access via OpenVPN.

Application

The developed system was tested in a laboratory setting with a reference current source to determine its sensitivity regarding dc and ac, as well as their superposition. A sensing head with a radius of $R = 8\,\text{cm}$ and $N \approx 150$ achieved a dc detection limit of around 0.2 A (Fig. 3). Measurements at lower currents are affected by optical noise and an imperfect $\lambda/4$ retarder. As demonstrated in [4], a sinusoidal ac will show as a rectified sensor signal and a superimposed dc will lead to a shift of the ac peaks. For an ac signal with $I_{peak} = 300\,\text{A}$, the standard deviation was 0.5 A, putting a limit on the detectable dc biases.

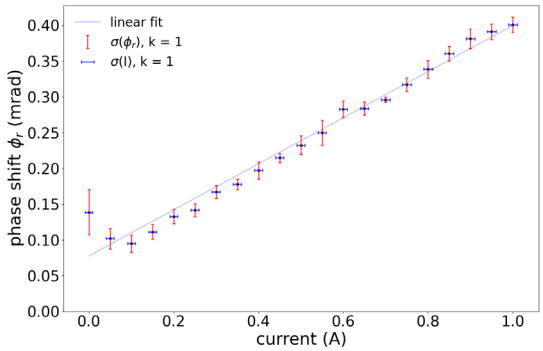

Fig. 3: Dc characteristic of developed FOCS from 0-1 A at room temperature: σ - standard deviation, k-factor = 1

The FOCS was installed at an electrical substation in Vienna, Austria. The optical elements as well as the electronics module (casted area in Fig. 1) were mounted in an electric cabinet next to the transformer and are kept at a constant temperature of 25° C. The fiber optic coil was placed on one phase of the 220 kV side of a Ynyn0 transformer. To fit the transformer turret, a new sensing head with a radius of $R = 24\,\text{cm}$ was constructed, resulting in $N \approx 50$. A reference zero-flux current transducer measures direct currents in the transformer neutral point (Fig. 4).

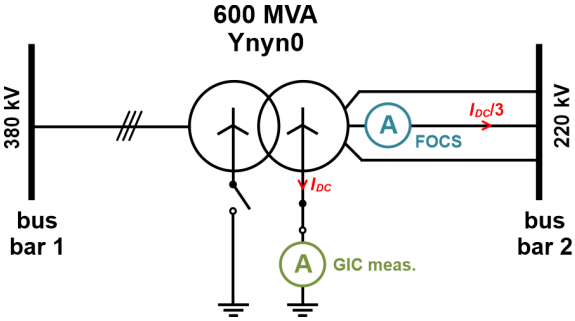

Fig. 4: Schematic of FOCS installation on one phase of a 600 MVA Ynyn0 transformer and comparison to a reference zero-flux GIC measurement system in the transformer neutral point.

Outlook

Given the current stage of the solar magnetic activity cycle, a frequent occurrence of GICs in the Austrian power grid with magnitude of several amperes is expected. The installed fiber optic sensor system will for the first time allow a direct measurement of GICs on the individual phases, and enable a comparison to ongoing GIC measurements in the transformer neutral point. The measurement campaign is planned for several months with the goal of monitoring the effects of geomagnetic storms on the power grid. In a follow-up study, the presented sensor setup will be improved by correcting temperature-induced performance variations in the sensor signal caused by a temperature-dependent Verdet constant and birefringence of the sensing fiber and an imperfect $\lambda/4$ retarder.

References

[1] D. Albert, P. Schachinger, R. L. Bailey, H. Renner, and G. Achleitner, “Analysis of long-term gic measurements in transformers in austria,” *Space Weather*, vol. 20, no. 1, pp. 1–16, 2022.

[2] R. M. Silva, H. Martins, I. Nascimento, J. M. Baptista, A. L. Ribeiro, J. L. Santos, P. Jorge, and O. Frazão, “Optical current sensors for high power systems: A review,” *Applied Sciences*, vol. 2, no. 3, pp. 602–628, 2012.

[3] G. Frosio and R. Dändliker, “Reciprocal reflection interferometer for a fiber-optic faraday current sensor,” *Appl. Opt.*, vol. 33, pp. 6111–6122, Sep 1994.

[4] J. Mandl, P. Trampitsch, P. Schachinger, D. Albert, R. Klambauer, and A. Bergmann, “Development of a fiber optic current sensor for low dc measurements in the power grid,” *IEEE Transactions on Instrumentation and Measurement*, vol. 73, pp. 1–8, 2024.

DOI 10.5162/SMSI2025/B5.1

Model-based Reconstruction of Freeform Surfaces with Radial Basis Functions

Friedrich Fleischmann[1], Tobias Binkele[2], Nils Müller[3], David Hilbig[1]
[1] Hochschule Bremen, 28199 Bremen, Germany
[2] OPTIMARE Systems GmbH, 27572 Bremerhaven, Germany
[3]ATLAS ELEKTRONIK GmbH, 28309 Bremen, Germany
friedrich.fleischmann@hs-bremen.de

Summary:
Optical elements with freeform surfaces open new degrees of freedom in the design of optical systems. Reliable measurement of shape is challenging, specially in case of strongly curved ones. A realization of deflectometry, Experimental Ray Tracing, has proven to measure those surfaces with high accuracy. A crucial step is integration of measured gradients from sampled and noisy data. A model based method for surface reconstruction based on Radial Basis Functions (RBF) using non-linear optimization is presented and compared to a new machine learning based RBF-Network approach.

Keywords: Freeform measurement, Deflectometry, Radial Basis Function (RBF), Radial Basis Function Network (RBFN), Experimental Ray Tracing (ERT)

Background and Motivation

In last decade, freeform surfaces on optical components have proven ability to reduce aberrations, size and weight of imaging and non-imaging optical systems [1]. While specific freeforms like aspheres already are measured with high accuracy, those with strong deviations from spherical or flat shape are still challenging [2,3]. Gradient based measurement techniques measure surface slopes instead of height, reducing complexity of setup and need for high dynamic range of sensor, but demand intensive post processing for surface reconstruction [4,5].

One of those, Experimental Ray Tracing (ERT), determines the direction change of a narrow beam passing an optical element. In previous work, method and setup to realize ERT for measurement of reflective surfaces was introduced and uncertainties were discussed [6].

Method

Here, we present the model-based reconstruction approach used, enforcing integrability and using integration of RBF by non-linear optimization and compare this to a new approach based on RBFNs.

The setup is sketched in *Fig. 1*. For measurement, the incident ray i is directed to the surface under test (SUT) and reflected, with new direction r depending on i and surface normal g at the point of reflection. Those vectors can be represented by direction vectors, and point of intersection by its position vector. Sampling the area $\boldsymbol{A}$ of SUT**,** one can derive surface normals in intersection points of area of interest $\boldsymbol{A}$ by

$$\boldsymbol{g} = \frac{\boldsymbol{r} - \boldsymbol{i}}{\sqrt{2(1 - (\boldsymbol{r} \cdot \boldsymbol{i}))}}$$

In *Fig.1*, relevant coordinate systems CS are introduced. Those are the CS of incident ray with the basis $\mathcal{I}$ describing vectors i , r, g, the

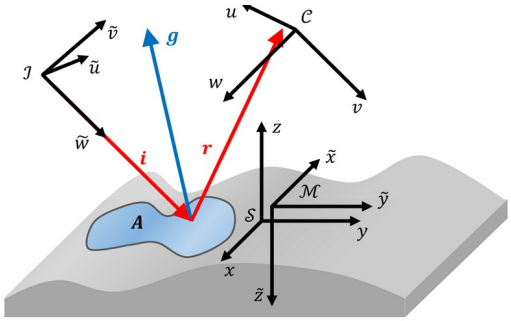

Fig. 1: Symbolic measurement setup. Device under test in grey, investigated area $\boldsymbol{A}$ in blue. Incident ray i, reflected ray r.

CS Camera $\mathcal{C}$ describing intensity distributions on sensor, CS of Measurement plane $\mathcal{M}$ identifying the direction of the sampling of the SUT, and CS of SUT with the basis $\mathcal{S}$ and axes x, y, z, describing the model function of SUT with height

$$z = s(\boldsymbol{x})\colon \mathbb{R}^2 \rightarrow \mathbb{R}, \text{ with } \boldsymbol{x} = (x, y)^T \in \boldsymbol{A} \quad (1)$$

Necessary coordinate transformation between CS is eased by homogeneous coordinates [7].

The surface normals are determined in CS $\mathcal{C}$, resulting in a surface normal at position $\boldsymbol{x}_i$ as $\boldsymbol{g}_i^{\mathcal{C}}$. Having all sample points acquired, normals are transferred into the CS $\mathcal{M}$. From normal's slopes a gradient field in CS $\mathcal{C}$ is derived. For numerical integration, a model of surface using RBS (Wendland functions) is used, with number of RBFs beeing identical to number of sample points and centers located in the measurement positions $\boldsymbol{x}_i$. Derivatives of RBF are fitted to measured gradients. Due to uncertainties and noise, an additional nonlinear optimization step is necessary. Flow of reconstruction process is depicted in *Fig. 2*.

The second method uses supervised learning for reconstruction. A "Growing and Pruning" RBFN was implemented, which uses derivatives of the Wendland function as a basis, see *Fig. 3*. That approach promises a reduction of compute time and memory, since model is optimized continuously by new measurement data.

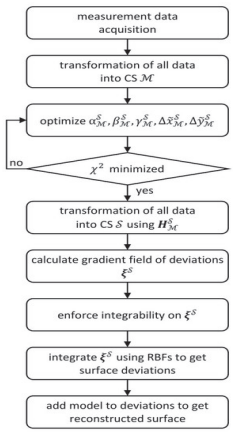

Fig. 2: Flowchart of the reconstruction process.

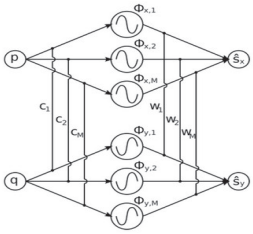

Fig. 3: Schematic Architecture for the RBF Network. Φ_x und Φ_y are derivatives of RBFs in x- and y-direction, c_i denotes i-th center position, p and q are the measured gradients in x and y direction and $\hat{s}$ are the approximated gradients in x and y direction.

Results

The reconstruction methods were applied in simulation as well as in measurement. For comparison reasons, here the outcome of simulated measurement of a "Franke-surface" is presented, see *Fig. 4* and *5*. The surface was evaluated using nonlinear optimization and integration (compare *Fig. 2*) as well as using supervised learning with RBFN approach (*Fig. 3*). Both methods result in extremely small deviations. The optimization method also proved its performance with real live data.

Tab. 1: Comparison of reconstruction performance.

Method	RMS/normalized	t/s
Integration	2.560e-4	126.312
RBFN	8.623e-6	42.583

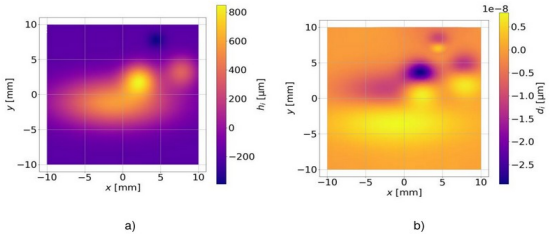

Fig. 4: Plots presenting a) the reconstructed "Franke" surface and b) its deviation from the surface model using RBF integration .

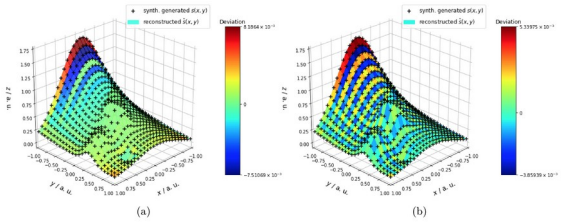

Fig. 5: Comparison of reconstruction using a) least-square RBFN and b) integration of RBF.

Conclusion

Two model-based techniques for reconstruction of freeform surfaces from gradient data are compared. In simulation, data-driven RBFN outperforms integration method especially in regard of processing time, but performance in real measurement has to be investigated further.

References

[1] K. P. Thompson and J. P. Rolland, Freeform Optical Surfaces: A Revolution in Imaging Optical Design, *Optics & Photonics News* 23(6), 30-35, (2012); doi: 10.1364/OPN.23.6.000030

[2] Ines Fortmeier *et al,* Results of round robin form measurements of optical aspheres and freeform surfaces *Meas. Sci. Technol.* **35** 085012 (2024); doi: 10.1088/1361-6501/ad4730

[3] M. Khreishi *et al*, Enabling precision coordinate metrology for universal optical testing and alignment applications, Opt. Eng. 60(3) 035106 (2021)

[4] Wagner, C., Häusler, G., Information theoretical optimization for optical range sensors, Appl. Opt. Vol. 42 No. 27 (2003).

[5] S. Ettl, J. Kaminski, M. C. Knauer and G.Häusler, Shape reconstruction from gradient data, Applied Optics 47, 2091-2097 (2008).

[6] T. Binkele, *et al*, Characterization of specular freeform surfaces from reflected ray directions using experimental ray tracing, *J. Sens. Sens. Syst.*, 10, 261–270 (2021); doi: 10.5194/jsss-10-261-2021.

[7] M. Duncan, Applied Geometry for Computer Graphics and CAD, 2nd edition, Springer, (2005)

DOI 10.5162/SMSI2025/B5.2

OPC UA for IO-Link Wireless in a Cyber Physical Finite Element Sensor Network for Shape Measurement

Henry Beuster[1], *Lars-Michel Bretthauer*[1], *Gerd Scholl*[1]
[1] Electrical Measurement Engineering, Helmut Schmidt University, Hamburg, Germany
firstname.lastname@hsu-hh.de

Summary: This paper presents the integration of OPC UA as a communication protocol in a wireless sensor network and the associated companion specifications as a semantic template for an information model. The Cyber Physical Finite Element Sensor Network (CPFEN) for Shape Measurements, a distributed wireless system, uses IO-Link Wireless for data transmission at the sensor level, OPC UA provides a unified interface for data access, configuration, monitoring, and calibration tailored to the needs of the CPFEN for all level above. This opens up additional possibilities, such as integrated quality assurance or creating a digital twin, while improving scalability.

Keywords: Sensor Network, IO-Link Wireless, OPC UA, Information Model, Shape Measurement

Motivation

The Cyber Physical Finite Element Sensor Network (CPFEN) for Shape Measurements proposed in [1] is a new approach addressing the challenges of precise real-time shape monitoring in industrial applications. It uses a network of interconnected sensor nodes like a finite element grid attached to the surface, enabling the continuous measurement of shape and deformation in large structures, as depicted in Fig. 1. This capability is critical for applications such as manufacturing process control and structural health monitoring. In this network, IO-Link Wireless (IOLW) connects sensor nodes to the Wireless-Master (W-Master), enabling the transmission of measurement data without the need for physical cabling. IOLW also enables centralized handling of calibration, configuration, and extended diagnostic data [2]. For higher-level communications, OPC UA provides a unified interface as communication framework. It extends across multiple W-Masters to the central measurement computer. A customized OPC UA information model is used to meet the specific requirements of the CPFEN. It provides a semantic structure for organizing sensor data, enabling monitoring, while ensuring easy scalability and remote configurability. This customization enables the integration of applications such as predictive maintenance and process optimization.

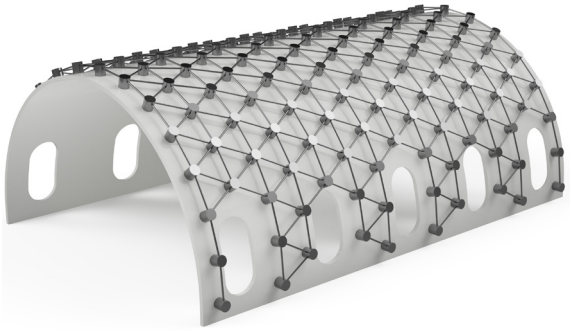

Fig. 1: Sensor network attached to the surface of a large structure.

Architecture and Sensor Information Model

The structure of the CPFEN, described from the lowest to the highest level, consists of up to 40 sensor nodes per IOLW W-Master. The W-Master is implemented on a TI TMDS64EVM evaluation board and provides dedicated cores for real-time processing of IOLW and sufficient processing power for communication applications such as OPC UA implemented on a non-real-time Linux [3]. In this configuration, the communication application based on the Open62541 stack serves as a gateway, providing both, the OPC UA server functionality and the ”Standardized Master Interface” of IOLW on the same network interface. In the subsequent layer, multiple W-Masters can be connected to a control and measurement computer via Ethernet or a corresponding wireless alternative such as 5G [4]. The sensor density is only limited by the capability of an IOLW cell, defined by the specification [5], which allows up to three W-Masters with 120 corresponding sensor nodes within a 10 m cell. A customized OPC UA information model, based on the ”OPC UA for IO-Link Devices and IO-Link Masters” specification [6], is adapted for the sensors of the CPFEN and the wireless multisensor system architecture. It comprises three key elements: firstly, sensor data of each node for easy access and integration; secondly, configuration and calibration parameters for centralized control of settings; and thirdly, diagnostic data for monitoring the sensor health and

communication status. The information model provides a flexible and scalable structure that allows efficient expansion and integration with higher-level applications such as quality assurance. Fig. 2 illustrates the mapping of the process input and output data to the corresponding physical measurement value, which reflects the sensor node structure as a representative of the other aspects mentioned. The sensor nodes consist of a central sensor probe with an acceleration sensor (index 0) and up to six mechanical interconnecting rods, each of which has an acceleration sensor and a distance measurement, of which up to three can be assigned to a node for the data connection (index i 1 to 3).

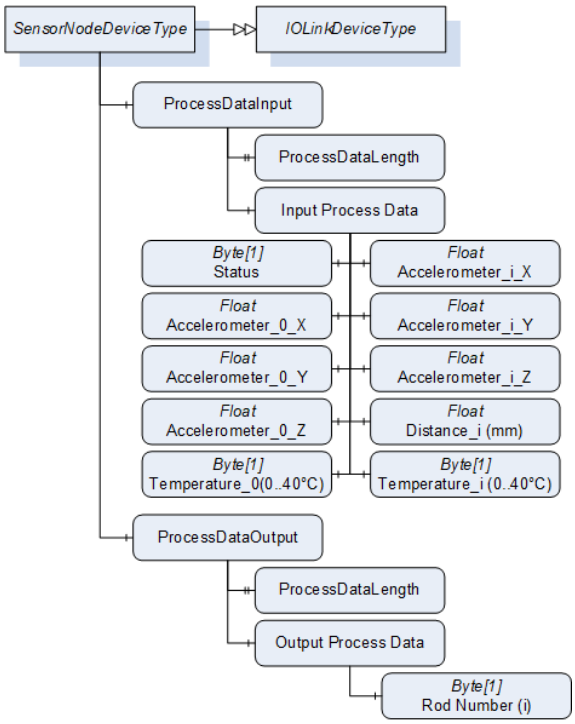

Fig. 2: Information model for the SensorNodeDeviceType according to [6].

Conclusion

The integration of OPC UA with IOLW in the CPFEN provides a modern architecture for precise wireless shape monitoring in industrial applications. OPC UA and the information model adapted to the CPFEN enable standardized communication, configuration and diagnostic handling and facilitate the deployment of the flexible sensor network in large structures. A promising direction for future research is to improve the real-time capabilities of OPC UA, as investigated by Pfrommer et al. [7]. They showed that OPC UA PubSub in combination with TSN can meet the demanding real-time requirements in industrial environments, which is also in line with the OPC UA Field eXchange specifications. Time-sensitive applications, such as dynamic condition monitoring of structures, automated quality control, or simply shorter process cycles and therefore also faster production, could be elevated by improved temporal precision and reduced latency. Enriching measurement data with semantics is an enabler for digital twin modeling, rapid integration, and new business models. Rentschler and Drath emphasized the use of AutomationML [8], while the similar approach with OPC UA also includes the communication protocol, and digital semantic models are largely convertible.

Acknowledgment

This research is funded by dtec.bw – Digitalization and Technology Research Center of the Bundeswehr. dtec.bw is funded by the European Union – NextGenerationEU (project “Digital Sensor-2-Cloud Campus Platform” (DS2CCP), https://dtecbw.de/home/forschung/hsu/projekt-ds2ccp).

References

[1] L.-M. Bretthauer, R. Heynicke, G. Scholl, Proposal of a Cyber Physical Finite Element Sensor Network for Surface Measurements, *IEEE International Instrumentation and Measurement Technology Conference*, (2024); doi: 10.1109/I2MTC60896.2024.10560668

[2] H. Beuster, K. Tebbe, T. R. Doebbert, G. Scholl, Measurements of the Safety Function Response Time on a Private 5G and IO-Link Wireless Testbed, *IEEE International Conference on Emerging Technologies and Factory Automation* 29, (2024); doi: 10.1109/ETFA61755.2024.10710762

[3] A. Morato, S. Vitturi, F. Tramarin, A. Cenedese, Assessment of Different OPC UA Implementations for Industrial IoT-Based Measurement Applications, *IEEE Transactions on Instrumentation and Measurement* 70, (2021); doi: 10.1109/TIM.2020.3043116

[4] T. R. Doebbert, C. Cammin, G. Scholl, B. K ¨archer, Study of a Safe and Secure Ecosystem based on IO-Link Wireless and a 5G Campus Network, *IEEE International Conference on Emerging Technologies and Factory Automation* 26, (2021); doi: 10.1109/ETFA45728.2021.9613484

[5] IEC 61139-3:2023 Industrial networks – Single-drop digital communication interface – Part 3: Wireless extensions

[6] OPC UA Companion-Specification 30120: OPC UA for IO-Link Devices and IO-Link Masters, V1.0 (2018)

[7] J. Pfrommer, A. Ebner, S. Ravikumar, B. Karunakaran, Open Source OPC UA PubSub Over TSN for Realtime Industrial Communication, *IEEE International Conference on Emerging Technologies and Factory Automation* 23, 1087–1090 (2018); doi: 10.1109/ETFA.2018.8502479

[8] R. Drath, M. Rentschler, Modeling and exchange of IO-Link configurations with AutomationML, *IEEE International Conference on Automation Science and Engineering* 14, 1530–1535 (2018); doi: 10.1109/COASE.2018.8560422

DOI 10.5162/SMSI2025/B5.3

OEFPIL: An Alternative Method for Curve Fitting

Anna Charvátová Campbell[1], Radek Šlesinger[1], Viktor Witkovský[2], Gejza Wimmer[3] and Martin Šíra[1]
[1] Czech Metrology Institute, Okružní 31, 638 00, Czech Republic
[2] Institute of Measurement Science, Slovak Academy of Sciences, Dúbravská cesta 9, 841 04 Bratislava, Slovakia
[3] Mathematical institute, Slovak Academy of Sciences, Štefánikova 49, 814 73 Bratislava, Slovakia
acharvatovacampbell@cmi.gov.cz

Summary: In recent years, as measurement processes have grown increasingly complex, curve fitting has become a vital tool for aligning theoretical models with observed data. As instrumentation improves, previously overlooked uncertainties must now be addressed for more precise measurements. Uncertainties as well as correlation in both dependent and independent variables should be taken into account. This is illustrated by applying the algorithm OEFPIL to the determination of the internal resistance of an AC source from its loading characteristics.

Keywords: curve fitting, errors-in-variables

Background, Motivation and Objective

Modern metrology extensively uses curve fitting, with non-linear least squares (NLS) being the most common method, although it assumes negligible uncertainties in the independent variable and no data correlation. Errors-in-variables (EIV) addresses these limitations by symmetrically treating uncertainties in both variables as well as taking into account possible correlations. Several approaches can be found in literature e.g. [1, 2, 3] which implement different methods for the estimation of the covariance matrix of the fitted parameters, The Monte Carlo method (MCM) constitutes yet another alternative for the uncertainty estimation. For some of the approaches software implementations are available, e.g. [2, 3] although neither one of them is fully general. In this contribution we present a method named Optimum Estimate of Function Parameters by Iterated Linearization (OEFPIL), which allows a general covariance matrix of the input variables as well as a general function of an arbitrary number of variables, both in implicit and explicit form, and illustrate its use by determining the internal resistance of an AC voltage source from its load characteristics. The internal resistance of the source must be known with high accuracy as it is needed for measurements with different voltmeters.

Method

OEFPIL is based on iterative linearizations of the EIV model with nonlinear parameter constraints specified in implicit form written as

$$\mathbf{X} = \beta + \epsilon, \qquad \mathbf{f}(\mu, \beta) = 0. \tag{1}$$

Here, $\mathbf{X}$ is the vector of direct measurements, μ the (unknown) expectations of $\mathbf{X}$, β the unknown parameters and ϵ the measurement errors. The expectation value of the measurement errors is assumed to be zero and their covariance matrix is assumed to be known. The constraint f is a general, continuous vector function. In terms of curve fitting, β corresponds to the parameters of the fitted curve, $\mathbf{X}$ to the input variables x_i and y_i and f is the function to be fitted (in implicit form). If the constraint is linear in the form of

$$\mathbf{B_1}\mu + \mathbf{B_2}\beta + \mathbf{b} = 0 \tag{2}$$

the estimates of the parameters β and measurements μ can be found using Best Linear Unbiased Estimation (BLUE) [4] as:

$$\hat{\beta} = -\mathbf{U}\mathbf{B_1}^T\mathbf{Q_{11}}\mathbf{b} + \left(\mathbf{I} - \mathbf{U}\mathbf{B_1}^T\mathbf{Q_{11}}\mathbf{B_1}\right)\mathbf{X} \tag{3}$$

$$\hat{\mu} = \mathbf{Q_{21}}\mathbf{b} - \mathbf{Q_{21}}\mathbf{B_1}\mathbf{X}, \tag{4}$$

where $\mathbf{I}$ is a unit matrix and the matrices $\mathbf{Q}_{ij}$ are blocks of the matrix $\mathbf{Q}$ defined as

$$\mathbf{Q} = \begin{pmatrix} \mathbf{Q}_{11} & \mathbf{Q}_{12} \\ \mathbf{Q}_{21} & \mathbf{Q}_{22} \end{pmatrix} = \begin{pmatrix} \mathbf{B}_1\mathbf{U}\mathbf{B}_1^T & \mathbf{B_2} \\ \mathbf{B}_2^T & \mathbf{0} \end{pmatrix}^{-1}. \tag{5}$$

If the constraint is nonlinear we iteratively linearize it at specific values μ_0 and β_0 and apply the BLUE procedure at each of these steps. Iteration is stopped when a specified criterion, such as the relative change in the parameter estimates, is met within a pre-defined tolerance.

Results

We shall demonstrate the use of OEFPIL on the determination of the internal resistance of an AC voltage source (SineWaveGenerator by CMI) from its load characteristic. The SWG was subjected to various loads by adding loading resistance R_s, and the resulting voltage drop on the output terminals was measured. Commercially available component resistors were used as the load. The output voltage was measured using a programmable josephson quantum standard (PJVS), which operated in the mode of an

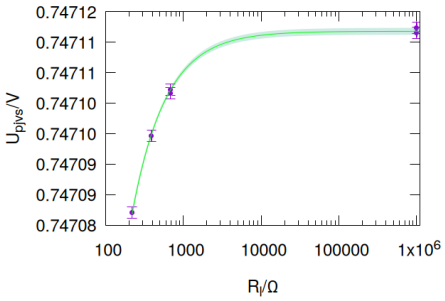

Fig. 1: Graph of relationship between the voltage measured by the PJVS and the applied load, including expanded uncertainties and bands.

AC quantum voltmeter. The PJVS itself introduces a load on the measured source through input impedance, R_d, of the sampling card (part of PJVS), so the total load on the SWG is the parallel combination of R_s and R_d. The SWG was modeled as a combination of an ideal voltage source U_s and the internal resistance R_s. The relationship between the voltage measured by the PJVS U_PJVS and the load R_l can be expressed as

$$U_\mathrm{PJVS} = U_\mathrm{s} R_\mathrm{l} / \left(R_\mathrm{l} + R_\mathrm{s}\right) \qquad (6)$$

where U_s and R_s are the voltage and internal resistance of the source and the total load R_l is given by the parallel sum of the input impedance of the sampling card R_d and the resistance of the component resistor R_s as $R_\mathrm{l}^{-1} = R_\mathrm{s}^{-1} + R_\mathrm{d}^{-1}$.
The uncertainties in the measured data arise from the calibration of the resistors, the estimation of the input impedance of the card based on literature, and the measurement of the AC voltage using the PJVS. An interesting question is the correlation of the data. Since we measure all voltage values with the same instrument, we can expect some correlation between them. The same holds for the resistance. However, the exact quantification remains an open question. In order to assess the effect correlation has on estimates and their uncertainties we considered constant correlation coefficients between any pair of resistances (denoted as ρ_R and any pair of voltage (denoted as ρ_V). Voltage and resistance values were assumed to be uncorrelated because of different traceability chains.

The data were fitted by OEFPI to the function (6). The fitted curve including expanded uncertainty bands is shown in Fig. 1. We verified the correspondence between the results obtained by OEFPIL and Monte Carlo method and found excellent agreement, see 1. It can be also seen that difference between NLS and OEFPIL without correlations is neglectable. The correlation between data obviously has a noticeable impact on the uncertainties whereas its effect on the estimated values is within error margins. This can be further elaborated creating maps for both estimated values as well as their uncertainties by varying the correlation coefficients. An example of such a map for the uncertainty of the resistance of the source is shown in fig. 2.

	R_s/mΩ	$u(R_\mathrm{s})$/mΩ
NLS	8.79364	0.148
OEFPIL (uncorr.)	8.79616	0.164
MC (uncorr.)	8.79636	0.164
OEFPIL (corr.)	8.79600	0.053
MC (corr.)	8.79619	0.053

Tab. 1: Internal resistance of the source obtained different fitting procedures: NLS, OEFPIL and Monte Carlo without correlations and OEFPIL and Monte Carlo with strong correlation $\rho_\mathrm{R} = \rho_\mathrm{V} = 0.9$.

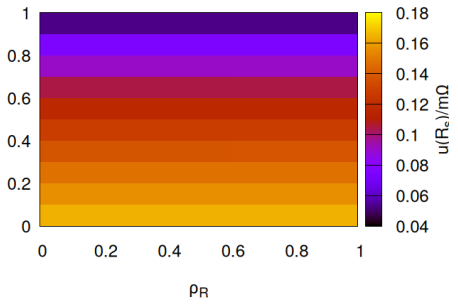

Fig. 2: Map of source resistance uncertainty depending on the correlation coefficients for voltage and resistance.

Conclusions

The use of OEFPIL has been illustrated on the determination of the internal resistance of an AC source. Uncertainty maps for different correlation assumptions can help to assess the impact of the correlation on the results.

Acknowledgements

This work was supported by the Czech Ministry of Education, Youth and Sports and the Slovak Research and Development Agency through the Inter-Excellence II program, project LUASK22008/SK-CZ-RD-21-0109

References

[1] A. Celmiņš, Least squares adjustment with finite residuals for non-linear constraints and partially correlated data, *Internal Report* (1973)

[2] P.T. Boggs et al., ODRPACK: Software for Weighted Orthogonal Distance Regression, *ACM T Math Software* 15,348 – 364 (1989); doi: 10.1145/76909.76913

[3] A. Malengo, F. Pennecchi, A weighted total least-squares algorithm for any fitting model with correlated variables, *Metrologia* 50, 654–662 (2013), doi: 10.1088/0026-1394/50/6/654

[4] L. Kubáček, Foundations of Estimation Theory, *Elsevier* (1988)

DOI 10.5162/SMSI2025/B5.4

Methods of uncertainty evaluation using virtual experiments with the example of the tilted-wave interferometer

Manuel Stavridis[1], *Manuel Marschall*[1], *Finn Hughes*[1], *Ines Fortmeier*[1] *and Clemens Elster*[1]
[1] *Physikalisch-Technische Bundesanstalt Braunschweig and Berlin*

Summary:
This paper uses virtual experiments to present a simplified uncertainty analysis for non-linear measurement methods. For these, the dependencies of the measured value on the uncertainty sources can often be regarded as sufficiently linear. This statement is examined for the example of a complex optical application based on the simplified version of the tilted-wave interferometer (TWI) by comparing the results of a simplified uncertainty evaluation with those of a Bayesian reference method.

Keywords: Uncertainty Evaluation, Virtual Experiments, Tilted-Wave Interferometer, Bayes, GUM, SimOptDevice

Bayesian uncertainty analysis (reference method)

In [1], a method for calculating the uncertainty for the TWI using virtual experiments (VEs) was presented. The Bayesian method described there includes an approximation, which leads to a Monte Carlo sampling procedure. For each sampling step, a call to the VE of the TWI is required, and a high-dimensional regression problem is solved.

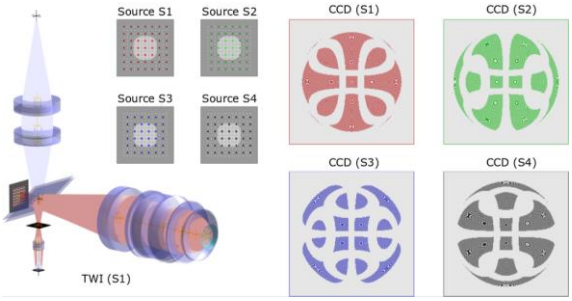

Figure 1: VE: Tilted-wave interferometer (left) and its simulated interferograms (right), (from [2], CC BY 4.0).

The VE of the TWI, as seen in Figure 1, includes a physical modelling of the measurement using ray tracing by SimOptDevice [2] up to the generation of the measurement data (interferograms).

The subsequent data analysis, with the aim of reconstructing the form of a sphere-, asphere- or freeform surface, again calls to the VEs in the context of a non-linear inverse problem.

Using the Bayesian uncertainty evaluation in [1], the point-wise standard uncertainty shown in Figure 2 was obtained for the polynomial fit (intermediate reconstruction step).

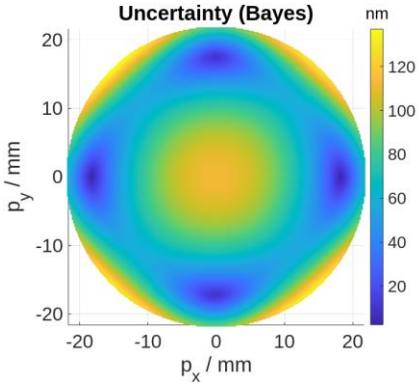

Figure 2: Point-wise standard uncertainty for the intermediate reconstruction step using the Bayesian method from [1].

Consideration of the uncertainty sources as linear

The GUM [3] serves as the de facto standard for uncertainty evaluation in metrology, and it propagates the uncertainties associated with the so-called input quantities to the quantity of interest, i.e. the measurand. Often a linearisation of this relationship is sufficient to provide an adequate uncertainty evaluation. An uncertainty evaluation using the linearised model and the "Law of propagation of uncertainty" (LPU) also requires the determination of the sensitivities or gradients of the VE. However, whether such a linearisation is sufficient or not needs to be checked.

Determination of the gradients for the sources of uncertainty using VEs

In the TWI, the VE is embedded in the measurement data reconstruction process. As a result, the VE models a physical-technical state in silico, in which the deviations from the real measured values (interferograms) have to be minimised within a numerical optimisation arising from an inverse problem.

The VE can then represent the dependencies between the actual measurand and the input quantities. In the linearised form, gradients can be calculated numerically by varying the input quantities and repeating the VE. SimOptDevice [2], a library for optical simulations, is also able to output these gradients analytically [4]. This is used to calculate the dependencies of optical elements or element groups regarding input quantities such as positioning or direction.

The basis for this is the change in the optical path length OPL with respect to the position of the surface $\frac{\partial OPL}{\partial p} = n_o\vec{e}_o - n_i\vec{e}_i$, where $\vec{e}_o$,$\vec{e}_i$ are the direction vectors of the beam and n_o, n_i are the refractive indices of the media before and after the surface, respectively [4]. The chain rule could also be used here to analyse dependencies on other quantities such as lens radii, directions, etc. [4].

Linearisation of the VE

After exporting the above sensitivities for the measurement, a linear model can be created:

$$x = G(y, z, \epsilon) \approx A_Y y + A_Z z + \epsilon \qquad (1)$$

x is the measurement data generated by the virtual or real experiment $G(y, z, \epsilon)$, y is a value for the measurand Y, and ϵ is a realization of observation noise, modelled as multivariate Gaussian distributed with covariance $\sigma^2 I$. The value z of a quantity Z represents additional input quantities that affect the measurement. With the TWI, x corresponds to the optical path length differences, which are simulated using the model or calculated accordingly from the measurement data.

In the simplified model (1), the matrices A_Y and A_Z represent the linear dependence of the measured value with respect to the measurand Y and the additional input quantities Z. In the simplified TWI, Y denotes the difference to the known design topography as well as the lateral position of the specimen. Z contains, for example, the positioning of the specimen along the optical axis and its tilt.

With consideration to (1), a possible approach for the linear reconstruction of the measurand Y and for setting up a measurement model according to GUM is as follows:

$$Y = A_Y^{-1}(X - A_z Z) \qquad (2)$$

Uncertainty according to GUM using LPU

According to GUM, the covariance V of the measurand Y can be determined with linear propagation using the following formula.

$$V = JUJ^T \qquad (3)$$

Here, J is the derivative of (2) with respect to X and Z, such that

$$J = [A_Y^{-1} \quad -A_Y^{-1}A_Z] \qquad (4)$$

and U is set up as follows:

$$U = \begin{bmatrix} U_x & 0 \\ 0 & U_Z \end{bmatrix}. \qquad (5)$$

Here, $U_X = \sigma^2 I$ is the assumed covariance of the measurement data and U_Z denotes the covariance of the additional quantities Z.

Applying this method to the analogue setting from [1], the point-wise standard uncertainty is obtained for the greatly simplified TWI method. If this result is compared with the corresponding case of the Bayesian method [1], it becomes clear that the uncertainty evaluation method presented here adequately replicates the Bayesian method. Furthermore, regarding computation time, the method presented here took significantly less time to achieve adequate results, which renders the usage in live applications much more feasible.

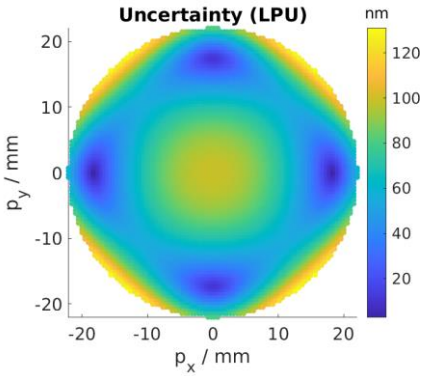

Figure 3: Point-wise standard uncertainty for the intermediate reconstruction step using the linearised model around the measured value.

Conclusion

We demonstrated for the example of the TWI that the uncertainty evaluation with a linear approximation of the influence of the input quantities essentially corresponds to that of a Bayesian reference method. The calculation of the linearised approach is significantly less time-consuming as Monte Carlo analyses with VEs are not required.

Acknowledgements

This research received funding by European Partnership on Metrology, co-financed from the European Union's Horizon Europe Research and Innovation Programme and by the Participating States, grant number 22DIT01 ViDiT.

[1] M. Marschall, I. Fortmeier, M. Stavridis, F. Hughes, C. Elster, Bayesian uncertainty evaluation applied to the tilted-wave interferometer, *Optics Express*: 32, 11, 18664 - 18683, (2024), doi: https://doi.org/10.1364/OE.524241

[2] R. Schachtschneider, M. Stavridis, I. Fortmeier, M. Schulz, C. Elster, SimOptDevice: a library for virtual optical experiments, *Journal of Sensors and Sensor Systems*: 8, 105 - 110, (2019), doi: https://doi.org/10.5194/jsss-8-105-2019

[3] BIPM, IEC, IFCC, ILAC, ISO, IUPAC, IUPAP, OIML, Evaluation of measurement data - Guide to the Expression of Uncertainty in Measurement, Joint Committee for Guides in Metrology, JCGM100, Sèvres, France, 2008.

[4] I. Fortmeier, M. Stavridis, A. Wiegmann, M. Schulz, W. Osten, C. Elster, Analytical Jacobian and its application to tilted-wave interferometry, *Optics Express*: 22, 18, 13 p. (2014), doi: https://doi.org/10.1364/oe.22.021313

DOI 10.5162/SMSI2025/B6.1

Fast Tracking using Event-based Vision Sensors and Binary Frames

Johannes Baßler[1] *and Michael Heizmann*[1]
[1] Karlsruhe Institute of Technology, Karlsruhe, Germany
johannes.bassler@kit.edu

Summary: A novel tracking algorithm for high-speed object tracking using event-based Vision (EBV) sensors and binary frame representation is presented. The method transforms sparse event data into binary frames, enabling precise and robust particle tracking at $2\,\mathrm{kHz}$ frequency by combining correlation-based matching and center of gravity alignment.

Keywords: Tracking, Event-Based-Vision, Realtime-Capable, Binary Frames, High-Speed

Introduction

This work is based on two key design elements: the use of Event-Based Vision sensors for high-speed tracking, and the representation of events through binary frames.
Event-Based Vision (EBV) sensors represent a promising new paradigm in the field of computer vision, offering high temporal resolution and low latency. These characteristics make **EBV sensors** particularly well-suited for tracking rapid movements. This paper presents a real-time, robust tracker that processes event data using binary frames, demonstrating its potential in applications such as bulk material sorting, where precise object tracking is crucial for pneumatic actuator control.
The proposed tracker operates at $2\,\mathrm{kHz}$, enabling precise tracking of particle trajectories in real-time. This performance level is challenging to achieve with conventional frame-based camera sensors due to limitations in costs, latency, and algorithm runtime. For comparison, the work of Maier et al. [1] utilizes conventional industrial-grade frame cameras, achieving only a $93\,\mathrm{Hz}$ tracking frequency. By leveraging the properties of EBV sensors, our approach overcomes these constraints, offering a significant advancement in high-speed object tracking. Moreover, there is potential to further increase the sampling rate if required for specific applications.
While existing event-based tracking literature, exemplified by Barranco et al. [2], focuses on direct sparse event processing, our work presents a paradigm shift through **binary frame representation**. The sparse spatio-temporal nature of event data poses significant challenges for classical computer vision algorithms, particularly in real-time scenarios with time-dependent data volumes. Our approach strikes a balance by generating binary frames that efficiently capture relevant information. These binary frames enable efficient morphological operations, support compression techniques like `RLE` and `CSR`, and minimize storage requirements through their boolean representation. This allows high frame rates and therefore a small but inherent loss in temporal resolution.

Method

Our tracking algorithm combines correlation-based matching to estimate object displacement with center of gravity alignment to refine tracking by maintaining the object's position within the reference frame. The method assumes a known initial position $\xi_{t_0,p}$ and reference frame $\mathbf{r}_{t_0,p}$ containing the tracking object, which in the context of bulk material sorting can be determined when a particle crosses a predefined boundary region in the direction of motion. The algorithm operates on binary frames accumulated over a fixed time interval τ. This accumulation period also defines the tracking frequency, as each new frame triggers a new iteration. This dual-step process is executed in parallel for each polarity p individually, providing shifts in both x and y directions.

Binary Frame Generation Binary frames are generated through temporal accumulation of the event stream. For each pixel location (x, y) and polarity $p \in \{+, -\}$, events are accumulated over a time window τ, resulting in binary frames $\mathbf{b}_{t,p}(x, y)$ defined as:

$$\mathbf{b}_{t,p}(x,y) = \begin{cases} 1 & \text{if } \exists e(x,y,t,p) \text{ in } [t, t+\tau] \\ 0 & \text{otherwise} \end{cases} \quad (1)$$

where $e(x, y, t, p)$ represents an event at position (x, y) with polarity p at time t. This results in two separate binary frames $\mathbf{b}_{t,+}(x, y)$ and $\mathbf{b}_{t,-}(x, y)$ for positive and negative events respectively. The accumulation time τ is a crucial parameter that needs to balance two competing requirements: it should be large enough to create coherent structures in the binary frames, yet

small enough to maintain sufficient temporal resolution for the tracking task. In our implementation, we set $\tau = 500\,\mu s$ to achieve a tracking frequency of $2\,kHz$.

Correlation-based Shift We compute the correlation map $\mathbf{c}_{t,p}$ by correlating the reference frame $\mathbf{r}_{t-1,p}$ with a constrained region $\tilde{\mathbf{b}}_{t,p}$ of $\mathbf{b}_{t,p}$. This region is delimited around $\xi_{t-1,p}$, extending d pixels beyond the size of $\mathbf{r}_{t-1,p}$ to capture the maximum expected particle displacement during τ, thereby reducing computational complexity significantly.

$$\mathbf{c}_{t,p} = \mathbf{r}_{t-1,p} \star \tilde{\mathbf{b}}_{t,p} \tag{2}$$

The correlation-based shift $\delta_{t,p}^{corr}$ is then determined by:

$$\delta_{t,p}^{corr} = \arg\max(\mathbf{c}_{t,p}) - C(\tilde{\mathbf{b}}_{t,p}) \tag{3}$$

where C represents the geometric center operation. Note, that $C(\tilde{\mathbf{b}}_{t,p})$ is equivalent to $\xi_{t-1,p}$ but referenced in the local coordinate system of $\tilde{\mathbf{b}}_{t,p}$ instead of the global coordinate system.

Center of Gravity Alignment Now, we extract an expanded preliminary reference frame $\tilde{\mathbf{r}}_{t,p}$ centered at the shifted position $\xi_{t-1,p}+\delta_{t,p}^{corr}$. The second shift $\delta_{t,p}^{grav}$ is computed as:

$$\delta_{t,p}^{grav} = \texttt{CoG}(\tilde{\mathbf{r}}_{t,p}) - C(\tilde{\mathbf{r}}_{t,p}) \tag{4}$$

where $\texttt{CoG}$ represents the center of gravity calculation. The actual reference frame $\mathbf{r}_{t,p}$ is then cut out of $\tilde{\mathbf{r}}_{t,p}$ w.r.t $\delta_{t,p}^{grav}$. This centering adjustment maintains the tracked particle within the reference frame, enhancing robustness by preventing positional drift across iterations. Morphological filtering of each reference frame enhances robustness against noise.

Final Position Estimation The total shift per iteration and polarity is $\delta_{t,p} = \delta_{t,p}^{corr} + \delta_{t,p}^{grav}$, yielding the next point $\xi_{t,p} = \xi_{t-1,p} + \delta_{t,p}$. Robustness is enhanced further by independent processing of positive and negative events, creating redundancy in the tracking process. The final object position is determined by $\xi_t = \frac{\xi_{t,+}+\xi_{t,-}}{2}$ where $\xi_{t,+}$ and $\xi_{t,-}$ represent the positions obtained from positive and negative events, respectively.

Results

The proposed tracking algorithm has been tested with numerous particle trajectories. Our experiments demonstrate the method's robustness and real-time capability, with processing times of approximately $200\,\mu s$ per iteration on a modern mid-range desktop processor, significantly lower than

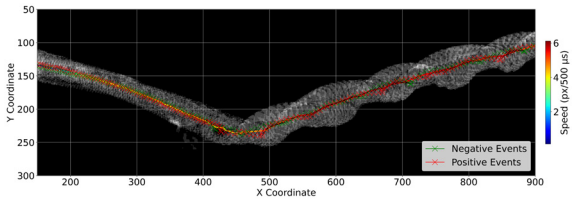

Fig. 1: Tracked particle trajectory with velocity estimation. The background image outlines the swept area of the particle during the flight.

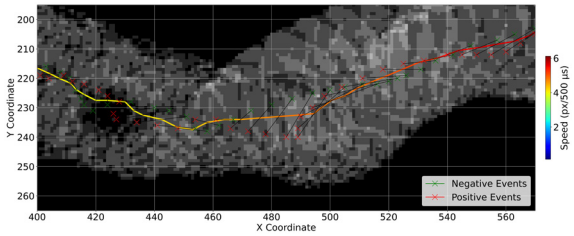

Fig. 2: Tracked particle trajectory with velocity estimation zoomed in at the interaction area between particle and pneumatic system.

$\tau = 500\,\mu s$ required for binary frame accumulation, posing the real time boundary. Figure 1 illustrates a representative tracking result, while 2 zooms in in order to reveal more details. The trajectory includes post-processed velocity estimations. More examples and videos illustrating the results for various examples in the context of bulk sorting can be found here: https://github.com/uwupl/FT_SMSI

Summary & Outlook

The tracking algorithm demonstrates significant potential for further development and practical implementation. Future work will focus on extending the method to track multiple objects simultaneously and incorporating rotational velocity estimation of the tracked objects. This extension would provide valuable information for more precise control of sorting actuators.
For optimal industrial performance, we are exploring FPGA implementation options. This hardware acceleration approach could significantly reduce processing latency and enable even higher tracking frequencies, making the system more suitable for high-throughput sorting applications.

References

[1] G. Maier, F. Pfaff, C. Pieper, R. Gruna, B. Noack, H. Kruggel-Emden, T. Längle, U. D. Hanebeck, S. Wirtz, V. Scherer, and J. Beyerer, "Experimental evaluation of a novel sensor-based sorting approach featuring predictive real-time multiobject tracking," *IEEE Transactions on Industrial Electronics*, vol. 68, no. 2, pp. 1548–1559, 2021.

[2] F. Barranco, C. Fermüller, and E. Ros, "Real-time clustering and multi-target tracking using event-based sensors," pp. 5764–5769, 10 2018.

DOI 10.5162/SMSI2025/B6.2

Performance Comparison of Area-scan and Event-based Image Sensors

Alkhazur Manakov and Bernd Jähne
IWR, Heidelberg University,
Berliner Straße 43, 69120 Heidelberg, Germany mr182@uni-heidelberg.de

Summary: Conventional area-scan and event-based sensors are compared in their performance using the event detectability ED, i. e., how much relative irradiance difference is required to detect an event and the latency to detect an event. In addition, the nonuniformity of event-based sensors is studied with respect to the false event detection probability (FDNU), the event detection nonuniformity (EDNU) and the latency at different irradiation levels.

Keywords: Sensor characterization, event-based, area-scan, performance, comparison

Introduction

Event-based cameras are bio-inspired sensors that differ from conventional area-scan cameras. They asynchronously measure pixel brightness changes, and output a stream of events that encode the time, location and sign of the brightness changes. This offers several advantages: high temporal resolution, very high dynamic range (120 dB), low power consumption, and a compressed output stream. Therefore, they have a large potential for robotics and computer vision in challenging scenarios for traditional cameras. A first proposal for a performance characterization of event-based sensors was made in [1] and the concept of change detectability was introduced by [2] to compare area-scan and event-based image sensors.

Here we add an analysis of nonuniformities and a direct performance comparison between three event-based and three conventional area-scan sensors: a) Prophesee, gen. 3.1 (15 µm pixel); b) Prophesee, gen. 4.1 (4.86 µm pixel); c) DAVIS 346, (18.5 µm pixel) and area-scan sensors with pixel sizes and spatial resolution comparable to the Prophesee, gen. 4.1: d) Sony IMX174, (5.86 µm pixel) t_{exp} = 9 ms, max frame-rate 105 fps, corresponds to 9.5 ms latency; e) Sony IMX287, (6.9 µm pixel), t_{exp} = 3.03 ms, max frame-rate 321 fps, corresponds to 3.12 ms latency; f) Sony IMX537 with binning, (5.48 µm pixel), t_{exp} = 1.3 ms, max frame-rate 582 fps, corresponds to 1.72 ms latency.

Event-based sensor characterization

Experimentally determining the irradiation contrast ΔE necessary for generating one event for given mean irradiance level E and event threshold settings consists in gradually increasing the stimulus step until an event is generated. In a noise-free world, minimal found stimulus amplitude always results in an event when applied. In the real world conditions, the very same pixel will react differently to the same stimulus due to its, possibly different, initial condition, electronic noise, etc. Therefore, for event-based sensor characterization it has been proposed to operate with "event probability" instead [3, 1]. It is defined as $p = \frac{M}{N}$, where M the number of event responses, N the number of applied stimuli. Event probability dependency on the stimulus amplitude in the presence of noise has an "S"-shape, and is therefore named *S-curve*. The acquisition of S-curves has been done on an EMVA 1288 Standard conform setup as described in [2].

Event detectability ED

The S-curve shows how much irradiance change ΔE is required to detect an event. Here the *event detectability* ED is defined as

$$\text{ED} = \frac{\Delta E}{E_{50\%}} = \frac{1}{\theta} = \frac{1}{E_{50\%}\frac{\mathrm{d}S(E)}{\mathrm{d}E}}, \qquad (1)$$

where $E_{50\%}$ is the irradiance at the 50% probability of the S-curve and $\mathrm{d}S(E)/\mathrm{d}E$ the (steepest) slope of the S-curve at this point. ED is the inverse of the *change detectability* θ defined in [2]. Graphically, ΔE means the distance between the zero and one probability crossings of the $\mathrm{d}S(E)/\mathrm{d}E$ line. Thus ED is a good measure for the relative irradiance change required to detect an event. Depending on the required probability for event detection, the relative irradiance change might be smaller or larger than ED.

Event detection with area-scan sensors

In [2] it was shown that any area-scan sensor can be used for event detection that there is a direct relation between signal-to-noise ratio and change detectability for area-scan sensors with a latency, which is the inverse of the maximum frame rate of the sensor:

$$\text{ED} = \frac{2\sqrt{\pi}}{\text{SNR}(\mu_p)} = 2\sqrt{\pi}\frac{\sqrt{(\sigma_d^2 + \eta E A t_{\text{exp}})}}{\eta E A t_{\text{exp}}}. \qquad (2)$$

DOI 10.5162/SMSI2025/B6.2

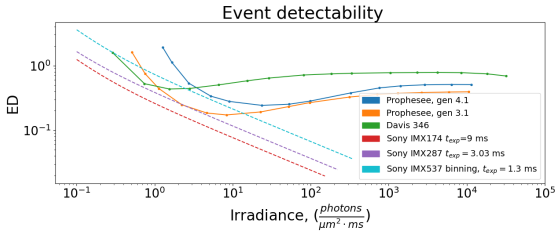

Fig. 1: Event detectability comparison for area-scan and event-based sensors.

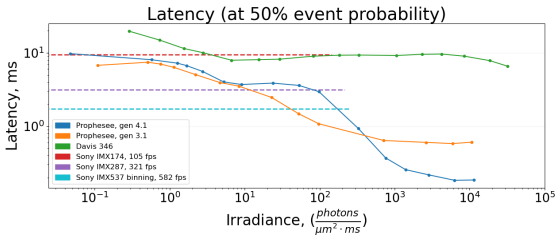

Fig. 2: Latency comparison for event-based and area-scan sensor

The equation on the right gives ED for a linear sensor with the variance σ_d^2 of the temporal dark noise and a quantum efficiency η according to the EMVA 1288 standard [4].

Results

Standard linear industrial area-scan sensors can detect events at lower relative irradiance changes but lack the high dynamic range of event-based sensors (Fig. 1). Event-based sensors have the additional advantage that the latency at high irradiation levels can be significantly lower than for area-scan sensors, where the latency is constant and just the inverse of the frame rate (Fig. 2).

The nonuniformity measurements of event-based sensors show several interesting effects. Firstly, the false event probability (FDNU), when no irradiance change happens, is irradiance dependent and can be quite high (Fig. 3). Secondly, the event detection nonuniformity (EDNU), defined by the irradiance required for each pixel

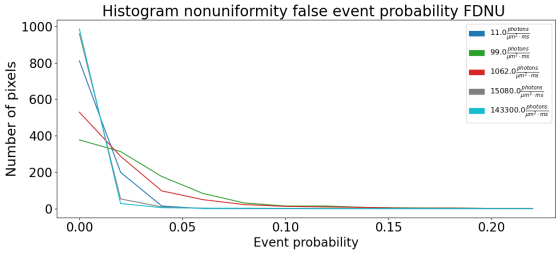

Fig. 3: Histogram of the false event detection probability under static irradiation for positive events with the Prophesee generation 4.1 sensor.

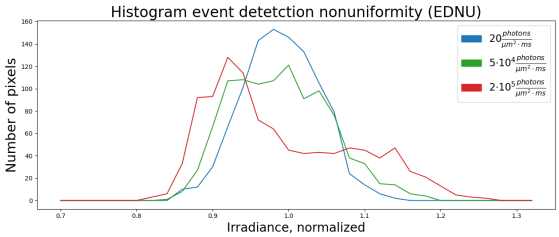

Fig. 4: Histograms of irradiance nonuniformity for 50% positive event probability for the Prophesee generation 4.1 sensor at irradiances as indicated.

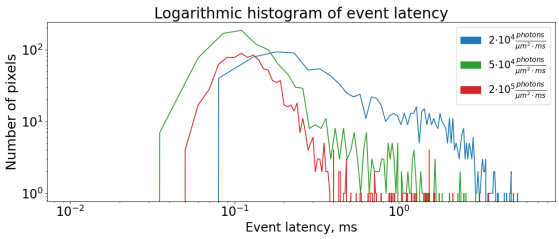

Fig. 5: Logarithmic histograms of positive event latency for 50% event probability at irradiances as indicated for the Prophesee, generation 4.1 sensor.

to reach a 50% event probability, is in the order of 10%. The distributions widens at higher irradiance and becomes skewed (Fig. 4).

Thirdly, the histogram for the latency measured at each pixel shows an even wider distribution (Fig. 5). At low irradiance a significant fraction of the pixels have a latency which is more than ten times higher than the average latency.

References

[1] A. Manakov and B. Jähne, “Characterization of event-based image sensors in extent of the EMVA 1288 standard,” in *Tagungsband ”Forum Bildverarbeitung 2020*, 2020.

[2] A. Manakov, H. Herrmann, and B. Jähne, “Performance comparison of area-scan and event-based sensors,” in *Tagungsband ”Forum Bildverarbeitung 2024*, 2024.

[3] C. Posch and D. Matolin, “Sensitivity and uniformity of a 0.18µm CMOS temporal contrast pixel array,” in *Circuits and Systems, ISCAS 2011, IEEE International Symposium*, pp. 1572–1575, 2011.

[4] EMVA 1288 Working Group, “EMVA Standard 1288 - standard for characterization of image sensors and cameras, release 4.0,” open standard, European Machine Vision Association, 2021.

DOI 10.5162/SMSI2025/B6.3

Motion Compensation of Event-Streams for Multitarget Tracking in Sensor-Based Sorting

Paul Bäcker [1] and Georg Maier[1]
[1] Fraunhofer IOSB, Fraunhoferstr. 1, 76131 Karlsruhe, Germany paul.baecker@iosb.fraunhofer.de

Summary: Event-based cameras excel in representing dynamic changes efficiently but can be overwhelmed in scenarios with strong global motion, such as conveyor belt systems. We propose a motion compensation method that filters events to focus on relative motion deviations. Our method significantly reduces the event-stream size while maintaining or even improving tracking accuracy. Our approach incorporates prior knowledge of global motion and demonstrates its efficacy in sensor-based sorting tasks.

Keywords: event-based vision, motion compensation, multitarget tracking, sensor-based sorting

Introduction

Event-based cameras efficiently capture dynamic scene changes by generating data only during motion or intensity changes, making them ideal for applications like multitarget tracking. However, in scenarios like sensor-based sorting on a conveyor belt with uniform motion, the constant motion generates a high volume of events, potentially overwhelming the system. To address this, we propose a method to filter event streams with a strong global motion prior, retaining only events corresponding to deviations from the expected motion.

Background, Motivation and Objective

Several works use contrast maximization techniques for compensation of scene motion in event-based vision [1]. Generally, these methods do not utilize a priori motion knowledge and therefore use computationally costly methods for estimating local scene motion from an event stream. [2] utilize a spiking neural networks for motion estimation and filtering, fully utilizing the asynchronous nature of event-based cameras. Although promising, spiking neural networks are still in their infancy, limiting their feasibility for widespread industrial application. [3] use on-sensor circuitry to extract object motion, by comparing local change-rates. However, some of their scene assumptions do not apply to our application. Further, to the best of our knowledge, the sensors are not commercially available. We propose a method, that efficiently filters events from commonly used event-based cameras by incorporating strong priors on global scene motion. The method is designed to be easily incorporated into tracking methods. We demonstrate our method on a multitarget tracking problem in sensor-based sorting, where we achieve equal tracking accuracy compared to a method using the full event-stream, while reducing the number of events by 70$\%$, reducing computational cost.

Method

We assume, that for a pure planar motion, every pixel of the event-based camera is expected to trigger the same amount of events. A property of the event-based sensor is, that on-events suffer from lower temporal jitter, than off-events. We therefore only consider on-events.

Consider $L(x,t)$ the radiance of a planar scene, we introduces $f(x,t)$ the motion compensated scene radiance.

$$L(x,t) = f(x + \boldsymbol{v}t, t) \tag{1}$$

relative to a planar transformation velocity $\boldsymbol{v}$ with $[v] = px/s$. A camera pointing towards a conveyor belt would capture radiance L, whereas a hypothetical camera moving along with the conveyor belt captures f. For a small temporal window δ_t we can assume a static scene $f(x)$. Using the event-generation equation from [1] we derive

$$\begin{aligned} pC &= L(x,t) - L(x,t_0) \\ &= f(x + \boldsymbol{v}t) - f(x + \boldsymbol{v}(t_0)). \end{aligned} \tag{2}$$

With p the polarity of the triggered event, $t_0 = t - \delta t$ the timestamp of the previously triggered event and C the contrast threshold of the event camera. Interpreting this, each event gives a measurement of the spatial change of a point in the scene, relative to the scene motion (e.g. the edge of a particle laying on top of a conveyor belt). However, since events suffer temporal jitter and only give binary information, we consider a spatio-temporal window around x, t for estimating the spatial gradient in ∇f relative to the speed v.

$$\nabla f(x,t)\boldsymbol{v} \propto \sum_{(x_i,y_i,t_i,p_i)\in\mathcal{E}} p_i \, \chi_x(x_i) \, \chi_y(y_i) \, \chi_t(t_i) \tag{3}$$

With $\mathcal{E}$ the event-stream and $\chi_x(x_i)$, $\chi_y(y_i)$, $\chi_t(x_i)$ indicator functions for whether event i is within the spatio-temporal window around x, t.

For every timestep Δt, we update all estimators for $\nabla f \boldsymbol{v}$. We choose Δt to be $1px/|\boldsymbol{v}| \approx 0.25ms$. The temporal window for the estimation of $\nabla f \boldsymbol{v}$ is chosen as $\Delta T = 5 \cdot \Delta t$, the spatial window a grid of 5 pixels around x. After updating the estimators, we compare $\nabla f(x,t)\boldsymbol{v}$ to $\nabla f(x,t_0)\boldsymbol{v}$, with t_0 the timestamp of the last motion compensated event, we triggered. Our event-trigger function $g(t)$ is defined as

$$g(t) = \begin{cases} 1 & \text{if } \nabla f(x,t)\boldsymbol{v} - \nabla f(x,t_0)\boldsymbol{v} > C_\nabla, \\ -1 & \text{if } \nabla f(x,t)\boldsymbol{v} - \nabla f(x,t_0)\boldsymbol{v} < C_\nabla, \\ 0 & \text{otherwise.} \end{cases} \tag{4}$$

Where C_∇ is the threshold for triggering an event. With 0 no event triggered, else $g(t)$ the polarity of the event. Figure 1 shows an example output of the motion filter algorithm.

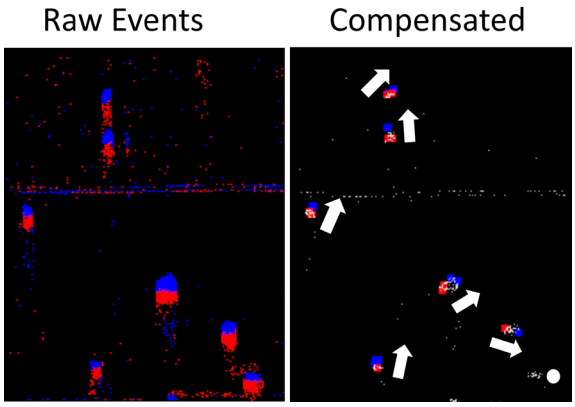

Fig. 1: Illustration of motion compensation. With index increasing proportional to the object speed, objects moving at the expected speed are projected to the same point in the compensated image (right). Using the relative position of the positive- and negative events, cues about object motion may be extracted, as indicated by the arrows.

Results

We apply the motion-filter to an existing event-stream, using different thresholds, resulting in different ratios of filtered events. In this work, we used an existing tracking approach using mean-shift tracking [4], with hyper parameters optimized using the full event-stream. We then applied different, motion-filtered event-streams without re-adjusting the tracking parameters. As shown in figure 2, we achieve a slight improvement of tracking accuracy, when reducing the number of events significantly, as only at very high filter ratios, the tracking accuracy is reduced. We further show that the filtered event-streams carry much more dense additional information, compared to the raw event-stream 1. This information could be used to further improve tracking accuracy.

Discussion and Future Work

Current method induces latency, since changes in event-frequency are only detected over time. Lower latency may be achieved by incorporating event-detection probabilities [5] or using more sophisticated changepoint detectors such as in [6]. The current implementation not optimized for realtime processing, but can be easily parallelized, since it applies operations globally.

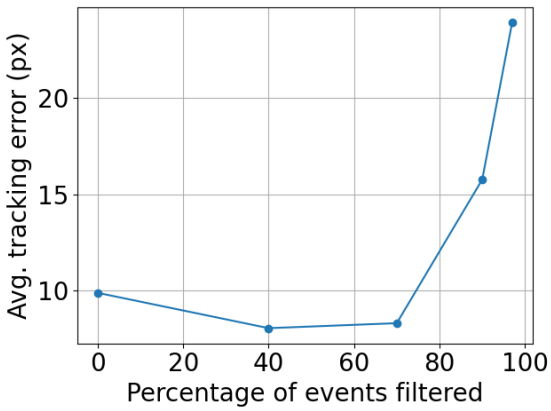

Fig. 2: Average tracking error, as given by distance to the ground-truth trajectory in pixels.

References

[1] T. Stoffregen, G. Gallego, T. Drummond, L. Kleeman, D. Scaramuzza, Event-Based Motion Segmentation by motion compensation, *2019 IEEE/CVF International Conference on Computer Vision (ICCV)*, 7243-7252 (2019); doi: 10.1109/ICCV.2019.00734.

[2] C. P. Rizzo, C. D. Schuman, J. S. Plank, Speed-based Filtration and DBSCAN of Event-based Camera Data with Neuromorphic Computing, *arXiv* (2024); doi: 10.48550/arXiv.2401.15212.

[3] S. Snyder, H. Thompson, M. A.-A. Kaiser, G. Schwartz, A. Jaiswal, M. Parsa, Object Motion Sensitivity: A Bio-inspired Solution to the Ego-motion Problem for Event-based Cameras, *arXiv* (2023); doi: 10.48550/arXiv.2303.14114.

[4] P. Bäcker, N. Terzer, G. Maier, U. D. Hanebeck, T. Längle, J. Beyerer, Fusion between Event-Based and Line-Scan Camera for Sensor Based Sorting, *10th Sensor-Based Sorting & Control 2024*, 89 (2024).

[5] A. Manakov, H. Herrman, B. Jähne, Performance comparison of area-scan and event-based camera, *Forum Bildverarbeitung 2024* (2024); doi: 10.5445/KSP/1000174496.

[6] V. Sundar, M. Dutson, A. Ardelean, C. Bruschini, E. Charbon, M. Gupta, Generalized Event Cameras, *arXiv* (2024); doi: 10.48550/arXiv.2407.02683.

DOI 10.5162/SMSI2025/B6.4

Ev2Gray: Generating Intensity Images from Event Streams

Johannes Baßler[1] *and Michael Heizmann*[1]
[1] Karlsruhe Institute of Technology, Karlsruhe, Germany
johannes.bassler@kit.edu

Summary: This paper presents a novel method for extracting absolute intensity information from event-based vision sensors, addressing their limitation in capturing static scene regions. Our approach utilizes a controlled occlusion mechanism that triggers events across both dynamic and static areas. By analyzing event patterns during occlusion and revelation phases, we reconstruct intensity values for each pixel.

Keywords: Event-based Vision, Intensity Reconstruction, Neuromorphic Sensing, Occlusion Mechanism, High Dynamic Range Imaging

Introduction

Event-Based Vision (EBV) sensors employ a fundamentally different output type compared to frame-based camera sensors. While frame-based camera sensors generate absolute intensity information for all image pixels at fixed time intervals, EBV sensors produce asynchronous and sparse events that encode relative brightness changes in the spatio-temporal domain. Each event e is represented by a tuple of four values: (x, y, t, p), where (x, y) denotes the pixel coordinates, t the timestamp, and p the polarity of the event, which defines the sign of the brightness change. This unique approach allows EBV sensors to offer significant advantages such as high temporal resolution, low latency, and high dynamic range. However, a critical limitation of event streams is their inherent difficulty in semantic interpretation of the scene, as they lack information about non-moving regions such as static backgrounds and do not provide comprehensive structural information. This absence of complete spatial context poses significant challenges for traditional computer vision algorithms and hinders direct semantic understanding, necessitating novel approaches to bridge the gap between event-based data and meaningful scene interpretation. Many state-of-the-art event-based vision methods still depend on structural information from frame-based cameras [1] – a requirement our approach aims to address. To address these limitations, we propose a novel method that, firstly, triggers events in all parts of the image, including static regions, in a controlled manner, and secondly, extracts absolute intensity images from the resulting event stream data without the need for an additional sensor. This approach aims to combine the advantages of event-based sensing with the comprehensive spatial information typically associated with frame-based cameras, potentially enabling more robust semantic interpretation of event-based data.

Related Work

While numerous methods, such as `E2VID` [2] and `ET-Net` [3], perform intensity reconstruction for videos using deep learning algorithms, to the best of our knowledge, there is only one other method capable of translating static scenes into intensity images using an event-based camera. The `EvTemMap` method initially darkens the scene completely using the aperture and then maps the timing of the first positive event for each pixel to absolute intensity values during the continuous opening of the aperture. As will be demonstrated, our method differs significantly in both the generation of occlusion and the computation approach. Unlike `EvTemMap` [4], our approach requires only partial occlusion and evaluates multiple events per pixel rather than just the first, which should positively affect noise performance.

Method

Event Generation Process We employ a moving opaque strip that traverses the entire image plane, completely occluding light from the scene in a spatially continuous and sparse manner. This strip induces controlled intensity changes across all pixels, regardless of whether they correspond to static or dynamic regions of the scene. As the opaque strip moves across the field of view, it creates two distinct transitions for each pixel:

1. **Occlusion Transition:** When the strip enters a pixel's view.
2. **Revelation Transition:** When the strip exits a pixel's view.

The number of events generated during these transitions is roughly proportional to the magnitude of the intensity change. The key insight of

our method is that the intensity level during full occlusion is uniform across all pixels. This provides a common reference point from which we can derive absolute intensity information.

Temporal Window Identification The first step in our procedure is to identify the relevant temporal windows for each pixel, specifically the occlusion and revelation phases. The method for determining these windows should be optimized based on the motion direction of the opaque strip. For instance, given a strictly horizontal motion of a vertical strip, we can select these time windows uniformly for all vertical pixel rows, resulting in a more robust and efficient determination of these regions. We define the temporal windows as:

$$T_{\text{occlusion}}(x,y) = [t^{\text{occ}}_{\text{start}}(x,y), t^{\text{occ}}_{\text{end}}(x,y)], \quad (1)$$

$$T_{\text{revelation}}(x,y) = [t^{\text{rev}}_{\text{start}}(x,y), t^{\text{rev}}_{\text{end}}(x,y)], \quad (2)$$

where x and y represent the pixel coordinates.

Intensity Value Assignment Once the temporal windows are established, we count the number of events generated during the occlusion and revelation phases with respect to the polarity of the events. We define the following quantities:

$$N_{\text{occ}}(x,y) = \sum_{t=t^{\text{occ}}_{\text{start}}(x,y)}^{t^{\text{occ}}_{\text{end}}(x,y)} \mathbb{I}\{e_{(x,y,t,-1)}\} - \mathbb{I}\{e_{(x,y,t,1)}\} \quad (3)$$

$$N_{\text{rev}}(x,y) = \sum_{t=t^{\text{rev}}_{\text{start}}(x,y)}^{t^{\text{rev}}_{\text{end}}(x,y)} \mathbb{I}\{e_{(x,y,t,-1)}\} - \mathbb{I}\{e_{(x,y,t,1)}\} \quad (4)$$

After calculating the sums based on the polarity and number of events in the respective phases, we compute the difference to assign a non-normalized intensity value to each pixel. This process can be formalized as:

$$I_{x,y} = N_{\text{occ}}(x,y) - N_{\text{rev}}(x,y), \quad (5)$$

where $I_{x,y} \in \mathbb{Z}$ represents the non-normalized intensity value for pixel (x,y). This integer value encodes the relative brightness of each pixel, with lower values indicating darker regions and higher values indicating brighter regions in the original scene. The final step involves normalizing the intensity values to obtain a standard 8-bit grayscale image. We employ min-max scaling to map the intensity values to the range $[0, 255]$:

$$I_{normalized}(x,y) = \left\lfloor \frac{I_{x,y} - I_{min}}{I_{max} - I_{min}} \cdot 255 \right\rfloor \quad (6)$$

This normalization produces a grayscale image compatible with standard image processing algorithms and display systems.

Results

We present a proof of concept for our proposed method using two examples: an ISO 12233 chart and a picture of the Karlsruhe Castle. These examples demonstrate our method's capability to reconstruct absolute intensity images from event-based data in both structured test patterns and complex real-world scenes. The experiments were conducted using a Prophesee EVK4 event camera, with a vertical black stripe moving horizontally across the scene to generate the controlled occlusion. These visual results validate the successful generation of intensity information from event streams, including static regions, while detailed quantitative evaluation is reserved for future work.

(a) Intensity reconstruction of the Karlsruhe Castle.

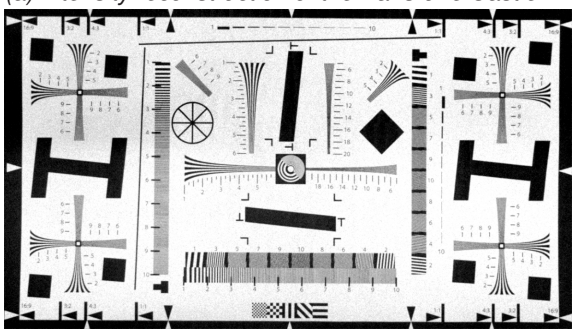

(b) Intensity reconstruction of an ISO 12233 test chart.

Fig. 1: Examples of intensity reconstruction using the proposed method.

References

[1] D. Cazzato and F. Bono, "An application-driven survey on event-based neuromorphic computer vision," Information, vol. 15, no. 8, 2024.

[2] H. Rebecq, R. Ranftl, V. Koltun, and D. Scaramuzza, "Events-to-video: Bringing modern computer vision to event cameras," IEEE Conf. Comput. Vis. Pattern Recog. (CVPR), 2019.

[3] W. Weng, Y. Zhang, and Z. Xiong, "Event-based video reconstruction using transformer," in Proceedings of the IEEE/CVF International Conference on Computer Vision (ICCV), 2021.

[4] Y. Bao, L. Sun, Y. Ma, and K. Wang, "Temporal-mapping photography for event cameras," 2024.

DOI 10.5162/SMSI2025/B7.1

Enhanced Signal Detection for Chlorophyll a Fluorescence Signal

Samaneh Baghbani , Ali Sarlak and Stefan J. Rupitsch
Department of Microsystems Engineering – IMTEK, University of Freiburg, Germany
Corresponding Author's e-mail address: samaneh.baghbani@imtek.uni-freiburg.de

Summary: Monitoring the quantum yield efficiency of Photosystem II evaluates plant health and stress by estimating electron transport rate in the photosystem. This measurement is typically performed using Pulse Amplitude Modulation (PAM) in combination with saturation pulses. The derived fluorescence signal is weak, often buried in noise, and has a low duty cycle. This contribution proposes a hybrid signal processing approach that combines aspects of boxcar averaging and lock-in amplification to extract low duty cycle signals from below the noise floor. We were able to detect the signals with a duty cycle of 0.01 %, with signal to noise ratio (SNR) up to –30 dB.

Keywords: Chlorophyll a fluorescence, Quantum yield's efficiency, PAM fluorometer, Lock-in amplifier, boxcar averaging

Introduction

The quantum yield efficiency of Photosystem II not only reflects how effectively plants utilize absorbed light but also indicates the electron transport rate within the photosynthetic system in vivo [1]. This efficiency is described by

$$\Phi_{\mathrm{PSII}} = \frac{F'_m - F}{F'_m}, \tag{1}$$

where F'_m is the maximum fluorescence and F denotes the variable fluorescence in light-exposed leaves. To separate the ambient light from the plant's fluorescence light, the fluorescence excitation light should be modulated [2]. Variable fluorescence is obtained by applying weak and short flashes of light (in the µs-range) called measuring light, to the leaf surface, ensuring no impact on the physiological state of the photosystem. Maximum fluorescence, on the other hand, is achieved by applying the same measuring light along with strong pulses that saturate all reaction centers in the leaf [3]. The modulated fluorescence signal is prone to noise interference, and an appropriate signal processing method could help detect the fluorescence changes. A Fast Fourier Transform (FFT) combined with a Welch window is used to recover the chlorophyll fluorescence signal [4]. The FFT method is computationally expensive and it is unable to detect the signals buried in noise.
Lock-in amplifiers are used for a wide range of applications where weak signals are obscured by noise and the frequency of the desired signal is known [5, 6, 7]. Low duty cycle signals spread across multiple harmonics in the frequency domain. Since lock-in amplifiers focus on the fundamental frequency, they fail to capture the information contained in the higher-order harmonics. In addition, the shorter the active signal duration, the more noise tends to dominate the overall measurement. In low duty cycle signals, boxcar averaging allows for recording during the short duty cycle, when the signal is present, and excluding the remainder where no relevant information exists to improve the signal to noise ratio [8].
In this contribution, we use boxcar gating to isolate the signal during the excitation pulse and an equivalent duration afterward, effectively increasing the duty cycle to 50 %. This adjustment allows us to apply a lock-in amplifier to the gated signal, taking advantage of the lock-in amplifier's strong capability to detect signals below the noise floor, even when the original duty cycle is low.

Experimental Setup

Fig. 1 shows the block diagram of the experimental setup to capture the chlorophyll a fluorescence signal from the leaf surface. It consists of (i) a sensor head, (ii) fluorescence excitation and detection circuitry, and (iii) a microcontroller.

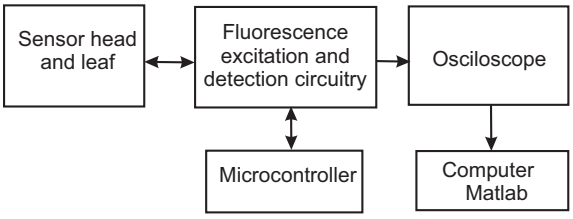

Fig. 1: Block diagram of the experimental setup

The sensor head includes a blue LED to excite the fluorescence and a PMMA plastic fiber to transfer the fluorescence light to the detector circuit. The LED is positioned at a 45 ° angle to the

leaf surface at a distance of 3 mm, while the plastic fiber is aligned to sample fluorescence from the same excitation point.

The LED excitation circuitry drives the LED to produce both measuring light and saturation pulses. The measuring light consists of 10 µs flashes at a frequency of 10 Hz with a current amplitude of 25 mA for assessing variable fluorescence. To measure the maximum fluorescence, 10 µs flashes of light at the frequency of 100 Hz are followed by saturation pulses with a current amplitude of 80 mA. The fluorescence detection circuitry includes a PIN photodiode covered by a longpass optical filter, which suppresses LED reflections and ambient light below its cutoff wavelength, 650 nm. A transimpedance amplifier then converts the detected fluorescence light into a voltage signal and amplifies it for further processing. The microcontroller controls the precise timing of the LED excitation signal and performs digital signal processing. For this study, we acquired the fluorescence signal using an oscilloscope, and the signal processing approaches were implemented in MATLAB software.

Results

The fluorescence signal in our measurements has a 0.01 % duty cycle. Simulation results show that combining the boxcar technique with a lock-in amplifier can effectively detect weak and low duty cycle chlorophyll fluorescence signals with an SNR as low as –32 dB, while boxcar averaging alone cannot detect signal even when the SNR is –16 dB (Fig. 2).

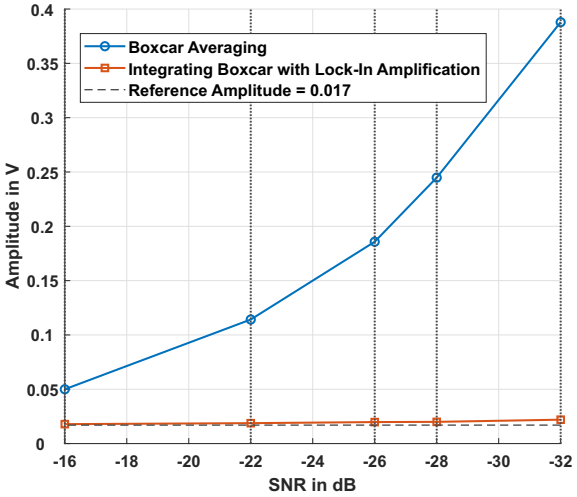

Fig. 2: Amplitude deviation across SNR levels for boxcar averaging and integrating boxcar with lock-in amplifier.

Conclusion

Lock-in amplifiers can detect signal amplitudes even when they are smaller than the noise floor. However, their efficacy will decrease when the duty cycle drops below 10 % due to energy distribution across harmonics. On the other hand, Boxcar averaging offers a high SNR value for very low duty cycle signals. While it effectively reduces noise, it mainly relies on averaging, which can struggle to extract the signal when it is deeply buried in noise. The proposed approach, which integrates boxcar and lock-in amplification, can detect the low duty cycle signals that are deeply buried in noise.

References

[1] B. Genty, J.-M. Briantais, and N. R. Baker, "The relationship between the quantum yield of photosynthetic electron transport and quenching of chlorophyll fluorescence," *Biochimica et Biophysica Acta (BBA) - General Subjects*, vol. 990, no. 1, pp. 87–92, 1989.

[2] W. B. U. Schreiber, U. Schliwa, "Continuous recording of photochemical and non-photochemical chlorophyll fluorescence quenching with a new type of modulation fluorometer," *Photosynth Research*, vol. 10, p. 51–62, 1986.

[3] U. Schreiber, "Pulse-amplitude-modulation (pam) fluorometry and saturation pulse method: An overview," *Advances in Photosynthesis and Respiration*, vol. 19, 01 2004.

[4] J. Reimer, S. Stöcklin, L. M. Comella, P. Woias, C. Werner, L. Reindl, and S. J. Rupitsch, "An autonomous and wireless pulse-amplitude modulated chlorophyll fluorometer," *tm - Technisches Messen*, vol. 88, no. 12, pp. 773–784, 2021.

[5] M. L. Meade, "Advances in lock-in amplifiers," *Journal of Physics E: Scientific Instruments*, vol. 15, p. 395, apr 1982.

[6] A. J. Harvie, S. K. Yadav, and J. C. de Mello, "A sensitive and compact optical detector based on digital lock-in amplification," *HardwareX*, vol. 10, p. e00228, 2021.

[7] C.-W. Kim, "A microcontroller-based lock-in amplifier for capacitive sensors," *Journal of Sensor Science and Technology*, vol. 23, 01 2014.

[8] K. Yamasue and Y. Cho, "Boxcar averaging scanning nonlinear dielectric microscopy," *Nanomaterials*, vol. 12, no. 5, 2022.

DOI 10.5162/SMSI2025/B7.2

A second generation dispatchable fibre-optic biosensor reader for monitoring sediment toxicity (Sundanse)

Abraham A. Paul [1], Gal Carmeli[1], Robert S. Marks[1,2]
[1] Avram and Stella Goldstein-Goren Department of Biotechnology Engineering, Ben Gurion University of the Negev, Be'er-Sheva 84105, Israel
[2] The Ilse Katz Center for Nanoscale Science and Technology, Ben-Gurion University of the Negev, Be'er Sheva 84105, Israel
rsmarks@bgu.ac.il

Summary:

This study presents a second-generation dispatchable fiber-optic biosensor reader optimized for in-field detection of sediment and water toxicity. The system utilizes bioluminescent whole-cell bioreporters immobilized in a calcium alginate matrix on fiber-optic tips. The newly enhanced biosensor is designed for improved portability, robustness, and ease of deployment, making it a versatile tool for real-time, on-site environmental monitoring.

Keywords: bioreporter, bioluminescent bacteria, optical fiber biosensor, water toxicity, sediment toxicity, in-situ monitoring, genotoxicity

Background, Motivation and Objective

Detecting toxicants in aquatic environments is critical for assessing the impact of pollutants on ecosystems. Conventional chemical analyses methods are often time-consuming and resource-intensive and may not fully capture bio-availability or cumulative pollutant effects. Whole-cell biosensors offer a rapid, biologically relevant method for assessing environmental toxicity.

Building on the previous generation of our fiber-optic biosensor, this study introduces a second-generation system that improves usability and field readiness while maintaining the core functionality of the original design. The upgraded incorporates additional features to enhance port-ability and ease of deployment in remote environments [1-3].

Description of the New System

Our previous system is a highly sensitive, photon-counting biosensor designed for detecting genotoxicants using genetically engineered bioluminescent bacteria. At its core is a photomultiplier tube (PMT) that detects low-intensity blue light emitted by the bacteria in response to toxicans. The bacteria are immobilized on the tip of a multimode optical fiber using a calcium alginate matrix, creating a disposable sensor probe. This probe is placed in a light-proof enclosure, with the fiber transmitting bioluminescence directly to the PMT without significant loss. The system provides a rapid, dose-dependent response, making it an efficient tool for environmental toxicity assessment [1]. The second-generation system features an upgraded photomultiplier tube (PMT) that is housed in a redesigned case with wheels for easy transport, with an optimized internal layout to accommodate the new components and improve user accessibility. Additionally, integrated satellite internet connectivity allows for real-time data transmission from remote locations, enabling immediate analysis. To ensure continuous operation in the field, the system is equipped with an internal power station and a solar panel array, providing a sustainable, self-sufficient power source for extended deployments. These advancements collectively improve the sensor's portability, functionality, and reliability, making it a robust solution for monitoring sediment toxicity in challenging environments.

Table 1 - Comparison of Previous and New Designs of the Bioluminescent Fiber-Optic Biosensor

Features	Previous Design	New Design

Portability & Transport	Fixed case, less portable	Redesigned case with wheels for easy transport
Data Connectivity	-	Integrated satellite internet
Power Supply	Small power supply unit for PMT	Internal power station with solar panel
Field Suitability	Limited to short-term deployments	Ideal for extended field deployments in remote areas
Commercialization Potential	Less practical	Enhanced for scalability, long-term storage, and field readiness

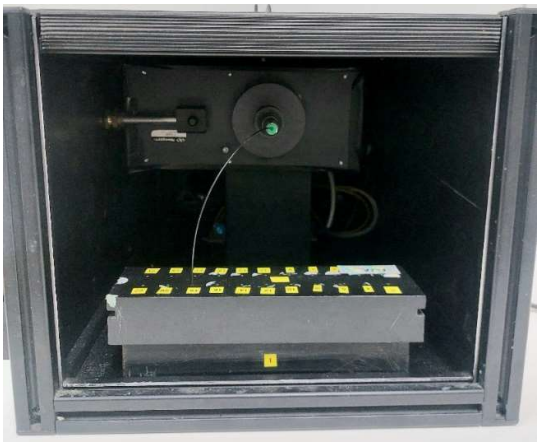

Figure 1 – Our previous design fot the optical-fiber, whole-cell biosensors.

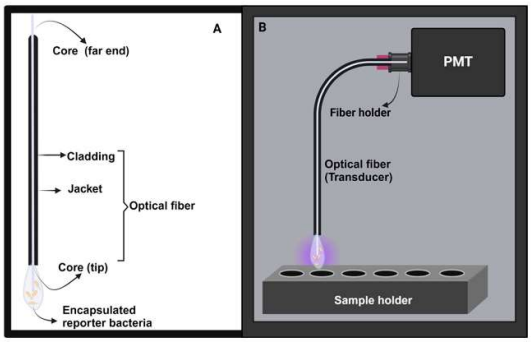

*Figure 2 - The basic components of the whole-cell, fiber-optic biosensors. (**A**) Optical fiber with a bioreporter immobilized unto the core. (**B**) Light–tight portable black box encasing all the biosensor components.*

Results

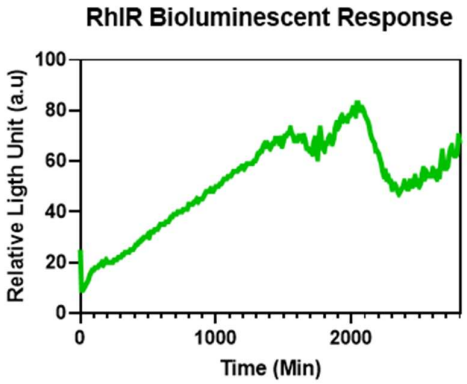

Figure 3 - Fiber optic detection of Pseudomonas aeruginosa via its secreted quorum sensing molecule.

Data Availability Statement

The original results presented in this study can be found in our records in footprints (link - https://footprints-b291f.web.app/), and authorization for its access may be granted by the corresponding author (paulab@post.bgu.ac.il)

Acknowledgement

This research is part of the project `**Innovative sediment management framework for a SUstainNable DANube black Sea system (SUNDANSE)**', co-funded by the European Union.

Disclaimer

Views and opinions expressed are however those of the author(s) only and do not necessarily reflect those of the European Union or the European Climate, Infrastructure and Environment Executive Agency. Neither the European Union nor the granting authority can be held responsible for them.

References

1. Polyak, B., et al., *Bioluminescent whole cell optical fiber sensor to genotoxicants: system optimization.* Sensors and Actuators B: Chemical, 2001. **74**(1): p. 18-26.
2. Eltzov, E. and R.S. Marks, *Parameters to consider in the construction of fiber-optic biosensors as alternative bioanalytical tools.* IEEE Instrumentation & Measurement Magazine, 2009. **12**(5): p. 10-16.
3. Ivask, A., et al., *Fibre-optic bacterial biosensors and their application for the analysis of bioavailable Hg and As in soils and sediments from Aznalcollar mining area in Spain.* Biosensors and

DOI 10.5162/SMSI2025/B7.3

Field Enabled Bioluminescent Fiber-Optic Whole-Cell Bioreporter Biosensors for Toxicity Monitoring of Water and Sediments (Sundanse)

Abraham A. Paul [1], Gal Carmeli[1], Ofir Menashe[3], Robert S. Marks[1,2]
[1] Avram and Stella Goldstein-Goren Department of Biotechnology Engineering, Ben Gurion University of the Negev, Be'er-Sheva 84105, Israel
[2] The Ilse Katz Center for Nanoscale Science and Technology, Ben-Gurion University of the Negev, Be'er Sheva 84105, Israel
[3] Water Industry Engineering Department, Achi Racov Engineering School, Kinneret College on the Sea of Galilee, D.N. Emek Ha'Yarden 15132, Israel
rsmarks@bgu.ac.il

Summary:

This study explores two configurations of bioluminescent fiber-optic whole-cell bioreporter biosensors designed for field-enabled monitoring of water and sediment toxicity. The first configuration uses alginate immobilization of genetically engineered reporter bacteria directly on a fiber optic tip, while the second utilizes encapsulated bacteria within bio-capsules with the fiber optic inserted within the capsule. Preliminary assessments indicate that both configurations demonstrate significant potential for environmental monitoring, with unique strengths in terms of sensitivity and stability, while the bio-capsule configuration offers improved storage via lyophilization – an important feature for commercialization.

Keywords: bioreporter, bioluminescent bacteria, biosensor, water toxicity, sediment toxicity, alginate immobilization, bio-capsule

Background, Motivation and Objective

Detecting toxicants in aquatic environments is crucial for monitoring and preserving water quality and ecosystem health. Traditional laboratory tests often rely on chemical analyses, which are time-consuming, resource-intensive, and fail to account for bioavailability, and cumulative and synergistic effects of pollutants on living organisms. Bioluminescent whole-cell microbial biosensors offer a rapid, real-time alternative for detecting bioavailable contaminants in water and sediments [1-7]. Building on this foundation, we aim to compare two configurations of biosensors to optimize performance and ease of use for field applications and commercialization.

Description of the Systems

Alginate Immobilization on Fiber Optic:

Genetically engineered *E. coli* cells were immobilized on a fiber optic tip using a calcium alginate matrix. This method enhances detection sensitivity by placing the bacterial cells in direct contact with the fiber optic surface, maximizing the bioluminescent signal in response to genotoxicants [1, 7].

Encapsulated Bacteria with SBP Bio-Capsules:

Utilizing encapsulation technology provided by BioCastle, this configuration involves inserting the fiber optic into a capsule containing lyophilized bioluminescent bacteria, enabling long-term storage. The freeze-dried bacteria can be rehydrated when needed, which significantly enhances the sensor's practicality for field deployment [8, 9]. In contrast, the alginate configuration cannot be stored in a freeze-dried state, limiting its shelf life.

Table 1 - Comparison of Alginate Immobilization vs. Bio-Capsule Encapsulation for Fiber-Optic Whole-Cell Bioluminescent Biosensors.

Features	Alginate Immobilization	Bio-Capsule Encapsulation
Bacterial Solid Phase Immobilization	✓	✓

Storage Capability	Limited (requires wet conditions)	Excellent (can be freeze-dried and stored)
Production Can be Automated	✓	✓
Field Suitability	Limited to short-term deployments	Ideal for long-term and field deployments

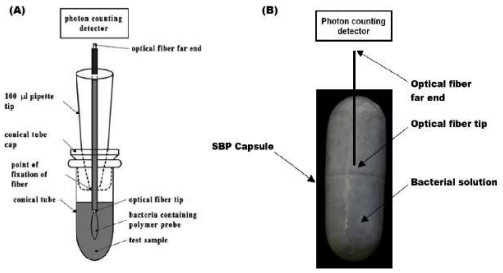

Figure 1 – (A) Instrument set-up demonstrating the components used in the experiments for the bioluminescent measurements using the optical fiber tip optrode whole-cell biosensor [1, 7]; (B) SBP BioCapsule experiment set up [9].

Results

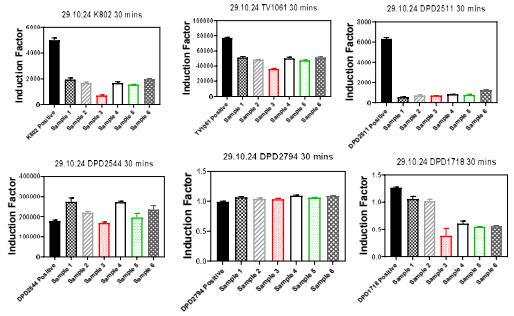

Figure 2 - Bioluminescent responses of six bioreporter bacterial strains exposed to contaminated sediment samples collected from six different sites within the Ramat Hovav industrial zone, southern Israel.

Conflict of Interest

Dr. Ofir Menashe is the founder and Chief Technology Officer (CTO) of BioCastle, the company that provided the bio-capsules used in the study.

Data Availability Statement

The original results presented in this study can be found in our records in footprints (link - https://footprints-b291f.web.app/), and authorization for its access may be granted by the corresponding author (paulab@post.bgu.ac.il)

Acknowledgement

This research is part of the project `**Innovative sediment management framework for a SUstainNable DANube black Sea system (SUNDANSE)**', co-funded by the European Union.

Disclaimer

Views and opinions expressed are however those of the author(s) only and do not necessarily reflect those of the European Union or the European Climate, Infrastructure and Environment Executive Agency. Neither the European Union nor the granting authority can be held responsible for them.

References

1. Polyak, B., et al., *Bioluminescent whole cell optical fiber sensor to genotoxicants: system optimization.* Sensors and Actuators B: Chemical, 2001. **74**(1): p. 18-26.
2. Eltzov, E., et al., *On-line biosensor for the detection of putative toxicity in water contaminants.* Talanta, 2015. **132**: p. 583-590.
3. Eltzov, E. and R.S. Marks, *Parameters to consider in the construction of fiber-optic biosensors as alternative bioanalytical tools.* IEEE Instrumentation & Measurement Magazine, 2009. **12**(5): p. 10-16.
4. Eltzov, E. and R.S. Marks, *Whole-cell aquatic biosensors.* Analytical and Bioanalytical Chemistry, 2011. **400**(4): p. 895-913.
5. Ivask, A., et al., *Fibre-optic bacterial biosensors and their application for the analysis of bioavailable Hg and As in soils and sediments from Aznalcollar mining area in Spain.* Biosensors and Bioelectronics, 2007. **22**(7): p. 1396-1402.
6. Eltzov, E., et al., *Flow-through real time bacterial biosensor for toxic compounds in water.* Sensors and Actuators B: Chemical, 2009. **142**(1): p. 11-18.
7. Polyak, B., et al., *Optical fiber bioluminescent whole-cell microbial biosensors to genotoxicants.* Water Science and Technology, 2000. **42**(1-2): p. 305-311.
8. Naramittanakul, A., et al., *Development of a continuous-flow system with immobilized biocatalysts towards sustainable bioprocessing.* Reaction Chemistry & Engineering, 2021. **6**(10): p. 1771-1790.
9. Kurzbaum, E., et al., *Encapsulated Pseudomonas putida for phenol biodegradation: Use of a structural*

DOI 10.5162/SMSI2025/C1.1

Comparison of Polyimide to Silicon Nitride Membranes for Robust Thermal Flow Sensors

Tobias Trautmann[1, 2], *Andreas Schander*[1, 2], *Michael Vellekoop*[1, 2, 3]
[1] *Institute for Microsensors, -actuators and -systems, University of Bremen, Bremen, Germany,*
[2] *Microsystems Center Bremen (MCB), Bremen, Germany,*
[3] *MAPEX Center for Materials and Processes, University of Bremen, Bremen, Germany*
ttrautmann@imsas.uni-bremen.de

Summary:
This work compares thin and robust polyimide membranes for thermal flow sensors to flow sensors based on silicon nitride membranes. Due to the low thermal conductivity of polyimide, the sensitivity measurements are showing only a small reduction in sensitivity of less than 20% when a polyimide membrane with a ten times higher thickness compared to a silicon nitride membrane is used. At the same time the polyimide membrane can withstand a 50% higher pressure difference which leads to a significant improvement of the robustness.

Keywords: thermal flow sensors, polyimide, silicon nitride, membranes, microfabrication

Introduction

Microfabricated thermal flow sensors are used in a wide range of applications like aerospace [1]. One commonly used method to measure the flow is the calorimetric principle. Here, the heat distribution generated by a heating wire is measured by thermistors, thermopiles or diodes [1]-[3]. The domains including the sensitive elements are often thermally insulated to reach a highly sensitive system with less heat losses [2], [3]. Thermal insulation can be achieved using a silicon nitride membrane by removal of the bulk material [3]. There is also research ongoing in using polyimide as a substrate material for thermal insulated calorimetric flow sensors [4]. Polyimide can be used due to its low thermal conductivity of 0.28 W/mK and its excellent robustness compared to silicon nitride membranes [5].

Although many approaches to polyimide-based flow sensors have already been investigated, a direct comparison between polyimide and silicon nitride membrane-based flow sensors has not been published until now to the authors' knowledge. Therefore, we compare the performance of flow sensors with a thinner polyimide membrane compared to the state of the art to one with a silicon nitride membrane.

Materials and Methods

To see the influence of the use of polyimide membranes on thermal flow sensors compared to conventional silicon nitride membranes the same pattern is used for the sensitive elements in both variations. The design consists of a heater in the center of the chip and symmetric thermistors on the up- and downstream side with a distance of 1 mm to the heater. Both, heater and thermistors, are placed on the membrane with a diameter of 4 mm. For electrical connection, bondpads for wire bonding are designed on the silicon bulk material.

The flow sensors are fabricated on silicon with a 1 µm thick layer of thermal silicon oxide for electrical insulation. Polyimide (U-Varnish-S, UBE Europe GmbH, Germany) is spin-coated on the wafer with a thickness of 4.7 µm, while silicon nitride is deposited with LPCVD method with a thickness of 500 nm. The heater and the thermistors are made of platinum with a thickness of 200 nm. To realize a membrane, the bulk material under the sensitive elements is removed by DRIE using SF6 and C4F8.

Experiments

Flow measurements are done in a wind tunnel with flow velocities up to 2.6 m/s. The heater is powered to 150 mW. Both sensors show no drift over 100 test cycles under thermal load.

To maintain the usability in fast reacting applications, the time response of both types of sensors is measured. For that, a flow is applied above the sensor and the change in resistance is plotted. In Fig. 1 such a plot is shown for a sensor with a silicon nitride membrane. The time response is calculated as the time difference between 10% and 90% of the mean value with/without a present flow. The flow sensors with silicon nitride membranes are showing a faster response time

of t_{SiN} = 16 ms compared to the t_{PI} = 28 ms of the ones with polyimide membranes.

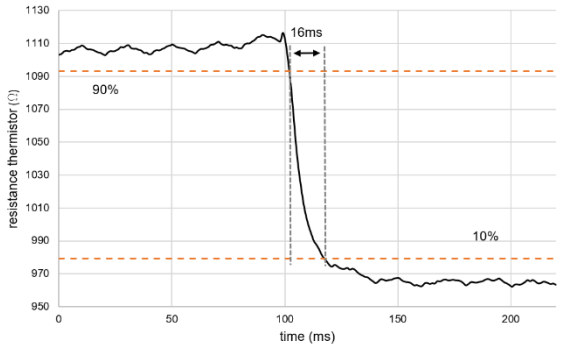

Fig. 1. Time response for the flow sensors with silicon nitride membranes.

Due to the different heat transfer in the membranes, the total change in resistance is limited by the materials used. Therefore, the difference in resistance between the thermistors up- and downstream is shown in Fig. 2 for different flow velocities. The output signal is up to 20% higher for the sensors with silicon nitride membranes compared to those with polyimide membranes.

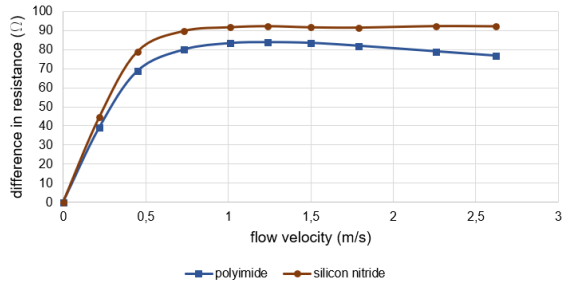

Fig. 2. Flow measurements with polyimide and silicon nitride membrane-based flow sensors.

A pressure difference is applied between both sides of the membrane to compare its robustness. In Tab. 1 the maximum pressure differences until a failure occurs are given. The polyimide membrane can withstand much higher pressure differences due to its high elasticity. Nevertheless, the heater and thermistors break at the same pressure since the strain is also increased due to the membrane deflection.

Tab. 1: The maximum pressure difference until the heater and thermistors or the membrane is damaged.

Membrane material	Heater and thermistors	Membrane
Silicon nitride	300 kPa	300 kPa
Polyimide	300 kPa	450 kPa

Conclusion and Outlook

This paper shows, that the time response is less than a factor 2 higher using a polyimide membrane, even though the thickness is approx. 10 times higher. The reason for that is the different heat capacity. Due to the lower thermal conductivity of polyimide, the difference in sensitivity is much lower. The flow sensors based on silicon nitride membranes are only up to 20% better. The major advantage of using flow sensors with polyimide membranes is the opportunity of using higher thicknesses than silicon nitride membranes without a significant reduction of sensitivity and time response. This leads to a more robust membrane, which can be used in e.g. aircraft applications for a stall detection sensor. Unfortunately, the sensing elements on the membrane cannot withstand the same pressure as the membrane itself. This could be solved by supporting the membrane structure with highly thermal insulating materials like aerogels. Also, the design needs to be optimized to increase the sensors range.

Acknowledgement and Disclaimer

This work is supported by the project Ultra Performance Wing (UP Wing, project number: 101101974) and by the Clean Aviation Joint Undertaking and its members. Co-Funded by the European Union. Views and opinions expressed are however those of the author(s) only and do not necessarily reflect those of the European Union or Clean Aviation Joint Undertaking. Neither the European Union nor the granting authority can be held responsible for them.

References

[1] L. Ribeiro, O. Saotome, R. d'Amore, R. de Oliveira Hansen, High-speed and high-temperature calorimetric solid-state thermal mass flow sensor for aerospace application: A sensitivity analysis, *Sensors*, vol. 22, no. 9: 3484 (2022); doi: 10.3390/s22093484

[2] B. W. van Oudheusden, A. W. van Herwaarden, High-sensitivity 2-D flow sensor with an etched thermal isolation structure, *Sensors and Actuators A*, vol. 22, pp. 425 – 430 (1990); doi: 10.1016/0924-4247(89)80007-X

[3] R. Buchner, M. Maiwald, C. Sosna, T. Schary, W. Benecke, W. Lang, Miniaturised thermal flow sensors for rough environments, *In Proceedings of the 19th IEEE International Conference on Micro Electro Mechanical Systems (MEMS 2006)*, pp. 582–585 (2006); doi: 10.1109/MEMSYS.2006.1627866

[4] T. Tsukada, R. Takigawa, Y. Hasegawa, M. S. Al Farisi, M. Shikada, Sensitivity enhancement of tube-integrated MEMS flow sensor using flexible copper on polyimide substrate, *Micromachines*, vol. 14, no. 1: 42 (2022); doi: 10.3390/mi14010042

[5] D. Briand, S. Colin, A. Gangadharaiah, E. Vela, P. Dubois, L. Thiery, N. F. de Rooij, Micro-hotplates on polyimide for sensors and actuators, *Sensors and Actuators A*, vol. 132, no. 1, pp. 317 – 324 (2006); doi: 10.1016/j.sna.2006.06.003

DOI 10.5162/SMSI2025/C1.2

Multichannel electrical conductivity sensor for gas-liquid flow imaging

Mathias Bliem[1], Stefan Puttinger[2], Marco Da Silva[1]
[1] Institute of Measurement Technology, Johannes Kepler University Linz, Austria
[2] Department of Particulate Flow Modelling, Johannes Kepler University Linz, Austria
marco.dasilva@jku,at

Summary:
Gas-liquid flows are ubiquitous in various industries, including oil and gas, chemical processing, and steel making. Accurate measurement of these flows is essential for optimizing process efficiency and ensuring safety. This work introduces a novel multichannel electrical conductivity sensor capable of directly imaging gas-liquid flows, eliminating the need for image reconstruction. The sensor offers a reliable, cost-effective, and robust solution for flow visualization. Validation against high-speed camera footage demonstrates excellent agreement.

Keywords: conductivity sensor, multichannel, flow imaging, two-phase flow

Introduction

Gas-liquid flow is found in many industries, such as oil and gas production, chemical reactors, or steel production. The flow itself often determines the efficiency and/or safety of processes, making online flow monitoring crucial for control purposes. In both cases, whether for in-line use or pilot plant studies, flow monitoring requires increasingly sophisticated flow sensors, with flow imaging offering the most detailed visualization of flow phenomena.

Process tomography has been widely used, but there is no universal technology that can measure the variety of situations [1]. Different tomography technologies have been used in the past. Optical tomography uses light to illuminate the flow field and capture images. While it provides high spatial resolution, it is limited to transparent or translucent fluids. Ultrasound tomography uses sound waves to probe the flow. It can penetrate opaque fluids and is relatively robust to interference. However, its spatial resolution is poor. X-ray tomography provides high-resolution images of the internal structure of opaque objects. However, X-ray sources can be expensive and require shielding, limiting their suitability for real-time monitoring of rapidly changing flow phenomena. Another promising technique for flow visualization is electrical tomography. By applying electrical currents to electrodes placed around the flow and measuring the resulting voltage differences, it can provide information about the electrical conductivity distribution within the flow. However, due to the inherent ill-posed nature of the inverse problem, image reconstruction can be quite complex.

In this paper, we present a multichannel conductivity sensor capable of generating images of gas-liquid flow, but without the need for image reconstruction. The idea is based on the work of [2], but the sensor is developed based on printed circuit technology (PCB), which is integrated into the sensor electronics, thus allowing a very simple integration into flow tubes via a flange system. In addition, the integration of the sensor into the sensor PCB allows for very good signal quality and therefore very fast measurements.

Multichannel electrical conductivity sensor (MECS)

The sensor consists of an excitation ring and a measurement ring, with the latter segmented into 16 electrodes of uniform size distributed evenly around the circumference of the pipe (Fig. 1). To determine the resistance between the excitation ring and an electrode on the measurement ring, an auto-balancing bridge, in conjunction with square wave excitation and an analog-to-digital converter is employed. For details on the electronic circuits see [3].

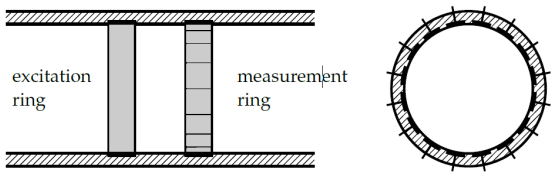

Fig. 1. Schematic illustration of the multichannel electrical conductivity sensor for flow visualization.

A technique known as side-plating, where the edges of the printed circuit board (PCB) are metallized, allows for the direct integration of electrodes into the PCBs. Figure 2 illustrates the installation of the sensor PCBs within a pipe using flanges. This installation mechanism considerably simplifies the production and assembly of the sensor by eliminating the need for manually attaching electrodes inside the pipe.

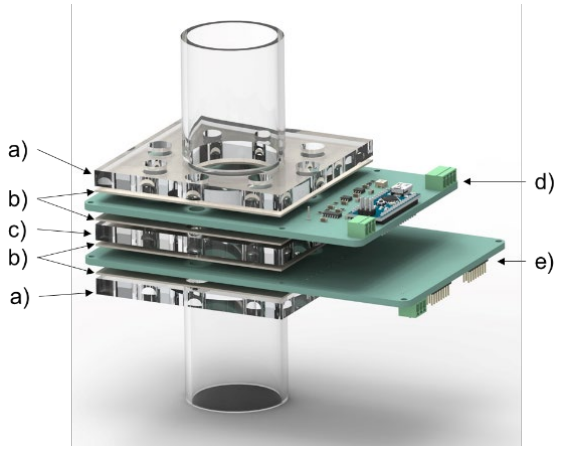

Fig. 2. Illustration of developed sensor attached to a pipe: a) Pipe with flange, b) Paper gasket, c) Spacer plate (8mm), d) Excitation PCB: generates symmetrical square wave signal, e) Measuring PCB: 16 measuring electrodes.

Results

The sensor's performance was rigorously tested through a series of experiments, including testing the measurement principle using a non-conductive object, comparing measurements in distilled and tap water, and examining its ability to detect bubbles and localize them using synchronized camera footage as a reference.

Figure 3 presents a side-by-side comparison of a camera image and a MECS surface plot, with the normalized electrode signals conventionally plotted below. To visualize the MECS measurements, the signals of the electrodes, which are positioned around the pipe's circumference, are flattened and displayed as surface plots. The horizontal red line in the surface plot indicates the sensor's position, corresponding to a specific moment in the camera recording. The color scheme ranges from blue (0, indicating water) to red (1, indicating air). Due to the lack of bubble velocity information, which requires two sensors and signal cross-correlation, the visualization time is set to an arbitrarily chosen value of 2.4 s.

The results showed a clear correlation between the sensor readings and the observed flow regimes, confirming the sensor's capability to distinguish between different flow patterns. Data processing techniques were applied to eliminate hardware irregularities such as excitation asymmetries and variations in the auto-balancing circuits. The resulting MECS signals are independent of the conductivity of the liquid phase, have the same baseline level, and are normalized such that a signal value of 0 corresponds to liquid and 1 to gas.

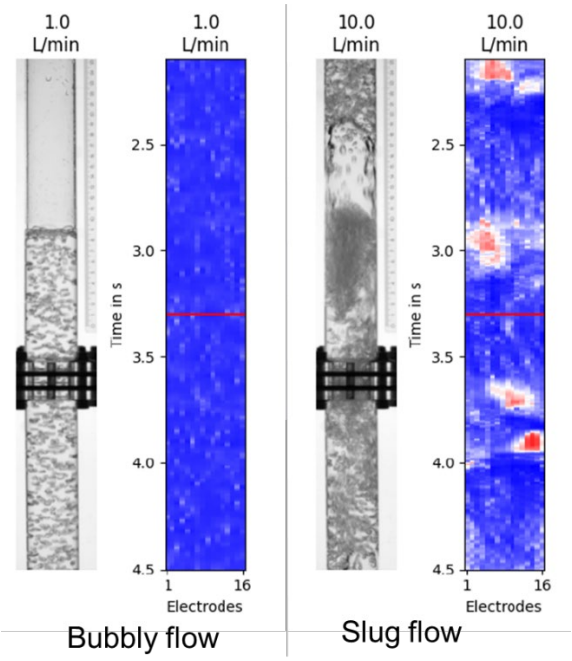

Fig. 3. Comparison of camera images and MECS measurements for two different flow rates and flow regimes.

Conclusions

This study presents a novel multichannel conductivity sensor that offers a reliable, cost-effective, and robust solution for flow visualization. The sensor's compact design and ease of integration into pipe systems make it suitable for a wide range of industrial applications. Future research will focus on automating flow regime identification using machine learning algorithms and validating computational fluid dynamics simulations with experimental data. Additionally, incorporating a second excitation plane will enable velocity measurements of flow structures, further enhancing the capabilities of this sensor.

References

[1] U. Hampel et al., A Review on Fast Tomographic Imaging Techniques and Their Potential Application in Industrial Process Control, *Sensors* 22, 2309 (2022) doi: 10.3390/s22062309.

[2] P. Seleghim Jr., E. Hervieu, Direct imaging of two-phase flows by electrical impedance measurements, *Measurement Science and Technology* 9, 1492–1500 (1998); doi: 10.1088/0957-0233/9/9/018.

[3] M. Bliem, Multichannel electrical conductivity sensor for the classification of flow regimes, *Master Thesis* at Johannes Kepler University Linz (2024) urn:nbn:at:at-ubl:1-75723

DOI 10.5162/SMSI2025/C1.3

Measurability of changes of the laminar-turbulent transition on wind turbines by means of thermographic flow visualization and a co-rotating measurement platform

Jakob Dieckmann[1], Nicholas Balaresque[2], Axel von Freyberg[1], Andreas Fischer[1]
[1] University of Bremen, BIMAQ, Linzer Str. 13, 28359 Bremen, Germany,
[2] Deutsche WindGuard Engineering GmbH, Überseering 7, 27580 Bremerhaven, Germany
j.dieckmann@bimaq.de

Summary:
Changes of the laminar-turbulent flow transition due to unsteady wind conditions influence the efficiency of wind turbines. In order to clarify the feasibility of monitoring these changes by means of thermographic flow visualization, a coupled thermal-flow simulation is performed indicating a feasible temporal resolution down to 50 ms, i.e. well below one rotor revolution. Further, a co-rotating measurement platform is presented that enables the continuous image acquisition of a rotor blade section at wind turbines.

Keywords: Thermography, co-rotating system, coupled thermal-flow simulation

Introduction

The laminar-turbulent flow transition position affects the efficiency of the wind turbine. Unsteady weather conditions as well as changing rotor blade positions during one revolution lead to varying laminar-turbulent transition positions. Hence, measuring these flow changes allows for future improvement and failure detection of the rotor blades.

Simon et al. [1] used infrared thermography (IRT) on a flat plate to determine the flow transition from laminar to turbulent and came to the conclusion that it is also suitable for measurements under unsteady flow conditions. Raffel and Merz [2] introduced differential infrared thermography (DIT) by subtracting one thermal image from another. This enables a visualization even before the surface has fully responded to the flow condition. DIT was shown by Gleichauf et al. [3] to be in principle capable of visualizing changes of the laminar-turbulent flow transition on wind turbines, with an image separation time of 50 s. Therefore, two open question are, if an increased temporal resolution in the order of a few seconds or even tenths of seconds is theoretically feasible, and how to realize a continuous image recording even during the blade rotation?

This work aims at both: approximating the theoretically achievable temporal resolution via simulation and create a measurement setup for visualizing changes close to that resolution.

Co-rotating measurement setup

The BIMAQ and the Deutsche WindGuard together are the first to develop a multisensor co-rotating platform to visualize the flow conditions on the rotor blades of wind turbines. The platform is shown in Fig. 1. It features an infrared camera for measuring the flow condition and a laser scanner as well as a visual light camera with the same field of view that allows to detect any deformations of the rotor blade. Additionally, it has four visual light cameras that picture the full rotor blade. The wind turbine's position and speed are detected with a small setter camera to control the co-rotation of the carrier platform including a kinematic compensation for the perspective distortion. The co-rotating measurement setup continuously visualizes the boundary airflow with a sampling period of the infrared camera which is 4 ms.

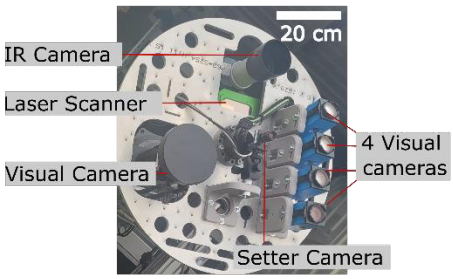

Fig. 1: Co-rotating measurement platform

Temporal resolution limit

For approximating the time t_{CNR} until a change of the boundary airflow is visible in the thermographic image, a thermal Computational Fluid Dynamics-simulation of a rotor blade segment is carried out. The rotor blade is modelled as a semi-infinite flat plate consisting of a 3 mm polyurethane (PU) coating on 17 mm glass-fiber-reinforced Polymer (GFRP), shown in Fig. 2.

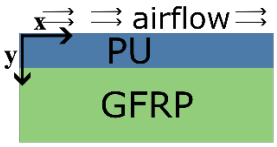

Fig. 2: 2D model of rotor blade

Convection is assumed to be the dominant heat transfer mechanism, which is supported by the fact that the Biot number is higher than one:

$$Bi = \frac{hL_s}{k_s} \geq 1.7\ , \qquad (1)$$

where $L_s = 2\,\text{cm}$ is the layer thickness, $k_s = 0.36\frac{W}{m\cdot K}$ is the weighted averaged thermal conductivity ($k_{GFRP} = 0.38\frac{W}{m\cdot K}$ [5], $\mathrm{k_{PU}} = 0.226\frac{\mathrm{W}}{\mathrm{m\cdot K}}$ [6]), and $h > 30\frac{W}{m^2K}$ (cf. Fig. 3) is the convective heat transfer coefficient. The heat transfer coefficient, which depends on the boundary airflow, is determined with a coupled Reynolds-Averaged Navier-Stokes (RANS) simulation. Here, an outer rotor blade section is studied for a Reynolds-number of $2.5 * 10^6$ considering a DU 96-W-180 blade profile as well as a solar-induced blade-air temperature difference of 5 K.

Fig. 3 shows the calculated heat transfer coefficient for two different blade angles of attack (AOA) over the chord-normalized position x/c. The laminar-turbulent transition is at $\frac{x}{c} = 0.25$ for an AOA of 4° and at $\frac{x}{c} = 0$ for an AOA of 18°.

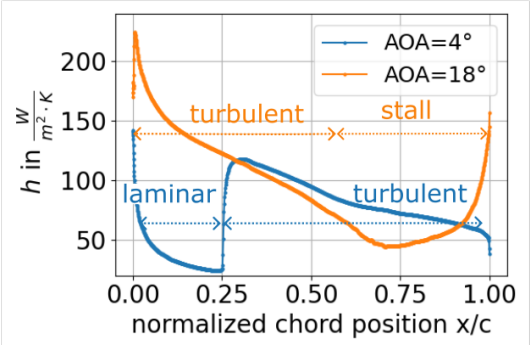

Fig. 3: Reynolds-Averaged Navier-Stokes (RANS) simulation of the heat transfer coefficient on a rotor blade profile at a Reynolds number of $2.5 \cdot 10^6$.

Considering the relative position $\frac{x}{c} = 0.25$, a change of the AOA thus leads to a change of heat transfer and therefore results in a step response of the surface temperature of the material that is simulated and shown in Fig. 4. The surface temperature declines after the boundary airflow has changed to turbulent. Already after $t_{CNR} = 50$ ms, the temperature difference is higher than the NETD given by the camera manufacturer InfraTec, which promises a theoretically reachable temporal resolution well below one second.

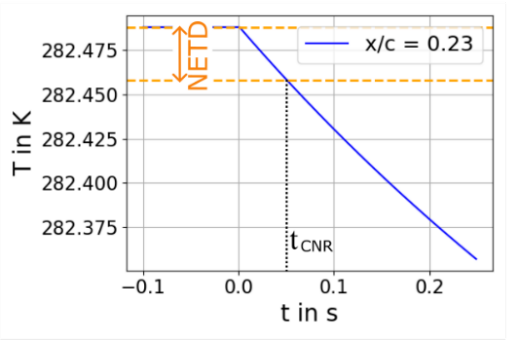

Fig. 4: Step response of the temperature after a boundary flow change from laminar to turbulent

Conclusion and outlook

The presented simulation results show that it is possible to thermographically visualize changes of the airflow with a contrast-to-noise ratio > 1 already 50 ms after a sudden change in the boundary airflow conditions. Furthermore, a co-rotating measurement system is realized for the first time that enables continuous thermographic images with a sampling period of 4 ms during the turbine revolutions and, hence, possibly facilitating measurements of flow changes close to the estimated temporal resolution limit.

The planned future research work is the use of the thermal images of the co-rotating platform to visualize position changes of the laminar-turbulent platform by means of DIT.

References

[1] B. Simon, A. Filius, C. Tropea, and S. Grundmann, 'IR thermography for dynamic detection of laminar-turbulent transition', *Exp Fluids*, vol. 57, no. 5, p. 93, May 2016, doi: 10.1007/s00348-016-2178-9.

[2] M. Raffel and C. B. Merz, 'Differential Infrared Thermography for Unsteady Boundary-Layer Transition Measurements', *AIAA Journal*, vol. 52, no. 9, pp. 2090–2093, Sep. 2014, doi: 10.2514/1.J053235.

[3] D. Gleichauf, F. Oehme, A.-M. Parrey, M. Sorg, N. Balaresque, and A. Fischer, 'On-site contactless visualization of the laminar-turbulent flow transition dynamics on wind turbines', *tm - Technisches Messen*, vol. 0, no. 0, Feb. 2023, doi: 10.1515/teme-2022-0120.

[4] P.-Y. Tsai, T.-E. Chen, and Y.-L. Lee, 'Development and Characterization of Anticorrosion and Antifriction Properties for High Performance Polyurethane/Graphene Composite Coatings', *Coatings*, vol. 8, no. 7, p. 250, Jul. 2018, doi: 10.3390/coatings8070250.

[5] T. Worzewski, R. Krankenhagen, M. Doroshtnasir, M. Röllig, C. Maierhofer, and H. Steinfurth, 'Thermographic inspection of a wind turbine rotor blade segment utilizing natural conditions as excitation source, Part I: Solar excitation for detecting deep structures in GFRP', *Infrared Physics & Technology*, vol. 76, pp. 756–766, May 2016, doi: 10.1016/j.infrared.2016.04.011.

DOI 10.5162/SMSI2025/C1.4

Advances in Magnetic Flow Metering: A Clamp-on Device

Leonhard Schmieder[1], *Peter A. Koss*[1]
[1] *Fraunhofer Institute for Physical Measurement Techniques IPM, Georges-Koehler-Allee 301, 79110 Freiburg im Breisgau, Germany*
Leonhard.Schmieder@IPM.Fraunhofer.de

Summary:

This study presents advancements in a clamp-on flow metering apparatus based on the magnetic flow metering procedure, with a focus on its non-invasive capabilities for the measurement of fluid flow across diverse pipe materials. The proposed metering methodology leverages novel optically pumped magnetometers (OPM), facilitating precise flow detection without disturbing the fluid dynamics of the system. We provide a detailed description of the essential components, including the pre-polarization magnet and the low-field nuclear magnetic resonance (NMR) region for signal preparation. This research represents a pivotal contribution to the ongoing evolution of the magnetic flow metering procedure, advancing its readiness for industrial application.

Keywords: Flow Metering, Non-Invasive, Quantum Sensing, Clamp-On, Magnetometry, NMR

Motivation

Clamp-on flow metering devices have emerged as crucial tools in the process industry, offering a non-invasive and efficient means to measure fluid flow. These devices provide significant advantages over traditional flow measurement techniques, including ease of installation, minimal maintenance requirements, and the ability to measure a wide range of fluid types without disrupting the flow or requiring system shutdowns [1, 2]. As industries strive for greater accuracy and reliability in their processes, the integration of clamp-on flow meters can enhance operational efficiency and reduce costs.
Our newly invented magnetic flow metering procedure [3, 4], which allows for a non-invasive flow detection with novel optically pumped magnetometers (OPM) through steel and plastic pipe materials [5], is constantly developed further to reach its full potential eventually [6]. In this article, we will outline our latest research achievements related to a clamp-on flow metering device based on this magnetic flow metering procedure. By leveraging the advantages of clamp-on technology described above, this method is particularly well-suited for non-invasive flow measurement, paving the way for its industrial applications.
The aim of our research presented is to develop clamp-on versions of the devices required for magnetic flow metering and to evaluate their performance against a stationary laboratory setup

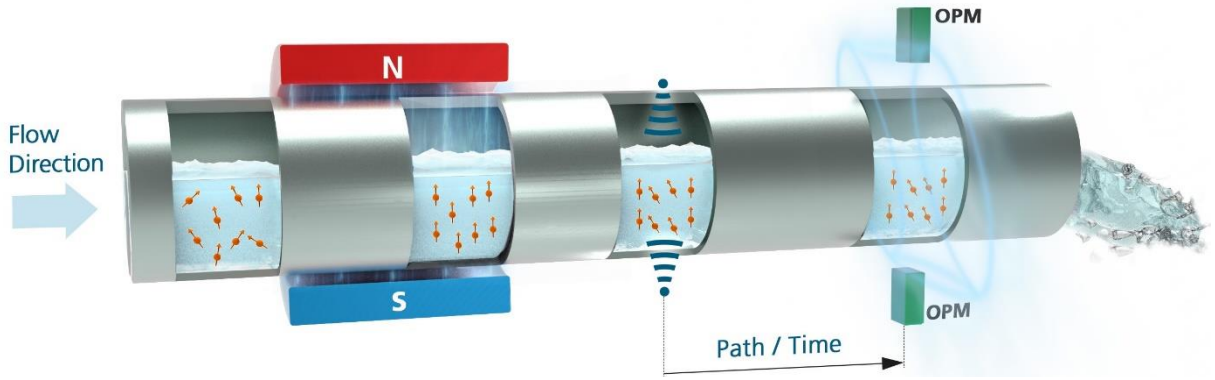

Fig. 1. Time-of-flight based measurement of a flow velocity. a) The fluid is magnetized by a strong magnet. b) A short and resonant RF pulse is applied to the fluid which creates a "notch" in a magnetized background. c) This notch is monitored by OPM downstream. The flow velocity is simply given by path over time where the timing information is given by the creation and detection of the notches.

and a commercial flow meter. The essential clamp-on devices include a pre-polarization magnet, a low-field nuclear magnetic resonance (NMR) region for signal preparation, and a magnetic shield that houses an optically pumped magnetometer (OPM) for signal detection. Although essential for the final apparatus, the OPM housing design is not yet complete at the time of this proceedings release; however, it is described in as much detail as possible.

Materials and Methods

Fig. 1 provides a schematic overview of the magnetic flow metering procedure. Short radiofrequency pulses are applied to a magnetically pre-polarized fluid. The local changes in the magnetic background field, detected by magnetometers positioned downstream, serve as timestamps for measuring the flow velocity in a time-of-flight fashion.

The design principle for the clamp-on Halbach magnet is shown in Fig. 2. The pre-polarization magnet is modelled after the research on clamp on magnetic systems in [7]. There, a new magnetic orientation design of a Halbach magnet allows for a forceless opening and closure of the magnet system, which is crucial for a simple operation in the field.

The RF interaction region and the detection region where the OPM is located must be magnetically enclosed to eliminate stray fields. To construct a clamp-on magnetic enclosure a press-on design of two half shells of mu metal around the pipe is used. Pressing the shells together ensures the connectivity of the mu-metal enclosure components. Separate enclosures are constructed for each region. The RF enclosure contains a built-in coil system to maintain a constant magnetic background field necessary for RF pulsing. Additionally, a clamp-on RF coil is fabricated using PCB manufacturing techniques.

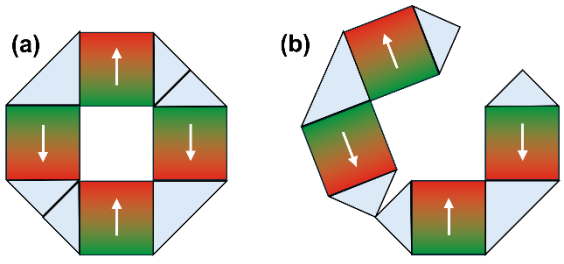

Fig. 2. Schematic arrangement of a clamp-on Halbach magnet with magnet orientation in open (a) and closed (b) depiction. The opening geometry allows for force free access. Image adjusted from [7], Fig. 3.

Results

The design of the clamp-on Halbach magnet is shown in Fig. 3. This magnet system is operated

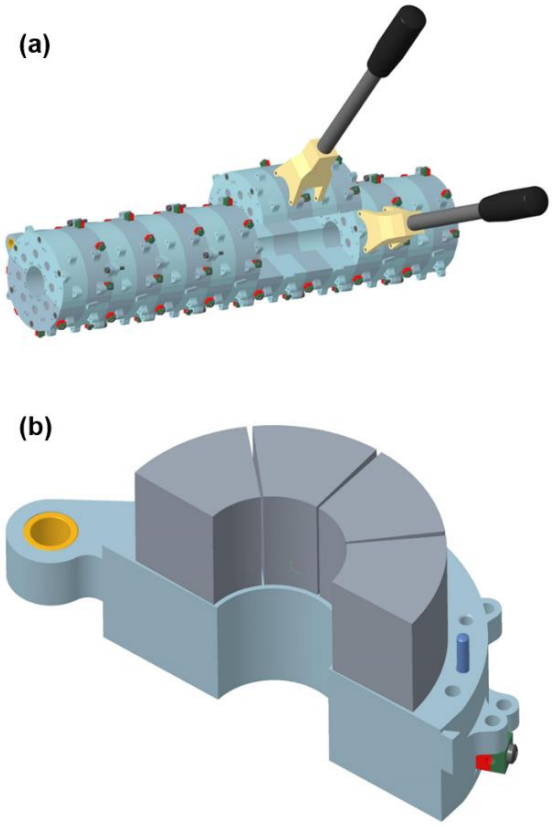

Fig. 3. Clamp-On Halbach system. In (a), a total view with opening levers is depicted. It consists of half shells which house trapezoid neodymium magnets. In (b), a close-up of a half shell is shown. The housed magnets are shifted outwards for an overview. The yellow ring is the hinge cylinder.

using two levers mounted on the exterior of the neodymium magnet housing. By pulling the levers apart, the half-shell magnet housing opens, allowing for effort-less deinstallation from the pipe due to the magnet's orientation. The magnetic field inside the Halbach system points perpendicular to the symmetry axis as the example shown in Fig. 2. The magnet system measures 416 mm in length and 86 mm in diameter. The modular construction enables the adjustment of the polarization length by adding or removing half shells from the magnet system.

The design of the RF magnetic enclosure is shown in Fig. 4. It has two layers mu metal pressed-on perpendicular to the symmetry axis and screws on both sides lock the layers into place. The enclosure measures 283 in length, 135 mm in diameter and has a simulated shielding factor on the order of 10^3. The inner coil system for RF pulsing and background field generation cannot be shown at the current development stage. The enclosure is manufactured by Sekels GmbH, Germany.

Although having more layers of mu metal and, thus a higher shielding factor, the magnetic enclosure for the OPM is manufactured in a similar

fashion as the RF magnetic enclosure but without a coil system in plan.

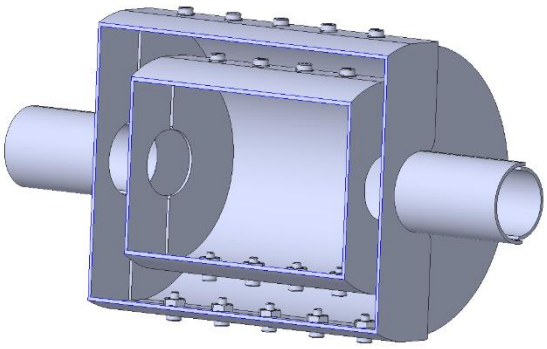

Fig. 4. Cross-sectional view of the clamp-on design for the interaction region enclosure. The magnetic field and RF coils are not depicted. The flow pipe is intended to run horizontally. Image provided by Sekels GmbH.

Discussion

This study presents advancements in clamp-on magnetic flow metering technology, emphasizing its non-invasive capabilities for measuring fluid flow in various pipe materials. By employing OPM, our method enables precise flow detection without disrupting the fluid dynamics, which is crucial for maintaining operational efficiency in industrial applications.

Our findings indicate that the clamp-on device, particularly the Halbach magnet design, allows for easy installation and removal, thus minimizing downtime. This reinforces the potential of our system to enhance measurement reliability while reducing maintenance needs.

The research contributes to the ongoing evolution of magnetic flow metering technology, showing promise for broader industrial applications. Continued development will focus on designing the OPM magnetic enclosure design and field tests when the apparatus is ready.

In conclusion, our clamp-on magnetic flow metering solution represents a pivotal step toward the industrial use as more efficient, accurate, and non-invasive flow measurement systems, aligning with the industry's increasing demands for sustainability and operational efficiency.

References

[1] Endress+Hauser GmbH+Co. KG, „Durchfluss-Messtechnik Für Flüssigkeiten, Gase und Dampf,“ [Online]. Available: https://portal.endress.com/wa001/dla/5000192/0856/000/01/FA00005DDE_1816.pdf. [Zugriff am 16 10 2024].

[2] Siemens AG, „Clamp-on ultrasonic flow measurement,“ [Online]. Available: https://www.siemens.com/global/en/products/automation/process-instrumentation/flow-measurement/ultrasonic/clamp-on.html. [Zugriff am 08 November 2024].

[3] L. Schmieder, P. A. Koss und F. Kühnemann, „Noninvasive magnetic-marking-based flow metering with optically pumped magnetometers,“ *Applied Sciences MDPI,* Bd. 12, Nr. 3, p. 1275, 2022.

[4] L. Schmieder, P. A. Koss und F. Kühnemann, „Verfahren und Durchflussmessgerät zum Erfassen einer Durchflusszeit eines Fluids“. Europa Patent EP4160159 A1, 5 April 2023.

[5] L. Schmieder, P. A. Koss und F. Kühnemann, „Magnetic Flow Metering with Optically Pumped Magnetometers (OPM),“ *SMSI Conference Proceedings,* pp. 69-70, 2023.

[6] L. Schmieder, P. A. Koss, F. Kühnemann und M. Bock, „Radio frequency pulse marking of nuclear magnetization for magnetic flow metering: The impact of the flow profile,“ *Journal of Applied Physics (JAP),* Bd. 135, Nr. 16, 2024.

[7] C. W. Windt, H. Soltner, v. D. Dagmar und P. Blümler, „A portable Halbach magnet that can be opened and closed without force: The NMR-CUFF,“ *Journal of Magnetic Resonance,* Bd. 208, pp. 27-33, 2011.

DOI 10.5162/SMSI2025/C2.1

„Sensor-Intelligence Devices (SID) for optimized condition and process monitoring“

K. Becker[1], D. Koster[1], H.-G. Herrmann[1];
[1]Fraunhofer-Institut für Zerstörungsfreie Prüfverfahren IZFP; Campus E3 1; 66123 Saarbrücken, Deutschland
kevin.becker@izfp.fraunhofer.de, Dirk.Koster@izfp.fraunhofer.de, Hans-Georg.Herrmann@izfp.fraunhofer.de

Summary:
In-memory computing (IMC) has gained significant attention in recent years, particularly in the context of energy-efficient sensor systems and the emerging field of ultra-low power and Tiny Machine Learning (TinyML).[3-4] In this work the capability of an SRAM memory to process Machine Learning algorithms for Sensor-Intelligence Devices (SID) could be demonstrated.

Keywords: SRAM, Machine learning processing, compute in memory, mixed-signal computing, analog in-memory computing

Background, Motivation and Objective

Intelligent sensor-systems are revolutionizing data processing by integrating AI directly into sensor systems, enabling real-time analysis and decision-making at the edge. Unlike traditional sensors, SIDs fuse multi-modal data, leverage neuromorphic computing, and utilize in-memory processing to maximize efficiency [1]. Techniques like compressed sensing and TinyML are enhancing this capability in reducing power-consumption and maintaining a high performance. Energy-efficient AI processors play a crucial role in advancing SIDs, particularly for edge computing. Innovations such as low-power NPUs, quantization, and sleep-mode optimization are enabling AI inference on battery-powered devices. Also extending operational lifetimes in remote and power-constrained environments. Near-sensor-computing is transforming industries such as material testing, manufacturing, healthcare, defense, and civilian security. In industrial applications, they enable predictive maintenance and automated defect detection, reducing downtime and improving quality control. In healthcare, wearable SIDs can provide real-time diagnostics. Deploying intelligent sensor-systems in remote and inaccessible locations presents challenges, including energy constraints, intermittent connectivity, and harsh environmental conditions. Advances in low-power design,

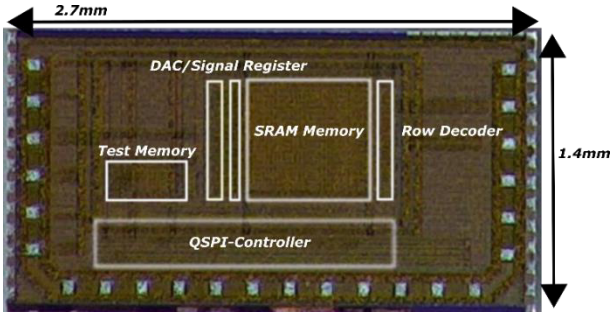

Figure 1 Picture of the chip. It includes the SRAM memory with its peripheral components

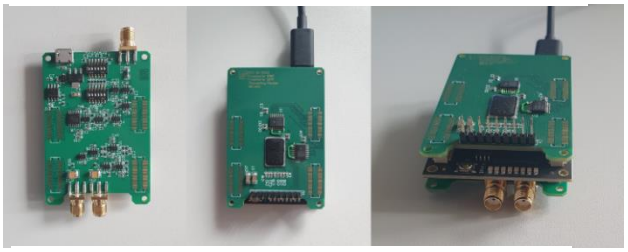

Figure 2 Eddy current transceiver, ASIC-PCB and completely stacked sensor-system

LPWAN communication, and self-diagnostic capabilities ensure long-term autonomous operation. By processing data locally, SIDs reduce cloud dependency, enhance privacy, and enable AI to function reliably in real-world, power-sensitive applications. These innovations pave the way for a new era of pervasive, low-energy AI, making intelligent systems more accessible and sustainable across diverse industries [2].

Description of the New Method or System

This work introduces a novel 6T-SRAM-based In-Memory Computing (IMC) method implemented in a 180nm technology node shown in *Fig.1*. The key innovation lies in the analog computation within the memory of the SRAM by integrating 128 polysilicon Digital-to-Analog Converters (DACs) near the memory. This enables data processing, in terms of efficient multiply an accumulate operations, with a minimal footprint, low power consumption, and high energy efficiency shown in Fig.4. The DAC generate an analog voltage, that modulates the conductance of pass transistors, effectively performing element-wise multiplication. The charge from all bitcells of the memory is then accumulated across the bitline. The voltage measured by the comparators at the bitlines is then used as activation function. The proposed method is designed for real-time sensor data classification, specifically targeting eddy current sensor systems. The classification process is executed directly within the SRAM, leveraging an in-memory algorithm that processes sensor data collected from an eddy-current transceiver *Fig.2*. The system incorporates an FPGA for signal preprocessing and sensor excitation, utilizing a transceiver to measure impedance variations across different materials. This approach offers significant advantages in performance density and energy efficiency. This new IMC approach paves the way for energy-efficient, high-performance machine-learning applications in embedded sensor systems.

Results

The SRAM-based In-Memory Computing (IMC) accelerator successfully classified real-world sensor data for nondestructive testing (NDT) using eddy currents. The fabricated chip achieves 3.2 TOPS/mm², while simulations of the 16kb IMC core predict 45 TOPS/W at 50 MHz. Experimental validation at 5 MHz confirms an energy efficiency of 3.4 TOPS/W. The system, including a sensor setup and computer interface for data storage, was tested with an external 5 MHz clock controlling the digital processing. The classification task demonstrated 98% accuracy in distinguishing different materials using multiple datasets across various bitlines. The measured power consumption of the chip averaged 48 mW,

Table I
CHIP SPECIFICATIONS

	Measurements and Specification
Process	180nm
Computation Type	IMAC
Architecture	Mixed-Signal
Cell Structure	6T
I/W/Out	8/1/1
Performance	3.2TOPS/mm^2
Efficiency	3.4TOPS/W
Circuit Area Overhead	6%
Core Size	670µmx900µm

Figure 3 Overview of the chip specification and measurements

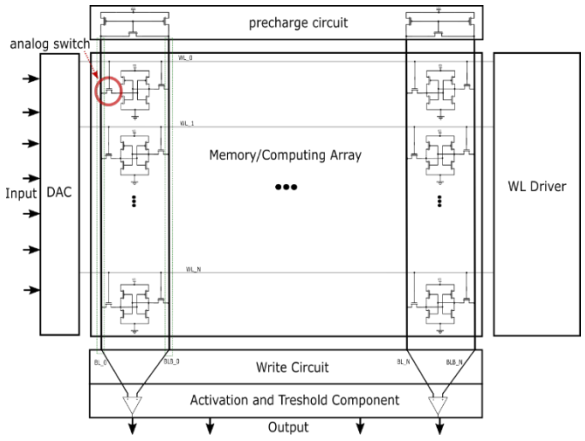

Figure 4 In-Memory Computing Technique within SRAM Memory

with an energy efficiency of 3.4 TOPS/W. Training all bitlines using an external PC took 1700 seconds per bitline over 20 iterations. For inference, the primary source of power consumption was identified as the DACs, leading to an optimized design that reduces DAC power consumption by a factor of 25, targeting a maximum current of 1 mA. This new version is currently under fabrication. The DAC power consumption varies based on the input signal due to the current drawn by the R2R ladder DACs, which depends on the digital input code. While larger DACs can reduce power consumption, they increase the overall chip size. However, using polysilicon resistors ensures high output linearity, making this design an effective trade-off. A key advantage of this approach is that standard memory components are repurposed for computation, enabling direct processing within memory rather than limiting the system to conventional read/write operations.

Conclusion

This work presents a high-performance IMC architecture that can be used for real-life datasets for eddy current testing while reaching an energy efficiency of 3.4 TOPS/W with a small area overhead, in concern of the integrated 128 DACs, of about 6% of the total chip area successfully implemented in different industrial projects, such as

for the investigation of load and the motion of wall anchors via accurate position- and distance measurements. Results in research projects for the determination of the humidity of concrete at bridges leading to structural damages like corrosion at the reinforcement or spalling due to volume increase are not yet available but look very promising.

Acknowledgement

This work was supported by the Saarland Ministry of Economic Affairs, Innovation, Digital and Energy (MWIDE) and the Fraunhofer Ge-sellschaft (High-Performance Center ‘Sensor-Intelligence’).

References

[1] S. Paul, R. Karam, S. Bhunia and R. Puri, "Energy-efficient hardware acceleration through computing in the memory," 2014 Design, Automation & Test in Europe Conference & Exhibition (DATE), Dresden, Germany, 2014, pp. 1-6, doi: 10.7873/DATE.2014.279

[2] H. Ahlendorf and L. Göpfert, "Hardware/software design challenges of low-power sensor nodes for condition monitoring," 2010 Design, Automation & Test in Europe Conference & Exhibition (DATE 2010), Dresden, Germany, 2010, pp. 659-659, doi: 10.1109/DATE.2010.5457122.

[3] S. K. Gonugondla, C. Sakr, H. Dbouk and N. R. Shanbhag, "Fundamental Limits on the Precision of In-memory Architectures," 2020 IEEE/ACM International Conference On Computer Aided Design (ICCAD), San Diego, CA, USA, 2020, pp. 1-9.

[4] N. Verma et al., "In-Memory Computing: Advances and Prospects," in IEEE Solid-State Circuits Magazine, vol. 11, no. 3, pp. 43-55, Summer 2019, doi: 10.1109/MSSC.2019.2922889

DOI 10.5162/SMSI2025/C2.2

Bioreactor Intelligence for Real-Time Monitoring and Automation of Stem Cell Cultivation

Dmitry Amelin[1], *Thorsten Knoll*[1], *Matthias Jochem*[1], *Saskia Altmaier*[1,2], *Franziska Musiol*[1], *Frank R. Ihmig*[1], *Michael M. Gepp*[1], *Roman Ruff*[1]
[1]*Fraunhofer Institute for Biomedical Engineering IBMT*
Joseph-von-Fraunhofer-Weg 1, 66280 Sulzbach, Germany
[2]*Department of Molecular and Cellular Biotechnology/Nanotechnology*
Saarland University, 66123 Saarbrücken, Germany
roman.ruff@ibmt.fraunhofer.de

Summary:
We present innovative approaches to develop novel sensor-intelligence devices for scaling up and standardizing the production of complex human induced pluripotent stem cells and their derivatives (e.g., neural cells). Preliminary results for the optical at-line sensors show good performance results for classification and segmentation of stem cell aggregates.

Keywords: deep learning, potentiostat, spheroids, embedded vision, process analytical technology

Motivation and Objectives

The quality-assured and reproducible production of complex cell models derived from induced pluripotent stem cells (iPSCs) is a fundamental prerequisite for the successful transfer of these models in e.g., drug development pipelines of pharmaceutical industry as well as cell therapy in clinical applications. Our research is pursuing several highly demanded approaches to develop new sensor-intelligence devices for scaling up and standardizing the production of complex iPSC-based three-dimensional (3D) cell models, known as spheroids or organoids.

The various approaches are to be integrated into a standard commercial suspension bioreactor system “CERO 3D Incubator & Bioreactor” (OMNI Life Science GmbH & Co KG, Bremen, Germany), which is commonly used for the cultivation of iPSC-derived 3D cell aggregates. The system does not yet measure parameters directly in the bioreactor tubes, except pH. This means that no statements can be made about e.g., glucose or lactate concentration, dissolved oxygen or other values relevant to spheroid maturation. Furthermore, quality control of the spheroids is a manual, invasive, time-consuming and user-dependent process. The concept of our sensor-intelligence device considering the following objectives:

- Scalable parallelization and automation of production processes for 3D cell cultures.
- Optimized cultivation and expansion of sensitive cell models, such as human iPSCs, and their differentiation into cardiomyocytes, neurons or lung cells using online sensors.
- AI-supported, non-invasive assessment of cell cultures (e.g. size, growth curve, morphology) during the ongoing production process, possibly with the option of feedback-control.
- Data connectivity and integration into quality assurance systems or laboratory information management systems by implementing standardized interfaces and protocols.

System Architecture

Our system employs optical and electrochemical sensors. Optical sensors capture morphological information of spheroids (e.g. size, shape, homogeneity), while electrochemical sensors measure characteristics of the medium (e.g. pH, dissolved oxygen, glucose / lactate). By combining this heterogeneous data, we plan to further assist biologists in the production of 3D cell cultures and to potentially fully automate the process in the future. Fig. 1 shows the demonstrator of the modified commercial bioreactor with integrated sensor intelligence.

Optical sensors are either integrated directly inside the incubator space (i.e. in-line) to monitor the spheroids inside the rotating tubes [1] or used at-line by attaching a microfluidic system to the bioreactor, where a microscope captures images of the spheroids drawn from the tubes [2]. Extraction of the spheroids is done by a special adapter with sterile metal straws which is inserted through a modified lid into the bioreactor.

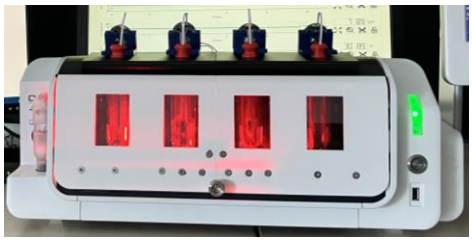

Fig. 1. Modified "CERO 3D Incubator & Bioreactor" with integrated sensor intelligence.

A peristaltic pump gently transfer the spheroids out of the tubes through a transparent microchannel, where images are taken for subsequent classification and analysis, and back to the tubes. Two separate deep learning models based on the YOLO5 (You Only Look Once) and YOLO8 architectures [3, 4] were trained respectively for these two types of optical sensors to detect, classify, and segment the spheroids. The results of the models are used to calculate morphological characteristics.

Electrochemical sensors are integrated inside the bioreactor tubes by the same adapter, which is employed for the spheroid extraction. Highly integrated measurement electronics with wireless data interface and four high-precision potentiostat circuits measures up to five parameters simultaneously (temperature, pH, glucose, lactate, and dissolved oxygen) per rotating tube. Sensor data is transmitted via Bluetooth Low Energy (BLE). Fig. 2 shows the compact measurement electronics with a diameter of 30 mm. Alternatively, the sensors are implemented into the microfluidic system leading to the at-line analysis. However, we focus on results for the optical at-line sensor in this paper.

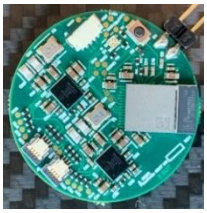

Fig. 2. Electrochemical measurement electronics with four potentiostat circuits and BLE interface.

Validation

The trained machine learning (ML) model for the optical at-line sensor processes each image in roughly 16 ms (± 6 ms), allowing the microscope camera to operate at around 40 FPS. Thus, the system can, in its current setup, process 5 ml sample volume per minute. Mean average precision at an intersection over union threshold of 0.50 (mAP50) of the trained model is 0.68. Throughout the process, the system provides real-time updates of descriptive statistics, offering an overview of the cultivation progress. Fig. 3 shows a visualization of the ML model's results. To assess the potential influence of spheroid transport through the peristaltic pump, we conducted two types of experiments:

1. On the third day, one tube was processed, leaving the final 10 mL untouched. This step was repeated twice on the same day using a tube with more than 10 mL of content. As a result, four tubes were obtained, each containing 10 mL of medium with spheroids.
2. In a separate experiment, 10 mL of medium containing spheroids was pumped through the at-line circuit and analyzed by the system on days 3, 5, and 7.

The spheroids in all 8 tubes were then cultivated under standard conditions for 10 days in total. Fig. 3 displays spheroids from human iPSC-derived neural stem cells (EBiSC cell line UKKi011-A) after 10 days of growth. The results suggest that the physical stress exerted by the system does not impact the spheroids' morphology.

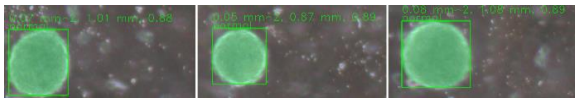

Fig. 3. Example of the ML model's output: classification, segmentation taken on day 10 of cultivation.

Conclusion

The reported outcomes indicate promising results for the optical at-line sensors. By enhancing the integration of our system, we will generate more data to further improve the performance and accuracy of our ML models and use heterogeneous data generated by the optical and electrochemical sensors to achieve our previously stated goals.

Acknowledgement

This work was supported by the Saarland Ministry of Economic Affairs, Innovation, Digital and Energy (MWIDE) and the Fraunhofer Gesellschaft (High-Performance Center 'Sensor-Intelligence').

References

[1] M. Carrillo, S. Altmaier, I. Meiser, F. Ihmig, Non-invasive and continuous monitoring of 3D stem cell culture in a bioreactor: An embedded machine learning approach, *Current Directions in Biomedical Engineering* 10(4), 148-152 (2024); https://doi.org/10.1515/cdbme-2024-2036

[2] D. Amelin, S. Ganz, T. Knoll, F. Musiol, S. Altmaier, M. Gepp, R. Ruff, AI based analysis of the spheroid cultivation process in real time, *Poster Session at ISSCR 2024 Annual Meeting*

[3] G. Jocher, ultralytics/yolov5: v7.0 - YOLOv5 SOTA Realtime Instance Segmentation, *Zenodo, Nov. 22, 2022*; https://doi.org/10.5281/zenodo.7347926

[4] G. Jocher, J. Qiu., A. Chaurasia, (2023). Ultralytics YOLO (Version 8.0.0) [Computer software]. https://github.com/ultralytics/ultralytics

DOI 10.5162/SMSI2025/C2.3

Real-time, Parallelized and Non-contact Read-Out of 3D Cardiac Tissue Models

Ronan Le Harzic[1], Frank Stracke[1], Dmitry Amelin[1], Roman Ruff[1], Ralf Kettenhofen[2], Franziska Musiol[1], Dominic Bauer [2], Sabrina Herrmann[2], Julia Neubauer[2], Heiko Zimmermann[1]
[1] Fraunhofer institute for biomedical engineering, Joseph-von-Fraunhofer-Weg 1, 66280 Sulzbach, Germany
[2] Fraunhofer Project Center for Stem Cell Process Engineering, Röntgenring 12, 97070 Würzburg, Germany
Corresponding Author: heiko.zimmermann@ibmt.fraunhofer.de

Summary:
We present a read-out technology for cardio high throughput screening of cardiac 3D tissue models. It is based on optical diffraction and allows non-contact, label-free and parallel operation on any 96 well plate formats.

Keywords: high throughput screening, cardiac tissue models, spheroid, Speckle, well plates

Background, Motivation an Objective

Pharmaceutical drug and toxicology screening is facing a paradigm shift today. For decades, compounds were tested on adherent, two-dimensional cell cultures. As endpoint, the cellular response to the respective candidate compound was determined using tailored assays. In future, three-dimensional tissue and organ models will increasingly replace the simple cell cultures [1]. These three dimensional models are far more physiological and render not only cellular functions, but also organ function beyond the cellular level [2]. This opens up the potential, to rule out much more candidates (false leads) from further examination at an early stage, saving time, resources and subsequent animal tests. The most prevalent pharmaceutical screen is evaluating compounds regarding their effect on the cardiac system. To this end, beating cardiomyocyte cell aggregates are exposed to drug candidates and the effect on the beating behavior is recorded. At present, confluent adherent cardiomyocyte cell cultures are grown on multi electrode arrays (MEA)]. But modern three-dimensional cardiac models are not suited to contact methods like MEA. Hence, a sensitive, contact-less read-out technology is needed, capable of parallel operation on multi-wall-plates and preferably automatable.

Description of the New Method or System

Here we present an optical non-contact and label-free technology based on Speckle diffraction. In contrast to imaging modes, diffraction methods reduce the 3D information to a 2D pattern, eliminating the need for delicate focusing and adjustments. Together with a signal analysis algorithm without any image rendering, the technology meets all requirements for high throughput screening (HTS) of cardiac 3D models [3].

The samples in the 96-well plate are illuminated by 96 laser diodes at a power of < 1 mW. Beam shaping is performed by 12×8-aperture array and a 12×8-lens array. Laser power may be adjusted individually for each well to ensure uniform signal amplitude over the well plate, alternatively to create power gradients or power patterns.

Since diffraction obeys different optical rules as imaging, a camera only may record the speckle pattern of the well on its optical axis. Instead of arranging 96 cameras under the well plate, we use a diffusive screen for Speckle pattern projection, transforming diffraction optic into imaging optics. The projection screen with 96 Speckle patterns may now be recorded by a single video camera. The video image is then segmented to 96 Speckle patterns, which are then analyses pixel-wise before summation:

$$\Delta D(t) = \sum_{n=1}^{N} |D_n(t) - D_n(t-1)| \quad (1)$$

The simple data processing allows to record the ΔD(t) of all 96 wells in parallel at a rate up to 50 Hz using a standard notebook computer.

Results

The technology was tested using spheroids of cardiomyocytes derived from induces pluripotent stem cells (hiPSC). Such spheroids are very basic heart muscle tissue models, exhibiting cardiac contractions at rates around 1 Hz. They consist of approximately 10.000 cells and are about 400 µm µm in diameter.

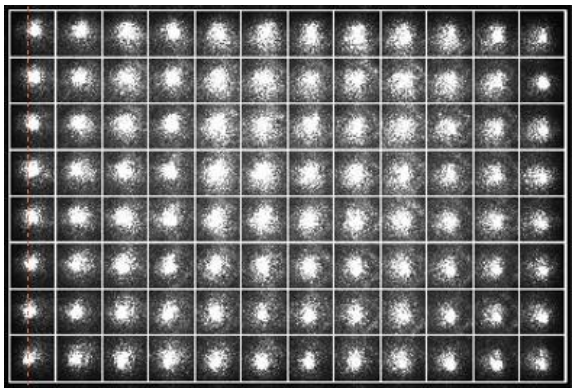

Fig. 1. 12×8 segmentation of the video signal into 96 individual Speckle patterns. The centered patterns appear brighter due to the angular dependence of diffuser scattering properties.

As a first result, the camera image displays appropriate Speckle patterns from the entire well plate. Slight dislocations of the well plate do not compromise the dynamic signal. The segmentation of the video signal works well and the contractions of the cardiac tissue models lead reliably to nicely modulated ΔD(t) readings.

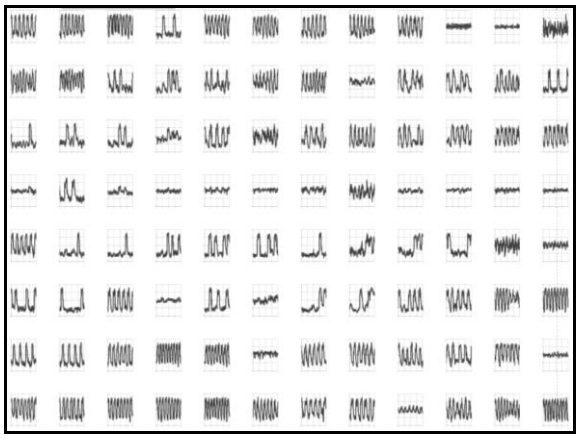

Fig. 2. Parallel in-line recording of ΔD(t) from all samples of the well plate. Some samples are inactive in this example, the beating frequencies vary significantly between the channels.

In order to extract the beating frequency of cardiac tissue model we calculate a frequency spectrum using Fast Fourier Transformation (FFT) and fit an error function to the data.

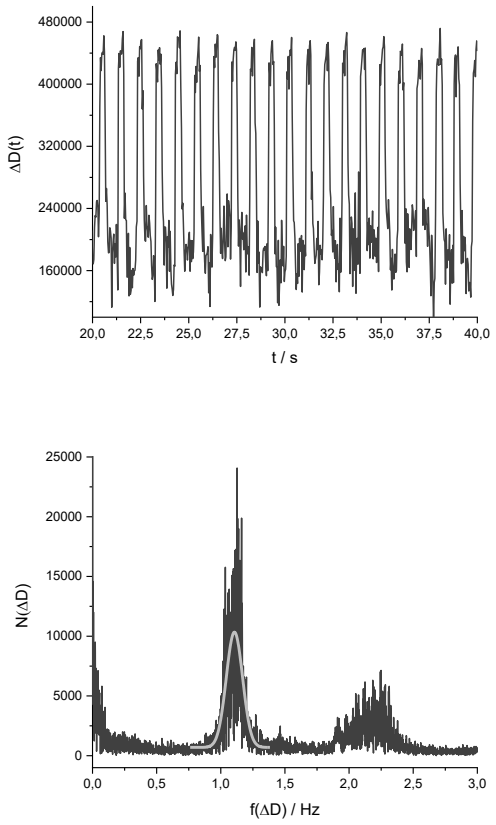

Fig. 2. A section of a ΔD(t) data set and the respective frequency spectrum.

The technology proved to be capable of sensitive HTS on modern cardiac 3D tissue models. The parallel operation and the insusceptibility to spatial dislocations, as well as the low requirements to data processing resources make the technology an ideal candidate for automated screening workflows.

Acknowledgement

This work was supported by the Saarland Ministry of Economic Affairs, Innovation, Digital and Energy (MWIDE) and the Fraunhofer Gesellschaft (High-Performance Center 'Sensor-Intelligence').

References

[1] R.M. Eglen, D.H. Randle, Drug discovery goes 3D: Goodbye to flat high-throughput screening? *ASSAY Drug. Develop. Technol*. 13, 262-265 (2015).

[2] F. Pampaloni, E.G. Reynaud, E.H.K. Stelzer, The third dimension bridges the gap between cell culture and live tissue, *Nature Rev: Mol. Cell Biol*. 8, 839-845 (2007).

[3] R. Le Harzic et al., Diffraction-based technology for the monitoring of contraction dynamics in 3D and 2D tissue models, Biomed. Opt. Expr. 11, 517-532 (2020).

DOI 10.5162/SMSI2025/C2.4

Implementation of Sensor-Intelligence Devices (SIDs) for Condition Monitoring Applications in the Sense of Smart Predictive Maintenance

Samuel Klein[1], Philipp Stopp[1], Dirk Koster[1]
[1] Fraunhofer Institute for Non-destructive Testing, Campus E3.1, 66123 Saarbrücken,
Fabian.Weber@izfp.fraunhofer.de, Philipp.Stopp@izfp.fraunhofer.de, Dirk.Koster@izfp.fraunhofer.de

Summary:
A condition monitoring and predictive maintenance testing system, called **M**odular **AU**tarkic **S**ensor platform (MAUS), is presented. Various applications are demonstrated and an outlook is given into further developments.

Keywords: Condition Monitoring, Predictive Maintenance, Sensor-Intelligent Device, EMAT, MAUS

Background, Motivation an Objective

Non-destructive approaches for the continuous monitoring of structures and components provide important information about their condition, service life and safety during operation. Especially in the area of critical infrastructure, exceptional situations in the form of impact events and dynamic processes - which cannot always be absorbed constructively - also influence the operating status of technical systems, which consequently require an as-built examination at regular intervals as part of Smart Predictive Maintenance models. Additional overlapping external influences such as extreme weather conditions, which can lead to age-related damage such as corrosion, or dynamic alternating loads, which can lead to material changes due to fatigue, require the recording and evaluation of relevant condition data in order to derive a damage assessment so that systems can be proactively monitored and subjected to preventive maintenance.

Description of the System

To address this challenge, an innovative solution known as the Modular Autarkic Sensor Platform (MAUS) has been developed. This modular, energy-efficient, and intelligent monitoring system utilizes state-of-the-art microelectronics to provide a plattform for many different sensor types, one of which uzilizes couplant-free ElectroMagnetic Acoustic Transducers (EMATs) to enable ultrasound ndt testing. MAUS is specifically designed for long-term monitoring of critical infrastructure components, primarily within the industrial and civil engineering sectors.

In order to enable combined monitoring system applications, the platform concept of the MAUS is split into different functional modules. These includes the base module, power supply module for tethered or autarkic supply, communication module for Wifi, LoRaWAN etc., up to different sensor modules for environmental data, position and vibration sensors as well as for different non-destructive sensors including ultrasound or eddy current testing.

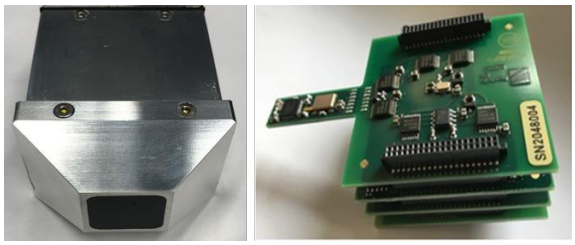

Fig. 1. Developed EMAT (left) and stacked functional blocks of the MAUS platform

The developed EMAT-based system was primarily designed for the local (see Fig. 2) and the mobile (see Fig. 3) ultrasound-based inspection of hard-to-access critical structures, such as wind turbines in the onshore and offshore sector or storage tanks including their in- and outlets, within the framework of operational monitoring in order to ensure the operating condition through permanent quality monitoring.

Results

Appropriate laboratory tests were carried out to investigate and evaluate the resolution and accuracy of the ultrasound-based wall thickness measurement of the system. For this purpose,

several reference specimens of steel have been manufactured, covering a wall thickness range of 2.5 mm up to 20 mm. In other applications similar test results were gathered through lab experiments and filed validation. A long term experiment monitoring overhead line anchors on building walls shows the reliabilty of an energy-constrained system.

Finally a high-performance multi-sensor approach is shown using fast vibration sensors that monitor automotive loads on driving surfaces. A field test setup is shown that demonstrates mulitple systems aquiring data at high speeds, which are capable of evaluating the data at real time to reduce data throughput to the acquisition site.

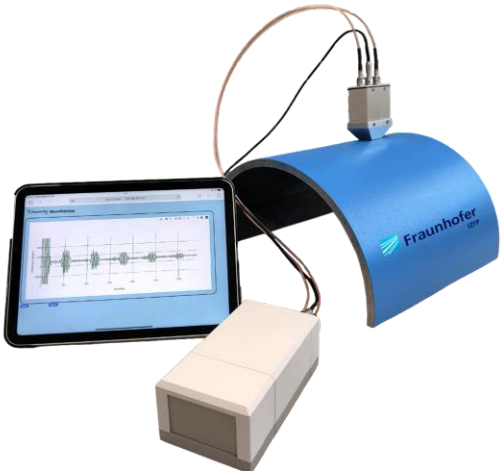

Fig. 2. Developed EMAT-SID concept applied to a half shell test specimen for stationary use including the wireless result display

Fig. 3. Developed MAUS-SID applied to line angle monitoring of wall anchors with constrained power

Conclusion

The system developed in this work excels to a:

- Scalable toolbox of hardware and software components
- High adaptability of the topology of the monitoring system
- Parameterization of the sensors to the test object geometry and damage mechanisms
- Sensor-related data reduction, -fusion and adapted signal evaluation directly in hardware

This system enables further use cases for the modular sensor platform combined with EMAT, covering applications in monitoring of critical infrastructure components and enhancing the detection of structural anomalies, assessing material integrity, and facilitating predictive maintenance to prevent catastrophic failures.

In addition, the MAUS platform as part of recently installed monitoring systems have been successfully implemented in different industrial projects, such as for the investigation of load and the motion of wall anchors via accurate position- and distance measurements [1]. Results in research projects for the determination of the humidity of concrete at bridges leading to structural damages like corrosion at the reinforcement or spalling due to volume increase [2][3] are not yet available but look very promising.

Acknowledgement

This work was supported by the Saarland Ministry of Economic Affairs, Innovation, Digital and Energy (MWIDE) and the Fraunhofer Gesellschaft (High-Performance Center ‘Sensor-Intelligence’).

References

[1] S. Philipp, SWO Netz installs smart wall anchors: Fraunhofer IZFP research project in Osnabrück, , Sep 2021, https://nachrichten.idw-online.de/2021/09/08/swo-netz-installs-smart-wall-anchors-fraunhofer-izfp-research-project-in-osnabrueck (abgerufen am 31.07.2024)

[2] https://imab-edge.de/

[3] Rapid-Prototyping für Monitoring-Anwendungen an Brückenbauwerken, Dirk Koster et al., BRÜCKENBAU, Issue 4 – 2024, Verlagsgruppe Wiederspahn

DOI 10.5162/SMSI2025/C3.1

3D Density Field Reconstruction of Vehicles Exhaust Plumes using Background Oriented Schlieren Tomography based on Windowed Fourier Transform and Graphical Phase Analysis

Hafiz Hashim Imtiaz[1], *Paul Schaffer*[1], *Thomas Forstinger*[1], *Martin Kupper*[1] *and Alexander Bergmann*[1]
[1] *Institute of Electrical Measurement and Sensor Systems, Graz University of Technology, 8010, Graz, Austria*
hafiz.imtiaz@tugraz.at

Summary:
This work presents a 3D Gas Schlieren Imaging Sensor (GSIS) system. The 3D-GSIS system allows to construct 3-D density fields of gas flows and vehicle exhaust plumes from conventional camera images, by using an innovative Windowed Fourier Transform-based Graphical Phase Analysis (WFT-GPA) algorithm and state-of-the-art Optical Flow techniques to calculate and construct density fields. The system will be combined with advanced remote emission sensing (RES) systems to measure the direct concentration of pollutants in the vehicle exhaust plumes.

Keywords: background oriented schlieren imaging, BOS tomography, 3D density fields, remote emission sensing, exhaust plume imaging

Background, Motivation and Objective

Air pollution is a significant public health issue, with on-road traffic emissions playing a pivotal role, especially in urban areas. Remote emission sensing (RES) is an advanced method for monitoring emissions from thousands of vehicles in real-world conditions. Advanced RES systems use absorption spectroscopic techniques to determine the concentration ratios of pollutants relative to CO_2, as this allows conclusions about the emissions related to fuel consumption.

To accurately measure the concentrations of pollutants in vehicle exhaust plumes, it is necessary to calculate the absorption path length, which refers to the extent of the exhaust plume in the direction of the laser beam from the RES system. Hence, if we can measure the size and extent of the exhaust plume in the direction of the laser beam of the RES system, we can measure the absolute concentration of pollutants according to Beer-Lambert Law [1]. The 2D Gas Schlieren Imaging Sensor (GSIS) System has been developed for qualitative and quantitative analysis of vehicle exhaust plumes [2]. It supports a vertical RES system, which means a laser transmitter is placed above the road and transmits a laser beam from the top toward the road. 2D images of exhaust plumes from single side only give enough information to calculate the laser beam's absorption path length in fixed setups.

This work presents a 3D-GSIS system that can construct the 3D density fields of vehicle exhaust plumes and other turbulent flows using background-oriented Schlieren (BOS) tomography. The 3D-GSIS system uses an advanced and efficient Windowed Fourier Transform-based Graphical Phase Analysis (WFT-GPA) and state-of-the-art Optical Flow (OF) techniques to calculate displacement fields and construct density fields. With the 3-D density fields of exhaust plumes, we can efficiently find the absorption path length of the laser beam from any direction.

Description of the System

The 3D-GSIS system is made of 8 cameras covering the angle of 160° from 0° to 160° as shown in Fig. 1.

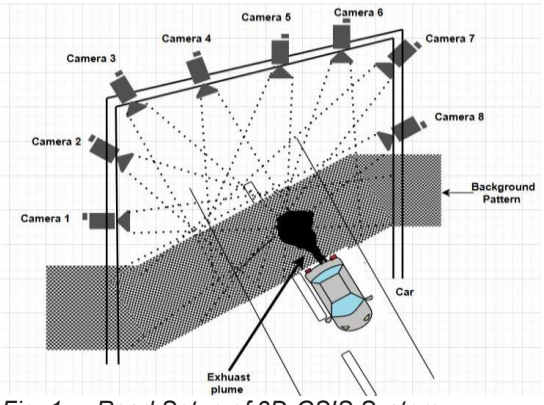

Fig. 1. Road Setup of 3D-GSIS System

The number of cameras can be adapted on the working conditions and applications, to adapt coverage and resolution. A pattern is placed in front of each camera unit. The gas flow and vehicle exhaust plume are located in the middle so that the plume is in the field of view of each camera. Each camera captures the image of the pattern board with and without the flow. The image pair is then used to calculate the displacement field using WFT-GPA and OF. The 2D line of sight integrated density fields are calculated using the displacement fields and solving the Poisson equation [3]. 3D density field is constructed using the tomographic reconstruction based on the Simultaneous Algebraic Reconstruction Technique (SART). The workflow of the 3D-GSIS system is shown in Fig. 2.

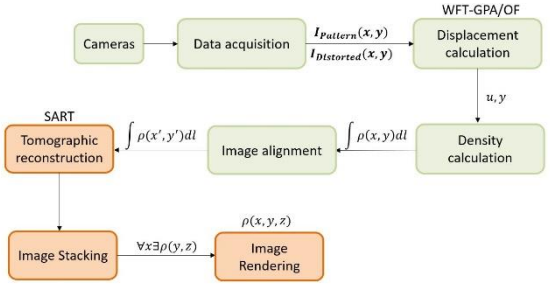

Fig. 2. Workflow of 3D-GSIS System

Results

The 3D-GSIS system was set up in the lab and tested with gas flows. Initially, the system experimented with the gas flow containing 10% air and 90% CO_2. The constructed 2D line-of-sight integrated density field and 3D density field are shown in Fig. 3 and Fig. 4.

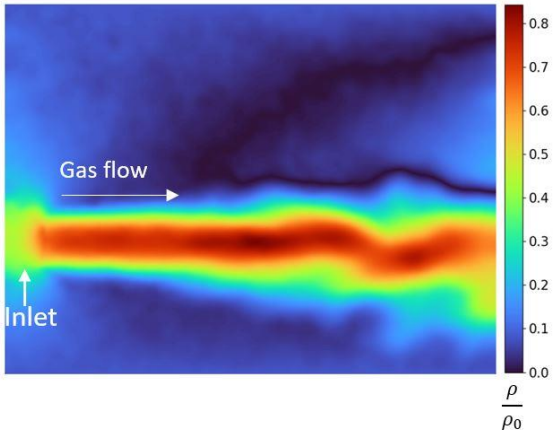

Fig. 3. 2D Density Field of Gas Flow

The 3D-GSIS system was also set up the Inffeldgasse campus of Graz University. It is being tested with passing cars. Fig. 5 and Fig. 6 show the constructed 2D and 3D density field of a car's exhaust plume.

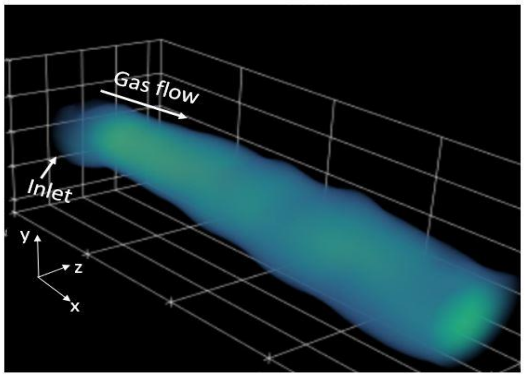

Fig. 4. 3D Density Field of Gas Flow

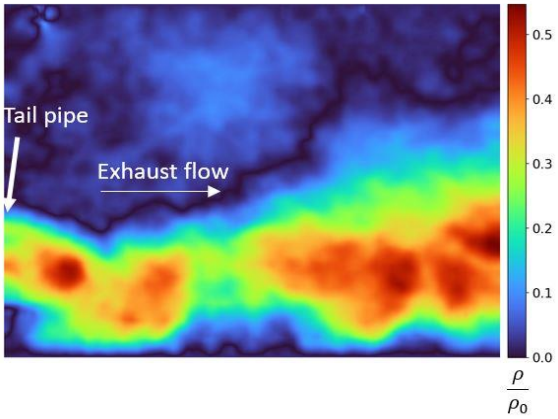

Fig. 5. 2D Density Field of Vehicle Exhaust Plume

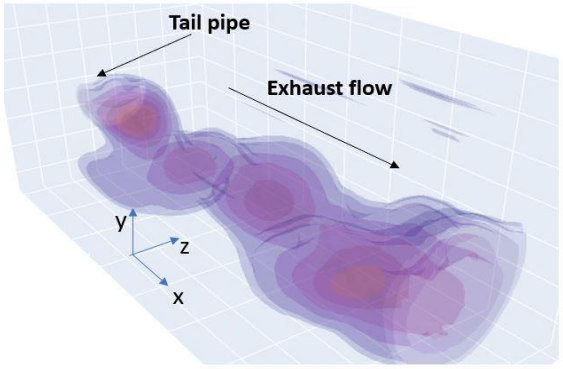

Fig. 6. 3D Density Field of Vehicle Exhaust Plume

References

[1] Popa, D.; Udrea, F. Towards Integrated Mid-Infrared Gas Sensors. *Sensors* 2019, *19*, 2076. https://doi.org/10.3390/s19092076

[2] Imtiaz, H.H.; Schaffer, P.; Liu, Y.; Hesse, P.; Bergmann, A.; Kupper, M. Qualitative and Quantitative Analyses of Automotive Exhaust Plumes for Remote Emission Sensing Application Using Gas Schlieren Imaging Sensor System. *Atmosphere* 2024, *15*, 1023. https://doi.org/10.3390/atmos15091023

[3] Venkatakrishnan, L., Meier, G.E.A. Density measurements using the Background Oriented Schlieren technique. *Exp Fluids 37*, 237–247 (2004). https://doi.org/10.1007/s00348-004-0807-1

DOI 10.5162/SMSI2025/C3.2

Fast Gas Chromatography Setup for Online Contaminant Monitoring in Plastics Recycling

Wolfhard Reimringer[1], *Oliver Brieger*[1], *Tilman Sauerwald*[2,3]
[1] *Saarland University, Lab for Measurement Technology, Saarbruecken, Germany*
[2] *Saarland University, Department of Systems Engineering, Saarbruecken, Germany*
[3] *Fraunhofer Institute for Process Engineering and Packaging IVV, Sensory Analytics and Technologies, Freising, Germany*
w.reimringer@lmt.uni-saarland.de

Summary:
This article presents a gas chromatography (GC) based solution for the online detection of contaminants in plastics recycling. The goal is to continuously assess post-consumer recycled plastics for adaptive treatment by stripping odorous substances and other contaminants in a compounding step. Based on earlier work, an automated sample transfer to a purpose-built GC setup has been devised. Steep heating rates and cooling rates exceeding −100 Kmin^{-1} allow for fast repetition of measurements and the integrated GC detector enables accurate peak reconstruction for dense short-column chromatograms.

Keywords: Gas chromatography, sampling, metal oxide sensor, plastics recycling, online monitoring

Introduction

Plastics recycling makes a significant contribution to sustainability as it helps to conserve finite fossil resources and reduce pollution. Therefore, legislation and commercial interests have led to recent developments in many aspects of the recycling loop. In order to reach the ambitious goals set by e.g. Directive (EU) 2018/852 [1], the recycling quota must be significantly increased. For post-consumer recycling (PCR), a major issue is the contamination of the collected material due to content residues and cross-contamination from other waste. One way to leverage PCR usage is to closely scrutinize the material at hand, ideally with continuous monitoring methods.

In prior work it has been found that a great variety of substances is present in PCR plastics processing [2], [3]. An interesting measuring location is the vacuum degassing of an extrusion process, such as the initial compounding or the recompounding steps; here, the overall conditions of molten material, high temperature and low ambient pressure force the phase change of contaminants to the headspace atmosphere [2]. However, this complicates the transfer of samples to the measurement system, especially when it needs a pressure gradient or temperature variation as it is the case with gas chromatography (GC) setups. The occurring phase transitions have been investigated [2] and a concept has been devised [3] and realized [4] to enable an online monitoring of relevant contaminants.

Materials and Methods

One main aspect of the sampling and measurement setup presented [4] is the need for fast temperature modulation of the system components. This includes the condensation/evaporation, adsorption/desorption parts as well as the GC oven and the detector; others can be stationarily tempered, e.g. valve blocks and connections. Heating can be accelerated by adding heating power when homogenous temperature spreading can be ensured [5]; however, temperature descents must be similarly enforced. This is realized by the integration of internal liquid cooling for all relevant parts. The cooling fluid is pre-cooled at −15 °C to reset starting conditions within 60 s from the components' maximum temperature, requiring cooling rates beyond −100 Kmin^{-1}. The complexity of the automated setup requires that an industrial PLC (*programmable logic control*) replaces the self-made control from the setup [2], which also enables future integration into the automation context of the processing machine.

At the heart of the GC setup, a radiation heated oven accommodates a capillary column of 0.5 m to 5 m length and is equipped with twofold cooling capabilities (air exchange and fluid cooling) and an integrated detector to prevent cold zones on the column. Low thermal mass and adjustable insulation allow for fast thermal ramps [4]. The use of a self-heating [6] or micromachined column [7] known from other fast and sensor GC applications was dismissed: Using the same FFAP as in the laboratory analyses allows to

maintain comparability with those analyses. Also, the focus in the current application is robust operation, rather than miniaturization.

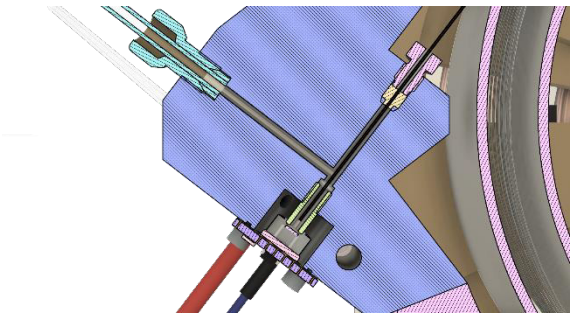

Fig. 1. Cross-section of the integrated detector in the GC oven. Makeup gas (top left) and eluents from the capillary column (top right) are applied directly to the gas sensor (bottom left).

Regarding the detector, metal oxide semiconductor (MOS) gas sensors have been found suitable as GC detectors, especially for fast GC setups with short gas peaks [8]. Certain aspects are crucial for effective detection, such as the gas transfer from the column to the sensing layer. Based on the approach shown in [9], the oven-integrated detector of Fig. 1 has a tailored nozzle that brings eluents and makeup gas directly to the sensing layer. As illustrated in Fig. 2 for a GGS 1330 (*Umweltsensortechnik GmbH, Geratal, Germany*), the resulting concentration profile at the sensor enables accurate peak reconstruction. Adding dead volume between column and sensor results in a significantly poorer gas profile as shown for the outlet of the sensor chamber.

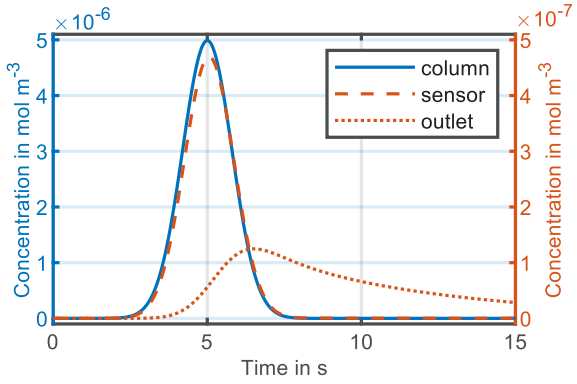

Fig. 2. COMSOL simulated peak concentrations in the column (left y-axis), on the sensing layer and at the sensor chamber exhaust (both right axis). Right y-axis scaled 10-fold to consider dilution by make-up gas.

The nozzle is exchangeable to adapt to various sensors. Fitting sensor boards have been made for analog thick-film and thin-film sensors as well as recent types with integrated digital interface.

Results and Outlook

The novel setup presented combines a complex process sampling method exploiting phase transition processes and an integrated GC oven with MOS sensor detector. This provides a fast and cost-efficient solution for the current task of contaminant monitoring in PCR plastics and will be demonstrated in on-site experiments at the compounding extruder. The setup also allows for extensive research on implementation details and adaptation to emerging applications.

Acknowledgements

This work has been funded by the German Federal Ministry of Education and Research (BMBF) under grant number 033KI116 as part of the innovation lab KIOptiPack.

References

[1] Directive (EU) 2018/852 of the European Parliament and of the Council of 30 May 2018 amending Directive 94/62/EC on packaging and packaging waste, vol. 150. 2018. [Online]. Available: http://data.europa.eu/eli/dir/2018/852/oj

[2] W. Reimringer, H. Haug, L. Seifert, and T. Sauerwald, “Sampling Apparatus for the Process Monitoring of Contaminants in Polyolefin Recycling,” in 2024 IEEE International Instrumentation and Measurement Technology Conference (I2MTC), May 2024, pp. 1–6. doi: 10.1109/I2MTC60896.2024.10560580.

[3] W. Reimringer, H. Haug, L. Seifert, and T. Sauerwald, “In-line gas phase sampling for contaminant monitoring in polyolefin recycling,” Journal of Sensors and Sensor Systems, 2025, doi: *in preparation.*

[4] W. Reimringer, H. Haug, and T. Sauerwald, “P05 - Entwicklung einer automatisierten Probennahme zur Online-Störstoffüberwachung im Polyolefinrecycling,” Poster, pp. 95–100, Nov. 2024, doi: 10.5162/17dss2024/P05.

[5] W. Reimringer, C. Bur, and T. Sauerwald, “Modular setup for temperature-controlled sampling of analytes using glassware with non-liquid thermal coupling,” Journal of Sensors and Sensor Systems, Sep. 2024, doi: *submitted.*

[6] M. D. Chopra, P. J. Müller, J. Leppert, M. Wüst, and P. Boeker, “Residual solvent analysis with hyper-fast gas chromatography-mass spectrometry and a liquid carbon dioxide cryofocusing in less than 90 s,” Journal of Chromatography A, vol. 1648, p. 462179, Jul. 2021, doi: 10.1016/j.chroma.2021.462179.

[7] S. Zampolli et al., “A palm-sized gas-chromatographic system for sub-ppb VOC detection in air quality monitoring applications,” in 2006 IEEE SENSORS, Oct. 2006, pp. 1163–1166. doi: 10.1109/ICSENS.2007.355837.

[8] T. Baur, C. Schultealbert, A. Schütze, and T. Sauerwald, “Novel method for the detection of short trace gas pulses with metal oxide semiconductor gas sensors,” Journal of Sensors and Sensor Systems, vol. 7, no. 1, pp. 411–419, May 2018, doi: 10.5194/jsss-7-411-2018.

[9] O. Brieger, S. Zhu, C. Bur, and A. Schütze, “OT5.202 - Characterization of a thick film MOS gas sensor as detector of short trace gas pulses,” Lectures, pp. 133–134, Sep. 2024, doi: 10.5162/EUROSENSORSXXXVI/OT5.202.

DOI 10.5162/SMSI2025/C3.3

Chromatographic VOC Sensing using Molecularly Cross-Linked Metal Nanoparticle Networks

Sophia C. Bittinger,[2] Lukas Mielke,[1] Jan-Niklas Beyer,[2] Tobias Vossmeyer,[2] and Hendrik Schlicke[1]
[1] Institute of Physical Chemistry and Polymer Physics, Leibniz IPF, Hohe Straße 6, 01069 Dresden, Germany.
[2] Institute of Physical Chemistry, University of Hamburg, Grindelallee 117, 20146 Hamburg, Germany
schlicke@ipfdd.de

Summary: Due to their perturbation-sensitive, tunneling-based charge transport, hybrid composite networks from molecularly stabilized and cross-linked metal nanopaticles are highly suited for the resistive detection of volatile organic compounds (VOCs). Herein we discuss recent investigations on the dynamic responses of such nanocomposite-based sensors, which are related to molecular transport phenomena. We further discuss the beneftis of employing dynamic features for the analysis of VOC mixtures and new integration schemes that enable chromatographic thin film VOC sensors for improved recognition of VOCs in complex mixtures.

Keywords: VOC sensors, gas sensors, metal nanoparticles, hybrid materials, sensor response dynamics

Chemiresistive sensing using metal nanoparticle composites[1] is enabled by the their highly perturbation-sensitive[2] charge transport mechanism, which is based on thermally activated inter-particle tunneling.[3, 4] The conductivity σ of metal nanoparticle networks is well-described by equation 1, where δ denotes the inter-particle distance, β the tunneling decay constant, E_A the charge transport activation energy, k the Boltzmann constant and T the temperature.

$$\sigma \propto e^{-\beta\delta} e^{\frac{-E_\mathrm{A}}{kT}} \quad (1)$$

Sorption of analytes, such as VOCs, within the organic material separating the nanoparticles (Figure 1a) induces swelling and consequently an increase of the inter-particle (tunneling) distance δ. This effect, as well as sorption-induced changes of the permittivity of the inter-particle organic matrix (these alter E_A), strongly affect the material conductivity.[3] Hence, via reading out the resistance of a nanoparticle composite sensing element, the presence of VOCs can be detected with high sensitivity.

Variation of the inter-particle organic material (ligands and cross-linkers with varying functional groups/polarity) influences the materials' sorption affinity and hence, their selectivity when incorporated into sensors. Since the pioneering work by Wohltjen and Snow[1] first reporting chemiresistivity in ligand-stabilized gold nanoparticle networks, tremendous research targeted altering the material systems to achieve broad variations of their selectivity and combination of different sensing elements to form sensor arrays (electronic noses).[6, 7]

While commonly (static) response amplitudes were used as sensing signals, the utilization of dynamic processes caused by molecular transport phenomena upon analyte sorption have been widely overlooked. In this contribution we present our recent advances in investigation, tuning and application of metal nanoparticle

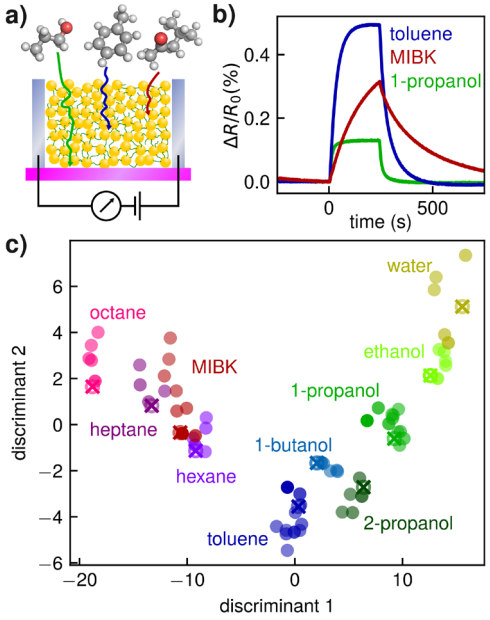

Fig. 1: a) Schematic depicting a chemiresistive sensor based on a molecularly cross-linked gold nanoparticle network. b) Resistive responses of a 1,6-hexanedithiol cross-linked gold nanoparticle chemiresistor upon transient exposure (240 s) to toluene, methylisobutylketone (MIBK) and 1-propanol at 400 ppm in nitrogen. c) Linear discriminant analysis of reponse data for a set of VOC, obtained from an array of 8 nanocomposite chemiresistors, taking into account quasi-equilibrium and dynamic features (Figure part c is reprinted with permission from [8]. Copyright 2021 American Chemical Society).

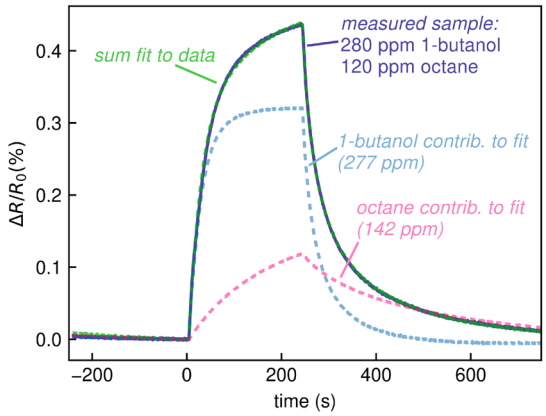

Fig. 2: Analysis of a chemiresistor response to transient exposure to a binary 1-butanol (280 ppm) / octane (120 ppm) VOC mixture. A weighted sum of transient response data previously recorded for pure components was fitted to the experimental data. Calculated concentrations correpsonding to the components' fit contributions are in good agreement with the set concentrations of the test mixture.

composite chemiresistors' dynamic responses. In a recent study, we investigated the response kinetics of dithiol cross-linked gold nanoparticle composite chemiresistors upon exposure to a set of VOCs.[8] Our results show that their sorption dynamics are selective and may be tuned via altering the composites' nanostructure, e.g., via using differently sized molecular cross-linkers or nanoparticles.
Figure 1b shows exemplary responses of a 1,6-hexanedithiol cross-linked gold nanoparticle chemiresistor to transient exposure to 1-propanol, toluene and methylisobutylketone (MIBK). Because the selectivities of dynamic response features (such as rise time or area below transient) and quasi-equilibrium features (such as sensor saturation response) differ, their combined use in conjunction with machine learning significantly improves the ability for analyte recognition. Figure 1c shows a linear discriminant analysis (LDA) employing a chemiresistor array of 8 sensors that was successfully used to discriminate between a set of analytes at varying concentrations using dynamic and quasi-equilibrium features.

While in the above experiments pure VOCs were targeted, applications in medical diagnosis via breath analysis or headspace analysis in food monitoring require discrimination between, and analysis of complex VOC mixtures. Herein, we present recent research on employing dynamic features for the analysis of binary VOC mixtures. Figure 2 exemplarily depicts a chemiresistor response to transient exposure to a mixture of 1-butanol and octane vapor. Fitting the response data with a weighted sum of response transients of the pure components yielded weights of their contributions to the fit. Based on calibration with the responses obtained for the pure VOCs, these weights are in good agreement with the set concentrations of the analyzed mixture.
These results obtained with a single chemiresistor device demonstrate that for the given set of analytes, the responses of the individual components of a VOC mixture do not interfere and superimpose to a sum response. In this contribution we discuss the benefits and applicability, as well as the limits of this linear model, when applied to a set of binary VOC mixtures.

Futher, we report current research activities aiming at the development of thin-film chromatographic gas sensor stacks. By vertical integration of multiple chemiresistive sensor layers into a device stack, spatiotemporal sensor responses are acquired upon entry of analytes. Hereby, responses with high information content for machine learning based analysis of analytes and analyte mixtures are obtained.

References

[1] H. Wohltjen, A. W. Snow, Colloidal Metal-Insulator-Metal Ensemble Chemiresistor Sensor, *Anal. Chem.* **1998**, *70*, 2856-2859, 10.1021/ac9713464.

[2] B. Ketelsen, H. Schlicke, V. R. Schulze, S. C. Bittinger, S.-D. Wu, S. Hsu, T. Vossmeyer, Nanoparticle-Based Strain Gauges: Anisotropic Response Characteristics, Multidirectional Strain Sensing, and Novel Approaches to Healthcare Applications, *Adv. Funct. Mater.* **2023**, *33*, 2210065, 10.1002/adfm.202210065.

[3] W. H. Steinecker, M. P. Rowe, E. T. Zellers, Model of Vapor-Induced Resistivity Changes in Gold-Thiolate Monolayer-Protected Nanoparticle Sensor Films, *Anal. Chem.* **2007**, *79*, 4977-4986, 10.1021/ac070068y.

[4] H. Schlicke, S. Kunze, M. Finsel, E. W. Leib, C. J. Schröter, M. Blankenburg, H. Noei, T. Vossmeyer, Tuning the Elasticity of Cross-Linked Gold Nanoparticle Assemblies, *J. Phys. Chem. C* **2019** *123*, 19165-19174, 10.1021/acs.jpcc.9b03553.

[5] R. A. Potyrailo, Toward high value sensing: monolayer-protected metal nanoparticles in multivariable gas and vapor sensors, *Chem. Soc. Rev.*, **2017**, *46*, 5311-5346, 10.1039/c7cs00007c.

[6] H. Schlicke, S. C. Bittinger, T. Vossmeyer, Lithographic Patterning and Selective Functionalization of Metal Nanoparticle Composite Films, *ACS Appl. Electron. Mater.* **2020**, 2, 3741-3748, 10.1021/acsaelm.0c00770.

[7] C.-Y. Liu, S. C. Bittinger, A. Bose, A. Meyer, H. Schlicke, T. Vossmeyer, Tuning the Interfacial Chemistry of Nanoparticle Assemblies via Spin-Coating: From Single Sensors to Monolithic Sensor Arrays, *Adv. Mater. Interfaces* **2024**, *11*, 2301058, 10.1002/admi.202301058.

[8] H. Schlicke, S. C. Bittinger, H. Noei, T. Vossmeyer, Gold Nanoparticle-Based Chemiresistors: Recognition of Volatile Organic Compounds Using Tunable Response Kinetics *ACS Appl. Nano Mater.* **2021**, *4*, 10399-10408, 10.1021/acsanm.1c01892.

DOI 10.5162/SMSI2025/C3.4

Towards Low-Cost Portable GC Systems for VOC Analysis

Omar Tarek Penagos Carrascal[1,2], Gina Zeh[1], Tilman Sauerwald[1,2]
[1] Fraunhofer Institute for Process Engineering and Packaging IVV, Department of Sensory Analytics and Technologies, Giggenhauser Strasse 35, 85354, Freising, Germany
[2] Saarland University, Campus A5.1, 66123 Saarbrücken, Germany
omar.tarek.penagos.carrascal@ivv.fraunhofer.de

Summary:
A gas chromatography system with a metal oxide semiconductor gas sensor as detector was designed, built, and tested for the detection of hexanal, octanal, and acetic acid. The system consisted of a manual sample injection using a gas-tight syringe (100 µL) and with helium as carrier gas. A free fatty acid phase column (L: 15 m x OD: 0.25 mm, coating: 0.25 µm), kept in an oven at 80°C, promoted the selectivity of the sensor via gas separation. The sensor used for detection was a Sensirion SGP40, whose four sensing layers were operated isothermally at 300°C. The system was able to measure the presence of individual compounds based on their retention times, specifically hexanal (RT ~70 s), octanal (RT: ~160 s) and acetic acid (RT: ~470 s). Sharp detector peaks were achieved from the first derivative of the sensor signal.

Keywords: Gas chromatography, VOC analysis, phase equilibrium, MOS sensor, system optimization

Introduction

Reducing the size and cost of gas chromatographs (GCs) to portable versions is a challenging task due to their high complexity. Traditional GCs incorporate expensive components to handle a wide range of applications and measure a broad range of substances. To make GCs portable and affordable, one strategy is to narrow the focus to specific applications. By doing so, it becomes possible to replace high-cost components with more affordable alternatives that can still provide adequate results for those specific scenarios.

The main objective of the current study is to conceptualize and demonstrate the feasibility of a portable GC comprising inexpensive components. The field of application is the measurement of volatile organic compounds (VOCs) for the analysis of polymer recyclates

For this purpose, it is necessary not only to build the device, but also to optimize its configuration by means of mathematical models that describe the phase equilibrium along the device, as well as to optimize the sensor system operation and data analysis. A practical approach to achieving this is to evaluate each stage of the GC process independently: Injection/sampling, separation, and detection [1]. This abstraction provides a clearer view of which parts can be simplified or replaced.

In VOC detection, a metal-oxide-semiconductor (MOS) sensor can be used as a lower-cost alternative to more complex detectors [2]. In applications where analyte concentrations are too low for detection, the use of a preconcentrator may be necessary to increase system sensitivity and maintain a reliable detection. This means that a sampling/injection system must be designed and optimized to achieve the highest preconcentration of the substance to be analyzed.

The separation takes place inside a GC column coated with a stationary phase that interacts with the different components in the sample. The difference between these interactions causes the compounds to flow at different rates through the column, resulting in separation. The challenge is to achieve a separation good enough to detect the substances of interest while keeping costs low (a GC column as short as possible and a suitable temperature program).

In this work, we present a demonstrator for the simultaneous detection of selected volatiles.

Materials and results

Helium is used as carrier gas and is introduced into the system through a mass flow controller (MFC) at a constant rate of 3 mL/min. Injection into the system was performed manually using a Hamilton gas-tight syringe, introducing a total sample gas volume of 100 µL. The syringe was used to take a headspace sample from a vial containing a mixture of the target substances. The following substances were chosen for a first qualitative test of the system: acetic acid, octanal

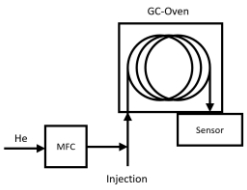

Figure 1: Process flow diagram of the system

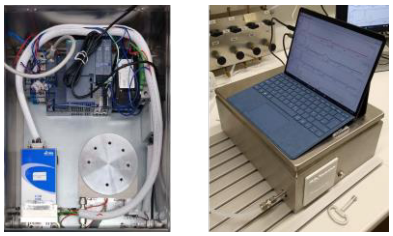

Figure 2: Interior (left) and exterior casing (right) of the system

and hexanal, which are all typical odorants in recyclates [3].

An oven was built containing a 40 W 24 VDC heating element from Triangle Labs. The temperature controller was a Wachendorff UR43838. An Agilent HP-FFAP GC column (L: 15 m x OD: 0.25 mm, coating: 0.25 µm) was installed and a sensor array SGP40 from Sensirion was connected at its outlet. The sensor system has four sensing layers, each of which deliver a signal. All sensor layers were held at 300 °C and the oven was operated isothermally (80 °C). The system was controlled by a Siemens PLC through Python using the snap7 package (see Figure 1 and Figure 2).

Figure 3 (left side) shows the signals emitted by the sensor system, with S being defined as the subtraction of the raw value from the maximum possible raw value ($S = 65535 - R$).

All four layers of the sensor show three maxima, showing that separation of the odorants within the gas mixture was successful, and the chosen sensor was able to detect the substances at the chosen concentrations. Tests with each of the substances individually confirmed that the peaks corresponded to hexanal, octanal, and acetic acid, respectively. Some peaks overlap (e.g., first sensor layer, red curve), which can make it difficult to measure the substances quantitatively or even to distinguish them. To overcome this issue, a first derivative analysis is performed on the sensor signal. For this, the curve was smoothed using the *gaussian_filter1d* function from the *SciPy* package for Python. The first derivative is shown in Figure 3 (right side).

Outlook

The developed system was able to separate the three selected substances. Further optimization and development work is currently in progress, including the design and optimization of a preconcentration/injection system to replace the manual injection, optimization of the detection stage, and evaluation with other analytes.

References

[1] M. Köhne, G. Zeh, C. Schmidt, and T. Sauerwald, “P13.4 - Entwicklung eines kostengünstigen Gaschromatographie-Systems für die Messung von Reifegas mit Kompensation der Temperatureinflüsse auf die Säule,” in *Poster*, Online: AMA Service GmbH, Von-Münchhausen-Str. 49, 31515 Wunstorf, Germany, 2021, pp. 338–342. doi: 10.5162/15dss2021/P13.4.

[2] A. Schütze *et al.*, “Highly Sensitive and Selective VOC Sensor Systems Based on Semiconductor Gas Sensors: How to?,” in *Environments*, Mar. 2017, p. 20. doi: 10.3390/environments4010020.

[3] M. Strangl, E. Ortner, T. Fell, T. Ginzinger, and A. Buettner, “Odor characterization along the recycling process of post-consumer plastic film fractions,” *Journal of Cleaner Production*, vol. 260, p. 121104, Jul. 2020, doi: 10.1016/j.jclepro.2020.121104.

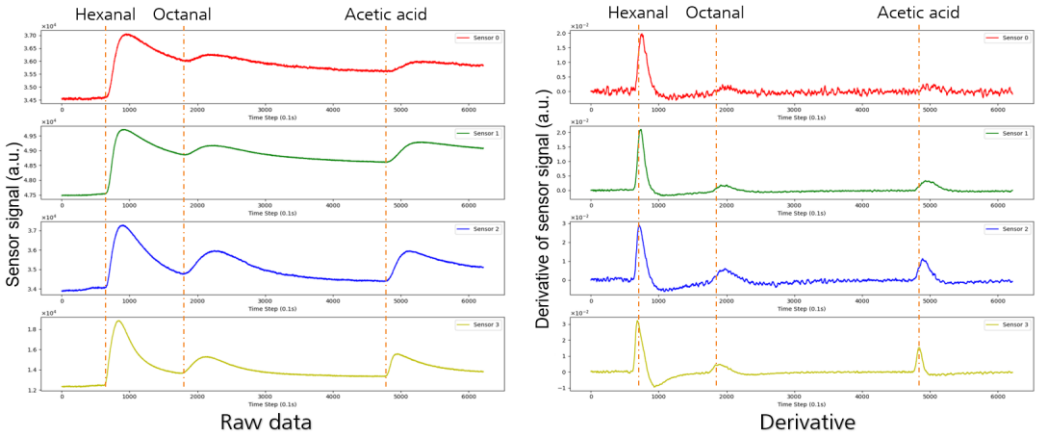

Figure 3: Measurement results, raw data (left) and derivative (right)

DOI 10.5162/SMSI2025/C4.1

Additive Manufactured Capacitive Sensor for Slip Detection with Seamless Integration of Object Recognition and Differentiation in Robot Grippers

Nikolai Hangst[1], Steffen Schröder[1], Thomas M. Wendt[1], and Stefan J. Rupitsch[2]
[1] Offenburg Universtiy of Applied Sciences, Work-Life Robotics Institute, Offenburg, Germany
[2] University of Freiburg, Department of Microsystems Engineering, Laboratory for Electrical Instrumentation and Embedded Systems, Freiburg, Germany
nikolai.hangst@hs-offenburg.de

Summary: In this contribution, we present a novel additive manufactured capacitive sensor for slip detection with seamless integration of object recognition and differentiation in robot grippers. The sensor consists of a measuring electrode in combination with guarding and shielding electrodes to reduce edge effects and disruptive influences. The results show precise slip detection through linear sensor behavior. In addition, object detection and differentiation are possible.

Keywords: Robotic, capacitive sensor, slip detection, object recognition and differentiation, additive manufacturing

Introduction

Safety in robotics is one of the central issues in shop floor scenarios with automated processes. The interaction between robots and humans must be safe [1]. This means safe gripping of the appropriate object and safe limitation of the gripping force [2]. In addition, the handling of sensitive and fragile components is essential. The components must be gripped without damage and prevented from slipping [3]. The combination of force and slip is usually determined tactilely by the coefficient of friction or by the deformation of the gripping surface [4]. Neither of these methods offers the possibility to detect and distinguish between objects. Therefore, this contribution presents a novel capacitive sensor for slip detection with additional object recognition and differentiation. The force measurement is performed separately as, for example, described in Hangst et al. [5].

Working Principle

In a configuration with two parallel gripper jaws in robotic grippers, as shown in Hangst et al. [5], the principle of a parallel plate capacitor is suitable as a sensor. The challenge of capacitive sensors in gripper technology is the individual freedom of movement and the associated unpredictable, disruptive influences. In addition, precise slip detection requires a homogeneous measuring field without edge effects. Fig. 1a shows the real world. The influences and edge effects can be reduced by applying guarding and shielding electrodes [6]. This results in an approximately idealized scenario according to Fig. 1b. The model can be described by

$$C = \varepsilon_0 \, \varepsilon_r \, \frac{A}{d}. \tag{1}$$

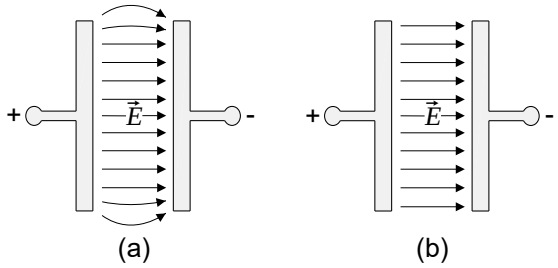

Fig. 1: Schematic representation of the electric field of a capacitive sensor. a) inhomogeneous electric field, b) homogeneous electric field.

ε_0 is the dielectric constant of vacuum, ε_r is the relative dielectric constant of the dielectric, d is the distance between the electrodes, and A is the sensor plate's area.

Sensor Design

The capacitive sensor designed by Hangst et al. [6] was utilized as the basis. The modification consists of a 1 mm thick insulating layer in the measurement area of both plates (see Fig. 2). This allows the additional possibility of gripping conductive parts. The sensor is utterly 3D printed except for the leads.

Experimental Setup

The experimental setup encompasses a capacitive sensor, an evaluation board, a PC, and an actuator. Slip detection validation was performed by pulling a 5 mm thick rectangular plastic component with uniform dimensions as the sensor out of the capacitor plates in 1 mm increments via an actuator. Capacitance measurement was performed with an EVAL-AD7747 Ca-

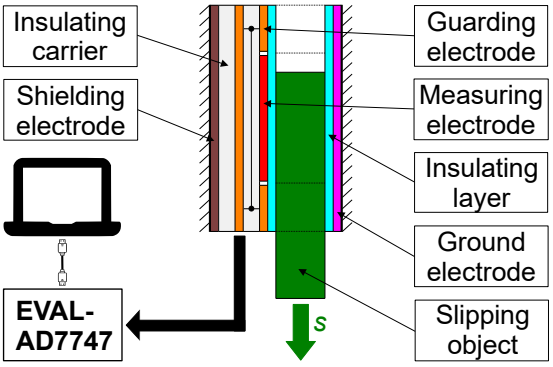

Fig. 2: Schematic experimental setup.

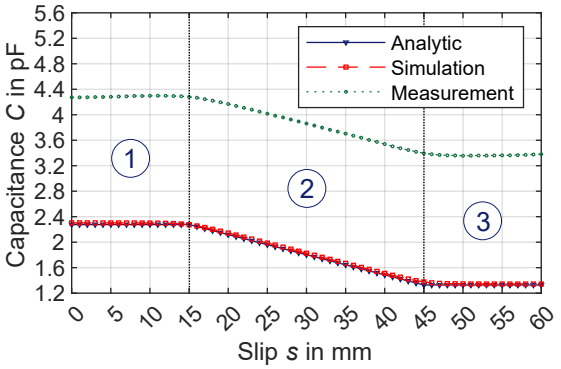

Fig. 3: Results of the analytical approach, simulation and measurement for the slip.

pacitance Digital Converter (CDC) with an accuracy of ± 10 fF and a linearity of ± 0.01 %. The CDC has a connection for an active shielding. The shield is connected to the guarding electrodes. For a statistically significant result, 100 measurements were taken, and the mean was calculated. The Data were analyzed in MATLAB. The schematic experimental setup for slip detection is shown in Fig. 2.

Results and Discussion

Fig. 3 shows the theoretical and experimental results of the sensor behavior. The analytical approach for the measuring electrode was calculated according to

$$C(s) = \frac{1}{\frac{1}{C_i} + \frac{1}{C_a + C_o}}. \qquad (2)$$

C_i is the capacitance of the insulating layer, C_a is the capacitance of the air volume, and C_o is the capacitance of the object. The simulation was carried out via COMSOL 6.2. The previously unknown relative dielectric constant of the component was obtained from the measurements. The value determined was 2.0, which is close to the values found in the literature for plastics. The sensor shows a linear behavior in the measurement area (Fig. 3, region 2). Certain deviations can be seen at the edges. The capacitance is almost constant in the area of the guarding electrodes (Fig. 3, region 1 and 2). There is an offset between analytic / simulation and measurement that can be ascribed to the parasitic capacitance of the connecting wires.

The advantage of the sensor is the possibility of additional object recognition and differentiation. This can be applied to handling other sections after determining a reference value for the capacitance in the gripped state of a component. A comparison with the reference value indicates whether or not the correct object has been gripped. The limitations of the sensor are due to the fact that the slip is detected after the displacement, not when the displacement occurs. A change in the component's material properties or geometry must also appear in the measurement field. The ideal solution is a stepped edge. In the case of homogeneous components, no slip can be detected in the measurement field.

Conclusion

In this contribution, we presented an additive manufactured capacitive sensor for slip detection with additional object recognition and differentiation. Despite the low dielectric constant of plastics in the range of 2, slip detection was possible. The capacitance measurement is linear and independent of external influences using additional guarding and shielding electrodes. The position of the subsequent gripper in space is irrelevant. An advantage of this sensor is the supplementary possibility of object detection and differentiation based on capacitance.

References

[1] A. Narendiran, B. George, Capacitive tactile sensor with slip detection capabilities for robotic applications, *IEEE Int. Instrum. & Meas. Tech. Conf. (I2MTC)*, Pisa, Italy, 464-469, (2015); doi: 10.1109/I2MTC.2015.7151312

[2] S. Blankemeyer, T. Recker, A, Raatz, Hardwareseitige MRK-Gestaltung, *Handbuch Mensch-Roboter-Kollaboration*, Hanser, Munich, 37-70, (2019); doi: 10.3139/9783446453760.002

[3] J. Yu, S. Yao, X. Li, A. Ghaffar, Z. Yao, Design of a 3-D Tactile Sensing Array for Incipient Slip Detection in Robotic Dexterous Manipulation, *IEEE Trans. Instrum. Meas.*, vol. 73, 1-14, (2024); doi: 10.1109/TIM.2024.3436064

[4] R. A. Romeo, L. Zollo, Methods and Sensors for Slip Detection in Robotics: A Survey, *IEEE Access*, vol. 8, 73027-73050, (2020); doi: 10.1109/ACCESS.2020.2987849

[5] N. Hangst, S. Junk, T. Wendt, Method for Producing a Robotic Element, in Particular a Gripper, by Means of 3D Printing, *US 11,491,717 B2*, (2020)

[6] N. Hangst et al., Design of a Grounded Low-Cost Capacitive Liquid Level Sensor for Robotics Applications, especially in the Field of Gastronomy, *ITG-Fachbericht*, vol. 303, Berlin, Offenbach, 85-89, (2022); ISBN: 978-3-8007-5835-7

DOI 10.5162/SMSI2025/C4.2

Novel Characterisation and Modeling of the Thermal Behavior of Multi-Wire SMA Actuators for Robot Grippers

Thomas M. Wendt[1], *Alexander Dierle*[1], *Thomas Seifert*[1] *and Andi Schnebel*[1]
[1]Offenburg University of Applied Sciences, Badstraße 24, 77652 Offenburg, Germany
alexander.dierle@hs-offenburg.de

Summary: This study describes the behaviour of a multi-wire shape memory alloy (SMA) actuator, with the bending angle expressed as a function of the actuator surface temperature. The temperature behaviour is quantified based on data obtained from an infrared sensor, and the hysteresis behaviour of the SMA actuator is modelled applying a sigmoid function. The least squares method is employed to identify the parameters of the sigmoid function, thereby enabling the positioning of the actuator with an average deviation of 0.5°. These results provide a foundation for position control in SMA-based robotic grippers.

Keywords: shape memory alloy, nitinol, actuator, surface temperature, robot grippers

Introduction and Motivation

Shape memory alloys (SMAs) are among the so-called 'smart materials' that have been identified by researchers as a potential avenue for application in the field of robotic grippers [1], [2]. The thermal activation of SMA can result in a change in shape between two states, a phenomenon known as the 'two-way' effect. This change is based on a transformation in the crystal structure between the martensite and austenite states [3]. The application of SMA as actuators provides a more compact alternative to servomotors, which are characterised by high volume and weight [4].

One challenge to the widespread adoption of SMA actuators is their restricted force output. While thicker SMA wires do result in an augmented force output, this also leads to an extension of the already considerable cycle time. This restricts their viability for incorporation into robotic applications [4]. Determining the position of the SMA actuators represents a challenge due to the temperature-dependent hysteresis. This can only be addressed through approaches such as the Lagoudas or Souza-Auricchio model [1], [4].

In this paper, the existing knowledge regarding the temperature-dependent deformation of SMA is applied to a SMA multi-wire actuator. This study examines the bending angle of a SMA multi-wire actuator in relation to the surface temperature of the SMA multi-wires. This provides a new foundation for control or determination of the opening angle in robot grippers, which has the potential to advance SMA technology in industrial robotics.

Methods

In order to enhance the output force without significantly extending the cycle time, a SMA actuator with a parallel configuration of four Nitinol wires with a diameter of 0.5 mm is employed. The output force increases in proportion to the number of wires up to a maximum of 7 N at the actuator edge [4], [5].

The temperature of the SMA wires is controlled by a pulse-width modulation (PWM) signal, which ensures that a predefined shape, specifically a designated angle, is attained. The surface temperature is monitored with an infrared sensor, and the heating power is adjusted based on the temperature to achieve the desired angle. Fig. 1 illustrates the measurement setup.

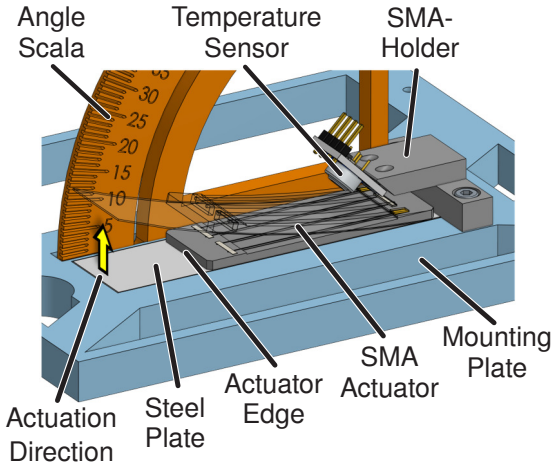

Fig. 1: Measurement setup

The COMPAKTIV 3920H is employed as the SMA actuator. It is fastened to one side and mounted on a steel plate. The Hailege MLX90614 infrared sensor is utilised as the temperature sensor. An Arduino MEGA 2560 is employed to controll the SMA. The actuator is supplied with a maximum current of 3 A.

Results

The thermal behaviour of the actuator surface was investigated experimentally, whereby the surface temperature was increased from 23 °C to 85 °C in 1 °C increments. The bending was recorded (see Fig. 2 Meas. heating/cooling). The maximum temperature of 85 °C was selected because it corresponds to the maximum bending of 20° after the permissible excitation time. The hysteresis behaviour of Nitinol can be simplified through the use of sigmoid functions. If the parameters of the function are based on the data sheet of the SMA multi-wire actuator, the observed behaviour, and a review of the relevant literature [1], [6], the experimental results are not described well (see Fig. 2 Calc. heating/cooling).

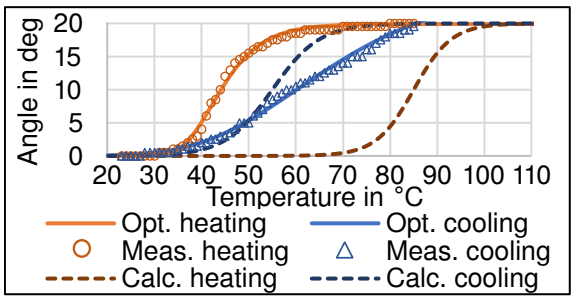

Fig. 2: Hysteresis of SMA actuator surface temperature with sigmoidal modeling

The study by Kciuk et al. provides a description of the SMA hysteresis behaviour, which offers a reference point for further analysis. The adapted formula for calculating the bending angle $\alpha_{bending}$ as a function of the surface temperature (T) is presented below [6]:

$$\alpha_{\text{bending}}(T) = \frac{\alpha_{\text{max}}}{((1+\exp(-\beta \cdot (T - T_0)))^n} \quad (1)$$

In accordance with the results of the measurement, the least squares method, as outlined by Kciuk et al., is applied to ascertain the parameters α_{max} (max. bending angle), β (max. slope of the hysteresis curve), T_0 (the mean of the start and end surface temperatures of a phase transition) and n (exponent for curve asymmetry, limited to 10 to prevent overfitting). The start and end points were given more weight to ensure consistency during cooling and heating. The results are shown in Tab. 1.

Tab. 1: Optimised parameters

Parameter	Heating	Cooling
α_{max}	19.9°	26.1°
β	0.17 1/°C	0.05 1/°C
T_0	28.87 °C	16.46 °C
n	10	10

The overall RMSE is 0.5° (see Fig. 1 Opt. heating/cooling).

Discusion

The position of a multi-wire SMA actuator can be determined by measuring the surface temperature using an infrared sensor and creating a model with an average deviation of 0.5°. A sigmoid function can be employed for the purpose of providing a simplified mathematical description of the angle change. The parameterisation of this function can not be based on standardised or manufacturer-provided data, as the measured surface temperature differs from the wire temperature. Apart from a shift in the temperature, the heating curve exhibits a similar shape (see Fig. 2 Opt./Calc. heating). The discrepancies observed in the cooling curve at temperatures exceeding 55 °C can be attributed to the non-linear hysteresis exhibited by the material and the spring-like behaviour of the steel plate. The parameters in Tab. 1 apply from 23 °C to 85 °C. It is necessary to recalculate the parameters for each distinct configuration of the SMA actuator.

Conclusion

The study demonstrates that the actuation angle of a multi-wire SMA actuator can be determined by a sigmoid function based on the surface temperature. This finding provides a basis for the position control of SMA-based robot grippers.

References

[1] S. Langbein and A. Czechowicz, *Formgedächtnistechnik: Entwickeln, Testen und Anwenden*. Wiesbaden: Springer Fachmedien, (2021); doi: 10.1007/978-3-658-17904-5

[2] M. N. Islam, M. B. Gonzalez, S. Tabassum, and K. M. M. Billah, “3d printed shape memory alloy wire embedded actuator,” in *2024 IEEE 17th Dallas Circuits and Systems Conference (DCAS)*, ISSN: 2766-5186, (2024), pp. 1–5; doi: 10.1109/DCAS61159.2024.10539916

[3] G. Stano, S. M. A. I. Ovy, J. R. Edwards, M. Cianchetti, G. Percoco, and Y. Tadesse, “One-shot additive manufacturing of robotic finger with embedded sensing and actuation,” *The International Journal of Advanced Manufacturing Technology*, vol. 124, no. 1, pp. 467–485, (2023); doi: 10.1007/s00170-022-10556-x

[4] D. Kumar, J. Daudpoto, and B. S. Chowdhry, “Challenges for practical applications of shape memory alloy actuators,” *Materials Research Express*, vol. 7, no. 7, p. 073 001, (2020), Publisher: IOP Publishing; doi: 10.1088/2053-1591/aba403

[5] CompActive GmbH, “Datenblatt sample actuator curve plugged a3920e20,” n.d.

[6] M. Kciuk, K. Chwastek, K. Kluszczyński, and J. Szczygłowski, “A study on hysteresis behaviour of SMA linear actuators based on unipolar sigmoid and hyperbolic tangent functions,” *Sensors and Actuators A: Physical*, vol. 243, pp. 52–58, (2016); doi: 10.1016/j.sna.2016.02.012

DOI 10.5162/SMSI2025/C4.3

Optimized Grasp Planning for Bin-Picking Robots with 2D and 3D Sensor Data

Roman Haas[1], *Nikolai Hangst*[1] *and Thomas M. Wendt*[1]
[1]Offenburg University of Applied Sciences, Work-Life Robotics Institute, 77652 Offenburg, Germany
roman.haas@hs-offenburg.de, nikolai.hangst@hs-offenburg.de, thomas.wendt@hs-offenburg.de

Abstract: Bin-picking systems face challenges in fully emptying containers due to collision risks in real-world scenarios. In this contribution, we present a grasp planning approach that combines 2D and 3D sensor data to ensure collision-free handling. The method is successfully tested on objects with eccentric centers of mass and is implemented directly on the robot's control unit, eliminating the need for separate computing hardware.

Keywords: robotics, bin-picking, grasp planning, sensor fusion, object detection

Introduction

Robotic bin-picking tasks are essential in industries such as manufacturing, warehousing, and logistics. Effective grasp planning remains challenging due to real-world complexities like eccentric centers of mass, the lack of collision checks with the bin, and the handling of tightly packed bins [1]. Existing methods often rely on point clouds, which are time-consuming to compute and fail to incorporate 2D information of the objects.

Related Works

Buchholz et al. [2] apply depth images and parallel projections of the gripper to evaluate various grasps from a given pose and defined degrees of freedom. Shi and Koonjul focus on automating the generation of grasps to reduce setup times in bin-picking systems [3]. Spenrath and Pott employ a heuristic tree search for grasp planning, leveraging a neural network-based approach that reduces computational time by 45 % [4]. Another approach involves the constrained placement of unknown objects, but faces problems with low accuracy and the lack of consideration for the center of mass [5].

Developed Method

The proposed grasp planning system combines 2D and 3D sensor data to localize objects within a bin. While 3D data is crucial for accurately determining object position and orientation, 2D data enhances object detection in tightly packed bins. Placement requirements of the objects can be met, as the surface texture provides feedback on the center of mass and object features that are not detected in the point cloud. Specially designed grippers reduce collision probability, but do not eliminate the need for grasp planning. Fig. 1 shows the bin-picking robot along with the coordinate systems involved.

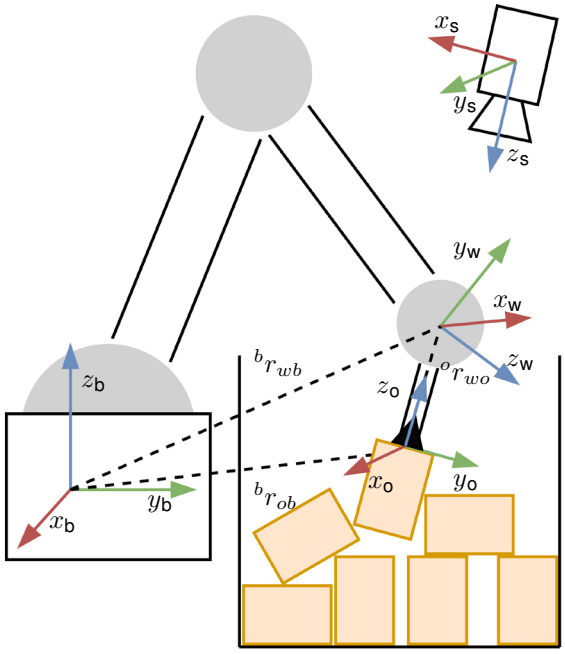

Fig. 1: Robot bin-picking with the required coordinate systems for the proposed grasp planning.

The method incorporates coordinate systems for the robot base, wrist center, sensor and object. This grasp planning approach relies on the position of the wrist center in base frame coordinates ${}^{b}r_{wb}$ (see Eq. 1).

$$ {}^{b}r_{wb} = {}^{b}r_{ob} + {}^{bo}T\,{}^{o}r_{wo} \tag{1} $$

The sensor, in combination with image processing, determines the position of the object in the sensor's coordinate system. With a valid hand-eye calibration, the object's position is then transformed to the robot base frame ${}^{b}r_{ob}$.

A three-dimensional space within the bin, where ${}^{b}r_{wb}$ is allowed during grasping, is defined by P as specified in eq. (2). In this context, all coordinates (x, y, z) refer to the base frame.

$$P = \left\{ (x, y, z) \in \mathbb{R}^3 \;\middle|\; \begin{array}{c} x_{\min} \leq x \leq x_{\max}, \\ y_{\min} \leq y \leq y_{\max}, \\ z_{\min} \leq z \leq z_{\max} \end{array} \right\} \quad (2)$$

The system is designed to be implemented on a robot controller with simple commands, without the need for additional computing power.

Experiments

We conducted experiments to test the grasp planning system, utilizing a *Yaskawa GP50* robot equipped with a vacuum gripper (see Fig. 2). For object detection, a *Roboception rcvisard 160 m-6* stereo sensor generates a 3D point cloud that includes 2D textures of the objects. The tests involved objects, which are characterized by eccentric centers of mass. For each object, multiple grasp options were defined, from which the system selected and executed a collision-free grasp with the developed method.

Fig. 2: Experimental setup of the robot performing a grasp in a bin with multiple objects with uneven center-of-mass

Results and Discussion

The experiments demonstrated that the proposed method successfully identifies collision-free grasps. The integration of 2D sensor data enhanced object detection in tightly packed bins, improving system reliability. The approach enabled the handling of objects with uneven centers of mass and features that 3D data alone cannot capture. Identifying the center of mass is critical for vacuum grippers, while small object features are essential for proper positioning, particularly when specific orientations are required. The current system does not account for potential collisions with other objects in the bin or along the robot's path to the object.

Conclusion and Outlook

The developed grasp planning system combines multimodal sensor data to increase object detection. By implementing coordinate transformations and predefined grasp points, the system calculates collision free grasping points. By considering the 2D textures of the objects, information about their center of mass can be inferred. The system operates efficiently without the need for additional computing hardware, reducing both complexity and cost.

Future work could focus on evaluating the robot's full path to the grasping point and incorporating self-learning capabilities for model-independent tasks. Key improvements could include integrating parameters such as weight, center of mass, and surface conditions to further enhance grasp reliability.

Tools

This paper benefited from OpenAI's ChatGPT, which was applied to improve grammar and sentence clarity.

References

[1] M. Schwarz *et al.*, "Fast Object Learning and Dual-arm Coordination for Cluttered Stowing, Picking, and Packing," in *2018 IEEE International Conference on Robotics and Automation (ICRA)*, May 2018, pp. 3347–3354.

[2] D. Buchholz, M. Futterlieb, S. Winkelbach, and F. M. Wahl, "Efficient bin-picking and grasp planning based on depth data," in *2013 IEEE International Conference on Robotics and Automation*, May 2013, pp. 3245–3250.

[3] J. Shi and G. S. Koonjul, "Real-Time Grasping Planning for Robotic Bin-Picking and Kitting Applications," *IEEE Transactions on Automation Science and Engineering*, vol. 14, no. 2, pp. 809–819, Apr. 2017.

[4] F. Spenrath and A. Pott, "Using neural networks for heuristic grasp planning in random bin picking," in *2018 IEEE 14th International Conference on Automation Science and Engineering (CASE)*, Aug. 2018, pp. 258–263.

[5] C. Mitash, R. Shome, B. Wen, A. Boularias, and K. Bekris, "Task-Driven Perception and Manipulation for Constrained Placement of Unknown Objects," *IEEE Robotics and Automation Letters*, vol. 5, no. 4, pp. 5605–5612, Oct. 2020.

DOI 10.5162/SMSI2025/C5.1

Programable Printing Technology Based on Spark Ablation for the Develoment of Gas Sensors

Leandro Nicolás Sacco[1], Larissa Egger[2], Maxim Popov[2], Christoph Dösinger[3], Nigel Rising[1], Lorenz Romaner[3], Niels Schouten[1], and Anton Köck[2]

[1] VSParticle, Oostsingel 209, 2612 HL, Delft, The Netherlands,
[2] Materials Center Leoben Forschung GmbH, Roseggerstrasse 12, 8700, Leoben, Austria
[3]Department of Materials Science, Montanuniversität Leoben, Franz-Josef-Straße 18, 8700 Leoben, Austria

Summary:
Herein, a manufacturing method is presented capable to screen multiple materials on a platform chip hosting 16 devices. This methodology relies on a dry printing process based on spark ablation that enable the deposition of nanoporous layers (NPLs). Different metal oxides semiconductors (MOS) compositions in form of NPLs were printed and tested as a gas sensors upon formaldehyde exposure. The focus of this work is not only on the sensing performance but also in the methods to accelerate the sensing layer production of single sensing units or an array of chemical sensors.

Keywords: Spark ablation, material screening, gas sensing, nanoporous layers, dry printing

Introduction

Gas sensing technology based on metal oxide semiconductors (MOS) needs to improve aspects related to the device selectivity [1], baseline signal drift over time [2], and power consumption [3]. Nanoengineering the sensing layers aroused as suitable approach to outperform the current device MOS device performance [4]. Then, a dry printing technology using a nanoparticle generator based on spark ablation is an attractive solution to produce nanopourous layers (NPLs) for gas sensor detection. Herein, 16 NPLs with different material compositions were printed on a platform chip [5] that were exposed towards formaldehyde gas molecules. The NPLs were based on mixtures of MOS (SnO_2, NiO, and ZnO) and metal catalysts (Ag and Au). Formaldehyde molecules at the 0.1 ppm level were detected with multiple NPLs. As a result, the presented methodology evidence the versatility and simplicity to produce: 1- gas sensing layers, 2- the screening possibility of multiple material composition in the same platform chip, 3- Fast production of an array of sensor or electronic nose.

Experimental section

Spark ablation working principle relies on generating high-energy electrical sparks between two bulk electrodes (metals or properly doped semiconductors) in a leak-tight chamber at atmospheric pressure where a high pure gas is flown. In short, the spark ionizes the gas and ablates the material from the electrodes, creating a vaporized material that rapidly cool down due to temperature difference between the spark zone and the surrounding environment [6]. If inert gas is used as a carrier, the formed NPs preserve the electrode (bulk) composition. Herein, up to three spark ablation generator VSP-G1 (VSParticle B.V.) were used to generate aerosols containing the ablated material in form of NPs [7]. Sn, Ni, Zn Au, and Ag (99.99 % purity) were used as electrodes. Argon was used as a carrier gas with a 1 liter/min flow. The spark power for each element was varied to achieve different material compositions (1.4 W- 13 W), for the catalyst content relatively low power conditions were considered to obtain a low catalyst contain in the aerosol mix (5 mol%<). Typically, Au ablation yield (even at relatively low power spark conditions) is higher than other base material [8]. Then, part of generated aerosol coming from the Au generator was removed (before the mixing aerosol zone) connecting a mass flow controller and an external pump. The generators were connected to a programmable fully dry printing system, named VSP-P1 (VSParticle B.V). NPLs were printed on a multi-sensor platform [5] hosting 16 sensors structures with a 4-probe configuration. The multi-platform chip was loaded into a chamber where the pressure is set at 0.15 mbar at room temperature. A nozzle with a 100 µm diameter orifice size was used and a throughput of 0.08 l/min. The substrate-nozzle distance was fixed at

300 µm. A 500 µm long line was printed on the sensing structure. The printing speed was set at 100 µm/s and the number of passes were varied to target a (5 ± 1) µm NPL thickness. To stabilize and fully oxide the NPLs, an annealing step was performed 400°C flowing in synthetic in a tubular furnace. For the gas sensing measurements, formaldehyde (ready-to-use mixture diluted in N_2) was introduced with stepwise concentrations of 0.1 ppm, 1 ppm and 10 ppm. Humidity level was set to 50% at 20°C, and the sensors operating temperature was 300°C. Sensor response was defined as in previous work [9].

Results and Discussions

Fig. 1 summarizes the resistance variation of 8 NPLs based on different compositions upon formaldehyde exposure steps.

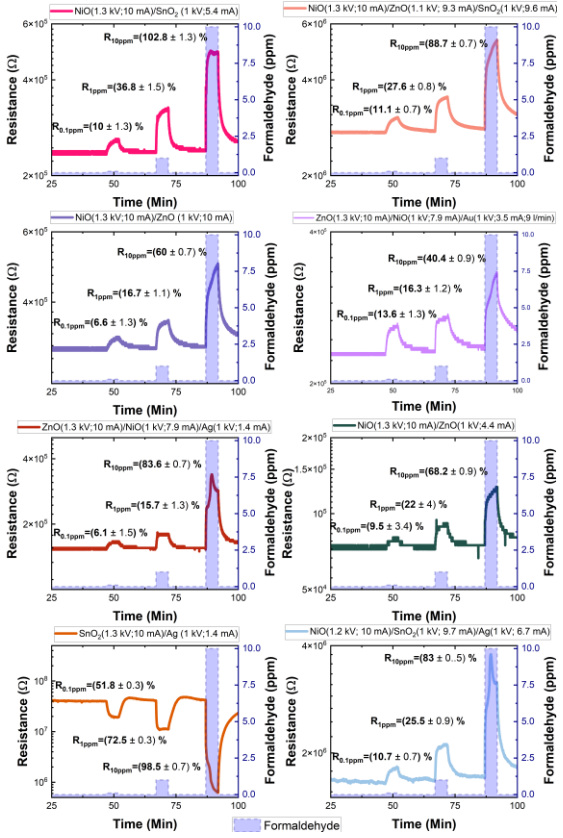

Fig. 1. Dynamic sensing response of NPLs with different material compositions upon exposure to formaldehyde gas in the concetration range from 0.1-10 ppm (Response value at each exposure are indicated).

The remaining 8 different NPLs compositions are not displayed because the device resistances were too high to measure with the used equipment. The resistance increase/decrease for each NPL under the same target gas is attributed to the p-type, n-type, p–n heterojunctions and the relative material compositions of the junctions. Remarkably, all the NPLs compositions are sensitive to 0.1 ppm formaldehyde gas molecules with relative high responses ranging from 6.1 % up to 51.8 % depending on NPL composition. Furthermore, the sensor response increases as the formaldehyde concentration continuously is increased from 0.1 ppm up to 10 ppm (no device saturation was detected).

Conclusions

Collectively, these results aim to dynamize the community work on the gas sensing sector. Firstly, showing that spark ablation coupled with programmable dry printed method can be used to produce high sensitive layers. Secondly, this methodology can substantially accelerate the material discovery to unlock new sensing layers were the current MOS based gas sensor are not capable to properly perform.

References

[1] N. Goel, K. Kunal, A. Kushwaha und M. Kumar, "Metal oxide semiconductors for gas sensing," *Engineering Reports,* 5,12604 (2023); doi: 10.1002/eng2.12604

[2] N. Dennler, S. Rastogi, J. Fonollosa, A. v. Schaik und M. Schmuker, "Drift in a popular metal oxide sensor dataset reveals limitations for gas classification benchmarks," *Sensors and Actuators B: Chemical,* 361, 131668 (2022); doi: 10.1016/j.snb.2022.131668 .

[3] A. Singh, S. Sikarwar, A. Verma und B. C. Yadav, "The recent development of metal oxide heterostructures based gas sensor, their future opportunities and challenges: A review," *Sensors and Actuators A: Physical,* 332,113127 (2021); doi: 10.1016/j.sna.2021.113127.

[4] L. Liu, Y. Wang, Y. Liu, S. Wang, T. Li, S. Feng, S. Qin und T. Zhang, "Heteronanostructural metal oxide-based gas microsensors" *Microsystems & Nanoengineering,* 8, (2022);doi: 10.1038/s41378-022-00410-1 .

[5] L. Egger, L. Reiner, F. Sosada-Ludwikowska, A. Köck, H. Schlicke, S. Becker, Ö. Tokmak, J. S. Niehaus, A. Blümel, K. Popovic und M. Tscherner, "Development of a Screening Platform for Optimizing Chemical Nanosensor Materials," *Sensors,* 24, 5565 (2024); doi: 10.3390/s24175565.

[6] R. Raymond und M. Akram, "Temporal investigation of a fast spark discharge in chemically inert gases," *Journal of Physics D: Applied Physics,* 30, 1125 (1997); doi: 10.1088/0022-3727/30/7/010.

[7] T. Pfeiffer, J. Feng und A. Schmidt-Ott,"New developments in spark production of nanoparticles," *Advanced Powder Technology,* 25, 56-70, 2014; doi: 10.1016/j.apt.2013.12.005.

[8] L. N. Sacco, L. Egger, M. Popov, C. Dösinger, N. Schouten, L. Romaner und A. Köck, "Printing Nanoporous Layers (NPL) Generated by Spark Ablation for Gas Sensing Applications," in *EUROSENSORS XXXVI*, Debrecen (2024); doi: 10.5162/EUROSENSORSXXXVI/OT5.252.

DOI 10.5162/SMSI2025/C5.2

Continuous Estimation of Particle Emissions in Flue Gas of Wood Combustion using Gas Sensor Measurements

Gunter Hagen, Ralf Moos
Zentrum für Energietechnik (ZET), Department of Functional Materials,
University of Bayreuth, D-95440 Bayreuth, Germany
gunter.hagen@uni-bayreuth.de

Summary:
Single-room wood-log fueled fireplaces are widely used but contribute significantly to harmful emissions such as carbon monoxide and fine dust. Automatically controlled operation might help to reduce health risks and environmental pollution. Therefore, in-situ measurements in the flue gas are necessary to intervene by controlling the combustion air stream automatically. As the detection of particulate matter in mass, concentration or size distribution is challenging – there are no suitable sensors available -, the particle emission shall be estimated by gas sensor data. We found correlations between hydrocarbon emissions and particulate data. The hydrocarbon concentration was evaluated from measurements with two gas sensors: an exothermicity sensor for reducing gases and a novel hydrogen sensor, both installed in the flue gas.

Keywords: biomass energy technology, wood combustion, particluate matter detection, thermoelectric CO/HC-sensor, hydrogen sensing

Background

Biomass offers a great potential to reduce greenhouse gas emissions (CO_2) from fossil sources. The use of renewable bio energy covers about 9 % of the primary energy consumption in Germany, mostly by heat generation. Wood burning comes along with massive particle emissions. In that field, more than 11 million single-room fireplaces in Germany are responsible for about 15.8 t of dust emissions [1].

In the past years, research and development efforts targeted the reduction of wood-log fueled fireplace emissions. To reduce gaseous pollutants, a sensor-based algorithm to control the primary and secondary air stream automatically in combination with the use of a ceramic noble-metal loaded catalyst was investigated. For particulate matter reduction, an electrostatic precipitator was used. Together, both concepts demonstrated to lower the total emissions of wood stoves by 80 % [2]. Of course, such systems cause high costs and will only be installed when required by law.

The aim of the present contribution follows a novel approach. Controlled operation should have high reducing potential when it is well-directed by additional in-situ information about the actual particle emission. As particulate matter detection in flue gas is challenging with sensor devices, we try to find correlations of particle data with continuous gas sensor data. Therefore, we evaluated the signals of two in-house developed gas sensors, suitable for harsh conditions. Gas data are compared to continuous particle data from a particle spectrometer (DMS 500, CAMBUSTION).

Experimental

Measurements were conducted in real exhaust from a wood-log fueled fireplace (LEDA UNICA). Sensors were installed in the vertical part of the chimney (ca. 30 cm above the burning chamber).

To detect the sum of reducing gas species (carbon monoxide and hydrocarbons), a CO/HC-sensor measures the heat generated by exothermic oxidation of the target gases at a catalyst by means of a thermopile structure. Details on the measuring principle can be found in [3], experiences when using such sensors in flue gas conditions are presented in [4]. The impressive correlation of such gas sensor response with analytics data from an FTIR is shown in [5]. A novel zeolite-based potentiometric H_2-sensor was used to determine hydrogen separately. Its general setup was formerly reported in [6]. Now, a novel thick-film-based transducer with internal heater was used to fit the needs of flue gas application. Lab measurements in synthetic gas atmosphere show the applicability (Fig. 1). Even in the presence of carbon monoxide (which is the leading component in the flue gas), the sensor responds selectively towards hydrogen.

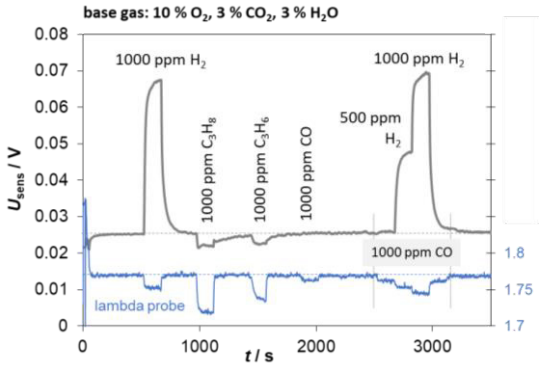

Fig. 1. Signal of a novel zeolite-based potentiometric hydrogen sensor device (H_2-sensor) in synthetic base gas with various test gases (details see text).

Results and Discussion

Several measurements with FTIR- and particle-analytics during wood combustion showed a possible correlation of hydrocarbon (HC) emissions with particle data.

To derive the HC concentration from sensor data and as the CO/HC-sensor measures a sum of CO and HC gas concentrations, we follow the consideration that the H_2- concentration in the flue gas is double the value of the CO-concentration (at least in the burn-out phase during CH_4 combustion [7]). So, the concentration values measured by the H_2-sensor divided by "2" were subtracted from the sum concentration values measured by the CO/HC-sensor (eq. 1).

$$c(HC) = c(CO/HC) - c(H_2)/2 \qquad (1)$$

Fig. 2 shows time continuous data during wood combustion exemplarily.

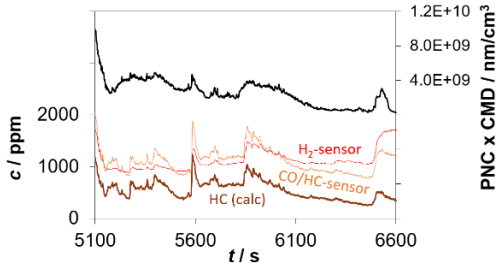

Fig. 2. Sensor measurements and particle analysis while one burning phase (stoking with "wood 3" until burn-out) as part of a combustion experiment. HC-concentration values are calculated from the sensor signals according to eq. (1).

Now, resulting continuous HC-concentration values are plotted against simultaneously collected particle data (here we used the product of the particle number concentration, PNC and the count media diameter, CMD). All data in Fig. 3 represent a more than 2-hour lasting experiment with different phases of wood burning (igniting the fire and stoking with different wood four times) with values every second.

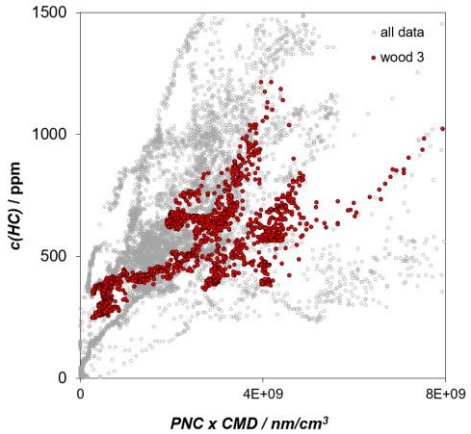

Fig. 3. Correlation of HC-concentration evaluated from two sensor measurements after eq. (1) with simultaneously collected data from a particle spectrometer (DMS 500). Highlighted points refer to data shown in fig. 2, background data to the whole experiment (more than 2 h, 9000 data points including ignition, cold start and four times stoking with wood.

Regarding the contiguous data for one burning phase ("wood 3" was the 3rd time of stoking with softwood of suggested humidity), significant correlation of the data gets visible although some assumptions might not be valid for the highly individual exhaust gas compositions during wood-log combustion. Furthermore, in comparison to the single sensor results (CO/HC or H_2), scattering of data in such display is significantly reduced. Future investigation should also take in account other secondary data such like residual oxygen concentration or temperatures to refine the results and elucidate more the interrelations of particle generation with operation parameters.

References

[1] Basisdaten Bioenergie Deutschland 2022, available online: Basisdaten.fnr.de

[2] X. Zhang, B. Ojha, H. Bichlmaier, I. Hartmann, H. Kohler, Extensive Gaseous Emissions Reduction of Firewood-Fueled Low Power Fireplaces by a Gas Sensor Based Advanced Combustion Airflow Control System and Catalytic Post-Oxidation, *Sensors* 23, 4679 (2023); doi: 10.3390/s23104679

[3] S. Wiegärtner, G. Hagen, J. Kita, W. Reitmeier, M. Hien, P. Grass, R. Moos, Thermoelectric hydrocarbon sensor in thick-film technology for on-board-diagnostics of a diesel oxidation catalyst, *Sensors and Actuators B* 214, 234–240 (2015); doi: 10.1016/j.snb.2015.02.083

[4] G. Hagen, J. Herrmann, X. Zhang, H. Kohler, I. Hartmann, R. Moos, Application of a Robust Thermoelectric Gas Sensor in Firewood Combustion Exhausts, *Sensors* 23, 2930 (2023); doi: 10.3390/s23062930

[5] G. Hagen, J. Herrmann, R. Moos, A. Müller, T. Wöhrl, Flue gas analysis of wood combustion, SMSI 2023, Nuremberg Germany, doi: 10.5162/SMSI2023/D3.4

[6] G. Hagen, R. Moos, Planar Zeolite-Based Potentiometric Gas Sensors, *Sensor Letters* 9, 1-4 (2011); doi:10.1166/sl.2011.1430

[7] T. Nussbaumer, Schadstoffbildung bei der Verbrennung von Holz, Ph.D. thesis (1989), ETH Zürich, Switzerland

DOI 10.5162/SMSI2025/C5.3

Optomechanical Gas Pressure Sensing over Broad Pressure and Temperature Ranges

Christoph Reinhardt[1], *Hossein Masalehdan* [2], *Sandy Croatto* [1], *Lea Stankewitz* [1,2], *Alexander Franke* [2], *Moritz Kunze* [1,2], *Jörn Schaffran* [1], *Nils Sültmann* [2], *Axel Lindner* [1], *Roman Schnabel* [2],
[1] Deutsches Elektronen-Synchrotron DESY, Notkestr. 85, 22607 Hamburg, Germany
[2] Institut für Quantenphysik (IQP) & Zentrum für Optische Quantentechnologien (ZOQ), Universität Hamburg, 22761 Hamburg, Germany
christoph.reinhardt@desy.de

Summary:
This paper presents novel optomechanical gas pressure sensors featuring a chip-scale mechanical resonator with ultra-low intrinsic loss, read out via an optical interferometer. In a recent experiment using a free-space optical Michelson interferometer, we demonstrated a single sensor with an unprecedented 10-decade measurement range from 10^{-7} to 10^{3} mbar. After providing a brief overview of our ongoing efforts to extend this range further towards lower pressures, we present developments of a compact, portable version of the sensor, using an optical fiber-based readout. We demonstrate this sensor's functionality over a broad temperature range from 77 K to 300 K.

Keywords: Gas Pressure Sensor, Interferometer, Nanomechanics, Vacuumtechnology, Cryogenics

Introduction

Chip-scale oscillating membranes have recently been shown to offer outstanding capabilities for gas pressure sensing. The demonstrated features are enabled by the membranes' ng-scale mass and ultra-low intrinsic loss, which are fully leveraged by measuring their oscillations using an optical interferometer.

In a recent study, we demonstrated such an optomechanical gas pressure sensor with an unprecedented measurement range, spanning 10 orders of magnitude [1]. Furthermore, a sensor for direct pressure measurements, independent of gas type, has been realized [2]. Work conducted at the National Institute of Standards and Technology (NIST) has demonstrated optomechanical pressure sensors with a total measurement uncertainty of $\sim 1\%$ [3], making them suitable as primary pressure sensors.

In this work we present our current efforts toward two main goals for optomechanical gas pressure sensors. First, we aim to extend the measurement range towards lower pressures, reaching into the ultra-high vacuum regime ($< 10^{-8}$ mbar). Second, we are developing a compact and portable version of the sensor that is applicable in typical vacuum setups. To this end the free-space optical readout is being replaced with an optical fiber interferometer.

Squeeze-Film Pressure Sensor

In Ref. [1], we present a single optomechanical gas pressure sensor covering a measurement range from 10^{-7} to 10^{3} mbar. The sensor's measurement principle relies on a pressure-dependent frictional force exerted on the oscillating membrane by impacting gas particles. This is reflected by a pressure-dependent mechanical quality factor Q, which, in the free molecular flow regime, is given by

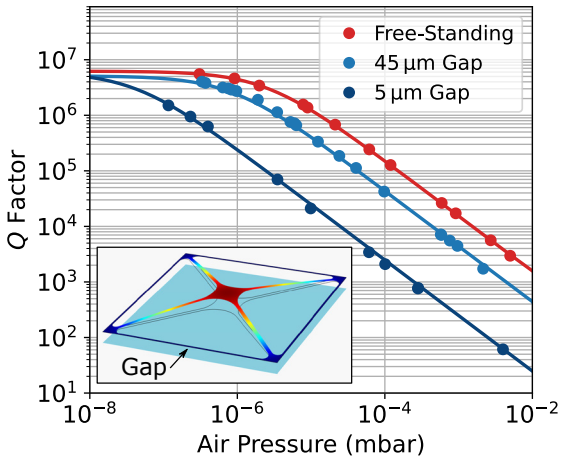

Fig. 1: Pressure dependency of the mechanical quality factor for three different trampoline pressure sensors. The inset shows a simulated oscillation mode profile of a mm-sized device, which forms a μm-scale gap with a neighboring surface.

$$Q = \left[Q_{\mathrm{in}}^{-1} + \xi \left(\frac{f \rho h}{P} \sqrt{\frac{\pi^3 k_{\mathrm{B}} T}{8m}} \right)^{-1} \right]^{-1}, \quad (1)$$

with intrinsic quality factor Q_{in}, resonance frequency f, mass density ρ, and thickness h of the membrane, as well as pressure P, temperature T, and particle mass m of the gas. The additional parameter ξ is explained in the following.

To extend the measurement range further toward lower pressures, we exploit squeeze-film damping. The inset of Fig. 1 shows a schematic of the corresponding setup. Here, a silicon ni-

tride trampoline membrane (details provided in Fig. 1 of Ref. [1]), comprising a central pad suspended by four tethers, is installed parallel to a neighboring surface, with a μm-scale gap in between. As the membrane oscillates, gas is shuttled in and out of the gap, which increases the pressure sensitivity compared to a free-standing membrane, used in the first generation of the sensor.

The red points and curve in Fig. 1 represent the measured and modelled pressure sensitivity of the free-standing trampoline, respectively (adapted from Fig. 4 of Ref. [1]). In the corresponding model function (Eq. 1), $\xi = 1$. Results for the novel squeeze-film sensor are represented by light and dark blue points and curves for 45 μm ($\xi = 4$) and 5 μm ($\xi = 62$) gaps, respectively. Compared to the free-standing trampoline, the onset of the pressure sensitivity for the squeeze-film sensor with a 5 μm gap is shifted to about sixty times lower pressure values. Overall, the relative deviation between data and respective model is within $\pm 15\,\%$.

Compact & Portable Pressure Sensor with Optical Fiber Readout

As the first step toward realizing a universally applicable version of our optomechanical pressure sensor, we replaced the free-space optical components with fiber optics. Figure 2(a) shows a schematic of the setup, where light from a laser, including an optical isolator, is split such that 90 % are directed onto photodiode 1, for monitoring laser stability, and 10 % to the membrane sensor, which reflects a fraction of this light back onto photodiode 2. The output voltages of the photodiodes are measured with a lock-in amplifier. Figure 2(b) shows a schematic of the sensor's key components, an optical fiber pointed at an oscillating square membrane. The membrane's oscillation is measured via amplitude modulation of the reflected light, which results from interference of the part directly reflected at the fiber tip and the part reflected by the membrane back into the fiber. Panel (c) shows a photograph of the membrane, suspended from a periodically patterned silicon chip (for suppressing the coupling to the support structure).

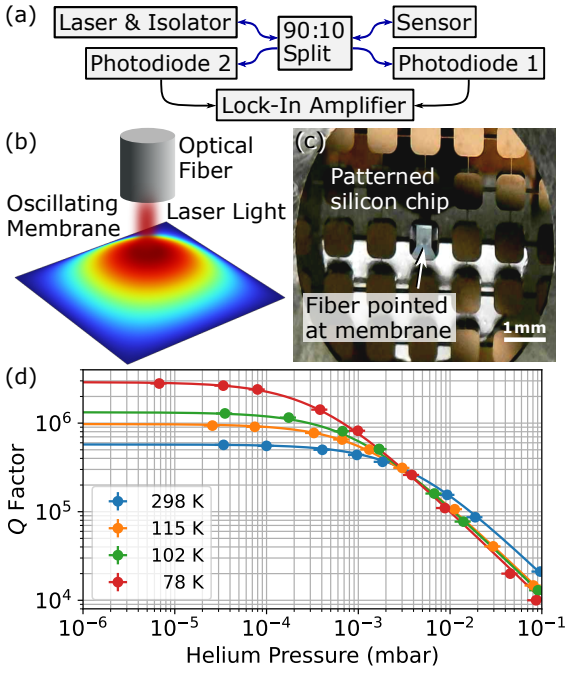

Fig. 2: Optomechanical gas pressure sensor with fiber-based readout setup (a) and key sensor components (b). (c) Photograph of the square silicon nitride membrane, suspended from a periodically patterned silicon chip. (d) Helium pressure dependence of the mechanical quality factor at different temperatures.

We measured the dependency of the sensor's mechanical quality factor on the surrounding helium pressure, inside a liquid nitrogen dipper cryostat. Figure 2(d) shows the results, at four different temperatures, where the data points are shown together with the corresponding model functions (Eq. 1, $\xi = 1$), each represented by a curve of the same color. The relative deviation between each data set and its corresponding model function is within $\pm 15\,\%$, as obtained for the squeeze-film sensor (presented above). The observed fivefold increase in the intrinsic quality factor from $Q_{\mathrm{in}} = 6 \times 10^5$, at 298 K, to $Q_{\mathrm{in}} = 3 \times 10^6$, at 78 K, follows the general trend for silicon nitride membranes.

Conclusion

We demonstrate that exploiting squeeze-film damping in optomechanical gas pressure sensors expands their measurement range to pressures sixty times lower than an otherwise identical sensor without squeeze-film damping. Furthermore, we developed a compact, portable optomechanical pressure sensor with fiber-optic readout. This sensor is compatible with cryogenic temperatures, where it provides an extended measurement range compared to room temperature, due to a fivefold increase in its intrinsic mechanical quality factor.

References

[1] C. Reinhardt, H. Masalehdan, S. Croatto, A. Franke, M. B. Kunze, J. Schaffran, N. Sültmann, A. Lindner, R. Schnabel, Self-Calibrating Gas Pressure Sensor with a 10-Decade Measurement Range, *ACS* Photonics, 11(4), 1438-1446 (2024); doi: 10.1021/acsphotonics.3c01488

[2] M. Salimi, R. V. Nielsen, H. B. Pedersen, A. Dantan, Squeeze film absolute pressure sensors with sub-millipascal sensitivity, *Sensors and Actuators A: Physical*, 374, 115450 (2024); doi: 10.1016/j.sna.2024.115450

[3] O. R. Green, Y. Bao, J. R. Lawall, J. J. Gorman, D. S. Barker, Accurate, precise pressure sensing with tethered optomechanics, *arXiv preprint* arXiv:2409.00256 (2024); doi: 10.48550/arXiv.2409.00256

DOI 10.5162/SMSI2025/C5.4

A Calibration-free Mid-Infrared TDLAS Sensor for Stand-Off Detection of Carbon Dioxide operating at 2004 nm

Paul Schaffer[1], Hafiz Hashim Imtiaz[1], Benjamin Lang[1], Martin Kupper[1], Alexander Bergmann[1]
[1] Institute of Electrical Measurement and Sensor Systems, University of Technology, Graz, Austria
paul.schaffer@tugraz.at

Summary:
This work presents a system concept for remote emission sensing, focusing of the design and validation of a calibration-free wavelength modulation spectroscopy (CF-WMS) approach. We show the applicability of a CF-WMS system for the detection of CO_2 emissions of on-road vehicles with laboratory validation measurements as well as first field tests.

Keywords: Remote Emission Sensing, Calibration-Free Wavelength Modulation Spectroscopy, TDLAS, Carbon Dioxide Monitoring, Vehicle Emissions

Introduction:

Emission regulations employed by institutions such as the European Union aim to reduce the emissions by vehicles on the road. These measurements have shown success for compliant vehicles, yet still 90 % of on-road emission are caused by 15 % of vehicles, commonly known as high emitters [1]. Identifying those high-emitting vehicles can help in the overall reduction of on-road emissions.

Remote Emissions Sensing (RES) has been shown to be a suitable tool for emission monitoring. In RES, the emissions of vehicles are measured by measurement systems installed at the roadside. This allows for a non-invasive measurement on the one hand, while one the other hand captures thousands of vehicles per day under normal driving conditions.

In the field of RES CO_2 emissions are commonly used in the determination of fuel related emission factors. Therefore, an accurate and reliable measurement of the emitted CO_2 and pollutant concentration is necessary.

In this work we present a system for calibration-free wavelength modulation spectroscopy for RES, characterization details and measurement results. The characterization of laser parameters omits the need for reference measurements during operation, while the principle itself has been shown to provide high accuracy, even in harsh conditions [2].

System Concept:

For our measurement system we use a DFB laser diode for the selected CO_2 absorption line at 2004 nm, as it shows limited cross interference to H_2O while having suitably high absorption, even at ambient CO_2 concentrations. Our system is additionally equipped with an ICL targeting NO_2 at 3421 nm, and an ICL for NO at 5263 nm is prepared. Furthermore, we aim to involve NH_3 measurements in the future.

Measurement Methods:

Wavelength Modulation Spectroscopy (WMS) is a specialized application of Tunable Diode Laser Absorption Spectroscopy. Here the injection current of the DFB laser is modulated by two superimposed sinusoidal signals: a low frequency scan (f_s = 11.92 Hz) and a high frequency modulation (f_m = 70 kHz).

The resulting amplitude modulation of the absorption feature is demodulated at f_m and $2f_m$ using a Lock-In amplifier. From the demodulated signals the resulting amplitude is calculated. As background absorption as well as nonlinear intensity effects can occur, both background and absorption *2f* signals must be normalized by the laser intensity contained in the *1f* signal [3]:

$$S_{2f/1f} = \sqrt{\left(\left(\frac{X_{2f}}{R_{1f}}\right)_{raw} - \left(\frac{X_{2f}}{R_{1f}}\right)_{bg}\right)^2 + \left(\left(\frac{Y_{2f}}{R_{1f}}\right)_{raw} - \left(\frac{Y_{2f}}{R_{1f}}\right)_{bg}\right)^2} \quad (1)$$

Here X_{2f} and Y_{2f} are the in-phase and quadrature components of the Lock-In Amplifier at *2f*, while R_{1f} is the root-sum-square of the *1f* outputs [3].

Measurement of Laser Parameters:

The emitted light of the laser can be described by its intensity and wavelength response. Accurately determining those laser parameters allows for a detailed modeling of the absorption process [4]. By simulating the Lock-In detection as well,

the signal, as detected in the measurement, can me modeled. This model is then used to determine the concentration from the measured signal by a fitting process.

Validation of Signal Reconstruction:

The CF-WMS approach was validated in terms of the reconstruction of concentration values from the measured WMS signal. Using a gas diluter, a range of gas concentrations were introduced into a gas cell with a pathlength of 2 m. Absorption spectra were recorded for each concentration. To account for absorption by ambient CO_2 concentrations the gas cell was filled with pure N_2 to record a background signal. Signals were averaged over 16.7 s.

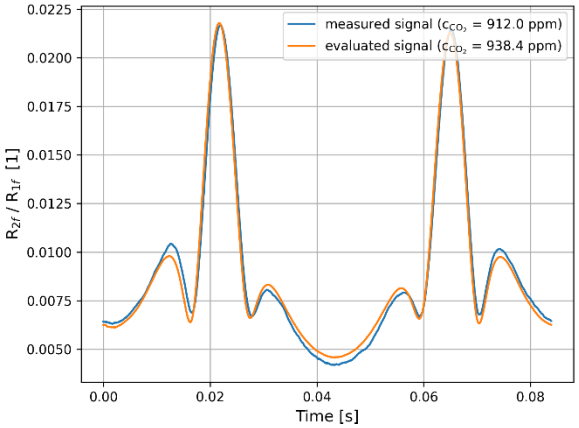

Fig. 1: Comparison between a measurement of 912 ppm CO_2 over a pathlength of 2 m and the corresponding evaluated concentration.

In Fig. 1 an example of measurement and evaluated spectrum is given. The evaluated measurement of the CO_2 concentration shows only an error of 2.98 %, which considering the low concentration and short pathlength shows to usability of this system concept for RES applications.

On-Road Measurement:

The CF-WMS system was further tested in a real-world scenario on the road. With the spectroscopy unit placed on one and the reflector unit on the side of the road a measurement pathlength of 10.18 m was realized. A diesel passenger car was used as a test vehicle. The considered measurement event started 2.5 s before the vehicle entered the measurement location. The Lock-In outputs were recorded for a total time of 22 s.

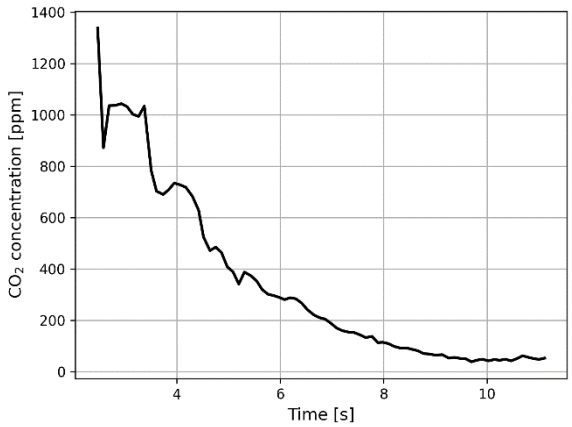

Fig. 2: Measured pathlength-averaged CO_2 concentration of a passing diesel vehicle.

Data collected before the vehicle entered the measurement location was used as the background signal and used in the background correction (1). The modeled absorption was then fitted to the background corrected signal to obtain the average CO_2 concentration over the pathlength of 10.18 m. In Fig. 2 the evaluated CO_2 concentration during the measurement event is shown.

Conclusions and Outlook

The presented CF-WMS setup has been validated in laboratory measurements showing its potential for a calibration free measurement of CO_2 concentrations, while first measurements in RES applications showed promising results.

The work regarding additional laser source for the detection of the pollutants described above is ongoing. Superimposing the laser beams for all analytes allows us to measure all concentrations simultaneously.

By combining this measurement approach with a gas imaging technique further enhances the systems capabilities to measure absolute concentrations for all targeted analytes [5].

References

[1] M. Bainschab, et. al., “Particle number measurements within periodic technical inspections: A first quantitative assessment of the influence of size distributions and the fleet emission reduction,” Atmospheric Environment: X, vol. 8 (2020); doi: 10.1016/j.aeaoa.2020.100095

[2] H. Li, et. al., "Extension of wavelength-modulation spectroscopy to large modulation depth for diode laser absorption measurements in high-pressure gases," Appl. Opt. 45, 1052-1061 (2006); doi: 10.1364/AO.45.001052

[3] G. Rieker, et. al., “Calibration-free wavelength-modulation spectroscopy for measurements of gas temperature and concentration in harsh environments," Appl. Opt. 48, (2009); doi: 10.1364/AO.48.005546

[4] C. Goldenstein, “Wavelength-modulation spectroscopy for determination of gas properties in hostile environments”, [Doctoral dissertation, Stanford University] (2014)

[5] H. Imtiaz, et. al., “Qualitative and Quantitative Analyses of Automotive Exhaust Plumes for Remote Emission Sensing Application Using Gas Schlieren Imaging Sensor System”, *Atmosphere* 15, no. 9: 1023 (2024); doi: 10.3390/atmos15091023

DOI 10.5162/SMSI2025/C6.1

Toward a Digital Twin of Hydrogen Pressure Vessels Enabled by Distributed Fiber Optic Sensors

Christos Karapanagiotis, Marcus Schukar, Mathias Breithaupt, Konstantin Hicke
Bundesanstalt für Materialforschung und-prüfung, Berlin, Germany
konstantin.hicke@bam.de

Summary:
We present a digital replica of a hydrogen pressure vessel enabled by distributed fiber optic sensors (DFOS). This digital replica dynamically displays and updates the vessel's structural condition by calculating strain residuals defined as the difference between the measured DFOS strain and the expected strain based on pressure data. As an example, we show the ability of the DFOS to detect and localize damage caused by drilling six holes into the vessel's body. This digital replica represents a foundational step toward a fully integrated digital twin for predictive maintenance and remaining lifetime prognosis.

Keywords: fiber optic sensors, structural health monitoring, predictive maintenance, hydrogen, digital twins

Introduction

The demand for composite overwrapped pressure vessels (COPVs) for hydrogen storage is expected to rise significantly in the future, driven by the ongoing energy transition toward sustainable sources. Therefore, an efficient and cost-effective solution to ensure safety and long-term sustainability is of high importance. Currently, COPVs are operated under strict regulations, including regular and time-consuming inspections to assess their structural integrity [1]. The need of these regular inspections could be partially eliminated by using DFOS for continuous and real-time monitoring. So far, DFOS have been used for COPV monitoring only under stable pressure conditions [2,3].

In this paper, we present, to the best of our knowledge, for the first time a digital replica of a hydrogen pressure vessel that dynamically updates the structural condition by analyzing real-time DFOS and pressure data. We show that digital twins based on data streams from DFOS could facilitate predictive maintenance and remaining lifetime prognosis.

Results

Fig. 1a shows a section of the tested COPV with surface-applied optical fibers, along with damage caused by drilling six holes into the composite structure. The optical fibers were wrapped circumferentially around the COPV with a relatively fixed wrapping angle, ensuring that the distance between two consecutive windings was approximately 20 mm. Because these fibers are generally sensitive to both strain and temperature, additional strain-free optical fibers were used to compensate the temperature effect. To render these fibers strain-free, they were placed inside capillary tubes glued along the vessel's horizontal direction. Two of these capillary tubes are visible in Fig. 1a.

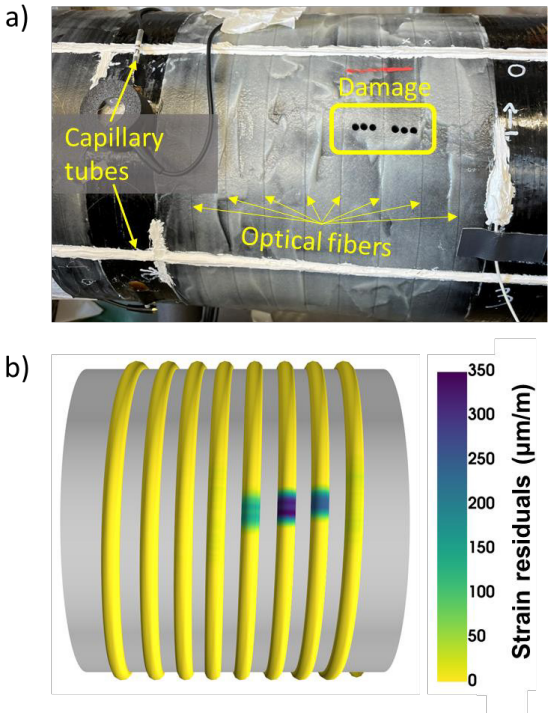

Fig. 1. A composite overwrapped pressure vessel (COPV) with damage caused by drilling six holes, monitored using distributed fiber optic sensors (a), and a 3D visualization of the calculated strain residuals.

Fig. 1b shows a 3D visualization of the DFOS results after drilling six holes of a depth and diameter of 8 mm and 4 mm, respectively. DFOS measurements were conducting using the commercial interrogator LUNA ODiSI 6100 (Luna Innovations Inc., Roanoke, VA, USA). Further details about the sensing technique can be found in [4]. We observe that DFOS are able to detect, localize and quantify the damage in terms of strain residuals. The strain residuals result from the difference between the measured strain and the expected one under normal (undamaged) conditions. The expected strain arises from a simple regression model that outputs strain based on pressure data [5].

Results from previous experiments show that DFOS are also capable of providing early indications of damage through strain residuals, even a few thousand of pressure cycles before failure [2]. These results, combined with the real-time sensing capabilities, can clearly open the way for the development of digital twins, such as the one shown in Fig. 2.

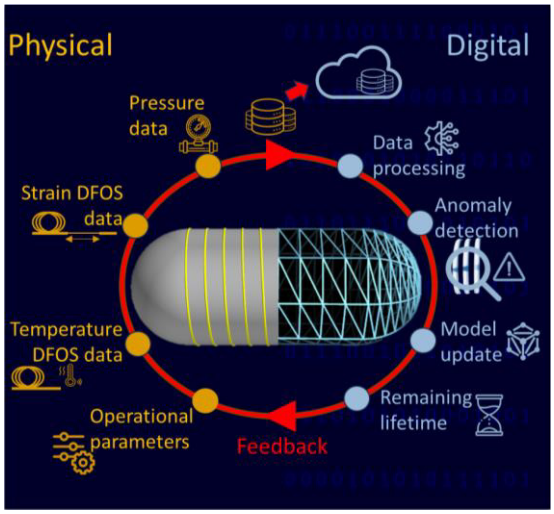

Fig. 2. The concept of a digital twin enabled by distributed fiber optic sensors (DFOS). DFOS and pressure data are sent in real-time from the physical to the digital domain. In the digital domain, the data are processed, anomalies are detected, remaining lifetime is predicted, and commands are sent back to the physical object.

The physical object is the real COPV instrumented with DFOS. The DFOS data along with pressure data are sent to a cloud. The digital replica is updated in real-time using the data stream from the physical object. In the digital domain, the data are processed and anomalies, like the one shown in Fig. 1b are detected. Then feedback is sent to the physical domain to determine whether to continue or terminate the operation.

While our system is able to detect early signs of damage in COPVs, it is currently unable to reliably assess the severity of the detected damage. Future work will focus on developing machine learning methods to classify damage severity and estimate the COPV remaining service lifetime. The estimation of the remaining lifetime is expected to reduce maintenance costs, enable more timely inspections, enhance the sustainability of the technology, and yield positive economic impacts overall. To achieve this, we will make use data from previous experimental campaigns as well as data to be collected from planned future experiments. However, we need to mention that due to the time-consuming and expensive nature of such experiments, simulations and probabilistic machine learning algorithms that can generalize well even with limited data should be employed.

Conclusions

We have reported to the best of our knowledge for the first time on a digital replica of a hydrogen pressure vessel enabled by DFOS data. Up to now, the digital replica allows for anomaly detection based on DFOS and pressure data. In the future, we will also include data from other COPVs that have already been tested and in combination with probabilistic machine learning, we will incorporate remaining lifetime prognosis.

Acknowledgements

We would like to acknowledge the funding received from the Federal Ministry for Economic Affairs and Climate Action. We would also like to thank Stephan Gohlisch for the technical support and all our colleagues from the QI-Digital project for the great collaboration.

References

[1] ISO 16528-1:2007. Boilers and pressure vessels. Part 1: Performance requirements, https://www.iso.org/standard/41079.html

[2] C. Karapanagiotis, M. Schukar, K. Krebber. Distributed fiber optic sensors for structural health monitoring of composite pressure vessels. *tm - Technisches Messen* 91, 168-179 (2024), doi:10.1515/teme-2023-0170.

[3] G. Souza, J.R. Tarpani. Using OBR for pressure monitoring and BVID detection in type IV composite overwrapped pressure vessels. *J Compos Mater* 55, 423-436 (2020), doi:10.1177/0021998320951616.

[4] M. Froggatt, J. Moore. High-spatial-resolution distributed strain measurement in optical fiber with rayleigh scatter. *Appl Opt* 37, 1735-1740 (1998), doi:10.1364/ao.37.001735.

[5] C. Karapanagiotis, M. Breithaupt, E. Duffner, M. Schukar. Real-time monitoring of hydrogen composite pressure vessels using surface-applied distributed fiber optic sensors. *JPhys: Photonics*, in press (2025), doi: 10.1088/2515-7647/adb9ac.

DOI 10.5162/SMSI2025/C6.2

Hydrogen Safety - Dealing with Closed Spaces

Keerthana Nattuveettil[1], Christian Liebner[1], Carlo Tiebe[1]
[1] Bundesanstalt für Materialforschung und -prüfung,
Keerthana.Nattuveettil@bam.de

Summary:
Hydrogen is under discussion as a potentially clean energy source, but its safe usage and handling in enclosed environments remains a critical challenge due to the properties of hydrogen. This work focuses on detecting and monitoring hydrogen concentration in closed spaces to improve safety by developing a sensor network-based leak detection system to prevent of the accumulation of hazardous mixtures. Furthermore, the study details the implementation of a hydrogen sensor network within a container, analysing sensor placement, data collection, and safety improvements. The findings contribute to better risk assessment and enhanced safety protocols in hydrogen storage and usage facilities.

Keywords: Hydrogen, Safety, Sensor network, Refuelling Station, Measurement Uncertainty

Background

In recent years, strategies for using hydrogen for decarbonisation have been proposed. An interesting example is the National Hydrogen Strategy of Germany [1]. These strategies also include increased research into the safety aspects of hydrogen to ensure public acceptance and reduce the risk of financial and human losses due to unforeseen hazards. This paper deals with the analysis of hydrogen release dynamics in an enclosed space and the use of sensor technology to detect a leak at an early stage and implement safety measures before potentially hazardous conditions are reached.

Introduction

Safe handling of hydrogen in enclosed spaces presents challenges due to its low molecular weight, high diffusivity, and wide flammability range [2]. A common practice in Europe is using containers to divide the hydrogen usage area with containers. As these areas are smaller and closed, a sensor network to find leaks is necessary [3]. Knowing the influence of ventilation on the dynamics of hydrogen in closed areas is essential to determine the placement of the sensors.

Figure 1 shows the flammability diagram for H_2-AIR-N_2 mixtures, which provides a critical framework for assessing hydrogen-related explosion hazards in enclosed environments. It graphically defines the flammable region where combustion can occur based on the volumetric composition of hydrogen (H_2), Air (Oxidizers in air), and nitrogen (N_2). The area is bounded by the lower flammability limit (LFL) and upper flammability limit (UFL), outside of which ignition is not sustainable [4].

In closed spaces, inert gases like nitrogen significantly influence flammability by suppressing flame propagation and altering the minimum ignition energy requirements. In less-ventilated areas, hydrogen accumulation can create flammable mixtures.

Understanding the flammability limits in confined spaces is essential for designing effective sensor networks, implementing ventilation strategies, and ensuring safe hydrogen storage and handling in industrial and energy applications.

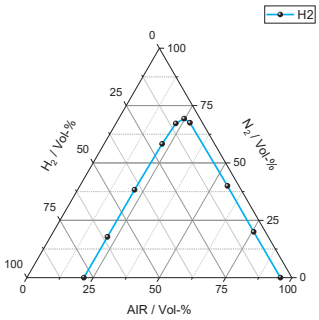

Fig 1: The flammability diagram for H_2-AIR-N_2 mixture.

The main goal of this experiment is to find the hydrogen dynamics in the container, exemplary for a hydrogen electrolyser unit. The time to disperse the hydrogen after a leak is determined to make a safety protocol.

Experimental Setup and Sensor Network

The experiment was conducted in different phases. Initially, a database of commercially

available sensors developed during the project H2-Sense [5] was updated to a Microsoft -Access based system. The sensor XEN-5320 from Xensor was selected for its fast response, making it suitable for leak detection.

The sensors are distributed across the container at different levels to determine the hydrogen volume fraction. As soon as the controlled release of hydrogen is stopped, the escape of the hydrogen in the containment is determined without external airflow. This will help continuously monitor the hydrogen concentration and help find the formation of potential explosion mixtures.

The two corresponding equations are:

$$\phi_{H2}(t) = \beta \cdot t + a \quad (1)$$

$$\phi_{H2}(t) = \phi_{H2-CRM} \cdot e^{-t \cdot \tau} \quad (2)$$

where β is the rate of increase of hydrogen concentration, φ_{H2} is the hydrogen concentration in Vol-%, a is the axis intercept, ϕ_{H2-CRM} is the volume fraction of the used certified reference material in Vol-% (“MXC-Mixture” with 5.55 Vol-% ± 0.11 Vol-% Hydrogen in Nitrogen, AirLiquide, i.e. this mixture can be mixed with any amount of air and will never form an explosive mixture), t is the time in min and τ is the loss constant / min.

Results

In this study, uncertainty was evaluated using the GUM (Guide to the Expression of Uncertainty in Measurement) framework, incorporating both Type A (statistical) and Type B (systematic) uncertainties. The expanded uncertainty for hydrogen concentration (φ_{H_2}) was determined to be 0.017% at a 95% confidence level, indicating the precision of the sensor measurements. Contributing factors include uncertainties in container volume (V_{con} = 26.16 m³ ± 0.02 m³), gas exchange rate (n = 0.72 h⁻¹ ± 0.05 h⁻¹), and retention time (τ = 5020 s ± 370 s). The discrepancy between theoretical and measured concentrations ($\Delta\varphi_{H_2}$ = -0.121% ± 0.080%) highlights the impact of sensor response variations and environmental conditions. Characterisation of these uncertainties ensures reliable hydrogen safety monitoring in closed spaces and supports the development of more robust detection strategies.

Figure 3 (a) shows the increase in the concentration during the hydrogen release and various alarm levels. Figure 3 (b) shows the distribution of hydrogen within the container by natural dispersion. The sensors closer to the windows show lesser concentrations, showing faster dissipation near the windows even when closed. The accumulation of hydrogen is first seen at the top of the container, with maximum accumulation near the leak source.

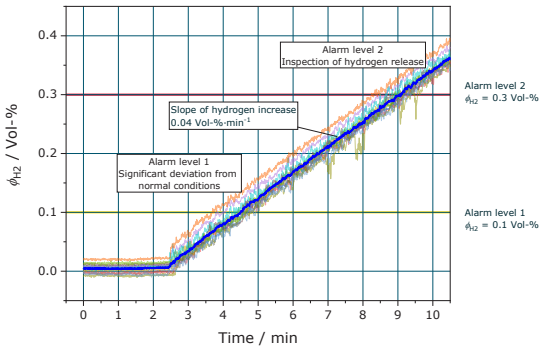

(a)

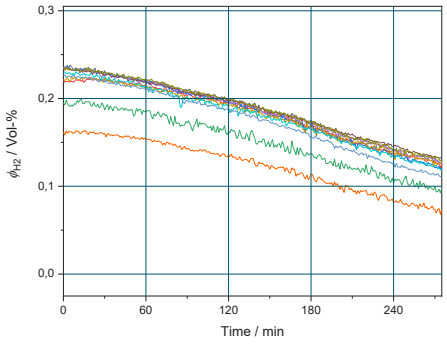

(b)

Fig 3: (a) shows the concentration increase in the container during the controlled release of hydrogen. (b) Shows the dispersion of hydrogen as detected by different sensors without any external ventilation

The findings validate the effectiveness of a sensor network for real-time leak detection and provide critical insights for optimising sensor placement and improving hydrogen safety strategies in closed environments.

References

[1] Die Nationale Wasserstoffstrategie https://www.bmwk.de/Redaktion/DE/Wasserstoff/Dossiers/wasserstoffstrategie.html

[2] Cameo chemicals, hydrogen https://cameochemicals.noaa.gov/chemical/8729

[3] Rao, V.C.M & Wen, J.X. (2019). Modelling approach for vented lean deflagrations in non-rigid enclosures. Proceedings Ninth International Seminar on Fire and Explosion Hazards (ISFEH9), 21-24 April 2019, Saint Petersburg, Russia, Vol. 1: 393-402. DOI 10.18720/SPBPU/2/k19-81

[4] M. Molnarne, T. Schendler, V. Schröder, in Sicherheitstechnische Kenngrößen, Vol. 2, Wirtschaftsverlag NW, Bremerhaven, 2008, pp. 1-539. https://www.chemsafe.ptb.de/home

[5] T. Hübert, (2016), H2Sense - Cost-effective and reliable Hydrogen Sensors for Facilitating the Safe Use of Hydrogen, urn: nbn:de: kobv:b43-387484

DOI 10.5162/SMSI2025/C6.3

Analysis of Methods for Predicting H_2 Sensor Responses

Raduan Sarif [1], Carlo Tiebe[1] and Christian Herglotz[2]
[1] Bundesanstalt für Materialforschung und -prüfung (BAM), Berlin, Germany
[2] Brandenburgische Technische Universität Cottbus-Senftenberg, Cottbus, Germany
Raduan.Sarif@bam.de

Summary: Hydrogen (H_2) is crucial for replacing fossil fuels and achieving net-zero emissions, but its flammability and explosiveness pose safety challenges. Rapid H_2 leak detection is essential for triggering emergency accidents. However, H_2 sensor response is constrained by material properties and gas flow dynamics, causing response and detection delays. Our current study explores various available algorithms for H_2 sensor response prediction from early responses with a small time window, accelerating leakage detection. Our findings identify the most efficient algorithms for real-time implementation, enhancing H_2 safety systems.

Keywords: H_2 safety,early H_2 leakage detection,stable H_2 value prediction, prediction algorithms

Introduction

(H_2) plays a significant role in clean energy, but its storage and transportation pose several challenges due to leakage and permeation. Leakage occurs through structural defects, while permeation involves the slow diffusion of hydrogen through materials. These risks are heightened in high-pressure storage, increasing the potential for rapid release and ignition. To address risk concerns, sensor systems with advanced predictive algorithms are essential for early hydrogen safety, especially leak detection. The algorithms improve detection speed and accuracy by analyzing transient response signals and estimating stable sensor values. Numerous studies have explored predictive modeling for hydrogen sensor response. Shi et al. applied a CNN-LSTM model to forecast hydrogen concentration for rapid detection [1]. Hübert et al. developed a mathematical approximation algorithm to estimate the sensor t_{90} response time [2]. Osorio-Arrieta et al. utilized the Gauss-Newton method to accelerate the measurement time by fitting transient response curves [3].

Existing literature primarily focuses on predicting sensor response using the entire H_2 sensor response. This study focuses on algorithms that predict H_2 entire sensor response from an early small time window of the sensor response. Our study evaluates various algorithms' mathematical feasibility and practical applicability for sensor response prediction while providing a comprehensive overview of methods used in H_2 sensor analysis.

Hydrogen Sensor Response Behavior

In gas measurement, a sensor reacts to a change in gas concentration, resembling a negative exponential curve as the hydrogen concentration increases [4, 5]. Ideally, the sensor response is stable when it reaches the targeted H_2 gas concentration. However, sensor response can be affected by both extrinsic and intrinsic factors. Extrinsic factors include gas delivery dynamics and data acquisition delays. In contrast, the intrinsic factors related to the sensor's physical properties influence the delay between hydrogen release and initial signal detection [2]. As illustrated in Fig. 1, we aim to predict the stable value of the sensor response (green curve) using a model (red curve).

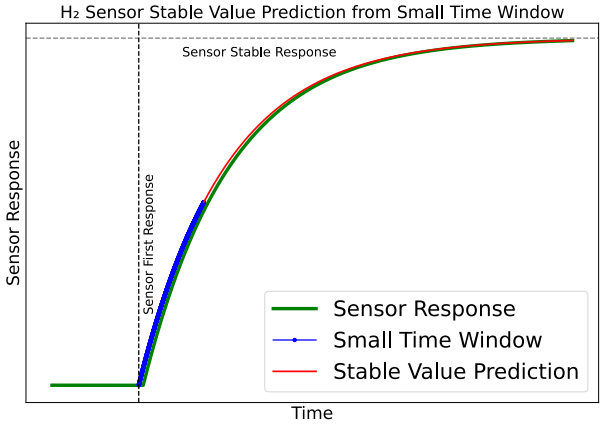

Fig. 1: Hydrogen sensor response with key features: sensor response, a small time window, and the predicted response

We will follow a structured workflow to predict H_2 sensor response from a small time window. First, raw time-series sensor responses will be collected from experiments and real-world use cases. Next, key variables—including the initial response, small time window, and stable sensor response—will be defined. Different prediction models will be selected based on their accuracy

and applied to estimate the stable response using small time data. In this research, we will present various prediction models in the following sections. The models' outputs will be analyzed and evaluated, taking into account uncertainties and potential errors in real-world sensor responses. Finally, we will identify the most effective model for H_2 sensor response prediction.

Classic Approximation (CA)

CA algorithms are based on analytical transfer functions that approximate hydrogen sensors' transient and steady-state response. They help estimate key response characteristics such as time delay and stable values. CA algorithms establish a clear analytical framework, enhancing interoperability and providing valuable insights into sensor dynamics. Different CA models, such as First-Order Plus Dead Time (FOPDT) and Second-Order Plus Dead Time (SOPDT), Exponential and Polynomial Curve Fitting explained in [6] are computationally efficient, requiring minimal processing power, which makes them well-suited for efficient applications.

Statistical Regression (SR)

SR algorithms predict sensor responses based on past sensor readings, making them practical for time-dependent predictions. In [7], various SR algorithms such as Auto-regressive (AR), Auto-regressive Moving Average (ARMA), and Auto-regressive Integrated Moving Average (ARIMA) are discussed, which provide a powerful approach for forecasting sensor values using historical data. These algorithms are particularly well-suited for time-series forecasting and real-time sensor response prediction. By leveraging past sensor readings, they can identify patterns and trends, making them valuable for long-term monitoring and adaptive calibration.

Machine Learning (ML)

ML is also a data-driven algorithm for predicting hydrogen sensor responses, leveraging large datasets for improved accuracy and robustness. It offers advanced, data-driven solutions for predicting hydrogen sensor responses, particularly in complex time-series data analysis. In [7], different ML algorithms such as Support Vector Machines (SVMs), Random Forest Regression (RF), Artificial Neural Networks (ANNs), Convolutional Neural Networks (CNNs), and Long Short-Term Memory (LSTM) Networks are discussed, which leverage large datasets to improve prediction accuracy and robustness. Unlike traditional classic and statistical algorithms, ML approaches can handle nonlinear sensor behaviors, adapt to environmental variations, and extract hidden patterns from sensor signals. However, ML models require large, high-quality datasets for training and can be computationally intensive, making them less suitable for low-power embedded sensor systems. Despite the limitations, ML-based sensor prediction models significantly enhance early leak detection and adaptive monitoring, making them a powerful tool in hydrogen safety applications.

Discussion

The H_2 sensor response is dynamic and influenced by ambient factors such as temperature, pressure, and humidity, which introduce uncertainties that should be quantified using appropriate error metrics and validation techniques. Our study starts with classical models (FOPDT, SOPDT), which estimate stable responses using a small time window. Furthermore, we will consider ARIMA for accurate prediction by considering uncertainties. Finally, we train the LSTM model to enhance real-time H_2 sensor response predictions in large-scale datasets.

Conclusion

In this study, our objective is to predict the H_2 sensor response using only a small time window from the early H_2 sensor response. Each model has its strengths and limitations—some algorithms excel at capturing specific features, while others offer higher accuracy with lower computational costs. Therefore, we are exploring the most efficient and reliable algorithms for quick H_2 sensor response prediction. In the future, we aim to test hybrid algorithm approaches by integrating CA, SR, and ML models to achieve optimal prediction accuracy.

References

[1] Y. Shi et al., "Rapid forecasting of hydrogen concentration based on a multilayer CNN-LSTM network," *Measurement Science and Technology*, 2023, https://doi.org/10.1088/1361-6501/acbdb5.

[2] T. Hübert et al., "Response time measurement of hydrogen sensors," *Hydrogen Knowledge Centre*, 2017, https:h2tools.org/sites/default/files/2019-09/211.pdf.

[3] D. L. Osorio-Arrieta et al., "Reduction of the measurement time by the prediction of the steady-state response for quartz crystal microbalance gas sensors," *Sensors*, 2018, https://doi.org/10.3390/s18082475.

[4] T. Hübert et al., "Time response of hydrogen sensors," *Hydrogen Knowledge Centre*, 2013, www.ichs2013.com/images/papers/124.pdf.

[5] *ISO 26142:2010: Hydrogen detection apparatus – Stationary applications*, International Organization for Standardization, 2010, https://www.iso.org/standard/52319.html.

[6] D. E. Seborg et al., *Process dynamics and control*. John Wiley & Sons, 2016, https://doi.org/10.1002/aic.11628.

[7] G. James et al., *An introduction to statistical learning*. Springer, 2013, https://doi.org/10.1007/978-1-0716-1418-1.

DOI 10.5162/SMSI2025/C6.4

Digital Certificates: Enabling Automation in Quality Assurance and Metrological Traceability

Michael Melzer, Nanine Brunner
Bundesanstalt für Materialforschung und -prüfung (BAM),
Unter den Eichen 87, 12205 Berlin, Germany,
michael.melzer@bam.de

Summary:
Automation in the metrological traceability of measurements bears high potential for a more effective quality management with less human interaction and reduced risks from manual data processing. For this purpose all metrological and administrative information in quality certificates must be provided in a fully machine-readable and machine-interpretable form. Following the well-established approach of digital calibration certificates (DCCs) also other digital quality certificates are currently under development.

Please describe briefly the highlights of your work. The summary of max. 6 lines should be typed across both columns. Please do not leave any spaces between the short paper and the title of your first section and please do not use symbols in the summary. (style “SMSI_Conference_Bodytext”)

Keywords: Digital metrology, calibration, reference materials, quality assurance, automation

Introduction

Conformity assessment documents, especially calibration and reference material certificates, contain valuable metrological information for laboratories and the industrial measurement technology. The correct handling and processing of this information can lead to more precise measurement results, more effective and resilient processes and increased yield. However, since a comprehensive metrological know-how and a well-documented quality infrastructure is necessary to enable these advantages, the information in these quality certificates often remains unutilized.

For the automated handling and processing of quality certificates, their quantitative and administrative data must be interpretable by machines and algorithms. In view of nowadays complex and globally entangled value chains the data structure of such digital certificates should be harmonized to be readily utilizable across all stakeholder communities.

The DCC as a Model for Digital Certificates

With XML being a markup language that is established and stable since decades, *Digital Calibration Certificates* (DCCs) were recently converted into a structured data format. For a fundamental harmonization an XML-schema was developed with the global participation of many stakeholders from the metrological and quality infrastructure sector, which is freely available and currently hosted by the *Physikalisch-Technische Bundesanstalt* (PTB). [1] This DCC-schema defines the basic architecture and terminology of DCCs, which is mainly regulated by the ISO/IEC 17025 standard [2]. Further harmonization within specific metrological areas is achieved by good practice definitions which are currently under development [3-6].

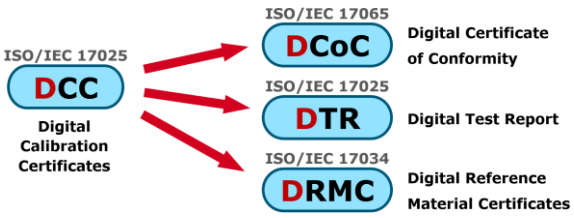

Fig. 1. The DCC-Schema is adapted for other digital quality documents.

Adaptations for Further Quality Certificates

Besides calibration certificates, there are other conformity assessment documents that could be processed automatically in a digital quality management environment. Although there are broad similarities, especially in terms of content and terminology of the administrative information, each of those document types has specific requirements, mainly determined by a respective standard of the ISO 17XXX series. Hence the established DCC-Schema is not suitable for other quality documents as a whole and is currently

adapted by experts for each certificate type accordingly (see Fig. 1).

Digital Certificates of Conformity (DCoC) [7] contain less quantitative information but require a clear semantic concerning the certification criteria which are mostly derived from harmonized standards. These standards are linked directly with a reference to the specific clause in DCoCs.

Digital Reference Material Certificates (DRMC) contain material properties as metrological information that are mostly represented in a similar way as in DCCs, including uncertainties. In both cases, this quantitative data is provided via the *Digital-SI* format which is directly included into both schemas. The D-SI implies a formalism for the machine-interpretable statements of units and their origin from the SI base units as well as the associated measurement uncertainties. [8] With a direct relation to the novel *BIPM SI-Digital Reference Point* [9], the interpretation of digital units becomes unambiguous around the globe.

Digital test reports (DTR) require a large variety of possible data representations and conformity assessment formats. First DTR realizations for specific testing procedures are currently under development will probably result in individual schema implementations. The universe of testing procedures is highly diverse and the harmonization between different testing communities beyond the administrative information will remain a challenge.

Digitally Verifiable Accreditation for Quality Services

Often, conformity assessment services are requested from accredited service providers to assure the defined requirements for the execution of their procedures are met. The fact that a conformity assessment service was provided within the scope of an accreditation needs to be apparent on the resulting certificate. On human readable certificates, this is usually represented by a logo of the national accreditation body and a reference to the accreditation case number for the respective service provider.

For the representation of the accreditation on machine-readable certificates, the *German Accreditation Body* (DAkkS) has set up the public key infrastructure (PKI) for a *Digital Accreditation Symbol* (d-AS). [9] This allows accredited bodies to equip their machine-readable certificates with an advanced electronic seal, which represents their digital identity as a holder of an active accreditation for their services at the time of final certificate authorization. As it also provides all other functionalities of an electronic seal, (*i.e.* data integrity and authenticity), it can fully replace a digital signature on accredited quality certificates (*eAttestations*). The verification on the receiver side can be fully automated and seamlessly integrated into digital workflows.

Fig. 2. The advantages of machine-readable certificates and an automated quality management.

Conclusion

Digital conformity assessment certificates enable the automatization of quality assurance in laboratories and the industrial measurement technology (see Fig. 2). The automated validation, transfer, and data processing releases manual workload and lead to more effective and resilient processes with reduced risks.

References

[1] www.ptb.de/dcc/ (accessed March 2025)

[2] ISO/IEC 17015:2017 “General requirements for the competence of testing and calibration laboratories”

[3] DKD-E 7-2 „Instructions on how to use the DCC schema to create a digital calibration certificate for weights” (2024); doi: 10.7795/550.20240119B

[4] DKD-E 4-3 “Anleitung zur Nutzung des DCC-Schemas für die Erstellung eines digitalen Kalibrierscheins für Parallelendmaße“ (2024); doi: 10.7795/550.20250131

[5] M. Melzer, R. Deschermeier, L. Bünger, M.-A. Demir, J. Schüür, Good practice definitions fort he DCC on temperature and humidity quantities, *Measurement: Sensors* (accepted); doi: 10.1016/j.measen.2024.101477

[6] S. Schönhals, M. Jordan, M. Melzer, D. Röske, Ideas for the transition from paper-based force and torque calibration certificates to machine-readable XML data, *Measurement: Sensors* (accepted); doi: 10.1016/j.measen.2024.101334

[7] T. Shevelena, G. Foyer, D. Knopf, Conceptual harmonization between D-COC and DCC data structures representing result documents in conformity assessment, *Measurement: Sensors* (accepted); doi: 10.1016/j.measen.2024.101472

[8] D. Hutschenreuter, F. Härtig, W. Heeren, T. Wiedenhöfer, A. Forbes, C. Brown, I. Smith, S. Rhodes, I. Linkeova, J. Sykora, V. Zeleny, B. Acko, R. Klobucar, P. Nikander, T. Elo, T. Mustapää, P. Kuosmanen, O. Maennel, K. Hovhannisyan, B. Müller, L. Heindorf, V. Paciello, SmartCom Digital System of Units (D-SI), *Zenodo* (2019); doi: 10.5281/zenodo.3522630

[9] https://si-digital-framework.org/ (accessed March 2025)

DOI 10.5162/SMSI2025/C7.1

Simulation and determination of the coupling efficiency to photoacoustic resonators

Daniel Sieg[1], Vincent Kuczius[1], Gabriel Rodriguez Gutierrez[1], Jonas Gaworski[1], Stefan Palzer[1]
[1] TU Dortmund, Professorship for Sensors, Friedrich-Wöhler-Weg 4, 44227 Dortmund, Germany
stefan.palzer@tu-dortmund.de

Summary:
Direct photoacoustic spectroscopy setups oftentimes employ acoustic resonators to enhance the photoacoustic signal and suppress acoustic noise from the environment. In this contribution the coupling of an idealized sound source to a cylindrical resonator is simulated and shows the dependence of the coupling efficiency on the relative position of the sound source with respect to the resonator. The simulations reveal the spatial dependence of the ideal incoupling positions as a function of the resonator modes. The results are important for setups that spatially separate acoustic sound generation and detection.

Keywords: direct photoacoustic spectroscopy, acoustic resonator, coupling simulation

Introduction

The use of resonator-enhanced, direct photoacoustic spectroscopy setups for gas monitoring is a versatile tool for sensitive [1] detection of the molecular number density. Laser or light emitting diode (LED) – based devices have been shown to achieve limits of the detection in the ppb range [2,3]. For scenarios, where the spectral bandwidth of the exciting light source is much narrower than typical absorption features, the performance in terms of selectivity exceeds that of indirect photoacoustic setups [4] and consequently, it is a complementary technology in this regard.

Typically, the photoacoustic wave generation is done within the acoustic resonator, i.e. the exciting light is funneled into the acoustic resonator, where it is absorbed according the Beer-Lambert law [5] ultimately leading to the generation of an acoustic wave, whose amplitude indicates the number density of the target molecules. A large overlap between the acoustic eigenmodes of the resonator and the light beam achieves an excellent coupling efficiency in case the overall absorption is weak, leading a nearly constant sound wave amplitude along the absorption path.

However, in case of strong absorption, the light absorption leads to exciting the molecules localized. In this case, the signal detected with a microphone may even decrease with increasing number density, since the coupling between generated sound wave and the resonator eigenmodes is weak.

In these cases, spatial separation of the sound wave generation and the acoustic resonator may offer systematic advantages, since signal generation and signal detection may be optimized independently. This may also be of relevance in setups aimed at detecting multiple gases with a single resonator [6]. In this case, the efficiency of coupling acoustic waves into a resonator becomes crucial. To this end, a simulation of a point-like sound source has been used to investigate the efficiency of photoacoustic wave coupling into acoustic resonators.

Setup of the Model

The simulation model is depicted in Figure 1 and features a point-source of sound in the vicinity of a cylindrical resonator.

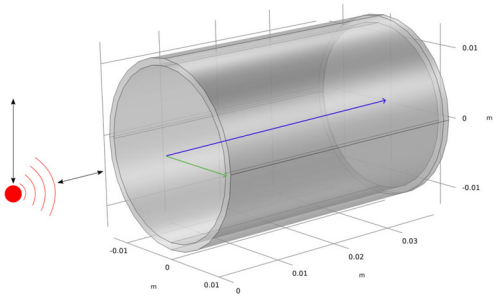

Fig. 1. The photoacoustic signal is modelled as a point source and the coupling efficiency into the resonator's eigenmodes is investigated as function of the distance from the opening and the radial offset from the symmetry axis.

The mode spectrum of a resonator with a diameter of 20 mm and a length of 35 mm is simulated in a modulation frequency range ω_{mod} between 2 kHz – 25 kHz. The amplitude of the different excited eigenmodes is used as a means to quantify the coupling efficiency as a function of the position of the sound source. Fig. 2 shows the frequency spectrum of the resonator.

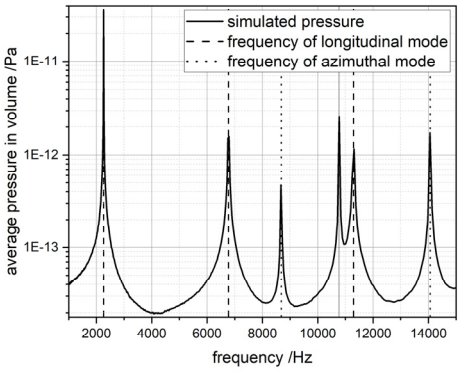

Fig. 2. The frequency spectrum of the longitudinal and azimuthal modes of the acoustic resonator.

The simulation results have been checked by exciting sound waves using a capacitor and a MEMS microphone inside the resonator. By scanning the excitation frequency of the capacitor, sound waves of equal frequency have been generated and the response to a frequency sweep has been analyzed using a Lock-In Amplifier.

Results

The spatial dependence of the efficiency of exciting acoustic waves inside the resonator as a function of the relative position of the sound source is depicted in Figure 3 and 4 for the longitudinal eigenmode at 13867 Hz and the azimuthal eigenmode at 20830 Hz in longitudinal and radial direction, respectively.

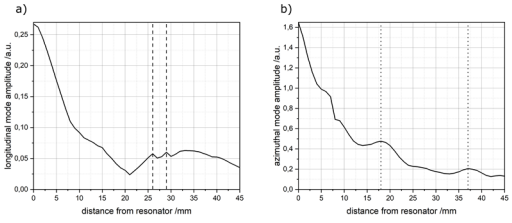

Fig. 3. Coupling efficiency to the longitudinal (a) and azimuthal (b) mode as a function of the longitudinal displacement.

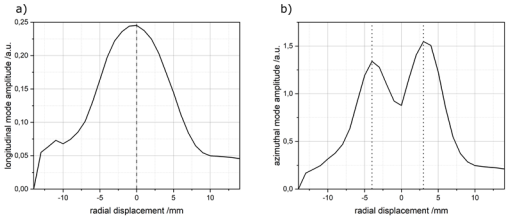

Fig. 4. Coupling efficiency to the longitudinal (a) and azimuthal (b) mode as a function of the radial displacement.

The measurements show fundamentally different behavior of the spatial dependence of the coupling efficiency for different classes of eigenmodes.

Conclusion

The spatial decoupling of photoacoustic signal generation and detection offers means to independently optimize the dynamic range and sensitivity of direct photoacoustic setups. The coupling efficiency hinges on the relative position of the sound source and may be tuned in order to optimized schemes for multigas detection further.

References

1. Miklós, A.; Hess, P.; Bozóki, Z. Application of acoustic resonators in photoacoustic trace gas analysis and metrology. *Review of Scientific Instruments* **2001**, *72*, 1937–1955, doi:10.1063/1.1353198.
2. Kapp, J.; Weber, C.; Schmitt, K.; Pernau, H.-F.; Wöllenstein, J. Resonant Photoacoustic Spectroscopy of NO_2 with a UV-LED Based Sensor. *Sensors (Basel)* **2019**, *19*, doi:10.3390/s19030724.
3. Patimisco, P.; Scamarcio, G.; Tittel, F.K.; Spagnolo, V. Quartz-enhanced photoacoustic spectroscopy: a review. *Sensors (Basel)* **2014**, *14*, 6165–6206, doi:10.3390/s140406165.
4. Palzer, S. Photoacoustic-Based Gas Sensing: A Review. *Sensors (Basel)* **2020**, *20*, doi:10.3390/s20092745.
5. Swinehart, D.F. The Beer-Lambert Law. *J. Chem. Educ.* **1962**, *39*, 333, doi:10.1021/ed039p333.
6. Rey, J.M.; Romer, C.; Gianella, M.; Sigrist, M.W. Near-infrared resonant photoacoustic gas measurement using simultaneous dual-frequency excitation. *Appl. Phys. B* **2010**, *100*, 189–194, doi:10.1007/s00340-010-3994-x.

DOI 10.5162/SMSI2025/C7.2

Design of a Refrigerant Leak Sensor based on the Photoacoustic Dual-Chamber Detection Method

Hassan Yassine[1], Christian Weber[1,2], Mahmoud El-Safoury[2], Nicolas Brugger[1], Katrin Schmitt[1,2], Jürgen Wöllenstein[1,2],
[1] Department of Microsystems Engineering-IMTEK, Laboratory for Gas Sensors, University of Freiburg, Georges-Köhler-Allee 102, 79110 Freiburg, Germany
[2] Fraunhofer Institute for Physical Measurement Techniques IPM, Georges-Köhler-Allee 301, 79110 Freiburg, Germany
hassan.yassine@imtek.uni-freiburg.de

Summary:
We present a concept for the development of a dual-chamber photoacoustic sensor for refrigerant leak detection using R227ea as an example. Photoacoustic detection allows a very compact sensor with high sensitivity and selectivity to be realized. The simulations presented in this paper demonstrate that the sensor can cover the concentration range of 0-5000 ppm R227ea, with a limit of detection (LOD) of approximately 20 ppm R227ea.

Keywords: Refrigerants, R227ea, dual-chamber photoacoustic detection method, simulations

Motivation

Refrigerants are gases or liquids, predominantly chemical compound with hydrogen and carbon atoms, deployed in cooling processes or other cooling applications. Some of these gaseous compounds are known for their high infrared (IR) absorption [1]. Therefore, they are among the gases whose emissions into the atmosphere must be monitored and whose use must be minimized. The detection of 1,1,1,2,3,3,3-heptafluoropropane (R227ea), a well-known refrigerant used in refrigeration applications [2], is of great significance. R227ea, whose absorption spectrum was previously measured [3], is one of the strongly absorbing gases in the IR. One sensor application is the detection of R227ea leaks in cooling applications. Such a leak is a possible reason for the undesired release of this gas into the atmosphere. In this context, a proper detection unit is needed to detect these leaks. The early detection of a gas leak allows to act as quickly as possible and to prevent the emission of R227ea into the atmosphere. We are investigating the feasibility of using a photoacoustic dual-chamber sensor for R227ea detection.

Sensor concept

The planned sensor consists of an IR source, a photoacoustic detector, and an absorption cell in in the optical path for gas exchange. The photoacoustic detector itself is a closed chamber with a MEMS microphone, which is filled with 100% R227ea. This detector chamber is sealed with a silicon window, that is transparent in the wavelength ranges of R227ea absorption. The IR source implemented for this application is a thermal IR emitter which covers all absorption bands of R227ea. The sensor is being developed to measure in the range 0-5000 ppm R227ea with a LOD in the low ppm range.

Simulations to determine the dimensions of the planned sensor including the optical path length (L_O), which is the length of the absorption cell, as well as the response of the planned sensor and its sensitivity to R227ea were carried out and evaluated.

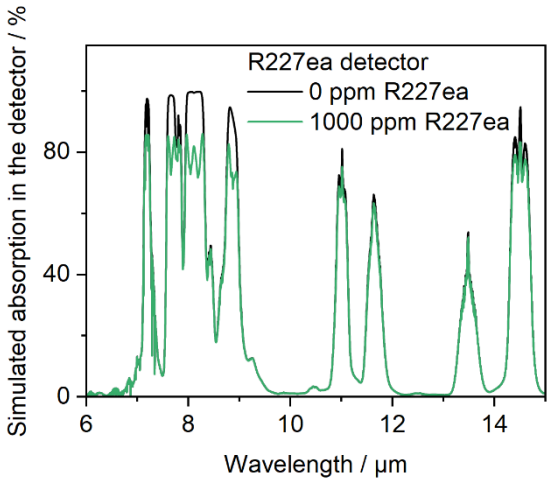

Fig. 1. Simulation of the absorption of a detector filled with R227ea with a detector length of 1.5 mm and its spectral response towards 1000 ppm R227ea in the absorption cell (L_O = 5 cm).

The calculations presented in this paper are based on the same formulas employed in the simulations published in [3,4]. The absorption inside a R227ea photoacoustic detector with a length of 1.5 mm was calculated and is plotted in Fig. 1. The detector contains 100 vol.-% R227ea and is the basis for all calculations. The results of the spectral calculations indicate that the absorption at 8.18 µm is of high relevance, because the spectral detector signal at this wavelength decreases to roughly 71.9 % when 1000 ppm R227ea is in the absorption cell (L_O = 5 cm). Furthermore, the absorption at 7.65 µm, 8.04 µm, 8.87 µm and at 14.5 µm are also relevant, because the spectral detector response at these wavelengths is also high and decreases strongly with the absorption of 1000 ppm R227ea. On the other hand, the R227ea detector shows at the other wavelength (11.01 µm, 11.63 µm and 13.48 µm) a slight change in the spectral detector signal. It seems that the very strong absorption bands have the highest influence on the signal change.

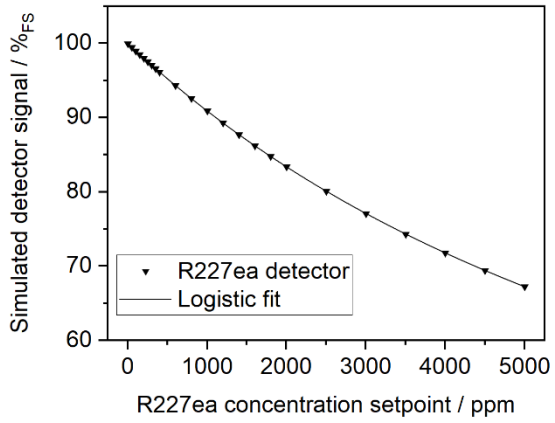

Fig. 2. Simulation of the response of the planned R227ea sensor (L_O = 5 cm) to R227ea in the desired concentration range (0-5000 ppm R227ea).

The results of the simulations with the sensor response and its calibration, including the logistic function that is a suitable function for the calibration, are shown in Fig. 2. The detector signal shows a linear decrease at low concentrations (up to 400 ppm R227ea) and tends to become more nonlinear with increasing R227ea concentration. The sensor shows a decrease in the full-scale (FS) signal with a decrease of about 9.59×10^{-3} %FS/ppm reaching 96.16 %FS at 400 ppm R227ea. This reflects and explains the sensitivity of the sensor to R227ea at low concentrations, which is about 0.19 %FS/20 ppm. At the upper concentration limit, the sensor achieves a response and a sensitivity of 67.3 %FS and 0.08 %FS/20ppm, respectively. The sensitivity of the sensor therefore dropped to more than half at 5000 ppm R227ea, which is due to the nonlinear decrease of the simulated response of the sensor.

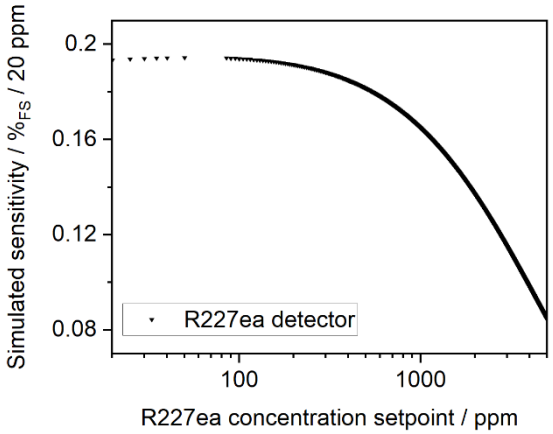

Fig. 3. Simulation of the sensitivity of the planned R227ea sensor to R227ea in the desired concentration range (20-5000 ppm R227ea).

The lowest concentration that can be measured using this setup is approximately 20 ppm R227ea.

Conclusion

A concept of a photoacoustic dual-chamber sensor was developed for leak detection of R227ea, relevant in cooling processes or refrigerant applications. The simulations presented in this paper demonstrate that the sensor can cover the concentration range of 0-5000 ppm R227ea, with the lowest possible detectable concentration of approximately 20 ppm R227ea. Next steps will include the fabrication of the sensor and characterization measurements.

References

[1] R. V. Kochanov, I. E. Gordon, L.S. Rothman, K.P. Shine, S.W. Sharpe, T.J. Johnson, T.J. Wallington, J. J. Harrison, P. F. Bernath, M. Birk, G. Wagner, K. Le Bris, I. Bravo, C. Hill, “Infrared absorption cross-sections in HITRAN2016 and beyond: Expansion for climate, environment, and atmospheric applications." *Journal of Quantitative Spectroscopy and Radiative Transfer* 230, 172-221 (2019)

[2] A. P. Fröba, C. Botero, A. Leipertz, “Thermal Diffusivity, Sound Speed, Viscosity, and Surface Tension of R227ea (1,1,1,2,3,3,3-Heptafluoropropane)”, *International Journal of Thermophysics* 27, 1609-1625 (2006)

[3] H. Yassine, C. Weber, N. Brugger, J. Wöllenstein, K. Schmitt, “Towards a Miniaturized Photoacoustic Detector for the Infrared Spectroscopic Analysis of SO2F2 and Refrigerants”, *Sensors* 23(1), 180 (2023)

[4] M. El-Safoury, C. Weber, O. Kiesewetter, Y. Hespos, A. Eberhardt, K. Schmitt, J. Wöllenstein, “Miniaturized photoacoustic detection of organofluorine-based refrigerants”, *Journal of Sensors and Sensor Systems* 9(1), 89-97 (2020)

DOI 10.5162/SMSI2025/C7.3

Optimizing Analog Front End Architectures for Enhanced SNR in Photoacoustic Imaging

S. Kindorf[1,2], C. Weber[1], B. Bierer[1], J. Wöllenstein[1,2]
[1] Fraunhofer Institute for Physical Measurement Techniques IPM, Georges-Köhler-Allee 301, 79110 Freiburg, Germany,
[2] University of Freiburg Department of Microsystems Engineering IMTEK, Georges-Köhler-Allee 102, 79110 Freiburg, Germany,
sebastian.kindorf@ipm.fraunhofer.de

Summary:
In the field of photoacoustic imaging, systems with light sources with low pulse energy are currently being investigated. This study presents an analysis of different analog front-end architectures for such imaging, in particular their impact on the signal-to-noise ratio (SNR). The focus is on systems with high pulse repetition frequencies (PRF) and sampling rates of up to 50 Mega-Samples per second (MSPS). The architectures, which is tailored to Piezoelectric and Capacitive Micromachined Ultrasonic Transducer (PMUTs & CMUTs), include combinations of analog front-ends (AFE), preamplifiers, transimpedance amplifiers, and analog-to-digital converters (ADC). For testing purposes, the MUTs are simulated and set up with passive components.

Keywords: readout, signal conditioning, digitalization, analog front-end, photoacoustic imaging,

Background Motivation

High-power lasers with low pulse repetition frequencies (~10-20 Hz with ~20 mJ/cm^2) are often used in photoacoustic imaging. To increase system integration, the pulse energies can be reduced when the PRF is increased (kHz-range with ~1mJ/cm^2) to generate an image by averaging. These reduced energies allow lasers with a smaller footprint to be used. Both variants aim to exploit the full maximum permissible exposure (MPE) [1].

In photoacoustic imaging with low pulse energy, it is necessary to make the signal amplification and acquisition as low-noise and sensitive as possible. In this work, an analysis of different analog front-end architectures for photoacoustic imaging, with particular emphasis on their impact on the SNR is presented. Different integration times (Allan deviation) and pulse frequencies are investigated.

Systems operating at high repetition rates with sampling rates of up to 50 MSPS are being investigated. The system has been tailored to suit PMUTs and CMUTs. The architectures include different combinations of AFE, preamplifiers, transimpedance amplifiers and ADCs. The potential of using different types of ADCs and AFEs to improve the system's sensitivity and SNR is also being explored. The aim is to optimize the sensitivity of AFE for sonography and especially photoacoustic imaging.

Readout architectures for MUTs

There are two main approaches for recording analog ultrasound signals. One approach is to use transimpedance amplifiers to amplify the charge generated from the MUT and convert into a voltage. This signal is digitized by an ADC. Another approach is to use a fully integrated circuit to amplify and digitize the data in one chip. A printed circuit board (PCB) is used to build and test various useful combinations of amplifier and digitalization components. The different system architectures are shown in Fig. 1.

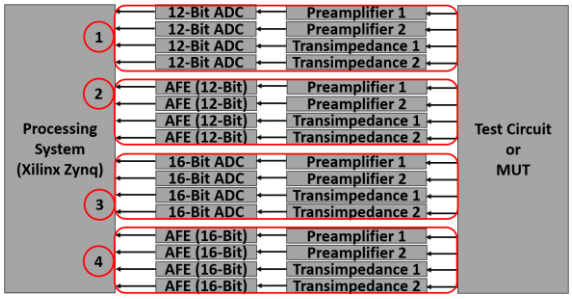

Fig. 1: Overview of the different system architectures. Four architectures with four channels each. 12- & 16-bit ADC and AFE with two different preamplifier and transimpedance amplifiers.

ADCs and AFEs are read out using serial low voltage differential signaling (LVDS). To ensure

comparability, all 16 channels are read out at a uniform sampling rate of 50 MHz. The readout is made by a Xilinx Zynq XC7Z020. This System-on-a-Chip (SoC) combines two ARM processor units with FPGA logic, providing high flexibility. The use of the Xilinx Zynq for data processing enables efficient management of multiple parallel input data streams from various channels.

Simulation of MUT

In photoacoustic imaging, typically small signals are recorded that follow a damped harmonic oscillation. Most ultrasound systems utilize lead zirconate titanate (PZT) transducers rather than CMUTs. MUT technology provide benefits such as enhanced bandwidth, the simplicity of constructing large, compact arrays, and the ability to integrate with supporting electronics [2]. MUTs can be used in pulse-echo mode for sonography or in receive mode for photoacoustic imaging. The received signals of both methods are similar. The main difference is that the signals in photoacoustics are an order of magnitude lower than in pulse echo, leading to a decrease in the SNR. Fig. 2 shows typical photoacoustic signals. High power lasers with low pulse repetition frequencies are compared with low power lasers with high repetition rates. The axes on the left and right illustrate the demands on the sensitive electronics since the signal decreases a hundredfold at low pulse energies.

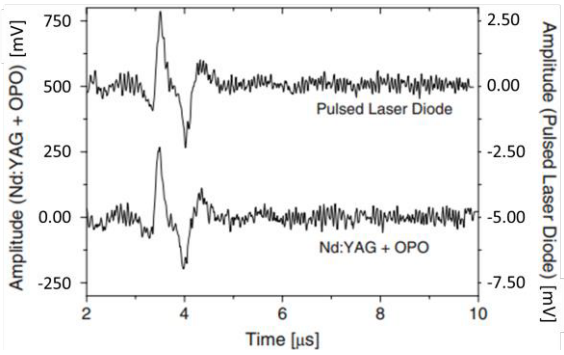

Fig. 2 Typical photoacoustic impulse response generated by a vessel in the hand. Comparison between high power Nd:YAG laser + optical parametric oscillator (OPO, single shot 0.45 mJ pulse) and low power pulsed laser diode (4.4 uJ averaged 10,000 times) [3] .

To study the different channel architecture of the AFE, a test circuit is developed to ensure comparability. In a multi-channel MUT, the photoacoustic signals are different depending on the position relative to the sound source. Another option, a digital-to-analog converter (DAC), can produce a synthetic fast waveform, but as a voltage source it does not simulate the reality of a MUT, which produces a finite charge. Both variants therefore do not provide reliable or realistic photoacoustic signals as from MUTs for a comparison of the channels and are therefore unreliable as a source. For this reason, a circuit is to be developed that uses an analog filtered pulse as a photoacoustic source. With the help of a simulation, a circuit consisting of passive components is developed that behaves like MUTs. In this way, millivolt signals with similar wavefronts and limited charge input can be generated to obtain a reliable method for validating the channels. This simulation is shown in Fig. 3. The attenuation, which determines the decay behavior, and the voltage amplitude, which influences the SNR, can be regulated by the values of the passive components.

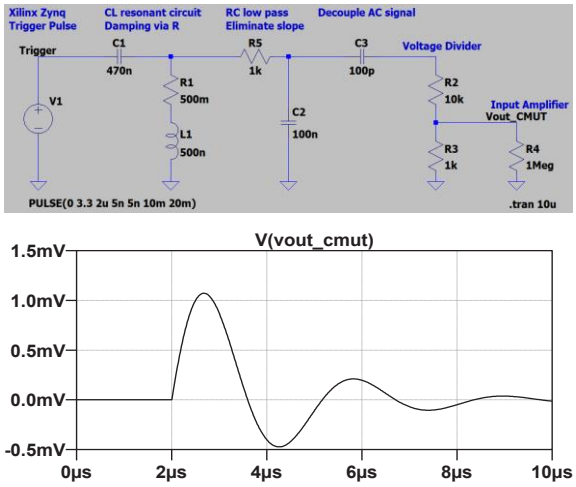

Fig. 3 The top image shows the setup using passive components in LTSpice, which behaves similarly to a MUT. The lower picture shows the simulation result.

Conclusion

In summary, this work demonstrates a way to characterize different analog front-end architectures for photoacoustic imaging using a synthetic signal. A simulation of a real MUT provides a reliable method to validate the channels using an analog filtered pulse as input signal.

References

[1] K. Sivasubramanian, M. Pramanik: “High frame rate photoacoustic imaging at 7000 frames per second using clinical ultrasound system”, DOI: 10.1364/BOE.7.000312

[2] Zhihong Wang et al.: “Micromachined thick film piezoelectric ultrasonic transducer array”, DOI: 10.1016/J.SNA.2005.10.054

[3] Roy G. M. Kolkman, Wiendelt Steenbergen, Ton G. van Leeuwen: “In vivo photoacoustic imaging of blood vessels with a pulsed laser diode”, DOI 10.1007/S10103-006-0384-Z

DOI 10.5162/SMSI2025/D1.1

eNDIRi² evaluation kit – evaluation system for IR components

Jeffrey Knossalla[1], Annett Isserstedt-Trinke[1], Andreas Sachse[1], Steffen Biermann[1]
[1] Micro-Hybrid Electronics GmbH, Heinrich-Hertz-Str. 8, 07629 Hermsdorf, Germany
j.knossalla@microhybrid.com

Summary:
The presented system for evaluation Infrared (IR) components enables high efficiently selection of IR detectors and infrared sources and their configuration for a wide range of application scenarios especially for optical gas sensors. The core components are the detector board, the emitter board and a central main unit that ensures high performance of the IR components and interface communication between as well as to an external PC. The detector interface performs signal amplification and digitization, while the emitter interface supplies a modulated and controlled power. The main unit connects all components and enables transparent data visualization as well as easy configurations via the developed PC software. The modular architecture enables multiple types of characterization of different IR components e.g. for environmental monitoring and medical diagnostics.

Keywords: eNDIRi², evaluation kit, IR component, IR emitter, IR detector

Motivation

In modern sensor technology, pyro- and thermopile detectors as well as infrared emitters play a crucial role in the detection of infrared light and thermal radiation. This paper describes the design and implementation of an integrated system which enables a high efficiently selection of IR detectors and infrared sources and their configuration for a wide range of application scenarios especially for optical gas sensors. By the versatile structure, an optimized couple of detector and source with optimal adapted working parameters can be implemented. The main components of the system are the detector interface, the emitter interface and the main unit which provides effective interface communication and performance control. Depending on the measurement task, the appropriate components are selected, combined and evaluated using a high user-friendly system. One of the biggest challenges is to combine in optimized way the wide variety of components (Fig.1) for an analysis device with the hardware and firmware into an easy-to-use system.

Fig. 1: IR components to be evaluated

System

The system design comprises several key components: The detector part and the emitter part, both connected to the main unit via SPI bus (Fig. 2). The detector, a pyro or thermopile sensor, is connected via a plug-in socket and coupled to a special detector interface that handles signal amplification, offset, digitization and sensor pin coding. The emitter is also integrated via a plug-in socket and will be supplied with modulated and controlled power via the emitter interface (Fig.3).

The central main unit controls the connection via the SPI bus, USB interface and other connectors. It stabilizes the voltage and acts as a converter and user interface. Incoming signals are collected and forwarded by the main unit and visualized on a connected PC using special high usability software developed for this purpose.

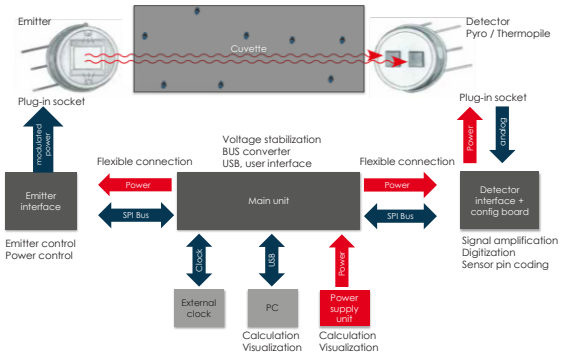

Fig. 2: block diagram of eNDIRi²

For the development of NDIR gas sensors the integrated gas cuvette enables initial functional measurements with test gases. A realistic test environment is provided were the extinction of the measuring signal based on filter configuration, absorption length and gas concentration can be easily evaluated.

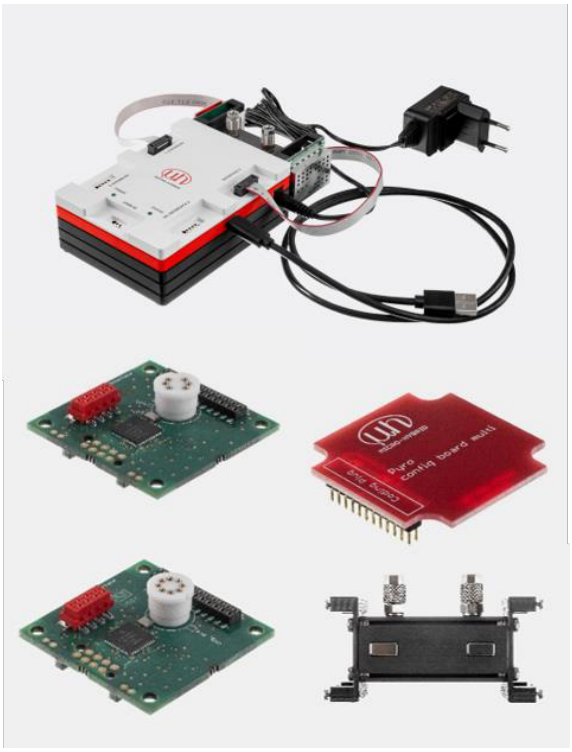

Fig. 3: system components of eNDIRi²

Results

The implementation of this system enables simple, precise parameterization, control and regulation of detectors and emitters. The use of flexible connections optimises adaptability, and the configuration of the power supply ensures that the system components can be operated stably and efficiently. Through signal amplification and digitization, the acquired data is processed with high precision, which represents a significant advance in sensor technology.

The eNDIR² software allows the emitter to be precisely controlled through settings of emitter type, clock source, chopper frequency and power, further increasing customisability and efficiency.

Pyro and thermopile sensors show different frequency responses and noise behaviour; pyro sensors offer a fast frequency response, while thermopile sensors stand out due to their low noise levels. Based on alternating current power mode @1 kHz high input power levels at low aging effects of emitters are possible. The eNDIRi² software supports comprehensive detector settings, including gain, offset and filter options, and offers four independent oscilloscope windows for detailed data monitoring. Selectable data sources and formula functions enable complex, time-resolved analyses of the measurement parameters, which further increases the system's range of applications and efficiency. The data recording via PC enables customized calculation and evaluations subsequent the measuring act.

Discussion

As a complete system for IR component characterization, it integrates a gas cuvette, emitter control, detector electronics and PC software, enabling comprehensive analysis. As a subsystem, eNDIRi² allows detailed characterisation of the emitters with power control, chopper function, clock input and clock output, as well as the detectors with adjustable analogue pre-stage and visualisation. This modular approach allows targeted optimisation of the system parameters of single-component systems, including adjustable preamplification and emitter power, as well as tuneable duty cycle, chopper and sampling frequencies.

The architecture presented combines flexibility and stability, making it an ideal candidate for applications in environmental monitoring, industrial process technology and medical diagnostics. The modular design allows for easy extensions and customisation to meet specific requirements. Future developments could focus on the further development of the user interface and the integration of advanced algorithms for data analysis to further increase the functionality and benefits of the system.

DOI 10.5162/SMSI2025/D1.2

Investigation of the suitability of MEMS-FPI-based NIR spectral detectors for the analysis of cooling lubricants

Janek Otto[1], *Karl-Ludwig Krieger*[1]
[1] Institute of Electrodynamics and Microelectronics (ITEM.ae), University of Bremen, Germany
janek.otto@uni-bremen.de

Summary: This paper presents a new approach to monitoring and analyzing cooling lubricants. For this purpose, a compact MEMS-FPI-based NIR sensor is used, which can be integrated online into a process and should enable conclusions to be drawn about the condition and various parameters of the cooling lubricant. Experimental investigations of different cooling lubricants of the NIR sensor are presented. The properties of the cooling lubricants differed not only in terms of type but also in terms of concentration and pH value. In addition, the analysis methods used are presented and evaluated in the context of parameter detection of cooling lubricants.

Keywords: NIR spectroscopy, MEMS sensors, cooling lubricant analysis, process technology, chemometrics

Introduction

In many metalworking production processes, cooling lubricants are a decisive factor that is essential for a high level of performance during machining. In addition to the main tasks of cooling and lubrication, they also ensure the continuous removal of metal chips and abrasion as well as corrosion protection, that protects the workpiece as well as tools and machines.

The components and composition of cooling lubricants vary depending on the type and area of application: In addition to a base oil (often mineral oil) and water in the case of water-miscible coolants, various additives are integral components to prevent corrosion and the formation of fungi, bacteria and foam, among other things.

In addition to a growing interest in sustainable management, increasing occupational health and safety requirements as well as a significant cost factor are decisive factors for an increasing interest in improving the service life and quality of cooling lubricants. In small individual systems, monitoring and maintenance is usually carried out by trained personnel at regular intervals.

In this article, we present a new approach to analyzing cooling lubricants. A compact NIR process spectrometer based on MEMS-FPI (Fabry-Pérot interferometer) sensor technology is used here, the aim of which is to analyze inline cooling lubricant parameters. The publication focuses on the analysis results obtained to determine various cooling lubricant parameters (including type, concentration, pH value) using chemometric and machine learning methods.

Experimental Setup

In order to be able to analyze the properties of cooling lubricants, various cooling lubricant samples were measured and examined using NIR spectroscopy. The focus here was on water-miscible cooling lubricants, as these are the most commonly used, accounting for over 90 %. The NIR spectral data was recorded using a MEMS-FPI spectral sensor, which covers a wide wavelength range by integrating several complementary narrowband detectors [1]. The application of the measurement principle of (diffuse) reflection according to Figure 1 also enables the measurement of cloudy and opaque cooling lubricants.

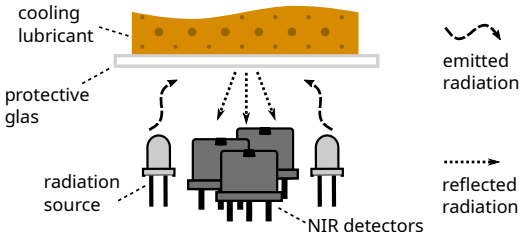

Fig. 1: Experimental setup for NIR spectroscopic investigation of cooling lubricants.

A total of around 500 samples were measured and different parameters of the cooling lubricant were systematically varied. In addition to different types of cooling lubricant, the concentrations and their pH values were also measured; crucial properties that allow conclusions to be drawn about the performance and condition of the cooling lubricant. The parameters of interest were recorded by corresponding reference measuring devices.

Analysis Methods and Results

The measured NIR spectra were pre-processed in a first step. In addition to smoothing using a Savitzky-Golay filter, a correction and normalization were carried out. A principal component analysis (PCA) was then applied to increase the information content of the measurement data

and to reduce redundant data to the relevant information content. A Support vector machine (SVM) was used to classify the different types of cooling lubricant. This was based on findings from [2]. Figure 2 shows the classification results plotted over the principal components. The left graph shows the explained variance with increasing number of principal components. The right graph shows the average accuracy of the classification of the cooling lubricant type.

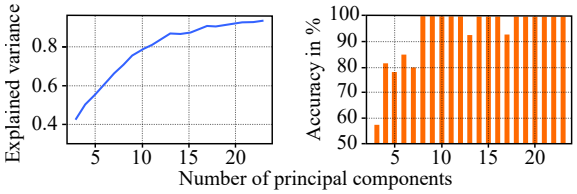

Fig. 2: Determining the type of cooling lubricant by using an SVM with different principal components.

The results were cross-validated and are independent of the concentration of the cooling lubricant used. A reliable statement about the type of cooling lubricant is already possible with a small number of principal components (almost 10).

In addition to the type of cooling lubricant, the concentration of the cooling lubricant was also analyzed and determined. For this purpose, corresponding samples were measured that differed in terms of this parameter. The applied linear regression methods were developed separately for the different types of cooling lubricant. To assess the quality of the regression, the coefficient of determination R^2 was used, which standardizes the difference between the prediction and the true value. Figure 3 shows the course of the coefficient of determination plotted against the number of main components used for two different cooling lubricants.

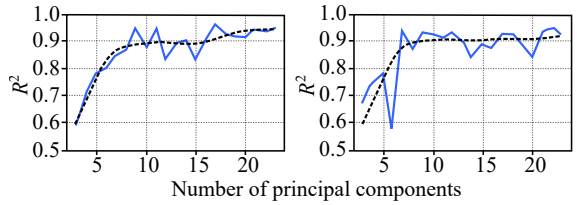

Fig. 3: Determination of the concentration of two cooling lubricants using linear regression with different number of principal components.

As was to be expected, the accuracy of the regression model increases as the number of main components used rises. However, the gain in quality per additional feature decreases sharply from around 8 features and the risk of overfitting increases. It should be noted that the results shown in Figure 3 are predictions in a large variation range of the concentration. In the typical application range of about 5 - 12 %, the predictions could be improved to a value of approx. R^2 = 0.95.

Finally, the pH value of the cooling lubricants was to be determined, which is a frequently considered parameter for assessing the condition of the cooling lubricant. Measurements were carried out at a constant concentration of 5 % in a pH value range of approximately 4 to 10 and then analyzed. The best results were achieved with a partical least square regression (PLSR). Figure 4 shows the measured over predicted test values of the optimized prediction model. The algorithm used achieves an R^2 of 0.92 with a root mean square error (RMSE) of 0.28.

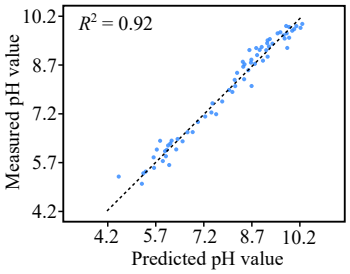

Fig. 4: Regression of the ph value of a cooling lubricant at a constant concentration used PLSR.

Conclusion

In this work, the analysis of cooling lubricants using MEMS-FPI-based NIR sensors was presented. For this purpose, cooling lubricant samples were systematically measured by NIR spectroscopy and different parameters such as type, concentration and pH value were varied. The spectra were then pre-processed and analyzed. The results obtained were used to prove that the MEMS-FPI NIR sensors used are suitable for determining the parameters of cooling lubricants in conjunction with appropriate analysis methods.

The knowledge gained here serves as a basis for determining other relevant parameters such as nitrite content or tramp oil and to develop a multifunctional, integrable cooling lubricant analysis sensor.

Acknowledgment

This work is funded by the German Federal Ministry for Economic Affairs and Climate Action project OPTSee (KK5039206DF3).

References

[1] J. Otto, K. -L. Krieger and H. Andreesen, “Development of a compact NIR sensor using MEMS-FPI NIR spectral detectors,” Sensors and Measuring Systems; 21th ITG/GMA-Symposium, Nuremberg, Germany, 2022, pp. 192-199

[2] Zhang W., Kasun LC., Wang QJ., Zheng Y., and Lin Z., “A Review of Machine Learning for Near-Infrared Spectroscopy.” Sensors. 2022; 22(24):9764. https://doi.org/10.3390/s22249764

DOI 10.5162/SMSI2025/D1.3

A gonioreflectometer for the measurement of bidirectional reflectance distribution functions in the thermal infrared

Hoschang Noori [1], *Ke Ma*[1], *Robert Schmoll*[1] *and Andreas Kroll*[1]
[1] Department of Measurement and Control, University of Kassel, Mönchebergstr. 7, 34125 Kassel, Germany
hoschang.noori@mrt.uni-kassel.de

Summary: An in-plane-gonioreflectometer was developed to measure bidirectional reflection distribution functions (BRDF) for opaque surface materials. The emissivity can be determined by integrating the BRDF over the hemisphere for surfaces with diffuse scattering properties. A gonioreflectometer generally consists of a radiation source, a detector and some robotics to vary radiation and viewing angles. An integrating sphere operating in a broadband infrared wavelength was selected as radiation source. An LWIR and an MWIR thermal imaging camera were selected as detectors. The gonioreflectometer and the results of the first measurements are presented here.

Keywords: emissivity, emittance, gonioreflectometry, BRDF, thermal infrared, in-plane-scatterometry

Background, Motivation and Objective

The bidirectional reflectance distribution function (BRDF) is a very useful function for characterising scattering and surface roughness, ray tracing, and determining reflectance of diffuse scattering surfaces [1], the last point being particularly interesting for thermal imaging for emissivity determination. This paper describes an in-plane-gonioreflectometer with thermal imaging cameras as detectors. The measurement procedure is described and the first results are presented.

Description of the Gonioreflectometer

First, the theory about BRDF measurements is presented. Then the measurement device and the measurement procedure is presented.

BRDF Theory

The BRDF for in-plane measurements is defined in radiometric terms as the ratio of the surface radiance in a particular viewing direction $dL(\theta_\mathrm{i}, \theta_\mathrm{o})$ to the surface irradiance resulting from the radiation incident from a particular direction of irradiation $dE(\theta_\mathrm{i})$, see eq. (1)[2].

$$f_\mathrm{r}(\theta_\mathrm{i}, \theta_\mathrm{o}) = \frac{dL_\mathrm{o}(\theta_\mathrm{i}, \theta_\mathrm{o})}{dE_\mathrm{i}(\theta_\mathrm{i})} \tag{1}$$

with θ_i as incident angle and θ_o as viewing angle (see Fig. 1). For a radiation source that can be assumed to irradiate a surface uniformly this simplifies to eq. (2) [1]

$$f_\mathrm{r}(\theta_\mathrm{i}, \theta_\mathrm{o}) = \frac{L_\mathrm{o}(\theta_\mathrm{i}, \theta_\mathrm{o})}{L_\mathrm{i} \cos(\theta_\mathrm{i}) \Omega_\mathrm{i}} \tag{2}$$

This means that two radiometric quantities ($L_\mathrm{o}(\theta_\mathrm{i}, \theta_\mathrm{o})$, L_i) and a geometric quantity, the solid angle of irradiation Ω_i, must be determined. Physical plausible isotropic BRDF must have the following properties [3]:

- Positivity, $f_\mathrm{r}(\theta_\mathrm{i}, \theta_\mathrm{o}) \geq 0$
- Helmholtz-reciprocity, $f_\mathrm{r}(\theta_\mathrm{i}, \theta_\mathrm{o}) = f_\mathrm{r}(\theta_\mathrm{o}, \theta_\mathrm{i})$
- Energy conservation $\int_{\phi_\mathrm{o}} \int_{\theta_\mathrm{o}} f_\mathrm{r}(\theta_\mathrm{i}, \theta_\mathrm{o}) \cos(\theta_\mathrm{o}) d\Omega_\mathrm{o} \leq 1$

Positivity means that the BRDF value cannot be negative, Helmholtz-reciprocity guarantees that when radiation and detector angle are exchanged, the resulting BRDF is the same and energy conservation says that the integration of the BRDF detection solid angle Ω_o over the hemisphere with viewing azimuth angle ϕ_o cannot be greater than 1.

Measurement device

The measurement device is shown in Fig. 1. The MWIR thermal imaging camera has two High Dynamic Range (HRD) modes which can measure temperatures between $0°\mathrm{C} - 800°\mathrm{C}$ and $300°\mathrm{C} - 1800°\mathrm{C}$. The integrating sphere is described in [4]. An optical chopper is used to subtract out disturbing ambient radiation and the self radiation of the surface in the thermal images. Two rotary tables are used to rotate the sample holder and integrating sphere with respective angles α, β, which are converted to the BRDF angles $\theta_\mathrm{i}, \theta_\mathrm{o}$. The source angle θ_i is determined by its rotary table. Before a measurement run the average radiance L_i from the exit port of the Integrating sphere is measured. The exit port radius r is known and with distance d_i the incident irradiation solid angle can be determined with $\Omega_\mathrm{i} = \frac{\pi r^2}{r^2 + d_\mathrm{i}^2}$.

Measurement procedure

Thermal images are taken for source angles $\theta_\mathrm{i} \in [1°, 89°]$ in $1°$ steps and detection angles $\theta_\mathrm{o} = \{10°, 20°, 30°, 40°, 45°, 50°, 60°, 70°, 80°\}$. Then a circle Region-of-Interest (ROI) with the same

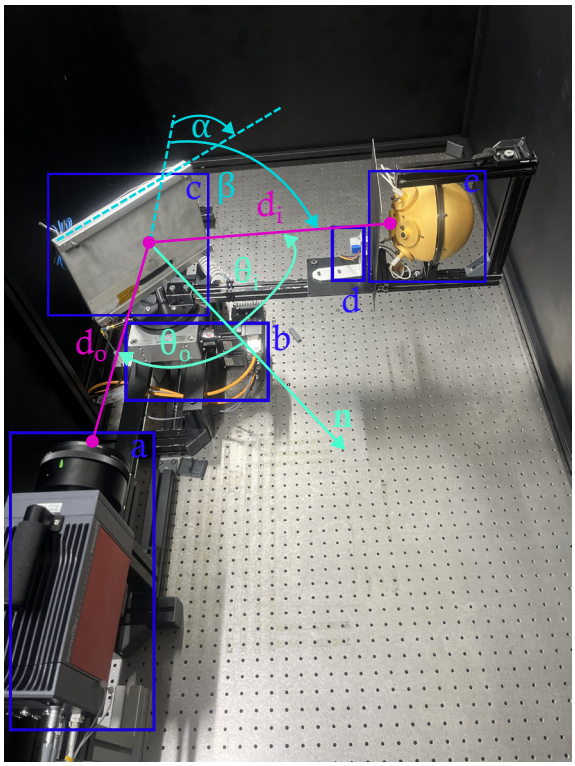

Fig. 1: Gonioreflectometer setup on an optical table in a dark room: a) Thermal imaging camera b) Rotary tables c) Sample holder d) Optical chopper e) Integrating sphere with an aperture

radius as the exit port around the specular reflection center $\theta_\mathrm{i} = \theta_\mathrm{o}$ is defined and the average radiance is taken as $L_\mathrm{o}(\theta_\mathrm{i}, \theta_\mathrm{o})$, which is weighted by $\cos(\theta_\mathrm{o})$ to account for the projected solid angle.

Results

The BRDF measurements of sandblasted steel (Fig. 2) and sandblasted aluminium (Fig. 3) for three different camera angles are presented here. Both show typical behaviour of diffuse reflecting surfaces. Sandblasted steel also has a specular component, especially recognizable for $\theta_\mathrm{o} = 20°,\ 40°$. For $\theta_\mathrm{o} = 60°$ the specular peak is less noticeable because of the rise of the diffuse BRDF component for growing detector angles. The measured BRDF with diffuse scattering properties show physical plausibility.

Conclusions

A measurement device was built for BRDF measurements in thermal infrared. The measurement procedure was described. First results were shown. The measurement device has to be validated by a sample with known BRDF and the uncertainty has to be analyzed. It must be tested for which surfaces emission values can be determined.

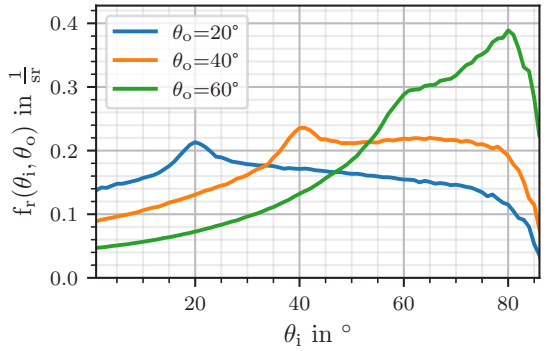

Fig. 2: BRDF measurements of sandblasted steel for $\theta_\mathrm{o} = \{20°, 40°, 60°\}$ with visible specular peaks.

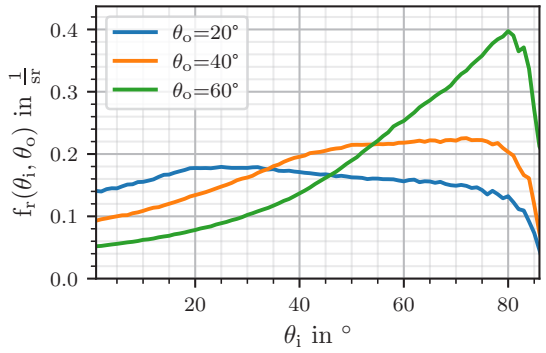

Fig. 3: BRDF measurements of sandblasted aluminium for $\theta_\mathrm{o} = \{20°, 40°, 60°\}$.

Acknowledgements

The project *Emissivity determination through the identification of a bidirectional reflection distribution function in the thermal infrared (e-BRDF)* is sponsored by the Federal Ministry of Education and Research of Germany under the funding code 13N16468.

References

[1] T. A. Germer, J. C. Zwinkels, and B. K. Tsai, *Spectrophotometry: Accurate measurement of optical properties of materials*. Elsevier, 2014.

[2] F. E. Nicodemus, J. C. Richmond, J. J. Hsia, I. W. Ginsberg, T. Limperis, S. Harman, and J. J. Baruch, *Geometrical considerations and nomenclature for reflectance*, vol. 160. US Department of Commerce, National Bureau of Standards Washington, DC, USA, 1977.

[3] J. R. Howell, M. P. Mengüç, K. Daun, and R. Siegel, *Thermal radiation heat transfer*. CRC Press, 2020.

[4] H. Noori, R. Schmoll, and A. Kroll, "Homogeneity and angular distribution of the radiance of an integrating sphere and a parabolic reflector in middle- and long-wavelength infrared," in *Optical Modeling and Performance Predictions XIV*, vol. 13129, p. 131290A, International Society for Optics and Photonics, SPIE, 2024.

DOI 10.5162/SMSI2025/D1.4

Development of a Computationally Efficient Person Detection Procedure for Low-Resolution Infrared Sensor Arrays

Alexander Rehmer
Heimann Sensor GmbH, Maria-Reiche-Str. 1, 01109 Dresden, Germany
rehmer@heimannsensor.com

Summary: A computationally highly efficient Computer Vision algorithm for detecting and tracking persons in low-resolution infrared images is introduced an its performance compared to a Deep Learning model in a case study.

Keywords: computer vision, object detection, person detection, infrared, thermopiles

Motivation

The progress made in Computer Vision during over the last two decades can mainly be attributed to the development and application of very complex models, which require virtually unlimited amounts of data as well as the employment of massive resources (storage, egenery, time, money) . Applicatons which pose restrictions on the availability of any of these resources (e.g. low-cost solutions, edge-computing applications, application on data from non-ubiquotus sensors) can not benefit from the progress made. Therefore, for some applications the development of highly tailored Computer Vision solutions is still necessary. Such a solution is presented in this work.

Introduction

Object Detection is one of the main tasks in computer vision. Its comprises the correct classification and localization of an instance of a semantic class in a digital image or video [1]. Localization is typically performed by drawing a bounding box as close as possible around the detected instance. Object recognition, as opposed to object detection, merely detects instances of a class, but does not necessarily provide their location. Object tracking is the task of tracking an identified instance of a class as it moves through the image plane from frame to frame. Since this entails an initial identification of an instance and some sort of re-identifaction in subsequent frames, object tracking usually presupposes object detection. Object detection algorithms, henceforth referred to as detectors, can be roughly divided into two classes [2]:

- Two-Stage Detectors work in two consecutive stages: A region proposal stage and a classification stage. During the first stage an algorithm identifies regions of interest (RoI) in an image that may contain an object and in the second stage these proposed regions are evaluated by one or multiple classifiers on whether they contain an instance of the
- One-Stage Detectors process the whole image in a single step by dividing it into a grid of cells and trying to detect objects centered in each of the cells.

In theory, One-Stage Detectors should provide more accurate results than Two-Stage Detectors, since they can be trained end-to-end. This is not possible with Two-Stage Detectors, since proposal generator and classifier are two seperate models. In practive however, Two-Stage Detectors surprisingly outperform One-Stage Detectors [3, 4]. While Two-Stage detectors can be realized using computationally very efficient traditional Computer Vision methods, One-Stage detectors are exclusively Deep Learning models. As such they need large amounts of training data (millions of datapoints) to achieve satisfactory performance as well as powerful hardware to process a frame in a reasonable amount of time [2].

To give even a brief overview over the current state of the art of tracking algorithms would exceed the scope of this article. Nevertheless it should at least be mentioned, that a detector can be extended of even be converted to become a *Tracktor* [5], i.e. a detector with tracking capabilities.

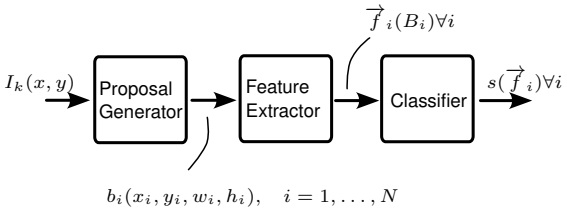

Fig. 1: Processing steps of a Two-Stage Detector.

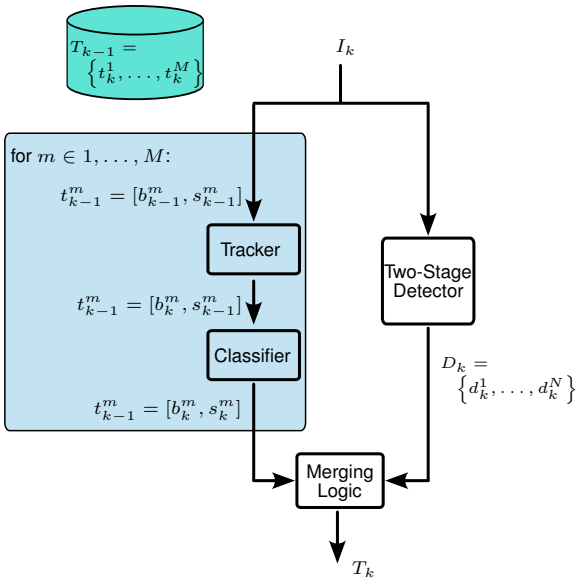

Fig. 2: Processing steps of the LRI-Tracktor.

LRI-Tracktor: A Person Detection and Tracking Procedure for Low-Resolution Infrared Sensor Arrays

Due to the higher accuracy and the possibility to employ computationally efficient traditional Computer Vision methods it was decided to developed a Two-Stage Detector specifically tailored to low-resolution infrared images. To this end, for each of the processing steps in Fig. 1 a method was carefully chosen (or developed if necessary) that fit the characteristics of the sensor data best and therefore yielded the highest performance.

In order to further enhance the performance of the developed detector, i.e. to handle occlusion, maintain instance identities across frames and improve detection accuracy, it was extended with tracking mechanisms. The resulting algorithm is named LRI-Tracktor due to the circumstance that it is tailored to **L**ow-**R**esolution **I**nfrared images. Fig. 2 provides a rough insight into the inner workings of the LRI-Tracktor. It maintains a list T_k of M active tracks $\boldsymbol{t}_k^m$, $m = 1, \ldots, M$, i.e. objects to be tracked. Each track consists of bounding box coordinates $\boldsymbol{b}_k^m$ and a classifier score s_k^m, i.e. $\boldsymbol{t}_k^m = [\boldsymbol{b}_k^m, s_k^m]$. The LRI-Tracktor first applies a tracking procedure to each of the tracks, shifting their bounding box positions from frame I_{k-1} to new positions in the new frame I_k, i.e. $\boldsymbol{b}_{k-1}^m \rightarrow \boldsymbol{b}_k^m$. Each of the shifted boxes is then evaluated by the detector's classifier, yielding a new score for each track, i.e. $s_{k-1}^m \rightarrow s_k^m$. The frame I_k is passed to the detector as well, yielding a number of detections D_k. Finally, the updated tracks $\hat{T}_k$ and the detections D_k are merged to the final result T_k using simple logic, e.g. killing tracks with low scores, initializing new tracks and updating tracks that have been found by the detector.

(a) 32x32 *(b) 60x40*

Fig. 3: Frames containing one person from a 32x32 and a 60x40 pixel thermopile array.

Tab. 1: Performance of YOLOv5m and the presented LRI-Tracktor on test data. Performance was measured in terms of the Mean Average Precision (mAP).

		Num. of Persons		
		3	4	5
YOLOv5m	$\mathrm{mAP}_{.5}$	**0.84**	**0.80**	**0.55**
	$\mathrm{mAP}_{>.5}$	0.36	0.28	0.15
LRI-Tracktor	$\mathrm{mAP}_{.5}$	0.76	0.64	0.40
	$\mathrm{mAP}_{>.5}$	**0.36**	**0.32**	**0.16**

Case study

The purpose of the following case study is to show that the developed LRI-Tracktor can achieve similar performance to state-of-the-art Deep Learning Computer Vision models on low-resolution infrared image sequence. As comparison model to the LRI-Detector the YOLOv5m Single-Stage detector was chosen. Unfortunately, the data on which YOLOv5m was evaluated is not available anymore, therefore the performance metric are not directly comparable. The LRI-Detector was applied to data of a 60x40 pixels thermopile array (perspective: bird's-eye view). YOLOv5m was applied to data of a 32x32 pixels thermopile array (perspective: top view). Fig. 3 shows an exemplary frame of each thermopile array. Multiple datasets were recorded with each sensor, containing from three up two five persons. The datasets were split into training and validation datasets. The performance on the validation data is documented in Tbl. 1. The results show, that YOLOv5m detects persons correctly more often than the LRI-Tracktor, but locates them only with low precision (rows with $\mathrm{mAP}_{.5}$). THe LRI-Tracktor on the other hand correctly detects persons with higher precision more often (rows with $\mathrm{mAP}_{>.5}$).

References

[1] A. Mauri, R. Khemmar, B. Decoux, N. Ragot, R. Rossi, R. Trabelsi, R. Boutteau, J.-Y. Ertaud, and X. Savatier, "Deep learning for real-time 3d multi-object detection, localisation, and tracking: Application to smart mobility," *Sensors*, vol. 20, no. 2, p. 532, 2020.

[2] N. O'Mahony, S. Campbell, A. Carvalho, S. Harapanahalli, G. V. Hernandez, L. Krpalkova, D. Riordan, and J. Walsh, "Deep learning vs. traditional computer vision," in *Advances in Computer Vision: Proceedings of the 2019 Computer Vision Conference*

(CVC), Volume 1 1, pp. 128–144, Springer, 2020.

[3] X. Lu, Q. Li, B. Li, and J. Yan, "Mimicdet: Bridging the gap between one-stage and two-stage object detection," in *Computer Vision–ECCV 2020: 16th European Conference, Glasgow, UK, August 23–28, 2020, Proceedings, Part XIV 16*, pp. 541–557, Springer, 2020.

[4] M. Carranza-García, J. Torres-Mateo, P. Lara-Benítez, and J. García-Gutiérrez, "On the performance of one-stage and two-stage object detectors in autonomous vehicles using camera data," *Remote Sensing*, vol. 13, no. 1, p. 89, 2020.

[5] P. Bergmann, T. Meinhardt, and L. Leal-Taixe, "Tracking without bells and whistles," in *Proceedings of the IEEE/CVF international conference on computer vision*, pp. 941–951, 2019.

DOI 10.5162/SMSI2025/D2.1

Innovative Sensor Technologies for Agrifood Quality Assessment

Francesca Venturini [1,2]
[1] *ZHAW Zurich University of Applied Sciences, School of Engineering, 8401 Winterthur, Switzerland,*
[2] *TOELT LLC, Research and Development, 8600 Duebendorf, Switzerland*
francesca.venturini@zhaw.ch

Summary:
In the agrifood sector, ensuring product quality and authenticity is critical for both producers and consumers. Optical sensor technologies, such as fluorescence and Raman spectroscopy, integrated with machine learning, enabling rapid, non-invasive, and cost-effective analysis and have still a large potential for real-time monitoring of agrifood products. Particularly for portable sensing devices, data-driven prediction models can improve transparency and sustainability in the agrifood supply chain. An example is the quality determination of extra virgin olive oil and wine.

Keywords: Fluorescence spectroscopy, deep learning, food quality, machine learning, olive oil

Introduction

Optical sensing offers rapid, non-invasive, and cost-effective analysis, enabling real-time monitoring of complex systems with minimal sample preparation. To develop affordable, portable, and precise sensors, hardware capabilities must remain constrained, making innovation in software, particularly using machine learning and deep learning (DL), a crucial enabler for applications such as chemical and biological analysis.

DL has shown significant potential in spectroscopy, as it can increase both the quality of information, by learning to extract physico-chemical signatures from noise, and the quantity of information through the automated extraction of relevant spectral features.

Advanced quality control techniques for agrifood products, powered by DL and optical sensing, are crucial to address increasing global demands, resource constraints, and the reduction of waste throughout the production process.

Current Challenges

Deep learning offers significant potential in spectroscopy but faces several key challenges. The first issue is the data availability: spectroscopy datasets are often small, heterogeneous, and expensive to acquire, limiting model training and generalization capability. A second issue is the lack of transparency on how a DL model learns during the training (functioning as black box), making it difficult to interpret predictions and reducing the trust in critical applications such as food quality. Furthermore, standard DL architectures are not optimized for high-dimensional, correlated spectral data, in contrast to other fields of application such as computer vision. Finally, begin DL computationally hungry, is not suited for deployment on real-time and field-ready devices.

Application to Olive Oil

quality control of extra virgin olive oil (EVOO) is an example of challenging use-case. EVOO is a high-quality product that is widely consumed for its health benefits and culinary properties. However, both during production process and storage, its quality continuously deteriorates due to oxidation processes. It is impossible for producers to determine olive oil quality during the oil lifecycle effectively and frequently enough.

This issue can be solved using a simple minimalistic low-cost sensor to overcome the limitations of traditional methods for evaluating olive oil quality, that are expensive and time-consuming, requiring multiple chemical analyses. The schema and photo of such a device are shown in Fig. 1.

Such portable device requires advanced software to extract efficiently quality indicators of olive oil. By using one-dimensional convolutional neural networks (1D-CNNs) it is possible to extract key physicochemical parameters, such as acidity, peroxide value, and UV spectroscopic indices, from a single fluorescence spectrum without any pre-processing (Fig. 2) [1].

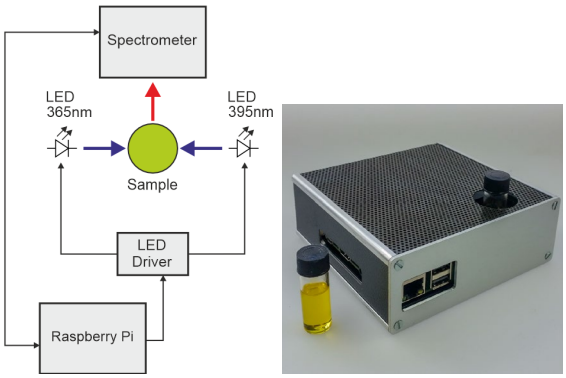

Fig. 1. Schematics (left) and photo (right) of the minimalist fluorescence sensor. Blue: Excitation light, red: Fluorescence.

While the results are promising, the small dataset and limited diversity in oil samples indicate the need for further studies with larger and more varied datasets.

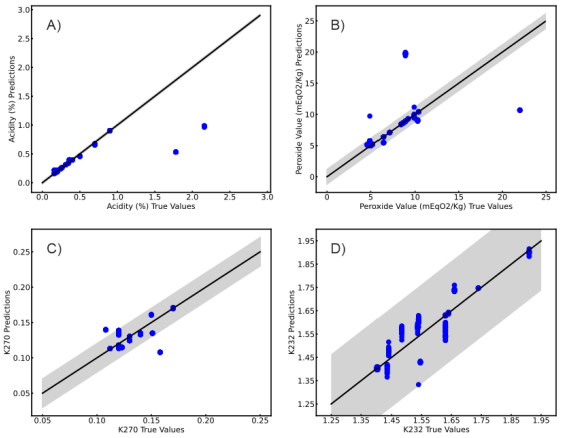

Fig. 2. Comparison of the predicted and measured (true) of the quality indicators parameters: A) acidity, B) peroxide value, C) K270 and D) K232. The solid line corresponds to predictions equal to the true labels. The grey area illustrates the experimental error on the true values. (Taken and adapted from [1]).

An approach to overcome the limitation of sparse or scares datasets is to train models on synthetic data or other type of data and exploit transfer learning to adapt it to the spectral data (e.g. fluorescence spectra) [2]. Additionally, using multidimensional data, in particular excitation-emission matrices (EEM, Fig. 3, top panel), it is possible to obtain detailed insights into the absorption and emission characteristics of substances, thereby acting as an effective fingerprinting tool. Furthermore, the fusion of deep learning and domain adaptation allows understanding and predicting the oxidation state of extra virgin olive oil with a high accuracy. By using a pretrained MobileNetv2 neural network model, trained on a large dataset of photographical images, and fine-tuning it for spectroscopic data, it is possible to effectively predict quality indicators (K232 and K268) related to oxidation processes with small datasets [2]. Such an approach also shows high interpretability, transforming deep learning from a black-box tool into a mechanism for understanding complex processes.

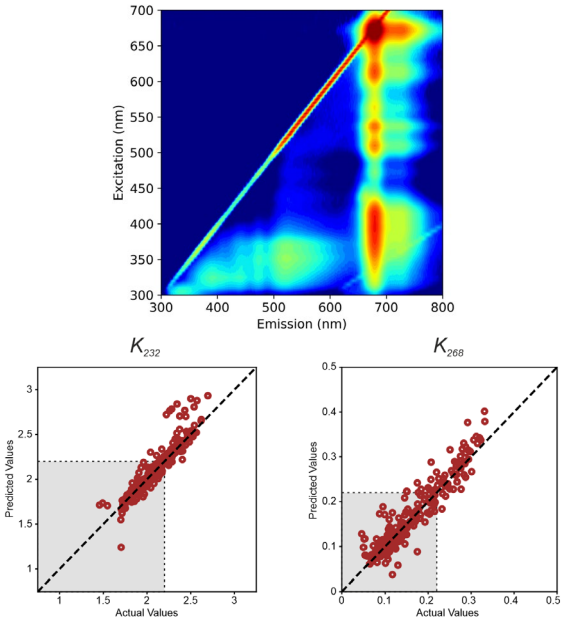

Fig. 3. Top: Excitation–emission matrix of EVOO. Bottom: Comparison of predicted and measured (actual) values of the quality indicators K232 and K268. The grey area in each plot marks the limit set by the Food and Agriculture Organisation of the United Nations and by the European Union. (Taken and adapted from [2])

Conclusions

The combination of optical sensors and DL offers substantial potential for improving agrifood quality assessment. Portable, low-cost devices powered by specific models enable accurate real-time monitoring of key parameters, as demonstrated in extra virgin olive oil. These innovations support sustainable and scalable solutions for food quality monitoring and open the door to a new generation of portable devices.

References

[1] Venturini, F., Sperti, M., Michelucci, U., Gucciardi, A., Martos, V.M. and Deriu, M.A., Extraction of physicochemical properties from the fluorescence spectrum with 1D convolutional neural networks: Application to olive oil. *Journal of Food Engineering* (2023), 336, p.111198); doi:10.1016/j.jfoodeng.2022.111198

[2] Michelucci, U. and Venturini, F., Deep learning domain adaptation to understand physico-chemical processes from fluorescence spectroscopy small datasets and application to the oxidation of olive oil. *Scientific Reports* (2024), 14(1), p.22291; doi:10.1038/s41598-024-73054-

DOI 10.5162/SMSI2025/D2.2

Quality assessment of raw fresh milk from several sources by no-destructive Raman sensor

Ilaria Petrignani[1], , *Salvatore Almaviva*[1], *Antonia Lai*[1]
[1] ENEA, Italian National Agency for New Technologies, Energy and Sustainable Economic Development.
Via Enrico Fermi, 45, I-00044 Frascati, Italy
Ilaria.petrignani@enea.it

Summary:

Raman spectroscopy has emerged as a powerful, non-destructive tool for assessing the quality and authenticity of dairy products, particularly fresh milk from a variety of sources. By producing detailed molecular 'fingerprints' in the 200-2000 cm-¹ range, Raman spectroscopy enables rapid identification of milk composition and detection of potential adulterants, offering significant advantages such as faster analysis times, reduced costs and minimal sample preparation. Combined with multivariate statistical analysis, Raman spectroscopy offers a promising solution for authenticating milk and ensuring quality control throughout the dairy supply chain. In this study, Raman spectra of different milk types (cow, sheep) were collected and compared, revealing unique and common spectral features related to their composition. Although not aimed at detecting adulteration, this analysis highlights the potential of Raman spectroscopy as a tool for differentiating milk types based on their spectral characteristics, suggesting a potential application in milk quality control.

Keywords: Raman spectroscopy, milk adulteration, non-destructive analysis, food quality

Background, Motivation an Objective

The quality of milk and dairy products is fundamental to food safety and consumer confidence. In the dairy industry, the composition of milk varies significantly between species, and these molecular differences influence nutritional value, flavour and end product applications. Sheep and cow's milk have unique profiles due to their different chemical composition. Traditional methods of milk quality analysis, such as electrophoresis or chromatography, are complex and time-consuming, making them impractical for rapid and continuous screening [1].

The use of an accurate, non-destructive tool to characterise these differences in-situ and in real-time could be useful for the dairy product chain.

Growing interest in more rapid and sustainable analytical solutions has focused attention on spectroscopic techniques, such us Raman spectroscopy, for the evaluation of dairy products. Raman spectroscopy offers a non-destructive, rapid and accurate approach to milk analysis, enabling the acquisition of unique molecular spectra or 'fingerprints', that reveal compositional details without the need for sample pretreatment [2].

With this technique, we have analysed different samples of milk, such as sheep and cow, to identify the fingerprint of each sample and any compositional changes that may occur as a result of freezing. Differences in spectral peaks can be used to identify and monitor specific quality markers in both fresh and frozen milk in the supply chain, for milk quality.

Description of the System

Raman spectroscopy is a well-known laser based technique, based on molecular vibrations/inelastic light scattering [3].

For this study, the analysis was carried out using a table-top portable Raman system (i-Raman by B&W TEK Inc.), equipped with a GaAlAs diode laser at 785 nm with tunable power (300 mW max, limited to 70 mW in the present measurements) and an optical fiber probe. The measurements were performed on raw samples of cow's and sheep's milk taken from milkings of 24 and 72 hours duration, respectively, under fixed stall conditions. Some of the samples were frozen at -30°C and analysed after thawing at +4°C for 24 hours.

We immersed the optical fiber probe directly into 60 ml of raw milk at room temperature (see Fig. 1). This contact-based method preserves the natural state of the milk and allows accurate analysis of its molecular composition. The laser source was set to a power of 70 mW for 50 s, and data were acquired in the 200-3000 cm-¹ range. To increase accuracy and reliability, each sample was measured 10 times under the same

conditions, ensuring consistent and reproducible spectral profiles for fresh and frozen milk.

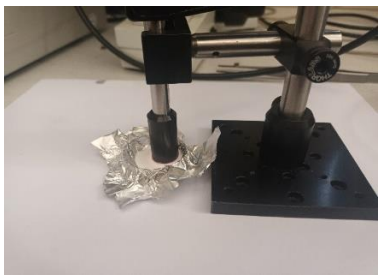

Fig.1 Adopted measurement procedure

Results

The results obtained highlight slight differences in the spectral features between fresh and thawed cow's and sheep's milk (see Fig.2 and Fig.3). According to the literature [4,5] the bands at 870, 1076, 1296-1300, 1440, 1650, 1744, 2800-2900 cm^{-1} were detected in all samples, with evident variations observed in the intensity and in the shape of the bands.

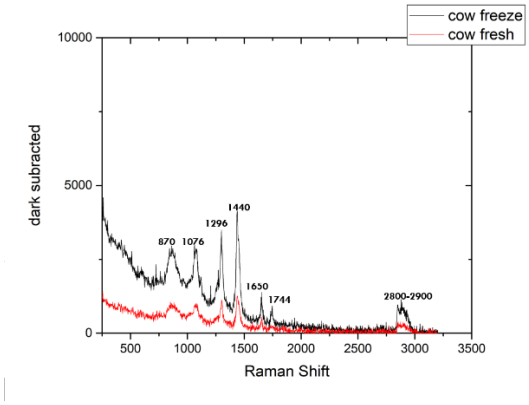

Fig.2 Raman spectra of fresh raw and freeze cow milk samples

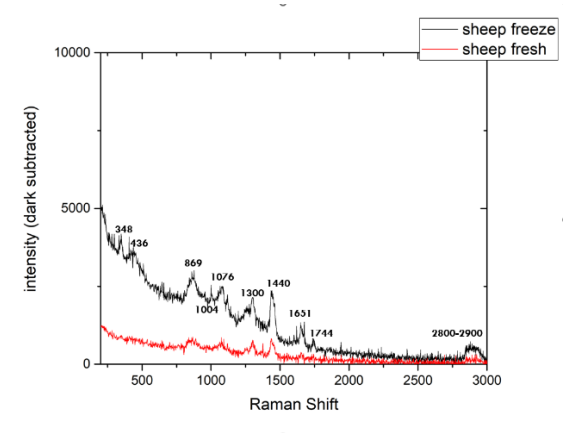

Fig.3 Raman spectra of fresh raw, dry and freeze sheep milk samples

The identified peaks are due to the main components of milk such as lipids, proteins and carbohydrate (lactose) [4,5], and the results for the frozen sheep milk samples showed a peak at 343 cm^{-1} representing the stretching and bending vibrations of the C-O-C [6].
Although there were variations in the Raman spectra of the milk samples, the visual discrimination of the latter by these spectral variations, was difficult and subjective. For this reason, future studies of the spectra, will be based on multivariate analysis, for example by using Principal Component Analysis (PCA).

Aknowledgments

This study was carried out within the Agritech National Research Center and received funding from the European Union Next-GenerationEU (PIANO NAZIONALE DI RIPRESA E RESILIENZA (PNRR) – MISSIONE 4 COMPONENTE 2, INVESTIMENTO 1.4 – D.D. 1032 17/06/2022, CN00000022). This manuscript reflects only the authors' views and opinions, neither the European Union nor the European Commission can be considered responsible for them.

References

[1] Bharti, A., Jain, U., & Chauhan, N. (2024). Progressive analytical techniques utilized for the detection of contaminants attributed to food safety and security. Talanta Open, 10, 100368.

[2] Silva, M. G., de Paula, I. L., Stephani, R., Edwards, H. G. M., & de Oliveira, L. F. C. (2021). Raman spectroscopy in the quality analysis of dairy products: A literature review. Journal of Raman Spectroscopy, 52(12), 2444–2478. https://doi.org/10.1002/jrs.6214

[3] Jones, R. R., Hooper, D. C., Zhang, L., Wolverson, D., & Valev, V. K. (2019). Raman Techniques: Fundamentals and Frontiers. Nanoscale Research Letters, 14(1), 231. https://doi.org/10.1186/s11671-019-3039-2

[4] Huang, W., Fan, D., Li, W., Meng, Y., & Liu, T. C. (2022). Rapid evaluation of milk acidity and identification of milk adulteration by Raman spectroscopy combined with chemometrics analysis. Vibrational Spectroscopy, 123, 103440. https://doi.org/10.1016/j.vibspec.2022.103440

[5] Yazgan, N. N., Genis, H. E., Bulat, T., Topcu, A., Durna, S., Yetisemiyen, A., & Boyaci, I. H. (2020). Discrimination of milk species using Raman spectroscopy coupled with partial least squares discriminant analysis in raw and pasteurized milk. Journal of the Science of Food and Agriculture, 100(13), 4756–4765. https://doi.org/10.1002/jsfa.10534

[6] Boyaci, I. H., Temiz, H. T., Geniş, H. E., Acar Soykut, E., Yazgan, N. N., Güven, B., Uysal, R. S., Bozkurt, A. G., İlaslan, K., Torun, O., & Dudak Şeker, F. C. (2015). Dispersive and FT-Raman spectroscopic methods in food analysis. https://doi.org/10.1039/C4RA12463D

DOI 10.5162/SMSI2025/D2.3

Investigating biotic and abiotic stresses on green-leaf plants by means of hand-held Raman spectroscopy

Lorenzo Pandolfi[1], Guido Faglia[1], Niccolò Miotti[2], Massimo Turina[2], Marina Ciuffo[2], Emanuela Gobbi[2], Teodora Tonto[3], Vittoria Locato[3], Laura de Gara[3] and Camilla Baratto[1]
[1] CNR-INO and University of Brescia, Via Branze 45, 25123 Brescia, Italy
[2] CNR-IPSP, Strada delle Cacce 73, 10135 Turin, Italy
[3] Università Campus Bio-Medico di Roma, 00128 Rome, Italy
camilla.baratto@ino.cnr.it

Summary:
Raman spectroscopy is a non-invasive technique that can be adopted for the in-field monitoring of crops and early detection of plant pathogens. Combining its sensing capabilities with chemometric analysis, it is possible to classify plants as healthy or infected by evaluating the leaf pigment content. The method is currently under investigation to characterize both abiotic stresses and biotic infections at the lab scale.

Keywords: Raman, spectroscopy, precision agriculture, chemometrics, plant pathogens

Introduction

Nowadays, while world population and food demand are rapidly growing worldwide, the yield and the quality of agricultural products are greatly affected by plant diseases, devastating entire crops, and causing severe economic losses. [1] For these reasons, expensive chemical treatments and pesticides and drugs are needed in modern agricultural and food production. Nevertheless, irrational or excessive usages of these chemicals cause severe concern for environmental and food safety reason. Thus, to limit the use of phytosanitary treatments, rapid detection of pathogen-infected plants is an important first step in plant disease management. Most disease symptoms usually manifest only at relatively later stages of infection or when it is already too late for a possible precision therapeutic intervention. [2] Therefore, early detection of infected plants would allow their rapid and selective removal, thus greatly reducing the opportunity for further disease spreading. This approach falls more generally into what is defined as "precision agriculture", a protocol of tailored treatments applied only when they are really needed, for a more sustainable farming. [3] Currently, the gold standard methods for analyte detection correlated to the presence of plant pathogens are chromatographic-based techniques. Although these methods are sensitive, accurate and reliable, the major limitations are the requirement for dedicated lab space, prolonged analyses, costly systems with expensive upkeep and the need for highly trained operators, as well as cumbersome analyte extraction and time-consuming sample preparation steps. [1] The use of Raman spectroscopy in agriculture is recently emerging for its relatively fast and non-destructive analysis that does not require sample preparation and offers selective and early detection of biochemical markers (*i.e.*, carotenoids, chlorophylls and anthocyanins) over multiple stress conditions. [4] By comparing the differences in the Raman spectra of a diseased sample vs. a healthy leaf, compositional analysis, rapid diagnosis of plant diseases, and biotic and abiotic stress response of plant tissue can be easily evaluated. [2][5] Most importantly, the recent development of portable and handheld Raman spectrometers allows for a quick and easy on-field monitoring, reducing the gap between sample collection and laboratory analysis. Finally, compared to already existing near-infrared monitoring techniques, the Raman spectrum is of much simpler interpretation. In the CN-Agritech project, the feasibility of the application of Raman spectroscopy in precision agriculture was evaluated, with the aim of analyzing biotic and abiotic stresses in green-leaf plants.

Results

In this work we have optimized an experimental protocol for the early detection of plant pathogens, starting from the study of different types of green-leaf plants (*i.e.*, tomato, rocket). Many physical variables which could affect the measurement were tested, including the working wavelength and the leaves to be chosen. Rocket plants have been sowed simulating a saline accumulation in the soil, in order to study the abiotic stress, while tomato plants were infected with a commercially interesting virus, to evaluate

the outcomes of biotic stresses. In particular, rocket plants were grown in a greenhouse: a control group was left without treatment, one group was treated with 150 mL NaCl solution, and another group was treated with 300 mL NaCl solution. Similarly, three tomato plants were infected by *Tomato Spotted Wilt virus* (TSWV) and three plants were used as a control group. The Raman measurements have been recorded either with a Horiba iHR 320 microspectrometer coupled with a 532 nm laser line, or a Rigaku Progeny hand-held Raman spectrometer in contact mode, with excitation wavelength at 1064 nm. Strategies to remove the stray light in outdoor environment were studied. Since signal variations were small and biological variability very high, a chemometric statistical approach was required to analyze the data collected. In fact, machine-learning algorithms (*e.g.*, PCA, LDS, PLS-DA) are at the core for predictive classification methods. Concerning rocket leaves, tests on fresh and lyophilized leaves were performed. The use of either 532 nm or 1064 nm as excitation source was achieved for fresh leaves, while with lyophilized specimens, intense fluorescence signal impeded the use of visible light. The interest in measuring dried samples consisted in the possibility to freeze the leaf and to exchange samples between different laboratories to compare and correlate conventional analytical techniques with Raman spectroscopy. The investigated data range was from 700 a 1700 cm^{-1}, as in this region, the Raman spectrum of green-leaf plants essentially displays the vibrational patterns of bio-pigments and metabolites, *e.g.*, carotenoids, chlorophyll, and polyphenols (Fig. 1). The classification accuracy strongly depends on the data collection method and was as high as 97.5% for lyophilized samples. For tomato plants, the aim of the investigation was to detect any Raman signal that could be correlated with the infection, before the appearance of any symptoms on the leaf. For this, infected leaves and mock-infected ones have been analyzed after three, six and nine days after the virus injection. After nine days each leaf measured has been evaluated with the destructive Polymerase Chain Reaction (PCR) diagnosis test. After data processing with PLS-DA, we demonstrated that a classification of healthy *vs.* infected plant was achieved by means of the multivariate analysis and that the error rate diminishes as the time increases. It is very interesting to consider that the technique is somewhat independent of the plant type. It is therefore potentially usable for leaf crops other than those considered in this study.

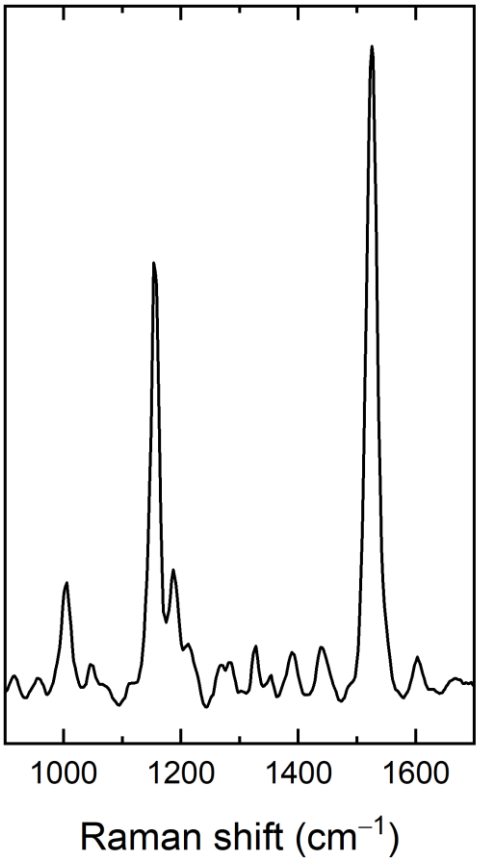

Fig. 1 *Raman spectrum of a fresh tomato leaf, recorded with the hand-held device (1064 nm).*

References

[1] S. Weng, X. Hu, J. Wang, L. Tang, P. Li, S. Zheng, L. Zheng, L. Huang, Z. Xin, “Advanced Application of Raman Spectroscopy and Surface-Enhanced Raman Spectroscopy in Plant Disease Diagnostics: A Review”, Journal of Agricultural and Food Chemistry, 69 (10), 2950-2964, 2021, DOI:10.1021/acs.jafc.0c07205

[2] P. Chung, G. Singh, C. Huang, S. Koyyappurath, J. Seo, H. Mao, P. Diloknawarit, R. Ram, R. Sarojam, N. Chua, “Rapid Detection and Quantification of Plant Innate Immunity Response Using Raman Spectroscopy”, Frontiers in Plant Science, 12, 2021, DOI:10.3389/fpls.2021.746586

[3] R. Gebbers, V. I. Adamchuck, “Precision Agriculture and Food Security”, Science, 327, 828-831, 2010, DOI: 10.1126/science.1183899

[4] S. Yeturu, P. V. Jentzsch, V. Ciobota, R. Guerrero, P. Garrido, L. Ramos, “Handheld Raman spectroscopy for the early detection of

plant diseases: Abutilon mosaic virus infecting Abutilon sp.”, Analytical Methods, 8 (17), 3450-3457, 2016, DOI: 10.1039/c6ay00381h

[5] M. Roy, A. Prasad, “Raman spectroscopy for nutritional stress detection in plant vascular tissue”, Materialia, 24, 2022, DOI:10.1016/j.mtla.2022.101474

DOI 10.5162/SMSI2025/D2.4

Portable Raman Spectroscopy Based Prototype for the Clostridia Detection in Milk

Daniele Barbiero[1,2], Fabio Melison[1], Lorenzo Cocola[1], Massimo Fedel[1], Christian Andrighetto[3], Paola De Dea[3], Luca Poletto[1]
[1] Institute for Photonics and Nanotechnologies, National Research Council, Padua, Italy
[2] University of Padova, Department of Information Engineering, Padova, Italy
[3] Veneto Agricoltura, Istituto per la Qualità e le Tecnologie Agroalimentari, Thiene, Italy
daniele.barbiero@pd.ifn.cnr.it

Summary:
In the dairy industry the detection of Clostridia is a remarkable issue. These bacteria are known for their hydrogen and carbon dioxide production, which compromises the shape and flavor of the cheese in which they reside. Early *Clostridia* detection allows infected milk to be redirected to less-aged products without any loss of quality, thus avoiding economic losses. Current methods are time-consuming and not specific for *Clostridia*, this paper presents a portable instrument based on Raman gas spectroscopy tailored to the detection of Clostridia and a test routine developed to simplify the experimental setup.

Keywords: Raman spectroscopy, *Clostridium*, Food Quality, Gas analysis, Hydrogen

Motivation

Clostridium detection in milk is crucial because these bacteria can survive pasteurization and then return to their active form. Their metabolism produces large amounts of hydrogen and carbon dioxide which leads to late blowing defects like cracks and slits in cheese. This not only changes the taste and appearance of the cheese but also contributes to food waste. Milk contaminated with *Clostridium* can still be used in making less aged cheeses. Thus, it is important to identify its presence as quickly as possible. Rapid microbiological methods are available [1], but they are expensive and require skilled operators, while the standard method [1], though inexpensive, lacks in specificity for *Clostridium*. The proposed solution is represented by a portable instrument based on Raman spectroscopy adapted to detect *Clostridium* through the hydrogen they release in the headspace of culture vials, as they are the only hydrogen-producing bacteria commonly found in milk. The developed instrument is specific for detecting *Clostridia*; unlike the traditional method, it has also proven to be faster [1,2,3]. Significant effort has been made in making it portable, allowing the direct use in its field of application.

Experimental setup

For the Raman scattering excitation, a 532 nm Nd:YAG DPSS laser with an power output of 1 W was employed. The laser beam is focused into the headspace of the vial under exam. After the interaction with the sample, the beam is directed towards a light trap and absorbed. The scattered radiation is collected by a custom made spectrometer positioned orthogonally to the laser path. The Raman signal is imaged onto the spectrometer focal plane with a pair of Hastings achromatic triplets. In the collimated light region between the two triplets, a 550 nm long-pass interferometric filter is placed in order to reject the strong Rayleigh scattering. The compact f/2.8 spectrometer setup includes an entrance objective lens, an additional long-pass filter, a diffraction grating, and a CMOS camera equipped with its objective lens. The instrument is also equipped with a linear translator useful to move a batch of vials and analyze them one at a time. Additionally, a pulley is placed in order to rotate the vials during the measurements. The entire instrument is enclosed in a controlled temperature box (53 cm x 38 cm x 40 cm) which is internally stabilized at 37 degrees Celsius by a heater. For this specific test the pulley could be

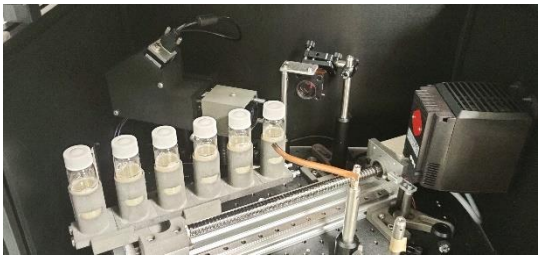

Figure 1: Experimental setup

disabled so during the measurements it is possible to rotate or just translate the vials.

Spectra generation

Raman spectra are generated by averaging several rows of the acquired frames. An example spectrum is shown in Figure (2). This technique is sensitive to most gas molecules, allowing the simultaneous detection of hydrogen, water vapor, nitrogen, oxygen, and carbon dioxide.

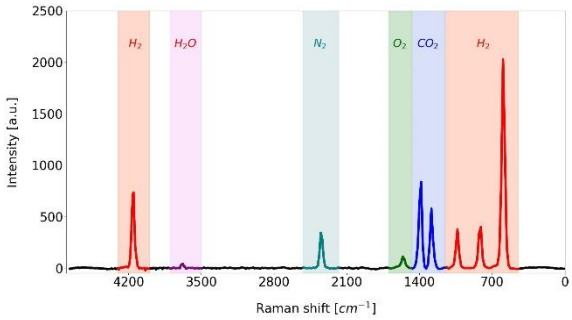

Figure 2: Example of Raman spectrum

The proposed method operates on a threshold based algorithm to determine the *Clostridium* contamination of a vial. A vial is considered contaminated if the hydrogen peak integral (587 cm^{-1}) exceeds the background mean plus 5 times its standard deviations in the same spectral region. The main limit to the measurement is represented by scattering and fluorescence caused by dirt, condensation, or milk droplets on the walls of the vials since those phenomena can lead to partial or complete saturation of the detector. For this reason, the idea is to rotate or translate the vial until an acceptable measurement condition is achieved. In any case, as long as the contribution of fluorescence does not lead to saturation of the detector, it can be subtracted by fitting with a 3rd degree polynomial equation.

Testing

To compare the effects of the two movements, rotation and translation, 24 vials containing a concentration expected to yield 19 positive results were prepared. The vials were measured by testing both rotations and translations. The sample preparation and image processing procedures followed standard methods used in previous measurements [1]. For each vial, 5 camera frames were acquired while rotating the vial around its vertical axis, subsequently 5 images were acquired after translating the vial 1 millimeter in both directions around the center (defined as the position when the laser passes through the vial's diameter). A measurement of 24 vials takes approximately 23 minutes. After choosing the most effective measurement strategy, the analysis time can possibly be reduced. To validate the experiment, a control test was conducted with the standard method on samples containing the same concentration of spores per volume unit.

Results

The method based on Raman spectroscopy revealed 7 positive vials out of 24 after 48 hours; while the standard method detected only 1 positive vial after the same incubation time. After 3 days, the number of positive vials detected by Raman spectroscopy increased to 20, while the standard method identified 16 positive vials.

Conclusions

The developed prototype was able to detect 35% (7/20) of the positive vials within 48 hours, whereas the standard method detected only 6% (1/16) as positive, showing the potential for a faster and more specific testing method. Measurement through successive translations did not present particular issues compared to rotation, leading to a possible simplification of the hardware setup. Future tests will be conducted to validate the proposed method and for further hardware and software improvements.

Acknowledgments

This work has been partially financially supported by Progetti@CNR–SCAN4FOOD–Early Detection of Contaminants in Food–CUP B55F21007800005. This study was partially carried out within the Agritech National Research Center and received funding from the European Union Next-Generation EU (Piano Nazionale di Ripresa e Resilienza (PNRR)–Missione 4 Componente 2, Investimento 1.4–D.D. 1032 17/06/2022, CN00000022).

References

[1] Barbiero D, Melison F, Cocola L, et al. Raman Spectroscopy Applied to Early Detection of Clostridium Infection in Milk. Applied Spectroscopy. 2024;0(0). doi:10.1177/00037028241252693

[2] Daniele Barbiero, Fabio Melison, Lorenzo Cocola et al., "Detection of bacteria contamination in milk through H2 and CO2 measurements by Raman gas spectroscopy", Sensing for Agriculture and Food Quality and Safety XVI, 16, (2024); doi:10.1117/12.301299

[3] Daniele Barbiero, Fabio Melison, Lorenzo Cocola et al., "Determination of hydrogen-producing bacteria contamination in milk by Raman gas spectroscopy", Proc. SPIE 12879, Photonic Technologies in Plant and Agricultural Science, 1287908 https://doi.org/10.1117/12.2692490

DOI 10.5162/SMSI2025/D3.1

Rapid measurement of the Size-of-Source Effect by using an Iris aperture

Miguel Mendez[1], *Robert Schmoll*[1] *and Andreas Kroll*[1]
[1] University of Kassel, Mönchebergstraße 7, Kassel, Deutschland
miguel.mendez@mrt.uni-kassel.de

Summary: The source size effect (SSE) is a systematic error in thermography cameras, where the measured radiance temperature varies with object size. The SSE is measured by capturing deviations in the camera's response across defined object sizes. These methods must ensure that the calculated differences are distinguishable from of measurement uncertainty and that any thermal effects unrelated to the measurement process are minimized. This often requires considerable effort, especially when the number of points to collect increases. This paper proposes an alternative method using an iris aperture for continuous SSE measurement, which yields results comparable to those of the conventional discrete method, while providing three times more data points and reducing measurement time by 98 %.

Keywords: Infrared thermography, Size-of-Source Effect, Iris aperture

Introduction

As with pyrometers, the accuracy of temperature measurements with thermography cameras depends not only on the emissivity of the objects to be measured, but also on their size, among other factors. This is known as the Size-of-Source Effect (SSE), and the associated deviations can exceed the uncertainty reported by manufacturers [1]. To study this systematic error and its causes—such as diffraction, scattering, and sensor signal digitization—a proposed method of measurement must be precise enough to clearly represent the behavior of the sensor-optical system under test [2]. Since the SSE is often represented as differences in measured quantities, the reported values can easily be contaminated by side effects, such as thermal drift due to heat convection. This complication increases the complexity of experimental setup and the effort required to measure the SSE. This paper presents a rapid method for measuring the SSE of a thermal imaging camera using an Iris aperture.

Measurement of the Size-of-Source Effect

The SSE evaluation is typically performed by recording the deviation of the measured radiance temperature of an object observed by the camera as the object size changes. To do this, the traditional approach, referred to as the discrete approach, positions a series of circular apertures, each with a different diameter, in front of a black body surface (BBS) with a known radiance temperature. These apertures are changed from smallest to largest, with a waiting period, of 2 min in this paper, between each change so that the thermal behavior stabilizes after the positioning of the apertures. The present paper proposes an alternative that uses an Iris aperture, which will be referred to as the continuous approach. It consists of capturing a sequence of frames to measure the change in temperature as the BBS is enlarged by hand sliding the pin lever of an Iris aperture, which adjusts the diameter of the circumference formed by the leaves. The Iris was mounted on a 3D-printed bracket, which was attached to a stainless steel plate (see Fig. 1). This bracket was designed for smooth insertion, but with sufficient stiffness to restrict the displacement of Iris while the circumference is being adjusted. The stainless steel plate was coated on the front with a high-emissivity reference paint, whereas the back side was left untreated to minimize heating up on the black surface.

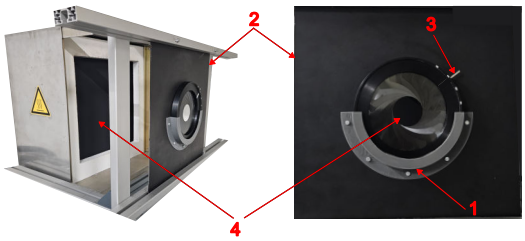

Fig. 1: Experimental set-up. The 3D printed mounting bracket (1) is attached to the high emissivity coated metal sheet plate (2) by means of conventional screws. The Iris aperture (3) is then placed into the mounting bracket and the size of the observed black body surface (4) is adjusted by moving the pin lever.

Results

The SSE was evaluated using the discrete and continuous approaches for a cooled midwave infrared camera, with a frame rate of 200 Hz for

both measurements. A relative diameter $d_{\text{rel,i}}$ in % is determined as

$$d_{\text{rel,i}} = d_{\text{px,i}} \cdot 100 / V_{\text{res}} \quad (1)$$

with $d_{\text{px,i}}$ the diameter of the circle in thermogram number i, determined with an image processing algorithm, and V_{res} the vertical resolution of the camera. The SSE is evaluated through the calculated temperature deviations

$$\Delta\theta_j = \theta_j - \theta_{\text{ref}} \quad (2)$$

where θ_j is the mean value obtained over a concentric circular region of interest (ROI), with a radius of 5 px, in an averaged thermogram j. In the discrete approach, for each diameter, this thermogram j was obtained by averaging 50 consecutive frames. In the continuous approach, for a set of predefined values of $d_{\text{rel,j}}$, all thermograms in the frame sequence with similar diameters $d_{\text{rel,i}}$, within a tolerance range of $\pm$ 0.5 %, were grouped together. Each set, with at least 20 members, was averaged pixel by pixel, resulting in thermogram j. Then θ_{ref} corresponds to the value obtained at the largest circle for each measurement.

The temporal evolution of d_{rel} and the measured radiance temperature θ is presented in Fig. 2-a). The contraction of the observed BBS is reflected in a reduction of the measured temperature, as well as the opposite, which is congruent with the well known behaviour of the SSE. The temperature deviations are presented in Fig. 2-b). It can be observed that both curves overlap, except for the point enclosed by the red circle, which deviates slightly from the trend observed in the other points of both curves. Notwithstanding, the superposition of the curves suggest that, the SSE of the optical system (camera and optical objective) was reproduced well enough by both approaches.

Table 1 lists the time spent performing each measurement and the number of points obtained with each approach. The use of the Iris aperture made it possible to collect 3 times more measured points, at a cost of 2 % of the time spent for the continuous measurement. This improves significantly the resolution of the resulting curves, facilitating a more accurate interpretation of the measured SSE and related phenomena. However, it requires 6 more times disk storage capacity.

Summary and Outlook

This paper has presented the use of an Iris aperture to measure the Size-of-Source Effect of a thermography camera. The size of the object is adjusted by sliding the pin lever of the Iris aperture. The temporal evolution of the measured temperature decreases as the observed diameter is reduced. Both this method and the traditional method provide the same relationship between these variables, but an improvement in the resolution of the curve was achieved, along with a notable reduction in measurement time ($> 98\%$) by using the Iris aperture. However, this came at the cost of requiring 10 times more disk space. In future work, the Iris aperture will be automated so as to provide a more uniform and reproducible variation in the diameter.

Tab. 1: Summary statistics of the measurements

Approach	Discrete	Continuous
Total measurement time in s	1020	18
Number of samples obtained	8	29
Required storage disk space in MB	163	1120

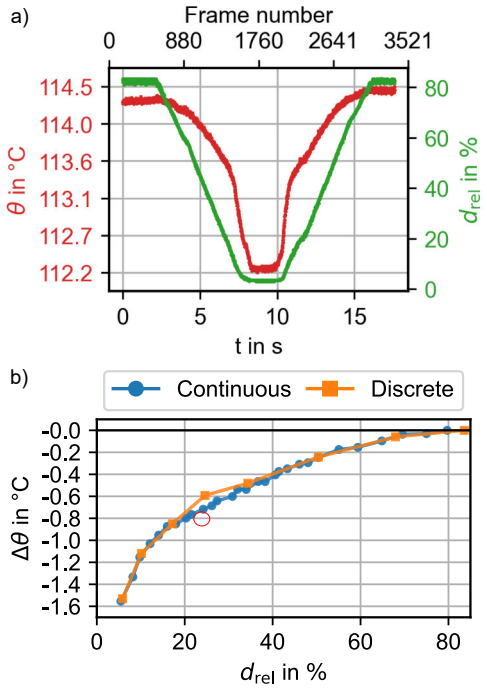

Fig. 2: Measured Size-of-Source Effect. a) Time series of the temporal evolution of the measured radiance temperature and b) the calculated temperature deviations.

Acknowledgments

This work is supported by the Federal Ministry for Economic Affairs and Climate Action (BMWK) on the basis of a decision by the German Bundestag.

References

[1] S. König, B. Gutschwager, R. D. Taubert, and J. Hollandt, Metrological characterization and calibration of thermographic cameras for quantitative temperature measurement, *Journal of Sensors and Sensor Systems*, 9, 425–442 (2020), doi: 10.5194/jsss-9-425-2020.

[2] M. Ohtsuka and R. E. Bedford, Measurement of size-of-source effects in an optical pyrometer, *Measurement*, 7, pp. 2–6 (1989), doi: 10.1016/0263-2241(89)90019-5

DOI 10.5162/SMSI2025/D3.2

Fast MEMS-IR-Emitters for NDIR Sensors

Toni Schildhauer[1], Andreas T. Winzer[1], Julia Baldauf[1], Thomas Ortlepp[1]
[1] CiS Forschungsinstitut für Mikrosensorik GmbH, Konrad-Zuse-Str. 14, 99099 Erfurt, Germany
tschildhauer@cismst.de

Summary:
Infrared emitters based on MEMS technology are ideal for miniaturizing NDIR spectrometers. However, commercial MEMS-IR emitters typically reach their operational limit at measurement frequencies around 20 Hz, while certain applications, require frequencies up to 100 Hz. To meet this demand, we have advanced our MEMS-IR emitters by optimizing both chip architecture and assembly techniques for high-speed NDIR spectroscopy. These enhanced IR sources enable gas analysis in the 2-20 µm wavelength range at pulse frequencies up to 100 Hz.

Keywords: NDIR, MEMS, infrared, emitters, gas sensors

Background and Motivation

NDIR (non-dispersive infrared) sensors are widely used for analyzing various gases. MEMS-based infrared (IR) sources are broadband, emit up to at least 12 µm, can be electrically pulsed, are resistant to minor vibrations and temperature fluctuations, and are cost-effective. Therefore, they currently represent the best solution for miniaturized NDIR sensors. However, commercially available IR emitters can only be effectively pulsed up to about 20 Hz. Although some emitters are listed with cutoff frequencies of up to 40 Hz [1, 2], our tests have not confirmed any cutoff frequency above 25 Hz.

The aim of this study was to optimize our own membrane-based MEMS-IR emitters for higher modulation frequencies while keeping sufficient intensities for our customer's NDIR-applications. Therefore, we built a model of our current chip in the simulation software Comsol Multiphysics Version 6.1 and tested various parameters before manufacturing and assembling new emitters.

Model Building

The parameters of the membrane layers deposited in our cleanroom required for a thermoelectrical model are yet unknown and can only be approximated roughly using values from the literature. Direct measurement of these material parameters is currently not feasible, so they were determined via an algorithm comparing simulation results with measured data.

First, we measured the temperature and electrical resistance of our legacy infrared (IR) emitter as a function of applied electrical power, at atmospheric pressure and in vacuum. The resulting characteristic curves served as target values for the development of the COMSOL model. Initially, physically meaningful boundary values were set for the desired material parameters, which guided the initial simulations. The simulated curves for temperature, electrical resistance, and power were used as input data of a neural network, which derived new estimations of the material parameters by comparing the simulation results with the measurement data. This process was repeated iteratively, with each simulation refining the parameters based on the neural network's outputs, gradually building a dataset.

This iterative process of simulation, comparison, and parameter adjustment eventually converged to a unique parameter set defining the thermoelectrical properties of the membrane layers. Figure 1 shows the comparison between simulation with these parameters and the measured values, demonstrating excellent agreement.

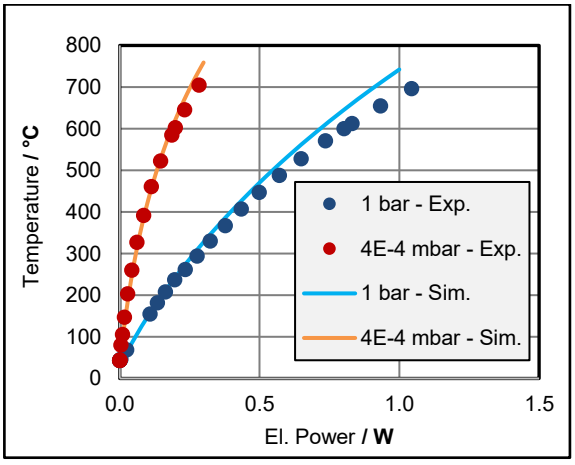

Figure 1: Comparison of the temperature-power curves (at two different pressures) between the

measured results (dots) and simulations (curves) based on the identified material parameters.

Design Study

With the obtained Comsol model, we were able to simulate over a hundred of different heating membrane geometries and the electric control. We analyzed potential designs before manufacturing with respect to resistance, power consumption, intensity and dynamic. The most promising designs were then chosen to be manufactured and assembled in our clean room facility.

Results

The dynamic response of MEMS-based infrared emitter chips is critically influenced by their physical dimensions. Larger chips possess a higher thermal capacity, which inherently slows their response times. Conversely, smaller chips, though more dynamic due to their reduced thermal capacity, often exhibit significantly lower intensity. Due to these limitations, we pursued two distinct approaches. First, we optimized the design of an existing larger chip, aiming to enhance its response speed while preserving as much emission intensity as possible. Second, we developed a single-chip-array of heating membranes, which combines the advantages of both high total emission area for increased intensity and small individual membrane size for improved thermal dynamics. In addition to fabricating newly optimized emitter chips, we successfully assembled highly compact emitter arrays from individual chips.

Extensive testing of these advanced emitter modules demonstrated noteworthy performance improvements. For instance, by implementing minor design modifications to our legacy chip, we achieved a 10% increase in modulation depth across a frequency range of 10 to 50 Hz. Furthermore, our novel in-chip array design, which retains the dimensions of the original chip, was able to deliver a 65% increase in emission intensity at 60 Hz without increasing electrical power consumption.

Moreover, our assembled 16-chip array exhibited the same intensity at 100 Hz as the legacy chip operating at 10 Hz. Despite being housed within the same TO-39 socket and therefore keeping the same packing size, the multi-chip array consumes three times the power of the legacy chip. Although the assembly of such a multi-chip array is complex and incurs higher production costs, it underscores the potential of this approach, particularly for high-value applications such as clinical breath analysis, where performance benefits justify the increased cost and power consumption.

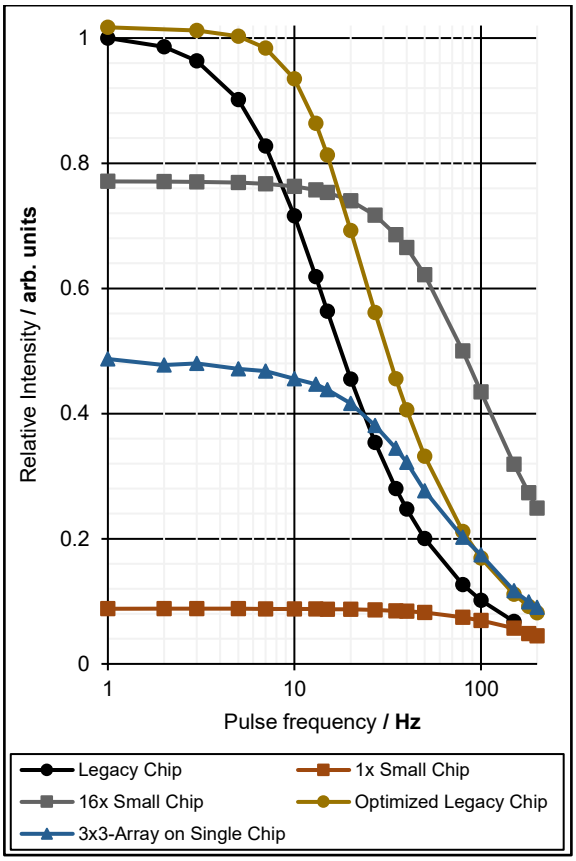

Figure 2: Comparison of the new IR-emitters to our legacy chip. The intensities are referenced to the legacy chip. The emitters were pulsed with a square-waved power signal at different frequencies and peak-to-peak intensity was measured.

References

[1] https://www.infrasolid.com/en/products, 11/13/2024

[2] https://cmosir.com, 11/13/2024

Acknowledgements

This research was funded by the German “Bundesministerium für Wirtschaft und Klimaschutz” (BMWK) within the project „FIRE“ (Innokom, 49MF220020).

DOI 10.5162/SMSI2025/D3.3

Accelerated Life Tests for Determining the Expected Lifetime – Test Strategy for IR-MEMS-Emitter

Luisa Bindel[1], *Franz Huwald*[1], *Lea-Sophie Oechler*[1], *Annett Isserstedt-Trinke*[1], *Steffen Biermann*[1]
[1] *Micro Hybrid Electronic GmbH, Heinrich-Hertz-Str. 8, 07629 Hermsdorf, Germany*
l.bindel@microhybrid.com

Summary:
A procedure for estimating expected lifetime of IR-MEMS-emitters was developed. A pre-test to examine the main influencing factor that limits lifetime has been carried out. Membrane temperature of the IR-MEMS-emitters was identified as the main influencing factor for electromigration, reducing lifetime. For this reason, the Arrhenius life stress model, a temperature based physical model, is used for calculating expected lifetime at nominal conditions.

Keywords: IR-MEMS-Emitter, Arrhenius life stress model, expected lifetime, membrane temperature

Background and Motivation

IR-MEMS-emitter are silicon-based hotplate infrared sources with an optimized emission in mid-infrared range between 2 and 15 µm wavelength. The emitter is a multilayer system, whereby the emission layer on the top side determines the emission range. The heating layer defines the resistance of emitter types. If an input voltage is applied, membrane temperature of heating layer rises and the hot resistance increases with defined temperature coefficient. Resistance, emission spectrum and temperature distribution over the membrane are the most important quality properties of IR-MEMS-Emitters. Stressed emitters show shifts in emission spectrum and a material shift in heating layer, which is called electromigration, and changes membrane temperature distribution. Resistance of emitters increases as electromigration continues. To better assess the effects of influencing factors on emitter lifetime, a test strategy has been developed that enables a statement of lifetime via accelerated lifetime tests. A test to evaluate expected lifetime based on an Arrhenius life-stress model was conducted. In addition, the correlation between electromigration and emission shift has been numerically quantified.

Arrhenius life stress model and Weibull-distribution

Prior testing to identify whether membrane temperature or strength of electrical field is the main influence factor of electromigration has been done. These tests showed that there is a strong correlation between emitter failure and high membrane temperatures. On the other hand at the evaluated operating point ranges, there was no connection between strength of electrical field and emitter failure observed. Therefore, simple Arrhenius life-stress model can be applied. This model is a physics-based model derived from temperature dependence [1], used for temperature-accelerated tests. From of at least two test groups with higher working temperatures the expected lifetime under normal conditions can be calculated. The membrane temperature is a function of the electrical input power and was measured by a suitable IR-camera. To estimate the characteristic lifetime of higher stress groups the 2-parameter Weibull distribution was used [2]. The 95 % confidence interval and median of parameters is determined via non-parametric bootstrapping, with 20,001 resamples.

Test setup

Tab. 1: Example distribution of test groups

Power [W]	#Samples Not IM	#Samples IM
0.65	32	8
1.05	48	8
1.2	48	8
1.35	48	-

For calculating expected lifetime, the resistance change of several emitters, running continuously at different power inputs and therefore temperatures, was measured in a special emitter test chamber. Furthermore, emission spectrum via FTIR-spectroscopy with a special external

emitter input and membrane temperature distribution via IR-camera were measured at regular intervals for a subset IM (intermittent measurements) of emitters. Tab. 1 shows the resulting test groups.

Results - Expected Lifetime

Based on Weibull distribution, the characteristic lifetimes of the temperature stressed test groups were calculated with results shown in Tab. 2.

Tab. 2: Example characteristic lifetimes of stressed test groups

P [W]	T_{mem} [K]	Characteristic Lifetime[h]
1.05	1026	4194
1.2	1111	679
1.35	1152	210

Logarithmizing the Arrhenius life-stress model leads to

$$ln\left(Lifetime(T_{mem})\right) = ln(C) + \frac{B}{T_{mem}} \qquad (1)$$

with parameters B and C obtainable via linear regression. Using *(1),* expected lifetime at nominal power has been determined. A service lifetime of minimum 1e5 hours at nominal input power of 650 mW was reached (Fig. 1).

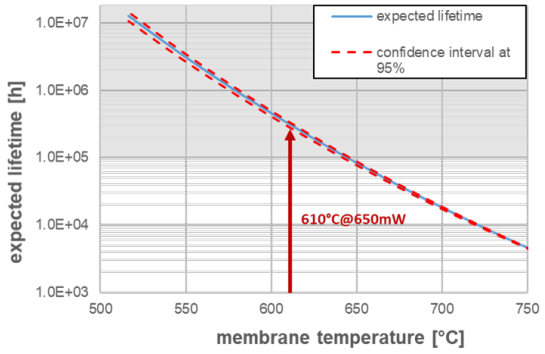

Fig. 1: expected lifetime of CMOSI500 vs. membrane temperature: nominal input power 650 mW @ 610 °C is marked

Electromigration

Electromigration was numerically quantified by IR-pictures showing membrane temperature distribution. Over the operational time of an emitter, position of the hot spot on the membrane and shape of the hot spot, defined by calculating the ratio of height and width (shape ratio) of the 10 % highest temperature pixels, were determined. While there is no change in location and shape ratio of the hot spot in test groups with nominal power, in stressed test groups the hot spot moves in one direction until some upper boundary. Afterwards the hot spot becomes more elliptic, indicated by an increasing shape ratio.

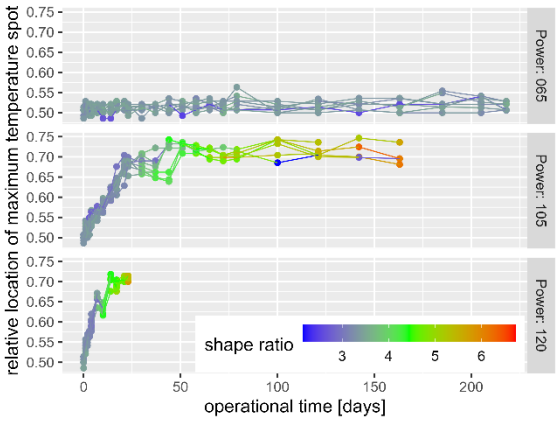

Fig. 2: numerical evaluation of IR-pictures

Emission shift

In four wavelength intervals, change of amplitude was measured by FTIR-spectroscopy. In higher stress groups there is a change of around 10 % in every wavelength interval, while in nominal power there is no change over operational time.

Discussion

To verify if there is a correlation between emission shift and electromigration the amplitude change of measured spectrometer data in the different wavelength were compared to calculated spectra of the temperature distribution measured by IR-camera. For every temperature pixel a Planck spectrum was calculated and summarized to a total spectrum. Both calculated and measured amplitude change are showing the same behaviour over time. This proves the correlation between emission shift and electromigration. Long-term tests had shown the main force that limits lifetime of IR-MEMS-emitter is electromigration, which can be attributed to a high membrane temperature. The material shift leads to changed radiation characteristics in emission spectrum caused by hot spot displacement and changes in hot spot shape. Finally the material shift leads to a rupture in membrane. The AC-Mode of IR-MEMS-emitters should contribute to the reduction of migration effects and thus to lifetime extension, which needs to be evaluated in further long-term tests.

References

[1] A.L. Hartzell, M.G. da Silva, H. Shea, MEMS Reliability, *Springer* (2011); ISBN: 978-1-4419-6017-

[2] W. Weibull, A Statistical Distribution Function of Wide Applicability, *Journal of Applied Mechanics* 18, 293-297 (1951); doi: 10.1115/1.4010337

DOI 10.5162/SMSI2025/D3.4

Power control and app connection via Bluetooth for NDIR-Sensor-applications

Moritz Ueberschär, Manuel Jung, Falk Liebold
Cooperative University Gera-Eisenach; Department of Technology;
Electrical and electronic Engineering; Weg der Freundschaft 4, 07546 Germany
falk.liebold@dhge.de

Summary:
For NDIR gas analysis, a constant emission spectrum of the integrated IR emitter is necessary. This requires the supply of constant electrical power. An electronic circuit is designed that enables the power implemented at the emitter to be set and measured. A digital controller with dynamic parameter determination is implemented in a microcontroller. A mobile smartphone application is created to display measured values and set the reference variable. Bluetooth communication enables cyclic data exchange between the app and the microcontroller.

Keywords:
Infrared emitter, digital power control, microcontroller, smartphone app, Bluetooth communication

Infrared emitter
One method in the field of gas sensing is non-dispersive infrared gas analysis (NDIR gas analysis).[1] Infrared emitters are used whose emission spectrum depends on the electrical power supplied.[2] It is therefore important for the measurement process to keep this power constant. Due to a non-linear relationship between the emitter temperature resulting from a certain emitter power and the resulting spectral energy density in the range of the wavelength used for analysis, even small power fluctuations cause a significant measurement error in NDIR gas measurement.[3]

Circuit design
A transistor serves as the power control actuator, which is controlled by a 32-bit microcontroller using the pulse width modulation method. A current regulator defines the operating range of the actuator and decouples it from the supply voltage. A smoothing capacitor generates a DC voltage from the PWM voltage and creates a quantifiable time constant for the dynamic transmission behavior of the circuit. The power measurement is carried out indirectly via two differential amplifier circuits for measuring current and voltage. The current is measured via a measuring resistor and the voltage is measured directly across the electrical load. A parallel resistor optimizes the adjustment range with regard to optimal utilization of the available PWM range to the specified working range and thereby maximizes the effectively usable resolution.

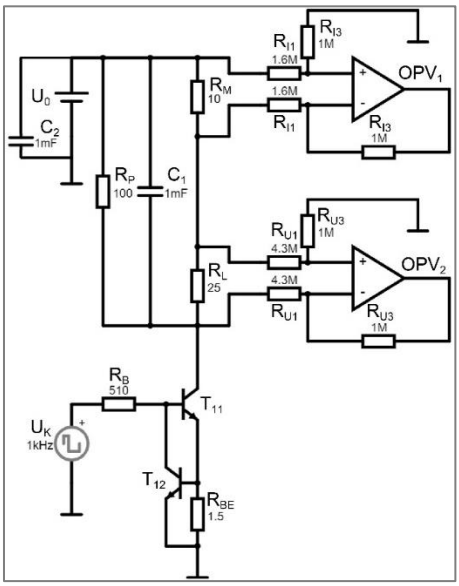

Fig. 1 Circuit Design

Controller
The electrical circuit of the power control can be described mathematically within the working area by the following relationship:

$$P_{RL}(s) = \frac{{I_{max}}^2}{1 + s \cdot T_1} \cdot \left(\frac{R_P}{R_L + R_M + R_P}\right)^2 \cdot R_L \cdot K(s)^2$$

[1] cf. [Wie22] pp. 393 f.
[2] cf. [MH24b] p. 3
[3] cf. [Wie22] pp. 1219-1221, [INS21] p. 2

$$T_1 = \frac{R_P}{R_P + R_M + R_L} \cdot (R_M + R_L) \cdot C_1$$

The squared influence of the duty cycle K(s) of the PWM voltage represents a static non-linearity. This is linearized by implementing a square root function as an inverse non-linearity in the microcontroller. The measured values of current and voltage are denoised in the microcontroller using a digital filter in the form of a T_1 element. The T_1 element has a limit frequency of $\omega_0 = 200$ s^{-1} and thus generates a delay element with $T_2 = 5$ ms. Overall, this results in a PT_2 controlled system with the following transfer function:

$$G_S = \frac{K_{PS1}}{(1 + sT_1) \cdot (1 + sT_2)}$$

$$K_{PS1} = \left(\frac{R_P}{R_L + R_M + R_P}\right)^2 \cdot R_L \cdot {I_{max}}^2$$

Closed loop control

The following figure shows the control loop consisting of the controller G_R and the controlled system.

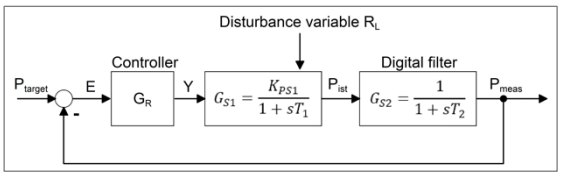

Fig 2 Digital control loop

A PI controller is used to control the PT_2 system, the parameters of which are determined using the method of compensating the largest system time constant[4]:

$$T_n = T_1$$

$$K_{PR} = \frac{T_1}{2 \cdot K_{PS1} \cdot T_2}$$

The resistor R_L represents a disturbance variable that can be determined from the current measured values for current and voltage measurement. In order to achieve a homogeneous response behavior over the entire working range of the control, the current resistance value is used to determine the controller parameters during the microcontroller's runtime from the context of the mathematical system model and thus dynamically adapt them.

Program structure of the microcontroller

In order to optimally use the microcontroller's computing power, the program is divided according to the different time requirements of individual functions, see the following figure.

Bluetooth communication works with a cycle time of 100 ms, as this has the lowest real-time requirement and the graph in the app is also displayed at a 0.1 Hz rate.

The cycle time of the controller was selected to be sufficiently short at 0.5 ms with system time constants of T_1=16.7…47.4 ms and T_2=5 ms in order to achieve a quasi-continuous behavior of the control loop.

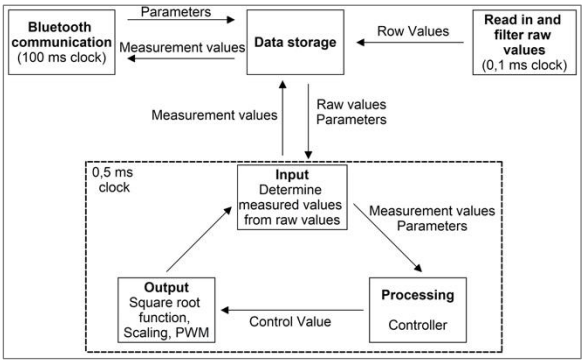

Fig 3 Program structure

The raw values of the current and voltage measurement are read and filtered in a cycle of 0.1 ms. This oversampling, in conjunction with the digital T_1 element, improves the quality of the measurement signals through reduced noise behavior.

The different cycle times are implemented using function calls in the interrupt service routines of various cyclic timer interrupts.

Smartphone application

The smartphone app enables communication between the user and the circuit via Bluetooth with the microcontroller. The target power value can be set using a slider or a text field. The current performance value is displayed in another text field. In addition, current, voltage, resistance and power curves are displayed in a graph.

Bluetooth data exchange

The data is transmitted cyclically as a character string. Semicolons are used to separate the individual pieces of information. The data sent from the microcontroller to the app contains the current measurements of current, voltage, resistance and power of the IR emitter. The data sent by the app to the microcontroller contains the setpoint of the control, controller parameters Kp and Tn, as well as the operating mode of the controller.

[4]cf. [Zac22] S. 21

Results

When testing the system, it was shown that the power of the electrical load can be controlled within the assigned working range. The measured value display in the app shows that the actual value follows the target value quickly and fluctuates around the target value with a deviation of 1 mW. The control behavior is examined using step responses and corresponds to expectations. Fig 4 shows the behavior based on a sudden change in resistance from 19 ohms to 80 ohms at 500 mW.

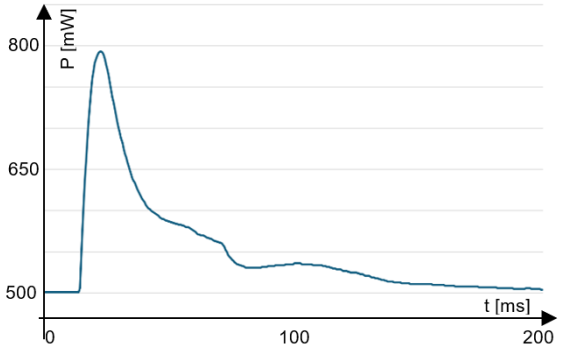

Fig 4 Control loop reaction to a disturbance

The transmission and display of the measured values in the mobile application works without interruption and has no noticeable delay. This means that the operator can use the app to monitor the current status of the circuit through the time curves displayed. The specification of the setpoint and the selection of the operating mode of the controller including parameter input works as expected.

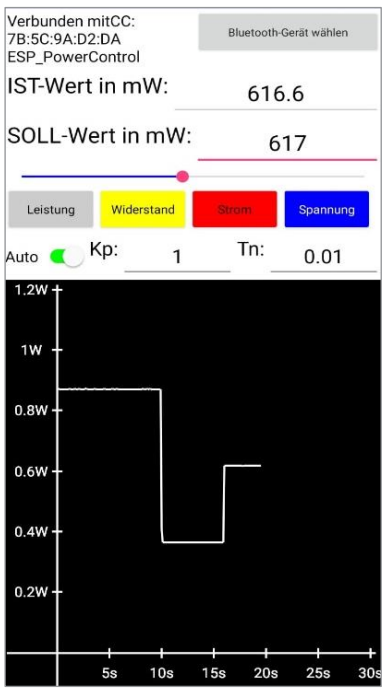

Fig 5 Mobile application

Conclusion

A digital power control of an electrical load was successfully implemented and visualized via an app. The implementation developed represents a prototype that fulfills the required functionality. Future developments can build on this.

References

[INS21] Infrasolid: "WHITE PAPER The Art of fastest Precision“, Infrasolid GmbH accessed on 02.11.2024 retrieved from: https://www.infrasolid.com/data/doc/White-paper/Whitepaper-The-Art-of-Fastest-Precision.pdf?c=20220609123356

[MH24b] Micro-Hybrid Electronic GmbH, "MH-Datasheet IR Strahler JSIR-350-4" accessed on 02.11.2024 retrieved from: https://www.microhybrid.com/de/shop/ir-strahler/ir-strahler-to39-mit-reflektor-und-filter-a1/

[Wie22] Wiegleb, G.: "Gasmesstechnik in Theorie und Praxis", 2. Auflage, Springer Vieweg, Wiesbaden, 2022

[Zac22] Zacher, S.: "Drei-Bode-Plots-Verfahren für Regelungstechnik", 2. Auflage, Springer Vieweg, Wiesbaden, 2022

Contact

Prof. Dr.-Ing. Falk Liebold
Cooperative University Thuringia
Electrical and Industrial
electronic Engineering
falk.liebold@dhge.de

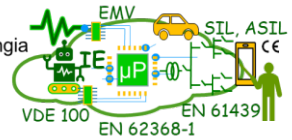

DOI 10.5162/SMSI2025/D4.1

Thin-film sensors on thrust bearing washers for temperature measurement directly in the mechanical rolling contact

Tobias Steppeler[1], Dennis Konopka[2], Rico Ottermann[1], Florian Pape[2], Folke Dencker[1], Gerhard Poll[2], Max Marian[2,3], Marc Christopher Wurz[1]
[1] Institute of Micro Production Technology, Leibniz University Hannover, An der Universität 2, 30823 Garbsen, Germany
[2] Institute of Machine Design and Tribology, Leibniz University Hannover, An der Universität 1, 30823 Garbsen, Germany
[3] Department of Mechanical and Metallurgical Engineering, Pontificia Universidad Católica de Chile, Vicuña Mackenna 4860, Macul 6904411, Región Metropolitana, Chile
steppeler@impt.uni-hannover.de

Summary:
The article shows the production and evaluation of directly deposited thin-film temperature sensors on a thrust cylindrical roller bearing washer in and near the tribo-mechanical rolling contact. The production was carried out using sputtering, photolithography and etching processes. Due to the frictional forces, a 12 % (3.6 °C) higher temperature was measured in the mechanical rolling contact and a 5.3 % (1.6 °C) higher temperature near the mechanical rolling contact compared with the conventional temperature sensor on the outside of the bearing washer.

Keywords: thin-film sensors, direct deposition, bearing washer, temperature measurement, harsh environment

Introduction

Frequent maintenance of systems and machines can prevent downtimes and reduce costs. To improve maintenance intervals, conventional machine elements, such as gears or rolling bearings, can be used in combination with a compact electronics solution by means of sensor integration for intelligent system monitoring [1,2]. Commercial applications for large rolling bearings are already available. Here, the operating states are monitored via condition monitoring systems (CMS) with external vibration and temperature sensors [3]. However, in order to maximize information about local bearing conditions (normal and tangential forces, temperature), the measuring position must be located directly in the bearing. For this purpose, thin-film strain gauges and temperature sensors can be used as an array directly or in the immediate vicinity of the tribological contact on the rolling element raceway [4,5]. This article focusses on manufacturing directly deposited thin-film temperature sensors on thrust roller bearing washers and qualify them in a component test bench.

Sensor Manufacturing

For the production of the thin-film sensors, sputter deposition was used. Thus, thin-film strain sensors and temperature sensors were applied, whereby this contribution focuses on temperature sensors. An axial cylindrical roller bearing washer (GS89312) was used as substrate. The mean roughness depth R_z was 0.68 ± 0.06 µm and the arithmetic mean roughness value R_a was 0.08 ± 0.01 µm as tactilely determined (HOMMEL-ETAMIC W5, JENOPTIK). First, the bearing washer surface was cleaned using acetone and isopropanol. A sputter etching process was then carried out in the SenVac Z550 sputtering system to increase the adhesive strength of the subsequent insulation layer out of alumina (Al_2O_3), which was applied with a power of 350 W. A 6 µm thick layer was deposited in steps of 1 µm with intermediate chemical cleaning steps. The layer for the temperature sensors was produced using the Kenotec MRC sputtering system with a power of 200 W and shadow masks dividing the washer area into different regions for strain gauges and temperature sensors. An adhesion promotion layer of titanium with a thickness of 10 nm was applied before the sensor layer made of platinum with a thickness of 230 nm was deposited. Finally, a 500 nm thick gold layer was applied to the edge of the bearing washer for the contact pads. Once the layer system of the sensors had been applied, the thin-film sensors were structured using photolithography with the resist AZ 10XT. Ion beam etching was used to remove the material that was not covered by the resist. After removing the resist, a 4 µm thick alumina layer was applied as a wear protection layer using the SenVac Z550 sputtering system and the

settings described above. The bearing washer with the thin-film sensors is shown in Figure 1.

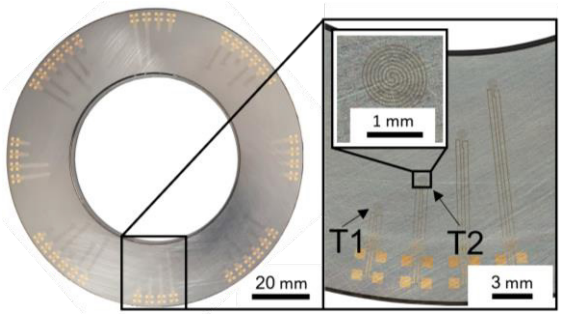

Fig. 1. Thrust roller bearing washer with sensors.

Measurement Results

To characterize the temperature sensors, the temperature coefficient of resistance (TCR) was determined using a hot plate and calculated according to (1) with the temperatures LT = 20 °C and HT = 80 °C.

$$TCR = [(R_{HT} - R_{LT})]/R_{LT}]/[HT - LT] \quad (1)$$

The temperature sensors had an average TCR of 744.6 ± 90.3 ppm/°C. For the investigations of the integrated sensors, the bearing washer was mounted in an FE8 test rig (DIN 51819-1:2016-12), which enables cylindrical roller thrust bearings to be loaded and operating under constant operating conditions. The selected rotational speed was 500 rpm and an axial load of 7.5 kN was applied, corresponding to an Hertzian pressure in the roller-raceway contacts of 750 MPa. Grease (ISOFLEX NBU 15) was selected as lubricant. After a test period of 60 minutes, the highest temperature of 33.6 ± 0.1 °C was measured with the thin-film sensor (T2) directly in the mechanical rolling contact. This was followed by the thin-film sensor (T1) close to the mechanical rolling contact with a temperature of 31.6 ± 0.1 °C. A temperature of 30 ± 0.1 °C was measured with the PT100 temperature sensor at the edge of the bearing washer (Figure 2).

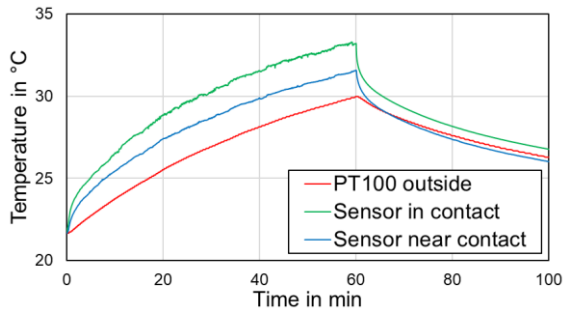

Fig. 2. Temperature signals from differently positioned sensors.

Due to the frictional heat caused by the frictional forces and the high sliding components caused by the contact kinematics, the measured temperatures in and near the rolling bearing contact are higher than the temperature of the PT100 at the edge of the bearing washer. The test was repeated four times with reproducible signals.

Conclusion

Thin-film temperature sensors were applied to a thrust roller bearing washer to measure the temperature in and near the mechanical rolling contact. The sensors were produced using cathode sputtering, photolithography and ion beam etching. Due to the frictional forces, various temperatures were measured in and near the tribo-mechanical contact as well as at the edge of the bearing washer when it was tested in a component test rig. The results show that after 60 minutes, a temperature 12 % (3.6 °C) higher in the mechanical rolling contact and 5.3 % (1.6 °C) higher near the mechanical rolling contact could be determined with the directly deposited sensors than with a conventional PT100 at the edge of the bearing washer. Thus, a more accurate and faster temperature determination is possible with the help of thin-film sensors directly in the tribo-mechanical contact, as well as more precise validation of simulation models.

Acknowledgment

The authors thank the German Research Foundation (DFG) that funded this work within the research project “Integrated sensors for intelligent large-diameter bearings” (project number 466778958) as part of the Priority Program 2305 “Sensor-integrating machine elements” (project number 441853410).

References

[1] E. Kirchner et al., A Review on Sensor-integrating Machine Elements, Advanced Sensor Research, (2024); doi: 10.1002/adsr.202300113

[2] T. Steppeler et al., Entwicklung einer Messelektronik zur Zustandsüberwachung von Wälzlagern mittels Integration von Dünnfilmsensoren, DMK2024, 161-176, (2024); ISBN: 978-3-96548-194-7

[3] Z. Liu, J. Chen, Monitoring and Diagnosis Technique on Slewing Bearing, Advanced Materials Research 156-157, 1478-1483, (2010); doi: 10.4028/www.scientific.net/AMR.156-157.1478

[4] D. Konopka et al., Advancements in monitoring of tribological stress in bearings using thin-film strain gauges, 10th ECCOMAS Thematic Conference on Smart Structures and Materials, Patras, (2023); doi: 10.7712/150123.9934.443603

[5] R. Ottermann et al., Degeneration Effects of Thin-Film Sensors after Critical Load Conditions of Ma-chine Components, Machines 2022, 10, 870, (2022); doi: 10.3390/machines10100870

DOI 10.5162/SMSI2025/D4.2

Characterization of the Thermal Conductivity of Silica Aerogels

T.M. de Rijk[1,2], T. Wendland[1] and M.J. Vellekoop[1,2,3]
[1] Institute for Microsensors, -actuators and -systems, University of Bremen, Germany
[2]Microsystems Center Bremen (MCB), Germany
[3]MAPEX Center for Materials and Processes, University of Bremen, Germany
TRijk@imsas.uni-bremen.de

Summary: This study presents a simple and accurate method for quantifying the thermal conductivity of silica aerogels which are well-known for their low thermal conductivity ($< 0.02\,\mathrm{W\,m^{-1}\,K^{-1}}$) and their highly porous structure [1]. In this setup, two aerogel blocks (diameter 2 cm, thickness 8 mm) are stacked with a small platin-based heating structure in-between and thermistors (diameter 7.5 mm) on the outside. This approach minimizes heating losses by ensuring the heat is transferred through the aerogel and measured by the sensors. The thermal conductivities found are in the range of 0.015 - 0.024 $m^{-1}K^{-1}$, corresponding well to the values found in the current literature.

Keywords: High porosity, Silica Aerogel, Thermal conductivity, Thermal Insulation

Introduction

The use of aerogels in microfluidic devices is very attractive due to their extremely high thermal insulation, which can be used in thermal micro-devices. Silica aerogels obtain their high insulation properties due to the high porosity (up to 99% [2]), and surface area. These properties and the fact that aerogels can be manufactured in all custom shapes make them ideal candidates for thermal insulation of microfluidic devices.

Measurement principle and setup

The measurement principle to determine the thermal conductivity is based on the 'Absolute Method'. One side of the sample is placed on a heating structure with a set power, the other side is positioned on a temperature sensor (with heat sink). The thermal conductivity (λ) can be determined from the temperature difference. The relation is shown in eq. (1) [3]. Here, $\dot{Q}$ is the heat flow, s the height of the sample, A the cross-sectional area and ΔT the temperature difference.

$$\lambda = \frac{\dot{Q} \cdot s}{A \cdot \Delta T} \tag{1}$$

The experimental setup is shown in Fig. 1. Sensors are glued with silver glue (Elecolit 414) to the aerogel samples and connected via 150 μm wires to a digital multimeter (Keithley DMM6500). The heater is connected to a power supply, which is selected to give a total input power of 60, 220 and 450 mW.

Sensor fabrication and characterization

The silica aerogels are manufactured based on the sol-gel process. First, Tetraethylorthosilicate (TEOS) is added to ethanol, DI water, and HCL to start the Hydrolyses reaction at 45°C. After 90 minutes, the temperature is decreased to 35°C, and Ammonia is added to start the condensation reaction. After roughly 50 minutes, the gel is formed and the samples are placed in the mold (diameter 2 cm, height 8 mm). The samples are aged in a mixture of TEOS / ethanol and dried using CO_2 critical drying (Leica CPD300). The complete process and molar ratios are shown in previous work [4].

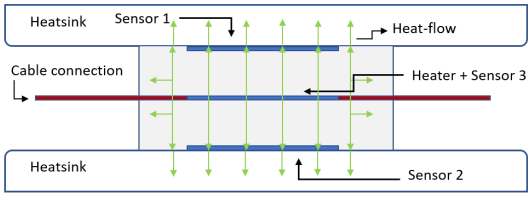

Fig. 1: Schematic side view of the setup. The green arrows indicate the flow-profile. Sensor 3 measures the temperature directly at the heater (T_{Heater}).

The sensors are manufactured on silicon wafers and are based on a 5 μm thick spin-coated polyimide layer (precursor U-varnish-S with 20% wt - polyamic acid content, UBE Europe GmbH) and 200 nm thick sputtered platin structures (100 μm linewidth) that serve as both a thermistor and a heater. The average resistances are 320 Ω and 1650 Ω, respectively. With a voltage applied, the aerogel structure heat up, changing the resistance of the thermistors. The relation between the actual temperature (in °C) and the resistance of the thermistors is give by eq. (2). These gave an average value for α of 0.0023 K^{-1}.

$$R(T) = R(T_0)(1 + \alpha_{T_0} \cdot (T - T_0)) \tag{2}$$

Results

An input power of 60, 220 and 450 mW was applied to the heaters, and the resistance of the sensors (including the sensor directly next to the heater T_{Heater}) was continuously monitored. The temperature is calculated from the resistance according to eq. (2), and the results are shown Fig. 2.

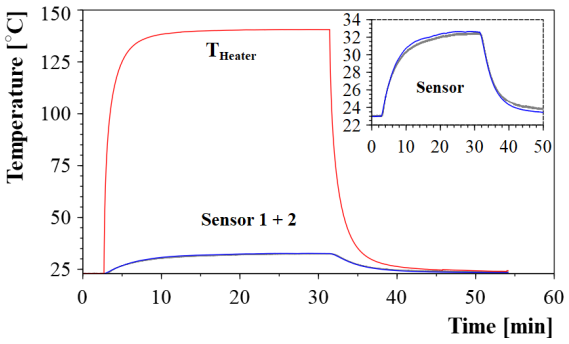

Fig. 2: Temperature response for 220 mW applied to the heater.

The responses to a stepwise increase in the heating temperature is shown in Fig. 3, with a temperature of 70 to 230°C. Both sensors detect identical temperatures, confirming the robustness and reliability of the measurement setup.

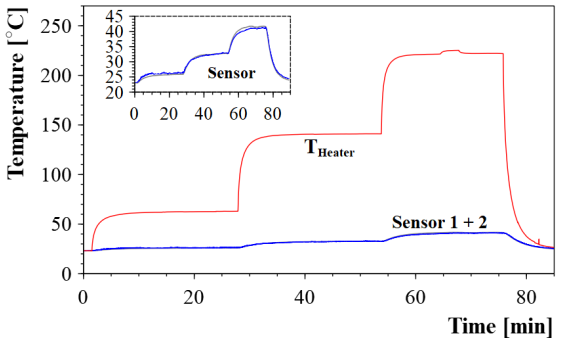

Fig. 3: Sensor response for step-wise increase of the heater power.

The calculated thermal conductivities (λ) for the measurements are shown in Fig. 4. The values for λ changes slightly depending on the temperature of the aerogel, which is a known occurrence. The objects thermal properties are related by the objects temperature [5].

Every manufactured sensor consists of a heater and a thermistor. Therefore, it is possible to additionally measure the temperature with the heater structures on the outer sides of the aerogel blocks. This gives extra confirmation of the temperature, as shown in Fig. 4. The calculated values (with the heater structures) show identical values, validating the determined thermal conductivities.

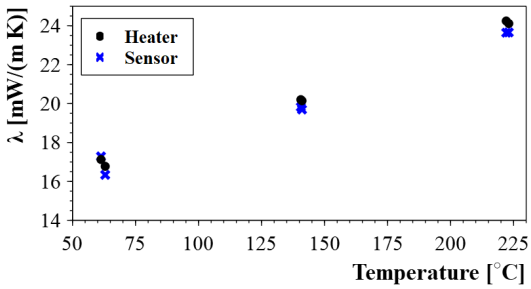

Fig. 4: Thermal conductivity of aerogel samples at different heating temperatures.

Conclusions and Outlook

This abstract presents a reliable method for determining the thermal conductivity of samples with extremely low values. The thermal losses in the setup are minimized by placing the sensor between two small aerogel blocks. This inhibits heat flow around the samples and also ensures that all heat goes in the aerogel (evenly distributed in both samples). The measurement setup features a total of five temperature sensors, enabling for accurate temperature readings and calculated thermal conductivities. The thermal conductivities (0.015 - 0.024 $m^{-1}K^{-1}$) found in this research can help further research to minimize heat losses in micro-chambers/reactors and/or other insulation in microfluidic devices. Future research will focus on integrating the aerogels with IC technology to improve the connections between the aerogel and the sensor.

References

[1] Michel A Aegerter et al. *Springer handbook of aerogels*. Springer Nature, 2023. DOI: 10.1007/978-3-030-27322-4.

[2] Faheem Akhter, Suhail Ahmed Soomro, and Vassilis J Inglezakis. “Silica aerogels; a review of synthesis, applications and fabrication of hybrid composites”. In: *Journal of Porous Materials* 28.5 (2021), pp. 1387–1400. DOI: 10.1007/s10934-021-01091-3.

[3] Peter Böckh and Thomas Wetzel. *Wärmeübertragung: Grundlagen und Praxis*. Springer-Verlag, 2018. DOI: 10.1007/978-3-662-55480-7.

[4] Ana Luiza S. Fiates et al. “Silica Aerogel in Microfluidic Channels: Synthesis, Chip Integration, Mechanical Reinforcement, and Characterization”. In: *ACS omega* (2024). DOI: 10.1021/acsomega.4c05019.

[5] Young-Geun Kwon et al. “Ambient-dried silica aerogel doped with TiO2 powder for thermal insulation”. In: *Journal of materials science* 35 (2000), pp. 6075–6079. DOI: 10.1023/A:1026775632209.

DOI 10.5162/SMSI2025/D4.3

Enhancing Dynamic Measurement Methods: From Concepts to Calibration Standards

Bayan Tallawi[*], *Jacques-Olivier Favreau, Kevin Romieu*
LNE-CETIAT, 69603 Villeurbanne Cedex, Lyon
bayan.tallawi@cetiat.fr

Summary:
Dynamic measurements, particularly in thermometry, are crucial for capturing rapid variations in physical systems. However, such measurements face challenges due to noise, system distortions, and the inherent uncertainty of capturing time-dependent phenomena. This study presents a methodological approach to improve dynamic measurements through advanced signal processing and calibration model enhancement. By integrating Fourier transforms, dynamic Kalman filtering, and temperature correction models, the research aims to enhance precision while ensuring traceability. The results demonstrate the effectiveness of these approaches in providing reliable, accurate, and standardized measurements for industrial and scientific applications.

Keywords: dynamic measurements; calibration; response time; metrology.

Introduction

Dynamic measurements are indispensable in fields like fluid dynamics, thermometry, and acoustics, where rapidly changing conditions demand accurate and responsive measurement techniques. Traditional static calibration methods, designed for steady-state scenarios, often fail to account for the transient and time-dependent behaviors of dynamic systems. This limitation necessitates the development of dynamic calibration methodologies, which incorporate sensor response times and temporal variations to ensure reliability and accuracy.
Key advancements include Monte Carlo simulations for uncertainty evaluation (1), frequency response and impulse response testing to characterize system behavior (2) (3) (4), and real-time data processing with compensation filters to manage large data volumes and correct distortions (5) (6).
These innovations, combined with fast-response sensors and adaptive signal processing techniques, address critical challenges in capturing accurate data in evolving conditions (7) (8). However, gaps in existing standards, such as the GUM (14) and VIM (15), highlight the need for greater emphasis on dynamic considerations, particularly in accounting for sensor response times, to improve replicability and precision in dynamic measurement systems.
In this study, calibration models are enhanced to better account for sensor response times and reduce uncertainties, enabling accurate measurement of rapid changes. Advanced data processing methods, including adaptive and real-time algorithms, are employed to optimize noise reduction and manage system uncertainty.

Methodology

Signal Processing

A robust signal processing framework was developed to address the challenges of dynamic measurements. The first step involved applying Fourier transforms to filter out noise and reconstruct the original signal. This technique effectively isolated the relevant frequency components, allowing for more accurate signal analysis.
A dynamic Kalman filter has been used to estimate the measurand by optimally balancing noise reduction and system uncertainty.

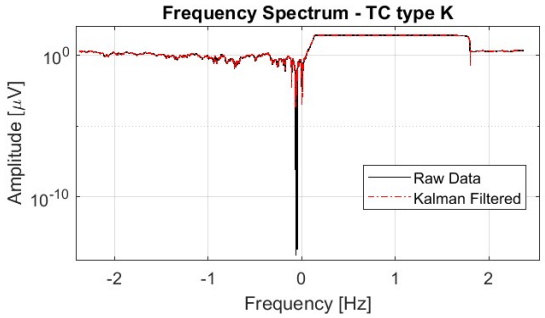

Figure 1 : application of Kalman filter on raw data of thermocouple type K.

Next, an inverse transfer function $(H_{inv}(\omega))$ was designed to correct distortions introduced by the measurement system. By restoring the original

signal, this approach improved the fidelity of the measured data. Finally, a dynamic Kalman filter was employed to optimally balance noise reduction with system uncertainty. This adaptive filtering technique allowed for real-time adjustments, ensuring the accuracy of the measurements under varying conditions.

Sensor temperature correction

This phase assesses thermocouple response time to ensure accurate and reliable dynamic temperature measurements. The thermocouple operates on the Seebeck effect (20), here two different metals generate an electrical voltage at their junction, which is temperature-dependent (21). Thermocouple temperature readings often deviate from the actual surrounding temperatures due to factors like radiation, convective heat transfer, and the thermocouple's response time. To account for these discrepancies, adjustments are made to the measured temperature, as explained by Pitts et al. (22). The formula that relates the environmental temperature (T_g) to the measured temperature (T_j) incorporates these elements and is given by:

$$T_g = T_j + \tau \frac{dT_j}{dt} + \frac{\epsilon\sigma}{h_{cov}}(T_j^4 - T_w^4)$$

Results and Discussion

The study demonstrates the effectiveness of the proposed methodologies in enhancing dynamic measurements.

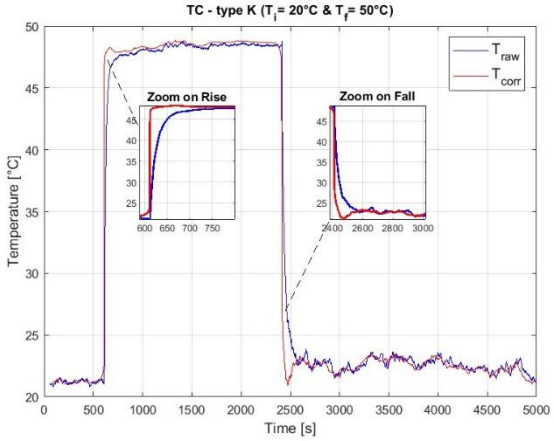

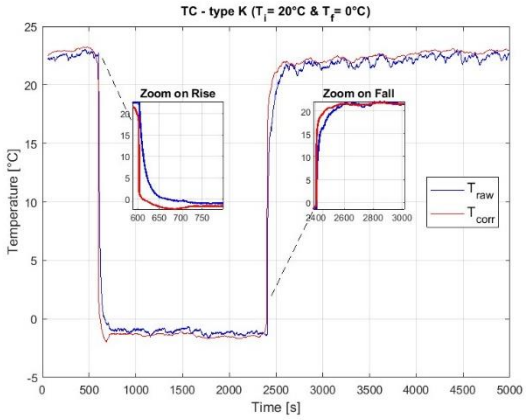

Figure 2 : example of temperature correction for a thermocouple Type K at two different temperatures.

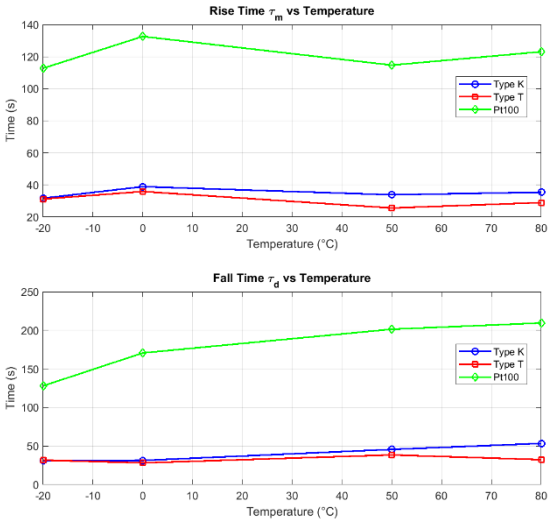

Figure 3 : Sensor Response Times vs. Temperature

The comparison of response time of different types of sensors like Pt100, TC type K and TC type T. It shows that Pt100 sensors have significantly slower response times compared to Type K and T thermocouples, making them less suitable for dynamic environments. In contrast, Type K and T thermocouples exhibit faster, consistent response times. Dynamic signal processing techniques reduced uncertainties, leading to more precise measurements. The temperature correction model addressed environmental and system-specific distortions, aligning measurements with metrological standards. The study also emphasized the importance of uncertainty propagation, with noise, filtering, and modeling errors identified as key contributors. The methodologies effectively minimized these uncertainties.

References

[1] S. Eichstädt, A. Link, P. Harris and C. Elster, Efficient implementation of a Monte Carlo method for uncertainty evaluation in dynamic measurements.,

Metrologia, 2012, 49(401). DOI: 10.1088/0026-1394/49/3/401.

[2] A. Oppenheim, R. Schafer, Discrete-Time Signal Processing, Engineering, Computer Science;1989.

[3] A. Oppenheim, R. Schafer, Discrete-Time Signal Processing, Engineering, Computer Science;1989.

[4] R. Pintelon, J. Schoukens, System Identification: A Frequency Domain Approach, Wiley-IEEE Press 2012, ISBN: 978-0-470-64037.

[5] Bernard Widrow, Samuel D. Stearns, Adaptive Signal Processing, 1985.

[6] Simon Haykin, Adaptive Filter Theory, 1986. url : https://api.semanticscholar.org/CorpusID:267927124.

[7] W. Pitts, E. Braun, R.Peacock, H. Mitler, E. Johnsson, P. Reneke, and L. Blevins, Temperature Uncertainties for Bare-Bead and Aspirated Thermocouple Measurements in Fire Environments, American Society for Testing and Materials, 2002, DOI : 10.1520/STP10945S.

[8] J. Fraden, Handbook of Modern Sensors: Physics, Designs, and Applications. Springer,2010.

[9] A. L. Shestakov, Dynamic measuring methods: A review, ACTA IMEKO, 2019, 8(1), 64-76. DOI : 10.21014/acta_imeko.v8i1.568.

[10] Mc. Daniel, A. Tinjum, J. M. Hart, D. J. & D. Fratta, Dynamic Calibration for Permanent Distributed Temperature Sensing Networks, IEEE Sensors Journal, 2018, 18(6), 2342-2352. DOI : 10.1109/JSEN.2018.2795240.

[11] A. Garinei, E. Tagliaferri, A laser calibration system for in situ dynamic characterization of temperature sensors, Sensors and Actuators A: Physical, 2013, 190, 19-24. DOI : 10.1016/j.sna.2012.11.014.

[12] N. Furuichi, C. Kar-Hooi & T. Yoshida, Experimental study to establish an evaluating method for the responsiveness of liquid flow measurement, Flow Measurement and Instrumentation, 2021 82. DOI : 10.1016/j.flowmeasinst.2021.102067.

[13] Dr.Ing. Aguilera Mena, Jesús A. Jaime, Dynamic weighing calibration method for liquid flowmeters – A new approach, Thesis Report, Technischen Universität Ilmenau, 2013, url : http://www.db-thueringen.de/servlets/DerivateServlet/Derivate-24734/ilm1-2011iwk-125.pdf.

[14] JCGM, GUM: Evaluation of measurement data — Guide to the expression of uncertainty in measurement, 2008.

[15] JCGM 200 : 2012, Vocabulaire international de métrologie - Concepts fondamentaux et généraux et termes associés, 2008.

DOI 10.5162/SMSI2025/D5.1

Noncontacting Determination of the Piezoelectric Coefficient d_{33} of Lithium Tantalate up to 400 °C

Hendrik Wulfmeier[1], *Niklas Warnecke*[1], *Dhyan Kohlmann*[1], *Holger Fritze*[1]
[1] *Clausthal University of Technology, Am Stollen 19 B, D-38640 Goslar, Germany,*
hendrik.wulfmeier@tu-clausthal.de

Summary:
In this work the laser Doppler vibrometry (LDV) is applied to determine the piezoelectric coefficients of sensor and actuator materials. LDV is a noncontacting optical method and, thus, not inhibiting sample displacement allowing for highly precise material characterization. The piezoelectric constants are also directly evaluated from the measurement data. In this work, d_{33} of lithium tantalate is determined up to 400 °C. However, in principle, the application temperature is limited by the furnace only in which the samples are installed.

Keywords: piezoelectric coefficient, laser Doppler vibrometry (LDV), lithium tantalate, non-contact measurement, high-temperature sensorics

Introduction and Motivation

Piezoelectric materials are the basis of numerous applications, especially in sensor and actuator technology. Such applications require precise characterization of the piezoelectric properties of the materials used, even under demanding conditions.

Lithium tantalate ($LiTaO_3$, LT) is one such case: it has already proven to be a very good piezoelectric sensor material in acoustic sensor technology. In form of a solid solution with lithium niobate (LN), it is expected to be usable at elevated temperatures above 600 °C [1]. Consequently, these materials are of great interest to research and industry [2]. However, exploiting this potential at high temperatures includes high demands on the characterization of the piezoelectric properties of these materials.

Laser Doppler vibrometry (LDV) promises to meet these requirements. It allows the piezoelectric coefficient and the displacement due to excitation to be measured independently of the temperature of the material. The measurement is contact-free and allows the material to vibrate almost completely freely.

Objective

The following work tests the functionality of this method by examining the piezoelectric properties of LT at different temperatures up to 400 °C. Later LDV shall be applied to similar materials such as the aforementioned LN and lithium niobate-tantalate solid solutions.

For this, LDV measurements of the displacement due to excitation are examined and the piezoelectric coefficient is determined by these.

State of the Art – Measurements of the Piezoelectric Coefficient of Lithium Tantalate

There have already been several studies on the piezoelectric coefficient d_{33} of LT showing a broad range from 5.7–23.4 pm/V. A detailed list of these is provided in [3].

Most of these measurements were indirect: d_{xy} was calculated from measurements of the resonance and antiresonance frequency of the material in conjunction with other material constants, meaning that unknown influences may involuntarily been taken into account.

There are also a few direct measurements using piezoelectric d_{33} meters or piezoelectric force microscopy. The most comparable measurement to this work was performed using an optical heterodyne interferometer. In this case, however, there was no freely oscillating sample, but one that was firmly attached to a surface, requiring the use of a correction term to determine correct piezoelectric coefficients.

Laser Doppler Vibrometry

Z-oriented LT single crystalline discs (Precision Micro Optics, USA, thickness: 523 µm, diameter: 10 mm) are coated symmetrically with circular Pt electrodes (7 mm) by mesh printing and positioned in a furnace so that the whole electrode area oscillates freely.

A laser beam (λ = 532 nm) is directed at the electrode surface, reflected and then directed into the detector together with the reference beam. The detector signal, i.e. the phase shift of the laser beams, is forwarded to the decoder (OFV-5000, Polytec, Germany), which in turn forwards the measurement results to an oscillo-

scope (PicoScope 4824A, Pico Technology, UK), which also measures the excitation voltage. Details to the LDV setup used in this work are given in [3] and [4].

The LDV decoder translates this interference pattern into a time-resolved voltage signal that is converted into a frequency-resolved voltage signal using a fast Fourier transformation (FFT). The maximum displacement can then be determined from this [5] and is proportional to the measured displacement on the examined surface Δs in measuring direction (here: Z).

In the static case, i.e. far away from the resonance frequency, the piezoelectric coefficient d_{33} can be calculated by the quotient of displacement Δs and excitation voltage U_{exc} (peak-to-peak). This relation applies if, as here, mechanical / piezoelectric displacement and electrical excitation both point in the same direction.

An excitation voltage of 10 V_{pp} is used. At each temperature, the electrode surface is scanned using LDV. Two linescans (top-to-bottom and left-to-right) with equidistant 13 points each are performed. Five measured values per measuring point are averaged. The respective mean values of the displacements at all of these points are then used to calculate d_{33}.

Results and Discussion

The determined displacements are in the range of several ten to a few hundred pm and still exhibit a signal-to-noise ratio of at least better than 5, mostly being in the range of 10 to 20.

Figure 1 shows the individual piezoelectric coefficients distributed over the surface of the sample. As predicted by theory, the displacement should be homogeneous over the entire surface and have no significant minima or maxima. The fact that this is confirmed in the experimental data verifies the approach in such a way that it does not influence the vibration behavior. The complete displacement without mechanical disturbances and, thus, the correct undisturbed piezoelectric coefficient can be determined.

The mean values of d_{33} for each temperature are displayed in Figure 2. There is a slight increase in d_{33} over temperature, however, being small in relation to the statistical deviation.

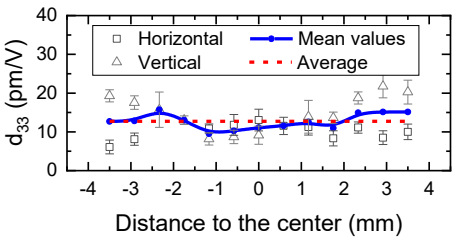

Fig. 1. Distribution and average of the piezoelectric coefficient d_{33} over the electrode surface in vertical and horizontal measuring direction at 200 °C.

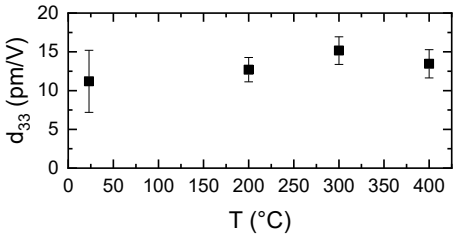

Fig. 2. Average values of d_{33} over the temperature. The errors correspond to the standard deviation of the spatial distribution (see Fig. 1).

Conclusions

The LDV is very well suited to measure the displacements of vibrating piezoelectric crystals. Displacements in the two-digit picometer range are possible to detect. The measurement can be carried out over the entire surface of the crystal in order to create a surface profile. The holder setup used allows the measurement of free vibrations. It is worth mentioning that LDV has no upper limit to the working temperature. The limiting factor here is the furnace used.

For LT piezoelectric coefficients d_{33} of (12.67 ± 1.75) pm/V are determined. There are no clearly recognizable trends regarding the course of the piezoelectric excitation over the surface. The piezoelectric coefficients also do not appear to follow a recognizable trend over the temperature.

References

[1] Y. Suhak, et al., Correlation of Electrical Properties and Acoustic Loss in Single Crystalline Lithium Niobate-Tantalate Solid Solutions at Elevated Temperatures, *Crystals*, 11, 398 (2021); doi: 10.3390/cryst11040398

[2] R.C. Turner et al., Materials for high temperature acoustic and vibration sensors: A review, *Applied Acoustics*, 41, 299–324 (1994); doi: 10.1016/0003-682X(94)90091-4

[3] N. Warnecke, Temperaturabhängige Charakterisierung der piezoelektrischen Eigenschaften von Lithiumtantalat mittels Laser-Doppler-Vibrometrie, Master thesis, TU Clausthal (2024)

[4] H. Wulfmeier, et al., Thin-film chemical expansion of ceria based solid solutions: laser vibrometry study, *Zeitschrift für Physikalische Chemie*, 236, 1013–1053 (2021); doi: 10.1515/zpch-2021-3125

[5] D. Kohlmann et al., Extraction of nanometer-scale displacements from noisy signals at frequencies down to 1 mHz obtained by differential laser Doppler vibrometry, *Journal of Sensors and Sensor Systems*, 13, 167–177 (2024); doi: 10.5194/jsss-13-167-2024

Acknowledgements

The authors would like to thank the German Research Foundation (DFG) for financial support of the projects FR1301/42-1/2 within the research group FOR5044 as well as the Research Center Energy Storage Technologies.

DOI 10.5162/SMSI2025/D5.2

Evaluation of piezoelectric micromachined ultrasonic transducers (PMUT) for the broadband detection of ultrasonic elastic waves

Henning Zeipert[1], Leander Claes[1], Chris Stoeckel[2,3] Shubham Mulay[2] and Bernd Henning[1]
[1] Measurement Engineering Group, Paderborn University, Paderborn, Germany
[2] Department Nano Device Technologies, Fraunhofer ENAS, Chemnitz, Germany
[3] Center for Micro and Nano Technologies, University of Technology Chemnitz, Chemnitz, Germany
zeipert@emt.uni-paderborn.de

Summary: Elastic waves in solids are frequently used for material characterisation or non destructive testing methods. For the detection of elastic waves with high sensitivity piezoelectric transducers are commonly used. This investigation compares the performance of a piezoceramic based ultrasonic transducer and a piezoelectric micromachined ultrasonic transducer (PMUT) for the detection of broadband acoustic waves in the spatial and temporal regime.

Keywords: Elastic waves, Non-destructive testing, Piezoelectric sensors, PMUT, Ultrasound

Motivation

In the interest of sustainable and cost-efficient processes the development of non-destructive testing (NDT) methods are a central aspect of contemporary research. Methods based on ultrasonic elastic waves are prevalent in this field, requiring specialised transducers for the excitation. Design goals for the detecting transducer are e.g. high sensitivity and a high bandwidth. This high bandwidth is especially important for material characterisation methods, as applied and developed by the authors [1]. While high temporal bandwidth can be achieved at the expense of the sensitivity in traditional, bulk piezoelectric transducers, high spatial bandwidth can only be reached by decreasing the sensors active area. The authors employ a specialised transducer based on an oblong, cuboid piezoceramic [2] to detect guided elastic waves to a high wavenumber or spatial frequency. These transducers are not commercially available and build in a manual process, which is incompatible with standard manufacturing techniques. To be able to deploy the aforementioned material characterisation methods in e.g. industrial applications an alternative to this custom build detection method, the performance of a piezoelectric micromachined ultrasonic transducer (PMUT) [3] is evaluated. To assess the bandwidth of the PMUT, broadband guided elastic waves in an aluminium plate are used as a benchmark.

Experimental setup

Ultrasonic guided waves are excited in an aluminium plate utilising ultraviolet pulsed laser radiation focused via a cylindrical lens onto a thin line ($\approx 0.1\,\mathrm{mm}$) on the surface of the specimen [2]. Due to a sufficiently low optical energy density the radiation results in a purely thermoelastical excitation without damaging the sample. A measurement routine is performed by moving the line of excitation in equidistant steps (e.g. $\Delta z = 0.1\,\mathrm{mm}$) along the plate and recording a signal at each step with the transducer coupled to the specimen. The resulting data matrix contains information in space-time-domain.

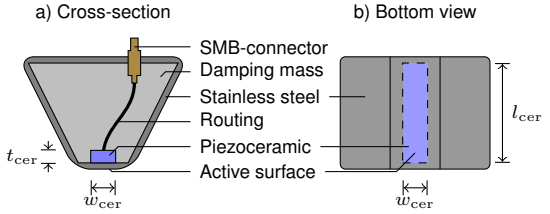

Fig. 1: Schematic of the piezoelectric transducer for the detection of broadband acoustic plate waves.

By applying a two-dimensional Fourier transform the data is transferred to the wavenumber-frequency-domain [4]. A depiction of the absolute value of the transformed measurement data shows detected propagating waves as ridges. The spatial and temporal bandwidth of the respective transducer can be assessed in these depictions by the range in which ridges are observed.

Piezoelectric transducers

For the purpose of detecting of propagating waves in the plate-like specimens with the measurement setup a piezoelectric transducer is designed (Figure 1). The active element is a strip-shaped piezoceramic (PIC255, PI Ceramic) with dimension $w_{\mathrm{cer}} = 1\,\mathrm{mm}$, $t_{\mathrm{cer}} = 0.5\,\mathrm{mm}$, and $l_{\mathrm{cer}} = 12\,\mathrm{mm}$. A sufficient amount of damping mass inside the transducer enclosure enables a reliable detection of broadband acoustic waves. Due to the laser radiation being focused onto a thin line and the strip-shaped piezoceramic excitation and detection are adequately matched.

The universal piezoelectric micromachined ultrasonic transducer (PMUT) used in this study comprises a number miniaturised sensors with an adaptive channel and chip size. For the electromechanical transducers a piezoelectric thin film AlN on a silicon oxide membrane and its necessary electrical components are used [3]. The universal PMUT technology is a patent pending technology, aiming a fast and resource-friendly production of application adapted sensors with-

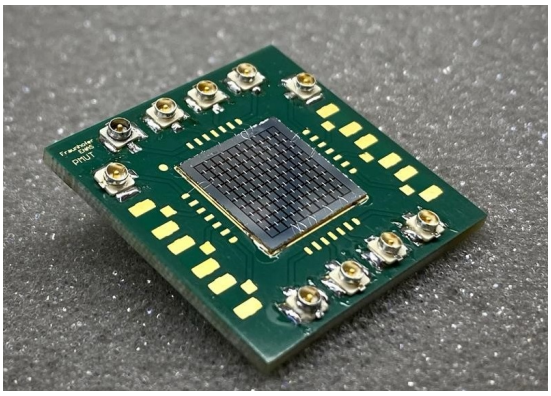

Fig. 2: PMUT with a membrane diameter of $100\,\mu m$ *and a linear wire bonding on a printed circuit board.*

out the setup cost for an application specific design and wafer run [5]. The design of the acoustic channels and chip size is based on piezoelectric transducer on a silicon wafer substrate divided into $1\,mm x 1\,mm$ unit cells. Each of these unit cells contains the miniaturised membranes ($50\,\mu m$ to $200\,\mu m$) with piezoelectric aluminium nitride as electromechanical transducer. Using an automatic wire bonding process those unit-cells can be electrically connected to create the desired geometry of the active elements of the final sensor (see Figure 2). This procedure enables the manufacturing of multichannel sensors from one wafer substrate with individual channel geometries. [5] For this investigation one single channel with a geometry of $1\,mm x 10\,mm$ and a membrane diameter of $100\,\mu m$ resulting a center frequency of $2\,MHz$ is used.

Experimental comparison

Figure 3 depicts a direct comparison of a measurement based dispersion diagram obtain with the piezoceramic transducer and the PMUT. Both measurements are recorded using the same $2\,mm$ thick aluminium plate and as well as the same process parameter and data processing algorithms. The depiction shows that both sensors have a sufficiently high sensitivity and therefore their measurement data provides clearly visible and distinguishable mode curves. The measurement using the traditional piezoelectric sensor contains modes up to $16\,MHz$ and $30\,rad\,mm^{-1}$, indicating that modes at least up to this frequency range are present in the specimen. The PMUT under consideration provides interpretable data up to $10\,MHz$ and $20\,rad\,mm^{-1}$ with reduced background noise.

Conclusion

The evaluation of a specially configured, universal piezoceramic micromachined ultrasonic transducer (PMUT) for the detection of elastic waves shows adequate spatial and temporal bandwidth. Given the fact that the PMUT examined in this work is not specifically build for this purpose, the test in the proposed application can be considered successful. Adapting the design of the PMUT to the task at hand, e.g. by

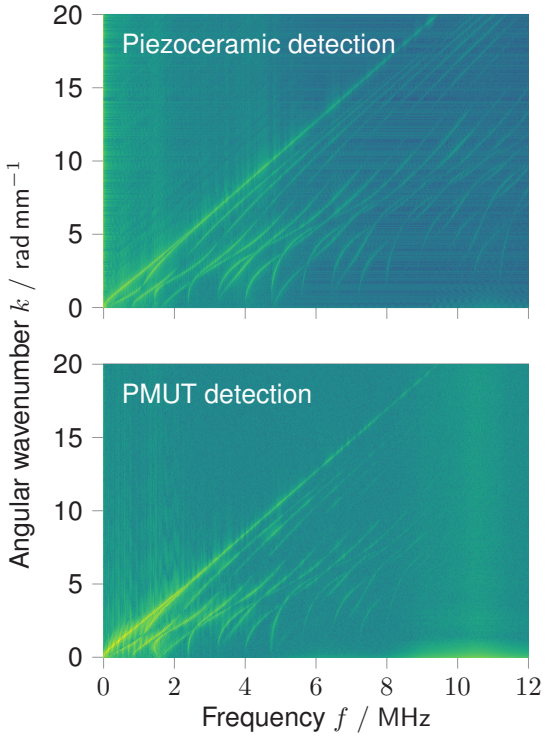

Fig. 3: Comparison of measured dispersion diagram of a $2\,mm$ *aluminium sample using the piezoceramic based transducer and the PMUT as the detecting sensor.*

adjusting the arrangement of the membranes, increasing the fill factor, using inner and outer electrodes and increasing the nominal resonant frequency, or using piezoelectric transducers with high piezoelectric coefficients and low permittivity such as AlScN, is expected to improve the results presented.

References

[1] S. Johannesmann, L. Claes, *et al.*, "Inverser Ansatz zur akustischen Charakterisierung plattenförmiger Materialproben," in *Fortschritte der Akustik - DAGA 2017*, Deutsche Gesellschaft für Akustik e.V. 2017, 2017, pp. 999–1002.

[2] L. Claes, T. Meyer, *et al.*, "Determination of the material properties of polymers using laser-generated broadband ultrasound," vol. 5, no. 1, pp. 187–196, 2016. DOI: 10.5194/jsss-5-187-2016.

[3] C. Stoeckel, M. Melzer, *et al.*, "Design and technology for uniform aluminum nitride piezoelectric micromachined ultrasonic transducers with radial array," in *2021 Smart Systems Integration (SSI)*, IEEE, 2021, pp. 1–4. DOI: 10.1109/SSI52265.2021.9467017.

[4] D. Alleyne and P. Cawley, "A 2-dimensional Fourier transform method for the quantitative measurement of Lamb modes," in *IEEE Symposium on Ultrasonics*, IEEE, 1990. DOI: 10.1109/ultsym.1990.171541.

[5] C. Stoeckel, K. Meinel, *et al.*, "Verfahren zur Herstellung eines mikromechanischen Ultraschallwandlers und Ultraschallwandler, TU Chemnitz," 20 2023 102 447 (utility model), patent pending, 2024.

DOI 10.5162/SMSI2025/D5.3

Experimental comparison of receive sensitivity of circular and ring piezo-electrodes geometries for PMUT resonator membranes designed in PiezoMUMPS process

Niko Plantak[1], Mihael Katalenić[1], Dinko Oletić[1]
[1] University of Zagreb Faculty of Electrical Engineering and Computing,
Unska 3, HR-10000 Zagreb, Croatia,
dinko.oletic@unizg.fer.hr

Summary:
Piezoelectric micromachined ultrasonic transducers (PMUT) elements in SOI technologies based on circular resonator membranes, often employ fully covered circular, or ring-shaped piezo-electrodes. However, depending on the exact piezo material stack, their placement and geometry may introduce mechanical clamping or residual stress, causing a loss of sensitivity, or unwanted resonant frequency shifts. Here we show early FEM and experimental results of geometric optimization of circular, and ring piezo-electrodes for 1 MHz PMUT resonator membranes designed in PiezoMUMPS process.

Keywords: ultrasonic, piezoelectric, PMUT, resonator, membranes.

Introduction

Piezoelectric micromachined ultrasonic transducers (PMUT) elements, designed in SOI technologies in form of circular-shaped device-layer silicon resonator membranes, most often use circular or ring-shaped piezo-electrodes [1], [2]. However, an exact set of material layers constituting the piezo-electrode stack, their mechanical properties, thicknesses, limitations of patterning individual layers etc. may introduce mechanical clamping or residual stress, causing a loss of sensitivity, or unwanted resonant frequency shifts [3, 4]. Therefore, it is necessary to specifically tailor the geometry, sizes, and alignment of individual thin-film piezo-electrode stack layers for a specific technological process. In this paper we do this by parametrizing circular, and ring piezo-electrodes geometries for PMUT membranes designed around 1 MHz in PiezoMUMPS process [5].

Methodology

In PiezoMUMPs (Fig. 1, left), a 10 µm P-doped silicon acting simultaneously as a structural device-layer defining PMUT membrane thickness, and as a relatively resistive bottom electrode. The piezo-electrode stack consists of AlN as a piezoelectric material, and a relatively thick 1 µm top metal electrode.

Modal response, and harmonic receive sensitivity (resonant frequency, displacement, piezo-voltage) of a PMUT were simulated by a harmonic coupled-physics FEM model (COMSOL), exploring the design-space of parametrized geometry elements (Fig. 1, right): membrane radius r_m, horizontal ring electrode thickness r_t, and position of the electrode's outer edge with respect to membrane. For each r_m, the design goal was to identify r_t, r_e, maximizing piezo-voltage, while minimizing relative frequency-shift Δf [%] and change in displacement Δd [%], compared to a referent PMUT design with a completely covered circular electrode aligned to the membrane edge ($r_t = r_m$, $r_e = 0$, Fig. 1, left). PMUT samples were microfabricated, and preliminary characterized by electrical impedance (Agilent), laser-doppler vibrometry (SmarAct), compensated for differences in membrane radius r_m due to back-side DRIE blowout.

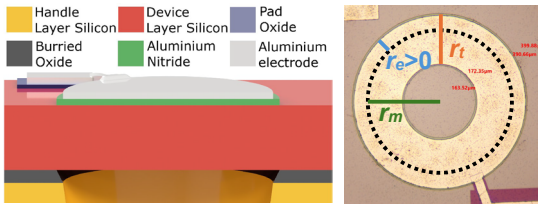

Fig 1. PiezoMUMPs technological cross-section (left), designed PMUT devices (right).

Experimental results

Compared to a fully covered membrane, frequency-shift can be minimized (Fig. 2, white iso-surface Δf = 0%) by designing thin ring-electrodes surpassing the membrane edge (r_e > 0, r_t << r_m,), with an optimal r_t changing more linearly starting from at least r_e > 15 µm. With smaller r_t resulting in lower Δd, Δd < -2% can

be expected in the region of intersection with the Δf = 0% iso-surface (Fig. 3, orange arrow). Voltage obtained at this intersection is maximized for r_e = 15 µm (Fig. 4, orange arrows). Optimal ring thickness r_t scales linearly with membrane radius r_m. If maintaining Δf = 0 is not relevant, Fig. 5 (orange arrows) confirms the presence of an additional piezo-voltage maximum, obtained for a thick ring-electrode, placed inside the membrane (r_e < 0) around the second point of maximal stress gradient, closer to its center. These findings were preliminarily confirmed by vibrometry (Fig. 6).

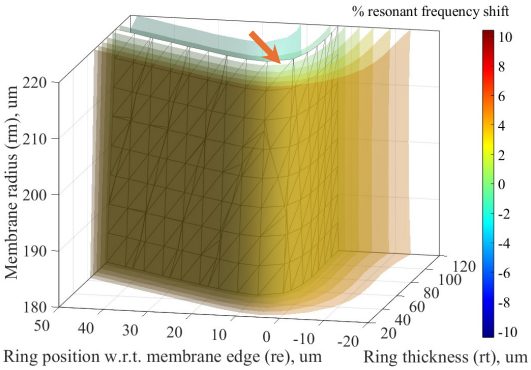

Fig. 2, Minimal change in resonant frequency Δf.

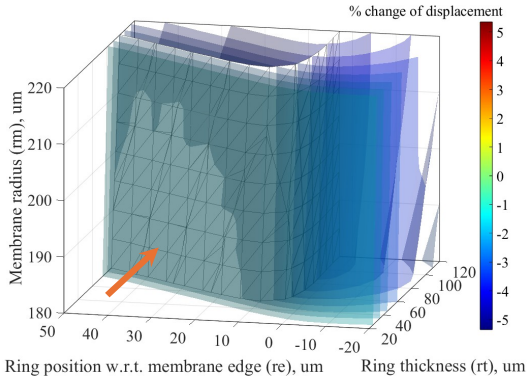

Fig. 3, Minimal change of displacement Δd, FEM.

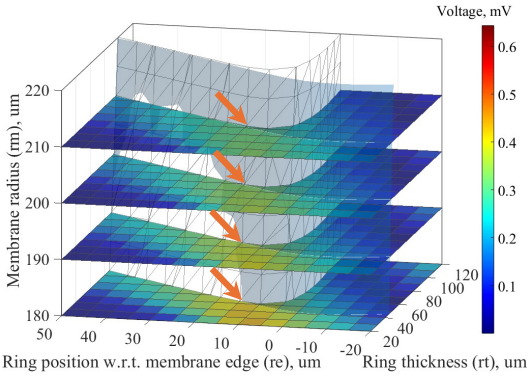

Fig. 4. Piezo-voltage for minimal Δf and Δd, FEM.

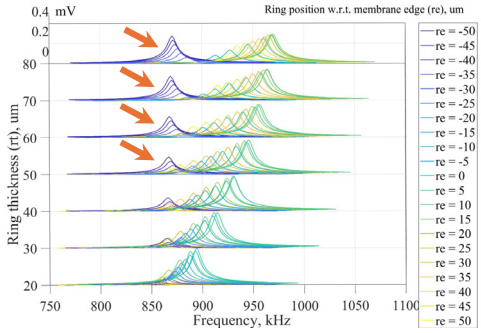

Fig. 5. Piezo-voltage, for fixed r_m = 200 µm, FEM.

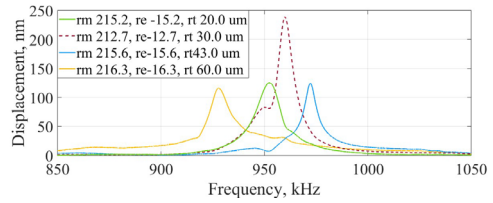

Fig. 6. Measured displacement, vibrometry.

Conclusion

An optimal placement and ring-thickness was derived for thin ring piezo-electrodes at the PMUT membrane edge, while minimizing the changes between the designed and obtained resonant frequency. More experimental work is planned to validate the FEM findings.

Acknowledgment

This work was partly Financed by European Union – NextGenerationEU under the Grant Agreement NPOO.C3.2.R2-I1.06.0090, and in part it was supported by an Industry Cooperation funded by Infineon Technologies Austria AG in the course of IPCEI Microelectronics.

References

[1] H. Wang, Y. Ma, H. Yang, H. Jiang, Y. Ding, and H. Xie, “MEMS Ultrasound Transducers for Endoscopic Photoacoustic Imaging Applications,” Micromachines, vol. 11, no. 10, Oct. 2020

[2] E. Moisello, L. Novaresi, E. Sarkar, P. Malcovati, T. L. Costa, and E. Bonizzoni, “PMUT and CMUT Devices for Biomedical Applications: A Review,” IEEE Access, pp. 1–1, 2024

[3] Y. Lu, D. A. Horsley, “Modeling, Fabrication, and Characterization of Piezoelectric Micromachined Ultrasonic Transducer Arrays Based on Cavity SOI Wafers,” J. MEMS., vol. 24, no. 4, 2015.

[4] F. Sammoura, et al., “Optimizing the electrode size of circular bimorph plates with different boundary conditions for maximum deflection of piezoelectric micromachined ultrasonic transducers”. Ultrasonics, vol. 53, no. 2, 2013.

[5] Science PiezoMUMPs technological process, https://science.xyz/docs/d/mems-piezo/index

DOI 10.5162/SMSI2025/D5.4

Impact of Damping Effects on Piezoelectric Actuation Used in Acoustofluidic Cell Trapping

*B. Leikam, S. Pandey*², O. Hayden*², *G. Schrag

*Professorship of Microsensors and Actuators, Technical University of Munich, Germany
*²Heinz-Nixdorf-Chair of Biomedical Electronics, TranslaTUM, Technical University of Munich, Munich, Germany
Contact: barbara.leikam@tum.de

SUMMARY

Acoustic trapping is increasingly recognized as an effective and gentle non-contact method for manipulating cells and particles within microfluidic systems, which is crucial for advancing research in drug development and medical treatments. A critical factor in the successful assembly of an acoustic trapping system is the design of the acoustic resonator, which must ensure the alignment of the resonance frequency between the piezoelectric element and the fluid-filled cavities. This paper focuses on characterizing piezo electrical damping effects essential for optimizing and advancing the acoustophoretic microsystem.

KEYWORDS: piezoelectric actuation, damping effects, acoustofluidics, acoustophoresis

BACKGROUND

Acoustic trapping, also known as acoustic tweezers, represents a promising technique in biomedical engineering, enabling various functions such as capturing, separation, filtration, and agglomeration of cells [1]. Utilizing this technology, a measurement setup and a prototype (Figure **1**) have been developed [2–4]. A crucial prerequisite for the propagation of Bulk Acoustic Waves (BAW) in both, the solid and the fluidic parts is the design and the positioning of the piezoelectric actuator. In acoustic trapping, the two phenomena decisive for successful operation are the acoustic radiation force (ARF) and the acoustic-streaming-induced drag force (ASF). The ARF is generated by pressure nodes and antinodes of standing acoustic waves, while the ASF results from the nonlinear attenuation of a propagating acoustic wave in a viscous medium. These forces are primarily determined by the acoustic resonator in combination with the generated BAWs and must be strong enough to counteract the velocity of the liquid medium. In this context, the impedance of the piezo and the deflection play a pivotal role. Preliminary studies revealed a zero-pressure node within the cavity at around 2 MHz, and the cell trapping conditions have been empirically met by sweeping the actuation frequency at the piezo within a certain range since neither the frequency characteristics nor the damping of the piezo material have been known precisely enough. However, operating the piezo at the dedicated and optimized operating frequency would be more energy-efficient and reduce system heating, which is particularly important if the device is extended to an extensive array system and/or applied in long-term studies like tumor cell interaction. Developing a second generation of cell trapping devices, specifically in an array configuration for parallelization of cell investigations and, hence, geometry and size changes in the system, necessitates dedicated characterization of the applied piezo element to ensure efficient wave transmission.

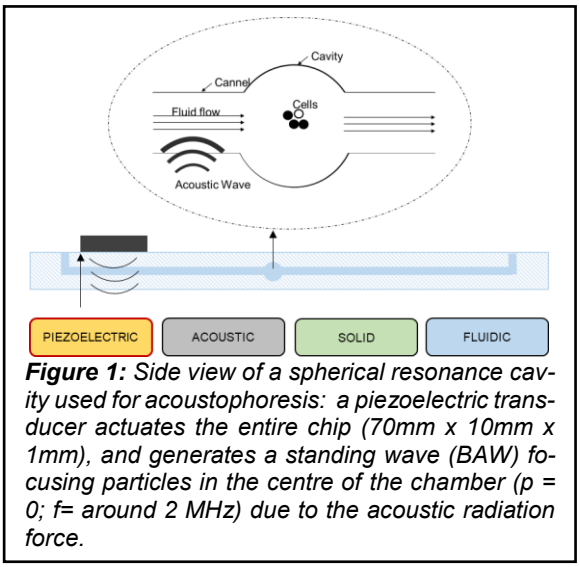

Figure 1: *Side view of a spherical resonance cavity used for acoustophoresis: a piezoelectric transducer actuates the entire chip (70mm x 10mm x 1mm), and generates a standing wave (BAW) focusing particles in the centre of the chamber (p = 0; f= around 2 MHz) due to the acoustic radiation force.*

RESULTS

In the first step, the unmounted piezoelectric actuator was excited by applying a voltage (V_{pp}= 10 V), with the system being in a vacuum and at a constant temperature, and its impedance was simulated and measured (**Figure 1**). In the second step, we introduced damping by applying an isotropic loss factor from the COMSOL material database. In theory, the minimum impedance of the piezo **(Figure 2)** occurs at the same frequency as the maximum deflection of

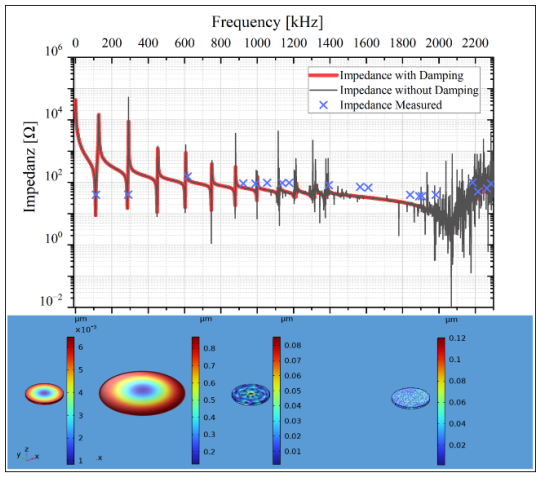

Figure 2: (Top) *Frequency-dependent impedance of a piezo element (Pz26) with a radius of 10 mm x 1mm. The minimum is located at* f_{min}*=2068 kHz.* ***(Bottom)*** *Modeshapes of the piezo at f= 1 kHz, 100 kHz, 868 kHz and 2068 kHz (from left to right).*

the piezo (**Figure 3 (A)**) shows that this is not the case when damping is considered. The maximum amplitude of the piezo is shifted to lower frequencies (110 kHz), and the maximum deflection decreases by a factor of 150. Next, we additionally took into account the gluing process (see **Figure 3 (B)**). As a result, the maximum impedance is shifted again to lower frequencies (blue), and the deflection decreases by 11% of the original deflection (red). Laservibrometer measurements show the most significant deflection at 6 kHz and 110 kHz for both the freely vibrating and glued disc, which compares well with the simulations.

CONCLUSION AND OUTLOOK

We characterized a piezoelectric actuator used in acoustophoretic devices for cell trapping by simulations and measurement to quantify the impact of material damping and of the glue used for mounting on the impedance of the piezo and the displacement induced by it. Both parameters are crucial for the design of the chips to get an optimized energy transfer and ensure frequency matching. It revealed that considering material damping, the maximum deflection is shifted to lower frequencies and – in contrast to theoretical expectations – does not coincide with the minimum impedance. Measurements by a Laservibrometer confirmed this trend. The outcome of this study will go into the design of more advanced cell trapping devices, e.g., the parallelization of cell investigations in arrays or the mixing of different liquid media.

REFERENCES

[1] Z. Wu, M. Pan, J. Wang, B. Wen, L. Lu, and H. Ren, "Acoustofluidics for cell patterning and tissue engineering," *Engineered Regeneration*, 2022, doi: 10.1016/j.engreg.2022.08.005.

[2] B. Sailer, R. Barnkob, and O. Hayden, "Acoustophoretic particle motion in a spherical microchamber, "*Physical Review Applied,* 2024, doi: 10.1103/PhysRevApplied.22.044034.

[3] B. Leikam, S. Pandey, O. Hayden, and G. Schrag, "Design Studies and Optimization of Acoustic Pressure in Acoustofluidic Cell Manipulation Platforms, "25th *EuroSimE*, 2024, doi: 10.1109/EuroSimE60745.2024.10491497.

[4] L. Fabiano, S. Pandey, Shilpi, M. Brischwein, M. Hasanzadeh Kafshgari, and O. Hayden, "Continuous Perfusion Experiments on 3D Cell Proliferation in Acoustic Levitation,", *Micromachines,* 2024, doi: 10.3390/mi15040436.

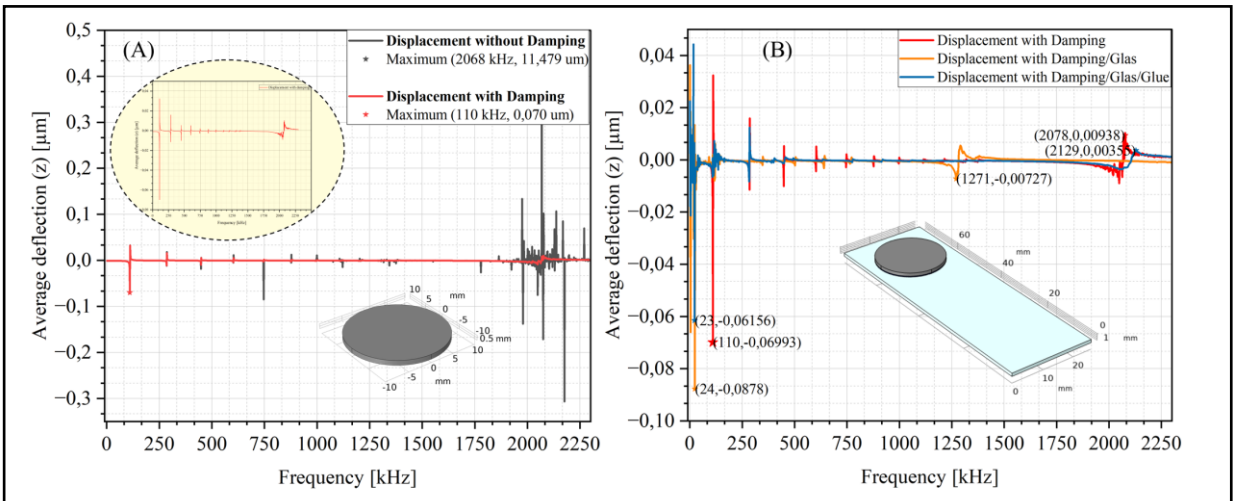

Figure 3*:* ***(A)*** *Average deflection of a freely vibrating transducer (PZ26) over frequency (*V_{pp}*= 10 V) without (grey) and with isotropic loss factor (red). The y-axis is limited to 0.5 µm for visualization, with the yellow background highlighting the zoomed-in region, where only the damping component is plotted.* ***(B)*** *Comparison of the average deflection of a freely vibrating transducer (red), fixed transducer on a glass slide (orange) and a transducer glued (*d_{glue}*=2µm) on a glass slide.*

DOI 10.5162/SMSI2025/D6.1

High Throughput Magnetron Sputtering of Tilted c-Axis AlN Films for Biosensing Applications

Patrick Bergmann[1], Enrico Loos[1], Matthias Nestler[1]
[1] scia Systems GmbH, Clemens-Winkler-Strasse 6c, 09116 Chemnitz, Germany
e-mail: p.bergmann@scia-systems.com

Summary:
A new two-step approach for high throughput magnetron sputtering of tilted c-axis aluminum nitride will be presented. This includes a slower growth of AlN in a tilted magnetron arrangement followed by a faster AlN deposition in a standard face-to-face sputtering arrangement.

Keywords: AlN; Tilted c-axis; Biosensors; Magnetron Sputtering

Motivation

Over the last decade, there has been an increasing development of biosensing applications using resonant vibrating bulk piezo devices, such as aluminum nitride, due to its excellent sensitivity and fast response [1]. The change in resonant frequency can be easily detected and is sensitive down to concentrations of <0.1 ng of molecules of interest. While standard resonators with vertical c-axis orientation suffer from significant attenuation in liquid, shear mode oscillators are advantageous.

We present the development of a magnetron sputtering process for the growth of polycrystalline aluminum nitride films with a defined oriented, tilted c-axis of the AlN grains. The high-vacuum tool employs an in-line principle with quasi-continuous substrate movement during deposition (Figure 1). Multiple wafers can be placed face down on a carrier tray as they move over the linear magnetron sputter sources.

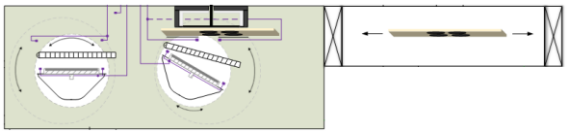

Fig. 1. Schematic illustration of the main components of the inline sputter tool scia Magna 200 Inline *with bulk and seed station (left) and load-lock (right), carrier tray for 4 wafers.*

Simulation

A particle-in-cell (PIC) simulation was used to define specific components and arrangements, in particular the tilt and orientation of the magnetron at the so-called seed sputtering station. At this position, a particle flux extracted from the sputter source with a wide angular distribution is parallelized by means of a collimator. The cell size and mechanical dimensions of the collimator are varied in order to achieve the highest flux at the substrate position while maintaining a well-defined growth of tilted grains with a small angular spread. Simulation results are presented (Figure 2). Nevertheless, the flux of sputtered particles through such a collimator is much lower than for an unrestricted sputtering arrangement. Therefore, the developed tool is equipped with a second sputtering station, the so-called bulk station, for subsequent fast growth by standard magnetron arrangement face to face with the substrate, which ensures a much higher rate than within the seed station.

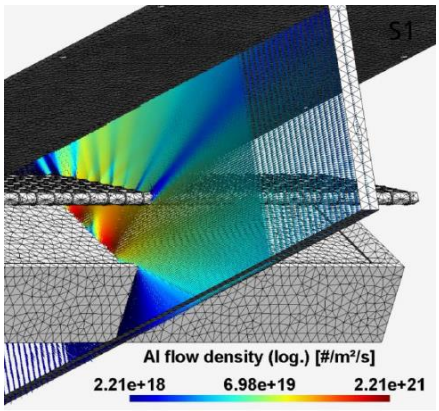

Fig. 2. Simulation result for a specific magnetron-collimator-substrate arrangement

Experimental

The quality of the grown films, in particular the crystal grain size and orientation, is investigated by XRD measurements such as theta-2-theta scans, rocking curves and pole figures.

We have found that an initial film thickness of about one hundred nanometers can be sufficient to act as a seed. The "seeded" tilted orientation is maintained for a few microns of film growth to

the desired thickness. This two-step approach allows the inline processes to be much better co-ordinated, without the throughput being limited by one of the steps. The influence of the initial substrate roughness is also known to be an important parameter for the seed of the tilted grains. Angles of tilt of >31° from the substrate normal have been achieved (Fig. 3).

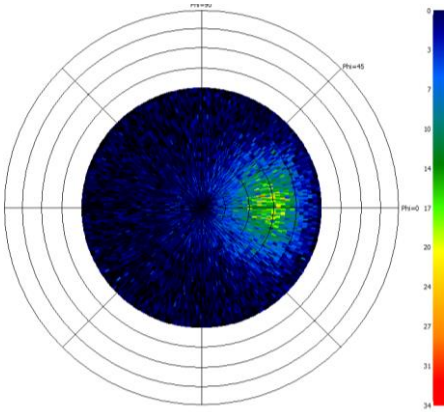

Fig. 3. Pole figure for an AlN film with 31° c-axis tilt represented by the (002) reflex

Outlook

Future developments will aim at a controlled switching of the tilt orientation after a certain film thickness as well as a change of the polarisation direction of the piezo crystallites.

References

[1] G. Wingqvist, J. Bjurström, L. Liljeholm, V. Yantchev, I. Katardjiev, Shear mode AlN thin film electro-acoustic resonant sensor operation in viscous media, *Sensors and Actuactors B 123*, 466-473 (2007); doi: 10.1016/j.snb.2006.09.028

DOI 10.5162/SMSI2025/D6.2

Noise in Piezoelectric MEMS: Modeling and Experimental Characterization

Sina Zare Pakzad[1,2] *Patrick Egger*[1] *Negin Rahnemai Haghighi*[1,2] *Shareena Muringakodan*[1,2]
Mahdi Mortada[1,2] Proloy T. Das[1,2] Keith C. Schwab[3,4] Ulrich Schmid[1] and Michael Schneider[1,2]
[1] Institute of Sensor and Actuator Systems, Gusshausstrasse, 1040, TU Wien, Austria
[2] Christian Doppler Laboratory for Piezoelectric Silicon MEMS with Enhanced Sensitivity and Responsivity, Institute of Sensor and Actuator Systems, Gusshausstrasse, 1040, TU Wien, Austria
[3] Kavli Nanoscience Institute and Thomas J. Watson, Sr., Laboratory of Applied Physics, California Institute of Technology, Pasadena, CA, 91125, USA
[4] Institute for Quantum Information and Matter, California Institute of Technology, Pasadena, CA, 91125, USA
michael.schneider@tuwien.ac.at

Summary: This study investigates noise mechanisms in piezoelectric MEMS membranes to identify and minimize performance limitations. A comprehensive noise model is developed, incorporating experimental measurements and the amplifier's noise floor, validated through close agreement with measured noise spectra. The noise is decomposed into distinct sources, which are identified within the developed model. The findings provide valuable insights for optimizing MEMS membrane design, enhancing noise performance, and enabling high-precision applications in sensing and actuation.

Keywords: Piezoelectric MEMS, noise measurement, noise modeling, alumninium nitride, thin-film sensors.

Introduction

Noise refers to unpredictable fluctuations or disturbances in physical quantities that inherently arise, impacting the performance of a system. In the context of microelectromechanical systems (MEMS), noise imposes critical limitations on the accuracy of sensors and actuators, with noise sources broadly categorized as either extrinsic or intrinsic. Piezoelectric MEMS have attracted considerable attention due to their ability to convert mechanical energy into electrical signals and vice versa, making them crucial for precision sensors, actuators, and energy harvesters. However, their performance is often constrained by noise, which can obscure weak signals and degrade measurement accuracy. The multilayer thin-film structures in piezoelectric MEMS, which typically include a piezoelectric layer, electrodes, and additional mechanical or electrical insulation layers, further contribute to noise. Understanding and mitigating noise contributions from these layers, as well as from the piezoelectric origin, is essential for advancing the design and functionality of such devices, particularly in the context of recent advancements in micro-/nanomanufacturing technologies [1].

Materials and Methods

Experimental Setup

The piezoelectric MEMS membrane, characterized by high impedance and low signal output, necessitates a low-noise signal conditioning circuit before interfacing with the data acquisition system. The experimental setup, illustrated in Fig. 1, incorporates a low-noise voltage amplifier to enhance the membrane's signal, given its capacitance in the range of hundreds of Picofarads (pF). The setup spans two dedicated rooms: a measurement room housing data control and environmental monitoring equipment, and a Faraday room designed for noise characterization under room-temperature conditions. Pressure and temperature sensors are employed to ensure stable environmental parameters, which are critical for consistent data collection. The low-noise amplifier (Sierra Amps., SA1) connects the MEMS membrane to a multifrequency lock-in amplifier (MLA-3) for data acquisition. Inside the Faraday room, the MEMS membrane, mounted on a custom PCB, undergoes visual inspection before measurements. SMA connectors and coaxial cables are used to maintain signal integrity within the vacuum chamber hosting the membrane. Temperature and pressure sensors continuously monitor the vacuum chamber to ensure stability during measurements. The low-noise amplifier, with an ultra-low noise floor of 300 pV/$\sqrt{\text{Hz}}$, interfaces the MEMS device output with the data acquisition unit. The MEMS membrane under investigation is fabricated using a silicon-on-insulator wafer with a 500 nm buried oxide layer and a 2 μm device layer. The fabrication process includes the deposition of a 330 nm oxynitride insulation layer, patterning of Cr/Au electrodes (50/200 nm), sputtering of a 400 nm AlN piezoelectric layer, and subsequent etching steps to release the membranes. The chips are then diced, bonded to a PCB, and each chip hosts multiple piezoelectric membranes dedicated to noise measurements.

Noise Modeling

Noise in piezoelectric MEMS membranes originates from various sources that significantly in-

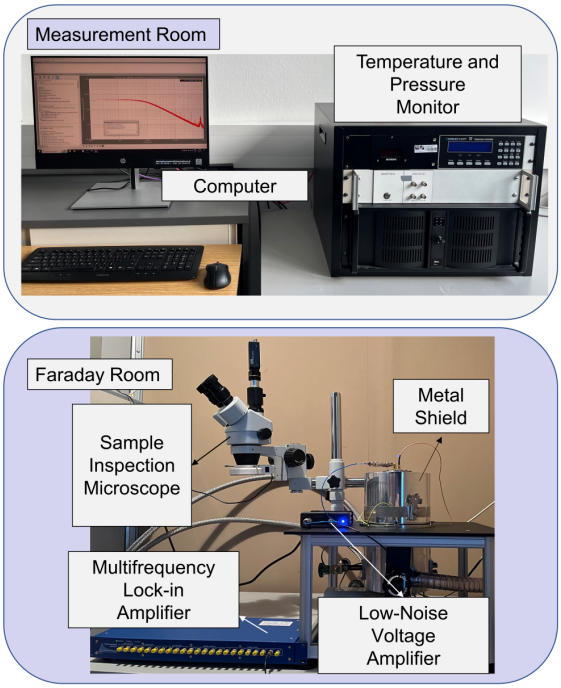

Fig. 1: Experimental setup for noise measurements of piezoelectric membranes, featuring a low-noise voltage amplifier for signal amplification, and a data acquisition system for noise characterization and spectral analysis.

fluence system performance. These sources are broadly classified as intrinsic noise, arising from the piezoelectric material, and extrinsic noise, introduced by the measurement and amplification setup. Thermal noise, also known as Johnson-Nyquist noise, is a fundamental contributor linked to the impedance characteristics of the piezoelectric membrane. This noise results from the random thermal motion of charge carriers within the material and depends on factors such as temperature, material properties, and operating frequency. Beyond thermal noise, the amplifier contributes noise components, including input voltage noise and current noise [2]. The input-referred voltage noise establishes the baseline noise floor of the measurement system, while current noise arises from gate leakage and capacitive coupling effects within the amplifier's input stage. Additional noise sources include the thermal noise of bias and load resistors, which propagate through the system and contribute to the total noise voltage at the amplifier's output. The interplay among these noise sources, the impedance of the piezoelectric membrane, and parasitic elements in the setup collectively determines the overall noise performance of the system. In this context, a model is developed based on individual noise sources that enables the interpretation of different factors that contribute to the total noise measured for the piezoelectric MEMS under investigation here.

Results

The noise spectral density measured at room temperature is presented in Fig. 2, comparing the experimental data, the modeled total noise, and the noise floor of the amplifier. The modeled noise closely matches the experimental measurements across the frequency range, confirming the validity of the noise decomposition. At higher frequencies, the noise approaches the amplifier's noise floor, while at lower frequencies, the measured noise exhibits a characteristic $1/f$ behavior. Peaks in the noise spectrum correspond to the structural resonances of the MEMS membrane, highlighting its vibrational response. The amplifier maintains a stable gain and noise characteristic within the frequency range of 1 kHz to 1 MHz, ensuring consistent noise performance. This comparison between the model and experimental data provides valuable insights into the dominant noise mechanisms and serves as a foundation for optimizing the membrane design and minimizing noise in future applications.

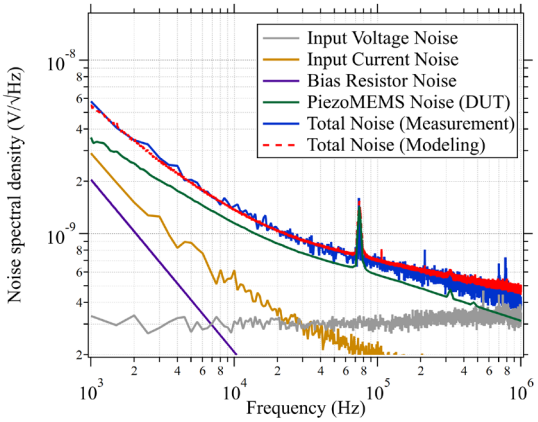

Fig. 2: Noise spectral density showing the total modeled noise compared to the measured noise for the piezoelectric membrane.

Acknowledgment

The financial support by the Austrian Federal Ministry of Labour and Economy, the National Foundation for Research, Technology and Development and the Christian Doppler Research Association is gratefully acknowledged.

References

[1] J. Liu, H. Tan, X. Zhou, W. Ma, C. Wang, N.-M.-A. Tran, W. Lu, F. Chen, J. Wang, and H. Zhang, "Piezoelectric thin films and their applications in mems: A review," *Journal of Applied Physics*, vol. 137, no. 2, 2025.

[2] F. A. Levinzon, "Noise of piezoelectric accelerometer with integral fet amplifier," *IEEE sensors journal*, vol. 5, no. 6, pp. 1235–1242, 2005.

DOI 10.5162/SMSI2025/D6.3

DC Voltage Induced Parametric Potential Energy Modulation in Bistable Piezoelectric MEMS Membranes

Shareena Muringakodan[1,2], Ulrich Schmid[1], Michael Schneider[1,2]
[1] Institute of Sensor and Actuator Systems, TU Wien, 1040 Vienna, Austria
[2] Christian Doppler Laboratory for Piezoelectric Silicon MEMS with Enhanced Sensitivity and Responsivity, TU Wien, 1040 Vienna, Austria
e-mail: shareena.muringakodan@tuwien.ac.at

Summary:
This paper explores the potential energy modulation of bistable PiezoMEMS membranes via stress tuning. The static deflection of the membrane is tuned by applying DC voltage, while external air pressure enables load-deflection measurements for the potential energy analysis. The effect of DC on the membrane is closely related to the membrane's stress and its initial static buckling height. Membranes that are already buckled and exhibit bistability demonstrate minimal changes when subjected to DC. In contrast, membranes that are buckled but remain monostable exhibit a significant response to DC.

Keywords: Bistability, Piezo, Membranes, potential energy, parametric.

Motivation and Objective

Bistable PiezoMEMS membranes are attractive for energy-efficient solutions, featuring two stable mechanical states [1,2]. However, the ability to precisely measure and control the potential energy landscape of these structures is a challenge. Hence investigating the influence of external factors like voltage and pressure on these membranes opens a new door for enabling tunable and adaptive bistable PiezoMEMS systems. Understanding how these factors interact with the membranes' properties can provide deeper insights into optimizing device performance and reliability.
The main objective of this research is to find the potential energy landscapes of PiezoMEMS membranes and investigate how their potential can be modulated by tuning the mechanical stress of the membrane by a DC voltage. With this approach, we are trying to establish a parametric correlation between the applied DC voltage and the membrane's potential landscape which helps to provide insights into dynamic stress control of bistable PiezoMEMS membranes. This approach is attractive for stress-modulated applications like varifocal MEMS mirrors [3].

Methodology

The silicon PiezoMEMS bistable membranes with diameters ranging from 600 to 800 µm and a thickness of ~3.43 µm were fabricated according to standard MEMS fabrication processes. The membrane has a stacked structure with a piezoelectric layer sandwiched between top and bottom electrode layers. Aluminum nitride (AlN) serves as piezoelectric layer whose stress is tuned to achieve the compressive stress needed to induce membrane buckling. Air pressure (both positive and negative) is applied as an external force perpendicular to the membrane surface (always from below the membrane) to conduct load-displacement measurements. Simultaneously, a DC voltage is applied to the system. The static deformation of the membrane under varying air pressures and applied voltages is measured with White Light Interferometry (WLI) (see Fig. 1).

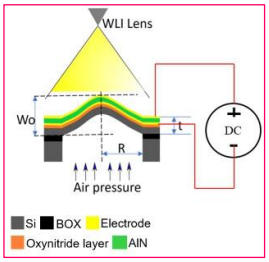

Fig. 1 Schematic of the measurement setup for DC voltage-induced parametric potential energy modulation in bistable piezoelectric MEMS membranes.

The parametrically modulated potential is derived from the load-deflection data corresponding to each applied voltage. To achieve a static buckling height (w_0>0), the membrane must exhibit compressive residual stress that exceeds its characteristic critical stress σ_c [1] given by eq. (1),

$$\sigma_c = -\frac{4 \cdot E_{eff} \cdot t^2}{3 \cdot R^2 \cdot (1-\nu_{eff}^2)} \quad (1)$$

where E_{eff} represents the effective biaxial Young's modulus of the membrane, t is the

membrane thickness, *R* denotes the membrane radius, and ν_{eff} is the effective Poisson's ratio.

Results

The stress within the whole wafer varied from the center to the edge of the wafer (see Fig. 2. (left)) resulting in the maximum static buckling height in the edge regions of the wafer ($\sigma_0 \approx 65$ MPa $\approx 3\sigma_c$), while the minimum was observed at the center ($\sigma_0 \approx 20$ MPa $\approx \sigma_c$), (see Fig. 2. (right)), marked as regions A, B, and C.

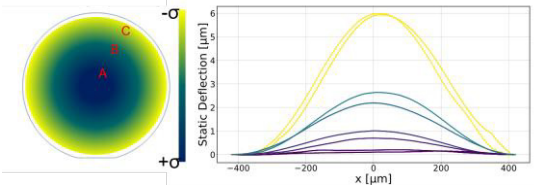

Fig. 2. Typical representation of stress variation in membranes across a wafer (left) and initial static buckling height of membranes with respect to its location on the wafer (right).

Experimental findings have shown that the effect of DC voltage on piezo membranes is strongly correlated with the initial stress and stiffness of the membrane. When DC voltage was applied, membranes in region A, which experienced minimal or no buckling, exhibited a negligible response, even when voltages as high as 60 volts were applied. This suggests that the voltage induced stress is not sufficient to achieve an effective membrane stress above σ_c. On the other hand, membranes in region C, which are highly buckled and exhibit bistability, also demonstrated only small changes in their static deflection (approximately 50 nm for 10 volts). This is because their mechanical stiffness has increased due to the buckling, making it more difficult to further deform the membrane. However, membranes in region B, the intermediate stress region, which are buckled but can remain only in one state, showed significant changes in buckling height when DC voltage was applied, approximately 500 nm for 10 volts (see Fig. 3 (top)). This is because the compressive stress in this region is still moderate, and the mechanical stiffness remains within an optimal range, allowing the voltage induced stress to effectively induce further deformation. These findings also open up new possibilities, where selectively adjusting the stress can transform a monostable membrane into a bistable one or modulate the deflection profile for tunable applications.

The potential energy of these membranes (see Fig. 3) was found from load-displacement measurements by applying air pressure steps *of* 30 mbar*,* generating forces that are orders of magnitude higher than those due to the applied DC voltage. Therefore, the distinct contribution of the DC voltage in the potential curves is "washed out" by the dominant air pressure effect.

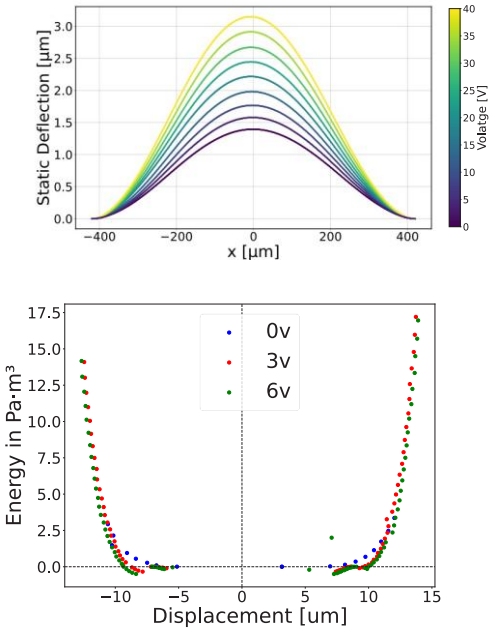

Fig. 3 DC Voltage response of a buckled monostable membrane from region B (top) and potential landscape of a buckled bistable membrane from region C (down).

Even if the membranes exhibited a linear response with DC voltage, under combined loading (air pressure + DC), air pressure induces larger deflections. But, in addition, their effective stiffness values increase and this minimizes the distinct contributions of the DC voltage to deflection and hence, we see minimal or even no changes in the potential profiles under DC voltage. To address this, membranes capable of withstanding higher DC voltages to achieve maximal deflection changes, while employing finer air pressure steps in the range of 1 mbar will help to capture parametric potential modulation accurately.

Acknowledgment

The financial support by the Austrian Federal Ministry of Labour and Economy, the National Foundation for Research, Technology and Development and the Christian Doppler Research Association is gratefully acknowledged.

References

[1] M. Dorfmeister, M. Schneider, and U. Schmid, "Static and dynamic performance of bistable MEMS membranes," *Sensors and Actuators A*, vol. 282, pp. 259-268, Oct. 2018.

[2] Liu, Jinpeng, et al. "Piezoelectric thin films and their applications in MEMS: A review." Journal of Applied Physics 137.2 (2025).

[3] Pribošek, Jaka, Markus Bainschab, and Takashi Sasaki. "Varifocal MEMS mirrors for high-speed axial focus scanning: a review." Microsystems & Nanoengineering 9.1 (2023): 135.

DOI 10.5162/SMSI2025/D6.4

Characterization of AlN-Based MEMS Kineto-Electric Transducer for Cultural Heritage Conservation

Carlo Trigona [1], Suhail Ahmed [1], Anna M. Gueli[2], Salvatore Baglio[1], Mariangela Liuzzo[3], Francesco Lo Iacono[3], Giacomo Navarra[3]

[1] *D.I.E.E.I., Dipartimento di Ingegneria Elettrica Elettronica e Informatica, University of Catania, Viale A. Doria 6, 95125 Catania, Italy*
[2] *Department of Physics and Astronomy "Ettore Majorana", University of Catania, Via Santa Sofia 64, 95123, Catania, Italy*
[3] *Department of Engineering and Architecture, University of Enna "Kore", Cittadella Universitaria, 94100, Enna, Italy*
carlo.trigona@unict.it

Summary:
In this study, an Aluminum Nitride (AlN) MEMS device is analyzed and characterized for kineto-electric conversion. The device has been designed, fabricated, and tested with the primary goal of being employed in the field of preventive conservation and conservation of cultural heritage. For this purpose, the system is capable of detecting low-frequency vibrations of weak intensity and has the ability to generate voltage, enabling kineto-electric conversion without relying on batteries. This feature significantly reduces the overall power consumption of the entire sensing system.

Keywords: AlN, Generating sensor, Kineto-electric conversion, MEMS, Preventive conservation

Overview and Motivation

The rise of low-power, wireless sensor nodes has spurred interest in vibration-based sensors, particularly energy-generating devices designed to replace or extend battery life. Materials such as PVDF, PZT, and AlN are widely used due to their ability to convert mechanical stress into electricity. AlN stands out for its CMOS compatibility, low toxicity, and stability, offering significant advantages in miniaturized, energy-efficient systems. Despite its lower piezoelectric coefficient, AlN achieves a competitive Figure of Merit, making it suitable for energy harvesting and sensing applications [1]. This study advances the state of the art by characterizing an AlN MEMS vibration-to-electricity transducer. Notably, the device is capable of generating voltage without the need for batteries. It has been specifically designed for use in conservation and preventive conservation within the field of cultural heritage. This application is critical for monitoring vibrations in compliance with regulations [2] or detecting mechanical shocks to protect or evaluate artifacts of historical and artistic significance. The results highlight the potential of the proposed MEMS for low-power, long-term applications, emphasizing its suitability for vibrational sensing technologies [3].

MEMS Process

The oscillatory behavior of the microsystem, based on a cantilever design, and the piezoelectric response of the AlN element in the MEMS are modeled (see Fig. 1) using a lumped-parameter system consisting of a mass (M), a spring (X), and a damper (C), which represent inertia, stiffness, and mechanical losses, respectively. For a given time-dependent motion z(t), a relative displacement y(t) occurs between the frame and the mass M due to inertia. The mass-spring-damper system, as a second-order system, enables the determination of the natural frequency f_n. The AlN acts as the transducer, capable of generating a variable voltage output and, in the presence of a load, a current I(t).

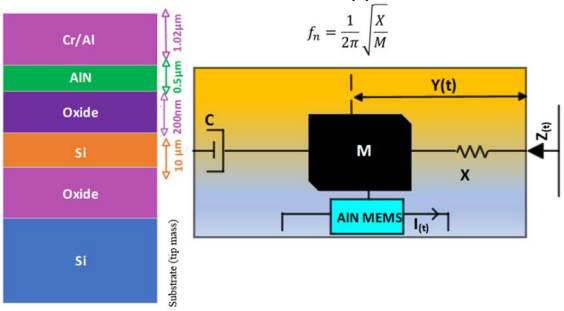

Fig. 1. Electromechanical model of the MEMS and its fabrication process

The fabrication of the piezoelectric cantilever-type AlN MEMS resonator involves an 8-step process, using an SOI wafer with a 0.5 µm device layer, a 1 µm buried oxide layer, and a 400 µm handle layer. Key dimensions, process steps, and film thickness values are shown in Fig. 1 and Tab. I respectively.

Methodology and Results

The measurement setup (see Fig. 2) is based on an APS 129 ELECTRO-SEIS® shaker for MEMS characterization. An automated system enables the measurement of the MEMS voltage output as a function of the applied z(t) excitations imposed by the vibrating platform. Signal post-processing was performed using MATLAB® routines. Fig. 3 shows the Frequency Response Function (FRF) obtained during the calibration process. The input to the shaker is a sine wave with a frequency linearly varying from 60 Hz to 70 Hz and a constant acceleration of approximately 0.5 m/s² (Root Mean Squared, RMS). The spike indicates the resonant frequency of the microsystem. Fig. 4 presents the calibration diagram of the MEMS device. The results show a maximum voltage of approximately 85 mV at 0.5 m/s². It is worth noting that the sensitivity is about 180 mV/m/s².

Conclusion

In this study, an AlN-MEMS device was characterized for kineto-electric conversion, with a focus on applications in the field of cultural heritage conservation. The device effectively detects low-frequency, weak-intensity vibrations and generates voltage, reducing the need for batteries and minimizing power consumption.

Tab. 1: Characteristics of the MEMS layers

MEMS Layer	Young's Modulus [N/m²]	Thickness [m]	Width [m]	Length [m]
Metal (Al)	0.68E+11	1.00E-6	800E-6	8000E-6
Metal (Cr)	1.49E+11	0.02E-6	800E-6	8000E-6
AlN (Piezo)	2.80E+11	0.50E-6	800E-6	8000E-6
Silicon layer	1.69E+11	10.00E-6	800E-6	8000E-6
Substrate (tip mass)	1.69E+11	400.00E-6	800E-6	800E-6

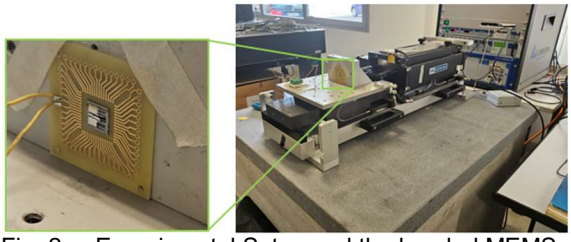

Fig. 2. Experimental Setup and the bonded MEMS

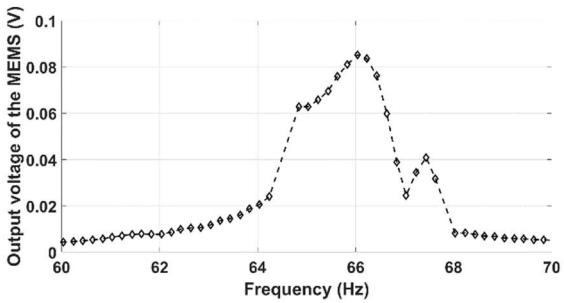

Fig. 3. FRF of the MEMS output with respect to a sweep sine input excitation

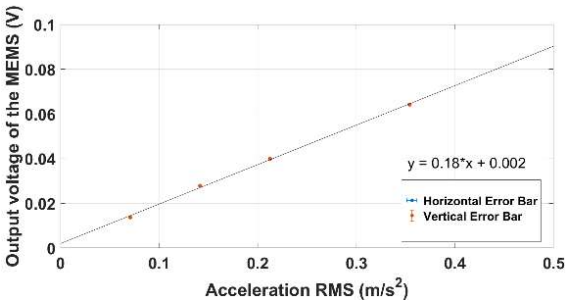

Fig. 4. Calibration diagram of the fabricated MEMS device

The results showed a resonant frequency between 60 Hz and 70 Hz and a sensitivity of approximately 180 mV/m/s², with a maximum output voltage of 85 mV at 0.5 m/s². These features make the device suitable for real-time monitoring of vibrations in situ or during transportation of historical artifacts and structures.

Acknowledgements

Authors would like to thank the European Union (Next Generation EU), through the MUR-PNRR project SAMOTHRACE (ECS00000022) "SicilAn MicronanOTecH Research And Innovation CEnter" – Ecosistema dell'innovazione (PNRR, Mission 4, Component 2 Investment 1.5, Avviso n. 3277 del 30-12-2021), Spoke 1 – University of Catania and University of Enna "Kore".

References

[1] Haider, S. T., Shah, M. A., Lee, D. G., & Hur, S. (2023). A review of the recent applications of aluminum nitride-based piezoelectric devices. Ieee Access, 11, 58779-58795.

[2] Trigona, C., Costa, E., Politi, G., & Gueli, A. M. (2022). IoT-Based Microclimate and Vibration Monitoring of a Painted Canvas on a Wooden Support in the Monastero of Santa Caterina (Palermo, Italy). Sensors, 22(14), 5097.

[3] Anton, S. R., & Sodano, H. A. (2007). A review of power harvesting using piezoelectric materials (2003–2006). Smart materials and Structures, 16(3), R1.

DOI 10.5162/SMSI2025/D7.1

Recognising Wild Animals on Roads: Radar-based Sensor Systems for Accident Avoidance

Michael Schneider[1], Hubert Mantz[1], Thomas Walter[1],
Mike Montoya-Capote[2], Jonas Berger[2], Andreas Reichel[2], Nils Hollmach[2]
[1] Ulm University of Applied Sciences, 89081 Ulm Germany,
[2] tecVenture, 04177 Leipzig Germany
michael.schneider@thu.de

Summary:
The objective of this study is to evaluate the potential of a 60 GHz radar system as a roadside wildlife detection system. The system can be integrated into a delineator, allowing roadside monitoring and the possibility of warning against wildlife accidents. This system is compared to a low-cost image-resolving thermal array sensing system. IR array sensors have limited range and are highly dependent on the environment, with a maximum distance of 18 m in cold environment.

Keywords: wildlife accident, radar system, IR-array sensor, range-doppler evaluation, sensor fusion, moving target indicator, wildlife protection, driver assistance

Introduction and Motivation

The increase in traffic on Germany's roads is contributing to a rise in the number of accidents involving wild animals. In order to assist drivers in avoiding accidents, car developers are turning to driver assistance systems [1]. Several pilot projects demonstrate how drivers can be actively warned. An electronic wildlife warning system has been tested and developed by the Forestry Testing and Research Institute in Baden-Württemberg, Germany, since 2007. This system involves the installation of a fence alongside the road to guide wild animals (e.g. deer) to a crossing area. At this point, infrared sensors detect the presence of an animal, and a sign then warns the driver [2]. The defining characteristic of existing sensor systems is that they monitor only short segments of road, typically between 5 and 7 m, with the remainder of the road secured by a fence. The system presented in this study employs the use of radar sensors to monitor the entire space between delineators. The range of a sensor mounted on a delineator covers an area within a maximum distance of 30 m as illustrated in Figure 1. They are capable of detecting wild animals as they approach the road. This sensor system monitors the entire area adjacent to the road, obviating the necessity for an additional barrier such as a fence.

Sensor Systems

The sensor system has been subjected to rigorous testing and validation in a portable measurement box.

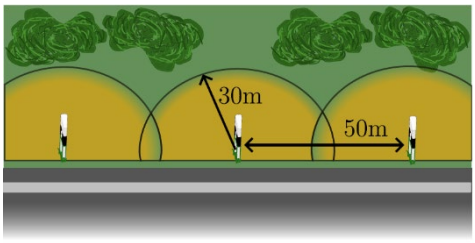

Fig. 1. The provided schematic depicts a road with integrated sensors within the delineator. The distance between the delineators is 50 m, and the sensing radius of the sensors forms a 30 m half circle radius around a delineator.

This box contains both the radar sensors developed in-house by TecVenture and a set of reference sensors. The radar sensors operate at frequencies of 60 GHz and 24 GHz, respectively. These comprise a 60 GHz radar sensor from RFbeam Microwave, referenced in [3], in addition to infrared measuring technology. This sensor type is based on the Infineon BGT60UTR11AIP. A custom-designed lens was constructed with the objective of limiting the field of view to a maximum of 60°. Additionally, a sensor with a frequency of 24 GHz, based on InnoSenT's SMR-334, was developed with the objective of extending the range of evaluation. Furthermore, a Moving Target Indicator (MTI) [4] was integrated into the radar developed by TecVenture, which is already capable of detecting motion. In order to more accurately assess the capabilities of the Boson 640 thermal camera [5], a comparison is made with IR measurement

technology. This is used for thermal validation of wildlife and to determine the maximum range of the camera in the context of existing systems. For this purpose, an IR array HTPA60x40d with a field of view (FoV) of 92° x 60° from Heimann Sensor is employed [6].

Results

The results of measurements conducted at a wildlife park indicate that deer can be detected at distances of up to 22 m using a radar-based detection system with a frequency of 60 GHz. Figure 2 illustrates the range Doppler map of the 60GHz radar sensor, indicating the presence of a target at a distance of 18m and a radial velocity of 0.8 m/s. A target of the same amplitude does also appear at 4 m. This is a radar artefact and not an object. It is of greater consequence to consider the radar and IR-array results in conjunction with the thermal camera data. The measurements presented were obtained at 08:00 on October 2024. The ambient temperature was recorded at 9°C. This resulted in a high degree of contrast relative to the deer's body temperature. As illustrated in Figure 3, the deer can still be detected by the IR array at a distance of 18 m. By the time the afternoon had elapsed, the ambient temperature had already reached 15 °C. Consequently, the detection capability of the IR array was reduced to a distance of 14 m. The thermal camera detects deer at any temperature, even from far away.

Discussion and Conclusion

The findings indicate that detection with the 60 GHz sensor is feasible at a distance of 22 m. During the measurement, no deer passed at a greater distance, which would have required a more comprehensive evaluation of the 24 GHz sensor. The configuration of the lenses and the orientation of the 60 GHz radar sensor permit the estimation of the direction from which the animal is approaching. Range-Doppler mapping techniques estimate the velocity of approaching animals, assessing their potential hazard to road traffic. However, the MTI cannot detect static or slow-moving targets. A mean value filter could enhance detection. Furthermore, the detection area was traversed by an agricultural machine, which demonstrated that the radar cross section signature can be employed to differentiate between animals and other targets. The evaluation of IR-array sensing technology has demonstrated that the detection range is significantly influenced by ambient temperature. This indicates that animals can be detected with greater efficacy and at a greater distance in the winter than when the ambient temperature is the same as the body temperature. The evaluation of the boson-thermal camera has demonstrated that an enhanced resolution results in a notable improvement in distance resolution. This is attributed to an elevated thermal energy per pixel. The camera has thus demonstrated its potential as a valuable instrument for validation. Subsequent series of measurements will be conducted to further investigate the random occurrence of game in the detection area. Additionally, the project entails the miniaturization of the system for integration into a delineator and the interface for the warning.

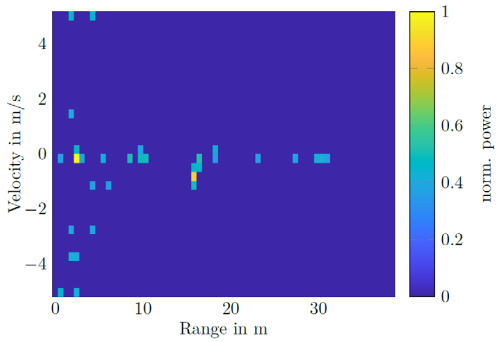

Fig. 2. The range-Doppler map of the 60 GHz Tecventure sensor in the absence of an MTI is presented herewith. The target is a deer situated at a distance of 18m and exhibiting a radial velocity of 0.8m/s.

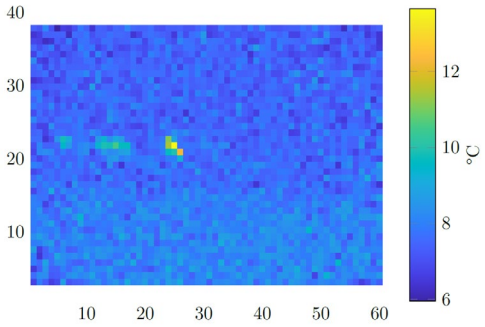

Fig. 3: The IR array image, captured concurrently with the data presented in Figure 2, reveals a thermal contrast at pixel (25,20) attributable to the presence of a deer at a distance of approximately 18 m.

References

[1] Kauer/DJV, "Wildunfallstatistik," 2023. https://www.jagdverband.de/,18.10.2024.

[2] FVA, "Pilotprojekt Elektronische Wildwarnanlage B292 bei Aglasterhausen" ,July 2008.

[3] "Md3-radar-transceiver," 2024. https://rfbeam.ch/product/v-md3-radar-transceiver/, 17.10.2024.

[4] E. Tohidi et al., "Compressive sensing in mti processing," in 2015 3rd International Workshop on Compressed Sensing Theory and its Applications to Radar,Sonar and Remote Sensing (CoSeRa), vol. 1, pp. 189–193, IEEE, June 2015.

[5] flir, "Boson640," 2024, https://www.flir.de/products/boson/ ,18.10.2024.

[6] "Heimann sensor," 2024. https://www.heimannsensor.com/, 20.10.2024.

DOI 10.5162/SMSI2025/D7.2

Portable Radar-Based Measurement System for Vibration Analysis of Large Infrastructures

Vivek Cherangil Ramankutty[1], Ron Martin[1], Christoph Sohrmann[1]
[1] Fraunhofer-Institut für Integrierte Schaltungen IIS,
Institutsteil Entwicklung Adaptiver Systeme EAS,
Münchner Straße 16, 01187 Dresden.
{vivek.cherangilramankutty,ron.martin,christoph.sohrmann}@eas.iis.fraunhofer.de

Summary: We report on the development and validation of a portable and cost-effective radar-based vibration measurement system. Vibration analysis is a powerful tool for structural health monitoring of critical infrastructure subjected to stresses, like environmental factors, loads, and wear over time. Using non-contact sensors avoids sensor installation and enables cost and time-efficient vibration measurements. We present a portable sensor concept based on FMCW radar technology. The system was successfully validated on a high-precision calibration system.

Keywords: Vibration, Infrastructure, Radar, FMCW, Condition Monitoring, SHM, Signal Processing

Introduction

Bridges, tunnels, energy facilities, or public buildings, are key components in the critical infrastructure. However, they are prone to damage and degradation from heavy loads and traffic. Structural health monitoring (SHM) technologies such as vibration analysis are essential to prevent failures and extend their lifespan. However, detecting small changes in vibration frequencies over time of large structures is still technically challenging. Our goal is the development of an accurate, highly portable radar-based measurement system [1]. Radar allows for non-contact measurements, is robust against harsh environmental conditions and captures multiple points simultaneously [2], supporting modal analysis.

Sensor System Hardware Setup

The setup includes a Frequency Modulated Continuous Wave (FMCW) radar, IWR6843ISK, combined with an FPGA, DCA1000EVM, from Texas Instruments (TI). The raw data from the sensor is acquired by the DCA1000EVM via the Low-Voltage Differential Signaling (LVDS) interface, then serialized and streamed via the Ethernet interface as User Datagram Protocol (UDP) packets. Since this setup usually requires TI's proprietary software components, we have developed a custom Python-based library for real-time data processing.

Data Processing Algorithm

The UDP packets obtained from the FPGA are parsed and the obtained IQ samples are processed. A high-level overview of the processing chain is given in Figure 1. A Range-FFT is performed on the IQ samples to determine the distance to the vibrating object under observation.

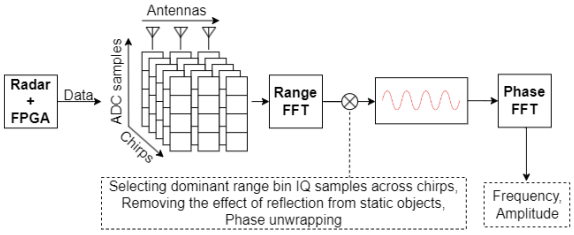

Figure 1: High-level flow of data processing chain

Once the range information is obtained, the dominant range bin is selected, and variations in the phase in that range bin are analyzed. The reflections from static objects are unfavorable as it introduces noise in the phases resulting in inaccurate low amplitude measurements. To remove this effect, data from multiple antennas are used to calculate the static vector and remove it [3]. To remove the phase discontinuities, unwrapping is performed. From the phase change, the displacement is calculated using

$$\Delta d = \left(\frac{c}{f}\right) * \left(\frac{\Delta\varphi}{4\pi}\right) * 10^3$$

where Δd is displacement in mm, c the speed of light in m/s, f the carrier frequency in Hz, and $\Delta\varphi$ the phase change in Rad. Various data processing steps, including scaling and windowing, are applied to refine the signal.

Validation of the Sensor System

As large structures have low fundamental frequencies [4,5], the sensor needs high resolution at those low frequencies. This can be achieved with longer measurement duration, which unfortunately contradicts portability and ease-of-use. Figure 2 shows the high-precision calibration system used to qualify the sensor accuracy at low frequencies and high amplitudes.

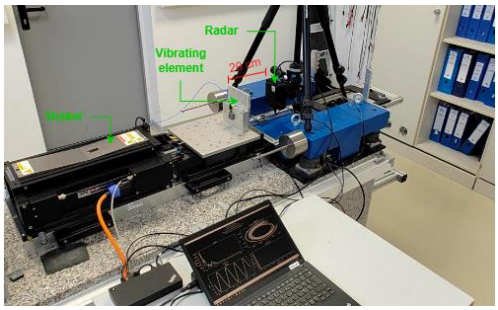

Figure 2: Long stroke vibration exciter APS 129 used for the sensor characterization

For various frequency-displacement combination within this regime, thirty data points for each setting are collected. Each data point is calculated from one second of radar data. The reference value and the measurement median value is shown in Figure 3 in red and black, respectively. The error is not visible within the scale of the plot.

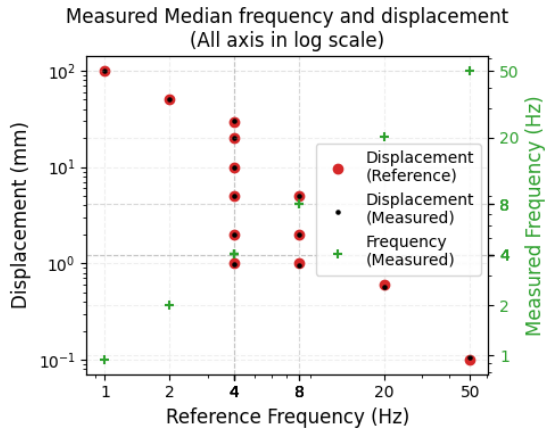

Figure 3: Measured frequency and amplitude

To quantify this, the median absolute percentage error is calculated for all the samples, see Figure 4 and Table 1.

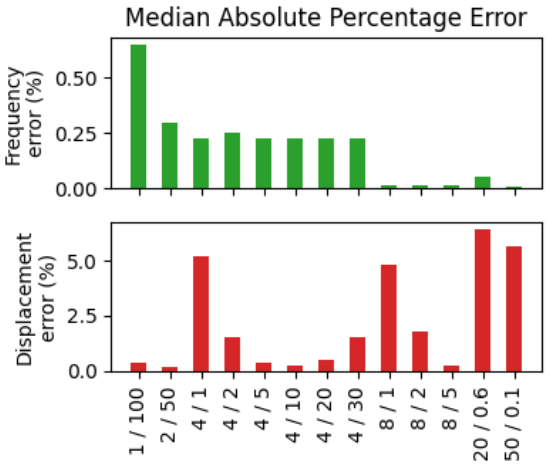

Figure 4: Median absolute percentage error; x-axis labelling: Frequency [Hz] / Displacement [mm]

Analyzing the displacement error across samples shows that the error decreases as the magnitude of displacement increases. This trend is particularly evident in the 4 Hz and 8 Hz samples. For the measured frequencies, the error decreases with increasing frequency.

Table 1: Median absolute percentage error across different frequency displacement combinations

Frequency in Hz \ Displacement in mm	0.1	0.6	1	2	5	10	20	30	50	100
1										0.646 0.388
2									0.296 0.183	
4			0.225 5.225	0.248 1.541	0.225 0.366	0.225 0.235	0.225 0.518	0.225 1.518		
8			0.01 4.779	0.01 1.793	0.01 0.238					
20		0.053 6.442								
50	0.01 5.655						Frequency error in % Displacement error in %			

Two main factors contribute to this trend: the limited duration of each measurement instance and the error metric used, which disproportionately penalizes small frequencies.

Summary and Future Directions

We have presented a FMCW-based vibration measurement system intended for SHM of large infrastructures. Radar offers many advantages over tactile sensors, such as robustness and portability. We have successfully validated the sensor on a commercial calibration system. While the error is generally very low, it will remain challenging to achieve a high measurement resolution at low frequencies under real-world conditions.

The radar cross section (RCS), material reflectivity, and surrounding noise are the main factors affecting the signal quality of a target. Future work will include advanced focusing techniques such as digital and lens-based beamforming, beam nulling, and algorithm improvements.

Acknowledgement: We gratefully acknowledge support by the Spektra GmbH for valuable discussions and testing time on the exciter system.

References

[1] Farrar, C. R., et al. (1999). “Microwave interferometers for non-contact vibration measurements on large structures”. Mechanical Systems and Signal Processing, 13(2), 241-253.
[2] Piotrowsky, L., & Pohl, N. (2020). “Spatially resolved fast-time vibrometry using ultrawideband FMCW radar systems”. IEEE T-MTT, 69(1), 1082-1095.
[3] Jiang, C., et al. "mmVib: micrometer-level vibration measurement with mmwave radar." Proceedings of the 26th Annual International Conference on Mobile Computing and Networking. 2020.
[4] Michel, C., and Keller, S. (2022). „Determining and Investigating the Variability of Bridges’ Natural Frequencies with Ground-Based Radar”. Applied Sciences, 12(11), 5354.
[5] Alsabagh, A. S. Y., et al. "Fundamental natural frequencies investigation for a typical 5-MW wind turbine blade" Noise&Vibration Worldwide 51.4-5 (2020) 77-84

DOI 10.5162/SMSI2025/D7.3

Millimeter-Wave Spectroscopy for Evaluating Blood Coagulation and Clotting

Tobias Liebchen[1,2], Giacomo Ulisse[1], Viktor Krozer[1,2]

[1]Physics Institute, Goethe Universität Frankfurt am Main, 60438 Frankfurt am Main, Germany,
[2]Ferdinand-Braun-Institut, 12489 Berlin, Germany

Correspondence to: Tobias Liebchen (Tobias.Liebchen@fbh-berlin.de)

Summary:

Millimeter-Wave spectroscopy is an emerging technology that has shown significant potential in medical diagnostics, particularly the measurement of blood coagulation is of crucial relevance in detecting stroke attacks. A promising approach is the utilization of dielectric changes in blood at frequencies in the 75-110 GHz range. This paper offers a novel approach to support and quantify the visualization of these biological processes.

Keywords: THz spectroscopy, medical, blood coagulation, blood clotting, PCA, FA

Introduction

Maintaining a healthy cardiovascular system is important for overall well-being. Millimeter-wave and THz signals exhibit a strong interaction with biological matter, which can be efficiently employed in biomedical applications due to the non-ionization properties of electromagnetic waves.

Measurement setup

The setup measures the absorption and reflection of THz radiation as it passes through a sample, to probe the molecular dynamics of blood components. Since these frequencies are highly sensitive to molecular vibrations and hydrogen-bonding interactions, they can provide detailed information about the structural and dynamic properties of biological molecules. In the context of blood coagulation, millimeter-wave spectroscopy can detect changes in the molecular structure of blood components as they transition from a liquid to a gel state during clot formation. The ability to determine the timestamp of clotting and detect the presence and effectiveness of blood thinners is vital for patient care. THz spectroscopy offers a powerful, non-invasive method for real-time monitoring of blood coagulation, providing valuable insights for both clinical diagnostics and pharmaceutical research.

The application of advanced algorithms for data analysis, including principal component analysis (PCA), has proven crucial for the interpretation of complex data sets, especially in medical diagnostics. This method allows the dimensionality of the data to be adjusted and reduced into manageable components, making it easier to identify significant patterns indicative of blood clotting. A factor analysis (FA) allows conclusions to be drawn about the points in time at which something is happening and provide another level of interpretation.

Conclusion

The effectiveness of anticoagulant medications is assessed by measuring their impact on coagulation time. Blood coagulation during surgeries or in patients with clotting disorders can be monitored in real-time. By measuring changes in blood coagulation time, Millimeter-wave spectroscopy can help ensure that patients are receiving the correct dosage of blood thinners. Interactions between blood thinners and other medications that may affect coagulation are identified. The use of AI-supported algorithms can considerably increase the efficiency of coagulation measurement by determining and evaluating schemes in the biological signals.

References

[1] Harder S, Santos SMD, Krozer V, Moll J. Surface Acoustic Wave-Based Microfluidic Coagulation Device for Monitoring Anticoagulant Therapy. *Semin Thromb Hemost*. 2019 Apr;45(3):253-258. doi: 10.1055/s-0038-1676318.

[2] Ulisse, G., Harder, S., and Krozer, V.: Millimeter wave spectroscopy system for blood coagulation measurements, 2019 *12th German Microwave Conference (GeMiC)*, Stuttgart, Germany, pp. 139-141, DOI: 10.23919/GEMIC.2019.8698158.

DOI 10.5162/SMSI2025/P01

Identification of Foraging Bumblebees by Pulse Compression of their Unique Doppler Radar Signature

Herbert Aumann[1], *Margery Aumann*[1], *Francis Drummond*[2]
[1]*Maine Biosensors LLC, Dover-Foxcroft, Maine, USA*
[2]*University of Maine, School of Biology and Ecology, Orono, Maine, USA*
herb@mainebiosensors.com

Summary:
A technique for observing foraging bumblebees with a 24 GHz continuous-wave Doppler radar is described. Upon departing from the colony, we discovered that foraging bumblebees accelerate briefly at a constant 9.8 m/sec^2, resulting in a distinct, linear frequency modulated (LFM) radar return. By correlating this return with an expected LFM template, departing bumblebees could be identified and counted while arriving bumblebees and other environmental effects are rejected.

Keywords: Foraging bumblebee counter, Doppler radar, pulse compression, template correlation

Introduction

Commercial bumblebees are effective pollinators of greenhouse and field crops, but a colony only lasts a few months. This paper describes a sensor for monitoring the pollination effectiveness of a bumblebee colony by counting the number of daily flights of bumblebees with a Doppler radar. A typical radar installation on a bumblebee colony is shown in Fig.1.

Fig. 1. Bumblebee colony with radar sensor

In a previous paper [1] on honeybees, we discovered that some honeybees departed the hive almost explosively, on a slightly ascending flight path, with a constant acceleration, quantitatively similar to gravitational acceleration. These bees were probably foragers looking for food in a distant location. We have observed the same behavior in less frequent flights of individual bumblebees. In [2], we exploited this characteristic to identify and count foraging bumblebees by applying a Hough transform to Doppler-Time-Images (DTI). Although the frequency-domain technique was successful, it exceeded a small, low-cost microprocessor's data storage and computational power. This paper uses the same Doppler radar [2] to implement an alternate, more straightforward technique of counting bumblebees based on template matching in the time domain.

Description of the New Method

We have shown in [1] that a 24 GHz Doppler radar, commonly found in automotive collision avoidance systems, can detect bees at a short distance. The unique acceleration characteristic of a foraging bee has a peculiar effect on the radar return. When a departing bee is illuminated by continuous-wave (CW) radar, the Doppler return from the bee is a nearly linear, frequency-modulated (LFM) waveform. For the 24 GHz radar, with λ = 12.5 mm and the flight parameters shown in Fig. 2, the Doppler frequency increases linearly from 0 Hz to 160 Hz in about 0.1 seconds.

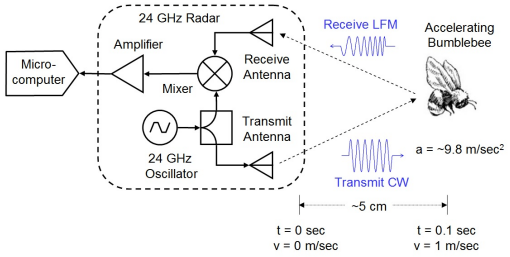

Fig. 2. Radar and bumblebee flight parameters

An LFM waveform, or chirp, is usually employed in a pulse compression radar to improve sensitivity and range resolution. Typically, the radar transmits an LFM waveform, receives an LFM waveform, and correlates it with an acceleration-corrected replica of the transmitted waveform [3]. The radar presented in this paper differs in that the radar transmits a CW signal, receives an LFM waveform, and correlates it with a synthetic LFM waveform based on the known target acceleration.

Results

We collected 24 GHz radar observations of bumblebees flying in front of a colony entrance by continuously recording the baseband signal in 19-sec segments at 800 samples/sec. A typical data file is shown in Fig. 3. More detailed pictures of departing (A, B) and arriving (C) bumblebees are shown in Fig. 4. The similarity of departing bumblebee radar returns is evident.

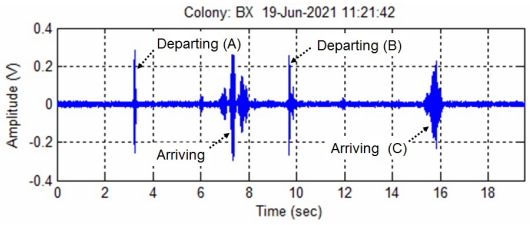

Fig. 3. Doppler radar baseband signal

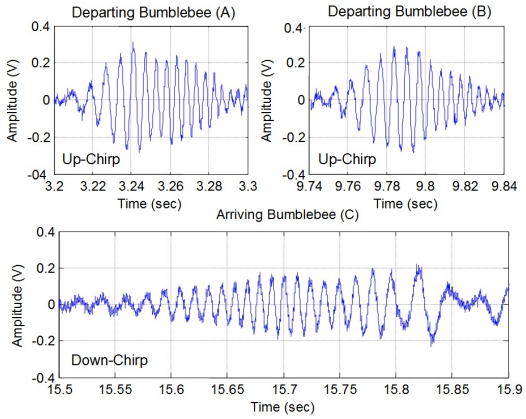

Fig. 4. Details of departing (A, B) and arriving (C) bumblebee Doppler radar baseband signals

We simulated a 0.1-sec 24 GHz Doppler radar return of a bumblebee departing with 9.8 m/sec^2 acceleration. The envelope of the simulated return was shaped to take the range geometry into account. A comparison of the Doppler return (A) with this template is shown in Fig. 5. We quantified the similarity between the two waveforms by Pearson's correlation coefficient, r = 0.86. This coefficient is independent of signal strength.

Due to differences in flight profiles, the measured departing bumblebee acceleration of 9.8 m/sec^2 had a standard deviation of 1.8 m/sec^2 [2]. Our technique is not particularly sensitive to the exact value of the actual acceleration. Setting a correlation threshold of r > 0.5 ensured correct identification of departing bumblebees.

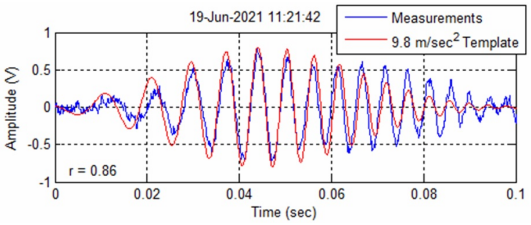

Fig. 5. Comparison of the departing bumblebee signal (A) with a 9.8 m/sec^2 acceleration template

Fig. 6 shows the correlation of the entire data segment depicted in Fig. 3 with the 9.8 m/sec^2 template in Fig. 5. Correlations with departing bumblebees are clearly above the threshold. In contrast, the correlations with arriving bumblebees are suppressed.

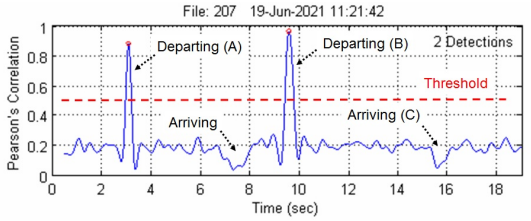

Fig. 6. Correlation of Doppler radar data in Fig. 3 with a 9.8 m/sec^2 acceleration template

We accumulated the count of departing bumblebee detections for each day from May to July 2021. Figure 7 illustrates the technique's effectiveness in monitoring the growth and decline of a bumblebee colony.

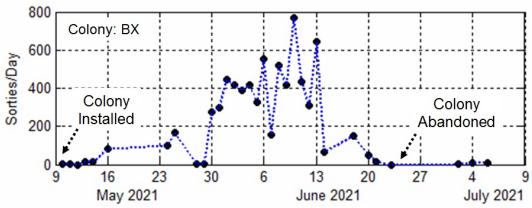

Fig. 7. Example of daily departing bumblebee counts

References

[1] H. Aumann, A Technique for Measuring the RCS of Free-Flying Honeybees with a 24 GHz CW Doppler Radar, *IET Conference Proceedings,* (2018); DOI: 10.1049/CP.2018.0540

[2] H. Aumann et al., The "Flight of the Bumblebee" by Hough Transform of Doppler Radar Images, *57th Asilomar Conference on Signals, Systems and Computers*, (2024); accepted for publication

[3] P. Bello, "Joint Estimation of Delay, Doppler, and Doppler Rate, *I.R.E. Transactions on Information Theory*, (1960); DOI: 10.1109/TIT.1960.1057562

DOI 10.5162/SMSI2025/P02

APPLICATION OF ENVIRONMENTAL MEASUREMENT IN PORTS USING CLEVER SENSE

García Fernández[12]
[1] *Geomodel 3DModeling Studio*
[2] *CIAUD Centre, University of Lisbon*
jorge@goclever.io

Summary:

Clever Sense is an automated, high-precision sensor-based system for quantifying and monitoring MARPOL V waste in port environments. Complying with international port regulations, Clever Sense provides accurate, real-time volume measurements, essential for regulatory reporting and environmental management. The system's robust architecture ensures precision, reliability, and scalability, directly supporting sustainable waste management practices in port operations.

Keywords: sensors, MARPOL V waste, environmental monitoring, IoT, port measurement

Background, Motivation an Objective

Port authorities are tasked with the challenging responsibility of managing and quantifying MARPOL V waste. According to MARPOL regulations, specifically Annex V of the International Convention for the Prevention of Pollution from Ships, ports must ensure that solid wastes generated by vessels are accurately quantified in terms of volume [1]. These regulations establish strict requirements for the handling and reporting of waste, making it critical for port authorities to have reliable and efficient systems that can measure waste precisely, support environmental sustainability, and ensure compliance with international standards.

Clever Sense was developed to address these operational and regulatory demands, automating the quantification of MARPOL V waste while minimizing human intervention. Unlike traditional manual methods, which are labor-intensive and prone to inaccuracies, Clever Sense deploys a network of high-precision sensors that continuously monitor waste volumes in real-time [2]. The data generated helps authorities document compliance, manage waste more effectively, and optimize resources for port waste management..

Description of the New Method

Clever Sense integrates an IoT-enabled sensor system with advanced data processing capabilities, offering automated, continuous monitoring of MARPOL V waste volumes. The system's sensors are strategically deployed within the port environment, where they capture real-time data on waste volumes from various waste management points. Designed to withstand harsh port conditions, Clever Sense's IP65-rated sensors provide highly accurate measurements that facilitate seamless integration into existing environmental monitoring frameworks [3].

Figure 1 shows the system installation at the Port of Barcelona, highlighting its adaptability to the port's layout and environmental conditions. The system's data processing module automatically aggregates and analyzes the captured data, offering insights into waste accumulation trends. Port authorities can access these insights through an intuitive interface, enabling them to monitor and document waste volumes efficiently. Furthermore, Clever Sense's scalability allows it to be adapted across multiple ports and waste categories, contributing to the consistent, compliant handling of MARPOL V waste in diverse port settings. This automated approach minimizes potential errors associated with manual waste measurement, significantly improving the accuracy and reliability of reported data [4].

Figure 1: Installation of Clever Sense system at the Port of Barcelona, illustrating sensor placement for optimized waste volume monitoring in compliance with MARPOL V standards.

Results

Field data confirmed that Clever Sense achieved a measurement accuracy of over 95%, meeting the stringent regulatory requirements for MARPOL V waste quantification [3]. By automating the data collection and processing workflow, Clever Sense eliminates the need for frequent manual checks, allowing port authorities to allocate resources more efficiently and focus on strategic environmental management. *Figure 2* illustrates a sample of the resulting point cloud data, which demonstrates the detailed, volumetric waste quantification that the system achieves. The success of Clever Sense in these pilot applications positions it as a scalable solution for broader adoption in global port operations.

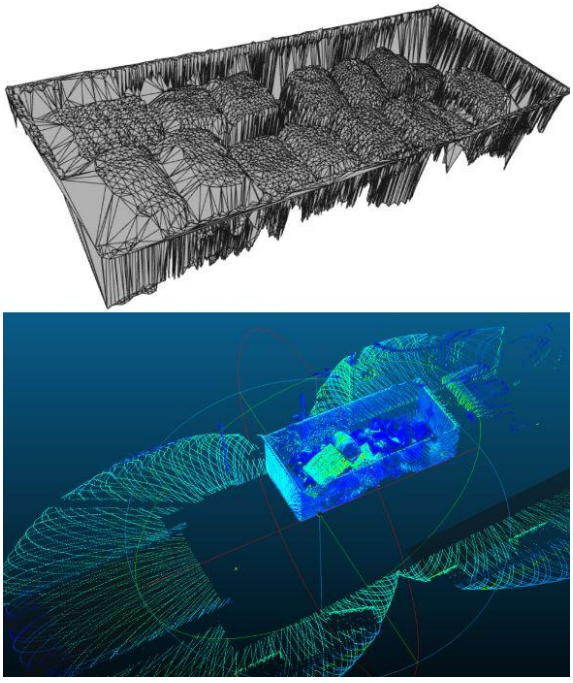

Figure 2: Mesh obtained from the triangulation of the point cloud (top), complete point cloud obtained from multiple convergent sensors (bottom). obtained from multiple convergent sensors (bottom)

Conclusion

Clever Sense, funded by **Puertos 4.0, Project 0062**, provides an efficient, automated solution for MARPOL V waste quantification, offering port authorities a tool that enhances both environmental compliance and operational efficiency. Its integration into IoT networks and robust sensor design make it an essential resource for modern, sustainable port waste management, supporting data-driven decisions in line with MARPOL regulations and reducing the environmental impact of maritime operations.

References

[1] MARPOL Annex V: International Convention for the Prevention of Pollution from Ships, *International Maritime Organization*, 2017.
[2] A. Silva, et al., *An Assessment of Errors and Their Reduction in Terrestrial Laser Scanner Measurements in Marmorean Surfaces*, Sensors Journal, 2021. DOI: 10.1234/sj.v3i8
[3] M. Gonçalves, et al., *Extending the Life of Virtual Heritage: Reuse of TLS Point Clouds in Synthetic Stereoscopic Spherical Images*, Digital Heritage, 2023. DOI: 10.1234/dh.v5i6
[4] L. Ramos, et al., *Terrestrial Laser Scanning and Digital Photogrammetry for Heritage Conservation: Case Study of the Historical Walls of Lagos, Portugal*, Applied Sciences, 2020. DOI: 10.1234/as.v7i10

The short paper should be submitted in a PDF-version at https://www.smsi-conference.com/submission-short-papers.

DOI 10.5162/SMSI2025/P03

NFC Based Current Sensor for Medium-Voltage Lines

M. Lenzhofer[1], D. Holzmann[1], D. Sturm[2]
[1] Silicon Austria Labs GmbH, Europastrasse 12, 9524 Villach, Austria,
[2] KNG-Kärnten Netz GmbH, Arnulfplatz 2, Postfach 200, 9020 Klagenfurt, Austria
Martin.Lenzhofer@silicon-austria.com

Summary:
The presented work focuses on developing a flexible NFC sensor patch, capable of being implemented in a medium-voltage underground cable. The measurement principle is based on the measurement of the magnetic field, which is directly proportional to the current in the cable. The sensor patch can be integrated into the cable, shielded, and covered with a shrinking repair sleeve. The measurement results prove the feasibility of such an NFC-based integrated sensor patch solution.

Keywords: NFC sensor, current measurement, Hall effect sensor, medium-voltage cable monitoring

Introduction

The actual current load is the main parameter to monitor in medium-voltage lines. The generated magnetic field under load conditions is proportional to the current within the conductor. Due to the cable's coaxial setup, an indirect measurement based on the magnetic field strength is the proper method [1].

A free-space configuration must be used for an integrated version, as it is impossible to attach any flux-concentrating magnetic materials around the wire or realize an inductive system like a Rogowski coil, [2]. The Hall sensor provides a measurable output voltage proportional to the magnetic field and therefore also proportional to the current according to Ampere's law given by (1),

$$\oint \vec{B} * d\vec{l} = \sum \vec{B} * \Delta\vec{l} = \mu_0 * I \qquad (1)$$

with the magnetic permeability of free space given by μ_0 = 4*π*10^{-7} Tm/A. As the medium-voltage cable is built up as a coaxial cable the field must be measured in offset to the central wire center, refer to Figure 1.

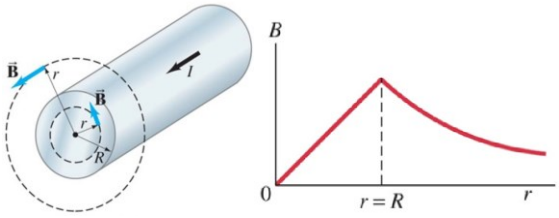

Fig. 1. Magnetic field characteristic of a single wire.

The current density or magnetic field *B* within the conductor of radius *R* is uniform. At the same time, it decays if the distance *r* is further increased *r* > *R*. By applying equation (1) and assuming a circular path around the wire, $\vec{B}$ is tangent to $d\vec{l}$ at every point, resulting in (2),

$$B = \frac{\mu_0 * I}{2 * \pi * r} \qquad (2)$$

Due to the specification of the medium-voltage cable of the type NA2XS(FL)2Y 1X95/25, the diameters of all the layers are known, and according to equation (2) the current can be calculated based on the measured magnetic field strength *B*.

Description of the System

As the sensor patch is wrapped around the cable, the printed circuit board (PCB) comprises a 300 µm thick flexible polyimide. The cable's shielding is conductive; therefore, to enable NFC communication "on-metal", the antenna must be electrically separated, which is realized using a ferrite antenna of the type W3509 of Pulse Electronics. To establish near-field communication (NFC), the NTAG 5 link IC of the type NP5332 from NXP Semiconductors is implemented. It enables the connection to any sensor chip featuring an I²C interface. The magnetic field is measured with a TLI493D sensor chip of Infineon. Figure 2 shows the realized sensor patch.

Fig. 2. Developed NFC-based magnet field measurement sensor patch.

Description of the Measurement Setup

Two medium-voltage cable samples of two meters in length were prepared, with the sensor patches integrated for testing. These two pieces were connected in the measurement setup, forming a short circuit loop. A plug-through transformer is used to generate the current flow, and an external Rogowski coil controls the current level. A high-voltage transformer generates the 11.55 kV, supplied to the connecting part of the cables forming the loop. The setup is shown in Figure 3. Commercially available NFC reader evaluation boards are used to read out the sensor patches. In this case, it is the RE12 development kit of Silicon Craft Technology.

Fig. 3. Measurement setup within the high-voltage laboratory.

Measurement Results

To verify the measurement principle, the current is increased stepwise from 50A to 250A every few minutes, and the measurement results are recorded with the reader kit connected to a computer, refer to Figure 4. The NFC sensor patches can be read out using special commands. As the NFC-based passive sensor patch is not intended for high sampling rates, the measured values depend on the current level of the 50 Hz current signal. The system is therefore strongly under-sampled, but as the current represents a periodic waveform, it is valid to sample over a longer time interval and capture the maximum occurring value.

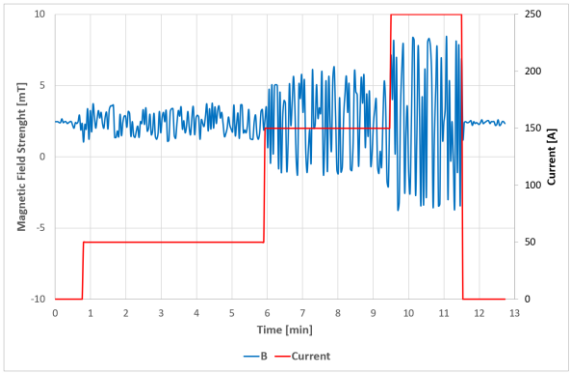

Fig. 4. Magnetic field (blue signal) versus applied current value (red signal). The current represents the effective value.

In a further postprocessing step, the adjusted current value is transformed to a *B* field value by applying equation (2). Before that, the respective effective value must be converted to the peak-to-peak value by multiplication with the factor of $2*\sqrt{2}$, as the sensor detects the magnetic field strength proportionally to the current signal. The table (1) shows the calculated values and the measurement results up to the tested maximum current level of 400 V_{eff}.

Tab. 1: Comparison of calculated values according to equation (2) and measured values.

I_{eff} [A]	Calculated [mT]	Measured [mT]
50	2.1	2.2
150	6.4	6.9
250	10.7	11.5
300	12.8	14.4
400	17.1	19.8

Conclusion and Outlook

Integrating a flexible sensor patch into a medium-voltage line with NFC current read-out was shown and verified. The read-out system works without interference even under load conditions with applied high voltage and high current levels. Minor deviations between the measured and calculated signal appear due to unstable control of the supplying current within the plug-trough transformer caused by temperature increase. In the next step, the sensor patch should be implemented in the medium-voltage grid, to investigate the behavior under real environmental conditions.

Acknowledgment

This work has been jointly supported by the industry partner KNG-Kärnten Netz GmbH and by Silicon Austria Labs (SAL), owned by the Republic of Austria, the Styrian Business Promotion Agency (SFG), the federal state of Carinthia, the Upper Austrian Research (UAR), and the Austrian Association for the Electric and Electronics Industry (FEEI).

References

[1] K. T. Selva, O. A. Forsberg, D. Merkoulova, F. Ghasemifard, N. Taylor, M. Norgren; Non-contact Current Measurement in Power Transmission Lines; Procedia Technology; Vol. 21; (2015); https://doi.org/10.1016/j.protcy.2015.10.034.

[2] Liu, Ji-Gou & Qiu, Jianhai. (2014). Simulation and Optimization of Conductor Structural Parameters of Free-space Hall-Effect Current Sensor. 10.13140/2.1.5126.0166.

DOI 10.5162/SMSI2025/P04

UHF RFID Based Strain Sensor for Hydropower Generators

M. Lenzhofer[1], A. Horn[1], S. Culetto[2]
[1] Silicon Austria Labs GmbH, Europastrasse 12, 9524 Villach, Austria,
[2] KELAG-Kärntner Elektrizitäts-Aktiengesellschaft
Außerfragant 72, 9831 Flattach, Austria
Martin.Lenzhofer@silicon-austria.com

Summary:
The presented work focuses on developing an RFID sensor capable of being implemented on the rotor of a power generator of a hydro storage plant to enable condition monitoring of dedicated positions suffering under stress in terms of start-stop operation scenarios. The strain sensor value is read out wirelessly via a UHF RFID system, which either supplies the sensor or transmits its measurement result. The analyzed measurements done in a post-processing step prove the possibility of using such technology within the generator use case.

Keywords: RFID sensor system, RFID technology, strain sensor, wireless measurement, sensor tag

Introduction

The generators in hydro storage plants are not operated continuously but are started and stopped as required. Due to this operation mode and also in case of load shedding resulting in overspeed conditions, high repetitive mechanical stress occurs at certain positions in the rotor, contributing significantly to the generator's aging. Available systems mainly just monitor the torque by flanged transducers, but there are no measuring systems monitoring stress, for example at the pole plates. Also, reliable transmission of measured values in such a harsh environment, which is characterized by the metallic housing, the high rotor speed of nominally 500 rpm, the high excitation voltage of 10.5 kV, and the generated power of up to 32 MVA, leading to high electromagnetic field strengths, remains challenging. The goal of this project was to develop a system that monitors the operating status of the rotor. On the one hand, it was necessary to find a suitable technology for transmitting measured values and, on the other hand, to realize a sensor that does not require an additional power supply. Additionally, the system should be as light as possible to avoid imbalance. Also, the fixture must be properly designed to avoid any damage to the generator in case of failure.

Description of the System

The proposed measurement system is based on ultra-high frequency (UHF) radio frequency identification (RFID) technology and consists of a commercially available reader unit and a developed passive sensor tag, [1,2]. Several vendors on the market currently provide RFID ICs combined with the ability to connect to external sensor circuits directly or via a digital bus interface. The main players are ASYGN, Farsens, Impinj and NXP. A chip of the type AS3212 from ASYGN was used for the implemented solution. The AS3212 is the first UHF RFID product that embeds a full analog sensor interface including a switched capacitor amplifier (SCA) and analog-to-digital converter (ADC) unit for monitoring external resistive sensors.

As all main modules are integrated within this chip, just a few components to match the antenna impedance, and the external sensor must be attached, refer to Figure 1.

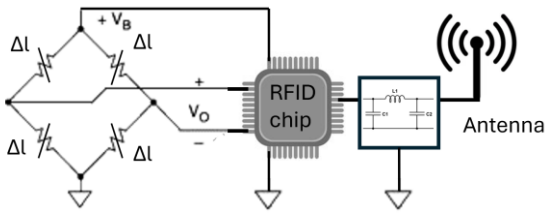

Fig. 1. Block diagram of the RFID sensor tag.

One main challenge is the implementation of the system in the generator. The developed solution is based on integrating a commercially available ceramic patch antenna of the type ISPC.86A.09.0092E from Taoglas, working as a director element. The reflector is realized through a conductive plane, which is proposed to be in the shape of the blade of the fan wheel of the generator. The blade profile in front of the antenna is realized with PEEK material and both parts are screwed together and secured by Nord-lock washers with additional adhesive,

refer to Figure 2. The profile is important to avoid disturbances in the cooling airflow. Also, the blade weight with the integrated antenna is matched to the blade weight of the original one to stay balanced.

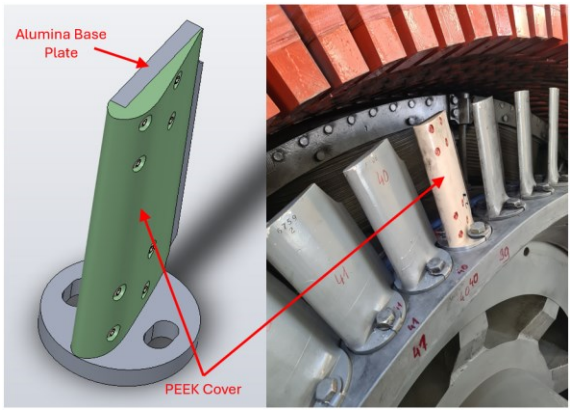

Fig. 2. The developed fan blade is built up by two parts with an integrated antenna.

As the connection to the sensing element must be as short as possible, the chip is integrated into a package with the matching network, and a long wire connects the antenna to the chip, refer to Figure 3. As this cable is a coaxial version it is shielded from disturbances. This wire is accordingly bandaged around the rotor and additionally fixed by adhesive. To read out the sensor two antennas are mounted on the stator side within the generator's housing that are connected to an RRU 4500 reader unit of Kathrein, refer to Figure 4.

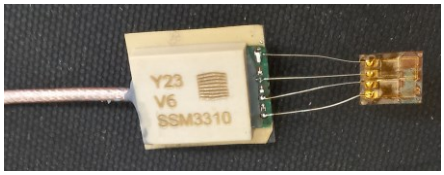

Fig. 3. Packaged RFID sensor with the connected strain sensor element SGT-2/1000-FB11 of OMEGA.

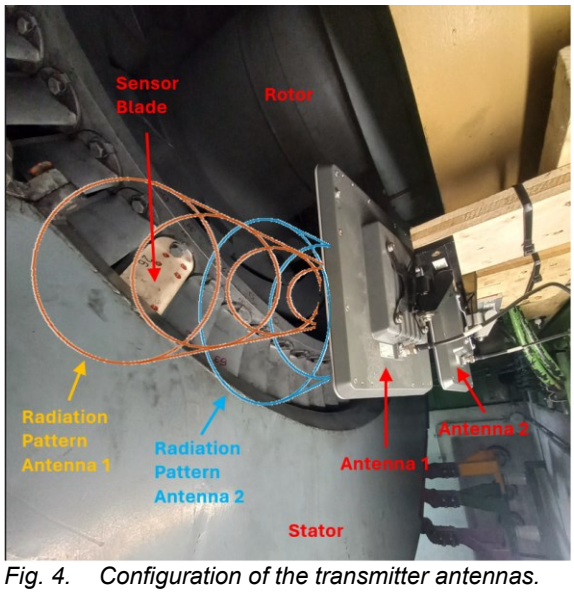

Fig. 4. Configuration of the transmitter antennas.

Measurement Results

The system is tested within a predefined procedure, where the turbine is first started up to start up the generator at a nominal speed of 500 rpm. After 5 minutes, the excitation voltage is switched on. After a further 5 minutes, the load of 20 MVA is activated, and another 5 minutes later, the generator is switched off again, refer to Figure 5. This step-by-step activation is necessary to examine the external influences on the measurement result.

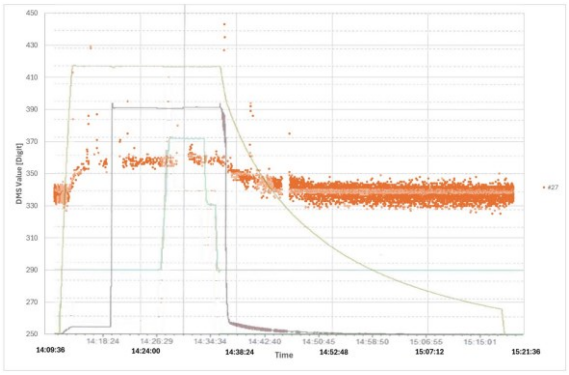

Fig. 5. Correlation of the measured ADC values (orange dots) with the generator characteristics, where the ochre curve represents the rpm value, the grey one the excitation voltage, and the green one the load cycle.

Conclusion and Outlook

Several test runs proved that strain on the defined position of the rotor in a hydropower plant generator can be measured. However, some issues regarding disturbances in the measurement result were identified, which need to be addressed in further optimization steps by providing a more stable power supply during the AD conversion.

Acknowledgment

This work has been jointly supported by the industry partner KELAG-Kärntner Elektrizitäts-Aktiengesellschaft and by Silicon Austria Labs (SAL), owned by the Republic of Austria, the Styrian Business Promotion Agency (SFG), the federal state of Carinthia, the Upper Austrian Research (UAR), and the Austrian Association for the Electric and Electronics Industry (FEEI).

References

[1] Senadeera, Praharshin & Wickramasinghe, Shyama & Jayasinghe, J.M.J.W.. (2024). Impedance Measurement of a Chip-Based Passive UHF RFID Sensor Transponder. 782-787. 10.1109/SoutheastCon52093.2024.10500136.

[2] Liu G, Wang Q-A, Jiao G, Dang P, Nie G, Liu Z, Sun J. Review of Wireless RFID Strain Sensing Technology in Structural Health Monitoring. *Sensors*. (2023); https://doi.org/10.3390/s23156925

DOI 10.5162/SMSI2025/P05

Self-built low-cost pyrolyzer using Curie-Point temperature coupled to a gas chromatograph-ion mobility spectrometer

Daniel Röckrath, Moritz Hitzemann, Martin Lippmann, Christian Thoben, Ayke Eckhardt, Stefan Zimmermann
Leibniz University Hannover, Institute of Electrical Engineering and Measurement Technology, Department of Sensors and Measurement Technology, Appelstr. 9A, 30167 Hannover Germany, Daniel.Roeckrath@geml.uni-hannover.de

Summary:
Pyrolysis is a well-known decomposition technique under inert gas for the analysis of liquids and solids by analyzing the volatile decomposition products. This work presents the design of a low-cost pyrolyzer based on the Curie-Point method. Using a 1 mm diameter Fe50Ni50 wire, the pyrolyzer heats up the wire carrying the sample to 520 °C within 3.71 s, verified by an optical infrared thermometer. For demonstration, this pyrolyzer was coupled to a gas chromatograph-ion mobility spectrometer (GC-IMS) and tested with Actimel yoghurt samples.

Keywords: Pyrolysis, Gas chromatography, Ion mobility spectrometry

Background, Motivation and Objectives

For onsite quantification of volatile compounds in more complex backgrounds, a mobile gas chromatograph-ion mobility spectrometer (GC-IMS) is a good choice, as it provides decent separation power and low limits of detection in the ppt_V-range while the instrumental effort is comparatively low. However, low- or non-volatiles need to be transferred into the gas phase before analysis by GC-IMS, *e.g.*, by thermal desorption. Another well-known method is pyrolysis.

Pyrolysis is defined as the thermal conversion process or decomposition of a sample in the absence of oxygen at temperatures exceeding 250 °C. The exclusion of oxygen prevents sample combustion. Over time, three methods of heating the sample until chemical bonds break and more volatile decomposition products are released have been established: Inductively (including the Curie-Point method) and resistively heated filaments as well as furnace pyrolyzers.

The Curie-Point method is explained in detail by Sobeih et al. [1]. It uses ferromagnetic wires inductively heated by a time-varying magnetic field. These wires are self-regulating at their specific Curie temperature, and thus allow for fast temperature ramping to their Curie temperature without any external temperature control.

As commercially available pyrolyzers are large in size and therefore not suited for mobile applications, we present a simple, miniaturized and low-cost setup.

Design

The Curie-Point method has been chosen due to the low instrumental complexity and the excellent reproducibility as a consequence of the used physical effect for end temperature control.

The Sectional view of the pyrolysis unit is visible in Figure 1. A 1 mm diameter ferromagnetic wire is used to minimize thermal mass. A glass liner from Agilent (5190-2292) flushed with nitrogen surrounds this wire. Around the glass liner is a single-wound copper coil with an inner diameter of 10 mm with a total of 15.5 windings. The coil has a total inductance of 600 nH.

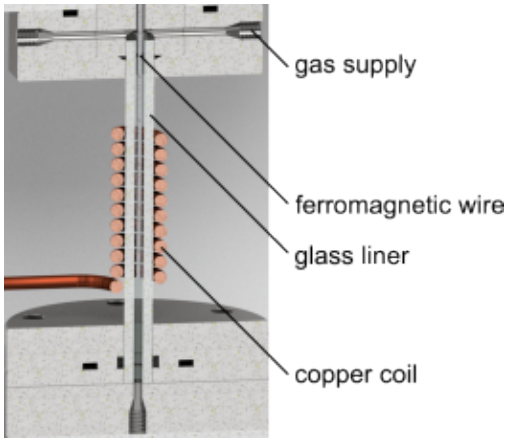

Figure 1 Sectional view of the pyrolysis unit structure

The generated pyrolysis products are transferred through a heated transfer line into the subsequent GC-IMS within pure nitrogen. The IMS is an ultra-fast polarity switching PCB-IMS with dual drift tubes for simultaneous recording of

positive and negative ions, as described by Hitzemann et al. [2].

The magnetic field in the coil is generated by a full bridge inverter with external frequency generation. A voltage-controlled oscillator allows for an adjustable frequency from 340 Hz to 1 MHz to control the full bridge inverter, which is fed by a supply voltage of up to 42 V.

Results

The rise time of the wire temperature and the temperature stability at Curie temperature were measured through the glass wall of the glass liner and a small gap between the windings of the coil using an optical infrared thermometer from Optris (CTlaser 3MH1 with CF2 lens giving a measurement spot of ≤ 0.5 mm and fast temperature recording rate of 1 kHz). The rise time is defined as the time required for heating from 10% to 90% of the Curie temperature beginning at ambient temperature. Unfortunately, the temperature measurement range of the used infrared sensor starts at 150 °C, which is above the 10% of the Curie temperature of the used wire, so that the rise time was estimated by using a linear regression fit function derived from the measured temperature ramp in the range from 150 °C to 467 °C. The heating process is considered to be completed when the slope of the temperature ramp falls below 10^{-3} K/s. The end temperature is calculated as the mean value of the following thousand measuring points. Figure 1 shows a measured heating curve of a 1 mm diameter and 60 mm long Fe50Ni50 wire. The final temperature of 520 °C matches the specified Curie temperature of 520 °C. The full bridge inverter is operated at 500 kHz and supplied with 20 V giving 60 of heating power. The temperature rise can be estimated to 3.7 s with a linear temperature ramp of 118.6 K/s from ambient temperature to 90% of the final temperature.

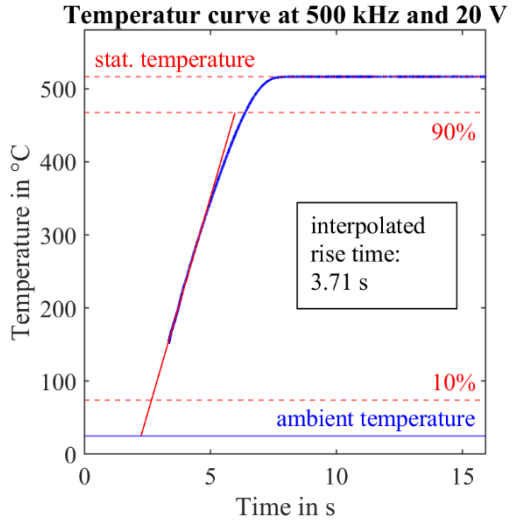

Figure 2 Heating curve of the Fe50Ni50 wire. The end temperature of 520 °C matches the specified Curie temperature of 520 °C. The full bride inverter is operated at 500 kHz and supplied with 20 V.

For demonstration of general feasibility, the developed pyrolyzer is coupled to a GC-IMS. Figure 2 shows the topographic plot of the measuring results when analyzing an Actimel yoghurt sample. Therefore, the previously described wire was simply dipped into yogurt and was directly transferred into the pyrolysis unit.

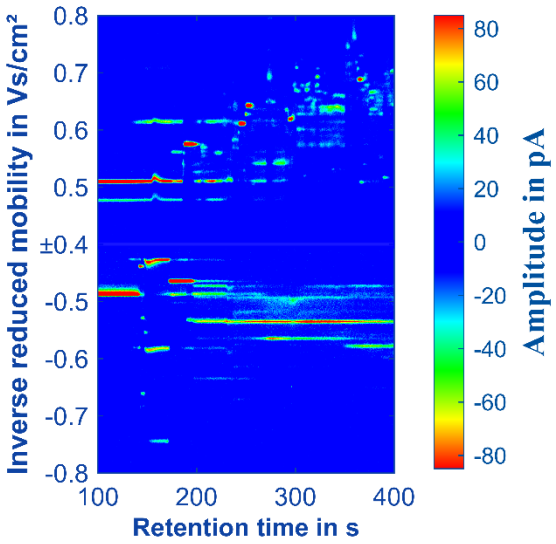

Figure 3 Topographic plot of an Actimel yogurt sample analyzed with Pyrolysis-GC-IMS.

Acknowledgements

Funded by the European Union

Funded by the European Union. Views and opinions expressed are however those of the author(s) only and do not necessarily reflect those of the European Union. The European Union cannot be held responsible for them.

This project has received funding from the European Defence Fund under grant agreement No 101103176 (TeChBioT).

Bibliography

[1] Sobeih, Karina L.; Baron, Mark; Gonzalez-Rodriguez, Jose (2008): Recent trends and developments in pyrolysis-gas chromatography. In: *J. Chromatogr. A* 1186 (1-2), S. 51–66. DOI: 10.1016/j.chroma.2007.10.017.

[2] Hitzemann, Moritz; Kirk, Ansgar T.; Lippmann, Martin; Nitschke, Alexander; Burckhardt, Olaf; Winkelholz, Jonas; Zimmermann, Stefan (2024): High-Resolution Drift Tube Ion Mobility Spectrometer with Ultra-Fast Polarity Switching. In: *Anal. Chem.* DOI: 10.1021/acs.analchem.4c03296.

DOI 10.5162/SMSI2025/P06

Comparison of Point-to-Point LPWA Smart Sensors with Low-Power Local Mesh Networking Solutions for Industrial Refrigeration and Operational Parameter Detection

In our presentation, we will outline the expectations for an effective IoT solution in industrial refrigeration, which is an excellent example. We will explore two distinct approaches to meet these requirements: cellular LPWA-based point-to-point solutions and local sub-GHz wireless ad-hoc mesh network-based distributed sensor systems. Our comparison will focus on technical, practical, and economic factors, complemented by application examples for both technologies.

We will discuss the challenges involved in parameter detection that support predictive maintenance, data collection for marketing purposes, and geolocation. Additionally, we will demonstrate how our E-IoT ecosystem addresses the needs of this industry by describing the complete asset chain, from sensors to the Cloud, encompassing wireless communication, Cloud services, and dashboard software.

Our presentation will provide insights into our hardware solutions for smart sensors, as well as our battery-operated local sensor networks and their gateways, which are designed for long service life.

We will include details on connectivity techniques, solution reliability, and data security protocols. On the hardware side, we will give an overview of the battery and circuit protection solutions that support operation in harsh environments.

The presentation offers best practices for engineers and data scientists active in the field of parameter detection, and data processing to be able to use the best smart sensor configuration to gather data for their analysis.

Endrich is committed to helping its customers leverage IoT technology to connect their traditional devices to networks and gather valuable data. This data can be utilized in a range of applications, including marketing, predictive maintenance, and remote monitoring. Our goal is simple: "We make your device smart."
In this summary, we'll showcase how we applied this approach to transform industrial refrigerators.

Advanced Collection of Refrigerator Data

Integrating traditional devices with the Internet opens a wide array of possibilities for collecting operational data and ensuring the appliance functions efficiently. By connecting for example a fridge or freezer to a cloud-based database, we can not only monitor its performance but also process and display this data in real time. This requires equipping the refrigerator **with various sensors** and a **reliable communication** channel, enabled by the hardware and software elements of the E-IoT (Endrich's own Internet of Things ecosystem) concept. The primary goal is to gather data that helps maintain optimal operating conditions, thus ensuring that the refrigerator operates effectively while providing valuable insights into its usage patterns. Of course, this system applies to any devices that need additional IoT functions.

Through continuous monitoring of critical parameters such as temperature and humidity, users can be assured that their refrigerator maintains the appropriate cooling environment for food storage. Additionally, these systems help to prevent mishaps such as the door being left open accidentally or detecting potential defrosting due to power cuts. The sensors can send alerts if such conditions arise, ensuring timely action to avoid food spoilage. This is particularly useful in cases where users are away from home for extended periods but still want to ensure that their stored food is safe.

The telemetry unit installed in these refrigerators offers a level of predictive maintenance that was previously unavailable in traditional appliances. By analyzing data related to power consumption, noise levels, and vibrations, the system can detect early signs of wear and tear or impending failures. This preemptive approach allows for repairs or maintenance to be performed before the refrigerator breaks down entirely, potentially saving significant costs and inconvenience for the user.

In terms of safety, the system plays a dual role. First, it monitors basic operational conditions, such as increasing internal temperatures, and can raise alarms if defrosting is imminent due to power failure or the door being left open. Second, it addresses the physical security of the appliance itself. For instance, built-in acceleration sensors or GPS-based tracking devices can alert the owner to unauthorized movement of the fridge, particularly in commercial or public spaces where theft or vandalism might be a concern. This ensures both operational and material safety are prioritized.

The ability to control and monitor the temperature of the refrigerator, as well as track energy consumption, also contributes significantly to more economical operation. Businesses can use this data to optimize cooling cycles, reducing energy costs without compromising food safety. In commercial environments, such as grocery stores or convenience shops, monitoring door openings provides valuable insights. The frequency and duration of door openings can help businesses understand customer behavior, track inventory flow, and calculate sales patterns. This data-driven approach can optimize store operations, minimize waste, and enhance marketing strategies.

The Endrich smart refrigerator concept offers several hardware solutions, all built around easy-to-install sensor modules. These sensors collect data on various parameters and wirelessly transmit this information to a dedicated cloud database. Transmission is achieved either directly through a mobile phone network or via a local mesh WLAN (Wireless Local Area Network) using a GSM gateway. Temperature and humidity sensors, light intensity detectors, and mechanical sensors such as acceleration sensors and MEMS microphones are strategically placed inside the refrigerator compartment to monitor key metrics.

For monitoring door status, the system offers flexibility. A magnetic sensor activated by the door magnet can detect when the door is opened or closed. Alternatively, a six-axis acceleration sensor can be used to measure the angle of the door opening, providing more detailed insights into

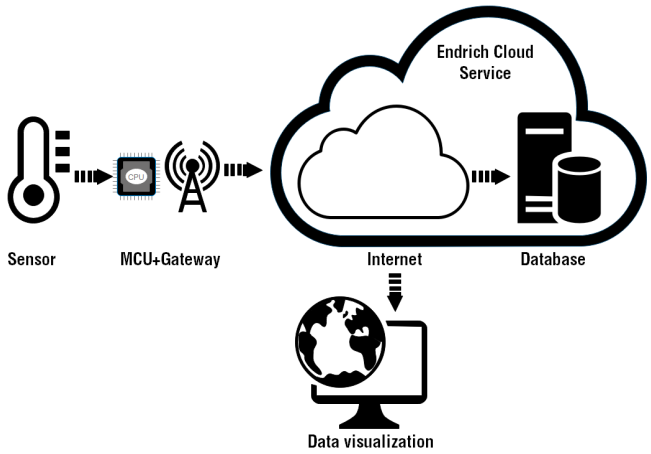

how the appliance is being used. Most of these sensor units are equipped with a backup battery offering seamless operation even in power failure situations. In freezers, where the harsh environment does not enable of using rechargeable batteries, special long-life disposable batteries are used. Depending on the frequency of data transmission, these low-power devices can operate for a long time and can report power failures as well thanks to the backup power solutions.

Communication between the sensors and the central system operates on the sub-GHz (868/915 MHz ISM) band, a low-power wireless communication channel that supports the installation of individual sensors in various locations inside the refrigerator. This approach allows for more flexible sensor placement, enhancing the system's ability to monitor different aspects of the appliance simultaneously. All sensor units form a local mesh network, which is connected to a WLAN-LPWA or LTE (Low Power Wide Area or 4G) gateway. This gateway is usually integrated into a power consumption monitoring device, enabling it to transmit all collected data to the cloud via a specialized NB-IoT/LTE-M/2G or LTE GSM modem.

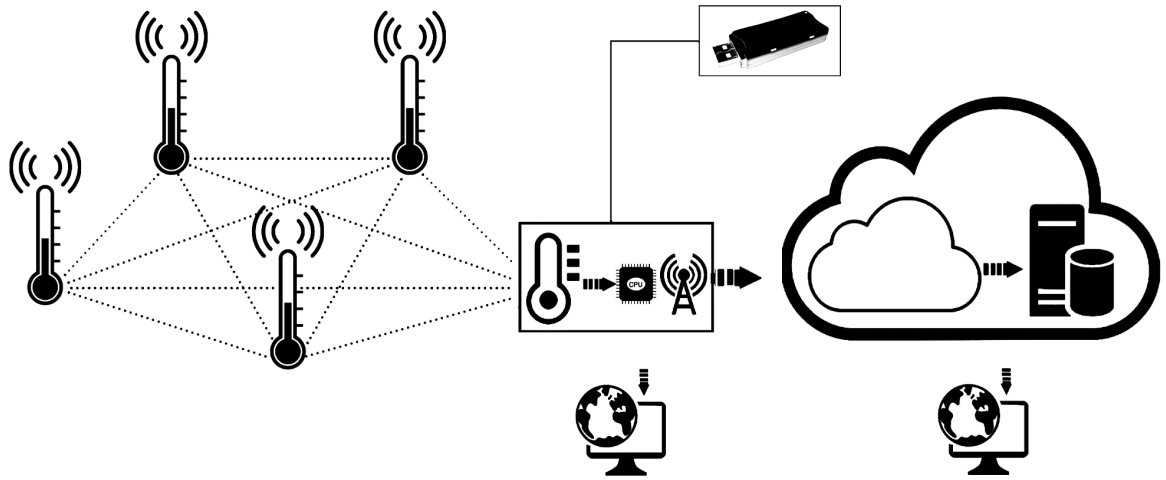

The advantage of this setup is clear: it not only monitors a single refrigerator but can also handle multiple units located in the same commercial building. For instance, a chain of refrigerators in a grocery store or gas station can all be connected to the cloud using the same system. Since the gateway operates on mains voltage, there are no concerns about power consumption during frequent data transmissions. In case of a power outage, an integrated supercapacitor provides enough reserve energy to send out one or two final status messages, alerting the user to the power failure and triggering preventive actions.

The LPWA communication technology (specifically NB-IoT) and the low-power ARM-M0+ microcontroller are designed to ensure long battery life for the sensors, minimizing the need for frequent recharging. This, combined with extremely low telecommunication costs—prepaid SIM cards can be purchased for just EUR 10, with 500 MB of data valid for 10 years—makes this an affordable and efficient solution for both consumers and businesses alike.

In terms of data utilization, several software services are available. Standard options include a smartphone app for real-time monitoring, a Data Access API for developers to integrate the system with other platforms, and a web-based interface for administration and data visualization. Custom software solutions can also be developed to meet specific customer needs, allowing businesses to leverage this data for unique applications.

In summary, by integrating our various sensors and IoT technologies into traditional refrigerators, we can transform them into smart appliances that offer a range of benefits. From improved energy efficiency and predictive maintenance to enhanced security and valuable business insights, these advanced systems represent the future of refrigeration in both residential and commercial settings. The ease of installation, combined with long-lasting, low-power operation, makes these solutions accessible and practical for various users, ensuring that refrigeration technology continues to evolve in line with the demands of modern life.

DOI 10.5162/SMSI2025/P07

A Concept for Form-Adaptive and Force-Controlled Gripping with Magnetorheological Material

Jennifer J. Blöchle[1], *Thomas M. Wendt*[1] *and Thomas Seifert*[1]
[1] Hochschule Offenburg, 77652 Offenburg, Deutschland
jennifer.bloechle@hs-offenburg.de

Summary: This paper presents a shape-adaptive gripper concept based on a 3D-printed structure made from TM5MED, filled with magnetorheological fluid (MRF). The gripper utilizes electromagnets to control the viscoelastic properties of the MRF, allowing for rapid shape adaptation. High-performance strain sensors made from flexible carbon nanotube (CNT) films measure pressure and deformation at the contact surface and along the sides, allowing for nuanced force control. This design concept is particularly suited for robotic applications that require flexible and safe object handling.

Keywords: Shape-adaptive gripper, smart material, magnetorheological material, strain gauge, Carbon nanotubes

Introduction

Handling fragile objects with different shapes is one of the main challenges in robotics [1]. Different grippers based on flexible materials, such as powder-filled vacuum grippers, have been developed to address this issue [2].This work presents a shape-adaptive gripper that can dynamically adapt to different object shapes. The gripper is based on a 3D-printed lattice structure and uses magnetorheological fluid (MRF), which changes its viscosity when exposed to a magnetic field.
Advances in materials science and manufacturing are enabling the development of flexible grippers that offer high precision and flexibility [1] [3]. MRF-based grippers achieve stiffness modulation with a trigger time at the millisecond level, substantially enhancing their efficiency in handling complex objects. 3D printing is also proving to be a key technology for producing complex gripper structures and customised designs [4] [5].
Control in adaptive grippers could potentially be enhanced by incorporating flexible and stretchable strain and pressure sensors made from Polymer/CNT (Carbon Nanotube) nanocomposites. These sensors aim to provide continuous data on deformation and applied force, which is crucial for the careful handling of delicate materials. Due to their flexibility and ductility, these sensors can adapt to the movements and shape changes of the gripper, making them highly suitable for dynamic gripping tasks. Integrating these sensors into robotic systems could significantly improve force control, thereby increasing the stability and safety of the gripping process. Initial research results indicate that this technology could further improve the handling of complex or fragile objects [6] [7].

Gripper design

The shape-adaptive gripper consists of a 3D-printed pad with an inner lattice structure and an outer shell made from TM5MED material. The sponge-like lattice structure (see Fig. 1) provides elasticity and ensures an even distribution of the magnetorheological fluid, preventing sedimentation. The stiffness of the MRF is intended to be controlled by a 24 V DC electromagnet, which regulates the material's rigidity through a magnetic field. The choice of a 24V system was made to make optimal use of the existing power supply in standard robotic systems.

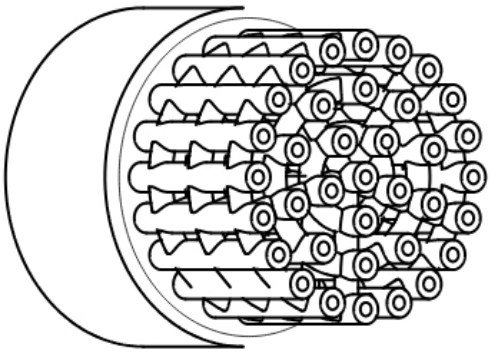

Fig. 1: Computer-aided design (CAD) model of the gripper's internal sponge-like architecture and electromagnet.

To enhance force control and prevent collisions, flexible strain and pressure sensors based on functionalized graphene nanoparticles were integrated, see Fig. 2. These sensors continuously detect deformation and applied forces, allowing adaptation to object shapes and preventing damage to the gripper from overload or

collisions [6]:

- **Strain Sensors**: Positioned on the outer side of the gripper, these sensors measure the overall deformation of the structure, ensuring the gripper adapts to the object's shape without compromising structural integrity.
- **Pressure Sensors**: Positioned at the contact interface, they measure the force exerted on the object, enabling immediate adjustment to prevent damage, particularly when handling fragile or irregularly shaped objects.

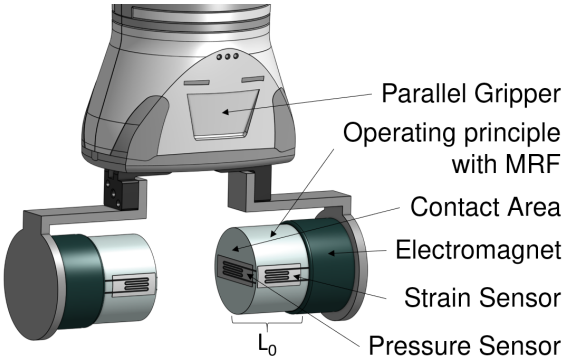

Fig. 2: Modeling Sketch of a parallel gripper.

Methods

The graphene-based strain and pressure sensors provide feedback to control the gripping process. The following methodology is employed:

Strain Measurement: Strain is calculated using the formula (1), where ϵ is the strain, ΔL is the change in length, and L_0 is the original length. This data helps adjust the MRF stiffness in real-time, allowing the gripper to conform to the object's shape.

$$\epsilon = \frac{\Delta L}{L_0} \tag{1}$$

Pressure Measurement: Pressure is measured by (2), where P is the pressure, F is the force applied, and A is the contact area. This enables force adjustment, ensuring a secure grip without damaging sensitive objects

$$P = \frac{F}{A} \tag{2}$$

Sensor response: The relative change in resistance of the graphene sensor, as described in equation (3), provides continuous feedback on strain and pressure. This feedback converts mechanical changes into electrical signals. This enables the gripper operation to be adapted.

$$\frac{\Delta R}{R_0} = f(\epsilon, P) \tag{3}$$

Discussion

Integration of flexible strain sensors and MRF in the shape-adaptive gripper is intended to enable controlled flexibility and force modulation, with the sponge-like structure considered a critical component. Internal tubes may exert excessive pressure under load or even rupture. The MRF volume may be insufficient to achieve the required stiffness. Additionally, there is a risk of uneven MRF distribution and sedimentation, which could impair adaptability. Validation of structure and flexibility is required for safe handling.

Conclusion

The shape-adaptive gripper utilizes MRF within a 3D-printed sponge-like structure, promoting even MRF distribution and preventing sedimentation. Strain and pressure sensors allow for variable stiffness and adaptation to object contours, facilitating a secure grip during handling. This technology is particularly suited for robotic applications requiring high adaptability and force control, especially when handling delicate or complex-shaped objects.

References

[1] M. Xu, Y. Liu, J. Li, F. Xu, X. Huang, and X. Yue, "Review of flexible robotic grippers, with a focus on grippers based on magnetorheological materials," *Materials*, vol. 17, no. 19, p. 4858, (2024), Number: 19 Publisher: Multidisciplinary Digital Publishing Institute; doi: 10.3390/ma17194858

[2] T. Wendt, F. Kirner, and N. Hangst, "D4.3 - 3d bin picking with an innovative powder filled gripper and a torque controlled collaborative robot," in *Lectures*, Nürnberg: AMA Service GmbH, Von-Münchhausen-Str. 49, 31515 Wunstorf, Germany, (2023), pp. 225–226; doi: 10.5162/SMSI2023/D4.3

[3] J. Cramer, M. Cramer, E. Demeester, and K. Kellens, "Exploring the potential of magnetorheology in robotic grippers," *Procedia CIRP*, vol. 76, pp. 127–132, (2018); doi: 10.1016/j.procir.2018.01.038

[4] J. Wang, Y. Yao, B. Yang, and Y. Liu, "3d printing of shape memory magnetorheological elastomers composites," *European Polymer Journal*, vol. 220, p. 113 403, (2024); doi: 10.1016/j.eurpolymj.2024.113403

[5] A. Pettersson, S. Davis, J. O. Gray, T. J. Dodd, and T. Ohlsson, "Design of a magnetorheological robot gripper for handling of delicate food products with varying shapes," *Journal of Food Engineering*, vol. 98, no. 3, pp. 332–338, (2010); doi: 10.1016/j.jfoodeng.2009.11.020

[6] O. Kanoun, A. Bouhamed, R. Ramalingame, J. R. Bautista-Quijano, D. Rajendran, and A. Al-Hamry, "Review on conductive polymer/CNTs nanocomposites based flexible and stretchable strain and pressure sensors," *Sensors*, vol. 21, no. 2, p. 341, (2021), Number: 2 Publisher: Multidisciplinary Digital Publishing Institute; doi: 10.3390/s21020341

[7] H. Yang and W. Wu, "A review: Machine learning for strain sensor-integrated soft robots," *Frontiers in Electronic Materials*, vol. 2, (2022), Publisher: Frontiers; doi: 10.3389/femat.2022.1000781

DOI 10.5162/SMSI2025/P08

The SI 2019 approach to redefine units does not apply to the mole

Raghu Kacker[1], Karl Irikura[1]
[1] National Institute of Standards and Technology, Gaithersburg, MD 20899, USA,
Email: raghu.kacker@nist.gov

Summary:

The SI (2019) claims that the Avogadro constant N_A may be used to redefine the mole. In particular, the expression $N_A = 6.022\ 140\ 76 \times 10^{23} \times \text{mol}^{-1}$ is a defining relation whose inversion provides the algebraic definition of the mole. This paper shows that the SI (2019) approach based on the defining relations that is used to redefine the other six base units does not apply to the mole.

Keywords: Avogadro constant, Avogadro number, Chemical measurements, Molar mass constant, Relative atomic mass

1. Introduction

This paper shows that the SI (2019) approach based on the defining relations that is used to redefine the other six base units (second, meter, kilogram, ampere, kelvin, and candela) does not apply to the mole. Let X denote a specified elementary entity of a stated substance, and N(X) denote the number of entities of type X in a sample. The SI (2006 and 2019) define *amount of substance* n(X) in that sample as $n(X) = N(X)/N_A$, where $(1/N_A)$ is a proportionality constant whose reciprocal N_A is called the *Avogadro constant*. The SI (2019 § 2.3.1) calls the numerical value of N_A the *Avogadro number*, conventional symbol $\{N_A\}$. Then the SI (2019 § 2.3.1) declares that $\{N_A\}$ is equal to the fixed number of entities in one mole. This declaration implies that one can substitute "1 mol" for n(X) and $\{N_A\}$ for N(X) in the SI definition $N_A = N(X)/n(X)$. Then $N_A = \{N_A\} \times \text{mol}^{-1}$. Thus, the Avogadro number $\{N_A\}$ and the Avogadro constant N_A represent the same quantity; namely, the fixed number of entities in one mole. The Avogadro number $\{N_A\}$ is dimensionless. The Avogadro constant N_A has the dimension mol^{-1}.

The unit mole has had only two SI definitions. The SI (1970) definition of the unit mole (with a clarification added in 1980) is stated in the SI (2006 § 2.1.1.6) as follows. "…The mole … contains as many elementary entities as there are atoms in 0.012 kilogram of carbon 12…." The SI (1970) Avogadro number is "as many entities as the ratio of the mass 0.012 kg to the mass of one atom of carbon-12 (unbound, at rest and in ground state)". The SI (1970) Avogadro number $\{N_A\}$ defines the SI (1970) mole.

The SI (2019 § 2.3.1) redefined the unit mole as follows. "… One mole contains exactly $6.022\ 140\ 76 \times 10^{23}$ elementary entities. …." The SI (2019) Avogadro number is "exactly $6.022\ 140\ 76 \times 10^{23}$ elementary entities". The SI (2019) definition of the mole consists of five sentences. The sentences 1, 2, and 5 define the mole completely. The SI (2019) Avogadro number $\{N_A\}$ defines the SI (2019) mole (sentences 1, 2, and 5) without referring to the Avogadro constant N_A.

2. The SI 2019 approach to redefine units does not apply to the mole

The magnitude of a quantity and a value assigned to that magnitude are different concepts. In the SI, a value is expressed as the product of a number and a unit. In nature, the magnitude of a quantity is unvalued. Usually, a value is assigned to the magnitude of a quantity by measurement. An unvalued magnitude is the input, and the assigned value is the output of measurement. A value assigned to the magnitude of a quantity by measurement is a quantitative description of that magnitude, and it carries uncertainty.

The SI (2019) uses the magnitudes of the defining constants and their established values, expressed in terms of the previous units, to redefine the units. A defining relation is an equation of the form: “magnitude of a defining constant = established numerical value × unit”. The SI (2019) inverts the defining relations to redefine (the magnitudes of) the units of the defining constants as proportional to the magnitudes of the defining constants as follows: “unit of a defining constant = magnitude of a defining constant / established numerical value”. The algebraic definitions of the units of the defining constants so obtained are solved to define the other SI units. The units second, candela, and meter were redefined based on the defining constants Δv_{Cs}, K_{cd}, and c in 1967, 1979, and 1983, respectively. The SI (2019) redefines the other base units.

Example: The defining relation corresponding to the transition frequency of the cesium-133 atom Δv_{Cs} is

$$\Delta v_{Cs} = 9\,192\,631\,770 \times \mathrm{s}^{-1} \,. (2.1)$$

Here, Δv_{Cs} is the constant magnitude of a property of the cesium-133 atom. The product 9 192 631 770 × s^{-1} is the established SI value of Δv_{Cs}. The time-duration ($1/\Delta v_{Cs}$) of one cycle of frequency Δv_{Cs} is a constant that exists independently of the magnitude of the unit of time, one second s, that is used to express its value. Therefore, the SI could logically use the defining relation (2.1) to redefine the unit s^{-1}. By inverting (2.1), the SI redefined the unit s^{-1} of Δv_{Cs} as

$$\mathrm{s}^{-1} = \Delta v_{Cs} / 9\,192\,631\,770 \,. (2.2)$$

By rearranging (2.2), the algebraic definition of one second is

$$1\,\mathrm{s} = 9\,192\,631\,770 \times (1/\Delta v_{Cs}) \,. (2.3)$$

Similarly, the SI (2019) units based on the six defining constants Δv_{Cs}, c, h, e, k, and K_{cd} are redefined by solving the algebraic definitions of the corresponding units s^{-1}, m s^{-1}, kg m^2 s^{-1}, A s, kg m^2 s^{-2} K^{-1}, and cd sr kg^{-1} m^{-2} s^3.

An essential requirement to redefine the units via the defining relations is that each defining constant must have an intrinsic magnitude that exists independently of the magnitude of the unit which that constant is used to redefine (to avoid circular reasoning). The magnitudes of the six defining constants Δv_{Cs}, c, h, e, k, and K_{cd} exist independently of the magnitudes of their units. Therefore, the SI could logically use the corresponding defining relations to redefine their units.

The SI (2019 § 2.3.1) claims that the expression

$$N_A = 6.022\,140\,76 \times 10^{23} \times \mathrm{mol}^{-1} \,. (2.4)$$

is the defining relation corresponding to the Avogadro constant N_A, and the expression

$$1\,\mathrm{mol} = 6.022\,140\,76 \times 10^{23} / N_A \,. (2.5)$$

is the algebraic definition of the unit mole.

The Avogadro constant N_A expresses the fixed number of entities in one mole as the SI value $N_A = \{N_A\} \times \mathrm{mol}^{-1}$ with the unit mol^{-1}. The description of the Avogadro number $\{N_A\}$ completely defines both the mole and the Avogadro constant $N_A = \{N_A\} \times \mathrm{mol}^{-1}$. So, the Avogadro constant N_A does not have an intrinsic magnitude that exists independently of its unit mol^{-1}. Therefore, the Avogadro constant N_A does not satisfy an essential requirement of defining relations. Consequently, the Avogadro constant N_A is not a defining constant, and the SI (2019) approach to redefine SI units based on defining relations does not apply to the mole. In particular, the expression (2.4) is not a defining relation, and the expression (2.5) does not define the mole.

Disclaimer: The opinions, recommendations, findings, and conclusions contained in this article do not necessarily reflect the views or policies of the National Institute of Standards and Technology (NIST) or the United States Government.

Acknowledgment: This paper is extracted from the reference [1]. Authors thank J. J. Scott, J. T. Hodges, D. W. Flater, B. K. Alpert, R. F. Boisvert, and the referees for their suggestions on the original paper.

References

[1] R. N. Kacker, K. K. Irikura, The Avogadro constant is not the defining constant of the mole, submitted to *Metrologia* as a Letter to The Editor (2024).

[2] SI (1970, 2006, 2019), The International System of Units (SI), Bureau International des Poids et Mesures (BIPM), Sèvres, France. https://www.bipm.org/en/publications/si-brochure

DOI 10.5162/SMSI2025/P09

Piezoelectric pressure mapping sensors using the poling effect induced by surface chemical modification

Daisuke Tadaki[1*], *Shintaro Matsumoto*[1], *Shin Yamamiya*[1], *Teng Ma*[2], *Yuji Imai*[3], *Ayumi Hirano-Iwata*[1], *Michio Niwano*[1]
[1] *Tohoku University, 2-1-1 Katahira, Aoba-ku, Sendai 980-8577, Japan*
[2] *Beijing Institute of Technology, 5 Zhongguancun South Street, Haidian District, Beijing 100811, China*
[3] *National Institute of Technology, Sendai College, 4-16-1 Ayashi-Chuo, Aoba-ku, Sendai 989-3128, Japan*
daisuke.tadaki@tohoku.ac.jp

Summary:
This paper presents a fabrication technology for a piezoelectric pressure mapping sensor with a PVDF film sandwiched between metal wire electrodes. A new approach is proposed for a poling treatment of the polymer films, which is generally required to obtain a sufficient voltage output from the sensor, using a simple solution-based method of drop-casting onto the chemically modified electrode surface. Here we report on the fabrication method and an investigation of the functionality of the fabricated novel mapping device, which can detect the applied position for a two-dimensional pressure mapping.

Keywords: pressure sensor, piezoelectric, PVDF, poling, surface modification

Introduction

Poly(vinylidene fluoride) (PVDF), an organic piezoelectric polymer, has so far been extensively studied for applications in flexible pressure sensors. To obtain a sufficient voltage output from pressure sensors based on piezoelectric polymer materials, including PVDF, a poling treatment of the polymer films is generally required. The conventional poling method usually requires a rather high electric field or a high annealing temperature, which leads to an increase in the sensor fabrication cost. A new approach to poling piezoelectric polymers, on the other hand, has been proposed using a simple solution-based method [1,2]. By drop-casting a PVDF solution in a polar solvent onto a chemically modified gold (Au) electrode surface, we have successfully formed a *β*-PVDF film with high piezoelectric properties and improved the sensitivity of PVDF pressure sensors [3]. For application to tactile sensing, which has recently attracted attention in healthcare fields, we are currently trying to develop a novel mapping device that expands the PVDF sensor to a two-dimensional (2D) system. In terms of obtaining the flexibility of a 2D device, these sensors using piezoelectric organic films have the advantage of requiring quite a simple fabrication method, whereas inorganic materials-based sensors usually require a complicated nanofabrication process to disperse the compressive stresses generated when pressure is applied. Here, we report on the fabrication method of a piezoelectric pressure mapping sensor with a *β*-PVDF film-based simple structure, and an investigation of the functionality of the novel device to detect the applied position for a 2D pressure mapping.

Experimental

Figure 1 shows (a) a top view and (b) a schematic diagram of the fabricated mapping sensor. Au (~60 nm) is mask deposited on a plastic (PET) substrate as the bottom (*x*) electrode and its surface is chemically modified with 1*H*,1*H*,2*H*,2*H*-perfluorodecanethiol (PFDT), a thiol agent with a high dipole moment. Subsequently, a PVDF solution containing hexamethylphosphoric triamide (HMPA) and acetone is drop-casted onto the substrate and thermally dried to form a PVDF film (~100 μm). Au (~60 nm) is finally mask deposited as the top (*y*) electrode perpendicular to the bottom (*x*) electrode. This novel method can thus provide the simplicity in fabrication process and reduction of the fabrication cost. The width of each Au wire on the sensor region is 150 μm, and the wire gap is 50 μm; i.e., the planar resolution is 200 μm. Electrical measurements were made independently at a single point (each three-dimensional intersection of the *x* and *y* electrodes) when a pressure jig with a square protrusion of 600 μm per side was periodically applied to the sensor region (Fig. 2).

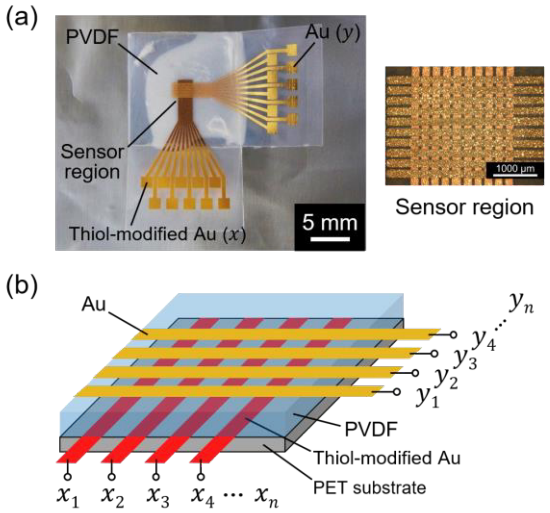

Fig. 1. (a) Photo image of the fabricated mapping sensor with an enlarged view of the sensor region. (b) Three-dimensional schematic of the sensor region. Each intersection of the x (bottom) and y (top) electrodes becomes a single measurement point.

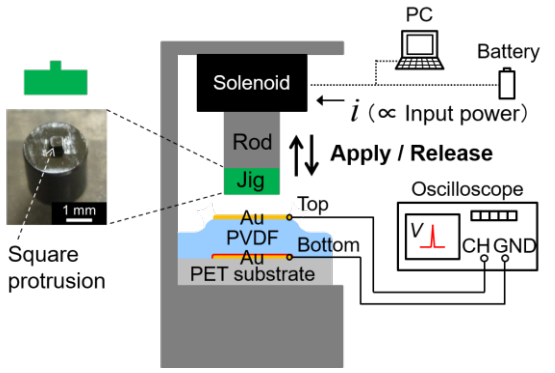

Fig. 2. Measurement system of the sensor device. A pressure jig with a square protrusion of 600 µm per side was periodically applied to the sensor region.

Results

Figure 3 shows the output voltage waveforms measured from point (*x*7,*y*5). It can be seen that a peak with an almost constant output voltage is reproducibly obtained by the periodically applying of the jig with protrusion. An increase ratio of the output voltage with the jig to without the jig is the largest at this point, reaching 34% (0.29 V → 0.39 V). Figure 4 shows a mapping of the output increase ratio (%) obtained from each point (64 points in total). It was found that the pressure applied to each point was clearly differentiated with a resolution of 200 µm, from which the approximate area of the applied position (black dashed box in the map) can be detected. We thus concluded that a 2D pressure mapping was successfully demonstrated with the fabricated novel device. Our main current issue is to further improve the output voltage (sensor sensitivity) for detecting more detailed 2D shapes of the applied objects.

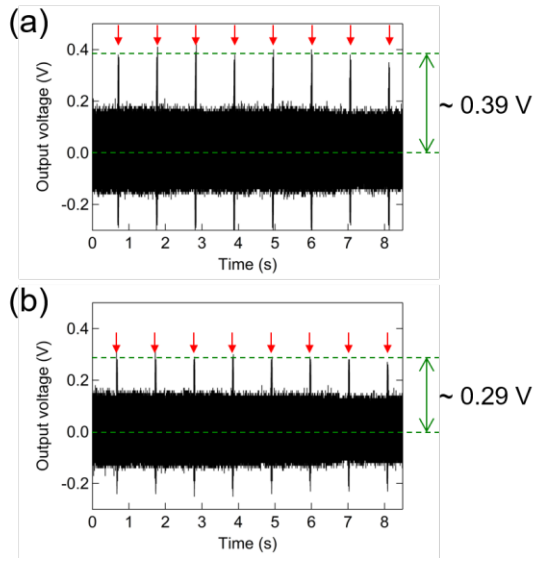

Fig. 3. Output waveforms at point (x7,y5) for the case of (a) with the jig and (b) without the jig (uniformly applied to the whole sensor region). The red arrow indicates each applied instant (~5 N, ~40 ms). The output increase ratio reaches 34% at this point.

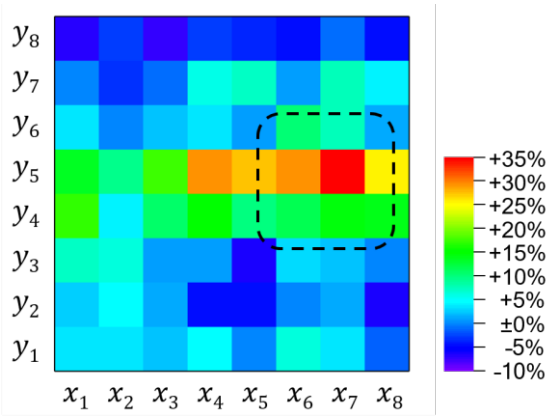

Fig. 4. Color distribution map of the output increase ratio (%) at each measurement point. Each segment corresponds to the planar resolution of 200 µm per side. The black dashed box indicates the approximate area of the applied position (600 µm per side).

References

[1] Y. Imai, Y. Kimura, M. Niwano, Organic hydrogen gas sensor with palladium-coated *β*-phase poly(vinylidene fluoride) thin films, *Applied Physics Letters* 101, 181907 (2012); doi: 10.1063/1.4764064

[2] Y. Imai, D. Tadaki, T. Ma, Y. Kimura, A. Hirano-Iwata, M. Niwano, Response characteristics of hydrogen gas sensor with porous piezoelectric poly(vinylidene fluoride) film, *Sensors and Actuators B* 247, 479-489 (2017); doi: 10.1016/j.snb.2017.03.001

[3] D. Tadaki, T. Ma, S. Yamamiya, S. Matsumoto, Y. Imai, A. Hirano-Iwata, M. Niwano, Piezoelectric PVDF-based sensors with high pressure sensitivity induced by chemical modification of electrode surfaces, *Sensors and Actuators A* 316, 112424 (2020); doi: 10.1016/j.sna.2020.112424

DOI 10.5162/SMSI2025/P10

Morphology Evolution of Snow-flakes Pattern and its Effect on Nano-/Micro-particles Embedded PbSe Photoconductive Thin Film Characteristics

Richard S. Kim[1], Sai Guduru[1], Yang Zhang[1], Kyung Hwa Lee[2], Jeung Hun Park[2], Sung Jin Kim[3]
[1] Laser Components Detector Group, Inc.,2277 N. Nevada St, Chandler, AZ 85225 USA,
[2] USMX Technologies LLC, 1455 E. Tropicana Ave Ste 275, Las Vegas, NV 89119 USA
[3] Electrical and Computer Eng., University of Louisville, 2301 S 3rd St, Louisville, KY 40292 USA
rkim@laser-components.com

Summary:

This study focuses on optimizing the fabrication of mid-wavelength infrared (MWIR) PbSe photodetectors, widely used in commercial, medical, environmental, industrial, and military applications due to their reliable, cost-effective performance at room temperature. Using chemical bath deposition (CBD), we identified unique snowflake-like patterns on PbSe surface, containing embedded nano-prisms. These formations are linked to PbSe recrystallization during the oxygen sensitization process. The research examines how these patterns evolve—forming, expanding, and eventually reducing—under varying oxygen exposure times and temperatures. Optimal detector performance is observed when snowflake density is highest, as indicated by enhanced photoluminescent (PL) output. Beyond a specific threshold, however, increased temperature leads to a reduction in pattern size and a decline in performance. By employing spectroscopic (PL/FTIR, UV-Vis) and structural (XRD, XPS, Hall-effect) analyses, the study demonstrates that snowflake morphology serves as a visible marker of ideal CBD conditions for producing high-sensitivity PbSe photoconductive detectors.

Keywords: lead selenide, photoconductive detector, nano-particle, nano-prism, snowflakes, sensitivity, responsivity, photoluminescent, sensitization, chemical bath deposition (CBD).

Introduction

Mid-wavelength infrared (MWIR) lead selenide (PbSe) detectors, produced via chemical bath deposition (CBD), have become essential in various commercial fields, including environmental monitoring, industrial sensing, medical diagnostics, and military applications. These detectors are favored for their reliability, cost efficiency, and effective room-temperature operation, making them an ideal solution for diverse sensing needs. Recent studies have highlighted the formation of distinctive snowflake-like patterns on PbSe active layer during oxygen sensitization. These patterns, containing embedded nano- and micro-particles—primarily nano-prisms—are thought to serve as visible indicators of PbSe recrystallization, reflecting crucial changes in detector properties and signaling optimal fabrication conditions.

In this work, we build upon previous research by introducing a novel approach to develop nanostructured PbSe thin-film photoconductive detectors [1], using snowflake patterns on the active region as observable markers for the crystallization process [2-3]. By systematically examining the formation and evolution of these patterns under varying oxygen sensitization conditions, we establish a clear correlation between snowflake morphology and detector performance. The characterization of these patterns and their effects on device functionality was carried out using spectroscopic techniques (PL/FTIR and UV-Vis) alongside structural analyses (XRD, XPS, and Hall-effect measurements). These methods confirm that snowflake density serves as a practical indicator for optimizing CBD conditions, advancing the development of high-performance PbSe detectors.

Results and Discussion

The results reveal key aspects of the snowflake-like pattern formation and its correlation with the performance of PbSe photodetectors. Figure 1(a) presents the initial appearance of snowflake patterns on the PbSe active surface, while Figure 1(b) highlights clusters of nano- and micro-particles beneath the snowflakes. Figure 2 shows the progression of snowflake patterns as a function of oxygen sensitization time at 415 °C, where the patterns first emerge, expand, and then reduce in size with prolonged

annealing. After wet-etching, Figure 3 reveals the active surface after removing the PbSe oxide phase, providing clearer insight into the pattern structure.

In Figure 4, snowflake development is depicted across different oxygen sensitization temperatures, showing a direct relationship between snowflake population density and the detector's signal response. This trend is further supported by the photoluminescent (PL) data in Figures 5 and 6, which demonstrate that shorter annealing times produce stronger PL signals at elevated temperatures, such as 415 °C, particularly at a wavelength of 4.0μm. Figure 7 shows the FTIR spectra (relative responsivity) of a 1x1 mm² PbSe detector at room temperature, indicating a peak in responsivity that coincides with optimized snowflake morphology.

Conclusion

In conclusion, the snowflake patterns observed on the active area of the PbSe detector represent a recrystallization phenomenon, serving as a visible and reliable indicator of detector quality. This morphology directly correlates with optimized chemical bath deposition (CBD) conditions, enhancing photodetector sensitivity and providing a straightforward, cost-effective approach to advancing high-performance MWIR PbSe detectors for commercial applications.

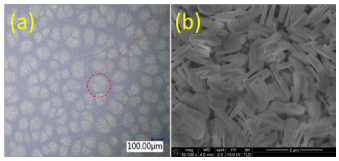

Fig. 1. A microscope photo showing the snowflakes patterns (a) and a SEM image of nano-/micro-particles formed beneath them (b).

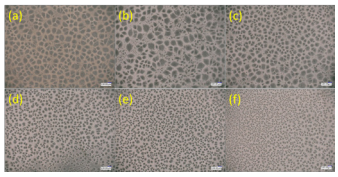

Fig. 2. Microscope images as a function of oxygen sensitization time at 415 °C. (a) 1min, (b) 2.5min, (c)5min, (d)7.5min, (e)15min, and (f)20min.

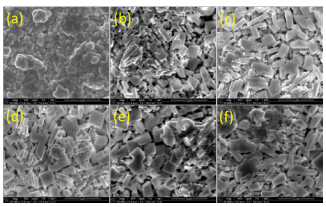

Fig. 3. SEM images showing the site of the evolution of nano-/micro-particles embedded PbSe thin film beneath snow-flakes pattern as a function of oxygen sensitization time. (a) 1min, (b)2.5min, (c)5min, (d)7.5min, (e)15min, and (f) 20min.

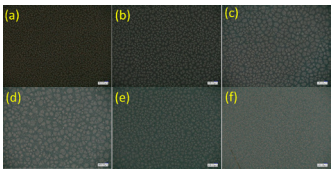

Fig. 4. Microscope photos showing the evolution of the snowflakes patterns as a function of annealing temperature in oxygen atmosphere. (a) 350°C, (b) 380°C, (c) 390°C, (d) 400°C, (e) 410°C, (f) 430°C.

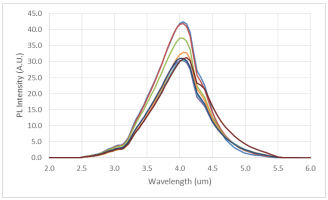

Fig. 5. PL spectra variation as a function of oxygen sensitization time with fixed 415 °C temperature.

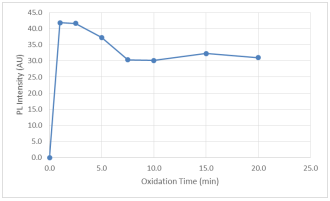

Fig. 6. PL intensity change as a function of oxygen sensitization time at λ=4.0μm at 415°C temperature (corresponding to Fig. 2).

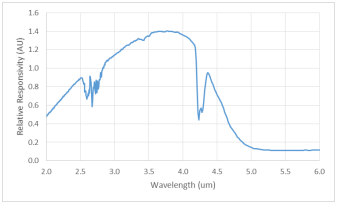

Fig. 7. Typical Sensitivity (Relative Responsivity) at 300K for 1x1mm² PbSe Detector with 5V DC supply.

References

[1] R.S. Kim, J.H. Park, R. Dahl, Snowflakes patterns formation enhances performance of nanostructure-based MWIR PbSe photoconductive detector, *The 16th international conference on Midinfrared optoelectronics: Materials and Devices (MIOMD 2023)*, MIOMD-Tup-17, 2023,

[2] R.S Kim, J.H. Park, Fabrication of PbSe nanostructures by employing chemical bath deposition (CBD) for photonics applications, *US Patent No. US2023/0160099 A1*, May 25, 2023.

[3] R.S. Kim, J.H. Park, Surface treatment strategies for iodine-doped PbSe thin films: Paving the way for low-cost focal plane array detectors, *IEEE/RAPID 2024 (invited)*, Aug 14, 2024.

DOI 10.5162/SMSI2025/P11

Split-Ring Resonator as Transducer for Metal-Organic Framework Based Sensors

Christian Thoben[1], Moritz Hitzemann[1], Lars A. Ruff[1], Charlotte Reinbacher[1], Tobias Hennig[2], Erik Rohloff[2], Andreas M. Schneider[2], Andreas Schaate[2], Stefan Zimmermann[1]
[1] Institute of Electrical Engineering and Measurement Technology, Leibniz University Hannover, Appelstr. 9A, 30167 Hannover, Germany
[2] Institute of Inorganic Chemistry, Leibniz University Hannover, Callinstr. 3-9, 30167 Hannover, Germany
thoben@geml.uni-hannover.de

Summary:
Split-ring resonators are electrical circuits, which enable highly sensitive readout of split capacity changes via measuring the shift in resonance frequency. Thus, functionalization of the sensitive area allows the development of selective sensors, where molecular interactions cause a change in permittivity and therefore a change in split capacity. Therefore, the split of a resonator is functionalized with metal-organic frameworks and the sensor response is investigated. Preliminary measurements show that introducing the anesthetic sevoflurane results in a significant shift in the resonance frequency.

Keywords: Split-ring resonator, SRR, UiO-66, metal-organic framework, MOF

Introduction

Split-ring resonators (SRRs) are easy-to-manufacture electric circuits built of two microstrip lines structured on printed circuit boards. One microstrip line is formed to a ring with a split that serves as the sensitive area, resulting in a resonator. The second microstrip line is used for coupling an electromagnetic wave into and out of the split-ring structure. The split-ring structure works as a RLC series resonant circuit where the conductor is the resistor, the ring is the coil, and the split is the capacitor. At resonance frequency, the electromagnetic wave couples into the split-ring structure and the transmission via the second microstrip line reaches a minimum. The resonance frequency changes with a change in the permittivity and conductivity of the sample in the split, resp. sensitive area. Therefore, SRRs are highly sensitive to changes of the electromagnetic properties at the sensitive area and can be used as sensitive sensors to measure the properties of liquids [1,2] or gases [3,4]. Graphene or carbon nanotubes are frequently employed as active surfaces for the detection of gases. An alternative approach uses metal-organic frameworks, which are currently being investigated in the context of sensor development [5].

Split-Ring Resonator

In the most basic setup, SRRs consist of a simple PCB with two microstrip lines, as shown in Fig. 1(a). Split-ring resonators can be described as RLC series resonant circuit with the basic equivalent circuit in Fig. 1(b).

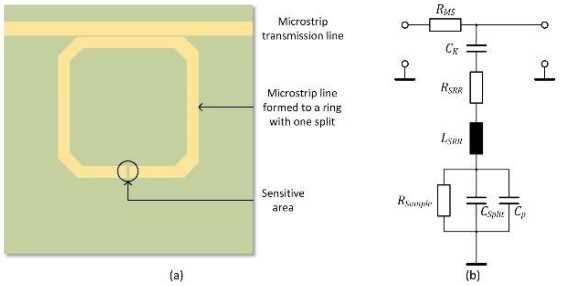

Fig. 1. (a) Schematic of a SRR consisting of a PCB with two microstrip lines, one for coupling electromagnetic waves (transmission line) into the other formed to a ring with a split; (b) equivalent circuit of the SRR with the electrical resistance of the transmission line R_{MS}, the coupling capacitance C_K, the electrical resistance of the ring R_{SRR}, the inductance of the ring L_{SRR}, the capacitance of the split C_{Split} and the parasitic capacitance C_p. Ohmic and dielectric losses of the split capacitor C_{Split} are represented by R_{Sample} [2]

From this very simple equivalent circuit diagram, the resonant frequency is obtained as a first approximation according to eq. (1), where C_K corresponds to the coupling capacitor, C_{Split} is the split capacitor including the dielectric, C_p summarizes the parasitic capacitances and L_{SRR} is the inductance of the ring.

$$f_{res} = \frac{1}{2\pi\sqrt{L_{SRR} \cdot C}}, C = \frac{C_K \cdot (C_{Split} + C_p)}{C_K + C_{Split} + C_p} \quad (1)$$

MOF UiO-66

Metal-organic frameworks (MOFs) are inorganic-organic hybrid materials composed of inorganic metal- or metal-oxo-nodes and organic linker molecules, which build up a framework structure with void spaces. Due to their high porosity and extensive chemical tunability through e.g. linker modification or post-synthetic methods, MOFs have received considerable attention over the last two decades in fields such as gas storage and separation, catalysis or sensing [6]. This tunability allows MOFs to engage in selective and high-affinity interactions with specific target molecules, enhancing their versatility in various applications. However, most MOFs lack chemical and thermal stability. A notable exception to this is the UiO-66-series, which displays exceptional stability due to its highly connected framework structure, formed by strong Zr-O coordination bonds [7]. We aim to employ UiO-66-type MOFs for gas sensing applications. Although this MOF has previously been used for both liquid and gas sensing, sophisticated detection methods, such as quartz-crystal microbalances, have been required to monitor analyte incorporation [8].

Measurements

Volatile anaesthetics are a potential hazard during occupational exposure, pregnancy or in individuals with existing disposition to malignant hyperthermia [6]. Sevoflurane was therefore selected as the analyte with the objective of developing a cost-effective sensor for trigger-free anaesthesia, which, up to now, can only be assessed using larger measuring systems [7].

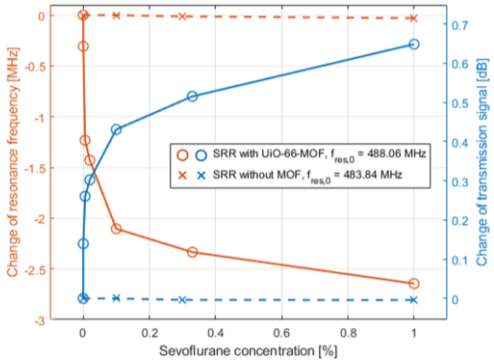

Fig. 2. Change of resonance frequency and transmission signal of the SRR functionalized with UiO-66-MOF (circles) and the unfunctionalized SRR (crosses) plotted against the sevoflurane concentration.

Fig. 2 shows the correlation between the sevoflurane concentration and the SSR response when functionalized with UiO-66-MOF in comparison to the SRR without functionalization. The functionalized SRR shows a significant resonance frequency shift of -1.23 MHz at a concentration of 58.8 ppm of sevoflurane and a difference in amplitude attenuation of 0.26 dB.

Acknowledgment

Funded by the Deutsche Forschungsgemeinschaft (DFG, German Research Foundation) - 511400779.

References

[1] M. Hitzemann, K. J. Dehning, A. V. Gehl, E.-F. Sterr, S. Zimmermann, Fast Readout of Split-Ring Resonators Made Simple and Low-Cost for Application in HPLC, *Electronics* 11, 1139 (2022); doi: 10.3390/electronics11071139.

[2] K. J. Dehning, M. Hitzemann, S. Zimmermann, Split-ring resonator with interdigital Split electrodes as detector for liquid and ion chromatography, *Sensing and Bio-Sensing Research* 44, 100645 (2024); doi: 10.1016/j.sbsr.2024.100645

[3] A. Javadian-Saraf, E. Hosseini, B. D. Wiltshire, M. H. Zarifi, M. Arjmand, Graphene oxide/polyaniline-based microwave split-ring resonator: A versatile platform towards ammonia, *Journal of hazardous materials* 418, 126283 (2021); doi: 10.1016/j.jhazmat.2021.126283

[4] S. K. Singh, P. Azad, M. J. Akhtar, K. K. Kar, Improved Methanol Detection Using Carbon Nanotube-Coated Carbon Fibers Integrated with a Split-Ring, *ACS Applied Nano Materials* 1, 4746–4755 (2018); doi: 10.1021/acsanm.8b00965

[5] P. Hajivand, J. Carolus Jansen, E. Pardo, A. Armentano, T. F. Mastropietro, A. Azadmehr, Application of metal-organic frameworks for sensing of VOCs and other volatile biomarkers, *Coordination Chemistry Reviews* 501, 215558 (2024); doi: 10.1016/j.ccr.2023.215558

[6] H. Furukawa, K. E. Cordova, M. O'Keeffe, O. M. Yaghi, The Chemistry and Applications of Metal-Organic Frameworks, *Science* 341, 1230444 (2013); doi: 10.1126/science.1230444

[7] J. H. Cavka, S. Jakobsen, U. Olsbye, N. Guillou, C. Lamberti, S. Bordiga, K. P. Lillerud, A New Zirconium Inorganic Building Brick Forming Metal Organic Frameworks with Exceptional Stability, *Journal of the American Chemical Society* 130, 13850 (2008); doi: 10.1021/ja8057953

[8] S. Okur, T. Hashem, E. Bogdanova, P. Hodapp, L. Heinke, S. Bräse, C. Wöll, Optimized Detection of Volatile Organic Compounds Utilizing Durable and Selective Arrays of Tailored UiO-66-X SURMOF Sensors, *ACS sensors* 9, 622–630 (2024); doi: 10.1021/acssensors.3c01575

[9] S. Heiderich, C. Thoben, N. Dennhardt, W. Koppert, T. Krauß, R. Sümpelmann, S. Zimmermann, W. Klingler, Low anaesthetic waste gas concentrations in post anaesthesia care unit, *European journal of anaesthesiology* 35, 534–538 (2018); doi: 10.1097/EJA.0000000000000785

[10] C. Thoben, N. Dennhardt, T. Krauß, R. Sümpelmann, S. Zimmermann, H. Rüffert, S. Heiderich, Preparation of anaesthesia workstation for trigger free anaesthesia, *European journal of anaesthesiology* 36, 851–856 (2019); doi: 10.1097/EJA.0000000000001086

DOI 10.5162/SMSI2025/P12

Multi-sensor pothole detection and monitoring system

Ivan Romero[1], *Hubert Mantz*[1], *Thomas Walter*[1], *Michael Schneider*[1]
[1] *Laboratory for Microtechnology, Ulm University of Applied Sciences, Ulm, Germany*
ivan.romero@thu.de

Summary: A pothole detection and monitoring system is designed and built to enhance maintenance planning by accurately localizing and assessing potholes as potential sources of danger for traffic. This multi-sensor system combines data from several sources. Two infrared cameras generate a depth image, an RGB camera captures visuals processed by AI-based algorithms for depth and segmentation, a radar sensor identifies surface irregularities, and a vibration sensor detects impacts from rough surfaces. By fusing the outputs of all sensors, the system achieves reliable pothole detection across diverse conditions. An integrated RTK GPS system helps to locate the events accurately.

Keywords: pothole detection, road surface observation, bicycle and pedestrian paths, depth imaging, stereo vision, radar analysis, vibration analysis, convolution neural network algorithms

Introduction and Motivation

As reported by the Germany Federal Statistical Office, a number of cyclist fatalities have been attributed to the lack of maintenance of cycling infrastructure [1]. This is largely attributed to the fact that many cities do not prioritize the development of such infrastructure [2]. These circumstances highlight the necessity for a system that can effectively detect and monitor potholes, with the aim of enhancing safety.

The current approach to pothole detection relies on a combination of manual inspections, citizen reports, and automated methods based on stereo vision [3,4], convolutional neural network (CNN) algorithms [5,6], radar sensors [7,8] and vibrations sensors [9,10]. However, each method has its own limitations. For instance, vibration sensors have been observed to generate false positives on stone roads, while stereo vision and CNN algorithms have shown to perform poorly in low-light conditions. Such limitations highlight the necessity for an alternative methodology to enhance the reliability and adaptability of pothole detections. The proposed system overcomes the limitations of a single-sensor system by integrating a multiple-sensor approach, which provides bicycle localization, facilitating road maintenance planning.

Sensor System

The system is mounted on a bicycle at a height of 0.8 m with its sensors facing downward as illustrated in Figure 1. The system comprises three modules connected to a computer via USB: the Intel RealSense D455 depth camera, the Infineon DEMO BGT60UTR11AIP radar sensor, and the UBLOX ZED-F9R GPS sensor. Two lamps are employed to enhance visibility in low-light conditions.

First, the depth camera computes a disparity map using stereo vision with two infrared cameras and an infrared projector, thereby enhancing depth accuracy on flat surfaces. Additionally, the module incorporates an RGB camera, which serves as an input for CNN algorithms to obtain depth and segmented images. The module Inertial-Measurement-Unit (IMU), comprising accelerometers and gyroscopes, is beneficial for the detection of vibrations. Next, the radar sensor employs the Infineon XENSIV 60 GHz platform, which is effective in distance and speed analysis in low-light conditions. Then, the GPS sensor obtains the longitude, latitude and altitude of the bicycle. This sensor supports both Real-Time-Kinematic (RTK) and dead reckoning. Finally, by integrating the information from all the modules, the system accurately detects and monitors potholes.

Fig. 1. Multi-sensor pothole detection system mounted on a bicycle at a height of 0.8 m

Results

The results of two road deformation scenarios are presented in Figures 2 and 3, which comprise four images each. The top-left quadrant (A) of each figure displays the depth image derived from the disparity map, while the top-right (B) displays the RGB image. In the bottom-left (C), the depth image generated by the "Depth Anything" CNN algorithm [11] is presented. Finally, the bottom-right (D) shows the image segmentation produced by the "Segment Anything" CNN algorithm [12].

Figure 2 illustrates a scenario featuring a road and a sidewalk. The disparity-based and the CNN-derived depth image both demonstrate a clear depth difference between the road and sidewalk. Additionally, the drain is visible in both images, with the CNN algorithm exhibiting superior performance. In the image segmentation, different segments are accurately identified from the RGB image.

Figure 3 illustrates a forested scenario with a bicycle path traversing it. The disparity-based depth image highlights a hole adjacent to the road, as well as leaves and rocks on the path. The CNN-derived depth image, while successful in detecting the leaves and rocks, does not capture the hole with the same accuracy. Conversely, the image segmentation identifies different segments derived from the RGB image.

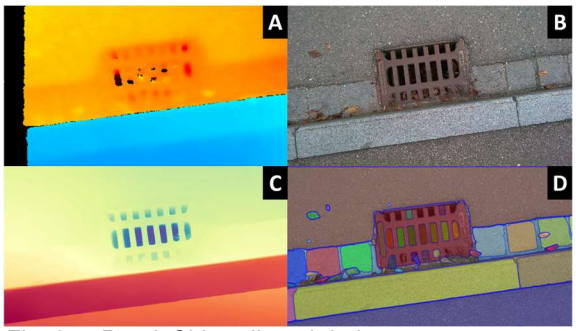

Fig. 2. Road, Sidewalk and drain.
(a) Disparity-based depth image, (b) RGB image,
(c) CNN-derived depth image [11],
(d) Image segmentation [12]

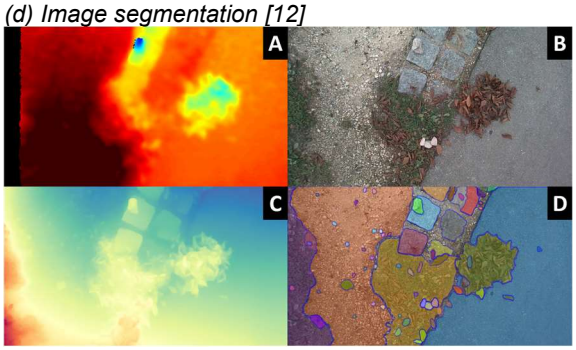

Fig. 3. Bicycle path traversing a forested area.
(a) Disparity-based depth image, (b) RGB image,
(c) CNN-derived depth image [11],
(d) Image segmentation [12]

Conclusions

The study presents a multi-sensor system for the detection and monitoring of potholes on cycling paths, with the objective of enhancing cyclist safety. By analysing depth data from disparity-based methods and CNN-derived algorithms, the system can detect the presence of potholes or deformities with reliability in multiple scenarios. This approach is further enhanced by performing the RGB image segmentation. The results validate the system's capacity to detect surface irregularities.

References

[1] Statistisches Bundesamt (Destatis), "Road traffic fatalities in Europe," Federal Statistical Office of Germany, 2021. Available: https://www.destatis.de/Europa/EN/Topic/Transport/road_traffic_fatalities.html. doi:10.1234/transport/fatalities2021

[2] ADFC, "ADFC Bicycle Climate Test 2022," Allgemeiner Deutscher Fahrrad-Club e.V., Apr. 2023. Available: https://www.ebike24.com/blog/adfc-bike-friendly-cities-rating-2022.

[3] Z. Zhang, X. Ai, C.K. Chan, et al., "An efficient algorithm for pothole detection using stereo vision," IEEE ICASSP, 2014.

[4] Y. Li, C. Papachristou, D. Weyer, "Road pothole detection system based on stereo vision," IEEE ICAL, 2018.

[5] M. Sathvik, G. Saranya, "An intelligent convolutional neural network-based pothole detection using YOLO-V7," ICACRS, 2022.

[6] R. Fan, H. Wang, Y. Wang, et al., "Graph attention layer evolves semantic segmentation for road pothole detection," IEEE TIP, 2021.

[7] R. Chen, et al., "Utilizing radar for road damage detection," in IEEE Robotics and Automation Letters, 2021.

[8] Y. Wang, M. Liu, et al., "Automated radar-based road surface analysis," IEEE Transactions on Geoscience and Remote Sensing, 2021.

[9] D. Chen, et al., "Real-time road pothole mapping based on vibration analysis in smart cities," IEEE Journal of Selected Topics in Applied Earth Observations and Remote Sensing, 2022.

[10] H. P.M., V. G., "Vehicle vibration signal processing for road surface monitoring," IEEE Sensors Journal, 2017.

[11] Depth Anything, "Depth-Anything-V2," Hugging Face, 2024. Available: https://huggingface.co/spaces/depth-anything/Depth-Anything-V2.

[12] Segment Anything, "Segment Anything Demo," 2024. Available: https://segment-anything.com/demo.

DOI 10.5162/SMSI2025/P13

Why a DCC Makes Life Easier with Multi-Component Sensors for Forces and Moments

Daniel Schwind
GTM Testing and Metrology GmbH,
Philipp-Reis-Str. 4-6, 64404 Bickenbach, Germany
Daniel.Schwind@gtm-gmbh.com

Summary:
DCC (digital calibration certificate) is in the starting blocks. The PTB working groups and countless experts from industry are contributing to the standardization and machine readability of the DCC and are in the final sprint [1]. The advantages of the DCC result from the automated management of thousands of sensor calibrations, and the associated economic savings are estimated at several billion euros per year in Germany only. This article shows another important aspect: the user-friendly simplification of complex calibration data.

Keywords: DCC, Multi-Component, Calibration, Certificate, Uncertainty Vector

Introduction

When the advantages of the DCC are discussed among experts, the focus is on simplifying the handling of large quantities of calibration certificates. For example, in a chemical factory where thousands of process monitoring sensors are installed and need to be traced back, an uninterrupted digital chain without media changes from the calibration laboratory to the application can save enormous amounts of time and greatly reduce the potential for errors.

However, the DCC is not only of interest in the cases mentioned above, but also in cases where complex data occur which are related to each other in some way. Or where large volumes of data are generated. A sensor that can metrologically competent reduce such complex data and present its performance to the user as simply as possible is called a smart sensor. The DCC can transport all the information required for a smart sensor. If the DCC is also cryptographically signed and stored on the sensor, a complex structure becomes a plug-and-play device.

Multi-component sensors are complex

Multi-component sensors are widely used in industrial applications like testing of components or structures, in robotics or crash testing in the automotive industry. These sensors provide information on externally applied forces and moments, usually oriented in a cartesian coordinate system. In most cases, monolithic base bodies made of steel or aluminium with strain gauge applications are used. These monolithic bodies exhibit a more or less good decoupling of the externally introduced force and moment vectors. The residue of the decoupling is often called crosstalk. This means a sensor that measures three forces and three moments requires at least 6 x 6 elements for its characterization. As the behavior can also have non-linear components, this can result in a multiple of the 6 x 6 matrix. It's easy to lose overview, apart from the fact that it's also not easy to check the accuracy or measurement uncertainty of the sensor. And it's even easier to lose focus when the expertise lies in the task of testing components or structures, in robotics or crash testing - and not in metrological subtleties.

State of the art of multi-component sensors and their calibration

There are countless multi-component sensor designs, each tailored to its application, and very little uniformity, for example in the testing area or in robotics. Only a few applications today allow integrated sensors, i.e. with corresponding amplification electronics, as the limited installation space of the integrated electronics may have a negative impact on the accuracy of the sensors. Apart from that, there are still not many calibration laboratories [2] that can calibrate multi-component sensors with the required precision and create a DCC with the necessary information for a smart sensor. However, with the increasing miniaturization of electronics and the increasing digital compensation possibilities, the number of possible applications is growing continuously. In

general, there are still no smart multi-component sensors, even if some manufacturers describe them as such. It is up to the smart user to configure their system, controller and electronics accordingly. Today, it is not enough just to have expertise in individual specialist areas - metrological expertise is also required.

DCC is the basis of a smart sensor

The steps that make up a smart multi-component sensor are as follows:

1. The sensor has an integrated or permanently connected (assigned) amplifier electronics
2. The electronics have one or more digital interfaces, which allows the transmission of data as well as the transmission of a DCC
3. The electronics have sufficient memory for DCC storage
4. The amplifier electronics understands the machine-readable DCC and configures itself accordingly
5. The multi-component sensor is calibrated in a laboratory, whereby the complexity of the sensor is considered and metrologically reduced to the data relevant for the application
6. The laboratory stores the cryptographically signed DCC on the sensor
7. The sensor is now plug-and-play - it spits out the metrologically evaluated data and provides the traceable calibration certificate

Of course, such systems are already in use in a similar form at some institutions. The revolutionary thing about the DCC is that the harmonization by the PTB and countless industry experts has created a globally standardized work. This provides a real basis for metrologists in calibration laboratories to competently calibrate the complex multi-component transducers and configure them using the DCC, so that the user – worldwide – does not have to make any complicated settings and is able to concentrate on its original tasks.

Requirements on calibration procedure

Unfortunately, there are no standardized calibration guidelines for multi-component sensors. This technical area is still in a development phase. There are various approaches to calibrate the forces and moments. For a smart sensor, moment-free forces and force-free moments are of course the first choice. The calibration procedure should provide information on the contribution's resolution, linearity, hysteresis, zero-return, repeatability and reproducibility and creep, unless the sensor is used in such a specific way that individual contributions can be excluded. To carry out the calibration as closely as possible to the application, mixed loads should also be applied in addition to uniaxial loads.

Fig. 1. Multi-component standard machine for uniaxial loading and mixed loading, performing forces moment-free and moments force-free

Requirements on DCC data

The certificate must contain at least the correction matrix with which the individual signals of the sensor are converted into the forces and moments. This is at least a 6 x 6 matrix, but can also be an 8 x 6 matrix, for example, if the transducer body has eight measuring bridges. And, as already mentioned, a multiple of the correction matrix may also be necessary for non-linear behavior.

A very important point for a smart multi-component sensor is the calculation of an uncertainty vector: as the forces and moments introduced are not scalar but vectorial, the calculated measurement uncertainty is also a vectorial quantity. Consequently, the DCC should also communicate the information for calculating this uncertainty vector to the smart sensor so that it calculates all measured values with the corresponding uncertainty vector.

Conclusion

With a DCC, it is possible to have complex requirements solved by experts from the calibration laboratories, so that the sensor user can concentrate on his core tasks.

References

[1] S. Hackel et al., Digitization versus Digitalization & Digital Transformation in the field of calibrations and their subsequent use (2024). Physikalisch-Technische Bundesanstalt (PTB). Available at: https://doi.org/10.7795/120.20240126

[2] D. Schwind, Multicomponent calibration of forces and moments – an overview of the various technical approaches, *XXIV IMEKO World Congress "Think Metrology"*, 2024, Hamburg, German

DOI 10.5162/SMSI2025/P14

Automatic Multisensory Measurement of the Borehole Length during Drilling of Inhomogeneous Materials

Adriano Boaron[1], Dirk Stöbener[1,2], Andreas Fischer[1,2]
[1] University of Bremen, Bremen Institute for Measurement, Automation and Quality Science, Germany
[2] MAPEX Center for Materials and Processes, University of Bremen, Bremen, Germany
a.boaron@bimaq.de

Summary:
Precise borehole length measurements are demanded in manufacturing and surgery, ideally with no additional time but as integrated part of the drilling process. For this purpose, an automatic detection of the material front and back surface position is proposed while monitoring the feed forward. The solution approach is realized by using a multisensory drive train and designing the signal processing for the sensor data fusion. As a result of experimental tests, the approach is validated, demonstrating an automatic measurement of the borehole length during drilling with a measurement uncertainty of 0.17 mm.

Keywords: Drilling, process monitoring, multisensory, composites, measurement uncertainty.

1. Introduction

In bone surgery, the fixation of metal implants on bones with screws requires to drill holes into the bones. Due to the small access to the bone, the borehole length measurement for the correct screw choice is difficult and could be improved by an integrated, automated length measurement during the drilling process.

Sorg et al. [1] published an approach for determining the borehole length when drilling pig bones by using a multisensory drive train and a manual analysis of the signals´ amplitudes in time domain. Guan et al. [2] proposed a method to detect the start and end of drilling in spinal pedicle screws by measuring both force and acoustic emission (AE) signals and processing them through an FFT, in the range of 10 kHz and 15 kHz. Furthermore, a method for the automatic drill breach detection during spine pedicle drilling based on vibroacoustic sensors has been developed by evaluating the spectrograms from the signals and using a neural network [3]. However, an uncertainty analysis for the borehole length was not conducted.

Therefore, the two aims of this paper are designing a signal processing for the automatic multisensory measurement of the borehole length during the drilling in bone-like inhomogeneous materials and determining the achievable measurement uncertainty. Here, the experiments are performed with an inhomogeneous composite material to mimic the structure of a bone.

2. Principle of the solution approach

The technological basis is the multisensory drive train proposed in [1], Fig. 1.

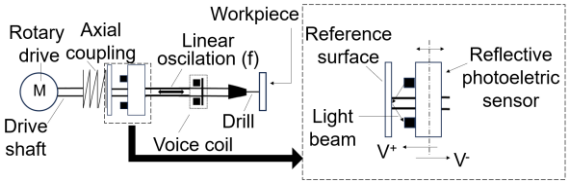

Fig. 1. Multisensory drive train from [1].

The drilling process rotational speed n and the feed velocity v_f are controlled and recorded, as well as the axial oscillation frequency f excited by a voice coil.

The signals of two integrated sensors (current sensor and reflective photoelectric sensor, RPS) are evaluated for deriving the front and the back surface position of the workpiece from in-process measurements. An additional optical sensor is used to measure the distance between the workpiece´s clamping and a fix structure on the drilling machine, which allows to measure the feed velocity during the process.

The current sensor installed on the rotary drive is used to indirectly measure the torque acting on the drill during the cutting process. The RPS mounted on the output movable shaft measures the relative distance between the sensor and a reference surface fixed on the shaft, which provides a measure for the acting feed force.

3. Experimental results

The experimental results related to the automatic multisensory method for measuring the borehole

length are based on a sensor signal analysis, which jointly evaluates the behavior of all sensor signals in time domain, see Fig. 2.

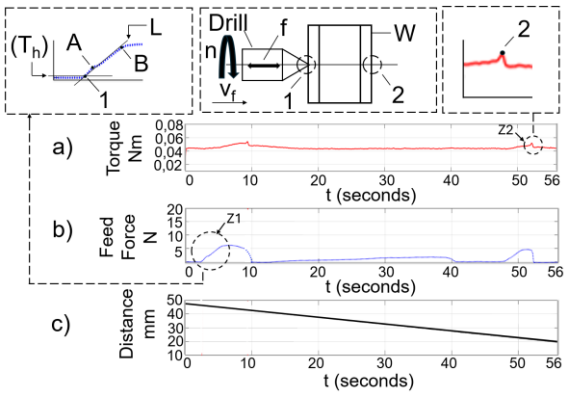

Fig. 2. Automatic multisensory measurement method of borehole length based on time domain signal processing.

Both the torque (Fig. 2-a) and feed force (Fig. 2-b) are obtained by filtering the original measured signals in order to eliminate inherent process noise. The combined analysis of both torque and feed force shows that there is a correlation between these signals. The initial slope observed in the torque and feed force refers to the instant in time in which the drill gets in contact with the workpiece W (material: composite with two PVC external layers and one internal polystyrene rigid foam XPS layer), whereas the drop of both signals noted in the end of the time duration refers to the breakthrough instant of the tool.

The feed force shows a higher sensitivity throughout the drilling process when compared with the torque sensor. This characteristic is used to recognize the initial contact between the tool and workpiece, which is defined by the intersection of the tangential line to the ground noise with an added threshold T_h and the best fit line L from the inflexion point A to the immediate change in curvature B (Fig. 2-b, zoomed view of point 1). The point in time associated with the breakthrough is then determined based on the maximum value shown by the torque signal (Fig. 2-a, zoomed view of point 2) which also matches the feed force signal for the given time instant. The time interval between the detected initial workpiece contact and the breakthrough represents the drilling duration $t_{1\text{-}2}$. The pattern shown by the distance signal (Fig. 2-c) confirms that v_f is constant throughout the drilling process and equals the set value of 0.5 mm/s. By using the combined information from all the sensors, the borehole length L_b is then determined by multiplying the time duration $t_{1\text{-}2}$ by v_f:

$$L_b = t_{1\text{-}2} \cdot v_f \qquad (1)$$

Fig. 3 shows the L_b values achieved when drilling the workpiece by using constant process parameters (n, v_f and f).

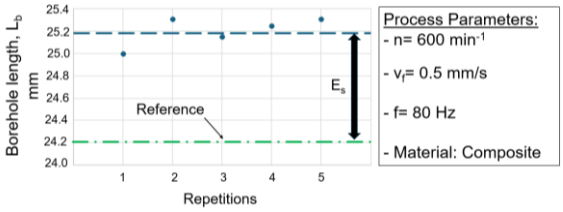

Fig. 3. Automatic borehole length L_b throughout experimental repetitions.

The measured L_b values are distributed around the mean μ = 25.2 mm (blue dashed line) with a small standard deviation σ = 0.06 mm, thus indicating a good precision afforded by the proposed sensor analysis. Considering both the L_b repeatability and the reference system resolution of 0.05 mm as the main sources of errors, and assuming a calibration to compensate for systemic errors, the achieved expanded measurement uncertainty for a confidence level of 95 % amounts to 0.17 mm.

4. Conclusion and Outlook

An automatic multisensory method for the indirect measurement of the borehole length during drilling of inhomogeneous composite material has been presented. The method relies on the evaluation of three different sensor signals to recognize both the initial and the breakthrough positions between the drill and the workpiece. This has resulted in sufficiently precise measurements of the machined borehole length, so that a systematic error dominates that requires a calibration. Therefore, next working steps are the in-depth understanding of the cause-effect chain between the mechanical machining and the sensor signals for improving the accuracy, as well as the investigation of additional sensors regarding their influence on minimizing the achievable total measurement uncertainty of the borehole length.

Acknowledgement

The authors gratefully acknowledge the financial support of the current research project by the Volkswagen-Stiftung within the scientific project SMILE (Sensitive machining of biological materials) – Funding ID: Momentum.

References

[1] M. Sorg, J. Osmers, A. Fischer, Methodical Approach for Determining the Length of Drill Channels in Osteosynthesis, *Sensors* 19, 1-10 (2019); doi: 10.3390/s19163532

[2] F. Guan, Y. Sun, X. Qi, Y. Hu, G. Yu, J. Zhang, State Recognition of Bone Drilling Based on Acoustic Emission in Pedicle Screw Operation, *Sensors* 18, 2-17 (2018); doi: 10.3390/s18051484

[3] A. Massalimova, M. Timmermans, N. Cavalcanti, D. Suter, M. Seibold, F. Carrillo, J. C. Laux, R. Sutter, M. Farshad, K. Denis, P. Fürnstahl, Automatic Breach Detection during Spine Pedicle Drilling Based on Vibroacoustic Sensing, *Artificial Intelligence in Medicine* 144, 1-9 (2023); doi: 10.1016/j.artmed.2023.102641

DOI 10.5162/SMSI2025/P15

Shape Measurement of Large Scale Components Employing Wireless Sensor Networks

Lars-Michel Bretthauer [1], *Gerd Scholl*[1] *and Ralf Heynicke* [1]
[1] Electrical Measurement Engineering, Helmut Schmidt University,
Holstenhofweg 85, 22043 Hamburg, Germany
firstname.lastname@hsu-hh.de

Summary: In this paper a wireless sensor network for measuring large scale components is presented. Accordingly, the methods of previous works for basic position calculations [1] and determining measurement uncertainties [2] are combined to implement a fully operational measurement system. Furthermore, a minimal-cost path is employed to optimize uncertainty in probe positioning calculations. Additionally, an approach for determining the structure shape via a least-square fit is demonstrated taking into account position uncertainty of each sensor probe. In order to demonstrate the feasibility a real-world measurement is presented.

Keywords: Sensor Network, Wireless, Shape Measurement, Large Structures Measurement, Least-Square-Fit

Motivation

Often it is not possible to measure the shape of a large object in real-time due to the large amount of time required. Therefore, we propose a wireless sensor network for determining the structure shape in real-time via distributed and interconnected sensors attached to the surface. Each probe measures the surface normal at its position and the distance to its directly neighboring probes. In recent works we demonstrated the construction of a sensor network capable of measuring the shape of an object in real time [1]. Additionally, we estimated the uncertainty of such a sensor network in accordance with the ”GUM” [3], resulting in an application dependent quality indication for uncertainty [2]. Moreover, we investigated the uncertainty estimation through the utilization of a Monte Carlo method employing a least squares fit, as detailed in [4]. In this work we want to combine the previous methods to prove the working principle within a network consisting of 22 sensor probes and 48 connections. Furthermore, we want to show the needed calculations to determine the shape of an object. The component with the sensor network is shown in Fig. 1.

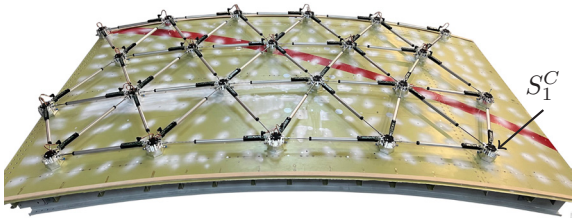

Fig. 1: Measurement object with the applied sensor network consisting of 22 sensor probes.

Shape Calculation

For the shape calculations each sensor probe position has to be evaluated in a reference probe coordinate system, which is used to translated into the component coordinate system. In our setup probe #1 (lower right in Fig. 1) is used as a reference probe denoted with the superscript ”C”. Due to the network structure each position can be calculated along serval paths. However, it is more practical to use the path with the lowest position uncertainty. This can be achieved by determining the minimal cost path by using the A*- Algorithm from [5]. Since the network can also mathematically be described as an undirected graph. The network structure with its interconnections is shown in Fig. 2. As weights between the nodes the Euclidean distance uncertainty of the probes position is used by applying the estimations from [2]. The result is a tree with interconnections, where the path through the branches with the lowest position uncertainty in respect to the reference node coordinate system is determined.

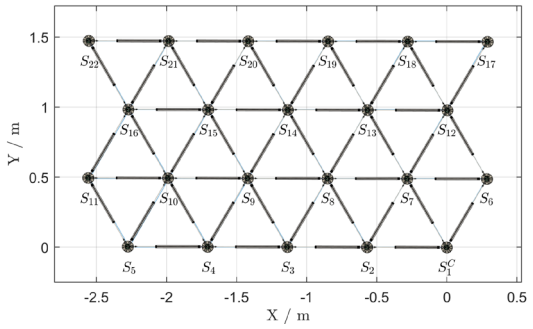

Fig. 2: Network structure of the applied sensor network from Fig. 1 with 22 nodes and 48 connections.

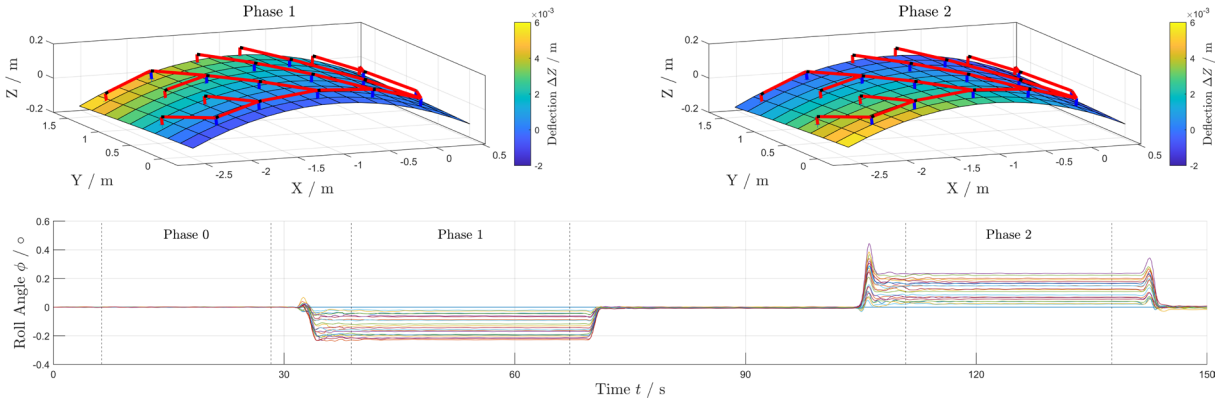

Fig. 3: Shape calculation of the component from Fig. 1 in phase 1 and phase 2, showing a deflection in Z direction to the phase 0. Results visualized as heat map with attached sensor network, minimal uncertainty path marked in red.

Subsequently, the surface shape can be reconstructed using a two-dimensional polynomial via a least-squares fit. The positions with the associated uncertainties are used for the fit calculation. For position estimation also the angles of the measuring probes can be used, as the angle information corresponds to the slope of the surface at the calculated probes position, respectively. This can be realized by extending the fit algorithm with the first derivative of the polynomial.

Measurement

Figure 3 shows the deformation resulting from lifting the component's edge $\approx 6\,\mathrm{mm}$ generating a torsional load on the component. The measurement is divided into three phases. Phase 0: initial shape, structure lies flat on the floor, phase 2: uplift of rear left corner and phase 2: uplift of front left corner. The two upper graphs show the calculated shapes of the component in phases 1 and 2 with the sensor networks minimal uncertainty path highlighted in red. The change in the Z direction with respect to the initial phase 0 is presented with the color map. Both phases show similar displacements. Also, the lifting point is visible on the heat map and shows that the component is lifted locally only on at a corner of the structure. The bottom graph shows the roll angle to illustrate the different stages in time. At the end of the measurement process the structure returns to its original shape.

Results

In this work we demonstrated that a real-time monitoring of large-scale structures with precise position and shape specifications is feasible, employing a wireless sensor network, which has been mounted on a test structure. Probe positions and the determination of the structure shape has been realized using a least-squares fit algorithm. In a future work the measurement results are cross-checked with a LASER-based reference measurement system.

Acknowledgment

This research paper out of the project "Digital Sensor-2-Cloud Campus Platform" (DS2CCP) is funded by dtec.bw – Digitalization and Technology Research Center of the Bundeswehr. dtec.bw is funded by the European Union – NextGenerationEU.

References

[1] L.-M. Bretthauer, R. Heynicke, and G. Scholl, "Proposal of a cyber physical finite element sensor network for surface measurements," *IEEE International Instrumentation and Measurement Technology Conference (I2MTC)*, pp. 380–387. (2024); doi: 10.1109/I2MTC60896.2024.10560668.

[2] L.-M. Bretthauer, R. Heynicke, and G. Scholl, "D5.1 - uncertainty modeling of a cyber-physical finite element sensor network for surface measurements," *GMA/ITG-Fachtagung Sensoren und Messsysteme 2024*, pp. 380–387. (2024); doi: 10.5162/sensoren2024/D5.1.

[3] BIPM, IEC, IFCC, ILAC, ISO, IUPAC, IUPAP, and OIML, "Evaluation of measurement data — an introduction to the "guide to the expression of uncertainty in measurement" and related documents." Published: Joint Committee for Guides in Metrology, JCGM 104:2009.

[4] L.-M. Bretthauer, R. Heynicke, and G. Scholl, "Monte carlo method for uncertainty estimations of cyber-physical finite element sensor networks," *tm - Technisches Messen*, vol. 91, pp. 32–37. (2024); doi: 10.1515/teme-2024-0050.

[5] P. E. Hart, N. J. Nilsson, and B. Raphael, "A formal basis for the heuristic determination of minimum cost paths," *IEEE Transactions on Systems Science and Cybernetics*, vol. 4, no. 2, pp. 100–107. (1968); doi: 10.1109/TSSC.1968.300136.

DOI 10.5162/SMSI2025/P16

Optical signal transmission solutions for electromobility and renewable energies in favor of a low carbon future

André Schäfer,
Hottinger Brüel and Kjaer GmbH (HBK),
Im Tiefen See 45, 64293 Darmstadt, Germany

Summary:
Wind energy and electromobility have the biggest share each in the production of renewable energies and a carbon-free use of them. Essential for very important basis for the transition to a low-carbon society the technical side of optical solutions shown in an optimized communication to power analyzers by optical remote probes and its versatile advantages with fiber optic technology as well as an optical pantograph monitoring solution for optimization of rolling stock is explained in here.

Keywords: electromobility, renewable energy, wind energy, electric motor, mechanical power, electrical power, efficiency, torque transducer, current transducer, power analyzer

Introduction

At the end of 2024, the UN Climate Change Conference took place in Baku, Azerbaijan showing there is no alternative to a world of 100 % renewables [1]. One of the results was that wind energy on the one hand and electromobility on the other respectively represent most important contributions to securing the global climate.

To secure further developing progress in these new technologies, solutions must be thought, better in comparison with current methods.

Resulting technical requirements

The Helmholtz Research Field Energy (HRFE) sees the task of developing a science and technology driven roadmap for energy research, to which we see ourselves as equally committed [2]. In several publications aspects of that progress has been described in detail. Increasing size of by wind turbines, makes torque generated rise to dizzying heights in the MN·m range. With the trend to offshore wind turbines the midterm horizon is nominal of 20 MN·m, necessary to be traced back as well [3;4], we offer reference standards. In this article now, the signal flow from sensors to DAQ should be the special topic.

Optical solutions vs electrical once

One of the most significant differences between optical interconnects and electrical interconnects is the speed and distance at which they can transmit data. Optical interconnects use light to transfer data, which allows for faster data transmission speeds. At the same time, they consume less power than the equivalent electrical interconnections and are more suitable for autarch or mobile solutions [5]. However, in the following solution advantages beyond that come into play.

Description of the new solution

In Electric Power Train testing for electromobility applications the parameters of the electric motor need to be investigated. Voltage measurement can be realized quite easily, current measurement needs special attention.

Current measurement is carried out by using the generated magnetic field, what has the specific advantage of being a non-contact i.e. isolated current measurement, so that the primary circuit does not need to be interrupted with the insertion of a lossy component like a shunt.

Fig. 1: Fluxgate current transducer HBK CTS200ID, manufactured by DaniSense, DK, Source: HBK

In an electric power test stand usually long cables from the current transducer are exposed to high voltage and often EMC problems. In case the new fiber optic remote probes feeding signals it into a power analyzer, this is not the case.

Fig. 2: Fiber optic remote probes for voltage (a) and current (b), for current optionally with integrated power supply (c)

The compete setup of an Electric Power Train test stand with fiber optical fusion probes and yellow optical cables to the power analyzer is shown below, allowing uncompromised safety and with shorter cable lengths to prevent reflections too [6].

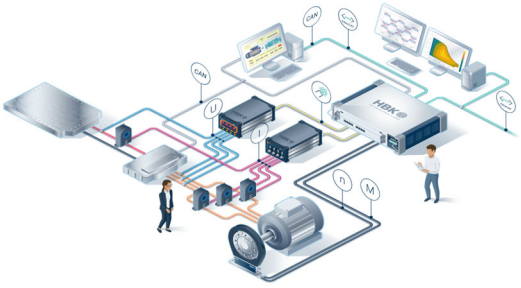

Fig. 3: Electric Power Train testing for electromobility with fiber optical fusion probes, saver and still more simple set-up

Integration into other optical solutions

The shown remote probes offer all the advantage of fiber optic technology to optimize communication ways to the power analyzer. However, their benefits can be further enhanced by combining them with other offers, complementary to other optical solutions HBK offers in the applications. So, for many years HBK offers already the HBK optical Structural health monitoring for wind energy applications [7].

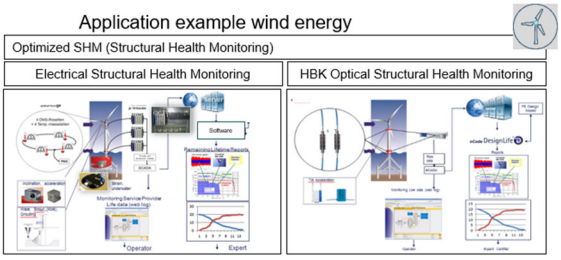

Fig. 4: HBK optical Structural health monitoring for wind energy applications

An example of a completely fiber-based measurement chain in electromobility is the newly developed pantograph optical monitoring providing optimized pick-up safety for rolling stock. High-voltage pantograph overhead-line monitoring can acquire optical sensor information in parallel to vehicle bus signals and position sensing (GNSS) allows you to build a graphical map of your infrastructure.

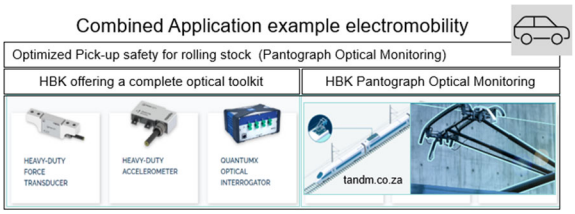

Fig. 5: HBK Optical pantograph monitoring solution for optimization in rolling stock

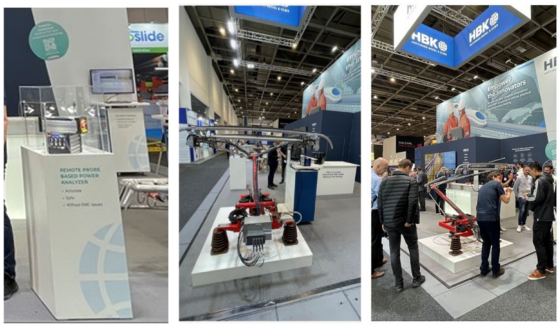

Fig. 6: Optical remote probe and optical pantograph solutions demonstrated

Both new optical solutions, the remote probes as well as a pantograph live demo have been presented at “InnoTrans 2024”- the leading international trade fair for transport technology, in September 2024 in Berlin, Germany (Fig. 6), and received great interest. We have more solutions in the pipeline and all the new solutions will be explained in detail in the oral presentation.

Conclusion

It could be shown that new optical solutions are not only superior in speed and distance, but it is over all the safety with which they are able to transmit signals despite of high voltages and harsh environments. The advantages will be presented in detail in the full paper and in the oral presentation.

References

[1] UN Climate Change Secretariat; *Agenda Expression of interest,* United Nations Climate Change Conference (COP 29) Baku, Azerbaijan (2024)

[2] Helmholtz Energy Transition Roadmap (HETR), Published by Helmholtz Energy Office; Karlsruhe Institute of Technology (KIT), Karlsruhe (2024)

[3] Schäfer, A. „Outlook regarding the growing importance of measurement in Wind energy”, *HBK Darmstadt Renewable energy*, Germany (2010)

[4] Weidinger, P. at al., Need for a traceable efficiency determination method of nacelles performed on test benches (2021), *Measurement Sensors 18(3):100159* DOI: 10.1016/j.measen.2021.100159

[5] Schäfer, A. Improved calibration and measurement capabilities-Basis of mechanical Engineering; *Congrès International de Métrologie* (*CIM),* Lyon, France (2023) DOI: 10.5162/sensoren2024/C1.1

[6] Schäfer, A.; Stock, A.; Torque as a key parameter for a better efficiency determination of electric motors and generators Conference: *XXIV IMEKO World Congress 2024*, Hamburg, Germany (2024)

[7] Schäfer, A. Efficiency determination of wind turbines by better capturing huge torque - a crucial factor of energy transition; 22. GMA/ITG-Fachtagung Sensoren und Messsysteme Nürnberg, Germany (2024) DOI: 10.5162/sensoren2024/C1.1

DOI 10.5162/SMSI2025/P17

Influence of Length on the Electromigration of Aluminum through Molybdenum disilicide Thin films

Julia Baldauf[1], Andreas T. Winzer[1], Thomas Ortlepp[1]
[1] CiS Forschungsinstitut für Mikrosensorik GmbH, Konrad-Zuse-Straße 14, 99099 Erfurt Germany, jbaldauf@cismst.de

Summary:
The effect of the length of the test structure on the electromigration of aluminum in encapsulated molybdenum disilicide layers has been investigated. Using the same measurement conditions an increase of the electromigrated volume of aluminum through the test structure with an increase of the length of the test structure could be observed.

Keywords: electromigration, molybdenum disilicide, thin film

Background and Motivation

Because of its high melting point molybdenum disilicide ($MoSi_2$) [1] is often used in heating devices such as MEMS micro heaters [2, 3]. Electromigration and diffusion of contact pad materials into $MoSi_2$ and electromigration within the $MoSi_2$ layer can cause device failure [3]. Electromigration in $MoSi_2$ has not been thoroughly been investigated. Some findings show the electromigration of aluminum through $MoSi_2$ [4 - 7] without mentioning influences of the length on the observed electromigrated volume. The length of lines under test influencing the electromigration is well known [8, 9] e.g in the Blech length or short-stripe effect [10] includes a decrease of the electromigration drift velocity with a decrease of the stripe length. During the electromigration the force onto an ion is:

$$\vec{F} = Z^* \cdot e\vec{E} - \Omega \frac{\partial \sigma_{xx}}{\partial x} \qquad (1)$$

wherein Z^* is the effective charge which includes the direction of the exchange of the momentum of the ions, e is the electron charge, Ω is the atomic volume σ_{xx} is the normal stress along the sample and x being the coordinate along the sample axis. For F=0 and therefore the mass transport J_{EM}=0 the critical product can be derived

$$(lj)_c = \frac{\Omega \, \Delta\sigma_{xx}}{eZ^*\rho} \qquad (2)$$

If the product of length and current density is bigger than $(lj)_c$ electromigration can occur.

The electromigrated volume V and the mass transport J_{EM} are related:

$$V = \Omega J_{EM} A t \qquad (3)$$

With A being the cross section of the electro migrating line and t being the time of the electromigration.

Experiments

P-doped silicon wafers with <100> orientation were used as substrates. A thin silicon oxide layer was grown, followed by the deposition of a silicon nitride layer (500 nm) and a high temperature silicon oxide layer as adhesion layer. On top of this a $MoSi_2$ layer (175 nm) was magnetron sputtered using a stochiometric target. Followed by an annealing process at 1000°C for 30 min in nitrogen atmosphere. This causes the $MoSi_2$ to be predominantly in the tetragonal phase. Different encapsulating layers were deposited using different wafers. All the $MoSi_2$ layers were contacted through an opening of the encapsulating layer with aluminum contact pads.

Tab. 1: Encapsulating layers

Thickness nm	material
20	High temperature silicon oxide (HTO)
60	High temperature silicon oxide (HTO)
25	Plasma enhanced silicon nitride (SixNy)
75	Plasma enhanced silicon nitride (SixNy)

A laser scanning microscope (Keyence VK-X200 series, objective lens CF Plan Apo 150X/ 0,95, wavelength 408nm). was used to measure the surface of the contact region of aluminum and $MoSi_2$ before and after current stressing for 7 min under ambient conditions to determine the volume of hillocks grown during the experiment.

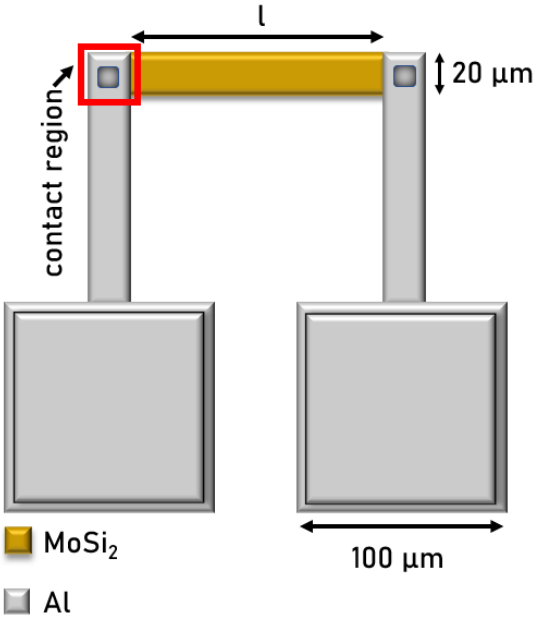

Fig. 1. Schematic of a line under test.

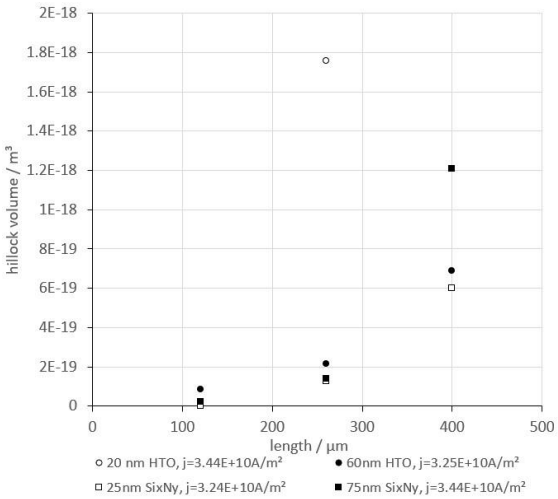

Fig. 2. Hillock volume dependent on the length of the line under test.

Similar to historic findings in other metals we observed a decrease of the electromigration with reducing the length of the line under test.

References

[1] A. B. Gokhale and G. J. Abbaschian, In Binary Alloy Phase Diagrams, vol. 2, T. B. Massalski (editor) (ASM, Ohio, 1986) pp. 1631, 2062.

[2] G. Beensh-Marchwicka, E. Prociów, and T. Berlicki, Thin film heater and thermopile built up using some silicides under thermal test, 2006 29th International Spring Seminar on Electronics Technology, St. Marienthal, 2006, pp. 475-478; doi: 10.1109/ISSE.2006.365152.

[3] Y. Ito, M. Sato, K. Wakisaka, and S. Yoshikado, Improvement of heating characteristics of molybdenum silicide thin film electrical heaters, Electrical Engineering in Japan 168 (2007),11-19; doi: 10.1002/eej.20806

[4] A. Zehe, A. Ramirez, Electromigration of Aluminium through Quasi Bamboo- Like Grain Blocked Silicide Interconnects, Crystal Research and Technology 35 (2000), 557-562; doi: 10.1002/1521-4079(200005)35:5<557::AID-CRAT557>3.0.CO;2-M

[5] A. Zehe, The stress-induced escape of migrating aluminium from silicide interconnects, Semicond. Sci. Technol. 16 (2001), 817-821; doi: 10.1088/0268-1242/16/301

[6] A. Zehe, A. Ramirez , A. Corona, Migration-forced metal extrusion from passivated molybdenum disilicide interconnects, Materials Letters 57 (2002), 55-58; doi:10.1016/S0167-577X(02)00698-5

[7] J. Baldauf, M. Schädel, Influences of the microstructure on the drift velocity of electromigrating aluminum through molybdenum disilicide thin films, SMSI 2021 Conference – Sensor and Measurement Science International (2021); doi: 10.5162/SMSI2021/B7.3

[8] C.E. Ho, W.Z. Hsieh, C.H. Yang, and P.T. Lee, Real-time study of electromigration in Sn Blech structure, Applied Surface Science 388 (2016) 339–344; doi: https://doi.org/10.1016/j.apsusc.2015.12.215

[9] Y.L. Cheng, M-K Shiau, W.Y. Chung, and Y.L. Wang, Competition of electromigration reliability in copper and nickel-silicide, Journal of The Electrochemical Society, 158 (2) H174-H177 (2011); doi: 10.1149/1.3526317

[10] E. E. Glickman, Short stripe effect and electromigration stress, Microelectronic Engineering 64 (2002) 383–389; doi: https://doi.org/10.1016/S0167-9317(02)00812-2

Acknowledgements

Parts of this research were funded by the german “Bundesministerium für Wirtschaft und Klimaschutz” (BMWK) within the project „DotIR“ (Innokom, 49MF240024).

DOI 10.5162/SMSI2025/P18

Changes in Amorphous Molybdenum Disilicide Thin Films Caused by Electrical Current Stressing

Julia Baldauf[1], Stephanie Reiß[1], Andreas T. Winzer[1], Thomas Ortlepp[1]
[1] CiS Forschungsinstitut für Mikrosensorik GmbH, Konrad-Zuse-Straße 14, 99099 Erfurt, Germany, jbaldauf@cismst.de

Summary:
We investigated the influence of electrical current on amorphous molybdenum disilicide layers. In our experiments we observed that current stressing causes a change of the layer composition of lines and aluminum electromigration from the contact pads into the top of the test structure.

Keywords: electromigration, molybdenum disilicide, amorphous, thin film, SIMS

Background and Motivation

Molybdenum disilicide ($MoSi_2$) has a high melting point [1] which causes its widespread use in heating devices such as MEMS micro hotplates [2, 3]. Electromigration and diffusion of metals from contact pads into $MoSi_2$ layers and electromigration within a $MoSi_2$ layer have been previously observed [3]. Electromigration in $MoSi_2$ thin films has not yet been investigated in detail. Some findings of electromigration in $MoSi_2$ show the electromigration of aluminum through $MoSi_2$ [4 - 7]. In this study we report findings of electromigration experiments conducted on amorphous lines under test.

Experiments

P-doped silicon wafers with <100> orientation were used as substrates. A thin silicon oxide layer (70nm) was grown using a dry oxidation process with HCl, followed by the deposition of a silicon nitride layer (500 nm) with reduced mechanical stress and a high temperature silicon oxide layer (40 nm) as adhesion layer. Finally, a $MoSi_2$ layer (60 nm) was magnetron sputtered on top of the dielectric layers. The annealing of the $MoSi_2$ layer was performed at 500°C for 60 min in a hydrogen atmosphere, causing the layer to be amorphous. A polycrystalline $MoSi_2$ layer was obtained via heat treatment in nitrogen atmosphere at 500°C for 60 min followed by a treatment at 900°C for 120min. The contact pads were made of aluminum.

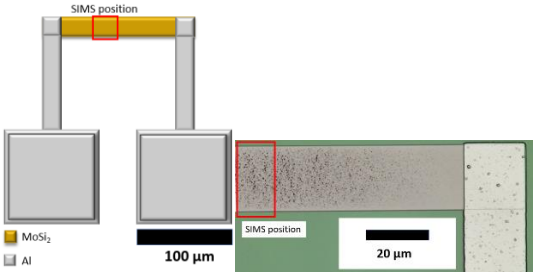

Fig. 1. Schematic of the line under test and light microscopy image of line after test.

The test structure shown in Fig. 1 was stressed with 3.47E+9 A/m² for 7 min under ambient air. The grain structure influences the electromigration [6, 7]. In amorphous $MoSi_2$ the electromigration may exceed the electromigration in polycrystalline lines stressed under higher current densities. Laser scanning microscopy (Keyence VK-X200 series, objective lens CF Plan Apo 150X/ 0,95, wavelength 408 nm) was used to measure the surface of the contact of $MoSi_2$ to aluminum before and after stressing and to determine the volume of the hillocks which is the deviation.

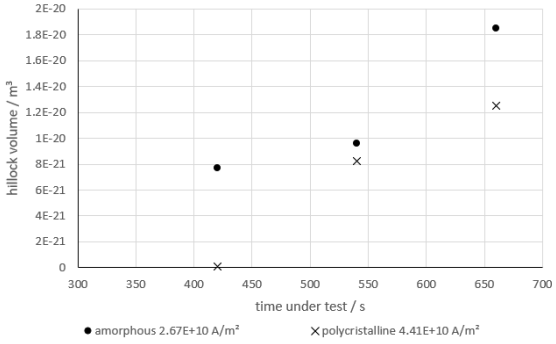

Fig. 2. Comparison of the volume of electromigrated hillocks of polycrystalline and amorphous $MoSi_2$ lines.

Secondary ion mass spectrometry (IMS7f auto by Cameca) was employed to investigate any changes of the test structure caused by stress. The systematic error for signal detection if repeated under same measurement conditions on a homogenous sample is less than 2%.

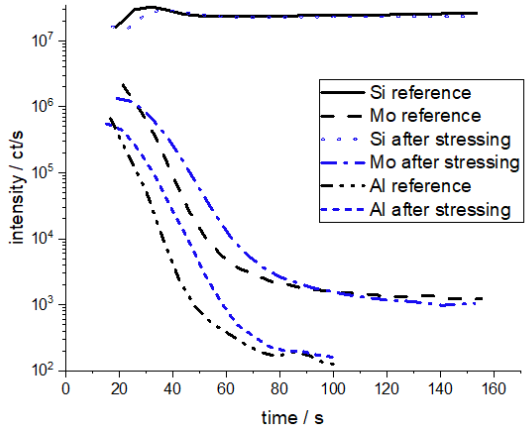

Fig. 3. Intensity of molybdenum, silicon, and aluminum detected via SIMS in ct/s over time in s.

A thin gold film (38 nm) was applied to avoid charging during SIMS analysis. Because of artefacts and the time required to reach the sputter equilibrium, the recorded element profiles of the first ~12 s do not reflect the actual depth profiles and are therefore not shown in the following data graphs.

Results

Fig. 3 shows the measured SIMS profiles of the $MoSi_2$ layer before (reference) and after stress. The Mo profile of the stressed layer is broadened and decreased in intensity at the surface compared to the one of the reference sample, pointing to a change in the contribution of Mo and hence, the Mo/Si ratio in the surface near region due to stress. In the recorded Al profiles, it can be seen, that after stress application the penetration depth of Al in the $MoSi_2$ is increased while its signal intensity at the surface itself remains unchanged, hinting to an accumulation of Al in the $MoSi_2$ layer during stress due to electromigration from the Al contact pads.

Possible falsifications of the SIMS profiles could be caused by inhomogeneities in the chemical composition of the $MoSi_2$ layers that could arise during their production process or by the small diameter (20 µm) of the lines that could lead to SIMS measurements including areas outside of the line of interest. The chosen raster size, apertures as well as egating for the SIMS measurements make the occurance of the later mentioned error source unlikely.

References

[1] A. B. Gokhale and G. J. Abbaschian, In Binary Alloy Phase Diagrams, vol. 2, T. B. Massalski (editor) (ASM, Ohio, 1986) pp. 1631, 2062.

[2] G. Beensh-Marchwicka, E. Prociów, and T. Berlicki, Thin film heater and thermopile built up using some silicides under thermal test, 2006 29th International Spring Seminar on Electronics Technology, St. Marienthal, (2006), pp. 475-478; doi: 10.1109/ISSE.2006.365152.

[3] Y. Ito, M. Sato, K. Wakisaka, and S. Yoshikado, Improvement of heating characteristics of molybdenum silicide thin film electrical heaters, Electrical Engineering in Japan 168 (2007),11-19; doi: 10.1002/eej.20806

[4] A. Zehe, A. Ramirez, Electromigration of Aluminium through Quasi Bamboo- Like Grain Blocked Silicide Interconnects, Crystal Research and Technology 35 (2000), 557-562; doi: 10.1002/1521-4079(200005)35:5<557::AID-CRAT557>3.0.CO;2-M

[5] A. Zehe, The stress-induced escape of migrating aluminium from silicide interconnects, Semiconductor Science and Technology 16 (2001), 817-821; doi: 10.1088/0268-1242/16/301

[6] A. Zehe, A. Ramirez , A. Corona, Migration-forced metal extrusion from passivated molybdenum disilicide interconnects, Materials Letters 57 (2002), 55-58; doi:10.1016/S0167-577X(02)00698-5

[7] J. Baldauf, M. Schädel, Influences of the microstructure on the drift velocity of electromigrating aluminum through molybdenum disilicide thin films, SMSI 2021 Conference – Sensor and Measurement Science International (2021); doi: 10.5162/SMSI2021/B7.3

Acknowledgements

Parts of this research were funded by the german “Bundesministerium für Wirtschaft und Klimaschutz” (BMWK) within the project „DotIR“ (Innokom, 49MF240024).

DOI 10.5162/SMSI2025/P19

Benchmarking Robot and Cobot Performance for an Assembly Application

Markus Gapp[1], Anke Fischer-Janzen[1], David Pfister[1], Thomas M. Wendt[1], Stefan J. Rupitsch[2]
[1] University Offenburg, Badstrasse 24, 77652 Offenburg, Germany,
[2] University Freiburg, Institut für Mikrosystemtechnik – IMTEK, Georges-Köhler-Allee 201, D-79110 Freiburg, Germany
markus.gapp@hs-offenburg.de

Summary
Over the past decade, the popularity of cobots (collaborative robots) has grown, largely due to their operator-friendly usage. When selecting a cobot or robot for a specific application, it is essential to consider which model best aligns with the desired process. The objective of this work is to introduce a method for evaluating the three-dimensional position performance of a given process to identify the optimal technical solution.

Keywords: Cobot, Robot, 3D-accuracy, Performance, Optical metrology

Introduction

The evaluation of robot performance must be conducted according to the ISO 9283:1998 standard [1]. Two essential parameters are absolute accuracy and repeatability, both in terms of pose and path. Absolute accuracy will be required when using offline programs or when programming a path. For assembly tasks, repeatability is more important to reliably move to any required process position.

There are ongoing efforts to optimize the evaluation of repeatability of pose (RP) especially for cobots according to their kinematic structure as outlined in [2]. The definition of ISO 9283 allows flexibility in performing repeatability measurements. The aim of this study is to focus on the issue of 3D-pose repeatability using a basic and inexpensive setup of high-precision standard industrial sensors.

Method and system setup

To compare RP, measurements were performed on a 6-DoF cobot (Fanuc CRX10iA) and a 6-DoF robot (KUKA KR16). Unlike [3], both robots were programmed to move from the upper ISO position to the centre of the robot's working range. This reflects our application of picking parts in a defined position while precise positioning. In [4], challenges were found in the precision of pose repeatability measurements. This setup was adapted accordingly. The sensor system was expanded by adding a 1D-laser sensor (OD2000) that measures the Y-coordinate in addition to the laser triangulation sensor (ECCO75.100) measuring X- and Z-coordinates for the purpose of ascertaining the third dimension. The setup is shown in Fig. 1.

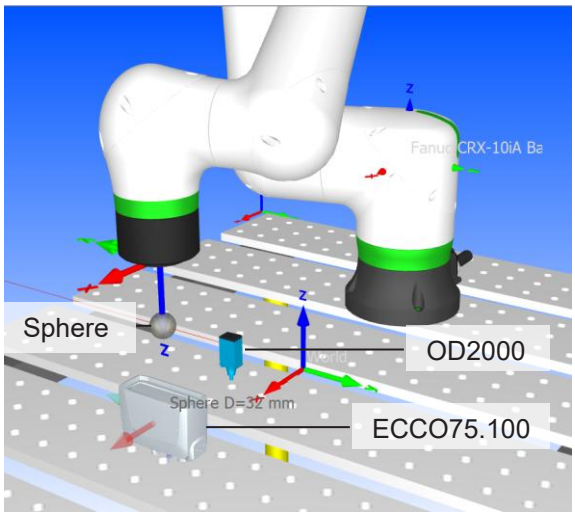

Fig. 1. Robot with sphere assembled at the flange and two laser sensors to detect the 3D-position of the sphere

The measured position of the sphere's centre was utilised for the robot position calculation. In order to facilitate a comparison of the measurement data, the speed and trajectory of the cobot and robot were unified, as required in [1]. The calculation of RP was performed in accordance with [1], utilizing $\bar{l}$ as the 3D mean position and S as the standard deviation.

$$RP = \bar{l} + 3S \qquad (1)$$

Results

In the data sheet, the repeatability of the industrial robot is specified as ±0.05 mm. The repeatability achieved with our system was 0.027 mm (S ±0.006 mm). In comparison to the reported repeatability of the cobot, which was found to be ±0.04 mm, we were able to determine a value of 0.037 mm (S ±0.008 mm).

Fig. 2 shows 30 measurements of the respective axes. The setup was aligned with the axes of the robot's base coordinate system to avoid possible error propagation that might occur during a required coordinate transformation.

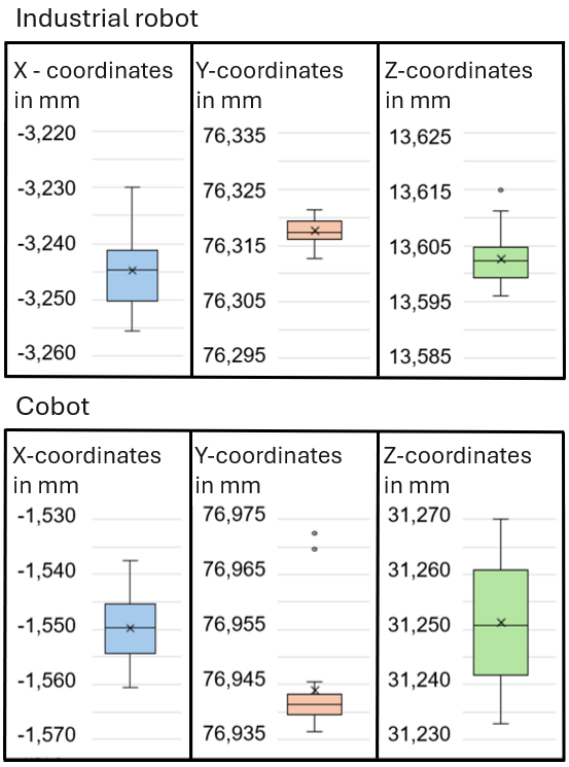

Fig. 2. Distance to sensors over 30 measurements shown in X-, Y- and Z-coordinates in mm. The upper boxplots show the values of the industrial robot and the lower boxplots those of the cobot.

Discussion

In our work, an easy to integrate process for evaluating the 3D position performance for our application has been demonstrated. Both robots are suitable for this application as they achieve the minimum tolerance. Although the test revealed that the industrial robot was more precise, we chose the cobot for our application based on the necessity to collaborate with humans.

The supposedly better repeatability of the cobots [5] was refuted in our test setup. This might indicate more restrictive requirements for purely industrial applications.

It is noticeable that the measured values of the Z-axis of the industrial robot show a significantly lower scatter. This could be due to the control structure of the robot's axes. Looking at the measured values of the Y-axis, there are clear outliers for the cobot. The reflective sphere's surface could also be a possible cause in addition. The potential impact of external factors, e.g. surface reflections, sphere smoothness, and varying loads at the robot flange, should be considered.

It is well known that accuracy critical processes like fitting are easier to realize with a robot. Therefore, additional values to determine the absolute accuracy and repeatability are important depending on the process in question. Table 1 provides an overview of the most important criteria of ISO 9283, which should be focused in further studies.

Tab. 1: Criteria of ISO 9283 as far as absolute accuracy and repeatability are concerned

	Absolute accuracy	Repeatability
Pose	x	x
Path	x	x
Distance	x	x
Multidirectional		x
Exchangeability	x	
Drift of pose	x	x

References

[1] ISO 9283:1998 Manipulating industrial robots – performance criteria and related test methods, 1998

[2] M. Hu, H. Wang, X. Pan, Y. Tian, Optimal synthesis of pose repeatability for collaborative robots based on the ISO 9283 standard, *Industrial Robot* 46(6), 812–818 (2019), doi: 10.1108/IR-03-2019-0056

[3] M. Vocetka, R. Hunady, M. Hagara, Z. Bobovský, T. Kot, V. Krys, Influence of the Approach Direction on the Repeatability of an Industrial Robot, *Appl. Sci.* (2020), doi:10.3390/app10238714

[4] T. M. Wendt, M. Gapp, A. Fischer, Innovative and cost-effective Measurement Setup to determine Robot Accuracy, *SMSI 2023 (2023)*; doi: 10.5162/SMSI2023/D4.4

[5] P. Amiri, M. Müller, M. Southgate, T. Theoridis, G. Wei, M. Rivhards-Brown, W. Holderbaum, A Statistical Analysis of Commercial Articulated Industrial Robots and Cobots, *J. Manuf. Mater. Process* 8(5), (2024); doi: 10.21203/rs.3.rs-3946319/v1

DOI 10.5162/SMSI2025/P20

Practical Realization of Johnson's Noise Thermometer

Jan Martinek[1,2], Václav Hortvík[1], Petr Klapetek[1]
[1] Czech Metrology Institute, Okružní 31, Brno, Czech republic
[2] Brno University of Technology, Žižkova 17, Brno, Czech republic
jmartinek@cmi.gov.cz

Summary: A practical realization of a thermometer utilizing Johnson's noise is presented. At 2019 new definition of SI units was adopted an Kelvin is not based on triple point of water as it used to be before. Boltzmann constant has a fixed value instead from which Kelvin could be derived in various ways.

Keywords: Johnson's noise thermometry, thermal noise, correlation, amplifier noise, electromagnetic interference, liquid nitrogen temperature

Introduction

The goal of the project was to construct a two-channel noise thermometer. This is a thermometer that must be calibrated using a single temperature point (e.g., the triple point of water), and thereafter, it is capable of measuring any other temperature. The range is limited only by the thermal endurance of the materials used, which can easily be selected so that the thermometer operates reliably from any cryogenic temperatures up to approximately 200 ℃ or even higher.

The temperature measurement is uniquely determined by fundamental physical principles, and thus any temperature point can be verified, which makes the noise thermometer well-suited for use in metrology.

The basic phenomenon utilized is the thermal noise of a resistor, which was first described in 1926 by John B. Johnson and further clarified in 1928 by Harry Nyquist. Ignoring the details, we can say that the principle is quite simple and easily applicable.

From the described properties, it might seem that the noise thermometer has excellent characteristics, its principle has been known for nearly a hundred years, and one might expect it to be widely adopted. However, the opposite is true. The noise thermometer is rarely used, almost exclusively in specialized applications—such as measuring the Boltzmann constant. In industrial practice, noise thermometers are a rare exception, found only in certain cryogenic temperature measurements.

The reason for the limited use of noise thermometers could be their slow response time, which is their main disadvantage. In principle, measurements need to be taken over an extended period to gather enough data. The uncertainty in the measured temperature depends on the measurement time, so measuring a single temperature can take several hours, which is a significant barrier for industrial applications. However, in metrology, long measurement times are quite common.

A noise thermometer is primarily an extremely sensitive device that cannot function properly if exposed to external electromagnetic interference. The measured values are so small that the main challenge in its implementation is designing the best possible shielding. As demonstrated during the research, mechanical vibrations are also highly detrimental.

Theory

A noise thermometer measures temperature based on the fact that the voltage noise of a resistor is proportional to the thermodynamic temperature T. Specifically, the average power on a resistor, resulting from the chaotic motion of electrons, can be expressed as:

$$P = 4kT\Delta f$$

where Δf is the bandwidth, and k is the Boltzmann constant, $k = 1.380649 \times 10^{-23}$ J/K. Electrical power can be expressed using the resistance R and voltage U, with $P = U^2/R$, which, together with the previous equation, leads to

$$U_{\mathrm{eff}} = \sqrt{4kTR\Delta f}$$

where U_{eff} is the effective value of the resistor's noise voltage.

For a resistor of 1 kΩ at a room temperature of around 300 K, and a measuring device operating with a bandwidth of 125 kHz, the effective noise voltage is approximately 1.29 microvolts. This voltage, after amplification, is supplied to the input of a measuring card with a range of ± 5 V. The amplifier gain should be such that the measuring range is optimally utilized without exceeding limit values. The peak value is significantly higher than the effective value. Assuming a factor of ten, this results in an exceedance in a statistically negligible number of cases. Then,

the amplifier gain is calculated as $A = 387597$. If we require measurements at higher temperatures than 300 K, the gain must be lower.

Two channel measurement

Every amplifier is a source of noise, which adds to the resistor's noise. In further processing, it is no longer possible to distinguish the level of noise produced solely by the resistor. Therefore, a dual-channel variant was assembled, allowing the resistor noise to be measured independently of the amplifiers, using two independent amplifiers. The principle relies on the fact that amplifier noises are completely independent, while the resistor noise affects both amplifiers simultaneously. It can be proven that the product of both channels has a mean value proportional only to the resistor noise. Based on this principle, a correlator (see Fig. 1) was programmed to calculate the mean value of the product of both channels, process blocks of digitized data, and output a value theoretically proportional to the thermodynamic temperature. Using two channels offers

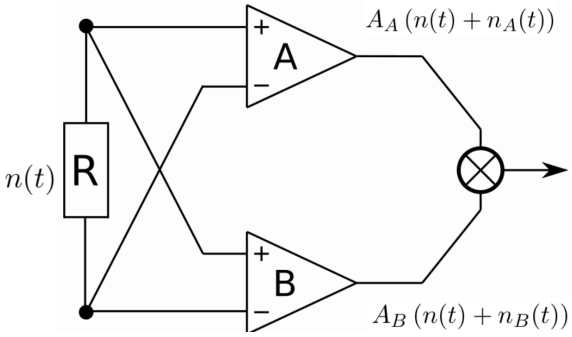

Fig. 1: A correlator made of two independent amplifiers

significant advantages. Not only is the correlator's response linear with respect to the resistor's temperature, but the line also starts from zero. Therefore, only a single temperature point is needed to calibrate the entire setup. Moreover, the temperature of the amplifiers does not need to be controlled, as their noise — dependent on the electronics' temperature — cancels out.

Results

The setup needs to be calibrated using one fixed temperature point. For this purpose an ice bath has been used to get proportionality constant. Afted this step the sensing resistor was immersed in liquid nitrogen with table value of temperature $-195.8°$ C. The response of the thermometer was monitored and the lowest measured stable value was 180 mK lower than the correct value, see Fig. 2.

Fig. 2: The time dependence of the measured temperature of liquid nitrogen shows a stable minimum temperature of $-195.98°$ C.

References

[1] Johnson, J. (1928). "Thermal Agitation of Electricity in Conductors". Physical Review. 32 (97): 97–109

[2] Nyquist, H. (1928). "Thermal Agitation of Electric Charge in Conductors". Physical Review. 32 (110): 110–113.

[3] Fischer, J; Fellmuth, B; Gaiser, C; Zandt, T; Pitre, L; Sparasci, F; Plimmer, M D; de Podesta, M; Underwood, R; Sutton, G; Machin, G; Gavioso, R M; Ripa, D Madonna; Steur, P P M; Qu, J (2018). "The Boltzmann project". Metrologia. 55 (2)

Conclusion

A practical implementation of a Johnson noise thermometer has been presented. Despite significant challenges related to shielding and overall noise immunity, results surpassing those of industry-standard Class AA platinum thermometers (Pt-100) have been achieved. Not only is the uncertainty lower across most temperature ranges, but the main advantage is that the thermometer's principle is derived directly from the Boltzmann constant, aligning with the redefined Kelvin in the SI system since 2019.

Acknowledgements

This work was supported by project JRP-i17 ThermoTRACE which has received funding from the European Partnership on Metrology, co-financed from the European Union's Horizon Europe Research and Innovation Programme and by the Participating States and by Institutional Subsidy for Long-Term Conceptual Development of a Research Organization granted to the Czech Metrology Institute by the Ministry of Industry and Trade of the Czech Republic.

DOI 10.5162/SMSI2025/P21

Elastically stable tensile force sensors for belt tension monitoring

A. Cyriax, Th. Frank, St. Hermann, A. Grün
CiS Forschungsinstitut für Mikrosensorik, Konrad-Zuse-Straße 14, 99099 Erfurt, Deutschland
tfrank@cismst.de

Summary:
In drive technology, timing belts and transmission belts are used to transmit large forces at large distances. Optimal power transmission depends on the belt tension. Consistently perfect belt tension increases service life and reduces wear. This ensures consistent quality and technical safety in the respective application. This article describes a silicon strain sensor and the necessary connection technology to enable continuous determination of the belt tension.

Keywords: silicon, piezoresistive, strain gauges, transmission belts, belt tension, force tensions

In drive technology, timing belts and transmission belts are used to transmit large forces at large distances. In order to withstand the operating conditions and force loads, the belts are combined with tension members made of steel cord or Kevlar. These run helically in the belt. In order to be able to detect the various changes in force acting on the belt, the sensor must be integrated on or in these tension members.

Miniaturized silicon-based strain sensors are used for the sensor, Fig. 1 left. Due to its small geometric dimensions of 500 µm x 500 µm, the strain sensor can be integrated into flexible arrangements. Based on the measuring principle and the small chip thickness, the smallest changes in force such as strain and tension can be detected. This makes them ideal for this application.

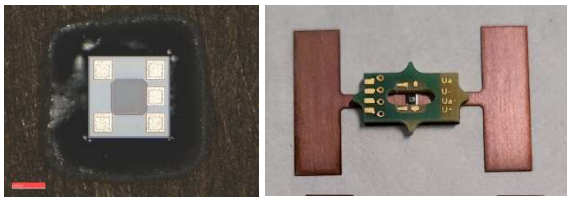

Fig. 1. Strain sensor (left) joined to mounting bracket (right)

To permanently determine the belt tension, the sensors must be directly coupled to the tension member. The coupling must completely enclose the tension member at the respective points. Fig. 2 shows the result of the simulation for coupling to the tension member.

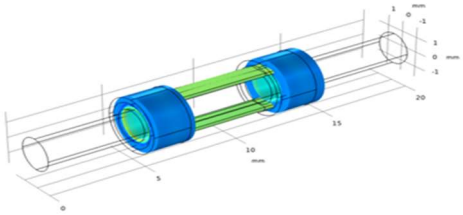

Fig. 2. Simulation of the coupling of the sensor system via mounting bracket to a tension member

H-shaped mounting brackets made of, for example, 1.4310, 1.4542, 1.4301 V2A are used for this, Fig. 1 right. The free ends are used for fastening to the tension member. Reinforcement with an adapted press sleeve is provided. For tension members made of steel cord, the two ends of the mounting bracket and the compression sleeve are optimally joined to the tension member using the laser welding process. In the case of tension members made of Kevlar, they are closed using a crimping process. Fig. 3 shows both variants.

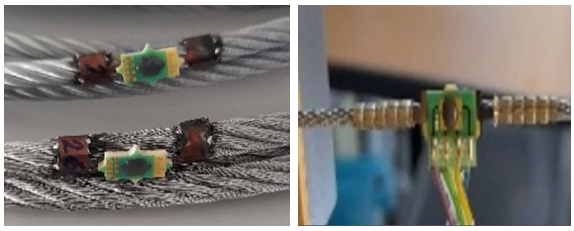

Fig. 3. Coupling to tension members with laser welding (left) and crimping (right)

This ensures that both joints are in contact with the same wires or threads. This significantly minimizes possible measurement errors.

Depending on the diameter of the existing tension members, different mounting brackets and correspondingly designed circuit boards are used for electrical contacting. The strain sensors are joined to the sensitive area of the mounting carriers using the glass frit method. Depending on the variant, the sensor and the contacting areas are encapsulated or covered to protect them from external influences.

The respective variants of the tensile force sensors were characterized according to the planned areas of application and showed positive results.

Fig. 4 shows the maximum change in the electrical sensor signal from the zero signal in relation to the measuring span of the sensors as a function of the temperature profile -10°C, +30°C, +85°C, +30°C and -10°C. With the exception of one setup variant, all show the same expected drift behavior.

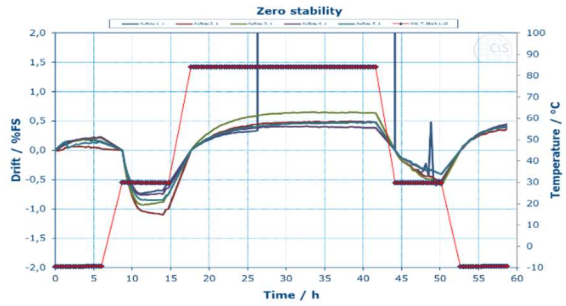

Fig. 3. electrical stability test at T = -10°C to +85°C

Long-term measurements were carried out at T = 25 °C, T = 85 °C, relative humidity <= 40 %, time = 168 h in order to rule out possible influencing factors due to the structure. Fig. 4 and Fig. 5 show that there is only a certain dependence on the relative humidity (red characteristic curve) at low temperatures (T=25°C, blue characteristic curve) due to the PCB material and the protective encapsulation used. Due to the planned application, integration of the sensor system into the transmission belt, this influence is no longer decisive later on. The integration is hermetically sealed. As a result, good long-term stability could also be demonstrated.

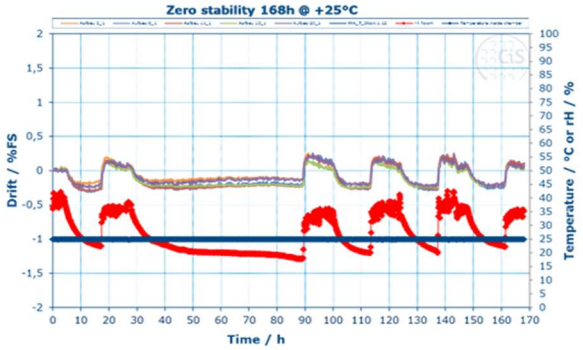

Fig. 4. Long-term stability measurement at T=+25°C

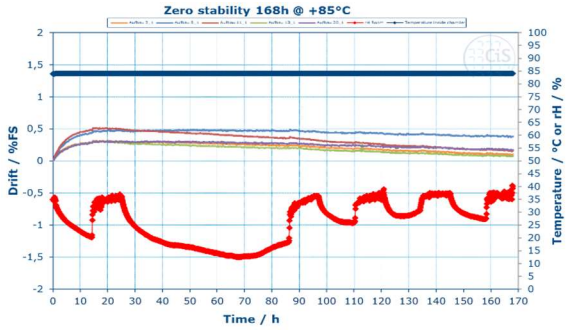

Fig. 5. Long-term stability measurement at T=+85°C

With the positive characterizations, the planned measurement deviation of 1 - 2 %FS at T = 25 °C and of 2 - 5 %FS in the range -10°C to +80°C for the mounted tensile force sensors could be successfully demonstrated.

The tension members (steel cord, Kevlar) were tested with the integrated tensile force sensors using various cable tensioning devices. For example, a force effect of up to 500N on a 2mm thick stainless-steel cord was detected for the tensile force sensor in Fig. 3 on the right, as shown in Fig. 6. The still low hysteresis is due to the crimp connection.

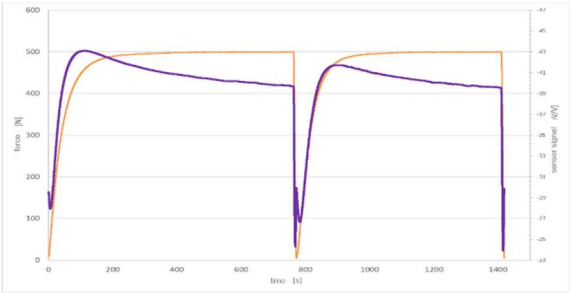

Fig. 6. Characteristic curves of tensile test up to 500N, force N on stainless steel cord (orange), sensor signal mV/V (purple)

This results in a signal change of 1mV/V per 50N of force applied for this cord variant. This corresponds to a sensitivity of 0.02 mV/V/N. And is therefore within the desired parameter range.

The tensile force sensor is used to monitor belt tension in drive technology systems, for example in sawing, cutting, milling and pointing machines, in packaging systems for conveyor belts or at test stations for table positioning. This allows maintenance intervals to be planned precisely, material fatigue to be detected at an early stage and unplanned downtime to be avoided.

Sources:

[1] Verwendung von Siliziumdehnungssensoren für makroskopische Prüfkörper, Th. Frank, St. Hermann, A. Grün, D. Hanig, M. Kermann, M. Hintz, A. Cyriax, R. Röder, U. Krieger, MST Kongress 2023, Dresden, 23.-25.10.2023

DOI 10.5162/SMSI2025/P22

Optimized hardness testing: Precise force application and measurement at low forces

Th. Frank[1], St. Hermann[1], A. Grün[1], H. Wünscher[1], P. Beisel[2]
CiS Forschungsinstitut für Mikrosensorik, Konrad-Zuse-Straße 14, 99099 Erfurt, Germany
KB Prüftechnik GmbH, Im Weichlingsgarten 10b, 67126 Hochdorf-Assenheim, Germany
tfrank@cismst.de

Summary:
In hardness testing, an indenter is pressed into the workpiece with a defined force to determine its hardness. It is important that the force builds up without shocks or vibrations and without overshoots. The ideal test sequence comprises four phases: approach without force contact, continuous application of force, holding the test force and finally withdrawal. The precise implementation of the test force is particularly demanding with small forces and requires sensitive force measuring cells and controls. The time of contact is critical, as too fast approaches can distort the measurement. With small forces, the approach speed must therefore be reduced. Distance sensors are used for optimization. Improvements include sensitive Si strain gauges and a two-stage spring for the indenter.

During hardness testing, an indenter is pressed into the workpiece to be tested with a defined force, the hardness of which is to be determined. The force applied during the penetration process should be free of shocks and vibrations and without overshoot. The idealized force curve during a test can essentially be divided into four phases (see Figure 1).

- Approach: the indenter approaches the test object; there is no force contact
- Application of force: after the force contact, the force is continuously increased so that the specified test force is reached after a specified time
- Stationary holding of the test force: the test force acts for a specified period of time
- Retraction of the indenter: the test force is reduced until there is no longer any force contact and the indenter is removed from the sample

The realization of the test forces, especially in the small and smallest force range, places high demands on the hardness test. There are various options here, using weights that are placed on in a controlled manner, hydraulically or by electric motor. The electric motor implementation of the test forces is widespread nowadays, as it allows very high precision with great flexibility and a wide range of test forces used - an almost mandatory requirement for testing machines. The force is applied in a closed control loop, which requires a force measuring cell to feed back the effective force. The smaller the test forces to be applied, the more delicate the force measuring cell must be, which increases its sensitivity to environmental influences. The aim is to create very rigid and very sensitive measuring cells.

Limits are set by the required penetration tools, which are attached directly to the force transducer. The most critical moment in the application of force is the time at which the indenter tip hits the DUT. If the approach speed is too high, the starting point on the surface of the test object immediately leads to a rapid increase in force, which would impair the entire measurement or render it unusable and for this reason must be checked as quickly as possible. However, the distance between the indenter tip and the test object surface is usually not known with sufficient accuracy in currently available systems, which is why the approach of the indenter must be slower the smaller the desired test force is. Currently available systems usually scan the surface using a tactile system to measure hardness and then detect the distance from the sample surface to the indenter tip using depth or length measurements on the test object. The approach takes a very long time when small test forces between 1 gf and 20 gf are implemented (approach speed in the last 100 µm above the test object approx. 1 µm/s).

In order to achieve a reliable assessment of the expected force contact and the associated

increase in force, the approach process must be examined using suitable distance sensors and included in the measurement so that the remaining distance between the indenter and the DUT, where the measurement is particularly slow, can be shortened from 100 µm to around 10 µm and the entire measurement can be accelerated. This not only increases the measurement and movement accuracy, but the distance detection between the indenter and the workpiece surface also optimizes the autofocus.

Some adjustments are made to optimize the process. Highly sensitive Si strain gauges with low temperature sensitivity of the measuring range. A two-stage spring for the indenter and a displacement measuring system for detecting the workpiece surface.

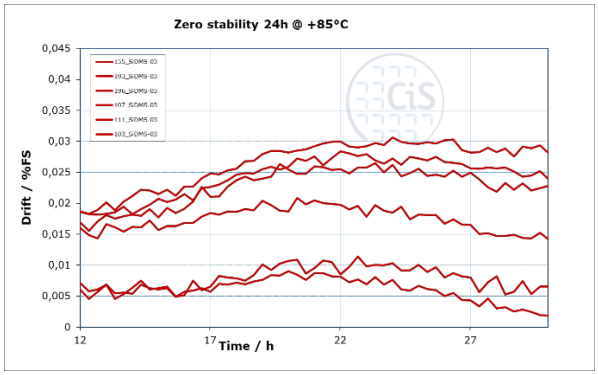

Fig. 1. Zero point stability, drift, at 85°C and 24h in % Full Scale Output (FS)

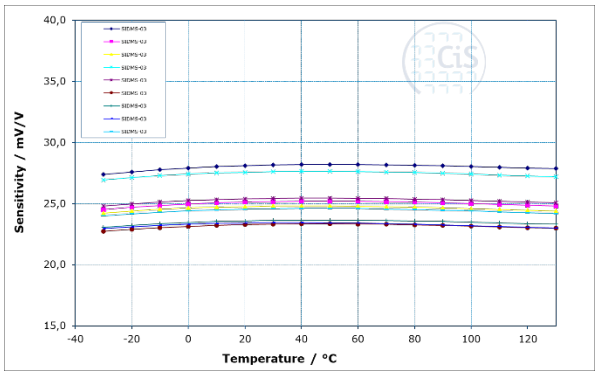

Fig. 2. Temperature dependence of the measuring range or sensitivity

The basis is a two-stage force sensor. This consists of two pairs of parallel springs, which are rotated by 180°, so that the unwanted movement on the side is compensated. In the first section, up to approx. 50 N, or 0.12 mm, only the outer springs work. After this, the inner, stiffer springs are connected in parallel. For this purpose, a drive pin is integrated into the spring. Fig. 1 and 2 show the characteristics of the system, the zero-point stability, 24 hours at 85°C and the temperature dependence of the measuring range.

Due to the very low temperature dependence of the measuring range, compensation of the temperature in the working area is not necessary. Fig. 3 shows the two-stage spring with attached Si-Strain Gauge without PCB. The characteristic curve of the spring is shown in Fig. 4. The distance sensors will be described later.

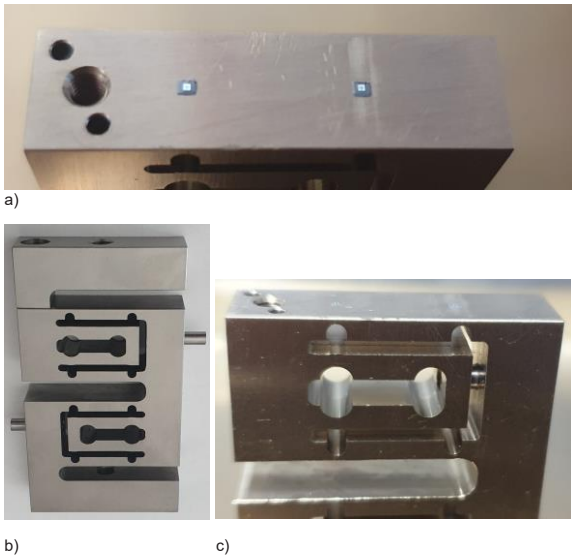

*Fig. 3. a) Assembled Si-Strain Gauge with glass frit, b) Two-stage spring body, 60 mm*30 mm*10 mm, stainless steel 1.4542 c) Focus on the inner parallel spring and the driving pin.*

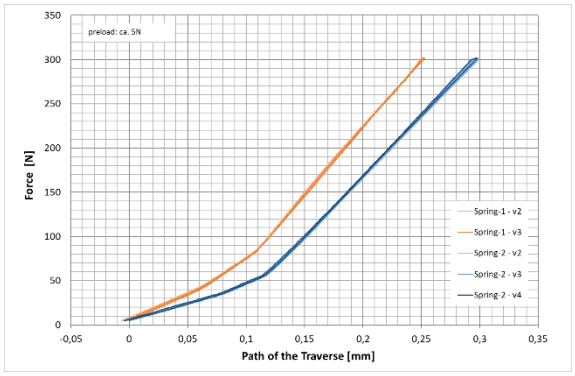

Fig. 4. Characteristic curve of the two-stage spring, blue line: softer inner spring

Literatur

[1] Thomas Frank, Stefan Hermann, André Grün, Danny Hanig, Manuel Kermann, Michael Hintz, Andrea Cyriax, Ralf Röder, Uwe Krieger, "Verwendung von Siliziumdehnungssensoren für makroskopische Prüfkörper", 10. MikroSystemTechnik Kongress 2023, Dresden, 23.-25.10.2023

DOI 10.5162/SMSI2025/P23

Signal evaluation of force sensors based on silicon strain gauges using artificial neural networks

Th. Frank, St. Hermann
CiS Forschungsinstitut für Mikrosensorik, Konrad-Zuse-Straße 14, 99099 Erfurt, Deutschland
tfrank@cismst.de

Summary:
Artificial neural networks (ANN) are used to evaluate signals from complex piezoresistive force sensors. The neural network is integrated into a microcontroller.

Silicon strain gauges are widely used elements for setting up force measurement. Their high sensitivity and precision make them ideal for applications where precise measurements are required. These strain gauges are particularly suitable for multi-component force transducers. These strain gauges contain a full bridge and are preferably joined to the spring body by glass frit bonding. These are electrically contacted by wire bonding. A description of the process can be found in [1]

In conventional multi-component force transducers, springs are available for each force direction. The aim of the design is for the springs to be designed in such a way that there is only minimal crosstalk between the force directions. Our own analysis of various force transducers shows that the force directions are better separated in a larger installation space. Crosstalk increases with compact force transducers.

For some sensors, the classic signal processing methods are not successful or are very complex. However, these can be successfully trained by using neural networks. The target values are provided by the test equipment during calibration. The training data is provided by the sensors, the signals from the strain gauges and the associated temperature sensors. This procedure is illustrated using two selected examples. Initial tests were carried out with an artificial neural network using the Python library "tensorflow.keras". These tests showed that there are applications in which the use of a neural network is advantageous compared to classic signal processing. This is particularly the case with multiple input variables and a strong hysteresis as in the examples.

Fig. 1 shows the selected sensors. Fig. 2 and Fig. 4 show the real signals under load. The hysteresis is clearly visible. Fig. 3 and Fig. 6 show the comparison of the prediction and the current value. Fig. 5 shows the absolute error of the evaluation for the ring force sensor. The result for the ring force sensor is better because significantly more data was available

Compact ring force sensor with 3 Si strain gauges to compensate for oblique forces. The ring force sensor is used to determine the screw preload force. The tolerance for parallelism in clamped components is 2°. This leads to an uneven load and an incorrect measurement result. This is partially compensated for by the 3 strain gauges, the average value from all 3 strain gauges is used. Due to non-linear relationships and non-identical sensitivity, this solution is not very precise. The characteristic curve also has a friction-related hysteresis. The comparison of the actual values shows a small error. In particular, the hysteresis was well compensated, Fig. 6.

3D force sensor, this has 4 Si strain gauges for 3 force directions. Calibration is extremely complex and not very precise either, as the crosstalk is very pronounced. In the Z direction, all Si strain gauges are loaded in the same direction, for the X or Y direction, the two corresponding Si strain gauges opposite are loaded in opposite directions. A force in the X or Y direction causes a moment around the Y or X axis. This leads to this load. When loaded in the X direction, the sensors in the Y direction are ideally not loaded, and the same applies to force in the Y direction. However, this is not the case. Due to the manufacturing tolerances, the ideal values are not achieved. Fig. 3 shows the characteristic curves when loaded in the Z direction. The slope of the four curves is identical, a friction-related hysteresis can be seen and the offset is different. The comparison of the predicted and actual values is very good despite the simple configuration of the

artificial neural network and the mechanical setup, Fig. 5.

Several different networks are investigated, especially for the data subject to hysteresis. To create a neural network that can handle a sensor with friction-related hysteresis, it must be taken into account that the sensor values depend not only on the current input values, but also on the previous direction and possibly on the previous values. This requires some form of memory or state awareness in the model.

One way to model these hysteresis effects is to use recurrent neural networks (RNNs) or long short-term memory networks (LSTMs). These networks are specifically designed to take sequence information and past states into account.

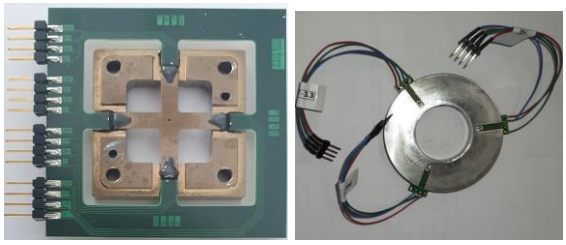

Fig. 1. Left: 3D force sensor, right: a compact ring force sensor

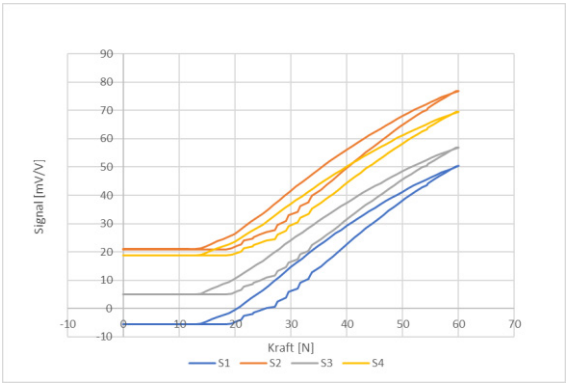

Fig. 2. Signals of the 4 strain gauges under load

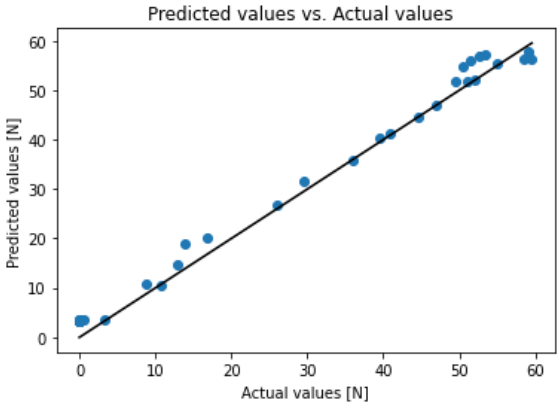

Fig. 3. The ANN of the 3D force sensor after training

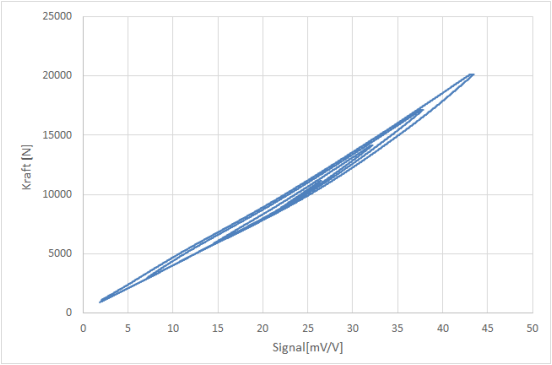

Fig. 4. Signal of the ring force sensor under load, sum of all 3 strain gauges

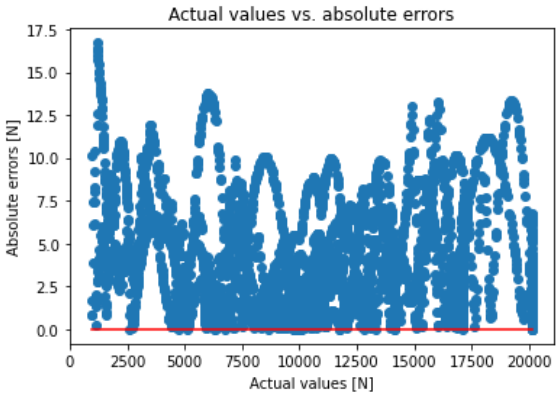

Fig. 5. The ring force sensor, absolute errors

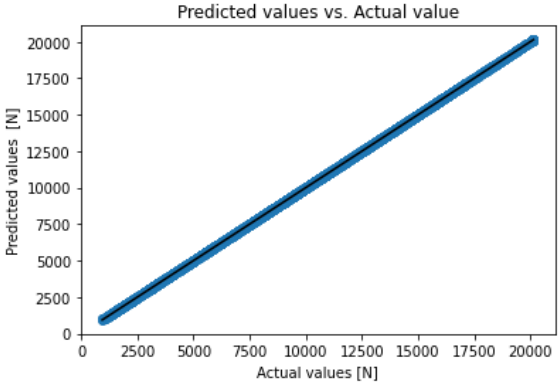

Fig. 6. The ANN of the ring force sensor after training

The last step is to implement the network on a chip for direct signal processing. Preferably, the final training takes place on the fully constructed sensor system. This has the advantage that all electronic components and their errors are incorporated into the parameters of the network.

References

[1] Thomas Frank, Stefan Hermann, André Grün, Danny Hanig, Manuel Kermann, Michael Hintz, Andrea Cyriax, Ralf Röder, Uwe Krieger, "Verwendung von Siliziumdehnungssensoren für makroskopische Prüfkörper", 10. MikroSystemTechnik Kongress 2023, Dresden, 23.-25.10.2023

DOI 10.5162/SMSI2025/P24

Add-on kit for non-invasive pressure measurement on process pipes

A. Cyriax, Th. Frank, A. Grün, St. Hermann, M. Kermann, St. Jagomast, A. Grün
CiS Forschungsinstitut für Mikrosensorik, Konrad-Zuse-Straße 14, 99099 Erfurt, Deutschland
tfrank@cismst.de

Summary:
This article presents a sensor system for non-invasive pressure measurement in process pipes. This is a back-fitting kit in the form of a sensitive sleeve with an integrated pressure sensor system. The direct coupling detects the exact changes in expansion of process pipes. When used as a monitoring system, statements can be made about material changes, wear mechanisms, maintenance, energy consumption under operating conditions or reactions to external influencing factors.

Keywords: non-invasive, silicon, piezoresistive, strain, force, pressure

Strain-based, non-invasive approaches for measuring pressure in piping systems are of great interest in the industrial plant sector due to their convenience and non-destructive installation.

Applications are possible for process pipes in systems for recording, digitizing, storing and evaluating condition variables. This provides information on material changes, wear mechanisms, maintenance, energy consumption under operating conditions or reactions to external influencing factors.

For non-invasive pressure measurement in process pipes, the back-fitting kit in the form of a sensitive sleeve with an integrated pressure sensor system should be used. The integrated pressure sensor system is realized on the basis of 500 x 500 µm small silicon-based strain sensors, shown in Fig. 1. These are applied to the sensitive area of the pipe sleeve using a micro-technical joining process.

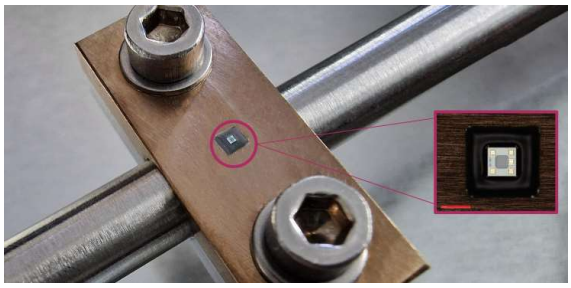

Fig. 1. Strain sensor joined to sensitive sleeve using glass frit

The direct coupling allows the exact expansion changes of the process pipe to be detected. Fig. 2 shows a simulation of the transfer of the pressure-dependent change in expansion of a process pipe to the sensitive pipe sleeve.

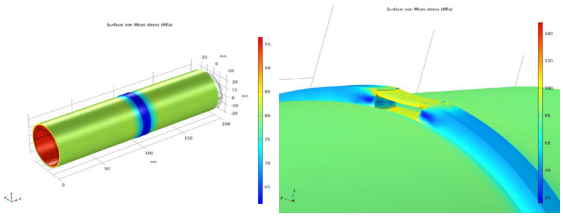

Fig. 2. Model of the direct coupling of the sensor system via a sensitive area in the pipe sleeve

The sensor system performs the following requirements:

- Non-invasive pressure measurement in pipes or pressure vessels without media contact

- subsequent installation on the process pipes (free mounting, surface mounting)

- Various geometry sizes/shapes possible depending on the application

- Easy installation, but slight loss of accuracy

- Measuring accuracy approx. 1% - 3% of the measuring range (4 to 300 bar)

- Possibility of temperature compensation of the raw signal

Source:

[1] Nachrüstsatz zur nichtinvasiven Druckmessung an Prozessrohren, Hannover Messe 2024, April 2024

DOI 10.5162/SMSI2025/P25

Membrane Characterization of Transparent Photodiodes

C. Möller[1], D.Mitrenga[1], T. Klein[1], A.T. Winzer[1], T. Ortlepp[1]
[1] CiS Forschungsinstitut für Mikrosensorik GmbH, Konrad-Zuse-Straße 14, 99099 Erfurt, Germany
cmoeller@cismst.de

Summary:
The paper reports the design, technology and mechanical and optical measurements on a transparent photodetector. We prepared different box layer thicknesses (500 nm, 250 nm, and 20 nm) and investigate the resulting membrane bow. OBIC measurements show the location-dependent photocurrent distribution on the membrane.

Keywords: photodiode, transparent, silicon-on-insulator, OBIC

Introduction

Interferometry enables very precise displacement measurements. In practice, the accuracy of the alignment of the components and their positional fidelity determine the achieved measurement accuracy. Due to its simple design without beam splitter and interference-prone reference beam path, the standing wave interferometer (SWIF) offers many advantages [1]. Very compact and robust systems can be achieved with this principle. A fixed laser shines light onto a movable mirror. The light reflected from the mirror forms a standing wave with the incident laser light [2]. By moving the mirror, the maxima and minima of the standing wave changes their position. With a suitable detector, the position of the standing wave in space can be recorded [1]. This enables a displacement measurement by knowing the displacement of the mirror. The basic requirement for this is a partial transparency of the detector.

Technology

The wavelength used for displacement measurement is 633 nm. To ensure the required transparency of the detector at this wavelength, the absorbing silicon layer must not be thicker than 600 nm. There is also another boundary condition: The thinner the detector, the more sensitive it is to the standing wave. If the thickness of the sensor is exactly the distance between maxima and minima, no signal change can be detected when the mirror is displaced. The optimal sensor thickness corresponds to λ/4 [1]. Using a helium-neon laser (633 nm) and the refractive index of silicon, this corresponds to 42 nm of silicon. To fabricate this thin silicon layer, the 500 nm thick device layer of an SOI wafer is thermally oxidized. The oxidation process “consumes” silicon - that means the remaining device layer gets thinner. Subsequently, the resulting silicon oxide can be selectively removed by wet etching. Several optically transparent layers are deposited to optimize the reflective properties. The layer stack is shown in cross-section in Figure 1. The doped regions are schematically drawn with the colors red and blue. Silicon removal from the backside is done by plasma-assisted etching. The box layer was etched to investigate different stress states of the membrane. Three different thicknesses are created and examined: 500 nm (not etched), 250 nm and 20 nm. To improve the optical properties, a further silicon nitride layer is deposited on the back of the membrane.

Three silicon device thicknesses were manufactured: 562 nm, 294 nm and 42 nm.

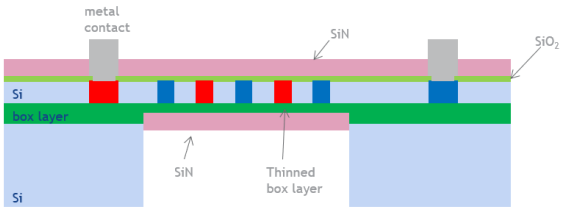

Figure 1: Layer stack of the transparent detector on SOI material. The red and blue areas in the silicon layer indicate boron and phosphorus doping, respectively. The box layer was etched in some samples to 250 nm or 20 nm thickness.

Chip Design

An example design of the transparent photodiode is shown in Figure 2. The depletion zone is formed between the doped fingers. And the capacitance of the photodiode can be adjusted by the spacing of the doped regions. Thus, the capacitance of the diode can be significantly reduced, resulting in a higher cutoff frequency. Membrane sizes were 1 mm, 0.8 mm and

0.6 mm. Distances between doped areas are available from 5 µm to 50 µm.

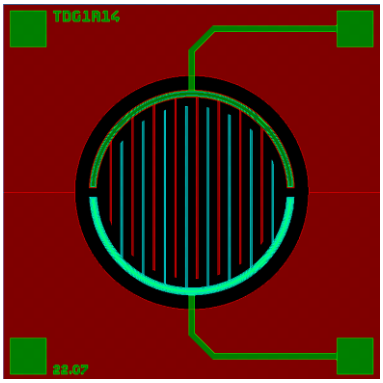

Figure 2: Design of a transparent photodiode with 50 µm distance between the doped regions and 1 mm membrane diameter. Red: boron doped, blue: phosphorus doped, green: metallization.

Membrane deformation

Caused by mechanical stress of the different layers (Figure 1), the membrane deforms after etching. Membrane geometry measurement was done with a laser scanning microscope. The bow of the membranes for different box layer thickness and 462 nm silicon is shown in Figure 3 as a line scan through the center of the chip. The greatest mechanical stress and thus deformation occurs at 20 nm box layer. Smallest bow appear at 250 nm.

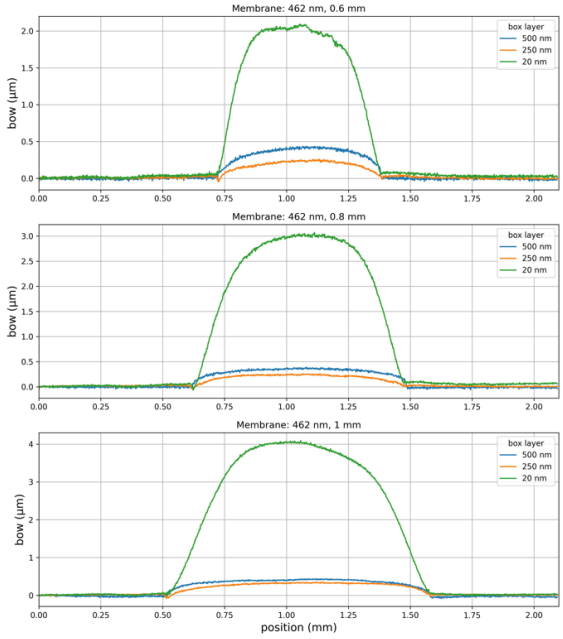

Figure 3: Comparison of the bow of different membrane diameters (1 mm, 0.8 mm, 0.6 mm) and box layer thicknesses of a 462 nm silicon thickness device.

OBIC measurement

The location dependent photocurrent on the membrane was determined with an optical induced beam current (OBIC) setup. The spot size of the 633 nm laser was about 6 µm with an optical power of 3 mW. The location dependent photocurrent is shown in Figure 4. The colors in the background define the different regions. Boron doping is located in the red region, phosphorus doping in the blue region. Light detection takes place only in the grey colored depletion region. This measurement was done in photoconductance mode.

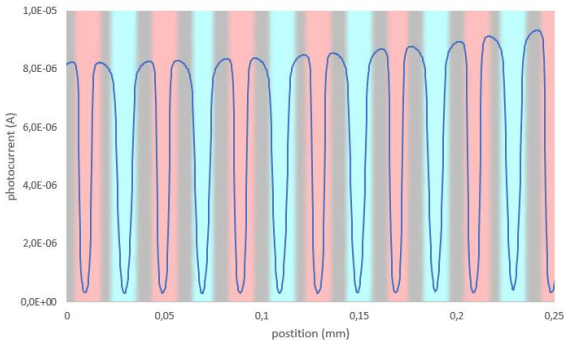

Figure 4: OBIC measurement of a photodiode with 10 µm spacing between the doping regions (10 µm).

References

[1] I. Ortlepp (2020): Mikrointerferometer auf Basis von interferenzoptischen Stehende-Welle-Sensoren. Ilmenau. Online unter: https://www.db-thueringen.de/receive/dbt_mods_00045571.

[2] I. Ortlepp *u. a.*, „Miniatur-Stehende-Welle-Interferometer auf Basis schneller, transparenter Photodioden“, *18 GMAITG-Fachtag. Sensoren Messsyst. 2016*, S. 418–424, 2016, doi: 10.5162/sensoren2016/6.1.2

Acknowledgements

This research were funded by the german “Bundesministerium für Wirtschaft und Klimaschutz“ (BMWK) within the project „KoSenDi“ (Innokom, 49MF220192).

DOI 10.5162/SMSI2025/P26

Combined Stationary Fluorescence and Nanosecond Time Resolved Laser Flash Photolysis Setup

Nele Lange[1], Martin Regehly[1]
[1] University of Applied Sciences Wildau, Hochschulring 1, 15745 Wildau, Germany
nele_sophie.wandel@th-wildau.de

Summary:
This paper presents a novel, adaptable setup for characterizing photoactive molecules, focusing on the determination of triplet state lifetimes and fluorescence spectra. The setup incorporates a custom-designed chopper wheel, which reduces the need for complex time control electronics. This configuration is easy to replicate and applicable across diverse fields. Initial tests with tetraphenylporphyrin demonstrate reliable lifetime and fluorescence measurements.

Keywords: laser flash photolysis, triplet state, fluorescence spectroscopy, chopper wheel

Motivation

The characterization of photoactive molecules is essential for numerous applications, including volumetric 3D printing [1], solar cells [2] or nanocircuitry [3]. Investigating triplet state properties, such as lifetime, can aid in designing molecules that are more efficient for targeted applications.

This laser flash photolysis setup is designed to be highly versatile, allowing for continuous modifications to meet specific experimental needs. It allows not only the determination of excited state lifetimes within the nanosecond range but also acquisition of fluorescence spectra.

Setup

The setup (Fig. 1.) primarily consists of standard laboratory components used in pump probe setups. Other components, like the cuvette holder, can easily be 3D printed. The laser must be capable of being triggered by the chopper controller.

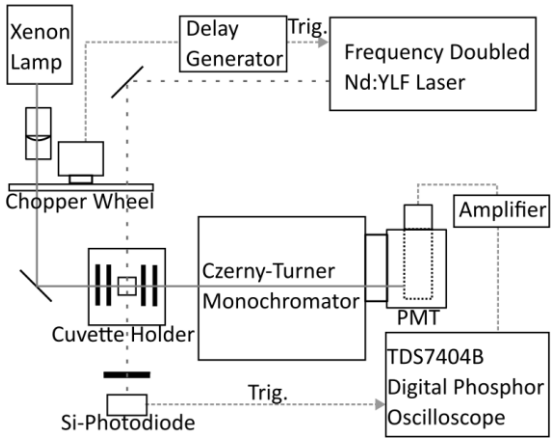

Fig. 1. Schematic drawing of the measurement setup

The pump beam is created by a diode-pumped, intercavity frequency doubled Nd:YLF laser that produces pulses exceeding 100 ns with single pulse energies between 0.1 mJ and 9.6 mJ. It passes through the chopper wheel, exciting the sample before reaching the Si-photodiode, which triggers the oscilloscope. The probe beam, generated by a xenon lamp, passes through the chopper wheel, reflects off a mirror, intersects the sample and the pump beam at a 90° angle, then continues through the Czerny-Turner monochromator before reaching the photomultiplier tube. The photomultiplier has a rise time of 2.2 ns. An amplifier transmits the data to the digital phosphor oscilloscope.

To acquire the laser-induced fluorescence spectrum, the xenon lamp and the chopper wheel are switched off and the monochromator is scanned across the desired wavelength range.

A key innovation of this setup is the chopper wheel (Fig. 2.) where both the probe and pump beam pass through at the same height, but in different locations.

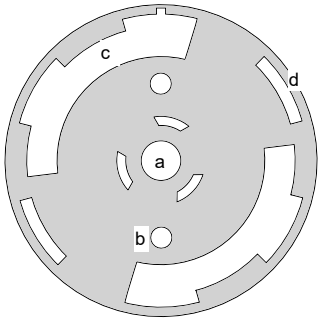

Fig. 2. Chopper wheel geometry a) mounting cut-out, b) pump laser openings, c) probe beam openings, d) feedback slots

The chopper wheel triggers the laser, allowing the pump laser frequency to be reduced by selectively opening sections in the inner ring of the disk (b). The chopper wheel also defines the measurement timing by opening and closing the probe beam path at precise intervals (c).

The setup's time resolution depends on the pump pulse duration and the photomultiplier rise time. The time window is defined by the slowest achievable repetition rate, with extended probe beam durations allowing for measurements over a broader timeframe.

Nanosecond Laser Flash Photolysis Results

Fig. 3. shows how the chopper wheel provides precise measurements with clear on/off intervalls, offering the 0% and 100% transmission values.

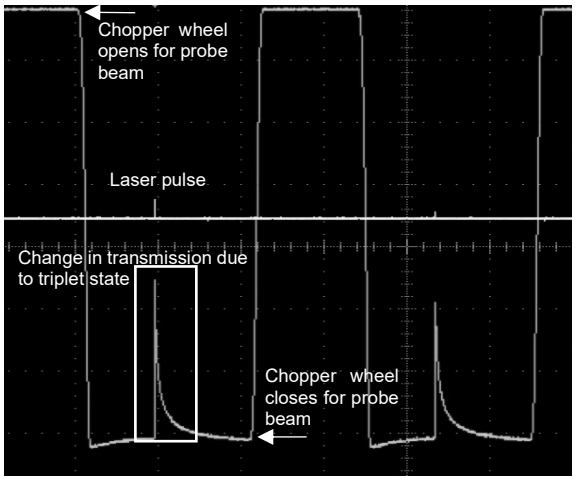

Fig. 3. Oscilloscope screenshot showing triplet state lifetime measurement

Upon excitation to the triplet state, tetraphenylporphyrin, exhibits a change in optical density influenced by the pump laser's energy and surrounding O_2 levels. This change is observed on the oscilloscope as a loss of intensity caused by the reduced transmission.

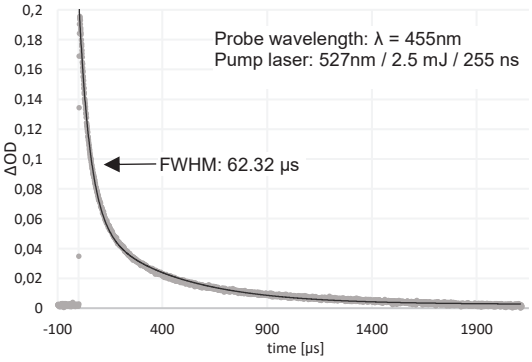

Fig. 4. Triplet state lifetime of tetraphenylporphyrin in toluene under nitrogen atmosphere

The change in optical density at a specified time ΔOD_t can be calculated using equation (1):

$$\Delta OD_t = -\log\left(\frac{I_t - I_0}{I_{max} - I_0}\right) \quad (1)$$

The results of the change in optical density can be seen in Fig. 4. A double-exponential curve fit yielded a half-life of 62.32µs for the triplet state.

Steady State Fluorescence Results

Tetraphenylporphyrin has a distinct fluorescence emission spectrum which was captured using this setup. Relative radiometric calibration was used to correct the data set, resulting in accurate fluorescence spectra, as illustrated in Fig. 5.

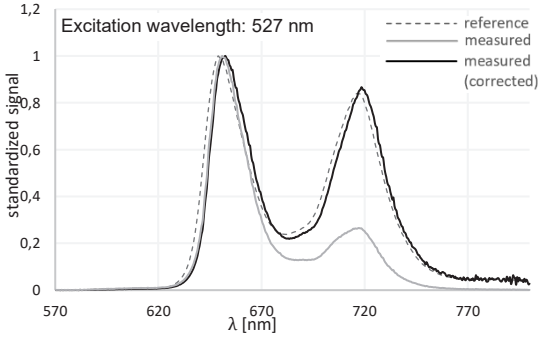

Fig. 5. Fluorescence spectrum of tetraphenylporphyrin in toluene

Conclusion

This work successfully demonstrates a versatile measurement setup capable of performing nanosecond laser flash photolysis spectroscopy and capturing steady state laser-induced fluorescence spectra, making it ideal for diverse applications. The innovative chopper wheel design and straightforward setup make replication feasible in any laboratory setting.

References

[1] Regehly, M., Garmshausen, Y., Reuter, M., König, N. F., Israel, E., Kelly, D. P., Chou, C.-Y., Koch, K., Asfari, B., & Hecht, S.,Xolography for linear volumetric 3D printing, *Nature* 588, 620–624 (2020); doi: 10.1038/s41586-020-3029-7

[2] Benduhn, J., Piersimoni, F., Londi, G., Kirch, A., Widmer, J., Koerner, C., Beljonne, D., Neher, D., Spoltore, D., Vandewal, K., Impact of Triplet Excited States on the Open-Circuit Voltage of Organic Solar Cells, Advanced Energy Materials 8, 21 (2018); doi: 10.1002/aenm.201800451

[3] Yang, C., Guo, Y., Masai, H., Iwai, T., Jie, J., Su, H., Terao, J., Guo, X., Logic operation and real-time communication via tunable excited states in a single-molecule optoelectronic chip, Chem (2024); doi: 10.1016/j.chempr.2024.01.005

DOI 10.5162/SMSI2025/P27

Improved Inductive Measurement System for Monitoring Electromagnetic Properties of Steel Sheets During Production

Marc Simoneit[1], Thomas Thuilot[1], Andreas Hennig[1], Olfa Kanoun[2]
[1] University of Applied Sciences Ruhr West, Mülheim an der Ruhr, Germany,
[2] Technical University Chemnitz, Chemnitz, Germany
Marc.Simoneit@hs-ruhrwest.de

Summary:
This work improves on a previously investigated inductive measuring system to monitor electromagnetic properties of steel sheet during production. The goal was to increase the measuring range. In comparison to the earlier method, a reference system was used to subtract the influence of the primary field. A simulation using COMSOL Multiphysics® was used to validate the proposal. The results obtained by simulation showed that microstructural transformation may be more easily observed with a different sensor configuration and improved postprocessing.

Keywords: sheet rolling mill, magnetic analysis, alternating current characterization, eddy current sensor, inductive sensor, non-destructive testing

Introduction

Steel is widely used in industries like electrical, mechanical, and civil engineering, each requiring specific properties. Electrical applications prioritize electromagnetic properties, while hardness, elasticity, and porosity are critical in others. These characteristics depend on steel's microstructure, making its monitoring essential for manufacturers. In-situ measurement techniques help assess if post-treatment is needed, allowing real-time corrections and reducing energy use compared to recycling faulty steel. This minimizes waste and supports greener production. [1]

Background, Motivation and Objective

This paper presents an improved method of a measuring strategy investigated in a past publication [2], demonstrated in a simulation using COMSOL Multiphysics® and the Jiles-Atherton-Model. It was shown, that by evaluating the phase shift between an exciting magnetic field H and the induced voltage U_{ind} in a measurement coil, the composition of the steel microstructure could be reliably monitored, with a method suitable for high speed, high temperature and resistant to dirt. A challenge remaining is the superposition of the weak measurement signal and the primary field reducing resolution and therefore informative value on the composition. This study examines the magnitude of the primary field's influence on measurement outcomes and assesses how subtracting an empty measurement without a steel sheet affects this influence. Such a subtraction of the primary field can be achieved by a thoughtful coil configuration as in [3] or by a reference system as in [4].

Approach

The measurement method used in this work is based on the evaluation of the phase shift between H-field and B-field. As shown in [2], this phase shift is influenced by the coercivity H_c of a hysteresis curve. The current in the field coil serves as an indirect measure of the H-field. The B-field is determined on the basis of the voltage induced U_{ind} in the measuring coil.

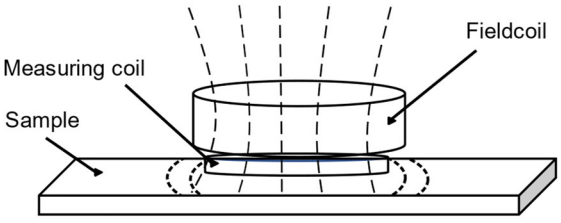

Figure 1: scheme of the simulation model

A flat measurement coil is positioned at a minimum distance of 7.5 mm above a sheet sample. Directly above the measurement coil, a second flat coil, designated as the field coil, is placed. The field coil is driven by a sinusoidal alternating current with an amplitude of 1,5 A. In the simulation, two hysteresis curves with different H_c were simulated in which small changes in H_c are generated by the pinning losses parameter. The two different hysteresis curves serve as model for

different microstructure compositions. However, since in this case the induced voltage U_{ind} is influenced by the sum of the primary generated field B_p and the opposing field generated by the eddy current B_{eddy}, the following equation is obtained:

$$B_{res} = B_p + B_{eddy}$$

$$\rightarrow \hat{B}_{res} \sin(\omega t + \varphi_{res})$$

$$= \hat{B}_p \sin(\omega t + \varphi_p) + \hat{B}_{eddy} \sin(\omega t + \varphi_{eddy}) \quad (1)$$

The following equation for the resulting phase position results from the sine addition theorem and transformations:

$$\varphi_{res} = \operatorname{atan} \frac{\hat{B}_p \sin\varphi_p + \hat{B}_{eddy} \sin\varphi_{eddy}}{\hat{B}_p \cos\varphi_p + \hat{B}_{eddy} \cos\varphi_{eddy}} \quad (2)$$

As the primary field can be used as a reference phase, it can be summarized as shown in Eq. 3

$$\varphi_{res} = \operatorname{atan} \frac{\hat{B}_{eddy} \sin\varphi_{eddy}}{\hat{B}_p + \hat{B}_{eddy} \cos\varphi_{eddy}} \quad (3)$$

This demonstrates that the resulting phase position is always compressed by the amplitude of the primary field. By subtracting an induced voltage from a reference measurement, the primary field can be suppressed and the measurable phase differences can be increased. For this purpose, the simulation from [2] was repeated and another one was done with a sample of air. The phase differences φ between the induced voltages and the exciting current were then observed.

Results

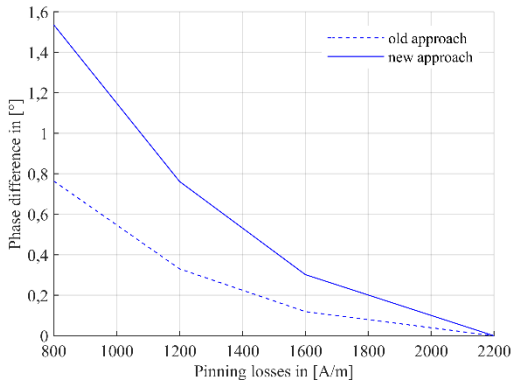

Figure 2: Phase difference over pinning losses for old and new approach relative to pinning losses at 2200 A/m

The results in Fig. 2 show an increase of the differences between all phase differences of the first hysteresis curve. For the first hysteresis curve, the difference increases by a multiple. For the second, at least twice as much. And the distance between the two curves increases by a factor of 5, as compared to the previous method (Tab. 1).

Tab. 1: Phase difference Δφ observed in simulation with (New) and without (Old) subtraction of a reference.

	Old	New
$\Delta\varphi_{max}$ curve 1	0.0155	0.4781
$\Delta\varphi_{max}$ curve 2	0.7639	1.5355
Δφ curves 1-2	-1.0679	-5.3351

Discussion

A substitute value φ_{res} for the coercivity H_c is measured by using inductive sensors, using a method that is directly suitable for in-situ applications. This method enables the value to be recorded precisely under real conditions without having to change the system or the measuring environment. The use of a reference system for the subtraction of the primary field leads to a considerable extension of the measuring range and thus offers higher accuracy and reliability compared to the previous method. For an application, the subtraction of the sample needs to happen in-situ, as a measurement with and without sample may not be possible to do simultaneously. With a thoughtful positioning form an extra set of coils it should be possible to measure the primary field without the field from the eddy current. [3] This paper show that it is beneficial to subtract the field generated by the primary coil from the field generated by the eddy current.

References

[1] P. Pugsley, P. Hunt, H. Yang, F. den van Berg, J. Mosk, A. Peyton, ON-LINE PHASE TRANSFORMATION MONITORING ON A HOT STRIP MILL. In: *Anais do Seminário de Laminação e Conformação*, 21–30. São Paulo: Editora Blucher; 27.09.2016 - 29.09.2016.

[2] M. Simoneit, J. Brodmann, S. Schulze, A. Hennig, J. Himmel, Usability Tests on the Temperature-Induced Changes in Magnetic Hysteresis During Steel Production. In: *2023 International Workshop on Impedance Spectroscopy (IWIS)*, 115–118. IEEE; 2023.

[3] Andreas Hennig, *RFID SysTech 2008: Feasibility of Deeply Implanted Passive Sensor Transponders in Human Bodies*. VDE Verlag, Berlin; 2008.

[4] H. Stroppe, K. Schiebold, *Wirbelstrom-Materialprüfung: Ein Lehr- und Arbeitsbuch für Ausbildung und Prüfpraxis*. Castell-Verlag GmbH, Wuppertal; 2011.

DOI 10.5162/SMSI2025/P28

Enhancing Predictive Maintenance with Temporal Convolutional Networks

Florian Rieger [1], *Raphael Schilling*[1], *Ferdinand Heinrich* [1], *Franz Wenninger* [1] *
[1] Fraunhofer Institute for Electronic Microsystems and Solid State Technologies
Hansastr. 27d, 80686 Munich
florian.rieger@emft.fraunhofer.de

Summary: Predictive maintenance is a crucial technique for reducing machine downtime. One challenge is the absence of labeled run-to-failure data. We propose a semi-supervised anomaly detection approach using Temporal Convolutional Networks, a regression model that has multivariate data as input and estimates vibration data. Our study reveals that our sensor signal estimation is quite accurate for normal data. The estimation error serves as a score that is useful for identifying anomalies.

Keywords: predictive maintenance, machine learning, vibrations, neural networks, temporal convolutional networks

Introduction

Predictive maintenance (PdM) is a crucial technique to reduce machine downtime and improve operational efficiency. Traditionally, PdM relies on labeled run-to-failure data to train machine learning models that can predict equipment failures. However, obtaining such data is often challenging and impractical in many industrial settings [1]. This paper addresses the challenge of detecting anomalies in machine behavior without labeled run-to-failure data by leveraging control loop data to predict system responses, particularly vibrations.

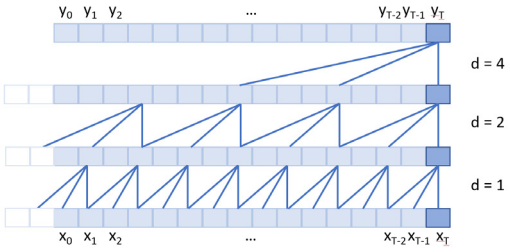

Fig. 1: Basic concept of a Temporal Convolutional Network. By using dilated causal convolutions, long-range dependencies (blue lines) can be captured without increasing the complexity of the model.

PdM finds applications across various industries, including oil, gas, and wind. The potential of PdM is significant, with studies estimating that a properly functioning PdM program can provide savings of 8% to 12% over preventive maintenance alone [2]. Depending on a facility's reliance on reactive maintenance and material condition, savings opportunities could exceed 30% to 40% [2].

This paper uses a Temporal Convolutional Network (TCN) approach as shown in Fig. 1 to perform anomaly detection on a die ejector machine. The die ejector is a critical component , where it is used to precisely place bare-dies onto substrates. The machine operates at high speed, which results in vibrations. Distinguishing normal from abnormal vibrations is a challenge. Using our adapted TCN-AD approach to predict the system's physical response to input signals, it is possible to detect anomalies in the die ejector's behavior, ensuring timely maintenance and reducing the risk of machine failure.

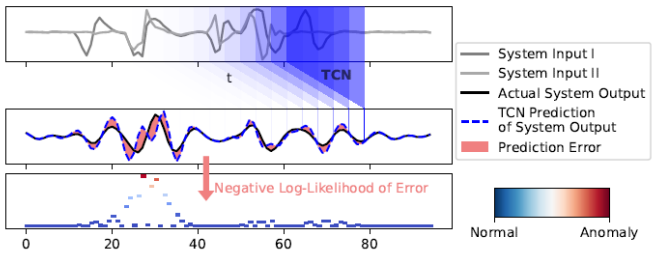

Fig. 2: Estimation error based anomaly detection using Temporal Convolutional Networks. Estimation errors lead to an increase in anomaly score.

Methodology

The methodology revolves around the development and evaluation of the Temporal Convolutional Network for Anomaly Detection (TCN-AD) approach, which was first used in [3]. What distinguishes our approach from that in [3] is that

*This research is funded by the Bavarian State Ministry of Economic Affairs, Regional Development and Energy under the identification number DIE0147.

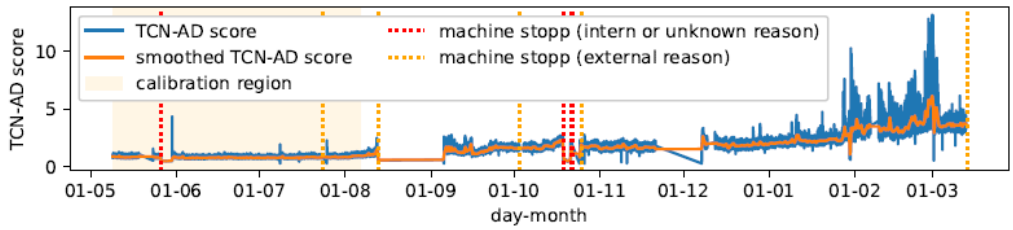

Fig. 3: TCN-AD anomaly score (blue) and smoothed score (orange) tracked over several month. Towards the end of the shown time period the machine condition gets worse, which already was indicated by our model.

there is no prediction of future time steps, but rather a regression of measured signals, in particular vibrations, based on a set of other signals, in our case control loop data. The primary goal is to detect anomalies in machine behavior by predicting the system's physical response to external impulses. In this way, the algorithm intrinsically models the physical system during normal operation. If the physical properties change over time, the regression error, which is the difference between the estimated and actual sensor signals, increases. Thus, this regression error makes a good indicator for anomalies (see Fig. 2).

The TCN model used in our approach consists of several key components, including dilated causal convolutions and residual connections. Dilated causal convolutions allow the model to capture long-range dependencies in the time series data without increasing the model complexity, while residual connections help in training deeper networks by allowing gradients to flow more easily through the network.

The model is trained using normal sequences of control loop data by minimizing the estimation error on these sequences. It is then validated with a separate set of normal sequences to ensure good generalization to unseen data. During anomaly detection, the trained TCN model estimates sensor signals for new input sequences, and sequences with high estimation errors are flagged as anomalies. What sets our approach apart from the state of the art is its ability to model the physical response of a system to input signals using control loop data, without relying on labeled run-to-failure data. This semi-supervised method is a robust and practical solution for predictive maintenance across various machines and systems without the need for extensive labeled datasets.

The approach is evaluated using a dataset that contains vibration data from a die ejector machine. The results demonstrate the effectiveness in detecting anomalies in machine behavior, highlighting its potential for improving predictive maintenance strategies and reducing machine downtime.

Results

The evaluation of the TCN-AD approach demonstrated its effectiveness in detecting anomalies in machine behavior using vibration data. The key findings from the evaluation are as follows:

The approach showed high accuracy in detecting anomalies in the vibration data of the die ejector machine. The estimation error, which is used as the anomaly score, effectively identified abnormal behavior in the machine's operations (Fig. 3). The model was found to be robust to noise in the sensor data. The use of dilated causal convolutions and residual connections in the architecture allowed the model to capture long-range dependencies and filter out noise, leading to more accurate anomaly detection. The model demonstrated good generalization to unseen data. During inference, the model successfully identified anomalies in new input sequences, indicating its ability to generalize well to new data.

The evaluation highlighted the advantages of using a semi-supervised learning method that uses normal operational data for anomaly detection, making it a practical solution for predictive maintenance. The findings from the evaluation in Fig. 3 suggest that the system changed significantly over time compared to the modeled one and thus the machine might have a damage.

Acknowledgements

We would like to thank our consortium partner *Mühlbauer* for giving us access to the data and providing us valuable feedback. In particular we would like to thank Patrick Grössing and Sebastian Heinrich.

References

[1] D. Kim, S. Lee, and D. Kim. An Applicable Predictive Maintenance Framework for the Absence of Run-to-Failure Data. *Applied Sciences* 11.11 (2021). doi: 10.3390/app11115180.

[2] G. Sullivan, R. Pugh, A. P. Melendez, and W. D. Hunt, Operations & Maintenance Best Practices - A Guide to Achieving Operational Efficiency (Release 3). 2010. doi: 10.2172/1034595.

[3] Y. He and J. Zhao, Temporal Convolutional Networks for Anomaly Detection in Time Series. *Journal of Physics* Conference Series 1213.4 (2019); doi: 10.1088/1742-6596/1213/4/042050.

DOI 10.5162/SMSI2025/P29

Non-radioactive Electron Capture Detection for Process and Quality Control in Brewery Production

Martin Lippmann[1], Modestus Wigger[2], Maximilian J. Kueddelsmann[1], Daniel Claassen[1], Max Kaschytza[1], Sabrina Deicke[1], Erik Bunert[1], Stefanie Sielemann[2], Stefan Zimmermann[1]
[1] Leibniz University Hannover, Institute of Electrical Engineering and Measurement Technology, Department of Sensors and Measurement Technology, Appelstr. 9A, 30167 Hannover, Germany,
[2] Hamm-Lippstadt University of Applied Sciences, Department HAM2, Marker Allee 76-78, 59063 Hamm, Germany
lippmann@geml.uni-hannover.de

Summary:
In beer fermentation, diacetyl and 2,3-pentanedione levels must be precisely controlled, with thresholds below 0.10 mg/L. Due to this low concentration, the Central European Brewing Analysis Commission recommends gas chromatography coupled to an electron capture detector as a sensitive analytical method. The new non-radioactive X-ray ECD achieves the necessary detection limit and linearity comparable to conventional radioactive ECDs, eliminating regulatory burdens tied to radioactive sources and allowing continuous concentration monitoring over the entire fermentation process.

Keywords: Gas chromatography, Non-radioactive Electron Capture Detector, X-ECD, Brewery, Food

Introduction

In beer production, managing diacetyl (2,3-butanedione) and 2,3-pentanedione levels is crucial, as concentrations exceeding 0.10 mg/L cause undesirable off-flavors. These compounds are by-products of yeast metabolism and undergo gradual breakdown during fermentation. However, due to variations in natural ingredients, breweries without analytical monitoring instruments often extend fermentation times, impacting process efficiency. To improve monitoring accuracy, the Central European Brewing Analysis Commission recommends gas chromatography with an electron capture detector (GC-ECD) [1]. Traditional ECDs, however, rely on radioactive sources, raising regulatory and operational challenges for breweries.

A non-radioactive ECD, the X-ECD, was recently developed at Leibniz University Hannover [2]. It offers sensitivity and linearity comparable to traditional radioactive detectors but avoids regulatory restrictions for handling radioactivity. This study aims to validate the detector's performance and suitability for its use in brewery applications, showing a safer, more efficient option for in-production monitoring of critical fermentation compounds.

Experimental

The X-ECD is based on a compact high energy photoionization source, enabling ionization of the carrier gas (nitrogen or argon) to generate the necessary free electrons, similar to traditional radioactive sources. The X-ECD was coupled with a Shimadzu GC 2010, while incubation and injection of headspace samples were managed through a Shimadzu AOC-5000 Plus autosampler into a split injector, with detailed operational parameters listed in Table 1. A short, heated transfer line at 100 °C connected the GC column to the X-ECD. Helium served as the carrier gas, and Argon was added as a make-up gas through a T-connector.

Calibration was performed using solutions of diacetyl and 2,3-pentandione in water with 5% ethanol, replicating typical beer conditions. These solutions allowed precise testing of the detector's response to various concentration levels.

Additionally, real beer samples were analyzed under the same conditions to prove the absence of any disturbing matrix effects from coeluting substances.

Tab. 1: Operational parameters of the GC and the X-ECD.

Vial volume	20 mL
Liquid sample	10 mL
Incubation	10 min at 60 °C
Head space injection volume	1 mL
Injector temperature	150 °C

Split	1:5
GC-Column	HP5-MS (30 m, 0.25 mm, 50 µm)
Carrier Gas	0.9 mL/min Helium
Oven temperature	40 °C (3 min hold) 10 °C/min 80 °C (2 min hold)
Transfer temperature	100 °C
X-ECD temperature	100 °C
Make-up gas flow	50 mL/min Nitrogen
ECD modus	Constant-Current
ECD pressure	Open / atmosphere

Results

Figure 1 shows the chromatograms of headspace injections of a water ethanol mixture (95/5) containing different concentrations of diacetyl and 2,3-pentandione. Both compounds can be clearly identified by two clearly separated peaks. A response of the high amount of injected oxygen and ethanol appears much earlier than the analyte peaks, ensuring no baseline interference in the target area.

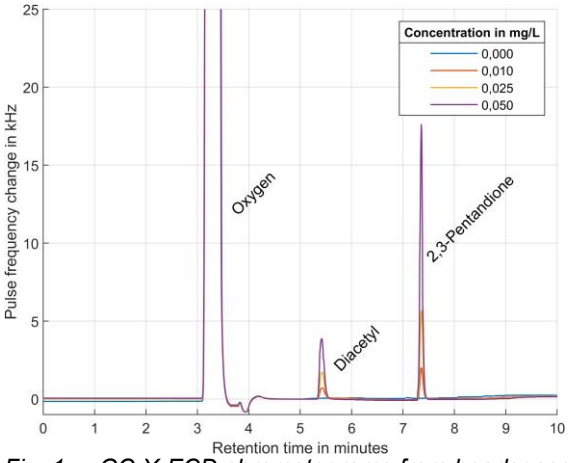

Fig. 1. GC-X-ECD chromatograms from headspace analysis of diacetyl and 2,3-pentanedione in an aqueous solution containing 5% ethanol, simulating a beer-like mixture.

The GC-X-ECD system detects concentrations as low as one-tenth of the threshold (0.1 mg/L). Our current work focuses on method development, enabling the full potential of the X-ECDs high dynamic range (starting already at a noise floor around 10 Hz in pulse frequency change) to cover the entire concentration range of the brewing process. This could enable real-time fermentation monitoring to adjust process parameters based on ingredient quality. Figure 2 shows measurements of two beer samples: one finished beer from the supermarket and one so called "young beer" with incomplete fermentation.

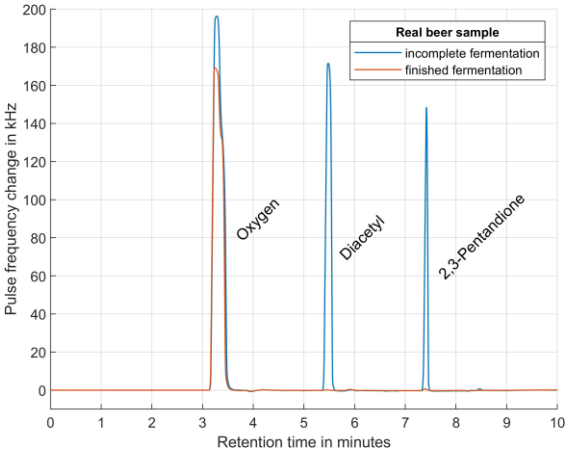

Fig. 2. GC-X-ECD chromatograms from headspace analysis of two real beer samples, comparing their profiles after incomplete and completed fermentation processes.

This illustrates the concentration variability present throughout the brewing process. Furthermore, the measurements demonstrate that no interfering substance peaks in real beer samples obstruct the identification and subsequent quantification of the two target compounds. In addition to achieving the required sensitivity and dynamic range, these results confirm the advantages of using an ECD over non-selective GC detectors, which may encounter challenges with coeluting substances within the complex beer matrix. Ongoing work aims to optimize method development to fully characterize the GC-X-ECD system, focusing on its limit of detection and linearity.

Acknowledgement

The project “Next Generation Electron Capture Detector – X-ECD” is funded by the German Federal Ministry for Economic Affairs and Climate Action and the European Social Fund as part of the EXIST program (Grant Number: 03EFNIO120).

References

[1] Brautechnische Analysenmethoden: Methodensammlung der Mitteleuropäischen Brautechnischen Analysenkommission (MEBAK). Band 3, (1996);

[2] Kueddelsmann, Stadtler, Kirk, Bunert, Zimmermann, Non-radioactive electron capture detector based on soft X-ray ionization for gas chromatography - A possible replacement for radioactive detectors, Journal of Chromatography A, 1711, 464453 (2023); doi: 10.1016/j.chroma.2023.464453

DOI 10.5162/SMSI2025/P30

Identification of plastics in foodstuff using Rapid-FLIM and neural networks

Sebastian Heitzmann [1] , *Aromal Somarajan Rajan* [1] , *Martin Versen* [1] , *Nina Leiter* [1]
[1] University of Applied Sciences Rosenheim, Rosenheim, Germany
sebastian.heitzmann@th-rosenheim.de

Summary: The analysis of fluorescence lifetimes has the potential to reliably differentiate plastics from foodstuffs. A setup for use in an industrial process is required to work in real time. The combination of Rapid fluorescence lifetime imaging microscopy (Rapid-FLIM) and neural networks shows significant improvements in capture time compared to other FLIM technologies, while achieving a reliable differentiation of foodstuffs and plastics.

Keywords: food safety, Rapid-FLIM, FD-FLIM, neural networks, MLP

Introduction

Plastics, due to their light weight and additional useful properties, are widely used in food packaging, both for the packaging itself and parts of machines in industrial food production. This prevalence leads to an issue of contamination with these ubiquitous materials through errors or wear of machine parts. Currently used detection processes struggle to differentiate organic materials like plastics from the inherently organic food stuffs processed.
The use of fluorescence lifetime for the detection of polymers in foodstuffs has been shown to be feasible [1]. This work aims to explore the potential of a frequency-domain based technology, focused on a faster measurement procedure while retaining the promising results of frequency-domain fluorescence lifetime imaging microscopy (FD-FLIM) [2].

State of the art

Fluorescence lifetime

Fluorescence describes the emission of a photon by a molecule or atom after absorption of a photon of shorter wavelength. Fluorescence lifetime, a material specific measure, is defined as the time between peak fluorescence intensity and $\frac{1}{e}(\approx 37\%)$ intensity [3].

FD-FLIM and Rapid-FLIM

The approach of FD-FLIM and Rapid-FLIM relies on the mathematical features of emission signals in the frequency domain.
The sample is excited by a modulated laser. For FD-FLIM, $n = 16$ images are captured, using a special pco.flim camera. Every image contains a Tap A and B, both capture half a period of the signal. The trigger switching Tap A and B is shifted by $\frac{1}{n} * 2\pi$ for every image relative to the laser modulation signal to allow a reconstruction of the emitted signal.

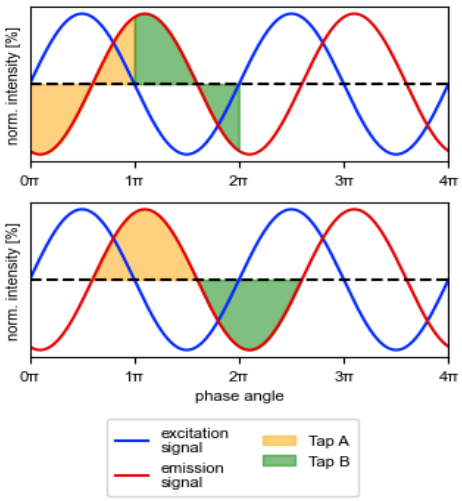

Fig. 1: Imaging process of Rapid-FLIM

From the phase-shift and amplitude dampening relative to the modulation signal, two distinct lifetimes are calculated. In contrast, Rapid-FLIM relies on two images, therefore reducing the capture time by a factor of eight. To gather the greatest amount of information within two images, the trigger-shift of the second image is set to maximize the intensity difference between the images, an example is shown in Fig. 1. Instead of a lifetime, an alternative measure, the normalized intensity difference, shown in equation (1), is calculated describing the normalized difference in the intensity of Taps A to the intensity of Taps B in a range from -1 to 1. A visualization as an image can be found in Fig. 2.

$$X_R = \frac{I_A - I_B}{I_A + I_B} \tag{1}$$

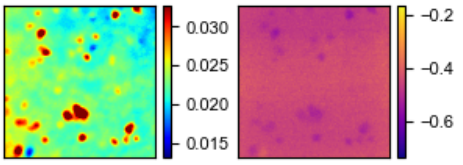

Fig. 2: normalized intensity and intensity difference of S015_M03_RF080

Tab. 1: Sample Overview

Sample	Product	Type
S001	Salami	food
S002	Ham	food
S004	Cheese	food
S005	Gouda	food
S006	Flour	food
S007	Sugar	food
S008	Oat flakes	food
S009	Ham fat	food
S014	Rubber gloves	plastic
S015	Conveyor belt front	plastic
S020	Conveyor belt back	plastic
S024	Yellow sausage	food

Sample Preparation and Data

The used dataset consists of 2362 measurements of twelve samples, ranging from processed foodstuffs, bought at a local supermarket, e.g., cheese and salami, to rubber gloves and conveyor belts. A complete overview of the samples including labels is given in Tab. 1.
Measurements are taken under a microscope, using a pco.flim FLIM-camera with a in house developed python-program and a $445\ nm$ laser as light-source. Measurements are saved as .npy files with sample name, measurement number and trigger phase-shift documented in the filename, e.g., “S001_M099_RF080.npy”.

Multilayer Perceptron

In the first run, the model is trained on 100 images of each sample, using k-fold cross validation (k=5) to increase the utilization of the dataset. Using a detailed confusion matrix, incorporating the differentiation of different food types as well, the developed MLP reaches a weighted F1-score of $77\ \%$. Shrinking this matrix to a binary classification of foods and plastics yields an F1-score of $82\ \%$. In the detailed confusion matrix, it can be seen, that three samples in particular are difficult to differentiate from plastics: S002, S005 and S0024, the individual F1-scores are shown in Tab. 2 in column ‘all’. For the following development, metrics are focused on those samples.

Tab. 2: Improvement of classification by measures

	all	data	features	filter
S002	$60.4\ \%$	$77.0\ \%$	$91.5\ \%$	$96.0\ \%$
S005	$85.7\ \%$	$95.0\ \%$	$95.8\ \%$	$97.8\ \%$
S024	$77.8\ \%$	$88.8\ \%$	$98.4\ \%$	$97.1\ \%$

The next version is focused on binary classification of the identified difficult food samples against plastics with a larger dataset consisting of 400 images for each food sample and 200 images for each plastic sample. The additional data improves the performance significantly, see Tab. 2 in column ‘data’.
To further boost the performance, additional statistical features of the images, namely the range, variance, and inter-quartile range (IQR) are implemented with good results, see Tab. 2 in column ‘features’.
Additionally, a change in the measurement setup, the change from a $460\ nm$ long pass filter to a $490/60\ nm$ bandpass filter increased the performance to the overall best results, see Tab. 2 in column ‘filter’.

Results and Conclusion

The results prove the feasibility of Rapid-FLIM to differentiate plastics from specific food samples. This training on a binary classification between one food sample and a range of plastics is close to a use case in industrial food processing, where process lines mostly are specialized for one type of food stuff.
The reduction of capture time by a factor of eight vastly improves on one of the flaws of FD-FLIM in real-time scenarios.

Acknowledgement

The authors thank Weber Maschinenbau GmbH for the supply of samples and advice on industrial processes.

References

[1] M. Versen, M. Wohlschläger, H. Langhals, and C. Laforsch, “The detection of organic polymers as contaminants in foodstuffs by means of the fluorescence decay of their auto fluorescence,” *Food and Humanity*, vol. 3, p. 100 363, 2024, ISSN: 29498244. DOI: 10.1016/j.foohum.2024.100363.

[2] S. Heitzmann, M. Wohlschläger, N. Leiter, M. Löder, M. Versen, and C. Laforsch, “Classification of foods and plastics using fd-flim and neural networks,” in *2024 IEEE Sensors Applications Symposium 2024*, pp. 1–6.

[3] J. R. Lakowicz, *Principles of Fluorescence Spectroscopy*. New York (USA): Springer Science+Business Media, 2006, ISBN: 978-0 387-31278-1.

DOI 10.5162/SMSI2025/P31

In-Situ and Operando Measurements for the Characterization of Next-Generation Sensor Materials

Rudi Tschammer[1], Carlos Morales[1], Carlo Tiebe[2], Karsten Henkel[1], Jan Ingo Flege[1]
[1] BTU Cottbus-Senftenberg, Konrad-Zuse-Straße 1, 03046 Cottbus, Germany
[2] Bundesanstalt für Materialforschung und -prüfung, Unter den Eichen 87, 12205 Berlin, Germany
tscharud@b-tu.de

Summary:
In this contribution, we highlight the use of *in-situ* X-ray photoelectron spectroscopy and *operando* spectroscopic ellipsometry for the characterization of ultra-thin (<20nm) atomic layer deposited layers for the use in next-generation miniaturized sensor devices. By targeting tin oxide layers, we show how we can use these techniques to gain insights into material composition, thickness, and optical properties, thus paving the way for unraveling the correlations between material properties and sensing performance.

Keywords: In-situ characterization, X-ray photoelectron spectroscopy, Ellipsometry, Tin oxide, Atomic Layer Deposition

Background and Motivation

Transitioning to an energy system based entirely on renewable energies requires significant use of energy carriers such as hydrogen (H_2) and its derivatives. While considerable effort is devoted to improving the generation, storage, and utilization of H_2, new developments for secondary components, such as gas sensors, will be necessary to ensure a swift and secure transition. Today's sensors rely on expensive materials such as noble metals for conductometric hydrogen sensors [1], expert personnel, careful maintenance, and high investment costs, making them unsuitable for large-scale deployment and necessitating the development of cheap, mass-producible gas sensors capable of operation near room temperature (RT) and without noble metals.

Among the available deposition methods, atomic layer deposition (ALD) has emerged as an attractive option for conformally depositing ultra-thin films with atomic-scale thickness control on the wafer scale [2]. In addition, ALD results in amorphous and defect-rich deposits, leading to material properties deviating from their crystalline and well-ordered counterparts. Interestingly, this has enabled us to demonstrate the sensing behavior of ALD-CeOx towards H_2 in O_2 (~1mbar) by near-ambient pressure X-ray photoelectron spectroscopy (XPS) [3].

Due to the low electrical conductivity of pure CeO_2, we aim to combine ALD-CeO_2 with other metal oxides, such as tin oxide (SnO_2), to lower the resistivity and improve electrical conductivity and gas sensing performance by exploiting interfacial interactions.

In this context, the sequential nature of the ALD process offers high flexibility for combining different materials during the growth process, either as heterostructures or mixed oxides, by using appropriate super-cycles [4]. However, this requires in-situ and operando material investigation techniques such as XPS and spectroscopic ellipsometry (SE) to control oxide composition and thickness during growth and monitor potential contaminants due to reaction residues. Combined with the amorphous nature of the thin films, this bottom-up approach allows for fine-tuning the deposit properties towards optimal gas-sensing performance, following a standard procedure to determine sensor characteristics for H_2/air or H_2/nitrogen.

Description of the New Method or System

From in-situ XPS and operando SE measurements of the SnO_2 film growth using TDMASn + O_3 at 160°C in our ALD cluster described elsewhere [5], we have analyzed the detailed evolution of material composition, thickness, and growth rate depending on the number of ALD cycles. In addition, preliminary gas-sensing measurements based on ALD-SnO_2 will be shown and correlated to material properties. Finally, the successful preparation of simple SnO_2/CeO_2 heterostructures will be demonstrated as a first step toward more complex material compositions and the impact on mate-

rial properties such as Ce cation oxidation state.

Results

Operando spectroscopic ellipsometry enables rapid ALD recipe optimization for TDMASn and O_3. The growth per cycle (GPC) has been determined to 0.6 Å to 0.7 Å between 0 and 750 cycles (0 and ~50 nm, respectively), in line with expectations based on the literature. No significant nucleation delay or change in the GPC for ultra-thin layers has been observed, showing ideal linear film growth on Si (see Fig. 1 as an example). A Drude-Lorentz model has been used to describe the SnO_2 layer.

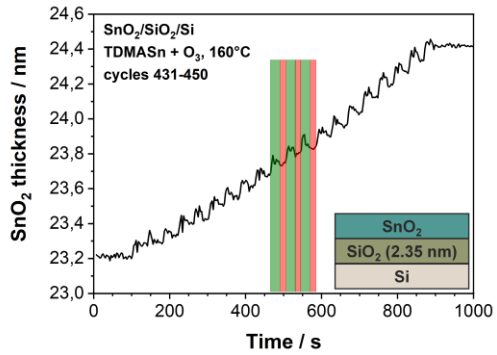

Fig. 1. The thickness evolution of SnO_2 was determined by operando SE during the ALD process. Green and red bars indicate the precursor and oxidant doses, respectively. The optical model is shown in the lower right.

In-situ Sn 3d XPS measurements during different stages of the deposition process indicate the absence of Sn metal in the ALD deposit. Early results from Auger parameter measurements hint at the presence of pure Sn^{4+}, with notable changes in the Auger parameter during the initial stages of growth. Together with information derived from the Si 2s core level associated with the native SiO_2 of the substrate, this is tentatively assigned to a change in the chemical environment, e.g., when transitioning from the SnO_2/SiO_2 interface to the SnO_2 film. This interfacial region could be especially relevant for ultra-thin SnO_2 films used in heterostructures or mixed oxides.

The amount of carbon and nitrogen residues from the TDMASn precursor in the film has been investigated by monitoring the C 1s and N 1s core level intensity evolutions with ALD cycles, respectively. Both show a noticeable intensity decrease compared to Sn 3d with increasing cycle number (cf., Fig. 2), indicating a difference in precursor reaction mechanism during the transition from hetero- to homoepitaxial growth [6], again relevant for use in future heterostructures.

Investigations of the sensing behavior of ALD-SnO_2 grown on sensor substrates with integrated electrodes are ongoing and will shed light on the influence of material properties on sensor response. In addition, surface decoration with small amounts of CeO_x nanoparticles and ultra-thin layers will be investigated to evaluate the impact of the heterostructure approach on operation temperature and sensor response.

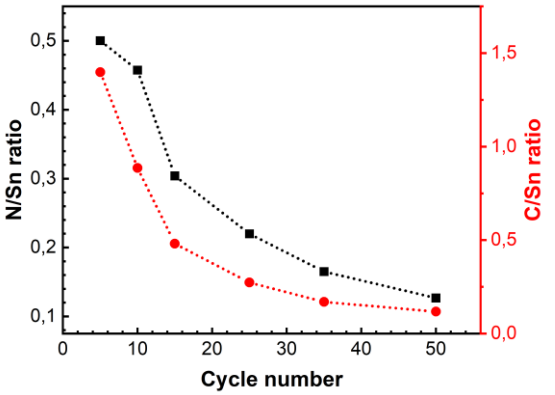

Fig. 2. Ratio of nitrogen and carbon to tin depending on ALD cycle number.

References

[1] T. Hübert, L. Boon-Brett, and W. Buttner, Sensors for Safety and Process Control in Hydrogen Technologies, 0 ed. CRC Press, 2018. doi: 10.1201/b19141.

[2] V. Cremers, R. L. Puurunen, and J. Dendooven, “Conformality in atomic layer deposition: Current status overview of analysis and modelling,” Appl. Phys. Rev., vol. 6, no. 2, p. 021302, Jun. 2019, doi: 10.1063/1.5060967.

[3] C. Morales et al., “Room temperature heterolytic H2 activation by ultrathin atomic layer deposited ceria for H2 sensing applications,” ChemSusChem, under review.

[4] A. J. M. Mackus, J. R. Schneider, C. MacIsaac, J. G. Baker, and S. F. Bent, “Synthesis of Doped, Ternary, and Quaternary Materials by Atomic Layer Deposition: A Review,” Chem. Mater., vol. 31, no. 4, pp. 1142–1183, Feb. 2019, doi: 10.1021/acs.chemmater.8b02878.

[5] C. Morales et al., “Combination of Multiple Operando and In-Situ Characterization Techniques in a Single Cluster System for Atomic Layer Deposition: Unraveling the Early Stages of Growth of Ultrathin Al2O3 Films on Metallic Ti Substrates,” Inorganics, vol. 11, no. 12, p. 477, Dec. 2023, doi: 10.3390/inorganics11120477.

[6] C. Morales et al., “In Situ X-Ray Photoelectron Spectroscopy Study of Atomic Layer Deposited Cerium Oxide on SiO_2 : Substrate Influence on the Reaction Mechanism During the Early Stages of Growth,” Adv. Mater. Interfaces, p. 2400537, Oct. 2024, doi: 10.1002/admi.202400537.

DOI 10.5162/SMSI2025/P

Measurement Systems for In-Situ Monitoring of Fuel Cell Systems Using Fiber Optical Sensors and Colorimetric Fluorescence Technology

Markus Reiter[1,2,3], *Gerald Auböck*[2], *Alexander Bergmann*[3], *Christof Sommitsch*[3], *Merit Bodner*[3]
Andreas Klug[1]
[1] *AVL List GmbH, Hans-List-Platz 1, 8020 Graz, Austria,*
[2] *Silicon Austria Labs GmbH, Sandgasse 34, 8010 Graz, Austria*
[3] *Graz University of Technology , Rechbauerstraße 12, 8010 Graz, Austria*
markus.reiter@avl.com

Summary:
Fuel cells (FC) are crucial in advancing sustainable transportation and energy production, though their industrial and automotive deployment remains limited. This research focuses on in-situ measurement solutions to enhance fuel cell performance, safety, and durability. Two instruments are being implemented: multiparameter fiber-optic (FO) sensors embedded in an additively manufactured bipolar plate (BP) for minimal invasive in-cell measurements and an online water analysis device for detecting degradation in FC wastewater. These solutions enable enhanced in-situ chemical and physical FC measurements.

Keywords: fuel cells, in-situ degradation monitoring, laser powder bed fusion, embedded fiber optical sensor, fluorescence sensor

Introduction

Innovative FC sensor solutions are essential for enhancing the development of proton exchange membrane (PEM) FCs, making them more affordable and durable. Real-time, in-situ measurements and characterization of inappropriate operating conditions is essential for better FC development and lifetime prediction. Dangerous conditions, such as an uneven humidity distribution or degradation of the perfluoro sulfonic acid (PFSA) Nafion® membrane material lead to membrane shrinkage and can cause irreversible damage to the FC. Monitoring spatially resolved membrane humidification and fluoride emission rates could be crucial for a more accurate FC system performance assessment. Additional in-situ data supports the development of simulation models and enhances their accuracy [1][2].

Methodology

A novel sensor solution for in-cell spatially resolved multiparameter monitoring is presented based on FO sensors embedded into an Additive Manufactured (AM) “smart” BP. The invention enables a minimally invasive multi-parameter measurement close to the chemical reaction of the FC. A Fiber Bragg Grating (FBG) technology is used for temperature and strain sensing, while tapered and laser-cut single-mode fibers are employed for humidity sensing [3].

Using the Laser Powder Bed Fusion (LPBF) process, a stainless-steel BP is 3D printed, embedding the fibers during process interruptions. However, this printing method encounters challenges, such as obtaining hydrogen gas tightness and ensuring that the BP's thermal, electrical, and fluid dynamical properties match those of standard BPs.

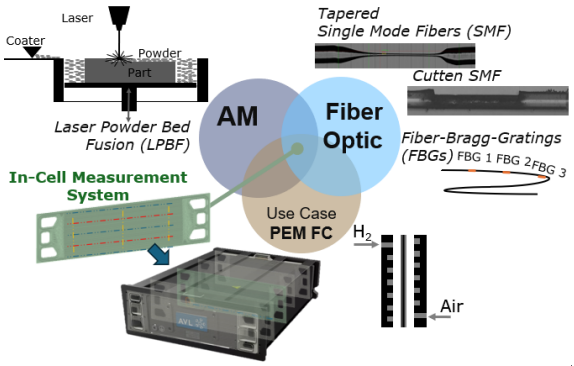

Fig. 1. Fusion of Additive Manufacturing and fiber optic sensors creates a “smart” bipolar plate for minimally invasive fuel cell application

Additionally, a real-time water analysis system for monitoring membrane degradation caused by free hydrogen radicals measures fluoride emissions in a time-resolved manner. This system uses a colorimetric fluorescent reagent with high selectivity for fluoride [4], laser excitation, and a

microfluidic cuvette to detect fluorescence, providing early indications of FC degradation. An integrated optical, microfluidic setup realized with an online sampling concept in the FC environment enables time-resolved measurement.

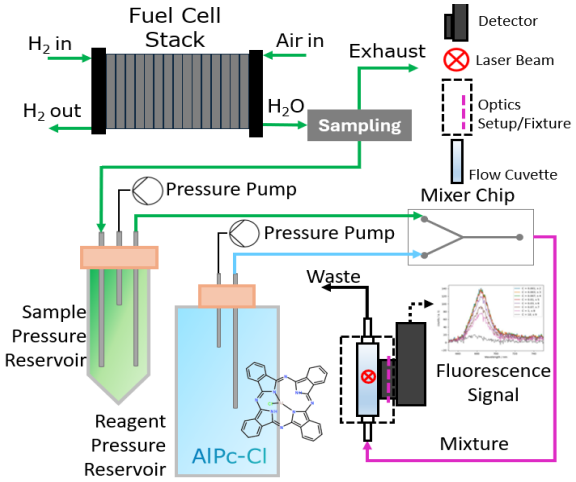

Fig. 2. Scheme of sensor concept for real-time fluoride measurement in PEM FC systems

Results and Discussion

The initial 3D printed BP was realized using 316L stainless steel, with the embedding OF for temperature and strain sensing based on FBG technology. AM prototypes successfully demonstrated H_2 gas tightness for FC applications. The first single-cell FC test bed application of a smart BP with embedded temperature OFs showed a good measurement correlation between detected hot spots and current density peaks measured with a shunt resistor current mapping board.

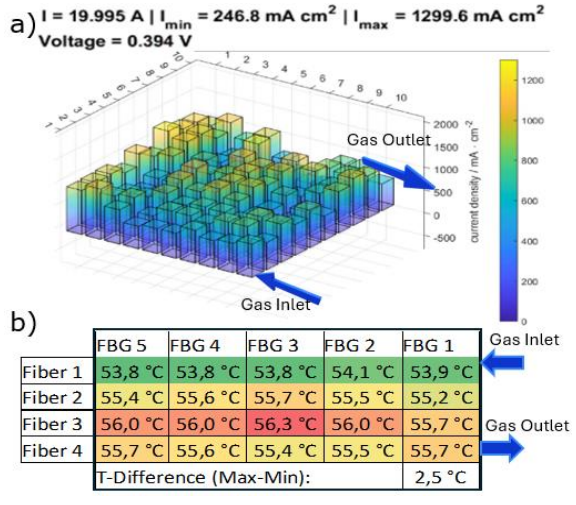

	FBG 5	FBG 4	FBG 3	FBG 2	FBG 1
Fiber 1	53,8 °C	53,8 °C	53,8 °C	54,1 °C	53,9 °C
Fiber 2	55,4 °C	55,6 °C	55,7 °C	55,5 °C	55,2 °C
Fiber 3	56,0 °C	56,0 °C	56,3 °C	56,0 °C	55,7 °C
Fiber 4	55,7 °C	55,6 °C	55,4 °C	55,5 °C	55,7 °C
T-Difference (Max-Min):					2,5 °C

Fig. 3. a) Current density distribution in a 5x5 cm single-cell FC test bed (cathode side). b) Temperature distribution in the smart bipolar plate (anode side)

Further enhancements aim to include humidity sensing using tapered or laser-cut single-mode fibers. Laser-cut fiber sensors demonstrated promising humidity correlation between 20%rH and 80%rH with ~1% accuracy. Improvements in fiber processing, such as debris cleaning and round edges design, enhance robustness in the embedding process and against rough environmental conditions in the FC.

A first research prototype for online sampling and time-resolved fluoride concentration measurements showed a detection limit below 10 ppb. The microfluidic system achieved accurate and bubble-free control of water analyte mixing with a constant flow rate of 15 µl/min and 10% water concentration. To achieve a faster aggregation of the F- with the reagent of approx. 6 minutes, the mixture was heated to 45°C, significantly improving PEM FC water quality assessment and membrane degradation detection.

Conclusion

Initial studies and implementations of the AM BP and the presented online product water analyzer show the potential of innovative sensor systems to identify and characterize unfavorable FC conditions. Preliminary lab and test bed applications demonstrated the potential for obtaining critical in-situ parameters and improving the identification of membrane degradation indicators, thus enhancing FC performance, lifetime, and safety.

Acknowledgment

This has been jointly supported by industry companies and an RTO owned by the Republic of Austria, the *Styrian Business Promotion Agency* (SFG), the federal state of Carinthia, *Upper Austrian Research* (UAR), and the *Austrian Association for the Electric and Electronics Industry* (FEEI) and research projects funded by the *Austrian Research Promotion Agency* (FFG), the *Climate and Energy Fund*, part of "*Zero Emission Mobility*" program.

References

[1] Nguyen, H.L.; et al., Review of the Durability of Polymer Electrolyte Membrane Fuel Cell in Long-Term Operation: Main Influencing Parameters and Testing Protocols. *Energies*, 14, 4048 (2021); https://doi.org/10.3390/en14134048

[2] Yuan, X.-Z.; et al. Degradation of a PEM Fuel Cell Stack with Nafion® Membranes of Different Thicknesses. Part II: Ex Situ Diagnosis. *Power Sources*, 205, 324–334 (2012); https://doi.org/10.1016/j.jpowsour.2012.01.074

[3] Korposh, S.; et al. Tapered Optical Fibre Sensors: Current Trends and Future Perspectives. *Sensors*, 19, 2294 (2019); https://doi.org/10.3390/s19102294

[4] A. Chatterjee; et al. Highly Sensitive Optical Sensor for Selective Detection of Fluoride Level in Drinking Water. *ACS Sustainable Chemistry & Engineering*, 9 (20), 7160-7170 (2021); 10.1021/acssuschemeng.1c02101

DOI 10.5162/SMSI2025/P33

MEMS-SPM for dynamic nanomechanical measurements of soft materials

Zhi Li[1], Uwe Brand[1]
[1] Physikalisch-Technische Bundesanstalt, Bundesallee 100, 38116 Braunschweig, Germany
Zhi.li@ptb.de

Summary:
High throughput nanomechanical characterization of soft materials including biomaterials demands further development of advanced nanomechanical measurement systems. A microelectromechanical system based scanning probe microscope (MEMS-SPM) for nanomaterial testing has been developed to bridge the metrological gap between typical nanoindentation instruments and nanomechanical AFMs. Proof-of-principle measurements of typical reference materials including PC with a bandwidth up to 20 kHz have been reported to validate the advanced measurement capability of the MEMS-SPM.

Keywords: Nanomechanical measurements, nanoindentation, nano-dynamic mechanical analysis (nano-DMA), microelectromechanical systems (MEMS), scanning probe microscopy (SPM)

Motivation

Quantitative measuring the mechanical properties of soft materials is essential in the field of biomedical applications such as tissue engineering and regenerative medicine, material development and quality control for soft robotics including soft robotic actuators and components, biophysics and cell mechanics.

To date, nanoindentation instruments with diamond Berkovich and ball-shaped indenters have proven to be qualified for mechanical measurements of bulk materials. However, their relatively poor force resolution has limited the application of nanoindentation instruments for biomaterial measurements. Nanomechanical AFMs have become powerful tools for biomaterial testing with relatively high lateral resolution. However, the indentation force and depth of AFMs are quite often inadequate for quality control of hybrid materials.

To bridge the metrological gap between nanoindentation instruments and nanomechanical AFMs, recently a MEMS-SPM has been proposed [1]. Quasi-static measurements of typical soft materials including various thermal plastic polymers with the MEMS-SPM have demonstrated the fundamental performance of the MEMS-SPM for nanomechanical measurements.

In this manuscript, the MEMS-SPM system has been further developed for the purpose of high-throughput nanomechanical measurements of soft materials.

Principle

The schematic of the MEMS-SPM for high-throughput nanomechanical measurements is illustrated in Fig. 1. It consists typically of a group of electrostatic comb-drives for force modulation and indentation depth sensing, and a passive cantilever gripper integrated on the main shaft of the MEMS-SPM. This gripper is especially optimized to hold non-contact AFM probes for material testing.

With this integrated cantilever gripper, nearly all commercially available AFM probes with a tip height larger than ~ 5 µm can be clamped by the MEMS-SPM head and utilized for material testing. For nanomechanical measurements of extremely soft biomaterials, ball-shaped AFM probes are recommended in [1].

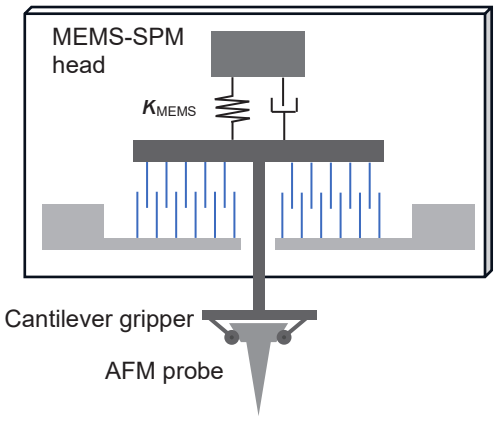

Fig. 1. Schematic of the MEMS-SPM head for nanomechanical characterisation of nanostructured materials.

In the case of quasi-static nanomechanical measurements, various capacitive sensors including commercial capacitance to digital converters (e.g. AD7745/46/47) can be utilized for indentation depth measurements with a resolution down to 10 Picometer.

To implement dynamic mechanical measurement methodology [2], a measurement system on basis of typical lock-in technique has been developed. As illustrated in Fig. 2, the carrier signal f_c overlapped with the modulation signal f_m is sent to the comb-drives within the MEMS for force modulation and indentation depth measurement. The through-put current coming from the MEMS is firstly converted to voltage signal and then sent into the lock-in amplifier for further analysis.

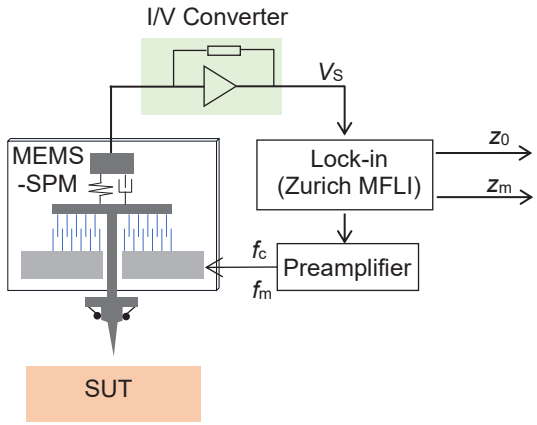

Fig. 2. Schematic of the signal processing and data acquisition system for dynamic mechanical measurement with the MEMS-SPM.

In our measurement system for dynamic measurements, the typical carrier signal f_c is set to 500 kHz for quasi-static indentation depth (z_0) measurement with subnanometric resolution and a bandwidth up to 300 Hz. The self-developed preamplifier for dynamic measurements features a DMA bandwidth up to 50 kHz.

Results

To demonstrate the capability of the MEMS-SPM for nano-DMA measurements, typical reference materials have been measured. Fig. 3 shows typical frequency-amplitude response of PC measured by the MEMS-SPM with a clamped diamond AFM probe. It can be seen that the MEMS-SPM head has a resonance frequency of about 2.9 kHz. After engagement with the reference sample, the contact resonance frequency of the measurement system is shifted to about 12.5 kHz.

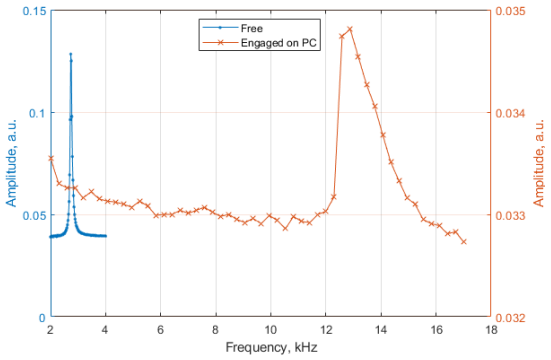

Fig. 3. Typical dynamic response of reference PC under MEMS-SPM measurements.

Summary and outlook

Quantitative data evaluation algorithm for MEMS-SPM will be further developed to extract the dynamic mechanical properties of soft materials including complex modulus and the loss factor. Quasi-static and dynamic nanomechanical measurements of the reference materials using commercial nanoindentation instrument (e.g. Hysitron Tiboindenter TI-950) will be performed.

The measurement uncertainty of the MEMS-SPM will be evaluated by means of the comparison measurements.

References

[1] Z. Li, S. Gao, U. Brand, K. Hiller, H. Wolff, A MEMS nanoindenter with an integrated AFM cantilever gripper for nanomechanical characterization of compliant materials, *Nanotechnology* 31, 305502 (2020); doi:10.1088/1361-6528/ab88ed

[2] S.R. Cohen, E. Kalfon-Cohen, Dynamic nanoindentation by instrumented nanoindentation and force microscopy: a comparative review. *Beilstein J Nanotechnol.* 4:815-33 (2013). doi: 10.3762/bjnano.4.93.

DOI 10.5162/SMSI2025/P34

Point Cloud Data Processing in Scanning Probe Microscopy

Petr Klapetek[1], *Miroslav Valtr*[1], *David Nečas*[2], *Edward Heaps*[3], *and Andrew Yacoot*[3]
[1] Czech Metrology Institute, Okružní 31, 638 00 Brno, Czech Republic
[2] CEITEC, Brno University of Technology, Purkyňova 123, 612 00 Brno, Czech Republic
[3] National Physical Laboratory, Hampton Road, Teddington, Middlesex, TW11 0LW, United Kingdom
pklapetek@cmi.cz

Summary: This work describes the methods for processing general XYZ data clouds which are the primary data coming from metrological Scanning Probe Microscopes (SPM).They can also be obtained also with other SPM instrumentation. XYZ data are more general than the normal raster scan data, typically used in SPM. The transition from raster data to point clouds allows much more complex scanning patterns to be used easily and makes the SPM sampling closer to that used in other 3D measurements systems such as coordinate measuring machines. The with all the benefits and drawback of this approach for scanning probe microscopes are discussed.

Keywords: Data Processing, Scanning Probe Microscopy, Metrology

Introduction

Scanning Probe Microscopy is a widely used measurement technique, suitable for determining dimensional and physical properties with nanometre resolution and with no need for sample preparation. It is based on use of a sharp probe that is physically scanned across the sample surface, while the force between the probe and surface is detected and used to establish a probe-sample distance feedback.

Conventional microscopes perform measurements in a raster pattern, *i.e.* the sample is scanned using an equidistant set of points lying on a rectangular grid. The benefit of this approach is that the results can be easily visualized. However, information on the sample is only rarely distributed homogeneously, so the sampling resolution is therefore in principle too low or too high on different areas of the scanned surface. Increasing the scan resolution, however, means increasing the scanning time, which leads to low throughput and increased impact of parasitic effects like thermal drift. When it comes to large area SPMs[1], designed to study industrially relevant sample areas scanning over millimetre ranges, raster patterns become highly ineffective. They are also unsuitable for high-speed SPMs[2], designed mostly for life-sciences applications as they contain too sharp turnarounds, leading to mechanical vibrations.

A solution is to use non-raster patterns, either optimized to obtain the information with density adapted to its local content or optimized to provide smooth mechanical motion. However, data processing techniques for non-raster data in SPM are highly underdeveloped. Here we describe some algorithms developed for the open source software Gwyddion[3] to treat general XYZ data, i.e. point clouds.

XYZ data acquisition

XYZ data sets are organized in a manner such that every sampled point comprises an x, y and z coordinate value. This is a natural way to store data from metrological systems where interferometric sensors are used to determine the probe or sample position in space.

To drive a microscope in a non-raster pattern we have used a Gwyscope open hardware digital signal processor[4] which is fully designed to work with general XYZ data sets. On top of it, every point is stored also with its timestamp, relative to the measurement start time. The microscope was based on use of a large area air bearings and voice coil motor based stage combined with a high-speed stage using piezoelectric transducers. Positions of both stages were measured using interferometers, as illustrated in Fig. 1.

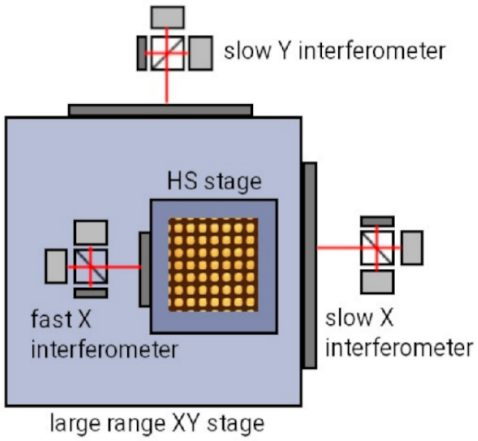

Fig. 1: Dual stage system with interferometers used to measure the XYZ data set

XYZ data processing

The XYZ point clouds in Gwyddion open source software are loaded as a special data type and dedicated data processing modules are provided for them. This includes the key operations that are needed to pre-process and evaluate the data: cropping data in time or space, organizing the point clouds data (merging, splitting, sorting), assigning the scales and units to them, etc. The data can be also filtered using Fast Fourier Transform, assuming that they were generated at constant sampling speed and they can be leveled to remove probe-sample tilt. Drift in the data can be estimated from the crossing points in the sampling pattern. Data can be at any moment rasterized to a regular grid to enable use of much wider set of data processing algorithms developed for the conventional scans, however this is not the goal. Algorithms are being developed for direct processing of XYZ data, e.g. for fitting a geometrical shape on it. All the algorithms discussed here are available in the open source software Gwyddion (http://gwyddion.net).

Results

Here we show an example of processing a XYZ data cloud from a measurement on a chessboard pattern calibration sample. The measurement was performed using a combination of a high-speed short range stage scanning in the x direction and large area stage moving in both x and y direction. This leads to a complex scan pattern on the surface. As the measurement was done using a simple setup that was not thermally optimised, there is a significant z drift in the data. In traditional raster data it would be easy to remove it by adjusting individual scan lines, however, for a general point cloud this is not possible. The drift was therefore detected from the crossing points,*i.e.* points where the scan path intersects itself. As all the data points also include a timestamp, we could evaluate the evolution of the z coordinates as a function of time and fit a polynomial drift model on these data. By removal of this polynomial the drift was significantly reduced, as seen in Fig. 2. It should be noted that there are also some other parasitic effect coming from mechanical oscillations of the test setup, nevertheless the data were significantly flattened using this approach.

Conclusions

A set of algorithms for XYZ point clouds generated in Scanning Probe Microscopy was developed and included in the Gwyddion open source software. It enables running advanced SPM experiments with more complex sampling patterns without need for developing the data processing tools from scratch. XYZ point clouds are a natural way how to extend the SPM functionality towards larger area and higher speed measurements.

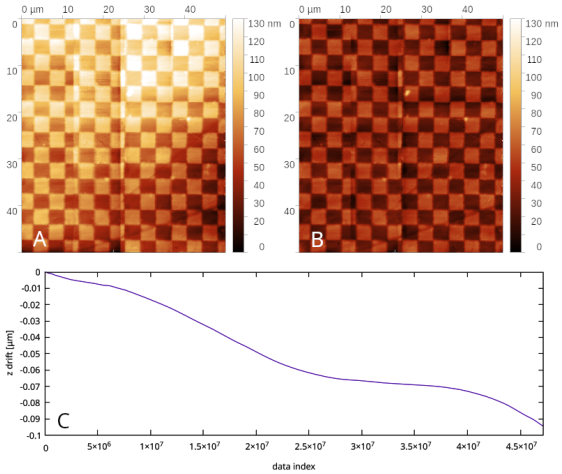

Fig. 2: Drift removal from XYZ data clouds measured on the checkerboard grating: A) raw data, B) processed data, C) estimated drift.

Acknowledgments

The work was supported by the 20IND08 MetExSPM project that has received funding from the EMPIR programme co-financed by the Participating States and from the European Union's Horizon 2020 research and innovation programme and by Institutional Subsidy for Long-Term Conceptual Development of a Research Organization granted to the Czech Metrology Institute by the Ministry of Industry and Trade of the Czech Republic. This work was additionally partly funded by the UK Government's Department for Science, Innovation & Technology through the UK's National Measurement System programmes.

References

[1] T. Hausotte, G. Jäger, E. Manske, N. Hofmann, and R. Mastylo, "Traceable nanometrology with a nanopositioning and nanomeasuring machine.," in *Proc. International Symposium on Precision Mechanical Measurements (ISPMM'2004)*, pp. 399–404, 2004.

[2] T. Ando, "High-speed atomic force microscopy coming of age," *Nanotechnology*, vol. 23, p. 062001, 2012.

[3] D. Nečas and P. Klapetek, "Gwyddion: an open-source software for SPM data analysis," *Central European Journal of Physics*, vol. 10, no. 1, pp. 181–188, 2012.

[4] M. Valtr, P. Klapetek, J. Martinek, O. Novotný, Z. Jelínek, V. Hortvík, and D. Nečas, "Scanning probe microscopy controller with advanced sampling support," *HardwareX*, vol. 15, p. e00451, 07 2023.

DOI 10.5162/SMSI2025/P35

Calibration of Temperature Probes on Heat Pipes

Jacques-Olivier FAVREAU[1], Eric GEORGIN[2],
[1] CETIAT, 25 avenue des arts 69100 VILLEURBANNE FRANCE,
Jacques-olivier.favreau@cetiat.fr

Summary:

For the past ten years, CETIAT has been working on the development of a new type of temperature generator. The goal is to reduce the stabilization time at calibration temperatures while ensuring an exceptional thermal quality of the comparison medium.

Heat pipe-based temperature generators are studied in several metrology institutes, such as INRIM and LNE. While water-based heat pipes have already been the subject of extensive research, the innovation introduced by CETIAT lies in the development of an ethanol-based heat pipe. This breakthrough enables coverage of a temperature range suitable for industrial calibrations, from -30 °C to 120 °C. This is made possible by combining two heat pipes: one using water and the other ethanol. These heat pipes are GCHPs: Gas-Controlled Heat Pipes.

The use of a heat pipe for calibrations at negative temperatures represents a first in metrology. In 2024, this calibration method was accredited by COFRAC. This article provides a summary of the results obtained and the calibration possibilities offered by this innovative technology.

Keywords: GCHP, Heat pipe, Calibration, metrology

1. Why use heat pipes as a comparison medium?

Heat pipes offer two major advantages: exceptional thermal homogeneity and robust, rapid implementation. The heat pipe effect relies on the liquid-gas phase change of a fluid, governed by Clapeyron's law. This phenomenon ensures an extremely stable phase transition temperature. The energy supplied to the system is absorbed during this phase transition, thus limiting the influence of external disturbances. When a heat pipe is connected to a regulated pressure circuit, it becomes possible to continuously adjust the temperature setpoints, as the adjustment parameters are temperature and pressure.

2. Operation of a heat pipe in metrology

The heat pipe effect is based on the liquid-to-gas phase change of a fluid. Clapeyron's law defines this phase change, which is extremely stable.

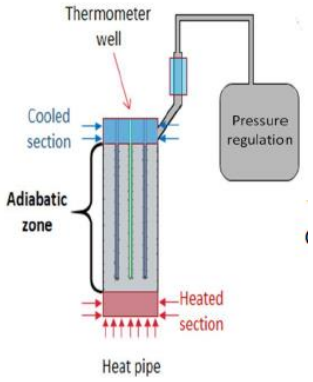

Fig. 1. Principle Diagram of the Heat Pipe Effect

A metrological heat pipe takes the form of a sealed cylinder. At its base, a fluid is heated and evaporates (evaporator). The resulting vapor condenses on a cooled upper surface (condenser), before flowing back by gravity to the evaporation zone. Between these two areas, a nearly adiabatic central region provides remarkable thermal homogeneity, making it ideal for calibration applications.

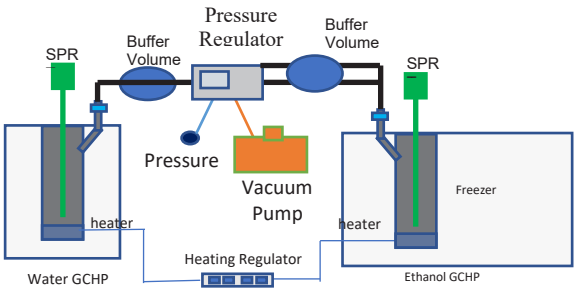

Fig. 2. Principle Diagram of the CETIAT GCHP

Compared to an overflow thermostat bath, the heat pipe offers superior thermal performance due to this effect. Additionally, regulation is provided by a pressure control system, which is more responsive than a traditional resistive device, allowing for quick adjustments of setpoints on heat pipe-based generators (GCHPs). Once the temperature and pressure conditions are defined, the heat pipe effect is established in a highly reproducible manner.

3. Adaptation to Calibrations

To transform a heat pipe into a temperature generator for calibrations, it is necessary to add inserts (heat sinks) for inserting the probes to be calibrated, like dry block ovens. Although the sensors are not directly immersed in a heat transfer fluid, as they would be in a calibration bath, the impact is negligible thanks to the excellent thermal characteristics of the heat pipe. Moreover, this setup also allows for the calibration of non-immersible sensors, provided their diameters are compatible.

Fig. 3. Photo of the CETIAT GCHP.

The GCHPs are thus ideal candidates for the realization of automated calibrations, combining precision, speed, and robustness.

4. Description of the Heat Pipes

The water-based heat pipe consists of a stainless-steel cylinder with a diameter of 114 mm and a length of 440 mm, featuring internally grooved walls. It is equipped with a removable lid that includes seven inserts (heat sinks) for inserting the sensors to be calibrated. These inserts, 400 mm in length and with an internal diameter of 10 mm, are particularly suited for calibrating long-stem reference probes such as SPRTs.

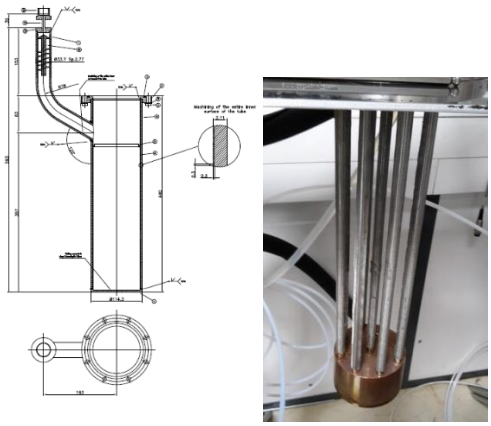

Fig. 4. Photo and diagram of the heat pipe

The walls immersed in the heat pipe are covered with a metallic wick that allows the flow of the condensate. A "gel tube" type cooling system maintains a constant temperature at the condenser throughout its use. The only variable parameters are the heating temperature at the evaporator and the pressure applied to the heat pipe. The pressure setpoint allows for precise definition of the internal temperature of the heat pipe, thanks to a pre-established pressure-temperature curve. Once configured, this system is easy to use.

Pressure regulation is achieved by a high-precision regulator, the Pace 6000, allowing adjustments to the nearest pascal. By knowing the pressure-temperature relationship, it becomes possible to quickly reach the desired temperature with excellent stability, making the heat pipe an ideal medium for calibrations.

5. Characterization of the GCHP

The two heat pipes at CETIAT have been characterized thermally according to the best current practices for characterizing temperature generators, including the use of a calibration bath. This characterization was carried out using reference thermometers, calibrated within the laboratory. We analysed the homogeneity and stability of the working volume over a period of at least 30 minutes, after the thermal steady state was established. The thermal load allowed us to evaluate the heat pipe's ability to compensate for the effect of a significant thermal load, such as the simultaneous calibration of six thermometers. Although the results obtained are lower than those from the National Metrology Laboratory

due to the traceability of the thermometers used, they still allow for an improvement in calibration uncertainty, reducing it from 0.03 °C to 0.02 °C.

Result /°C	Water	Ethanol
Homogeneity	0.001	0.005
Stability	0.003	0.009
Thermal loads	0.001	0.003

Fig. 5. Performance of the CETIAT GCHP.

6. Temperature Ranges and Innovations

The water-based heat pipe covers a temperature range from +30 °C to +120 °C. To extend this range, CETIAT has developed an ethanol-based heat pipe, a first in the field. This heat pipe is installed in a freezer maintained at a constant temperature of -80 °C, ensuring an ambient temperature lower than the operating temperature. This configuration allows the ethanol-based heat pipe to function effectively in a range of negative temperatures.

The thermal performance of the ethanol-based heat pipe is comparable to that of the water-based heat pipe. Together, these two devices provide CETIAT with high-quality metrological comparison media, covering a temperature range from -30 °C to +120 °C.

7. Validation and Implementation

The method was validated through an inter-laboratory comparison conducted with other laboratories accredited by COFRAC according to ISO 17025, with uncertainty levels that are closely aligned. The results showed a normalized deviation of less than 1, confirming the reliability of the method. In 2024, this approach was officially accredited by COFRAC.

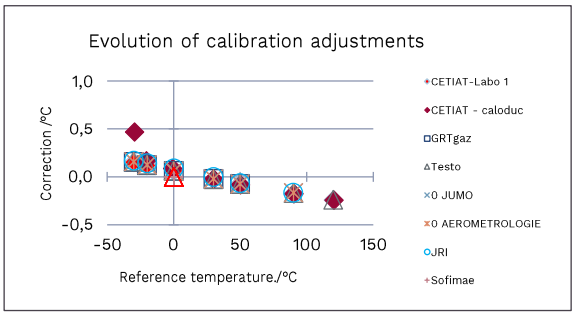

Fig. 6. *Results of the inter-laboratory comparison*

Today, CETIAT is able to perform temperature calibrations with an uncertainty of 0.02 °C. Initially, these calibrations will be reserved for internal use to allow laboratory technicians to gain expertise and experience. Ultimately, this expertise will be extended to commercial calibration services.

8. Conclusion

The implementation of pressure-regulated heat pipes as a comparison medium for temperature calibrations has been at the heart of extensive research, particularly in national metrology laboratories in France, Italy, and other countries. For the first time, CETIAT has developed a heat-pipe-based temperature generator intended for industrial calibrations.

To meet the needs of commercial calibrations, CETIAT has also innovated by designing a heat pipe capable of operating at negative temperatures, a first. This system relies on the integration of an ethanol-based heat pipe in a freezer, thereby opening up new possibilities.

The ongoing optimization of uncertainty budgets will ultimately allow for the offering of commercial calibrations with significantly reduced uncertainty levels compared to current solutions. Moreover, CETIAT is actively committed to promoting this type of high-quality generator, while highlighting its ease of use.

References

[1] Favreau J O, Georgin E, Savanier B and Merlone A 2017 International Journal of Thermophysics 38 11

[2] Rusby R L, Pearce J V, Elliott C J 2017 International Journal of Thermophysics 38 186

[3] Merlone A, 30 YEARS OF PROGRESS IN THE USE OF GAS-CONTROLLED HEAT PIPES FOR THERMODYNAMIC MEASUREMENTS, https://doi.org/10.1016/j.measurement.2020.108103 Measurement, Volume 164, November 2020, 108103

DOI 10.5162/SMSI2025/P36

Mass value correction method for weighing cell based on digital PID state-locking control

Pengpeng Sun[1], Jian Wang[1], Cheng Peng[1]
[1] National Institute of Metrology, Beijing, 100029, China
wjian@nim.ac.cn

Summary:
The weighing cells with electromagnetic force compensation are frequently employed for high-precision mass measurement. Digital control enables more comprehensive monitoring and facilitates the implementation of flexible control algorithms. However, due to the limited resolution of the digital-to-analog converter, small-step impacts exist in the electromagnetic force control process, adversely affecting the balancing process of the highly sensitive mechanical elastomer. The lever exhibits a discernible amplitude of vibration even in its stable stage, thereby inducing repetitive deformation in each flexible hinge and resulting in significant fluctuations of the measured values. A digital PID state-locking measurement method was proposed to reduce the influence of lever vibration on measurement results by fixing the states of input, output, and integration of the PID controller during stable stages, which disconnects the PID controller and the displacement of the mechanical elastomer. Additionally, mass values calculated using coil current are corrected by lever end displacement, leveraging the low stiffness coefficients exhibited by flexible hinges. Experimental results demonstrate that the proposed method effectively reduces fluctuation amplitudes in mass values during balance stages, thereby enhancing quality measurement accuracy.

Keywords: electromagnetic force compensation, weighing cell, digital PID control, mass correction.

Introduction

Weighing cells with electromagnetic force compensation is frequently used in high-precision mass measurement [1,2]. With the development of metrology digital transformation [3] and real-time control technology, digital control enables more comprehensive monitoring and flexible control algorithms for the weighing cells. However, due to the limited resolution of digital-to-analog converters (DAC), there is a small step shock in coil current control, resulting in excessive fluctuation. Additionally, the low natural frequency of highly sensitive mechanical elastomers makes feedback control of coil current susceptible to external signals, such as vibrations caused by lever movement during balance positioning. The adoption of digital control amplifies this vibration amplitude, which negatively impacts the measurement accuracy of the weighing unit. To mitigate mass measurement value fluctuations during steady stages, the displacement of the lever end is utilized to correct the mass value calculated by coil current.

Method

The weighing unit utilizes the lever balance principle to convert force signals into electrical signals for high-precision measurements. When balanced at the pivot hinge point, as shown in Fig. 1, the equilibrium equation can be expressed as eq. (1).

$$m_t g L_t = B I_{coil} L_{coil} L_l + k_{eq} \varphi \quad (1)$$

Where m_t is the mass value of the tested weight, L_t is the force arm of the tested weight relative to the fulcrum hinge, k_{eq} is the equivalent rotational stiffness coefficient of elastomer, φ is the rotation angle of the balance, B indicates magnetic induction intensity, L_{coil} refers to effective length of coil within magnetic field, I_{coil} is the coil current, and L_l is the equivalent lever of the lorentz force.

The tested mass can be expressed as eq. (2).

$$m_t = k_l I_{coil} + k_s s_{tail} \quad (2)$$

Where k_l is related to elastomeric link size, magnetic steel structure, permanent magnet strength, coil length and local gravity acceleration; while k_s is related to elastomeric link size, flexible hinge stiffness coefficient and local gravity acceleration among other parameters.

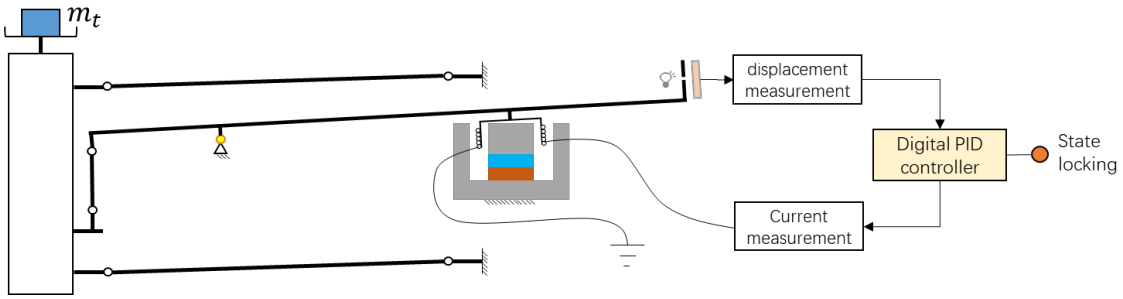

Fig. 1. Digital PID state locking measurement method of weighing cell.

The unbalance of the lever, as indicated by eq. (2), introduces a certain error in the calculated mass solely based on the coil current. However, this error can be corrected by the displacement at the end of the lever.

Therefore, the zero-order holder is utilized to lock states of the PID controller during the lever stabilization stage, as shown in Fig. 1. As a result, the negative feedback control channel of the electromagnetic force is interrupted, allowing the elastomer lever to freely balance under the tested weight and the electromagnetic force. Due to the mechanical properties of the elastomer and torque stiffness of the flexure hinge, a slight amplitude vibration eventually occurs at a specific position on the lever. The mass value calculated by coil current can be corrected based on Eq. (2) using the balance position of lever displacement vibration and the low stiffness coefficient to reduce the fluctuation of the steady-state stage of the weighing module under digital control. The stationary stage of the lever can be determined by whether or not its end displacement peak-to-peak value remains below a threshold value for a certain period.

Results

A weighing cell controlled by a digital PID controller was set up based on the TwinCAT development platform. The real-time control period was set to 2ms. Lever end displacement was measured by a photodiode and division amplifier circuit. The voltage and current acquisition cards were selected with 24-bit resolution, while the voltage DAC was selected with 16-bit resolution.

The experiment was carried out with a weight of 2g. Fluctuations in mass measurement results within the 60s during the stable stage were compared between analog circuit PID control, traditional digital PID control, and digital PID lock control, as shown in Table 1. The fluctuation error of traditional digital PID continuous control was the largest because of the resolution limitation of the voltage DAC. The results of the digital PID state-locking method exhibit the most minor fluctuation error, reduced by about 53% compared to traditional digital PID control and about 24% compared to analog PID control.

Tab. 1: The fluctuation results of the mass value in the stable stage during the mass measurement

Control Method	peak-to-peak value (μg)	standard deviation (μg)
Analog PID control	21.5	3.7
Traditional digital PID control	35.9	6.3
Digital PID state-locking control	16.9	2.8

Summary and Outlook

In conclusion, the proposed method of digital PID locking control and lever end displacement correction effectively reduces the amplitude of measurement result fluctuations and enhances the measuring accuracy of the digitally controlled weighing cells.

The future holds the potential for enhanced measurement accuracy of weighing units through real-time digital monitoring and control, enabling the integration of additional sensing capabilities such as ambient temperature and magnetic steel temperature, which will facilitate the establishment of digital twin models for weighing cells.

Acknowledgement

This work was funded by the National Natural Science Foundation of China (No. 52075515).

References

[1] M. Darnieder, M Pabst, R Wenig, et. al, Static behavior of weighing cells, Journal of Sensors and Sensor Systems, 7, 587-600(2018); doi: 10.5194/jsss-7-587-2018

[2] M Pabst, M. Darnieder, R Theska, T Fröhlich, Adjustment concept for compensating for stiffness and tilt sensitivity of a novel monolithic electromagnetic force compensation (EMFC) weighing cell, Journal of Sensors and Sensor Systems, 11, 109-116(2022); doi: 10.5194/jsss-11-109-2022

[3] Hackel Siegfried, Schönhals Shanna, et. al, The Digital Calibration Certificate (DCC) for an End-to-End Digital Quality Infrastructure for Industry 4.0, Sci, 5, 11(2023); doi: 10.3390/sci5010011

DOI 10.5162/SMSI2025/P37

Improved impulse magnetization of magnetic measurement scales

Dr., Rolf Slatter[1], *Bernd Böhle*[1], *Uwe Rother*[1]
[1] *ELSOMA GmbH, Kurzer Morgen 7, 58239 Schwerte, Germany*
rolf.slatter@elsoma.de

Summary:
Magnetic measurement scales, in the form of linear scales or multi-pole rings, are a key component in magnetic sensor systems for angle or length. Demands for longer scale lengths, increased accuracy, higher resolution and larger air gaps are pushing new developments, both in the field of new magnetic materials, and in the area of the magnetization technology used to encode the scales. A newly developed intelligent impulse magnetization head helps fulfil these new requirements and offers ways to remove some errors typically associated with magnetic measurement scales.

Keywords: measurement scales, magnetic sensors, angle measurement, length measurement, magnetization

Motivation

For several years, there has been a steadily increasing demand for magnetic-based measuring systems in industrial automation. Such measuring systems are characterised by a high degree of robustness and, at the same time, high cost-effectiveness [1]. In numerous areas of application, e.g. in semiconductor manufacturing, magnetic measuring systems have become the preferred solution for position and speed detection in moving machine axes.

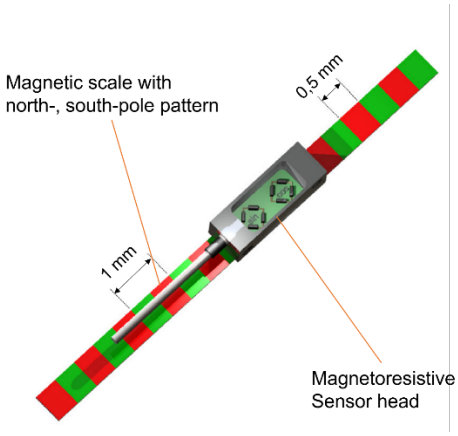

Fig. 1. Typical magnetic length measurement system

These measurement systems typically consist of magnetic sensors based on either magneto-resistive or Hall-effect technology, in conjunction with magnetic scales for linear and rotary motion. A pole pattern of north and south poles is written or encoded on the scale to enable both incremental and absolute distance or angle measurement (see Figure 1).

Different materials are used for the magnetic layer that can be written on. There have been some promising new developments in this area based on thin layers of hard magnetic materials that guarantee significantly better measurement accuracy and are even more resistant to contamination, high operating temperatures and high mechanical loads [2].

However, new requirements are emerging. There is a tendency towards larger measuring lengths, caused, among other things, by the trend towards the use of larger wafer formats in the semiconductor industry, which leads to longer travel distances for the testing machines used. In addition, even higher accuracies with a further improved price-performance ratio are required to make completely new applications accessible.

This could displace optical and inductive-based linear and angle measurement systems. To meet these market needs and to fully exploit the potential of new magnetic materials, the machines used to describe and encode the scales require significant further development.

In the BMBF-funded research project ELM2 ‘Development of a high-precision linear magnetising system for the description of magnetic scales’, which ran from July 2022 to December 2024, the Lahnau-based SME ITK Precisioning GmbH set itself the goal of enabling a higher level of

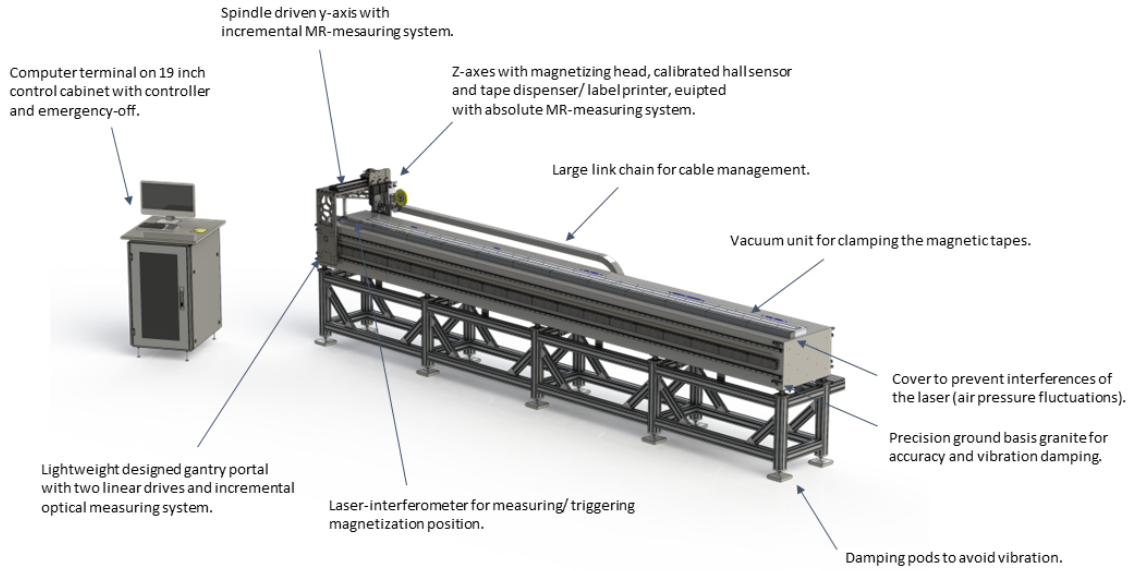

Fig. 2. Demontrator linear magnetization machine (Source: ITK Precisioning GmbH

magnetic measuring systems through the development of a new, high-precision linear magnetizing system.

Four essential developments were combined:

1. Based on FEM simulations, a thermally stable and rigid machine structure was designed to quickly and accurately describe scales up to 5 m in length (see Figure 2).

2. Direct drive technology, in the form of linear motors, in conjunction with lightweight structural elements, is intended to ensure higher machine dynamics and optimized throughput.

3. A new writing method has been established to enable pole correction and thus significantly higher scale precision.

4. Continuous writing and simultaneous writing and measuring (i.e. testing) should achieve a significant increase in productivity.

Development of a new impulse magnetization head

In order to deal with the third development area ITK approached ELSOMA GmbH, based in Schwerte, with the task of developing a new impulse magnetization head to be used in the ELM2 demonstrator machine.

The resulting ELSOPULS® IIM2k impulse-magnetization head (see Figure 3) is a microprocessor-controlled magnetizing device with integrated diagnostic and measuring functions. It is particularly suitable for magnetizing plastic-and elastomer-bonded hard ferrite magnets. The ability to emit very short magnetizing pulses enables the production of multi-pole magnets with pole pitches in the range of 1 to 5 mm. The short pulses lead to low thermal losses, which in turn, enables fast writing speeds.

Fig. 2. ELSOPULS IIM2k impulse-magnetization head (Source: ELSOMA GmbH

The new impulse head features a significantly higher magnetization field than previous solutions, so enabling the encoding of more coercive materials. Furthermore, the programmable current profile helps eliminate common errors e. g. by avoiding the start-pole error typically associated with multi-pole rings [3]

References

[1] Dixon, R.; „A market perspective on the opportunities for magnetoresistive technology “, Proc. of 15th xMR-Symposium, Wetzlar, 2019

[2] Bandorf, R., Ortner, K. & Krau, M.; „PVD-Abscheidung von CoSm-Schichten für magnetische Maßstäbe“, Vakuum in Forschung und Praxis, Vol. 32, No. 5, Oktober 2020

[3] Knoll, H. *et al*; Investigation and Assessment of the Magntization Accuracy for different Magnetization Technologies for long magnetic scales, 25th XMR-Symposium, Wetzlar, March 2025

DOI 10.5162/SMSI2025/P38

Fabrication and Characterization of CO_2 Sensor Using ZnO<In> Nanograins

M. Aleksanyan, G. Shahkhatuni, Z. Simonyan, G. Shahnazaryan, R. Papovyan, D. Kananov, A. Grigoryan, G. Gevorgyan, G. Stepanyan, A. Sayunts
Center of Semiconductor Devices and Nanotechnologies, Yerevan State University, 1 Alex Manoogian, 0025, Yerevan, Armenia,
Corresponding Author's e-mail address: sayuntsartak@ysu.am

Summary:
This work presents the development of a CO_2 gas sensor based on ZnO+0.5 at.% In_2O_3. The sensor, with a thickness of 40 nm, was prepared using the high-frequency magnetron sputtering method. The produced thin film exhibited excellent gas sensing characteristics towards CO_2 at an operating temperature of 265°C. In the presence of 5000 ppm of CO_2, the sensor demonstrated a decrease in resistance of approximately 2.3 times, indicating a linear dependence of the sensor response on gas concentration.

Keywords: Gas sensor, carbon dioxide, zinc oxide, greenhouse gases, nanograins

Title

As climate change becomes an urgent global issue, managing greenhouse gases, particularly carbon dioxide (CO_2), is crucial to mitigating its harmful environmental effects. The rise in CO_2 levels, primarily driven by industrial activities and the burning of fossil fuels, significantly contributes to global warming [1]. This increase in CO_2 accelerates shifts in weather patterns, the melting of polar ice caps, and the loss of biodiversity. Gas sensors play a vital role in monitoring CO_2 levels, a critical aspect of protecting human health, optimizing industrial processes, and addressing environmental challenges [2]. A key aspect of tackling these challenges is the creation of reliable and affordable gas sensors that can effectively detect and monitor CO_2 concentrations across different settings. Current sensors typically rely on resistive-type detection, where exposure to CO_2 causes measurable changes in the physical properties of the sensing material, such as resistance [3]. Ongoing advancements in sensor technology are enhancing the precision, high response, and cost-effectiveness of detection systems. These innovations enable the creation of real-time, highly accurate monitoring solutions that provide greater dependability while reducing maintenance expenses. As the demand for such devices grows, they are being incorporated into a wide range of applications, including workplace safety, residential automation, and environmental surveillance [4].

Metal oxide-based chemiresistive sensors offer a multitude of advantages, including straightforward fabrication, cost-effectiveness, adaptability, reliability, eco-friendliness, and compatibility with contemporary nano and micro systems. Zinc oxide (ZnO) is a chemiresistive material that is widely used for the detection of a wide range of gases, including CO_2 and methane, as well as ammonia and other volatile organic compounds (VOCs) [2]. Its high sensitivity makes it an ideal material for a variety of applications, including environmental monitoring and industrial safety [2].

Experimental

In order to prepare the chemoresistive sensor for CO_2 detection, the ZnO+0.5 at.% In_2O_3 polycrystalline target was synthesized in advance by means of the solid-phase reaction method. The zinc oxide and indium oxide (In_2O_3) nanopowders were previously weighed and thoroughly mixed until a homogeneous mixture was achieved. The resulting mixture was pressed into a tablet with a diameter of 50 mm and a thickness of 4 mm. The sample was subjected to annealing at temperatures between 800-1200°C for a period of 20 hours. Consequently, as a result of the solid-phase reaction, a ceramic target was formed, which served as a source of magnetron sputtering. Subsequently, nanograins were sputtered from the obtained target using the high-frequency magnetron sputtering method, condensing on a dielectric substrate. During the deposition process, the generator power was 70 W, the deposition duration was 20 minutes, and the temperature of the substrate was 200 °C. Then, palladium catalytic nanopar-

ticles were deposited on the surface of the resulting nanostructured film to improve the sensor performance. In the final stage of the production process, the sensor was subjected to thermal heating at 300 °C for four hours. Fig. 1 illustrates the scanning electron microscopy (SEM) image of the ZnO+0.5 at.% In_2O_3 thin film, which has a thickness of approximately 40 nm (measured by the Alpha-Step D-300 ,KLA Tencor, Milpitas, CA, USA profiler). It is obvious from the SEM image that average grain size in the film is within the range of 20–40 nm.

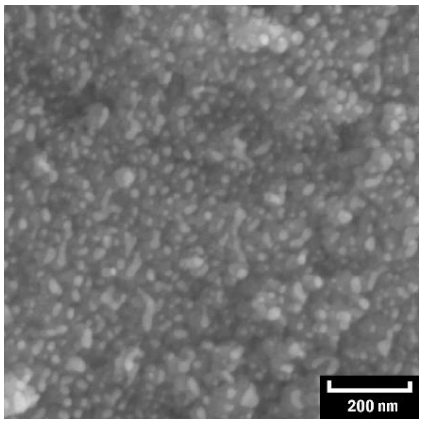

Fig. 1. SEM images of the ZnO+0.5 at.% In_2O_3 thin film with a scalebar of 200 nm.

Results

The gas sensing properties of the material were investigated using an automated gas sensor testing setup. The response of the sensor is defined as the ratio (R_a/R_g) of the sensor's resistance in air (R_a) and in the presence of the CO_2 (R_g). The sensing characteristics of the sensor were investigated over a temperature range of 25–300°C (Fig. 2).

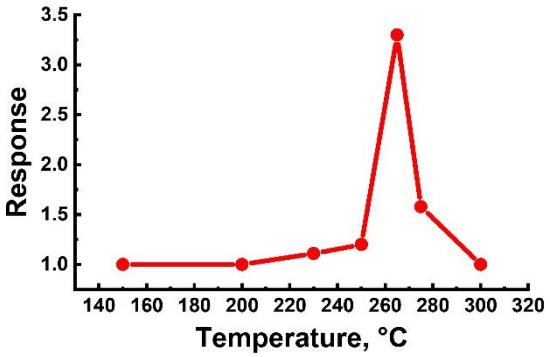

Fig. 2. Dependence of the ZnO+0.5 at.% In_2O_3 sensor response on temperature in the presence of 30000 ppm CO_2.

As Fig. 2 shows, the sensor exhibited a response to 30000 ppm of CO_2 started from 230°C and demonstrated its best result at 265°C operating temperature, where the resistance of the sensor changed approximately 3.3 times.

The dependence of sensor response on CO_2 concentration at 265°C operating temperature as well as the dynamic change in the sensor resistance under 10000 ppm of CO_2 concentration were shown in Fig. 3.

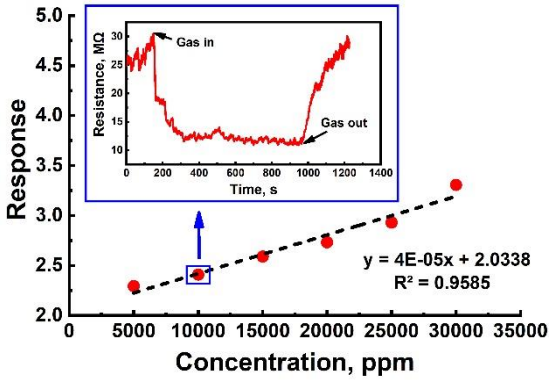

Fig. 3. Dependence of sensor response on CO_2 concentration at 265°C and the dynamic change in the sensor resistance under 10000 ppm of CO_2 concentration (inside of the picture).

It is crucial to highlight that the sensor response exhibits a linear correlation with CO_2 concentrations, enabling the estimation of varying concentrations of the target gas in authentic settings. The sensor response to the minimum CO_2 concentration (5000 ppm) was approximately 2.3, with a response and recovery times of 67 and 149 seconds, respectively.

Acknowledgment

This research was funded by the Higher Education and Science Committee of RA, grant number № 24FP-3B001.

References

[1] A. Molina, V. Escobar-Barrios, J. Oliva, A review on hybrid and flexible CO_2 gas sensors, *Synthetic Metals* 270, 116602 (2020); doi: 10.1016/j.synthmet.2020.116602

[2] C. Zhang, K. Xu, K. Liu, J. Xu, Z. Zheng, Metal oxide resistive senso rs for carbon dioxide detection, *Coordination Chemistry Reviews* 472, 214758 (2022); doi: 10.1016/j.ccr.2022.214758

[3] M. E. DMello, N. G. Sundaram, S. B. Kalidindi, *Assembly of ZIF-67* Metal–Organic Framework over Tin Oxide Nanoparticles for Synergistic Chemiresistive CO_2 Gas Sensing, *Chemistry – A European Journal* 24, 9220-9223 (2018); doi: 10.1002/chem.201800847

[4] Y. Jian, W. Hu, Z. Zhao, P. Cheng, H. Haick, M. Yao, W. Wu, Gas Sensors Based on Chemi-Resistive Hybrid Functional Nanomaterials, *Nano-Micro Letters* 12, 71 (2020); doi: 10.1007/s40820-020-0407-5

DOI 10.5162/SMSI2025/P39

Development of a universal instrument system for locking intramedullary nails

Thomas Reuter[1], *Andreas Grundmann*[1], *Sebastian Walther*[1]
[1] *Institut Chemnitzer Maschinen und Anlagenbau e.V.,*
Otto-Schmerbach-Straße 19, 09117 Chemnitz, Germany
t.reuter@icm-chemnitz.de

Summary:
In large animals, fractures of the upper long tubular bones such as forearm and humerus as well as lower and upper leg, continue to represent a major surgical challenge. Fixing these fractures with implanted nails has proven to be difficult and requires a high level of X-ray monitoring. Therefore, a camera-marker system was developed without the need for X-ray monitoring during drilling. The results showed that 8 of 10 implants could be securely fixed. However, the described method has great potential in both veterinary and human medicine and does not require X-ray exposure.

Keywords: Camera-marker system, Intramedullary nail, Femur, Implant locking, Osteosynthesis

Motivation

The horse population has grown significantly in the recent years, not only in Germany but worldwide. According to projections by the Federal Statistical Office, approximately 1.1 million horses and ponies are kept in Germany, which corresponds to a fourfold increase in the population over the past 40 years [1]. Not only the increase in absolute numbers of horses, but also tendential changes in the way horses are kept, lead to an increase of impact injuries and thus of fractures [2,3]. Therefore, an implant and a corresponding surgical procedure for intramedullary osteosynthesis in fractures of the long bones of large animals were developed [4]. Thereby, the fixation of the implanted nail - which is essential for rotational stability - is performed with the aid of an insertion guide and under X-ray monitoring. This causes a high radiation exposure for surgeon and patient. However, in human medicine, it was shown that it is difficult to securely fix the distal drill holes of the nail with the aid of the insertion guide [5]. Therefore, these abstract aims to present a newly developed screen-guided navigation system without the need for X-ray monitoring during drilling, consisting of two mutually sighting camera-marker modules, for the safe locking of nails during intramedullary osteosynthesis in large animals.

Methods

The development of the camera-marker system (CMS) is divided into three phases. The first phase includes the design of hard- and software. The second phase deals with the development of the algorithm for calculating the position data. In the third phase, the system was tested on equine femora. The locking of the intramedullary nail was evaluated according to the number of successful fixations of the distal drill holes. Secure locking was defined as all distal drill holes being fixed.

Camera-Marker System

The CMS utilizes two cameras which face each other, with one camera attached to the insertion guide of the nail and the other attached to the drilling machine. Figure 1 shows the experimental setup consisting of the two devices with attached CMS and the intramedullary nail.

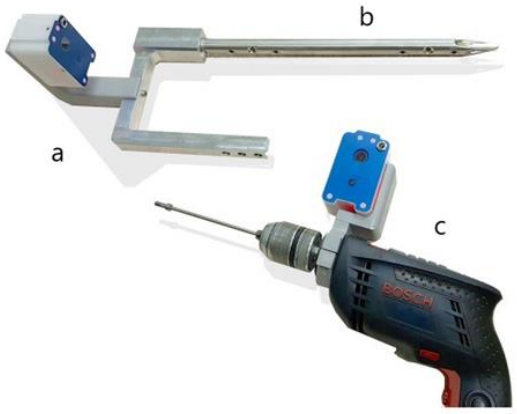

Fig. 1. Experimental setup: a.) insertion guide with CMS, b.) intramedullary nail and c.) drilling machine with CMS.

Four LED marker points on each camera surface emit infrared light, which allows the cameras to determine their relative positions to each other in

real-time through software with complex algorithms. The calculation of coordinates refers to determining the location of a point in each space based on its position relative to other known points (see Fig. 2). In order to calculate coordinates, a variety of factors must be considered, including the angles and distances between the known points, as well as any distortions or deviations in the measurements [4,5].

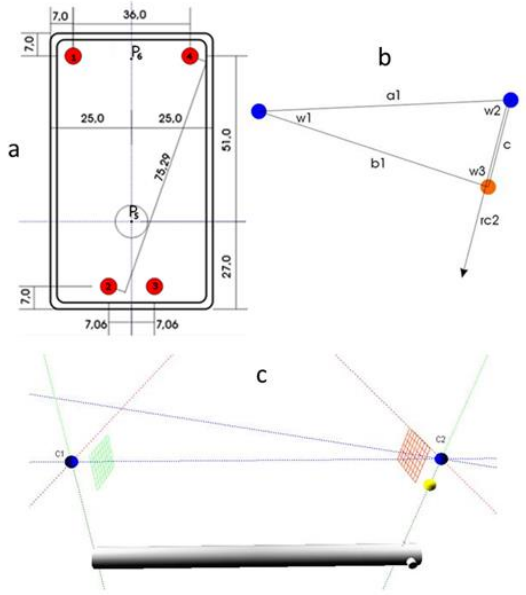

Fig. 2. Sketches about the calculation of the position data: a) CMS surface with dimensions (top left), b) vector calculation (top right) and c) relative angle determination (bottom).

The locking holes in the nail are calibrated to the system using a calibration pin according to the desired nail length. The challenge was to adapt the camera to the insertion guide, which required analyzing the anatomical features of horses and determining the ideal arrangement of the camera-marker modules in terms of opening angle and working distance. As a result of this adaptation, an extension arm was developed which can be mounted on the specific insertion guide in two different positions, covering the working range of the proximal and distal locking holes of intramedullary nails [4,5].

Experimental Setup

Ten femora from slaughtered horses (age 8 - 14 years) were collected from a local horse butchery for testing the CMS. The experimental procedure for testing the CMS can be divided into four steps: 1. preparation of the bone specimens, 2. mounting the CMS on the intramedullary nail and calibrating the system with the calibration pin, 3. nail insertion and proximal locking, 4. drilling and distal locking [4].

Results

The method developed here is suitable for locking intramedullary nails in large animals. The camera-marker system fits well into the surgical procedure and provides a high degree of accuracy. Likewise, the X-ray exposure for surgeon and animal can be reduced to a minimum. X-rays are only required for final locking control [4,5]. With sufficient training and practice, the surgeon can hit the distal locking holes with ease. The very first attempts already showed a hit rate of 80 % with fast improvement with increasing practice. Because of the very good results, the system could also bring great benefits in human medicine.

Outlook

Further work is planned to significantly improve handling and to develop a training concept for surgeons. The system will continue to be tested and iteratively improved in the future.

Author Statement

Research funding: The project is funded by the Federal Ministry for Economy and Climate Protection based on a resolution of the German Bundestag (Funding reference 16KN062326). Conflict of interest: Authors state no conflict of interest. Ethical approval: The conducted research is not related to human or animals use.

References

[1] W. Brade, O. Distl, H. Sieme, A. Zeyner, Pferdezucht, -haltung und -fütterung - Empfehlungen für die Praxis. Landbauforschung - vTI Agriculture and Forestry Research 2011; Sonderheft 353 / Special Issue 353.

[2] S. Hug, Epidemiologische Untersuchungen der Frakturpatienten der Pferdeklinik Bedeutung der Schlagverletzung als Ursache von Frakturen. Dissertation, Universität Zürich, 2009.

[3] A.N. Dimock, K.D. Hoffman, S.M. Puchalski, S.M. Stover, Humeral stress remodelling locations differ in Thoroughbred racehorses training and racing on dirt compared to synthetic racetrack surfaces. *Equine Vet J* 45(2), 176-181 (2013).

[4] S. Walther, T. Reuter, A. Grundmann, F. Preuß, D. Barnewitz, Development of a camera-marker system (CMS) for locking nails during intramedullary osteosynthesis in large animals – First results, *Current Directions in Biomedical Engineering* 9(1), 238-241 (2023); doi.org/10.1515/cdbme-2023-1060

[5] S. Walther, A. Grundmann, J. Biedermann, J. Wutzler, Process improvement of locking intramedullary nails, *Biomed Eng-Biomed Tech* 62(s1), 277 (2017).

DOI 10.5162/SMSI2025/P40

Branching Wall-less Vessel System in Tissue-Mimicking Materials for Magnetomotive Ultrasound Imaging

Christian Heim[1], Christian Huber[2,3], Ingrid Ullmann[3], Helmut Ermert[2], Stefan Lyer[2], and Stefan J. Rupitsch[1]
[1] Department of Microsystems Engineering (IMTEK), Laboratory for Electrical Instrumentation and Embedded Systems, University of Freiburg, Georges-Köhler-Allee 106, Germany
[2] Department of Otorhinolaryngology, Head and Neck Surgery, Section of Experimental Oncology and Nanomedicine (SEON), Professorship for AI-Controlled Nanomaterials (KINAM), Universitätsklinikum Erlangen, Glücksstraße 10a, Germany
[3] Institute of Microwaves and Photonics (LHFT), Friedrich-Alexander-Universität Erlangen-Nürnberg, Cauerstraße 9, Germany
Christian.Heim@imtek.uni-freiburg.de

Summary:
In this contribution, we present an extended manufacturing process and evaluation method of a branching wall-less vessel system in tissue-mimicking materials for the development of Magnetomotive Ultrasound (MMUS) imaging algorithms. Blood flow in vessels around a tumor can interfere with MMUS imaging and has to be considered for algorithm development. A water-soluble filament can be used to integrate a branching wall-less vessel system into phantom manufacturing. Branches can be evaluated exploiting 3D ultrasound imaging and vector-flow imaging in combination with a highly echogenic fluid.

Keywords: Magnetic Drug Targeting (MDT), superparamagnetic nanoparticles (SPIONs), Magnetomotive Ultrasound (MMUS), local cancer treatment, ultrasound imaging.

Motivation

Magnetic Drug Targeting (MDT) with superparamagnetic iron oxid nanoparticles (SPIONs) is an emerging cancer therapy with localized treatment. In combination with Magnetomotive Ultrasound (MMUS), the spatial distribution of the SPIONs can be monitored during enrichment [1]. A review of MMUS imaging can be found in [2]. MMUS is based on the time-tracking of magnetically induced small tissue displacements in the SPION-laden areas by applying time-varying magnetic fields. For the development of MMUS algorithms, ultrasound phantoms made of tissue mimicking materials (TMMs) are commonly used for baseline studies. However, real tumors have a branching vessel system as shown in Fig. 3 (left), which can interfere with MMUS imaging [1]. In order to extend phantoms by adding wall-less vessels, manufacturing methods for complex flow phantoms have been developed using different combinations of soluble 3D printing filaments [3, 4]. In this contribution, we present a manufacturing process using water-soluble polyvinyl alcohol (PVA) filament to manufacture a wall-less vessel system to improve phantom models for MMUS algorithm development. Branches have been evaluated exploiting 3D ultrasound (3DUS) and speckle tracking based vector-flow (STVF) imaging according to [5, 6].

Manufacturing Process

Phantom manufacturing involves many different methods and materials. A recent overview of ultrasound phantom manufacturing can be found in [7]. In this contribution, PVA (10 wt%, DuPont Elvanol 71-30) was chosen for the hydrogel due to its ability to harden phantoms with varying stiffness and to mechanically couple different phantoms. PVA can also be used as a water-soluble filament (Formfutura Atlas Support Natural) for vessels and as a scattering material (DuPont Elvanol 71-30) to mimic tissue echogenicity. To demonstrate the manufacturing process, we manufactured a wall-less vessel system around a SPION-laden phantom, as illustrated in Fig. 1.

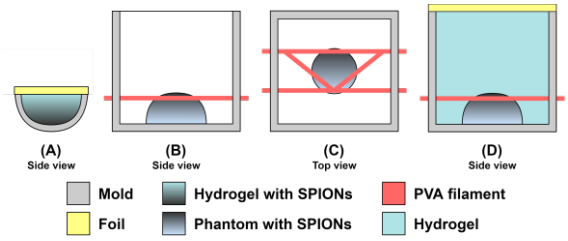

Fig. 1. Phantom manufacturing steps: (A) Pre-hardening with two freeze/thaw cycles of a SPION-laden tumor phantom with an iron content of 17.2 mg/ml, (B) Placement of tumor phantom and PVA filament, (C) Connect PVA filament parts using a heat gun, (D) Fill (4x4x4) cm mold with hydrogel and cover with foil.

After step (D), the final phantom was hardened in a climate chamber using two freeze-thaw cycles (FTCs). Fig. 2 shows the utilized temperature profile of one FTC. Finally, the PVA can be removed by placing the phantom in a water bath.

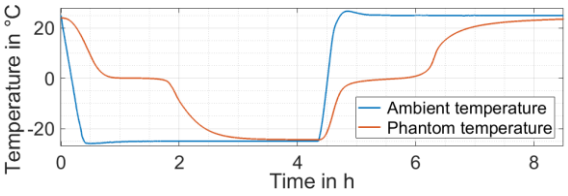

Fig. 2. Temperature profile of one FTC. The Phantom temperature was measured using a PT100 sensor placed in the center of a reference phantom.

Experiment and Results

To evaluate the braches, a highly echogenic fluid composed of the same hydrogel used to manufacture the phantom with 5 mg/ml PVA powder was utilized in combination with a Whadda WPM447 peristaltic pump to generate a fluid flow. Ultrasound data was collected by means of an Ultrasonix SonixTouch ultrasound scanner in combination with a L9-4/38 ultrasonic transducer exploiting STVF imaging and a 4DL14-5/38 ultrasonic transducer exploiting 3DUS imaging. The results are depicted in Fig. 3 and Fig. 4.

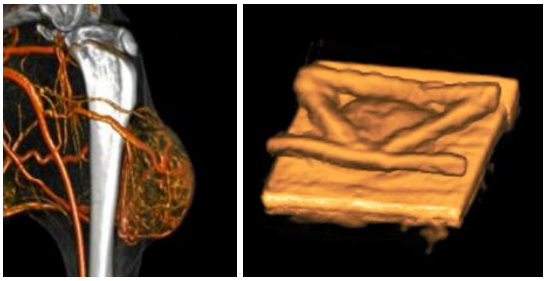

Fig. 3. Angiographic image of a VX2-tumor below the knee of a rabbit (left, SEON). 3DUS image of the phantom with a center frequency of 10 MHz, mechanical index of 0.28, and thermal index of 0.27 (right).

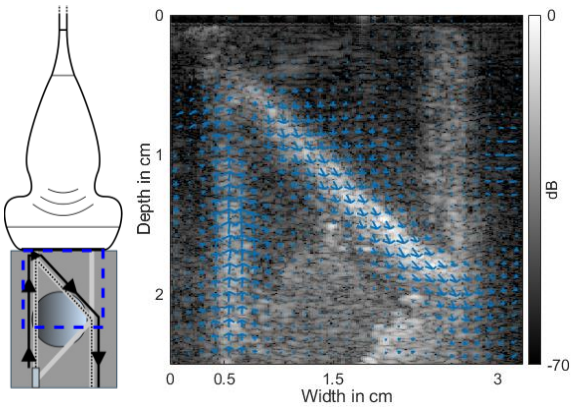

Fig. 4. STVF image with a center frequency of 6.6 MHz, 88 frames per second, mechanical index of 0.53, and thermal index of 0.37. Peristaltic pump is connected to inlet at (depth/width) of (4/0.5) cm. The blue box indicates the area used for the STVF image.

Conclusion and Outlook

This contribution demonstrates an extended manufacturing process for MMUS phantoms with a branching wall-less vessel system using water-soluble PVA filament. It could be shown that local heating using a heat gun can be used to connect PVA parts to build a branching wall-less vessel system around a tumor phantom. Furthermore, it could be shown that highly echogenic fluid enables evaluation of braches exploiting 3DUS imaging and STVF imaging. In addition, unlike Doppler imaging, STVF allows the characterization of speckle pattern movements independent of the orientation of the ultrasonic transducer. Future research will focus on disturbances caused by SPIONs in vessels and their impact on MMUS imaging.

References

[1] M. Fink, S. Rupitsch, S. Lyer, H. Ermert, In Vivo Study on Magnetomotive Ultrasound Imaging in the Framework of Nanoparticle based Magnetic Drug Targeting, *Current Directions in Biomedical Engineering* 6(3), 543–546 (2020); doi: 10.1515/cdbme-2020-3139

[2] K. Kubelick, M. Mehrmohammadi, Magnetic particles in motion: magneto-motive imaging and sensing, *Theranostics* 12(4), 1783–1799 (2022); doi: 10.7150/thno.54056

[3] C. Ho, A. Chee, B. Yiu, A. Tsang, K. Chow, A. Yu, Wall-Less Flow Phantoms With Tortuous Vascular Geometries: Design Principles and a Patient-Specific Model Fabrication Example, *IEEE Transactions on Ultrasonics, Ferroelectrics, and Frequency Control* 64(1), 25–38 (2017); doi: 10.1109/TUFFC.2016.2636129

[4] C. Huber, C. Heim, H. Ermert, S. Rupitsch, I. Ullmann, M. Vossiek, S. Lyer, Ultrasound Phantom of a Carotid Bifurcation Tumor Using Multiple 3D Printed Soluble Filaments, *Proceedings IEEE International Symposium on Biomedical Imaging (ISBI) 2024*, 1–5 (2024); doi: 10.1109/ISBI56570.2024.10635132

[5] V. Perrot, D. Garcia, Back to basics in ultrasound velocimetry: tracking speckles by using a standard PIV algorithm, *Proceedings IEEE International Ultrasonics Symposium (IUS) 2018*, 206–212 (2018); doi: 10.1109/ULTSYM.2018.8579665

[6] D. Garcia, Make the most of MUST, an open-source MATLAB UltraSound Toolbox, *Proceedings IEEE International Ultrasonics Symposium (IUS) 2021*, 1–4 (2021); doi: 10.1109/IUS52206.2021.9593605

[7] C. Heim, C. Huber, H. Ermert, I. Ullmann, T. Saleem, S. Lyer, S. Rupitsch, Modelling and Construction of Complex Shaped Polyvinyl Alcohol based Ultrasound Phantoms for Inverse Magnetomotive Ultrasound Imaging, *Proceedings 22. GMA/ITG-Fachtagung Sensoren und Messsysteme 2024*, 313–318 (2024); doi: 10.5162/sensoren2024/D1.4

DOI 10.5162/SMSI2025/P41

Innovating THz Detectors: Unmatched Sensitivity at Room Temperature, Infinite Possibilities

Adam Rämer[1], *Eric Nöske* [1], *Eugen Dischke*[1], *Viktor Krozer*[1], *and Wolfgang Heinrich* [1]
[1] Ferdinand-Braun-Institut, 12489 Berlin, Germany
adam.raemer@fbh-berlin.de

Summary: We have developed monolithically integrated THz detectors that operate at room temperature, covering a frequency range from 100 GHz to 1500 GHz with exceptional sensitivity and speed. These detectors are scalable to larger arrays, enabling the realization of THz imaging systems that were previously unattainable. In this paper, we present the THz detectors and a prototype THz scanner developed as a technology demonstrator, showcasing the groundbreaking capabilities of this innovative technology.

Keywords: monolithically integrated THz detectors, THz direct detectors, TeraFeT, THz scanner, THz camera

Introduction

The frequency range from 100 GHz to 1.5 THz offers unique opportunities for a wide range of applications. THz waves in this frequency range can penetrate non-conductive materials such as plastics, fabrics, and ceramics while being non-ionizing and safe for biological tissues and in industrial environment. These properties make THz technology particularly promising for material inspection, medical diagnostics and security screening.

THz direct detectors, which convert THz waves directly into DC electrical signals, play a crucial role in enabling real-time, high-resolution imaging systems without the need for complex intermediary steps [1]. Unlike other approaches, direct detectors eliminate the necessity for local oscillators.

Current THz detector technologies primarily use Schottky diodes, though their scalability to large arrays remains limited and 2D arrays are yet to be realized. Transistor based THz detectors have also been widely explored using CMOS, GaN HEMT and InP HBT devices [2, 3, 4]. Existing focal plane arrays have been realized by the authors using GaN technology [5] and other groups relying on Silicon [6], but their limited sensitivities lead to long image acquisition times and time-integration, significantly reducing readout speeds. Passive THz imaging [7] shows limited potential due to extremely long acquisition times of several hours and mechanical scanning, which is undesirable for many applications.

Highly sensitive and monolithically integrated detector arrays are essential for improving image quality and achieving faster scanning of broader areas. Image resolution of such detector arrays is dictated by the distance between the individual detectors on the chip. Large-scale detector array chips allow real-time imaging of larger areas and hence avoid complicated mechanical scanning, making such THz imaging systems suitable for real-world applications.

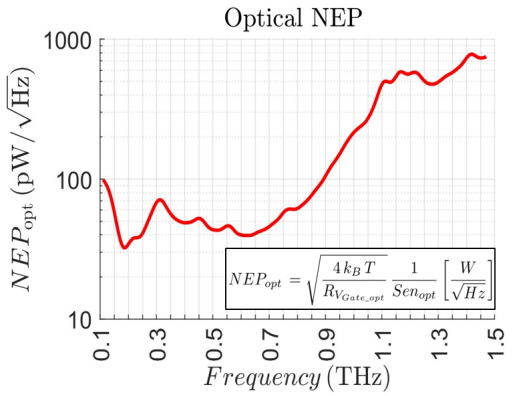

Fig. 1: Noise equivalent power (NEP) of a single detector

THz detector arrays

Figure 1 shows a single detector's outstanding noise equivalent power (NEP). The THz scanner line is made of up to 80 of these detectors. The line is 6 cm long and comprises 20 individual chips. Figure 2 shows the image of the line with the magnification of one chip. The distance from the center to the center point of the detectors is 640 µm. The patented array design of the detectors [8] avoids crosstalk to neighboring structures.

THz scanning system

The THz line scanner demonstrator operates at 300 GHz with a source power of 10 dBm illuminating an area larger than the THz detection array of 80 THz detectors each with a transimpedance amplifier providing a gain of 4 $M\Omega$

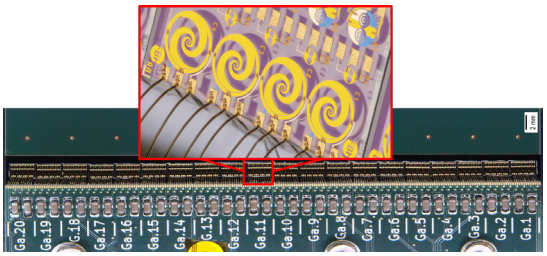

Fig. 2: THz scanner line; chip with 4 THz detectors per chip

and an analog-to-digital converter with 16-bit resolution and a sampling rate of up to 15,000 lines per second. The conveyor belt with a width of 27 cm is arranged between the signal source and the detectors with operating speeds of up to 1.5 m/s. The readout speed, determined by the electronics and system structure, can reach 2 GHz, with all detector pixels operating in parallel. This configuration enables efficient and high-speed data acquisition, making the setup ideal for real-time, high-resolution imaging. The figure shows a photo of 5 stacked Lego plates and the THz image generated by the THz scanner. The image presented in Figure 3 was captured in real-time on the conveyor belt. Each step of the stacked Lego plates can be identified due to increasing attenuation with plastic thickness. The small individual bumps, typical for Lego, can also be identified.

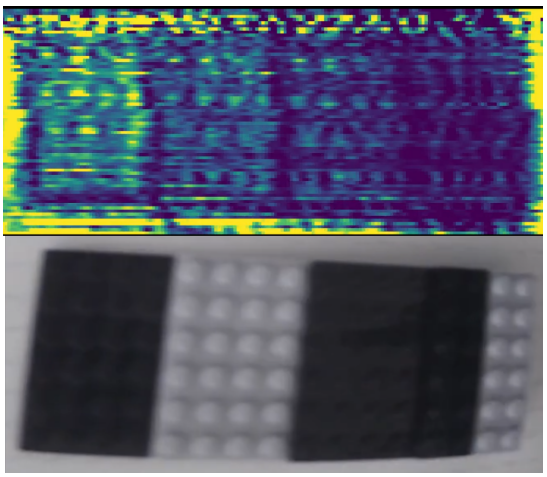

Fig. 3: Image of stacked Lego bricks and THz image, generation speed ¡ 1 s

Conclusions

The THz detectors and arrays presented here pave the way for the development of THz imaging systems that were previously unattainable, due to enhaced sensitivity and signal processing speed. To showcase these capabilities, we have constructed and demonstrated a real-time THz scanner. Videos of some scanning objects will be presented during the show.

References

[1] Leitenstorfer, "The 2023 terahertz science and technology roadmap," *Journal of Physics D: Applied Physics*, vol. 56, p. 223001, Apr. 2023. 10.1088/1361-6463/acbe4c.

[2] K. Ikamas, D. Cibiraite, M. Bauer, A. Lisauskas, V. Krozer, and H. G. Roskos, "Ultrabroadband terahertz detectors based on CMOS field-effect transistors with integrated antennas," in *2018 43rd International Conference on Infrared, Millimeter, and Terahertz Waves (IRMMW-THz)*, IEEE, sep 2018. 10.1109/irmmw-thz.2018.8510062.

[3] M. Bauer, A. Rämer, S. A. Chevtchenko, K. Y. Osipov, D. Cibiraite, S. Pralgauskaite, K. Ikamas, A. Lisauskas, W. Heinrich, V. Krozer, and H. G. Roskos, "A high-sensitivity algan/gan hemt terahertz detector with integrated broadband bow-tie antenna," *IEEE Transactions on Terahertz Science and Technology*, vol. 9, no. 4, pp. 430–444, 2019. 10.1109/TTHZ.2019.2917782.

[4] A. Rämer, E. Negri, H. Yacoub, J. Theumer, J. Wartena, V. Krozer, and W. Heinrich, "A monolithically integrated inp hbt-based thz detector," in *2024 54th European Microwave Conference (EuMC)*, pp. 1000–1003, IEEE, Sept. 2024. 10.23919/eumc61614.2024.10732183.

[5] T. Liebchen, E. Dischke, A. Ramer, F. Muller, L. Schellhase, S. Chevtchenko, W. Heinrich, and V. Krozer, "Compact 12×12-pixel thz camera using algan/gan hemt technology operating at room temperature," in *2021 46th International Conference on Infrared, Millimeter and Terahertz Waves (IRMMW-THz)*, IEEE, Aug. 2021. 10.1109/irmmw-thz50926.2021.9567181.

[6] E. Ojefors, U. R. Pfeiffer, A. Lisauskas, and H. G. Roskos, "A 0.65 THz focal-plane array in a quarter-micron CMOS process technology," *IEEE Journal of Solid-State Circuits*, vol. 44, pp. 1968–1976, jul 2009.

[7] D. Cibiraite-Lukenskiene, K. Ikamas, T. Lisauskas, A. Rysiavets, V. Krozer, H. G. Roskos, and A. Lisauskas, "Completely passive room-temperature imaging of human body radiation below 1 thz with field-effect transistors," in *2020 45th International Conference on Infrared, Millimeter, and Terahertz Waves (IRMMW-THz)*, vol. 9078, pp. 1–2, IEEE, Nov. 2020. 10.1109/irmmw-thz46771.2020.9370618.

[8] A. Rämer, S. Shevchenko, "Patent: Radiation detector and method for producing /de102017103687b3 / ep 3 449 508 b1/ us2019/0393374/ jp6914967b22021.8.4."

DOI 10.5162/SMSI2025/P42

Neuromorphic Spiking Sensory Conversion System Based on the STDP Learning Rule of Biological Synapses

Hamam Abd [1], *Anand Joshy*[1] *and Andreas König*[1]
[1] Lehrstuhl Kognitive Integrierte Sensorsysteme (KISE), EIT, Rheinland-Pfälzische Technische Universität Kaiserslautern-Landau, 67663 Kaiserslautern, Germany
habd@rptu.de

Summary: Developing a standard sensory system using advanced integration technologies presents both advantages and obstacles due to issues like noise, manufacturing deviations, and signal swings. Adopting a self-adaptive approach and shifting from traditional amplitude-based processing to a biologically inspired, adaptive spike-domain framework provides a practical solution. This work introduces a neuromorphic model of an adaptive spiking sensory front-end featuring self-X properties and capacitive storage. A learning loop enables continuous synaptic updates to prevent signal degradation, using spike-timing-dependent plasticity (STDP) for adaptation.

Keywords: Spike-domain code, STDP learning rule, self-X properties, Neuromorphic spiking sensory system

Background, Motivation and Objective

Sensory systems are rapidly evolving, with advances in transduction and integration enabling miniaturization and diverse applications, simplifying use but complicating electronic design [1]. Modern mixed-signal systems enhance efficiency and speed with lower voltages and capacitance but challenge traditional analog designs with increased noise, reduced signal amplitude, variability, mismatch, and lower gain. Reliable analog front-ends (AFEs) are critical for system performance, requiring robustness, accuracy, and self-X features like self-healing, self-calibration, and self-optimization. Fig. 1 shows a typical sensor interface with signal conditioning, amplification, filtering, and ADC. PGAs boost weak signals for ADC range, anti-aliasing filters reduce noise and align signals, and the ADC digitizes them for processing.

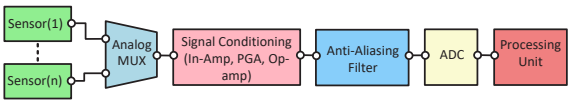

Fig. 1: The conventional AFE system chain.

Traditional AFEs relied on amplitude-coded signals, but modern CMOS technology's reduced transistor sizes and supply voltages shift the focus to time-coded signals, offering better adaptability and robustness. To address these limitations, we developed a neuromorphic spiking sensory system with adaptive capabilities, combining spike timing and an approach inspired by acoustic localization (Fig. 2) [2]. The system uses an adaptive synapse model with a CMOS-emulated memristor to mimic biological synapses [3] and was fabricated with XFAB CMOS 0.35 μm technology, featuring a self-adaptive spiking sensory front-end [4]. Previous systems used counters to control adaptive synapse weights [2]. This study replaces counters with capacitive storage, requiring periodic refreshing. A learning loop based on STDP, inspired by auto-zeroing techniques, reduces adaptation variables and transistors count compared to the previous implementation by using the counters, while enabling dynamic refreshing to prevent value degradation.

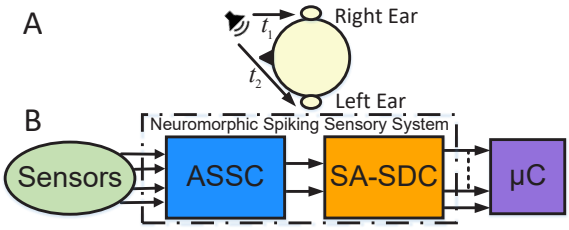

Fig. 2: A block diagram of neuromorphic spiking sensory systems, incorporating ASSC and SA-SDC.

Proposed Methodology and Results

The proposed neuromorphic spiking sensory system uses an adaptive sensor signal-to-spike converter (ASSC) and a self-adaptive spike-to-digital converter (SA-SDC), as shown in Fig. 2. The ASSC converts sensor signals into two spikes with a time difference (TD) representing the sensor output, while the SA-SDC generates digital codes from the TD. The ASSC aligns the SA-SDC input range with the sensor output through time-domain amplification and level shifting, avoiding data loss or costly range expansion. The SA-SDC comprises the Self-Adaptive Spike-to-Rank Coding (SA-SRC) and the Winner-Take-All (WTA) mechanism, as shown in Fig. 3. The SA-SRC encodes timing differences via spike order coding, based on spike

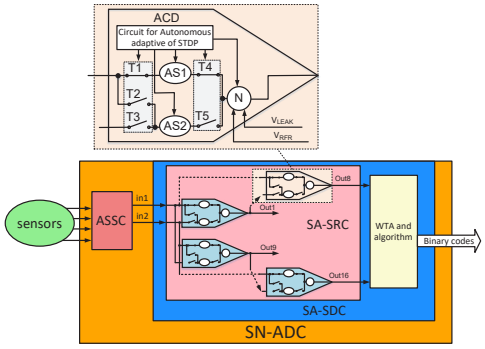

Fig. 3: The proposed neuromorphic AFE based on STDP adaptation

sequences in a neuron group. The WTA converts these patterns into digital signals. At its core, the SA-SRC uses an Adaptive Coincidence Detector (ACD) with two adaptive synapses (AS) and a neuron (N). The delay chain duration depends on the neuron's firing time, influenced by input current intensity and adjusted synaptic weights to match timing variations.

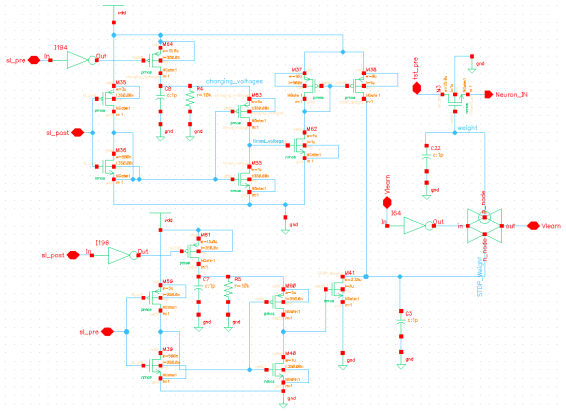

Fig. 4: Schematic of the proposed synapse.

Biological synapse models aim to replicate natural functions [6], but often require many adaptation parameters and transistors. For our ACD as a neural network time delay based on the STDP rule, we focused on key features. STDP, vital for learning and brain function, adjusts synaptic weights based on the timing difference between pre-and postsynaptic spikes [5]. The direction of weight change depends on whether this timing difference is positive or negative, continuing until the target weight is reached. We modified and optimized existing synapse models [6] to enable ACD to operate as a time delay element within a neural network using the STDP learning rule, as illustrated in Fig. 4. The STDP circuit has two sections: potentiation (top) and depression (bottom). Resistor-capacitor pairs set the time constant. The capacitor C3 influences the gate voltage of PMOS M3 by charging capacitor C22 during active learning. Once learning ends, C3 disconnects, leaving C22 directly linked to the PMOS gate. The synaptic weight controls neuron firing delay, adjustable between 3.7 ns and 11.6 ns by influencing the neuron's membrane capacitor charge.

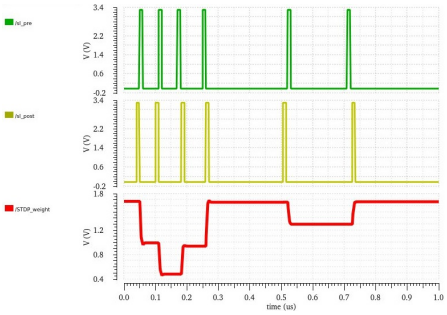

Fig. 5: The synaptic weight adjustments

The autonomous circuit regulates synaptic weights by leveraging pre- and postsynaptic spikes alongside the nominal delay. This adjustment occurs simultaneously across all ACDs by managing switches T1, T2, T3, T4, and T5. As a result, the adaptation time remains independent of the number of synapses since all are updated concurrently. In each ACD, the circuit adjusts the first synapse's weight by connecting it while disconnecting the second. Similarly, the weight of the second synapse is adapted in parallel. Fig. 5 illustrates the synaptic weight adjustments based on pre- and postsynaptic spikes. In the current phase of the design, pre- and postsynaptic spiking events emulate the generation and adaptation of pre-and postsynaptic spikes in the planned complete circuit. The next phase focuses on developing an autonomous circuit to control these events, marking the first step toward a physical demonstrator or chip.

References

[1] Luo, Yifei, et al. "Technology roadmap for flexible sensors." ACS nano 17.6 (2023): 5211-5295.

[2] Abd, Hamam, and Andreas König. "Design of a CMOS memristor emulator-based, self-adaptive spiking analog-to-digital data conversion as the lowest level of a self-x hierarchy." JSSS, 2022. 233-262.

[3] Abd, Hamam, and Andreas König. "Adaptive Spiking Sensor System Based on CMOS Memristors Emulating Long and Short-Term Plasticity of Biological Synapses for Industry 4.0 Applications." tm-Technisches Messen 88.s1 (2021): s114-s119.

[4] Abd, Hamam, et al. "Neuromorphic Spiking Sensory System with Self-X Capabilities." IEEE Access (2024).

[5] Gerstner, Wulfram, and Werner M. Kistler. Spiking neuron models: Single neurons, populations, plasticity. Cambridge university press, 2002.

[6] Bahuguna, Yash, et al. "32nm CMOS Analog Circuit Implementation of STDP for SNNs." 2023 14th ICCCNT. IEEE.

DOI 10.5162/SMSI2025/P43

Viscosity Analysis of Liquid Food Using Hyperspectral Imaging

Amira Ghezal [1], and Andreas König[1]
[1] Lehrstuhl Kognitive Integrierte Sensorsysteme, Fachbereich Elektrotechnik und Informationstechnik, RPTU University Kaiserslautern Landau, 67663 Kaiserslautern, Germany
ghezal@rptu.de

Summary: This study suggests the use of the third overtone region (675–965 nm) with an NIR hyperspectral camera as a first step toward a non-contact, mobile approach for estimating viscosity in liquid foods—a critical quality parameter. Key spectral features (such as normalized peak intensity, area ratios, FWHM, and peak position) were extracted from selected channel regions and input into a K-Nearest Neighbor (KNR) regression model (k=3), achieving high predictive accuracy (MAE = 0.141 Pa.s, MSE = 0.927 Pa.s², R^2 = 0.95) and accurately predicting sample viscosity across variations. These findings lay the groundwork for a compact, multi-spectral AMS-based device, supporting in-field quality control and food safety.

Keywords: Viscosity Prediction, Non-Invasive Measurement, KNR Regressor, Hyperspectral Imaging (HSI), Spectral Band Selection

Background, Motivation and Objective

Viscosity is a key quality parameter in liquid foods, impacting texture, consistency, and production processes [1]. Near-Infrared (NIR) spectroscopy, especially in the third overtone region, offers a promising non-contact alternative for real-time viscosity estimation by capturing the key absorption peaks relevant to molecular interactions linked to viscosity [2][3]. Besides, hyperspectral imaging (HSI) combined with machine learning has shown potential for quality control in food applications, enabling non-invasive prediction of physical properties and chemical composition [4][5]. This study suggests the use of the third overtone region in the NIR range (675–965 nm) for non-contact viscosity estimation in liquid foods. A K-Nearest Neighbor (KNR) regression model enables a preliminary investigation into a non-invasive alternative to traditional viscometers, focusing on key spectral features.

Methodology

We used a hyperspectral sensor (MV1-D2048x1088-HS02-96-G2-10, Photonfocus) [6] with an IMEC snapshot mosaic CMV2K-SSM5x5-NIR sensor, capturing 25 NIR channels (675–975 nm) at 2048×1088-pixel resolution. Samples (olive oil, water, honey, and milk) in glass containers were illuminated with two 50 W halogen lamps positioned at a 45-degree angle, 20 cm from the camera, to ensure consistent conditions. These samples were chosen to cover a range of viscosities and compositions, ensuring initial feasibility before expanding to a larger dataset. Calibration was conducted with reference white and dark images to correct for environmental and sensor-related inconsistencies. Regions of Interest (ROIs) were extracted from each sample's images, resulting in a data matrix (192660, 25). Reflectance values were normalized and converted to absorbance using Lambert-Beer's Law as shown in Eq. (1):

$$A = \log_{10}\left(\frac{1}{R_{\text{reflectance}}}\right) \tag{1}$$

where A is the absorbance and $R_{\text{reflectance}} = \frac{I_{\text{reflected}}}{I_{\text{incident}}}$ is the reflectance ratio.
For visualization, data preprocessing included Gaussian filtering for noise reduction and cubic spline interpolation for spectral smoothing. Spectral region selection targeted features associated with molecular interactions relevant to viscosity, specifically the normalized peak intensity ratio, normalized area ratio, Full Width at Half Maximum (FWHM), and peak position. A K-Nearest Neighbors (KNR) regression model (k=3) was used for simplicity and accuracy, trained on water, milk(H-milch 0.3% Fett), olive oil and honey (Wild Honey) samples.

Results and Discussion

The absorbance spectrum (Figure 1) reveals distinct peaks that correspond to molecular interactions impacting viscosity.

Water's peaks observed arise from O-H stretching overtones, enhanced by water's polarity and hydrogen bonding. Its low viscosity (0.001 Pa·s) is due to small molecular size and relatively weak intermolecular forces.

Milk shares these peaks (765 nm and 802 nm), modulated by interactions with proteins and fats. Reduced peak intensity reflects disrupted hydrogen bonding, while its higher viscosity (0.002 Pa·s) is due to colloidal suspensions increasing intermolecular friction.

Oil shows broad peak at channel8 (778 nm), associated with C-H stretching in hydrocarbons.

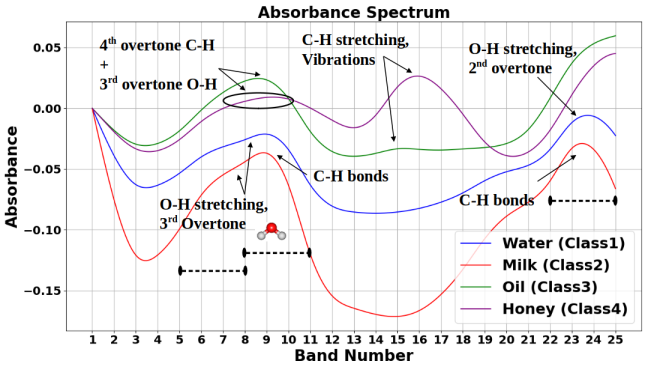

Fig. 1: Absorbance Spectrum and Channel Selection

Its higher viscosity (0.1 Pa·s) stems from large nonpolar molecules and van der Waals interactions, with minimal hydrogen bonding.

Honey's spectrum combines water, sugars, and organic acids. Broad bands arise from overlapping water and carbohydrate C-H stretching vibrations. Its high viscosity is due to strong hydrogen bonding between sugars and water, forming a dense molecular network.

Based on spectral analysis, channels 4–7, 7–10, 13-18 and 21–24 were selected as regions of interest, capturing O-H and C-H absorption bands sensitive to hydrogen bonding. Key peak properties intensity, area, and Full Width at Half Maximum (FWHM) were extracted to quantify intermolecular forces related to viscosity. dataset (192660, 20), created with three container volumes and balanced pixels per class, trained a K-Nearest Neighbors regressor, `n_neighbors=3`, `weights='distance'`, `algorithm='auto'`, and `leaf_size=20`. An 80/20 data split yielded an R^2(Regression metric) of 0.95, Mean Absolute Error (MAE) of 0.141 Pa.s, and Mean Squared Error (MSE) of 0.927 $(Pa.s)^2$, supporting effective viscosity prediction based on selected channels.

Figure 2 shows the model's accuracy in predicting viscosities for water (0.001 Pa·s), milk (0.002 Pa·s), oil (0.1 Pa·s), and honey (around 10 Pa·s). Minimal variance within each category demonstrates its robustness. Testing with varied container volumes and repeated measurements addressed uncertainties and enhanced real-world generalizability.

Conclusion

This study establishes a foundation for a portable, embedded device using the AMS AS7265x chipset, demonstrating the potential of NIR spectroscopy in the third overtone range for non-contact viscosity estimation in liquid foods. Initial experiments with a hyperspectral camera (675–965 nm) identified specific absorption peaks linked to viscosity-related molecular interactions. The AS7265x chipset, with its 18 channels spanning 410–940 nm, aligns closely with these peaks, making it well-suited for capturing critical molecular details. Future work will focus

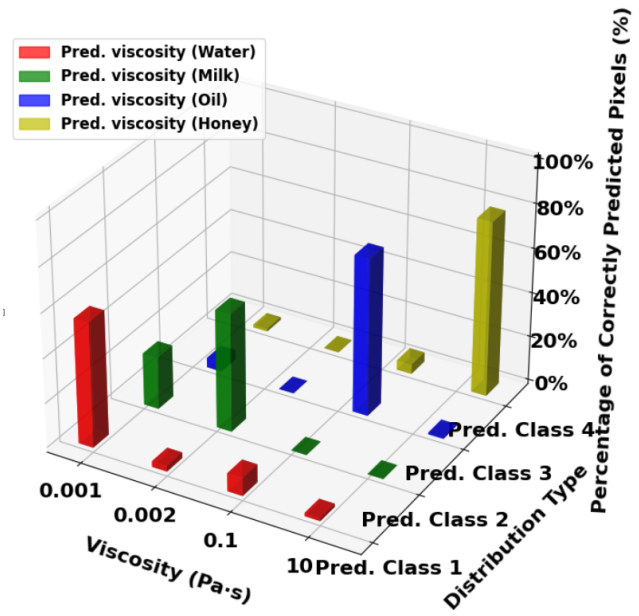

Fig. 2: Distribution of Predicted Pixels Across Viscosity Categories

on validating the chipset's performance across diverse samples, improving unknown sample detection, incorporating contactless temperature measurements with corrective adjustments, and expanding the dataset by including more samples, along with rotated measurements and additional containers, to enhance statistical robustness and invariance.

References

[1] R. Rodrigues, "The viscometer and its role in the food and beverage industry," 2024. Accessed: 2024-11-03.

[2] A. Badr Eldin, *Near Infra Red Spectroscopy*. 07 2011.

[3] D. Macleod, "The frequency of vibration of molecules in liquids and its relation to viscosity," *Proceedings of the Physical Society*, vol. 50, no. 5, p. 788, 1938.

[4] J. Hwang, K.-O. Choi, S. Jeong, and S. Lee, "Machine learning identification of edible vegetable oils from fatty acid compositions and hyperspectral images," *Current Research in Food Science*, vol. 8, p. 100742, 2024.

[5] M. Aqeel, A. Sohaib, M. Iqbal, H. U. Rehman, and F. Rustam, "Hyperspectral identification of oil adulteration using machine learning techniques," *Current Research in Food Science*, vol. 8, p. 100773, 2024.

[6] Photonfocus, "Photonfocus." Accessed: 2024-11-03.

DOI 10.5162/SMSI2025/P44

Supervised Self-Calibration for Fault-Tolerant xMR-Based Angular Decoders under Dynamic Perturbations

Elena Gerken[1], Andreas König[1]
[1] Cognitive Integrated Sensor Systems, RPTU University Kaiserslautern Landau, Deutschland, e.gerken@rptu.de

Summary:

This paper introduces a self-calibration methodology inspired by biological systems, focusing on its application in xMR angular decoders. Designed to address the limitations of static calibration, the approach effectively corrects mechanical misalignments and operational deviations. By leveraging simulated and empirical data to train machine learning (ML) models such as support vector regression (SVR), convolutional neural networks (CNN), and resource-allocating networks (RAN) with radial basis function (RBF) components, it enables real-time error compensation. Experimental results demonstrate a reduction in mean absolute error (MAE) from 2.06° to 0.08° and confirm a significant improvement in recovery efficiency, robustness, and reliability.

Keywords: Self-Calibration, TMR sensor, CNN, SVR, RAN.

Introduction

The ongoing advancement of sensor technology has led to an increase in the number and variety of low-cost, compact, and portable sensors on the market [1], establishing them as the foundation for real-time measurement, monitoring, and data analysis in key areas of Industry 4.0. However, the accuracy and reliability of data generated by these sensors can raise concerns, particularly in the absence of proper calibration [2]. Static calibration approaches, while initially effective, often fail to account for factors such as sensor degradation, environmental variability, and mechanical impacts, necessitating the development of more advanced methods [3]. Inspired by self-maintenance in living organisms, this research proposes a self-calibration approach as part of a broader self-X system, enhancing reliability and autonomy [4]. Although the self-calibration itself is static, the approach facilitates real-time error compensation by applying pre-trained models to dynamic data. This article compares supervised self-calibration methods, emphasizing ML-based models such as artificial neural networks, and their comparison with traditional methods like linear regression. Their effectiveness is evaluated in terms of enhancing fault tolerance and reliability under diverse dynamic perturbations [5].

Proposed Methodology

The proposed methodology employs a mathematical model to simulate sensor output signals under varying operational conditions, including both ideal scenarios and that representative of real-world distortions. By incorporating both simulated and real data, the methodology ensures comprehensive coverage of potential sensor behavior. ML models were trained using these datasets, with reference values serving as targets to guide the calibration process. The effectiveness of training was evaluated using key metrics: mean squared error (MSE) to measure prediction accuracy and the coefficient of determination (R^2) to assess the model's ability to describe data variability [5]. To implement the self-calibration process, algorithms such as SVR, CNN, and RAN were selected. The raw data was processed directly, without pre-extracted features. Additionally, trained CNN layers were used to generate high-level features. These frozen feature layers (FL) produced characteristics of the data, which were then fed into the RAN and SVR algorithms, replacing the standard fully connected layer typically used at the top of the CNN architecture. This approach allowed for a comparison of the effectiveness of using raw data versus high-level features generated by CNN.

Results

The study utilized both simulated and real-world data. Simulated data consisted of synthetically generated tunnel magnetoresistive (TMR) sensor outputs with injected errors, including phase shifts, amplitude imbalance, noise, and offset, allowing for an in-depth examination of self-

calibration responses to various types of distortions and their combinations (Fig. 1).

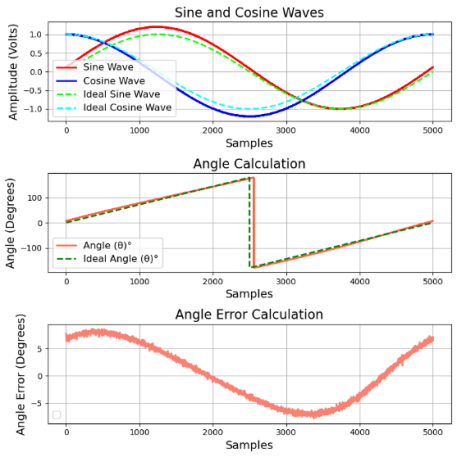

Fig. 1. Simulated ideal and corrupted TMR sensor outputs (10% amplitude imbalance, 1° phase shift, ±0.1 V offset, and 0.005 V noise).

Empirical data were collected using the experimental setup shown in Fig. 2, designed to simulate and introduce a variety of mechanical errors.

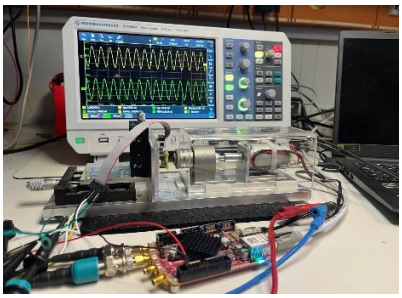

Fig. 2. Lab setup with fault injection capability.

Figure 3 shows TMR sensor outputs after displacements along the X, Y, and Z axes (10 mm, 15 mm, and 10 mm), simulating operational failures. The subplots illustrate sensor outputs, calculated versus reference angles, angle errors before and after calibration (with reduced residuals), and the error distribution shifting toward zero post-calibration. The dataset comprised 208,629 samples, randomly split into 80% for training (166,903 samples) and 20% for testing (41,726 samples). The results in Tab. 1 are averaged over 10 independent runs to ensure reliability and robustness, with standard deviations included for clarity. MAE represents the angular error after self-calibration. The hierarchical method, which integrates frozen CNN feature layers with RAN and SVR, significantly outperformed the direct application of these models, reducing the initial angle error from 2.06° to 0.08°. In RAN, 10 centres were used, while SVR utilized 6,407 support vectors. These results confirm the effectiveness of self-calibration in improving accuracy and reliability under dynamic perturbations. Future work will aim to develop adaptive and dynamic calibration methods for real-time error correction and improved sensor accuracy across varying operational scenarios.

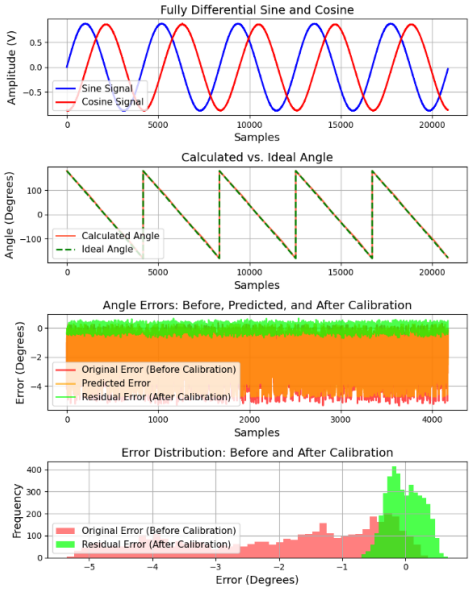

Figure 3. TMR outputs before/after calibration.

Tab. 1: Model evaluation results

Method	MSE [°²]	R^2	MAE [°]
CNN	0.02 (0.005)	0.99 (0.002)	0.11 (0.013)
SVR	0.05 (0.0002)	0.98 (0.0001)	0.18 (0.0008)
RAN	0.16 (0.053)	0.93 (0.022)	0.31 (0.061)
SVR (FL)	0.01 (0.0003)	0.99 (0.0001)	0.10 (0.0007)
RAN (FL)	0.01 (0.0011)	0.99 (0.0024)	0.08 (0.004)

References

[1] Barceló-Ordinas, José M., Messaoud Doudou, Jorge García-Vidal and Nadjib Badache. “Self-calibration methods for uncontrolled environments in sensor networks: A reference survey.” ArXiv abs/1905.11060 (2019): n. pag.

[2] Nalakurthi NVSR, Abimbola I, Ahmed T, Anton I, Riaz K, Ibrahim Q, Banerjee A, Tiwari A, Gharbia S. Challenges and Opportunities in Calibrating Low-Cost Environmental Sensors. Sensors. 2024; 24(11):3650. https://doi.org/10.3390/s24113650

[3] Pereira, J.D. Pressure Sensors: Working Principles of Static and Dynamic Calibration. Sensors 2024, 24, 629. https://doi.org/10.3390/s24020629

[4] Gerken, Elena, Qummar Zaman, Senan Alraho and Andreas König. “Development of a Self-X Sensory Electronics for Anomaly Detection and its Conceptual Implementation on an XMR-based Angular Decoder Prototype.” tm - Technisches Messen 90 (2023): 20 - 26.

[5] Badura, M., Batog, P., Drzeniecka-Osiadacz, A. et al. Regression methods in the calibration of low-cost sensors for ambient particulate matter measurements. SN Appl. Sci. 1, 622 (2019). https://doi.org/10.1007/s42452-019-0630-1.

DOI 10.5162/SMSI2025/P45

Determination of the phase proportions of austenitic steels using artificial intelligence

Thomas Schroeter[1], Galina Polte[2], Julia Wichmann[1], Leon Kaufhold[3]
[1] ifw Günter Köhler Institut für Fügetechnik und Werkstoffprüfung GmbH, Ernst-Ruska-Ring 3, 07745 Jena, Germany
[2] Technische Universität Ilmenau, Fakultät für Maschinenbau, Fachgebiet Qualitätssicherung und Industrielle Bildverarbeitung, Newtonbau
Gustav-Kirchhoff-Platz 2, 98693 Ilmenau, Germany
[3] Ernst Abbe-Hochschule Jena, Fachgebiet SciTec, Carl-Zeiß-Promenade 2, 07745 Jena, Germany
tschroeter@ifw-jena.de

Summary
Work on the development of an automated process for the metallography of metallic materials based on digital image processing and artificial intelligence is presented. This particularly involves the precise recording of the phase components of duplex stainless steel by evaluating metallic micrographs. The process can also be applied to other types of steel and other metallic materials.

Keywords: Metallography, Duplex Stainless Steel, Image Processing, Artificial Intelligence, Machine Learning

Motivation

Currently known evaluation strategies are based on algorithmic or visual methods for determining phase components of metallographic samples. Such as shown in Fig. 1.

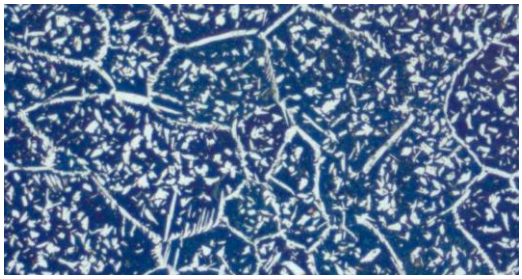

Fig. 1. Color-etched section of a sample of austenitic steel, magnified 500x

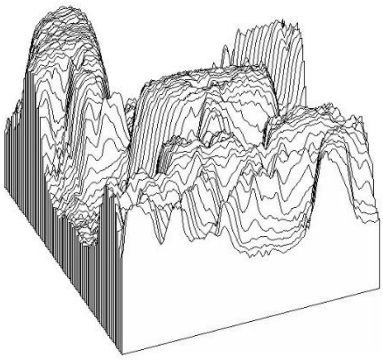

Fig. 2. Gray value distribution of the pixel amplitudes of an image section in Fig. 1

A recognized method is the point counting method, in which selected points of the microscope image of a sectional sample are visually examined by a measuring person and assigned to a phase [1]. However, this process is very complex and requires a lot of personnel. Automated evaluations are based on algorithmic methods such as threshold determination of the gray value histogram of metallographic images [2] or segmentation using edge detection. However, since the distribution of the pixel amplitudes is irregular (see Fig. 2), these methods have limits in terms of the achievable accuracy. Learning processes and artificial intelligence processes are therefore proposed as an alternative. The initial goal here was to achieve at least the same level of accuracy as the visual procedures.

Approach

The approach consisted of using artificial intelligence in the form of model-based and learning processes including neural networks, with the focus on the latter. The following methods, not based on neural networks, were examined: Support Vector Machine SVM [3], decision trees (random forest), Chan-Vese method [4]. In addition to some of the procedures, relaxation labeling – RL was used. In addition, various filter operators known from image processing were used to filter the images before further processing. The histogram method according to Otsu was also examined for comparison. A convolutional

network was used as the neural network (convolutional neural network - CNN, see Fig. 3).

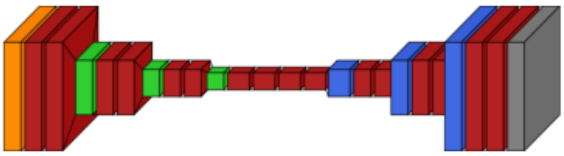

Fig. 3. Convolutional neural network used

orange: input layer, red: folding layers, green: pooling layers blue: upscaling layers, gray: output layer

In addition, a modified version was used, containing 21 layers each. In addition to the fully connected layers known from classic neural networks, they also contain mathematical convolution layers, pooling layers for data reduction and upscaling layers. The “Tensorflow” framework was used for this. A program was created in Python from Anaconda that can be used to access Tensorflow and configure networks. To obtain the image material for the investigations, material samples measuring approximately 10x2 mm2 were embedded, cross-sections were made and the samples were then color-etched. Microscopic images were then taken at 500x magnification and an image resolution of 2646 x 2056 pixels for further evaluation. In the learning methods, a training process was initially carried out using labeled pixels, i.e. pixels of known class affiliation (austenite or ferrite). To determine the actual class affiliation of these reference pixels, software was developed with which areas in pixel blocks of size 128 x 128 are marked using mouse support based on visual assessment and this area is then assigned to a phase. All pixels contained in the pixel block are then labelled and can be used as reference pixels. In addition to the real data from the metallographic samples, artificially generated images were also used to obtain reference patterns using so-called image augmentation [5].The systems of the learning procedures have now been trained with the help of the reference patterns provided. With the Support Vector Machine - SVM, individual pixels were trained and with the neural networks, blocks of 128 x 128 pixels were trained. Finally 128 x 128 pixels were available as a result at the network output.

Results

The individual methods were applied to labelled pixels in several images, as shown in Fig. 1). Understandably, the learning processes only used pixels that were not previously included in the training process. For the evaluation, the accuracy was determined, i.e. the number of correctly assigned pixels to the austenite and ferrite classes, based on the number of all evaluated pixels, also the pixels incorrectly assigned to the two classes. Table 1 shows the results for the individual procedures. For the methods not based on neural networks, only the best results are shown depending on various parameters. As can be seen, the accuracy results are all between 95% and 98%, which is in line with expectations. The best results were achieved with the modified convolutional neural network.

Tab 1. Accuracy values achieved for the examined procedures, RF – Random forest, RL Relaxation labelling

Procedure (see section Solution approach)	Accuracy
OTSU	0.956
ChanVese	0,960
ChanVese+RL	0,968
RF	0,973
CNN	0,973
CNN modified	0,977

Outlook

The actual work builds the foundation for the automatic determination of phase proportions in duplex stainless steel. Future work will concern further areas of application in metallography and ceramography as well as further increases in accuracy. Folding neural networks in particular still have great potential for this. Further possible future applications are the detection of grain and phase boundaries, the detection of alloy components and the detection of voids also in X-ray, CT or ultrasound images.

References

[1] ASTM E915 2021: Standard Test Method for Determining Volume Fraction by Systematic Manual Point Count, Verlag Information Handling Services 2019

[2] Nobuyuki Otsu (1979). "A threshold selection method from gray-level histograms". IEEE Transactions on Systems, Man, and Cybernetics.

[3] M. A. Hearst, S. T. Dumais, E. Osman, J. Platt, and B. Scholkopf. “Support vector machines.” Intelligent Systems and their Applications, IEEE, 13(4), pp. 18–28, 1998.

[4] Getreuer, Pascal: Chan-Vese Segmentation, Image Processing On Line, 2 (2012), pp. 214–224.

[5] Wunsch, L., Anding, K., Polte, G. Kun Liu, Notni, G.: Data augmentation for solving industrial recognition tasks with underrepresented defect classes, ACTA IMEKO, ISSN: 2221-870X, December 2023, Volume 12, Number 4, 1 - 5

DOI 10.5162/SMSI2025/P46

Soft Sensor Approach to Detect Failures in Circuit Breaker Components

Mona Fuhrländer [1], *Jörg Gebhardt*[1], *Hadi Rahmeh* [1] *and Aydin Boyaci*[1]
[1] ABB AG, Kallstadter Str. 1, Mannheim, Germany
mona.fuhrlaender@de.abb.com

Summary: A digital twin for circuit breaker monitoring has been developed, focusing on the trip coil and adjacent mechanisms. The twin is based on a fast-to-evaluate system of ordinary differential equations (ODEs). It works as a soft sensor which integrates measurements of observable quantities (e.g. current, force) and parameter identification algorithms. The approach allows to infer the drift of non-measurable quantities such as damping. This gives new options for predictive maintenance and increased reliability of circuit breakers. Calculational results demonstrate the digital twin's effectiveness in real-time monitoring and fault detection.

Keywords: predictive maintenance, soft sensor, circuit breaker, digital twin, optimization

Introduction

Reliability of switchgear systems is crucial for the energy transition, due to increased power demand and decentralized, generation. Frequent switching heightens the risk of failures, safety hazards and operational disruptions. Cost-efficient sensors in grid components are enablers for appropriate maintenance strategies.

Trip coils as circuit breaker components

The trip coils in a circuit breaker initiate the opening or closing operation [1]. If the circuit, e.g., is supposed to be interrupted, the opening coil is energized. The trip coil pin is driven upwards to initiate the kinematic chain ending with the release of the opening spring and the main contact separation. In Fig. 1 we see the interior or a circuit breaker drive with the trip coil highlighted.

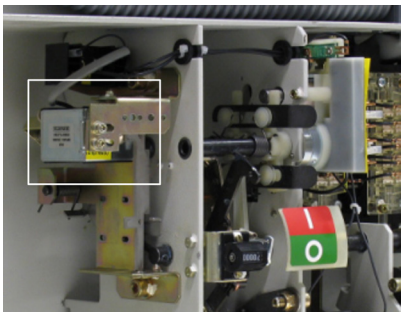

Fig. 1: Interior of a circuit breaker drive.

Physical model of the trip coil

We focus on the digital representation of the trip coil. Our aim is to have a system of ordinary differential equations (ODEs), which can be efficiently solved within the operating circuit breaker.

We obtain the following system

$$\frac{d\lambda}{dt} = U - R \cdot i(\lambda, x) \tag{1}$$

$$\frac{dv}{dt} = \frac{1}{m} \cdot F_{\text{coil}}\,, \quad \frac{dx}{dt} = v \tag{2}$$

where λ denotes the flux linkage, U the supply voltage, R the coil resistance, i the current, x, v the trip coil pin's vertical position and speed, and m the pin's mass. Equation (1) describes the electromagnetics of a linear reluctance motor [2]. Equation (2) is Newton's law for the pin dynamics. In F_{coil} all forces acting on the trip coil pin are summarized: The damping force F_{d}, the spring stiffness F_{s}, and the gravity force F_{g} have negative sign and tend to hold the pin at the bottom. The electromagnetic force F_{em} pushes the pin upwards (positive sign). The mechanical forces are defined by

$$F_{\text{d}} = -c(x) \cdot v \tag{3}$$

$$F_{\text{s}} = -k(x)(x - x_0) \tag{4}$$

$$F_{\text{g}} = -m \cdot g \tag{5}$$

with possibly non-linear damping coefficient c and spring stiffness k, and the spring equilibrium point x_0.

Soft sensor use case

This fast-to-evaluate model can be used for soft sensing potential drift of important parameters. With physical sensors, quantities such as i or F_{coil} can be measured in operation, thereby turning the model into a continuously updated digital twin. If a change in these measured quantities is observed, for maintenance reasons it would be useful to determine which model parameters have changed. Relevant degrading parameters include the damping of the pin or the spring stiffness. Possibly degrading parameters are then

set as optimization variables (e.g., the damping coefficient c). Then, we minimize the difference (according to a suitable norm $|.|$) between the force $F_{\mathrm{DT}}(c)$ calculated by the twin model as a function of the degrading parameter, and the force measured F_{m}, at a number of points in time, i.e. we solve the optimization problem

$$\min_{c} |F_{\mathrm{DT}}(c) - F_{\mathrm{m}}| \ , \ c \in A \subset \mathbb{R}^n. \qquad (6)$$

The optimal solution gives an estimate how much, in this case, the parameter set $c \in \mathbb{R}^n$ has drifted. In Fig. 2, an illustrative case with $n = 1$, the force F_{m} is plotted vs time in the reference state and after degradation. These curves can be measured in the field, however, in our test both are simulated using the digital twin model (1 - 2). In the reference curve, negligible damping is assumed, i.e., $c_{\mathrm{ref}} = 0$. To simulate a degradation, we set this coefficient to $c_{\mathrm{degr}} = 15$. Solving the optimization problem described above, we obtain the optimal solution $c^{\star}_{\mathrm{degr}} = 15.03$. The deviation between true degradation c_{degr} and the degradation measured with the soft sensor $c^{\star}_{\mathrm{degr}}$ is $0.2\,\%$. This result validates our approach.

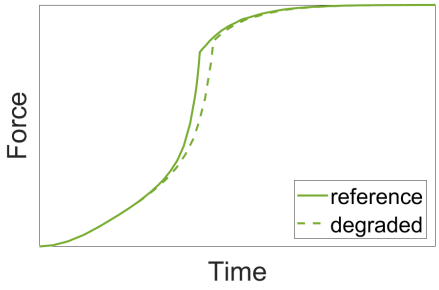

Fig. 2: Schematic representation: Trip coil pin's force vs. time during an opening operation. The degraded state shows a delayed force build-up as compared to the reference.

Digital twin of the mechanical part

Once the trip coil pin is pushed upwards by the electromagnetic force, a kinematic chain is initiated, as illustrated in Fig. 3. The pin hits a lever which is connected with the off (or on) button. This hits the antipumping part, which, after overcoming a clearance, hits the lever of the opening (or closing) shaft. The rotation of the shaft then starts the release of the opening (or closing) spring. Since relevant faults can occur in this mechanical subsystem, it needs to be included into the ODE system (2) in form of additional terms. The detailed formulation is beyond the scope of this paper, but the reasoning is given in (7). We replace F_{coil} in (2) by F_{total}, which is defined by

$$F_{\mathrm{total}} = \qquad (7)$$

$$\begin{cases} F_{\mathrm{coil}}, & \text{if } x < x^{\mathrm{c}} \\ F_{\mathrm{coil}} + F_{\mathrm{lever}}, & \text{if } \frac{L_{\mathrm{L}}}{L_{\mathrm{b}}} x_{\mathrm{b}}^{\mathrm{c}} + x^{\mathrm{c}} > x \geq x^{\mathrm{c}} \\ F_{\mathrm{coil}} + F_{\mathrm{lever}} + F_{\mathrm{shaft}}, & \text{if } x \geq \frac{L_{\mathrm{L}}}{L_{\mathrm{b}}} x_{\mathrm{b}}^{\mathrm{c}} + x^{\mathrm{c}}. \end{cases}$$

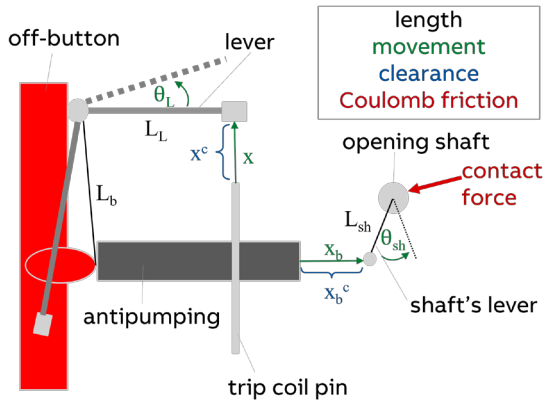

Fig. 3: Illustration of the circuit breaker drive's opening mechanism.

The meaning of the variables in (7) can be taken from Fig. 3. The force F_{total} acting on the coil pin now also includes contributions from lever and shaft. Both terms have negative signs, F_{lever} represents the inertia of the plastic lever, F_{shaft} contains the inertia of the shaft, the stiffness of the shaft's spring, and a damping force. The case distinction is required due to the clearances between pin and lever and between antipumping part and shaft. Hence, in the first case, if $x \leq x^{\mathrm{c}}$, the extended ODE system coincides with (1-2).

Conclusion

We presented an approach to use a digital twin of the trip coil and adjacent mechanisms of a circuit breaker as a soft sensor. It has been shown that degrading parameters can be identified, which are difficult to measure directly.
The twin, therefore, can continuously update its internal parameters according to the status of the real asset. This is an important element allowing predictive maintenance. We have already formulated the equations for the ODE system, including mechanical components behind the coil.
The next step is to integrate this system into the soft sensor to detect degradation in the mechanics of levers and shaft.

Acknowledgment

The project AProSys on which this paper is based was funded by the German Federal Ministry of Education and Research under the funding code 03EI6090A.

References

[1] A.A. Razi-Kazemi et al., Circuit-breaker automated failure tracking based on coil current signature, *IEEE Transactions on Power Delivery*, Vol. 29, No. 1, (2014); doi: 10.1109/TPWRD.2013.2276630

[2] M.F. Rahman et al., Position Estimation in Solenoid Actuators , *IEEE Transactions on Industry Applications* Vol. 32, No. 3,(1996); doi: 10.1109/28.502166

DOI 10.5162/SMSI2025/P47

Stop ignoring units outside the SI

Joaquín Valdés[1]
[1] *Universidad Nacional de San Martín, 25 de Mayo y Francia, 1650 San Martín, Prov. Buenos Aires, Argentina*
jovaldes1875@gmail.com

Summary:
In times of digital transformation, machines are expected to operate exclusively using the International System of Units (SI), something that humans have not yet fully achieved. This requires an internationally agreed database for converting to SI units the non-SI units that humans enter at the level of human-machine interface. This contribution considers additional requirements and possibilities for achieving this goal.

Keywords: metrology, digital SI, non-SI units, conversion factors, BIPM.

Non-SI units accepted and not accepted for use with the SI

On May 20, 2025, the 150th anniversary of the signing of the Metre Convention is celebrated. A scientific International Bureau of Weights and Measures (BIPM) with its headquarters in Paris was set up by the Metre Convention. The BIPM operates under the exclusive supervision of the International Committee for Weights and Measures (CIPM) which itself comes under the authority of the General Conference on Weights and Measures (CGPM). There are currently 64 States Parties to the Metre Convention and 37 Associate States and Economies. At that historic moment, the goal was to ensure standard units accessible to all the people for all time. With that purpose in mind, what we know today as the International System of units (SI) was being built. The core of the constituent parts of the SI are essentially seven base units, a set of derived units and the SI prefixes. The authoritative document of the SI is the SI Brochure [1]. The SI is the only internationally agreed system of units. It was expected that such a system, which did not belong exclusively to any nation, would be adopted by all. Cumbersome conversions between the many different existing units were gradually being overcome. Despite this great achievement of humanity, not all people currently use only SI units. A relatively small set of non-SI units that were difficult to stop being used by people continued to be accepted for use with the SI. Some of those units were gradually being removed. In addition to this short list, there are still a large number of non-SI units that continue to be customary used in some contexts and countries. Let's mention some current examples of commercial transactions and industrial applications in non-SI units. Gasoline is sold in U.S. gallons (gal). In the international petroleum market prices are given in U.S. dollars per barrel (bbl). The inch (in), foot (ft) and yard (yd) are also used as units of length in several countries. Vehicle efficiency is measured in the UK in miles per gallon. Beer is commonly sold in pints (pt). Food is sold by pounds (lb). In many countries tire pressure is measured in pounds per square inch (psi). Energy associated with fuels is expressed in British thermal units (Btu). The units knot and nautical mile, until recently accepted as non-SI units for use with the SI, are still widely used in both aviation and maritime navigation. There are also laws within sovereign states allowing the use of non-SI units alongside the SI. The logic underlying the gradual elimination of some non-SI units from the SI seems to find a limit in few units, such as day, hour and minute, that humans could not stop using because they are so familiar with them. This is an inference based on the common sense of humans. The logic of interaction between machines may be quite different.

Machines operating exclusively with SI units

The coexistence of SI units with non-SI units has been the cause of many important incidents. There are known cases of overweight flights due to ground crew assuming that kilogram weight markings on cargo were pounds. A plane that took off with about half the fuel it should have had because the pilots thought the figure for fuel weight on board was in kilograms when it was really pounds. The most resonant case was that of the Mars Climate Orbiter NASA´s spacecraft, which in 1999 unexpectedly crashed on arrival at its destination due to a mismatch of units. The

spacecraft engineers calculated some thrust forces in pound-force (lbf), whereas the team who built the thrusters were expecting a value in newton (N), according to specifications. One solution to these problems is to continue waiting decades until all humans become familiar with using SI units. Another solution would be to force all machines to communicate with each other using only SI units. The latter has been proposed in the SmartCom project [2] with the participation of several major National Metrology Institutes, universities and industrial companies, headed by Germany's PTB (Physikalisch-Technische Bundesanstalt). Machines use only SI units for machine-to-machine communication, while humans may still refer at the user interface level to non-SI units. The SmartCom Project started on 01 June 2018 and produced a Guide for the exchange of machine-readable data of digital measurement values in a given metadata-format. The fundamental goal of this development is machine communication using only the seven SI base units. A unit that only requires to interpret SI base units has the greatest importance for a highly machine-readable data representation. We have recently proposed to include at the BIPM website the conversion factors to the seven SI base units of most of the non SI units used worldwide for machine-to-machine communication [3]. Here we address additional considerations in this regard.

Stop ignoring units outside the SI

The global collaboration CODATA (Committee on Data of the International Science Council) formed also in 2018 the Task Group on Digital Representation of Units of Measurement (DRUM). The title of this contribution is inspired by that of a comment article appeared in Nature in 2022: "Stop squandering data: make units of measurement machine-readable" [4]. It was published by DRUM and other scientists participating in a Forum on Metrology and Digitalization, reporting to the CIPM. The document addresses a set of shortcomings related to a consistent, machine-readable description of units in data, such as the lack of broadly agreed technical specifications for representing quantities and their associated units without confusing machines. The technical requirements for detecting the origin of the data, the units associated with the incoming data, conversion and validation modules, their language and format, so as automation of the workflow, may improve over time.

However, the uniqueness of unit conversions with reference to the SI requires that a database of conversion factors be internationally agreed between States and then periodically updated with international agreement. In this regard, the information provided by the NIST Guide for the Use of the SI and the ISO/IEC 80000 series of standards would gain internationally authoritative status if it were approved by the CGPM and made official on the BIPM website. There is already formal cooperation between BIPM/CIPM with CODATA and its Task group DRUM. It seems then very feasible that scientific efforts will continue, aiming at the inclusion of a conversion factors database in a possible international agreement between States participating in the decision-making bodies of the Metre Convention. It should also be noted that ISO and IEC are independent, non-governmental organizations made up of members from the national standardization bodies, which can be either public or private. Within the framework of the Metre Convention, there are already historical precedents of collaboration involving both organizations. They participate together with the BIPM in the Joint Committee for Guides in Metrology. They are also signatory of a Joint statement of intent on the digital transformation.

The new message of universal unification emerging from those adhering to the Metre Convention could be: This is the SI, and these are the conversion factors to be used so that any other customary unit in use is discarded by using only SI units.

Acknowledgement

The author thanks to Héctor M. Laiz for helpful discussions.

References

[1] BIPM SI Brochure 9th edition 2019 (V3.01 August 2024) https://bipm.org/en/publications/sibrochure

[2] D. Hutzschenreuter et al. SmartCom Digital System of Units (D-SI), Version D-SI 1.3 (2019); doi: 10.5281/zenodo.3522631

[3] J. Valdés and H. M. Laiz, "An SI for humans and a digital SI for machines", Metrologia 62 1-5 (2025); https://doi.org/10.1088/1681-7575/ad94f8

[4] R. Hanisch et al., 'Stop squandering data: make units of measurement machine-readable', *Nature* **605**, 222-224 (2022): https://doi.org/10.1038/d41586-022-01233-w

DOI 10.5162/SMSI2025/P48

Application-Oriented In-Situ Testing Methods for Permanent Magnet Characterization

M. Lanz[1,2], G. Martinek[1], T. Kresse[1], A. Georgiadis[2], G. Schneider[1], D. Goll[1]
[1] Materials Research Institute, Aalen University, Aalen, Germany
[2] Faculty of Management and Technology, Leuphana University, Lüneburg, Germany
maximilian.lanz@hs-aalen.de

Summary:

The long-term performance of permanent magnets is critical, as even small variations in field or temperature can cause irreversible demagnetization. In this paper, a test framework is presented with three different setups that enable comprehensive magnetization analysis and monitoring of commercial magnets, capturing both direct and time-dependent losses, while bridging the gap between material testing and application requirements.

Keywords: testing methods and arrangements, in-situ demagnetization monitoring, application-oriented demagnetization measurements, permanent magnets behavior

Introduction

Permanent magnets play a crucial role in actuators, sensors, and measurement technology. Preventing irreversible magnetization losses is a key challenge, as demagnetization occurs due to field or temperature changes and time-dependent effects [1]. Integral methods like hysteresisgraphs, vibrating sample magnetometers (VSM) [2], and Helmholtz coils assess overall magnetization [3]. Hysteresisgraphs suffer from fluxmeter drifting, making them unsuitable for long-term studies. VSMs are limited by sample size [4], while larger moment measurement coils, typically in a Helmholtz coil arrangement, lack external field and temperature control. Local methods, such as field mappers, map the sample's field using a moving Hall probe, allowing the detection of field inhomogeneities but also lacking active field and temperature control. This highlights the necessity of a comprehensive framework that bridges material characterization with application requirements. To address this, three testing concepts are developed and tested. This study focuses on measuring and monitoring direct magnetization losses, time-dependent viscosity S, and the magnetic viscosity parameter S_v. S_v allows for the prediction of magnetization losses, by defining an effective fluctuation field: $H_{eff} = S_v * \ln(\Delta t)$ [1]. This enables the extrapolation of results over the entire lifetime of a component. Furthermore, the testing arrangement enable in-situ field scans for visualization of the demagnetization process.

Testbench Framework

Concept 1

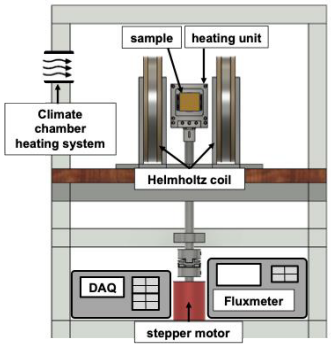

Fig. 1. General overview of concept 1.

The first concept, based on a classical Helmholtz coil with fluxmeter measurement, is enhanced by a stepper motor [5] for sample rotation (Fig. 1). Additionally, a heating unit capable of reaching temperatures up to 250 °C was integrated. The fluxmeter converts the induced voltage into magnetic flux. Fluxmeter drifting is minimized by rotating the sample within the Helmholtz coil, enabling long-term measurements (magnetic viscosity S) at various temperatures.

Concept 2

The second concept combines classical Helmholtz measurements with the functionality of a field mapper under varying field and temperature conditions (in situ) (Fig. 2) [6]. The sample, mounted on a rotating sample disc, can be heated up to 200 °C. During one rotation, it is

exposed to an external field within the yoke's air gap (H_{ext} = 1800 kA/m), measured integrally via the Helmholtz coil with a fluxmeter, and locally analyzed by a scanning Hall probe. This enables both the integral measurement of the entire demagnetization curve (hysteresis curve) and detailed local field mapping.

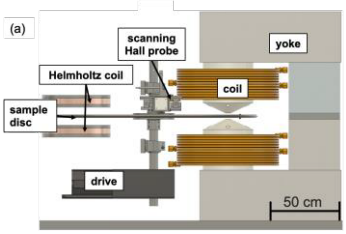

Fig. 2. General overview of concept 2.

Concept 3

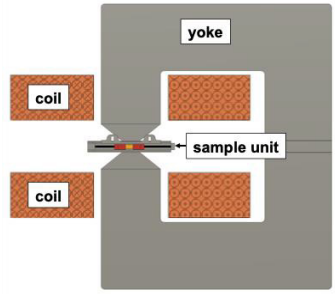

Fig. 3. General overview of concept 3.

The third concept enables both rapid field changes and constant fields. It is based on a yoke made of electrical steel sheet, with excitation coils generating external field strengths of up to 1500 kA/m (Fig. 3). The sample can be heated up to 250 °C and is measured using Hall probes in the air gap between the sample and the yoke. This setup is designed for measuring demagnetization curves as well as time-dependent behavior over short time frames. It enables the routine determination of the magnetic viscosity parameter S_v for full-size samples.

Data acquisition

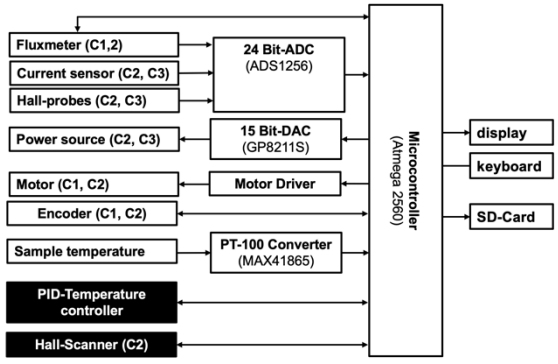

Fig. 4. General overview of the DAQ system with concept-specific components indicated in parentheses.

Measurement acquisition and process control are managed by an ATmega 2560 microcontroller. Each setup includes a microcontroller with an ADC (Analog-to-Digital Converter) for acquiring measurement signals, such as Hall probe readings and/or the magnetic moment from the fluxmeter (Fig. 4). This enables discrete data acquisition and precise control of process parameters (Tab. 1), including driving the current source via a DAC (Digital-to-Analog Converter) and controlling the motor drive. Additionally, Concept 2 includes a field mapping unit alongside the main acquisition and process control unit, synchronizing its stepper motor with the sample's rotation for field mapping.

Tab. 1: Summary of measurement methods, process parameters, and key results for all concepts.

Concepts	Measurement methods	Measurement variables	Relative measurement accuracy (at applied process parameters in medium conditions)	Process parameter	Key results
1	Helmholtz-coil with Fluxmeter	J [T]	J: ≈ 0.005 %	Temperature: 20-250 °C	Magnetic viscosity: *S*
	Thermocouples	T [°C]	T: ≈ 0.5 %	Time	Temperature ramps: *J(T)*
2	Helmholtz-coil with Fluxmeter	J [T]	J: ≈ 0.01 %	Field (H_{ext}): 0-1800 kA/m	In-situ field maps: *B(x,y)*
	Hall-probes	H [kA/m]	H: ≈ 0.1 %	Temperature: 20-200 °C	Hysteresis curves: *J(H)*
	Thermocouples	T [°C]	T: ≈ 2.5 %		
3	Hall-probes	J [T]	J: ≈ 0.1 %	Field (H_{ext}): 0-1500 kA/m	Magnetic viscosity: *S*
	Current Sensor	I [A]	I: ≈ 0.5 %	Temperature: 20-250 °C	Viscosity parameter: S_v
	Thermocouples	T [°C]	T: ≈ 1 %	Time	Hysteresis curves: *J(H)*

Conclusions

The proposed testing framework enables a detailed analysis of demagnetization effects in permanent magnets by combining integral and local measurement techniques. Concept 1 allows long-term monitoring of magnetic viscosity, concept 2 provides in-situ field mapping, and concept 3 determines viscosity parameters. These approaches bridge the gap between material testing and applications, improving the reliability of magnet stability assessments.

References

[1] R. Street, J. C. Woolley, Proc. Phys. Soc. A 62, 562 (1949); doi: 10.1088/0370-1298/62/9/303.

[2] S. Foner, Rev. Sci. Instrum. 30, 548–557 (1959); doi: 10.1063/1.1716679.

[3] S. Möwius, N. Kropff, M. Velicescu, ACTA IMEKO 7, 15 (2019); doi: 10.21014/acta_imeko.v7i4.572.

[4] T. Kresse, G. Martinek, G. Schneider, D. Goll, Materials 17, 243 (2024); doi: 10.3390/ma17010243.

[5] D. W. Carnegie, J. Timpf, Nucl. Instrum. Methods A 319, 97–99 (1992); doi: 10.1016/0168-9002(92)90537-E.

[6] M. Lanz, G. Martinek, G. Schneider, D. Goll, Metrology 4, 506–516 (2024); doi: 10.3390/metrology4030031.

DOI 10.5162/SMSI2025/P49

Modeling of High-Sensitivity SAW Magnetic Field Sensors with Au-SiO_2 Phononic Crystals

Mohsen Samadi[1,*], *Jana Marie Meyer*[2], *Fabian Lofink*[2,3], *Martina Gerken*[1]
[1]*Integrated Systems and Photonics, Department of Electrical and Information Engineering, Kiel University, Germany*
[2]*Fraunhofer Institute for Silicon Technology ISIT, Itzehoe, Germany*
[3]*Microsystem Materials, Department of Materials Science, Kiel University, Germany*
[*]*mosa@tf.uni-kiel.de*

Summary:
In this study, we present a highly-sensitive SAW magnetic field sensor that utilizes phononic crystal structures with Au pillars embedded in a SiO_2 guiding layer. The sensor's sensitivity is considerably improved due to increased interactions between the SAW and the magnetostrictive material, facilitated by resonance effects within the PnC structure. Our proposed sensor thus demonstrates significantly enhanced performance compared to sensors with continuous delay lines.

Keywords: magnetic field sensor, magnetostriction, phononic crystal, surface acoustic wave

Introduction

Magnetic field sensors are crucial in various applications for accurate measurement and detection of magnetic fields [1-4]. Surface acoustic wave (SAW) based magnetic field sensors have been exploited to detect minute changes in magnetic fields by utilizing the ΔE effect, where the Young's modulus of magnetostrictive materials changes under an external magnetic field, causing phase modulation of the SAW [5-8]. This modulation is detected and measured, providing information about the magnetic field strength. Phononic crystals (PnC), i.e., engineered materials with periodic arrangements, allow precise control over acoustic wave propagation and dispersion [9-15]. Integrating PnC structures into SAW magnetic field sensors enhances sensitivity and performance, promising advancements for applications that require accurate magnetic field detection [16].

Here, we model a SAW magnetic field sensor with a PnC structure embedded within the guiding layer. The proposed sensor is schematically illustrated in Fig. 1. A thick silicon substrate is coated by a 1 µm-thick $Al_{0.77}Sc_{0.23}N$ piezoelectric layer [17]. Two gold IDTs are devised on the surface of the AlScN layer to generate and detect a Rayleigh wave at a center frequency of approximately 250 MHz. A 2D square lattice of Au pillars is embedded within the SiO_2 guiding layer between the two IDTs. These pillars are of the same thickness as the guiding layer (h_P = h_{GL} = 4.5 µm). The entire PnC structure is then coated by a continuous FeCoSiB layer with a thickness of h_{MS} = 200 nm.

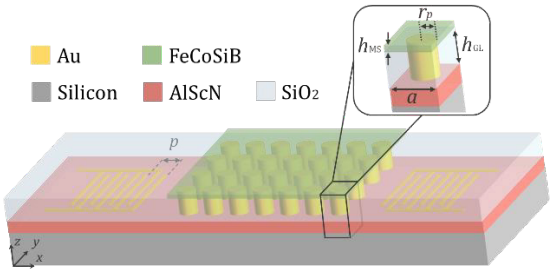

Fig. 1. SAW magnetic field sensor with Au-SiO_2 PnC. A magnified view of a unit cell of the PnC is shown with further details. a and r_p denote the lattice constant and the radius of the pillars, respectively. h_{GL} and h_{MS} represent the thicknesses of the guiding layer and the magnetostrictive layer.

Theoretical Model

To analyze the sensor's performance, we solve a set of coupled differential equations using the finite element method (FEM) [18,19]. For simplicity, we consider an isotropic magnetostrictive material whose mechanical stiffness tensor is determined by the Young's modulus (E) and Poisson's ratio (v).

Applying a magnetic field induces changes in the Young's modulus of the magnetostrictive material, denoted as the ΔE effect. The final value of the Young's modulus (E_f) is achieved by the superposition of the purely mechanical component (E_0) and the magnetically-induced component (ΔE) [20]. When accounting for a hard axis magnetization process:

$$E_f = \begin{cases} \left(\frac{1}{E_0} + \frac{1}{\Delta E}\right)^{-1} & |\mathrm{H}| < \mathrm{H}_K \\ E_0 & |\mathrm{H}| > \mathrm{H}_K \end{cases} \qquad (4)$$

Here, H_K denotes the effective anisotropy field and the magnetically-induced change in the Young's modulus (ΔE) can be obtained using the following formula:

$$\frac{1}{\Delta E} = \frac{9}{4}\frac{\mu_0 \lambda_S^2 \mathrm{H}^2}{K^2}\chi \qquad (5)$$

where μ_0, λ_s, and K are the magnetic vacuum permeability, the saturation magnetostriction, and the first-order anisotropy constant, respectively. Further details regarding the theoretical model and material parameters can be found in [16].

Results

We employed the finite element method (FEM) to calculate the band structure of the PnC and conducted a series of parameter sweeps using COMSOL Multiphysics to determine the optimal dimensions of the PnC for precise frequency matching between one of the PnC resonant modes with the center frequency of the Rayleigh mode generated by the IDT, i.e., *f*=250 MHz. The details of the simulation model can be found elsewhere [16]. Fig. 2(a) presents the band diagram calculated in Γ-X direction for a PnC with *a* = 5.6 µm and r_p = 0.25×*a* = 1.4 µm. The PnC dimensions are adjusted so that the second Rayleigh mode (R2) meets the frequency matching condition near the edge of the first Brillouin zone. In this region, formation of flat bands results in slower wave propagation for frequencies close to the band edges.

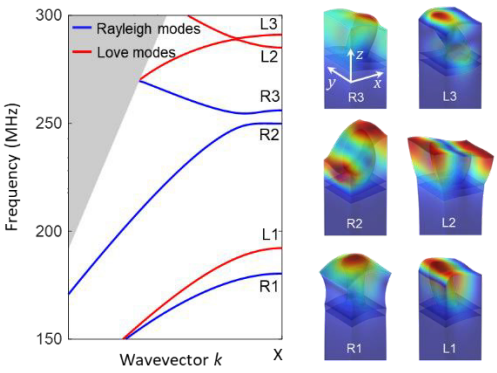

Fig. 2. Left: Band diagram of the PnC with a = 5.6 µm, r_p = 1.4 µm and h_p = 4.5 µm, calculated in the Γ-X direction of the first Brillouin zone. Rayleigh and Love modes are indicated by blue and red lines, respectively. The grey-shaded area outlines the sound cone. Right: Displacement profiles of the first three Rayleigh and Love modes calculated at the point X of the first Brillouin zone.

To investigate the sensitivity of our sensor, we subjected it to an external magnetic field in the range of $0.6\mathrm{H}_K < |\mathrm{H}| < 0.7\mathrm{H}_K$. Alteration of the magnetic field within this range induces a linear change in the Young's modulus of the FeCoSiB layer, ranging from 120 GPa to 115 GPa. This leads to a change in the SAW velocity and a phase shift in the output signal, which is analyzed to quantify the magnetic field strength.

The structural sensitivity of the sensor is defined as the change in the SAW phase velocity per unit change in the Young's modulus of FeCoSiB ($S_{str} = \partial v/\partial E_f$). Fig. 3(a) presents the band diagram of the second Rayleigh mode (R2 in Fig. 2) for two different Young's modulus values of 115 and 120 GPa. At the frequency of *f*=250 MHz, the phase velocity of the Rayleigh wave changes by Δ*v*~88 m/s, yielding a structural sensitivity of S_{str}~17.6 $\frac{m/s}{GPa}$. The Rayleigh mode propagating through the unpatterned guiding layer exhibits a phase velocity change of Δ*v*~7.5 m/s in response to the same variation in the Young's modulus of FeCoSiB, resulting in a structural sensitivity of S_{str}~1.5 $\frac{m/s}{GPa}$ (Fig. 3(b)).

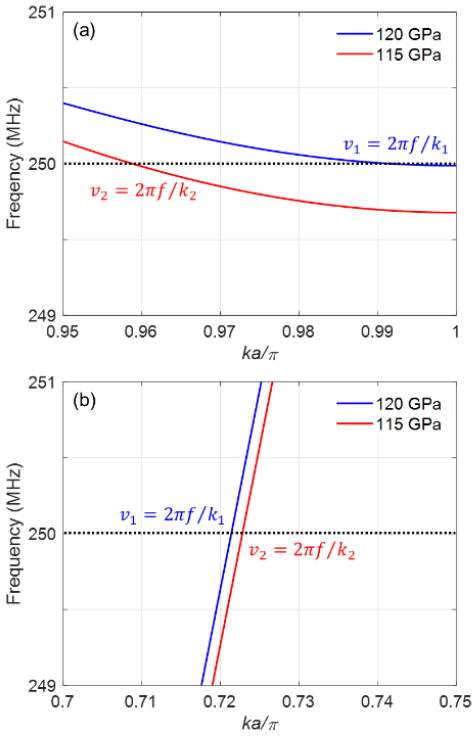

Fig. 3. Band diagrams of (a) the second Rayleigh mode of the PnC (R2 in Fig. 2) and (b) the Rayleigh mode propagating through the unpatterned guiding layer for the Young's modulus values of 120 and 115 GPa. v_1 and v_2 denote the phase velocity values acquired for 120 and 115 GPa, respectively.

The significant enhancement in the sensitivity of the SAW magnetic field sensor is attributed to resonance effects within the PnC structure. These effects cause the SAW to propagate through the PnC with an effectively lower velocity, resulting in an effectively increased interaction between the SAW and the magnetostrictive material, thereby improving the sensing capability of our sensor.

Acknowledgment

This work was funded by the German Research Foundation (Deutsche Forschungsgemeinschaft) via the collaborative research center CRC 1261 “Magnetoelectric Sensors: From Composite Materials to Biomagnetic Diagnostics”.

References

[1] J. Zhai, Z. Xing, S. Dong, J. Li, and D. Viehland, “Detection of pico-Tesla magnetic fields using magneto-electric sensors at room temperature,” *Appl Phys Lett*, vol. 88, no. 6, p. 62510, Feb. 2006.

[2] S. Zuo *et al.*, “Ultrasensitive Magnetoelectric Sensing System for Pico-Tesla MagnetoMyoGraphy,” *IEEE Trans Biomed Circuits Syst*, vol. 14, no. 5, pp. 971–984, Oct. 2020.

[3] D. Murzin *et al.*, “Ultrasensitive Magnetic Field Sensors for Biomedical Applications,” *Sensors*, vol. 20, no. 6, p. 1569, Mar. 2020.

[4] E. Elzenheimer *et al.*, “Quantitative Evaluation for Magnetoelectric Sensor Systems in Biomagnetic Diagnostics,” *Sensors*, vol. 22, no. 3, p. 1018, Jan. 2022.

[5] A. Kittmann *et al.*, “Wide Band Low Noise Love Wave Magnetic Field Sensor System,” *Scientific Reports*, vol. 8, no. 1, pp. 1–10, Jan. 2018.

[6] A. Kittmann *et al.*, “Sensitivity and noise analysis of SAW magnetic field sensors with varied magnetostrictive layer thicknesses,” *Sens Actuators A Phys*, vol. 311, p. 111998, Aug. 2020.

[7] P. Durdaut *et al.*, “Phase Noise of SAW Delay Line Magnetic Field Sensors,” *Sensors,* vol. 21, no. 16, p. 5631, Aug. 2021.

[8] J. M. Meyer *et al.*, “Thin-Film-Based SAW Magnetic Field Sensors,” *Sensors*, vol. 21, no. 24, p. 8166, Dec. 2021.

[9] S. Tamura, D. C. Hurley, and J. P. Wolfe, “Acoustic-phonon propagation in superlattices,” *Phys Rev B*, vol. 38, no. 2, p. 1427, Jul. 1988.

[10] V. Laude, M. Wilm, S. Benchabane, and A. Khelif, “Full band gap for surface acoustic waves in a piezoelectric phononic crystal,” *Phys Rev E Stat Nonlin Soft Matter Phys*, vol. 71, no. 3, p. 036607, Mar. 2005.

[11] S. Benchabane, A. Khelif, J. Y. Rauch, L. Robert, and V. Laude, “Evidence for complete surface wave band gap in a piezoelectric phononic crystal,” *Phys Rev E Stat Nonlin Soft Matter Phys*, vol. 73, no. 6, p. 065601, Jun. 2006.

[12] A. Khelif, B. Aoubiza, S. Mohammadi, A. Adibi, and V. Laude, “Complete band gaps in two-dimensional phononic crystal slabs,” *Phys Rev E Stat Nonlin Soft Matter Phys*, vol. 74, no. 4, p. 046610, Oct. 2006.

[13] A. Khelif and A. Adibi, “Phononic crystals: Fundamentals and applications,” *Phononic Crystals: Fundamentals and Applications*, pp. 1–245, Jul. 2015.

[14] M. Badreddine Assouar and M. Oudich, “Dispersion curves of surface acoustic waves in a two-dimensional phononic crystal,” *Appl Phys Lett*, vol. 99, no. 12, p. 123505, Sep. 2011.

[15] M. Oudich *et al.*, “Tailoring Structure-Borne Sound through Bandgap Engineering in Phononic Crystals and Metamaterials: A Comprehensive Review,” *Adv Funct Mater*, vol. 33, no. 2, p. 2206309, Jan. 2023.

[16] M. Samadi, J. Schmalz, J. M. Meyer, F. Lofink, and M. Gerken, “Phononic-Crystal-Based SAW Magnetic-Field Sensors,” *Micromachines*, vol. 14, no. 11, p. 2130, Nov. 2023.

[17] N. Kurz *et al.*, “Experimental determination of the electro-acoustic properties of thin film AlScN using surface acoustic wave resonators,” *J Appl Phys*, vol. 126, no. 7, p. 75106, Aug. 2019.

[18] C. Cordier and C. Dolabdjian, “Modeling of Delta-E Effect Magnetic Field Sensors,” *IEEE Sens J*, vol. 23, no. 3, pp. 2014–2020, Feb. 2023.

[19] J. Schmalz, E. Spetzler, J. McCord, and M. Gerken, “Investigation of Unwanted Oscillations of Electrically Modulated Magnetoelectric Cantilever Sensors,” *Sensors*, vol. 23, no. 11, p. 5012, May 2023.

[20] B. Spetzler, E. V. Golubeva, C. Müller, J. McCord, and F. Faupel, “Frequency Dependency of the Delta-E Effect and the Sensitivity of Delta-E Effect Magnetic Field Sensors,” *Sensors*, vol. 19, no. 21, p. 4769, Nov. 2019.

DOI 10.5162/SMSI2025/P50

Effect of Matrix Gas Variations on NO_2 Measurements by a PEMS Device for Real Driving Emissions Tests

Mi Eon Kim, Henning Bohlius, Volker Ebert, Javis Nwaboh
Physikalisch-Technische Bundesanstalt, Bundesallee 100, 38116 Braunschweig, Germany,
Javis.Nwaboh@ptb.de

Summary:
For legally required Real Driving Emissions measurements, the quantification of NO_2 amount fractions is performed using Portable Emission Measurement System (PEMS). Although a PEMS must be accurately calibrated, the typical NO_2 calibration gas matrix composition (e.g. synthetic air) differs significantly to that of car exhaust gas. This study shows that a change in matrix composition can cause considerable deviations in PEMS NO_2 results. We found a slope difference of up to about 30 % between measurements performed in synthetic air and a matrix gas mimicking real exhaust gas composition.

Keywords: Nitrogen dioxide (NO_2), Gas matrix effect, Portable emission measurement system (PEMS), Calibration, Optical gas standards (OGS).

Introduction

Nitrogen dioxide (NO_2), one of the major species of nitrogen oxide (NOx), is a reactive gas and an air pollutant that has hazardous effects on human health. In addition to its health effects, NO_2 further contributes to degradation of air quality as it is a precursor of secondary pollutants [1]. The European Commission has defined rigid emission limits for combustion engine vehicles. NOx is one of the key pollutant groups under the emission regulation. To overcome the discrepancies between laboratory tests and real vehicle operation, the concept of real driving emission (RDE) measurements was developed and adopted in the European vehicle regulations. RDE measurements should be performed during realistic road emission tests using portable emission measurement system (PEMS) devices [2]. In the last years, there has been a strong need to calibrate PEMS devices using reference gases that better reflect the real application in particular the real exhaust gas composition. Here, the real exhaust gas composition includes additional molecules such as NO, CO, CO_2 and H_2O, while the common components N_2 and O_2 appear in largely different amount fractions. However, for NO_2, PEMS are typically still calibrated using NO_2 in oversimplified gas matrices such as nitrogen or synthetic air, which leads to matrix composition dependent calibration deviations compared to real exhaust gas. Hence, it is important to determine which effect the different matrix gas composition has on the calibration accuracy of the PEMS. Due to the complex composition of real exhaust gases, there has also been a strong necessity to investigate whether calibration of PEMS devices in nitrogen or synthetic air gas matrix produces valid results when measuring in the real-world application i.e. car exhaust gas analysis. Therefore, in this study, we focused on the investigation of matrix gas effects on the performance of a commercial PEMS device that was calibrated using NO_2 in synthetic air. This is done by measuring NO_2 amount fractions in various gas matrix compositions. The results from the PEMS device are compared to those of a reference device at PTB for a cross check and validation of the observed effects.

Method

Fig. 1 shows a schematic diagram of the setup used for NO_2 measurements. The International System of Units (SI) – traceable static gas reference materials prepared in cylinders or dynamically prepared gas mixtures were used to interrogate the PEMs device. The dynamic gas mixtures are prepared via dilution of the static gas mixtures. In parallel with the PEMS device, there is a reference device (Non-Dispersive Ultraviolet spectrometer) that also monitors the NO_2 amount fraction (concentration) for cross check and validation of the measured effects. Matrix effects on the response of the reference device were previously validated via a comparison with the PTB direct tunable diode laser absorption spectroscopy (dTDLAS) instrument [3] and found to be insignificant. The dTDLAS instrument is being developed to be operated as an optical gas standard (OGS) and fully accounts for matrix gas effects via the fitting of the absorbance data [3]. The work with the dTDLAS instrument is planned for a separate publication.

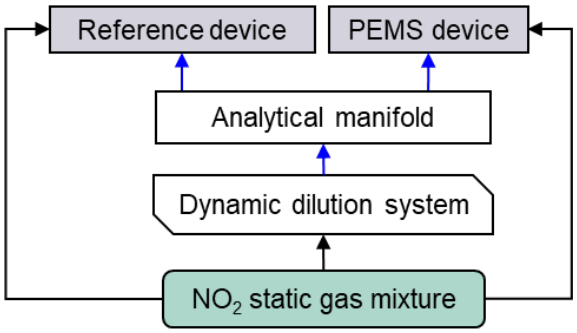

Fig. 1. Schematic diagram of the setup used for NO_2 measurements.

By means of the dynamically generated gas mixtures as shown in Fig. 1, multiple NO_2 amount fraction steps can be measured by both the PEMS device and the reference instrument simultaneously. For the matrix effect studies, dynamically prepared gas mixtures with NO_2 in different matrices, e.g. (a) synthetic air (79 % N_2, 21 % O_2), (b) synthetic air plus argon (78 % N_2, 21 % O_2, 1 % Ar), and (c) 85 % N_2 plus 0.5 % O_2, 0.2 % NO, 0.02 % C_3H_8, 0.5 % CO and 14 % CO_2 were used. For all gas matrices, the H_2O level as specified by the producer was well below 2 $\mu mol mol^{-1}$. The multi-component matrix (c) was prepared to mimic real car exhaust gas composition.

Results

As shown in Fig. 2, the results from the PEMS device are compared to those from the reference device by plotting the measured NO_2 amount fraction as a function of dynamically generated NO_2 amount fraction values. For the PEMS and reference instrument, a good linearity is derived for the NO_2 amount fraction results for the difference as matrices as presented in Fig. 2. For the reference device, the slope values are almost identical (within ±0.01) for matrix a, b and c, i.e. 1.09, 1.08 and 1.09, respectively. However, for the PEMS device, the slope values for the different matrix compositions a, b, and c vary up to about 30 % (i.e. 0.98, 0.97, and 1.29 respectively), and demonstrate a strong matrix effect on the PEMS device.

It is concluded here that, if air-based matrix reference materials are applied to calibrate a PEMS device, it can lead to a considerable deviation of the NO_2 amount fraction in car exhaust measurement in real world scenarios. Future measurements are planned to calibrate the PEMS device with the dTDLAS OGS which provides direct traceability of the results to the SI. This will enable the PEMS device to be used in real world applications, providing accurate and reliable NO_2 measurements in car exhaust gases.

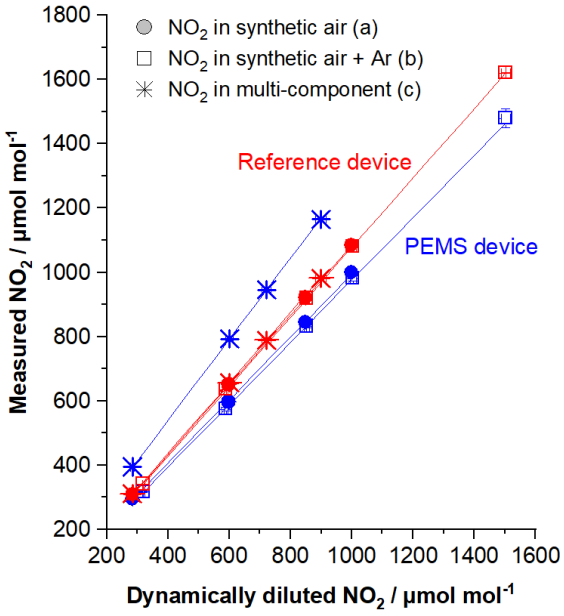

Fig. 2. Plot of measured NO_2 amount fraction as a function of dynamically generated NO_2 amount fraction values, PEMS device (blue) and a reference device (red).

Acknowledgement

This work was supported by the European Metrology Programme for Innovation and Research (EMPIR) project “Improved vehicle exhaust quantification by portable emission measurement systems metrology (MetroPEMS)” and the European Partnership on Metrology (EPM) project “Metrology for green maritime shipping: Emission control through traceable measurements and machine learning approaches (23IND09 MaritimeMET)”. The project 23IND09 MaritimeMET project has received funding from the EPM, co-financed from the European Union’s Horizon Europe Research and Innovation Programme and by the Participating States.

References

[1] WHO global air quality guidelines: particulate matter (PM2.5 and PM10), ozone, nitrogen dioxide, sulfur dioxide and carbon monoxide (2021); https://iris.who.int/handle/10665/345329

[2] European Commission Regulation (EU) 2023/443 of 8 February 2023 amending Regulation (EU) 2017/1151 as regards the emission type approval procedures for light passenger and commercial vehicles (2023); https://eur-lex.europa.eu/eli/reg/2023/443/oj

[3] J. A. Nwaboh, Z. Qu, O. Werhahn, V. Ebert, Towards an Optical Gas Standard for Traceable Calibration-Free and Direct NO_2 Concentration Measurements, *Applied Sciences* 11(12), 5361 (2021); doi: https://doi.org/10.3390/app11125361

DOI 10.5162/SMSI2025/P51

ThinKIsense – Thin Edge Artificial Intelligence for Process Automation

Erdler, Gilbert; Klehr, Stefan; von Dosky, Stefan; Siemens AG, DI PA MI ST IP;

Mussler, Marvin; Siemens AG, DI PA ST&T TI PD;

Östl. Rheinbrückenstr. 50, 76187 Karlsruhe

In cooperation with NXP GmbH Hamburg, TU Darmstadt, FZI Karlsruhe, Netzsch GmbH Waldkraiburg

- Calculation of process variables like pressure, volume flow and turn speed out of pump vibration as well as an anomaly classification direct at the sensor microcontroller
- Comparison of different AI technologies including efficiency

1. Motivation

State of the art: Battery powered sensors collect structure-borne sound and air-borne sound, raw data is send to edge or cloud to process them using AI methods

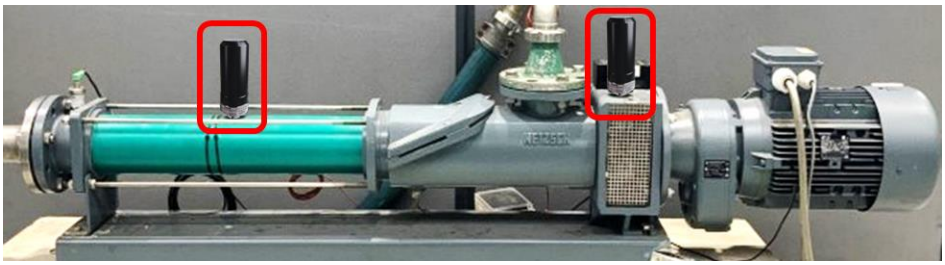

Wireless transmission of huge data sets

High energy demand

3 years battery lifetime

2. Targets

Processing of sensor data with AI directly in the multisensor, only KPIs are sent to the cloud. Resilience with end-to-end security from edge to cloud.

The battery life of the sensors is expected to be several years to be able to use them in complex systems with long maintenance intervals.

Simple and reliable fault detection is intended to enable plants to operate longer. Pumps without connection to an automation system are observable using implemented long range wireless network interface NB-IoT.

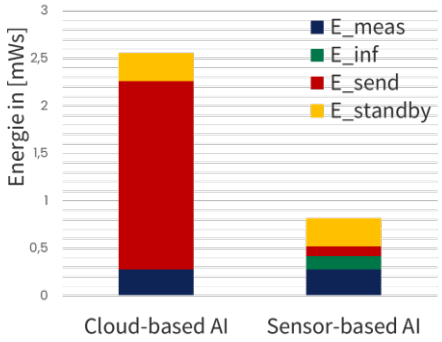

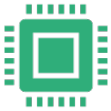

Wireless transmission of huge data sets

Enable detailed maintenance planning

8+ years battery lifetime

3. Test

Benchmark of 3 AI processors inside ThinKIsens sensor: ARM, RISC-V extended and neuromorphic hardware. Battery lifetime versus prediction accuracy is tested at a pump flow rig.

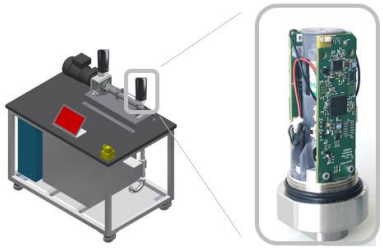

DOI 10.5162/SMSI2025/P52

Modelling Membrane-Based Compact Fiber-Interferometric Gas Pressure Sensors in Cryogenic Environments

Daniel Hartwig[1], *Christoph Reinhardt*[1], *Lea Stankewitz*[1, 2], *Sandy Croatto*[1], *Hossein Masalehdan*[2], *Sven Karstensen*[1], *Jörn Schaffran*[1], *Nils Sültmann*[2], *Axel Lindner*[1] *and Roman Schnabel*[2]
[1] Deutsches Elektronen-Synchrotron DESY, Notkestr. 85, 22607 Hamburg, Germany
[2] Universität Hamburg, Luruper Chaussee 149, 22761 Hamburg, Germany
daniel.hartwig@desy.de

Summary: Ultra-thin nanomechanical membrane oscillators are used in various technological applications. Recently, the ability to sense gas pressures across a ten-decade measurement range was demonstrated by interrogating the motion of a silicon-nitride trampoline membrane with a free-space interferometer. To increase the flexibility and compactness of this sensing solution, the use of optical fibers is a promising pathway toward broad applicability. Here, we model the interface between an optical fiber and a silicon-nitride membrane, and verify pressure readings from a prototype sensor inside a cryogenic vacuum system using a rarefied gas simulation. We find the fiber-based sensor to have a comparable readout sensitivity to a free-space setup while delivering predictable and precise pressure readings even in cryogenic environments.

Keywords: interferometry, MEMS, vacuum, cryogenics, gas pressure sensing, silicon-nitride membranes, finite-difference time-domain method, rarefied gas simulation

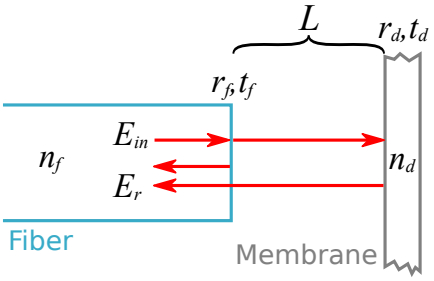

Fig. 1: Schematic of the fiber-membrane interferometer. A part of the incoming light wave E_{in} is reflected at the fiber tip while another part propagates in free space to the membrane, which itself reflects a part of this light. Back at the fiber tip, the two components recombine and interfere, forming the reflected wave E_{r}. Adapted from [2].

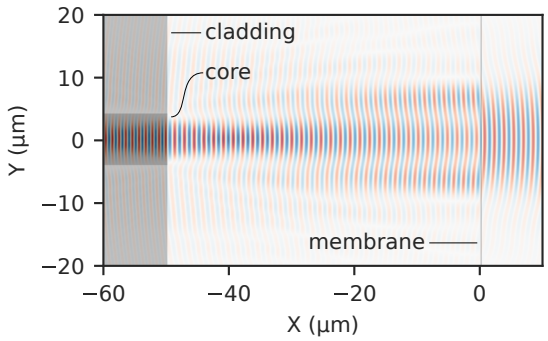

Fig. 2: Simulated electrical field pattern for the fiber-membrane interferometer. A continuous wave is emitted from the fiber core (dark gray) on the left of the image. The membrane (thin line at $X = 0$) reflects a part of the light back into the fiber, while some light is lost by transmission through the membrane or reflection into the fiber cladding.

Pressure Sensing Principle

A 50-nm-thick silicon nitride membrane is immersed in the gas to be analyzed. Through its high internal stress and frame design, the membrane with a sidelength of approx. 1 mm is able to oscillate in its drum mode with very low internal friction. Any presence of residual gas particles increases the damping of the membrane oscillation, reducing its mechanical ringdown time. By measuring this ringdown time interferometrically, the pressure of the surrounding gas is reconstructed as demonstrated before with up to a ten-decade measurement range [1].

Modelling the Fiber-Membrane Interface

The interferometer for detecting the membrane motion is formed right in the space of approx. 100 µm between the fiber tip and membrane surface, see fig. 1. As the membrane oscillates, it modulates the distance between the fiber tip and the membrane surface and, consequently, the phase of the light reflected by the membrane. This light then interferes inside the fiber with the light that was internally reflected at the fiber tip, modulating the total reflected optical power.

As the membrane oscillation is converted to a modulation of the light power reflected by the interferometer, the modulation amplitude and the photonic shot noise of the power measurement fundamentally determine the smallest detectable membrane displacement. To estimate the displacement signal and shot noise of the fiber-

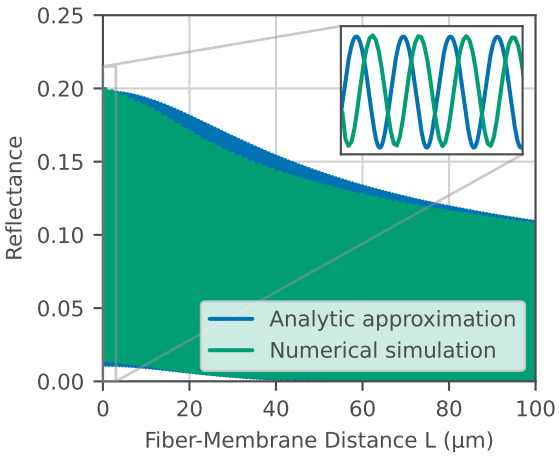

Fig. 3: Modelled reflectance of the fiber-membrane interferometer as the distance between fiber tip and membrane is varied. The analytic approximation assumes a gaussian mode profile of the light exiting the fiber, while the numerical simulation is the result of a finite-difference time-domain (FDTD) optics simulation [3] implementing the actual fiber eigenmode.

membrane interferometer, the interferometer reflectivity as a function of distance L between the fiber tip and the membrane was estimated using both a numerical simulation (fig. 2) and an analytic method, which differ by 7 % at most.

Fig. 3 shows the predictions of the interferometer reflectance. The highest signal-to-noise ratio is achieved at small gaps L, where the interference signal has the highest amplitude. In this case, no reflected light is lost due to mode mismatch between the reflected beam and the fiber eigenmode, which corresponds to the performance of a free-space interferometer. At a distance of 100 µm, more than half of the maximum signal is still conserved. In a shot-noise-limited scenario, this equates to losing less than 30 % in signal-to-noise ratio.

Modelling Pressure Gradients in Cryogenic Environments

To demonstrate the pressure sensing ability of a fiber-based prototype sensor at cryogenic temperatures, it was placed in a vacuum chamber immersed in liquid nitrogen (fig. 4(a)). Nearby, a controlled stream of gas entered the chamber to control the gas pressure. The pressure reading from the membrane sensor was compared to a commercial pressure gauge placed in the room-temperature top part of the system [4]. However, due to pressures being in the free molecular flow regime, the pressures inside the vacuum system varied substantially by location inside the system, leading to differences between the pressure reading in the two locations. To verify the measured pressure differences between the top and bottom of the vacuum system, a finite-elements simulation [5] was conducted, see fig. 4(b). It verified the pressure differences to within 15 % of the observed values.

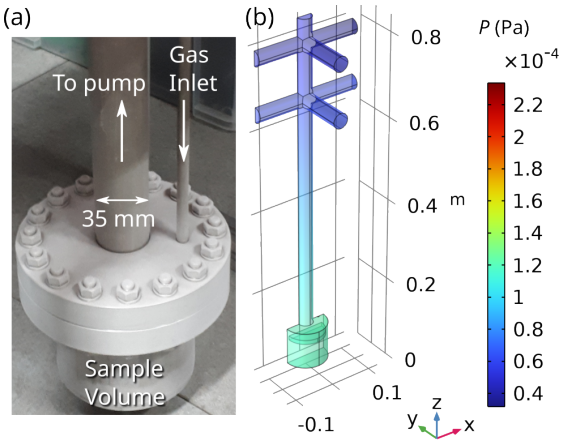

Fig. 4: (a) Photograph of sample volume in cryostat. (b) Model geometry and simulated pressure distribution in cryostat vacuum system. Gas is injected in the bottom chamber at cryogenic temperature and pumped out of the system near the top at room temperature.

Conclusion

By modelling the fiber-membrane interface, we estimated the shot-noise-limited readout sensitivity of portable cm-scale fiber-interferometric pressure sensors to reach at least 70 % of a free-space table-top Michelson interferometer. Further, molecular flow simulations of the pressure gradients inside a cryogenic test setup match the measurements within 15 %. Overall, the presented simulations support the development of our novel, broadly applicable gas pressure sensor combining a nanomechanical resonator with a compact and flexible fiber-based readout, especially for applications in cryogenic environments.

References

[1] C. Reinhardt, H. Masalehdan, S. Croatto, A. Franke, M. B. K. Kunze, J. Schaffran, N. Sültmann, A. Lindner, and R. Schnabel, "Self-Calibrating Gas Pressure Sensor with a 10-Decade Measurement Range," *ACS Photonics*, vol. 11, pp. 1438–1446, Apr. 2024.

[2] C. Reinhardt, *Ultralow-Noise Silicon Nitride Trampoline Resonators for Sensing and Optomechanics*. PhD-Thesis, McGill University, Canada, Aug. 2017.

[3] "NanoComp/meep." Open-source FDTD electromagnetics simulation software.

[4] L. L. Stankewitz, "A Compact & Portable Nanomechanical Gas Pressure Sensor for Cryogenic Applications," Master's thesis, Universität Hamburg, Hamburg, Germany, Nov. 2024.

[5] "COMSOL: Multiphysics Software for Optimizing Designs."

DOI 10.5162/SMSI2025/P53

Simultaneous DTGS and DTS Measurements for Temperature Estimation in a Bubble Column Reactor

Danilo Fernandes Gomes[1], Guilherme Heim Weber[1], Yannik Schick[3], Mark W. Hlawitschka[2], Cicero Martelli[1], Marco José da Silva[3]
[1] Federal University of Technology - Paraná UTFPR, Av. Sete de Setembro 3165, Brazil
[2] Institut für Verfahrenstechnik, Johannes Kepler Universität, Altenberger Straße 69, 4040 Linz, Austria
[3] Institut für Elektrische Messtechnik, Johannes Kepler Universität, Altenberger Straße 69, 4040 Linz, Austria
marco.dasilva@jku.at

Summary:
This study demonstrates the combined use of DTGS and DTS for temperature estimation in a bubble column reactor. DTS provides absolute temperature, while DTGS precisely detects rapid thermal variations. Results show bubble-induced convection enhances heat distribution, emphasizing the benefits of integrating both techniques for advanced process monitoring.

Keywords: DAS/DTGS, DTS, temperature measurement, bubble column reactor, fiber optics

Introduction

Distributed Fiber Optic Sensing (DFOS) technologies have revolutionized monitoring in harsh environments, offering remote sensing capabilities with high sensitivity, linear response, and discreet deployment. Among these, Distributed Temperature Sensing (DTS) leverages Raman scattering to provide absolute temperature measurements over distances of up to 70 km. However, its temperature resolution is limited to approximately 2°C, and its sampling rate is relatively slow [1],[2]. Conversely, Distributed Acoustic Sensing (DAS) utilizes Rayleigh scattering to detect variations in the optical path caused by strain and refractive index fluctuations. This allows a broadband response from high frequency acoustic signals to low frequency temperature gradients and deformation, supporting the terms low frequency-DAS (LF-DAS) and Distributed Temperature Gradient Sensing (DTGS). Although DAS does not provide absolute measurements, it offers exceptional precision, with sensitivity on the order of nε and µK, while maintaining a rapid response time [3]. Previously we have demonstrated the measurement of the movement of bubbles in an experimental column reactor using DAS [4]. In this work, we extend capabilities to temperature estimation combining simultaneous DAS/DTGS and DTS measurements to enhance process control.

Methodology

The bubble column reactor setup (Figure 1) features a 2-m-high acrylic pipe with a 150 mm outer diameter and 5 mm wall thickness, filled with water and open at the top. Air bubbles were sparged into the reactor through a controlled air inlet at the bottom. The Fiber Under Test is a duplex round cable (9/125µ G652.D, 3 mm outer diameter), with one fiber dedicated to DAS/DTGS and the other to DTS measurements. Two key sections were instrumented: Outside wrap, a 137 m-fiber helically wrapped around the column's outer surface, covering 85.8 cm in height. The Inside wrap section is 22 m-long fiber, similarly wound near the top inside the column.

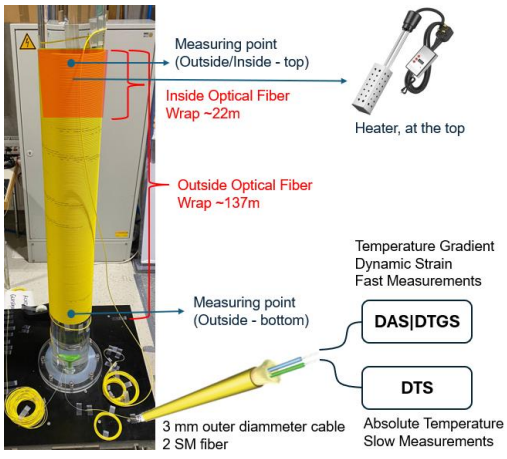

Fig. 1. Experimental setup for the measurement of temperature in a bubble column reactor.

DAS/DTGS and DTS data were acquired using a single interrogator unit at JKU's Institute of Measurement Technology, sampled with a 14-bit, 500 MS/s acquisition card at 10 kHz and a 40 ns spatial resolution. The experiment lasted

600 s. Initially, the column contained still water. At 80 s, a water heater positioned near the top was activated, gradually increasing the temperature. At 260 s, an automated valve periodically opened the air inlet, producing bubbles that ascended to the surface. Their movement induced fluid circulation within the column.

Results

Figure 2 presents the results from both sensing technologies. The DTS signal is depicted in the upper colormap, while the DAS in the lower colormaps. The Outside wrap section extends from 50 to 187 m, while the Inside wrap spans 203 to 225 m. Within these ranges, both signals exhibit a similar trend, showing a gradual increase in intensity over time, though with varying gradient periods. To provide a more detailed analysis, local signals are plotted at three key positions: outside bottom, outside top, and inside top, as indicated in Figure 1. At the start, the DTS signals reflect the outer wall temperature of the column, which is expected to be close to ambient temperature, averaging approximately 23°C, with a variation of ±1°C across different heights. Meanwhile, the inside wrap of the column registers an initial water temperature of approximately 27.5°C due to heating prior to the experiment. In contrast, DTGS signals all start at zero, as they measure relative variations over time rather than absolute temperature. However, DTGS responds more rapidly to thermal changes. At 80 s after the start of the experiment, the water heater was turned on, triggering a temperature increase that is first detected at the inside top position, followed by a delayed response at the outside top measurement points. The bottom measuring points remain largely unchanged until approximately 260 s, when the automated air inlet valve begins periodic operation. Up to this moment, heat propagation within the column is primarily driven by natural convection. However, once air bubbles are introduced, they induce fluid circulation, significantly enhancing heat distribution throughout the column at all levels. This transition is clearly observed in the local signals, where temperature evolution follows distinct gradients at different heights, highlighting the effect of bubble-induced mixing on thermal dynamics. Additionally, DAS data is displayed, where a 20 Hz high-pass filter has been applied to extract vibration and acoustic phenomena. The filtered signal reveals periodic pulse-shaped patterns after 260 s, corresponding to the opening of the air inlet valves and the periodic formation of bubbles. This process is closely aligned with the change in thermal dynamics observed in both DTS and DTGS signals, confirming the strong influence of bubble-induced convection on heat distribution.

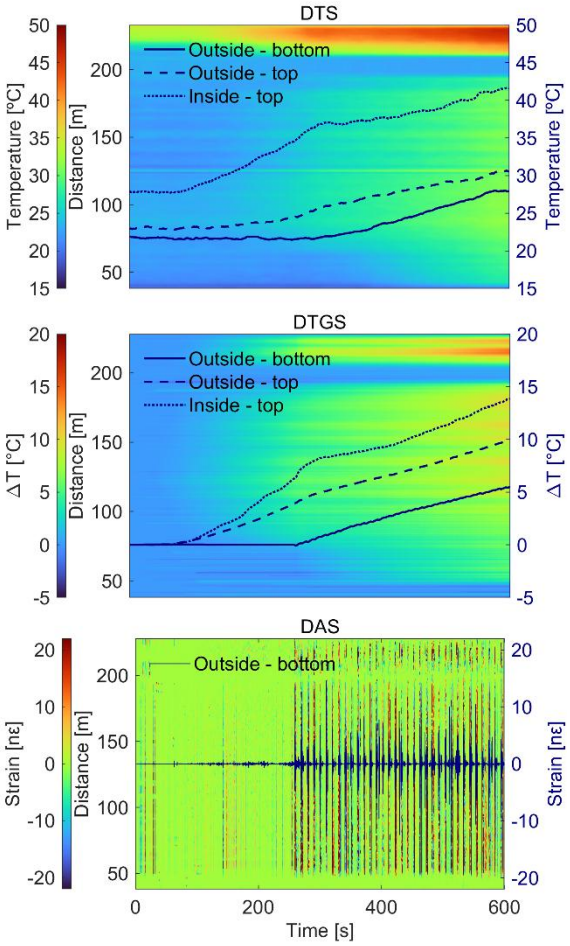

Fig. 2. Simultaneous temperature measurement using DTS (top) and DTGS/DAS (center and bottom).

Conclusion

The integration of DTS and DAS/DTGS enables precise absolute temperature monitoring with fast thermal response and acoustic analysis. This synergy enhances process monitoring and opens new possibilities for data fusion, improving accuracy and real-time insights into thermal and fluid dynamics.

References

[1] LAUBER, Thomas et al. Physical limits of raman distributed temperature sensing-are we there yet?. In: Optical Fiber Sensors. Optica Publishing Group, 2018. p. WF30.

[2] UKIL, Abhisek et al. Distributed temperature sensing: Review of technology and applications. IEEE Sensors Journal, v. 12, n. 5, p. 885-892, 2011.

[3] PELAEZ QUIÑONES, Julián David et al. High resolution seafloor thermometry for internal wave and upwelling monitoring using Distributed Acoustic Sensing. Scientific Reports, v. 13, n. 1, p. 17459, 2023.

[4] SCHICK, Yannik et al. Flow monitoring in a bubble column reactor by Distributed Acoustic Sensing. Technisches Messen, vol. 91, no. s1, 2024, pp. 14-19. https://doi.org/10.1515/teme-2024-0048